Designing Metalloenzymes by Controlling the First and Second Coordination Spheres Using Non-Traditional Design Strategies

by

Winston Cole Pitts

A dissertation submitted in partial fulfillment
of the requirements for the degree of
Doctor of Philosophy
(Chemistry)
in the University of Michigan
2024

Doctoral Committee:

Professor Vincent L. Pecoraro, Chair
Professor Jennifer Bridwell-Rabb
Professor Bruce A. Palfey
Professor James E. Penner-Hahn

Winston C. Pitts

wcpitts@umich.edu

ORCID iD: 0000-0001-8964-8441

© Winston C. Pitts 2024

To my family

Acknowledgements

I am immensely grateful to have reached this milestone in my academic journey by completing this Ph.D. thesis. I am grateful to everyone who took part in my work and so kindly gave of their time and knowledge. This accomplishment would not have been possible without the support, encouragement, and contributions of individuals to whom I extend my heartfelt appreciation. I would like to acknowledge and sincerely thank those who have helped me get to this point.

First, I would like to thank my advisor, Vince. Your encouragement and support carried me through all the critical stages of my research, my writing, and my independence as a scientist. While in your lab, I have had the opportunity to problem-solve, learn new techniques, and collaborate with others from around the world, and I truly benefited from these experiences. I am grateful for your advice and critiques throughout my time in his lab which have undoubtedly made me a better scientist.

I also want to extend my gratitude to my committee members, Professor James Penner-Han, Professor Bruce Palfey, and Professor Jennifer Bridwell-Rabb for their mentorship at different times during my PhD. Professor Penner-Han, thank you for teaching me how to have a keen and skeptical eye for Copper XAS and the numerous discussions we have had. Your fruitful collaboration over the years has made me a better scientist. Professor Palfey, thank you for passing on your wisdom in kinetics both through our conversations and through your kinetics class, all of which I will carry with me throughout my career. Professor Bridwell-Rabb, thank you for opening up your lab and willingness to collaborate at any point in time. And of course, thank you to all my collaborators for their discussions and scientific contributions: Dr. Aniruddha Deb (for teaching me all things beamline and the many laughs), Dr. Anabella Ivancich (for all of the knowledge and

wisdom on heme proteins, as well as your time mentoring me in Ann Arbor), and Dr. Debashish Sahu (for all of the help and discussions about high field protein NMR).

Thank you to all the Pecoraro lab members, past and present, who have helped me along the way with words of encouragement, support, and fruitful conversation: Tyler, Karl, Audry, April, Elvin, Bernadette, Wenqing, Tim, Valentina, Jean, Gretchen, Marla, Salvatore, Iago, Soroush, Sonja, John, Valerie, Jacob, and Sahil. You all have made my time in the lab a fun and memorable experience. I would also like to thank Jill from Nicolai's group and Andrew from the Buss group for their scientific and spontaneous conversations.

Last, but certainly not least, I would like to express my deepest gratitude towards my family. Without their support, I would not be here today. To my mom and dad: thank you for always believing in me and providing opportunities in my childhood that allowed me to grow into the person I am today. Your constant encouragement throughout my life has been pivotal. To my amazing wife, Megan, without you at my side, I could not have progressed as far as I have. I appreciated your patience while I was away from home, working in the lab, and the many times you kept me company during all the late nights. This would not have been the same without your love, encouragement, and support. I can't wait to see what our future holds on this next journey.

Table of Contents

Dedication ii
Acknowledgements iii
List of Tables viii
List of Figures x
List of Abbreviations xix
Abstract xxi
Chapter I. Customizing Nature: Engineering and Designing Metalloproteins Using Novel Design Strategies 1
Introduction 1
Copper in Natural Proteins 2
Native Protein Engineering and *de novo* Design 13
2A. The Engineer: Metalloproteins from a Synthetic Inorganic Chemist's Viewpoint 13
2B. Applications of protein redesign to Cu enzymes 16
2C. Non-Heme *de novo* Design 19
Stammers and Stutters: A Twist on Protein Design 42
Thesis outline 55
References 59
Chapter II. Exploiting Non-Coded Amino Acids to Enhance the Activity of Designed Copper Nitrite Reductases 75
Introduction 75
Materials and Methods 78
Results 84
Discussion 105
Conclusion 118

References 119
Chapter III. Exploring Nitrite Binding at Both the Oxidized and Reduced Enzyme Form in *de novo* Designed CuNiRs 125
Introduction 125
Materials and Methods 128
Results 133
Discussion 152
Conclusion 169
References 170
Chapter IV. Stretch, Twist, and Switch: *de novo* Designed Copper Nitrite Reductase Mimics with Sequence Discontinuities 176
Introduction 176
Materials and Methods 180
Results 185
Discussion 202
Conclusion 214
References 215
Chapter V. Conclusion and Future Directions 219
Designing 3SCC with features important to catalysis 220
Further investigation into the mechanism underlying CuNiR activity in 3SCCs 224
Expanding on stammers and stutters within GRAND homotrimers 225
References 230
Appendix A. High Resolution Nuclear Magnetic Resonance Spectra of *de novo* Designed Apo-3SCC and Copper(I)/(II)-3SCC 233
Introduction 233
Methods 233
A.1 Chapter II and Chapter III Nuclear Magnetic Resonance Data (TRI and TRIW Proteins) 237
Protein: TRIW-H2 237
Protein: TRI-4'Py and TRIW-4'Py 242
Protein: TRI-4'Py L19A and TRIW-4'Py L19A 253

Protein: TRI-3’Py.....261
A.2 Chapter IV Nuclear Magnetic Resonance Data.....267
Protein: GRW-3’Py.....267
Protein: $GRW_{stam27(AE3'Py)}$.....274
Protein: GRW-4’Py.....281
Protein: $GRW_{stam27(AEL)}$L33-4’Py.....287
Protein: $GRW_{stam27(AEA)}$L33-4’Py.....290
References.....295

List of Tables

Table I-1: Common Geometries found in Cu(I) and Cu(II) proteins 3

Table I-2: Kinetic parameters for hydrolysis of *p*NPA by Zn(II)-Peptides at pH 9.5 27

Table I-3: Kinetic parameters of Pecoraro *et al.* designed CuNiRs 33

Table I-4: Key parameters for CuNiR (pH 5.8) and Zn-*p*NPA hydrolysis (pH 9.5) 54

Table II-1: Stability parameters determined from the chemical denaturation curves in Figure II-4A 86

Table II-2: Stability parameters determined from the thermal denaturation curves in Figure II-4B-D 87

Table II-3: Dissociation constants based on fluorescence tryptophan quenching experiments at pH 5.9.....89

Table II-4: Structural parameters of the best fits to the Cu(I) EXAFS 96

Table II-5: Nitrite reduction kinetics parameters fitted at pH 5.9 101

Table II-6: ^{1}H and ^{13}C chemical shifts for TRI-3'Py and TRI-4'Py L19A during the Cu(I) titration 107

Table II-7: UV-VIS and EPR parameters of relevant designed Cu(II)-proteins Cu(II) model Complexes.....108

Table II-8: Summary of bonding parameters of Cu(I) pyridine and histidine complexes 111

Table II-9: Kinetic parameters for native, small molecule and designed NIRs 114

Table III-1: Summary of each Cu(I)-CI adduct's fits at pH 5.9 133

Table III-2: EPR parameters of oxidized forms with 50 eqv. $NaNO_2$ at pH 5.9.....142

Table III-3: Summary $K_{i,Cl}$- values for each enzyme and their steady state parameters resulting from each method used 147

Table III-4: Summary of relevant distances in Cu(I) complexes 156

Table III-5: Relevant NiR activity comparisons between CuNiR mimics 158

Table III-6: Relevant Cu(II) EPR comparisons 166

Table IV-1: Stability parameters determined from the chemical denaturation curves 185

Table IV-2: Apparent dissociation constants based on fluorescence tryptophan quenching experiments a pH 5.9 187

Table IV-3: X-band EPR parameters of the oxidized enzyme at pH 5.9 (T=90-100 K).....189

Table VI-4: Summary of EXAFS fits for reduced pyridine and histidine designs 192

Table VI-5: Nitrite reduction kinetics parameters fitted at pH 5.9 199

Table VI-6: Summary of Nitrite reduction kinetics in 3SCC.....203

Table VI-7: Summary of EXAFS fit for Cu(I) pyridine and histidine enzymes.....204

Table V-1: First-shell EXAFS fits of stutter sites 226

List of Figures

Figure I: The bioinorganic chemistry of the primary coordination sphere of copper....4

Figure I-2: An example of early protein design from horseshoe crab hemocyanin (pdb:1NOL)....6

Figure I-3: Overview of the Type 1 and Type 2 Copper center....8

Figure I-4: Crystal Structure of various binding modes of nitrite to CuNiR....10

Figure I-5: CuNiR mechanism based on crystallography and kinetics in solution....11

Figure I-6: Examples of *protein redesign*....15

Figure I-7: Representation of monomeric bovine pancreatic polypeptide (pdb:1BBA)....16

Figure I-8: Protein redesign of Lytic polysaccharide monooxygenases....17

Figure I-9: Helical Wheel diagram different oligomerization states of parallel coiled coil....20

Figure I-10: First *de novo* design protein....21

Figure I-11: Crystal Structure of $[Hg(II)]_S[Zn(II)]_N(CSL9PenL23H)_3$ (pdb:3PBJ)....25

Figure I-12: Summary of *de novo* designed CuNiR within 3SCCs....32

Figure I-13: X-ray structure of the Cu(II)-ArCuP (pdb:7L33)....36

Figure I-14: Electrocatalytic reduction of hydrogen peroxide with ArCuP....38

Figure I-15: Overview of the design of a type 3 copper site in Due Rame 1 (DR1)....41

Figure I-16: Overview of the coiled coil architecture with stammers and stutter....43

Figure I-17: Effects of heptad breaks on the packing of the α-carbons in (2SCC)....44

Figure I-18: Overview of discontinuities in SadAK3 protein....48

Figure I-19: SadAK3 sequences and plots of their coiled-coil parameters....49

Figure I-20: Side-on view of superimpositions of the native ORF1pCCD (from residues 92Glu-155Glu) with *de novo* design proteins 52

Figure I-21: Model of $GRW_{stam27(AEL)}L33H$ (green) overlayed with GRCSL16CL30H (blue) modelled with a diamagnetic Zn(II) 54

Figure II-1: Comparison of 3SCC (pdb: 3PBJ) with two-domain CuNiR from *Bradyrhizobium* (pdb:6THF) 76

Figure II-2: Overview of chemical structures of N-heterocycles discussed in relation to the position in the 3SCC 77

Figure II-3: CD spectra of apo, Cu(II), and Cu(I) designed enzymes 85

Figure II-4: Chemical and thermal denaturation of designed T2Cu centers.....86

Figure II-5: Cu(II) UV-VIS titration confirming a Cu(II)/Trimer ratio of 1 to 1.....88

Figure II-6: Fluorescence quenching of the N-terminal tryptophan as a function of $CuSO_4$ 90

Figure II-7: UV-VIS and EPR of oxidized designed T2Cu centers.....91

Figure II-8: NMR Cu(I) Titration of TRI-3'Py (pH 5.9, 298 K).....92

Figure II-9: NMR Cu(I) Titration of TRI-4'Py L19A (pH 5.9, 298 K) 93

Figure II-10: K-edge Cu(I) XANES of designed T2Cu Centers at pH 5.9.....95

Figure II-11: EXAFS of Cu(I) designed T2Cu centers at pH 5.9 98

Figure II-12: Models of the metal binding sites of designed Cu(I) proteins 99

Figure II-13: Kinetics progress curves of nitrite reductase assay at pH 5.9 102

Figure II-14: Nitrite reduction pseudo first-order rate plots at pH 5.9.....104

Figure II-15. CuNiR Michaelis-Menten kinetics curves at pH 5.9.....105

Figure II-16. Cu(I) XANES at pH 5.8/5.9 comparing the pyridine constructs with histidine active sites 109

Figure II-17: X-ray structures of model Cu(I)-pyridine complexes in Table II-9.....112

Figure III-1: Inhibition patterns and reaction schemes 126

Figure III-2: Simple scheme highlighting the scattering paths, and their associated initial parameters used to fit k^3-space.....134

Figure III-3: *k*-space weighted by k^3 (*left*) and associated Fourier Transform (right) of Cu(I)-TRIW-3'Py L19A (400 mM NaCl) fits.....135

Figure III-4: *k*-space weighted by k^3 (*left*) and associated Fourier Transform (right) of Cu(I)-TRIW-3'Py (400 mM NaCl) fits.....136

Figure III-5: *k*-space weighted by k^3 (*left*) and associated Fourier Transform (right) of Cu(I)-TRIW-4'Py (400 mM NaCl) fits.....137

Figure III-6: *k*-space weighted by k^3 (*left*) and associated Fourier Transform (right) of Cu(I)-TRIW-4'Py L19A (400 mM NaCl) fits.....138

Figure III-7: XANES (derivative, *right*) comparison between the reduced enzyme with 4'Py sites in the presence and absence of NaCl 140

Figure III-8: XANES **(**derivative, *right***)** comparison between the reduced enzyme with 3'Py sites in the presence and absence of NaCl 141

Figure III-9: X-band EPR of Cu(II)-TRIW-4'Py L19A in the presence of 50 eqv. $NaNO_2$ (50 mM) at 90 K.....143

Figure III-10: X-band EPR of Cu(II)-TRIW-3'Py L19A in the presence of 50 eqv. NaNO (50 mM) at 90 K.....144

Figure III-11: X-band EPR of Cu(II)-TRIW-3'Py in the presence of 50 eqv. $NaNO_2$ (50 mM)at 90 K.....144

Figure III-12: UV-Vis spectra (d-d region) in the presence of increasing equivalents of NaCl (0 mM-279 mM) and 250 μM Cu(II)-Trimer.....145

Figure III-13: X-band EPR of Cu(II)-TRIW-4'Py L1A in absence (*black*) and presence of 400 eqv. (400 mM) NaCl at 95 K (*green*).....146

Figure III-14: Progress curves of the background reaction between nitrite and sodium ascorbate at various NaCl concentrations (200 mM $NaNO_2$, 1.5 mM NaAsc) 148

Figure III-15: Steady-state plots showing competitive inhibition of TRIW-3'Py by Cl^- 149

Figure III-16:Steady-state plots showing competitive inhibition of TRIW-3'Py L19A by Cl^-...150

Figure III-17: Plots showing competitive inhibition of TRIW-4'Py L19A by Cl^- 151

Figure III-18: Models highlighting 3-coordinate adduct less sterics interactions than a 4-coordinate tetrahedral adduct.....154

Figure III-19: Mechanism in native and designed CuNiRs 159

Figure III-20: Binding isomers to the Cu(I) enzyme and proposed enzyme substrate complex..... 161

Figure III-21: Fourier Transform of 3'Py sites with and without Cl^-.....162

Figure III-22: Possible Cu(II) nitrite adducts consistent with the X-Band EPR.....168

Figure IV-1**:** Summary of impacts of stammer inserts on 3SCC 177

Figure IV-2**:** Overview of the design process of stammers into the GRAND scaffold.....178

Figure IV-3**:** CD and chemical denaturation of designed proteins.....186

Figure IV-4: Fluorescence quenching curves of the N-terminal tryptophan as a function of $CuSO_4$ 188

Figure IV-5: UV-Vis spectra of the oxidized forms at pH 5.9.....190

Figure IV-6: EPR spectra of the oxidized forms at pH 5.9 of Cu(II)-GRW-3'Py and Cu(II)-$GRW_{stam27(AEL)}$L33-3'Py 191

Figure IV-7: XANES comparison between the reduced enzyme resting state at pH 5.9.....193

Figure IV-8. Simple scheme highlighting scattering paths and their associated initial parameters used to the fit k^3-space 194

Figure IV-9: EXAFS fits of Cu(I)-GRW-3'Py (*left* **A**-**C**) and Cu(I)-GRW-4'Py (*right* **D**-**F**).....195

Figure IV-10: EXAFS fits of Cu(I)-GRW$_{stam27(AEL)}$L33-3'Py (*left* **A**-**C**) and Cu(I)-GRW$_{stam27(AEA)}$L33-3'Py (*right* **D**-**F**) 196

Figure IV-11: EXAFS fits of Cu(I)-GRW$_{stam27(AE3'Py)}$ (*left* **A**-**C**) and Cu(I)-GRW$_{stam27(AEH)}$ (*right* **D**-**F**).....197

Figure IV-12: EXAFS fits of Cu(I)-GRW$_{stam27(AEA)}$L33-4'Py 198

Figure IV-13 CuNiR Michaelis-Menten kinetics of designed histidine sites 200

Figure IV-14: CuNiR Michaelis-Menten kinetics of pyridine sites with and without stammers .....

.....201

Figure IV-15: A case of asymmetry in the primary coordination induced with the Co(II) (AEL) stammer.....202

Figure IV-16: Cu(I) XANES comparison of TRIW and GRAND-stammer designs with 4'Py sites 206

Figure IV-17: Cu(I) XANES comparison of TRIW and GRAND-stammer designs with 3'Py sites and AlphaFold assisted modeling of the reduced enzyme.....208

Figure IV-18**:** XANES of Cu(I) in 2-, 3-, and 4-coordinate pyridine complexes.....209

Figure IV-19: Cu(I) XANES comparison of TRIW and GRAND-stammer designs with histidine sites and AlphaFold assisted modeling of the reduced enzyme.....211

Figure IV-20: XANES derivative spectra of the reduced copper-histidine enzymes 212

Figure IV-21: Summary of orbital interactions of the Cu(I) XANES.....213

Figure V-1: Limitations of the Asp^{d} design with Cu(II) by highlighting Asp. binding within Co(II) heterotrimer.....223

Figure V-2: Cu(II)-TRIW-3'Py L19A azide titration at pH 5.9 224

Figure V-3: Summary of stutter peptides.....226

Figure A-1**:** ^{1}H-NMR of apo-TRIW-4'Py at pH 5.88 (Region: Aliphatic).....237

Figure A-2: ^{1}H-NMR of apo-TRIW-4'Py at pH 5.88 (Region: Aromatic/Amide) 238

Figure A-3: ^{1}H-^{1}H NOESY of apo-TRIW-H pH 5.86 (Region: Aromatic/Amide) 239

Figure A-4: ^{1}H-^{1}H NOESY of apo-TRIW-H pH 5.86 (Region: Overview) 240

Figure A-5: ^{1}H-^{1}H NOESY of apo-TRIW-H pH 5.86 (Region: Aliphatic) 241

Figure A-6: ^{1}H-NMR of apo-TRIW-4'Py at pH 5.88 (Region: Aliphatic) 242

Figure A-7: ^{1}H-NMR of apo-TRIW-4'Py at pH 5.88 (Region: Aromatic) 243

Figure A-8: ^{1}H-^{15}N NOESY of apo-TRW-4'Py at pH 5.88 (Region: Amide) 244

Figure A-9: ^{1}H-^{13}C HSQC NMR of apo-TRI-4'Py pH 5.00 (Region: Aromatic) 245

Figure A-10: ^{1}H-NMR of Cu(I)[MeCN]$_4$ titration TRI-4'Py 10% D_2O v/v at pH 5.90 (Region: Aromatic) 246

Figure A-11: Progression curve of Cu(I)[MeCN]$_4$ titration of TRI-4'Py following the meta-proton on the pyridine ligand 247

Figure A-12: ^{1}H-^{13}C HSQC NMR of 1.04 eqv. Cu(I)[MeCN]$_4$ TRI-4'Py at 10% D_2O v/v pH 5.90 (Region: Aromatic) 248

Figure A-13: ^{1}H-^{15}N HMBC of 4.239 eqv Cu(I)[MeCN]$_4$ TRI-4'Py 10% D_2O v/v at pH 5.90 (Region: Aromatic) 249

Figure A-14: ^{1}H-NMR NaCl titration of Cu(I)-TRI-4'Py [1 eqv. Cu(I)[MeCN]$_4$] 10% D_2O v/v at pH 5.90 (Region: Aromatic) 250

Figure A-15: Progression curve of NaCl titration of Cu(I)[MeCN]$_4$ titration of Cu(I)-TRI-4'Py following the meta-proton on the pyridine ligand 251

Figure A-16: ^{1}H-NMR NaCl titration of Cu(I)-TRI-4'Py [1 eqv. Cu(I)[MeCN]$_4$] 10% D_2O v/v at pH 5.90 (Region: Aliphatic) 252

Figure A-17: ^{1}H-NMR pH Titration of apo-TRI-4'Py L19A in 10% D_2O v/v (Region: Aromatic) 253

Figure A-18: ^{1}H-^{13}C HSQC NMR of apo-TRI-4'Py L19A at pH 2.90 (Region: Aromatic) 254

Figure A-19: ^{1}H-^{13}C HSQC NMR of apo-TRI-4'Py L19A at pH 3.99 (Region: Aromatic) 255

Figure A-20: ^{1}H-^{13}C HSQC of apo-TRI-4'Py L19A at pH 5.97 (Region: Aromatic).....256

Figure A-21: ^{1}H-^{13}C HSQC NMR of apo-TRI-4'Py L19A at pH 9.84 (Region: Aromatic) 257

Figure A-22: ^{1}H-^{13}C HSQC of apo-TRI-4'Py L19A at pH 5.94 (Region: Aliphatic-sidechains)..... 258

Figure A-23: ^{1}H-^{13}C HSQC NMR of 3.7 mM TRI-4'Py L19A 0.3 eq. $CuSO_4$ (10 eq. sodium ascorbate) at pH 5.94 (Region: Aromatic) 259

Figure A-24: ^{1}H-^{13}C HSQC NMR of 3.7 mM (TRI-4'Py L19A)$_3$ 0.7 eq. $CuSO_4$ (10 eq. sodium ascorbate) at pH 5.94 (Region: Aromatic) 260

Figure A-25: ^{1}H-NMR of Cu(I)-TRI-3'Py at pH 5.91 vs. the oxidized enzyme (Region: Aromatic) 261

Figure A-26: ^{1}H-^{13}C HSQC NMR of 2.2 mM TRI-3'Py 0.3 eq. $CuSO_4$ (10 eq. sodium ascorbate) at pH 5.93 (Region: Aromatic).....262

Figure A-27: ^{1}H-^{13}C HSQC NMR of 2.2 mM TRI-3'Py 0.5 eq. CuSO4 (10 eq. sodium ascorbate) at pH 5.93 (Region: Aromatic).....263

Figure A-28: ^{1}H-^{13}C HSQC NMR of 2.2 mM TRI-3'Py 0.7 eq. $CuSO_4$ (10 eq. sodium ascorbate) at pH 5.93 (Region: Aromatic).....264

Figure A-29: ^{1}H-^{13}C HSQC NMR of 2.2 mM TRI-3'Py 1.0 eq. $CuSO_4$ (10 eq. sodium ascorbate) at pH 5.93 (Region: Aromatic).....265

Figure A-30: ^{1}H-^{15}N NOESY of apo-TRI-3'Py at pH 5.88 (Region: Amide) 266

Figure A-31: ^{1}H-NMR of apo-GRW-3'Py at pH 5.97 (Region: Overview) 267

Figure A-32: ^{1}H-NMR of apo-GRW-3'Py at pH 5.97 (Region: Amide/Aromatic) 268

Figure A-33: ^{1}H-^{13}C HSQC NMR NMR of apo-GRW-3'Py at pH 5.97 (Region: Aromatic).....269

Figure A-34: ^{1}H-^{13}C HSQC of apo-GRW-3'Py at pH 5.97 (Region: Aromatic) 270

Figure A-35: ^{1}H-^{1}H NOESY of apo-GRW-3'Py at pH 5.90 (Region: Overview).....271

Figure A-36: ^{1}H-^{15}H NOESY of apo-GRW-3'Py at pH 5.90 (Region: Amide/Aliphatic).....272

Figure A-37: ^{1}H-^{15}H NOESY of apo-GRW-3'Py at pH 5.90 (Region: Amide/Amide).....273

Figure A-38: ^{1}H-NMR of apo-$GRW_{stam27(AE3'Py)}$ at pH 5.97 (Region: Overview).....274

Figure A-39: ^{1}H- NMR of apo-$GRW_{stam27(AE3'Py)}$ at pH 5.97 (Region: Aromatic).....275

Figure A-40: ^{1}H-^{13}C HSQC NMR of apo-$GRW_{stam27(AE3'Py)}$ at pH 5.97 (Region: Aromatic).....276

Figure A-41: ^{1}H-^{13}C HSQC NMR of apo-$GRW_{stam27(AE3'Py)}$ at pH 5.97 (Region: Aromatic).....277

Figure A-42: ^{1}H-^{1}H NOESY of apo-$GRW_{stam27(AE3'Py)}$ at pH 5.97 (Region: Overview).....278

Figure A-43: ^{1}H-^{1}H NOESY of apo-$GRW_{stam27(AE3'Py)}$ at pH 5.97 (Region: Amide/Aromatic) ..279

Figure A-44: ^{1}H-^{1}H NOESY of apo-$GRW_{stam27(AE3'Py)}$ at pH 5.97 (Region: Amide/Aliphatic)...280

Figure A-45: ^{1}H-NMR of apo-GRW-4'Py at pH 5.90 (Region: Aliphatic) 281

Figure A-46: ^{1}H- NMR of apo-GRW-4'Py at pH 5.90 (Region: Amide/Aromatic) 282

Figure A-47: ^{1}H-^{13}C HSQC of apo-GRW-4'Py at pH 5.90 (Region: Aromatic) 283

Figure A-48: ^{1}H-^{1}H NOESY of apo-GRW-4'Py at pH 5.90 (Region: Overview).....284

Figure A-49: ^{1}H-^{1}H NOESY of apo-GRW-4'Py at pH 5.90 (Region: Amide/Aliphatic).....285

Figure A-50: ^{1}H-^{1}H NOESY of apo-GRW-4'Py at pH 5.90 (Region: Aliphatic).....286

Figure A-51: ^{1}H-NMR of apo-$GRW_{stam27(AEL)}$L33-4'Py at pH 5.97 (Region: Aliphatic).....287

Figure A-52: ^{1}H-NMR of apo-$GRW_{stam27(AEL)}$L33-4'Py at pH 5.97 (Region: Aliphatic).....288

Figure A-53: ^{1}H-^{15}N NOESY of apo-$GRW_{stam27(AEL)}$L33-4'Py at pH 5.97 (Region: Overview) 289

Figure A-54: ^{1}H-NMR of apo-$GRW_{stam27(AEA)}$L33-4'Py at pH 5.87 (Region: Aliphatic).....290

Figure A-55: ^{1}H- NMR of apo-$GRW_{stam27(AEA)}$L33-4'Py at pH 5.87 (Region: Amide/Aromatic) 291

Figure A-56: ^{1}H-^{13}C HSQC NMR of apo-$GRW_{stam27(AEA)}$L33-4'Py at pH 5.87 (Region: Aromatic) 292

Figure A-57: ^{1}H-^{1}H NOESY of apo-$GRW_{stam27(AEA)}$L33-4'Py at pH 5.87 (Region: Overview) 293

Figure A-58: ^{1}H-^{1}H NOESY of apo-$GRW_{stam27(AEA)}$L33-4'Py at pH 5.87 (Region: Amide/Aliphatic) 294

List of Abbreviations

2SCC:	Two stranded coiled coil
3'Py:	3-(3-Pyridyl)-L-alanine
3SCC:	Three stranded coiled coil
4'Py:	3-(4-Pyridyl)-L-alanine
4SCC:	Four stranded coiled coil
CA:	Carbonic anhydrase
CC:	Coiled coil
CD:	Circular dichroism
CuNiR:	Copper Nitrite Reductase
DIC:	diisopropylcarbodiimide
T1Cu:	Type I copper center
T2Cu:	Type II copper center
$T2Cu_{ox}$	Oxidized Type II copper center
$T2Cu_{red}$:	Reduced Type II copper center
T3Cu:	Type III copper center
ESI-MS:	Electrospray ionization mass spectrometry
EXAFS:	Extended X-ray absorption fine structure
His:	Histidine
HPLC:	High pressure liquid chromatography
ICP-MS:	Ion coupled plasma mass spectrometry
NaAsc:	Sodium Ascorbate
N_{δ}:	Delta nitrogen on histidine
N_{ε}:	Epsilon nitrogen on histidine
MES:	2-(N-morpholino)ethanesulfonic acid
NMR:	Nuclear magnetic resonance

XANES:	X-ray absorption near edge spectroscopy
XAS:	X-ray absorption spectroscopy

Abstract

This thesis extends or introduces innovative approaches to *de novo* design to interrogate metal binding, structure, and catalytic activity using a copper nitrite reductase (CuNiR) model. These designs will be used to investigate, at a molecular level, how the first and second coordination spheres influence the copper's coordination number and, in turn, modify nitrite reduction in a well-folded 3-stranded α-helical coiled coil (3SCC). The non-coded amino acids 3'Pyridyl alanine [3'Py] and 4'Pyridyl alanine [4'Py] side chains were first designed into the 3SCC forming sequence [Ac-G WKALEEK $(LKALEEK)_2$ PyKALEEK G-$NH_2]_3$ (*i.e.*, TRIW) to enforce the ε-nitrogen of histidine within the core of the assembly (*i.e.*, authentic pyridine type nitrogens). The pyridyl sites formed 3-coordinate cuprous sites and 4- or 5-coordinate cupric geometries which yielded an unnatural type 2 copper center (T2Cu). The cuprous state favored a more 2-coordinate linear geometry by designing space above the active site through the mutation of the leucine layer to an alanine layer (L19A), highlighting the impact of distant residues on protein structure around a metal. CuNiR kinetics were investigated under conditions favoring the binding of nitrite to the cuprous state (*i.e.*, Abraham's mechanism) which is the alternate, unexplored pathway of native CuNiRs. Compared to the natural histidine site, the pyridine ligands enhanced CuNiR activity by a factor of 400. Interestingly, while the k_{cat} values were maximized (~3 s^{-1}), the catalytic efficiency was doubled (k_{cat}/K_m= 5 M^{-1} s^{-1} vs. 11 M^{-1} s^{-1}) which depended on the ligand's orientation within the active site. The catalytic efficiency is further enhanced by shifting to a 2-coordinate Cu(I) enzyme which resulted in a decrease in the K_m from 600 mM to 50 mM and k_{cat}/K_m of 39 M^{-1} s^{-1}. Detailed structural experiments and inhibition kinetics resulted in competitive inhibition between Cl^- and NO_2^- providing strong evidence of nitrite binding to the reduced enzyme during the catalytic cycle. This demonstrated the formation of a Cu(I)–NO_2 adduct and

highlighted the Cu(I) enzyme as the important oxidation state controlling catalytic efficiency. It is argued that NO_2^- displaces one pyridine ligand in the 3-coordinate cuprous complex (verses forming a 4-coordinate Cu(I)$(Py)_3$-NO_2), analogous to what is observed with the Cu(I)–Cl adducts as a result of the steric constraints of the interior of the core. Collectively, the rationale for a 3-coordinate Cu(I)-NO_2 enzyme-substrate complex is explored within the context of the sterics between the primary and secondary coordination spheres.

This work will also describe an alternative, novel strategy to repack side chains within the 3SCC using 3-residue non-canonical inserts (*i.e.*, stammer) to overwind the coiled coil to explore nitrite reduction. Stammers will be explored in terms of their ability to change the metal-coordination number or rotate solvent-exposed residues (*i.e.*, glutamate) into the core in proximity of the copper center. While this approach generates 3-coordinate cuprous enzymes for both the 3'Py and 4'Py ligands, 2-coordinate resting states are achieved by implementing two different stammers for either ligand (*i.e.*, AEA and AE3'Py), all of which are distinct from the cuprous states of the Leu/Ala designs in terms of their electronic structure. Each stammer explored resulted in slight variations in the kinetics which impacted only the K_m values in the range of 100-400 mM. This study will emphasize yet another approach to controlling the coordination number of copper active sites to tune the catalytic efficiency.

Chapter I

Customizing Nature: Engineering and Designing Metalloproteins Using Novel Design Strategies.

Introduction:

The field of *de novo* designed proteins strives to build proteins that are unique in structure and function to those found in nature. This is accomplished by using unique sequences or amino acids that the designer believes will confer some shape or, in general, a property that will result in a particular structure or function. While we know that the protein amino acid sequence is very important in determining the overall fold of the protein and, therefore, its function(s), we have yet to design proteins from a general theory of protein folding and accurately predict the lowest energy state of a protein from a given sequence. This is one of the main issues in protein design, and it gets considerably trickier when a metal is added to the protein structure. Despite this, *de novo* proteins have emerged as a result of 1) recent advancements in ab initio and artificial intelligence prediction methods that predict proteins' 3D structures from their primary amino acid sequence with accuracy comparable to that of experiments, and 2) lessons learned from engineering natural proteins.[1–3] Different approaches are required to clarify structure/function relationships in metalloproteins. Enzymological studies of native or engineered metalloproteins provide useful insights and small molecules provide precise parameters for the metal and manipulations such as low temperature trapping of intermediates.[4,5] However, there are many advantages to using *de novo* designed proteins to understand the relationship between metal catalysis and protein structure. The emerging field of *de novo* protein design is both a field of chemistry and structural biology whose explicit goal is to create novel proteins with specific functions using computational design, spectroscopy, library screening, and synthetic biology. The field has made progress,

considering structural predictions with deep learning methods that have been developed within the past 10 years. As examples, designers have created metalloproteins that are comparable to the diferrous sites in ribonucleotide reductase,[6] iron-sulfur clusters,[7,8] native rubredoxins,[9,10] and cupredoxins.[11–13]

In this chapter, I focus on natural copper proteins, with an emphasis on those relevant to the history *de novo* design of metalloproteins and native copper nitrite reductases (Section I). In Section II, I discuss the state of the field of protein redesign (2A and 2B), and I discuss *de novo* designed metalloproteins with a focus on coiled coil structures, highlighting non-heme copper metalloenzymes (Section 2C). Section III covers unique alterations to coiled coil proteins (*i.e.*, heptad breaks) that lead to predictable changes in their tertiary structure. Chapter IV of this thesis will utilize these modifications to alter further metalloprotein design. Finally, each of the thesis's subsequent chapters is briefly summarized in Section IV.

I. Copper in Natural Proteins:

Copper proteins are wide-ranging in their function. For the first two billion years of life, the lack of oxygen and the 10^{-3} M concentration of H_2S meant that the atmosphere was strongly reducing which resulted in water insoluble forms of copper (*i.e.*, Cu(0) and Cu(I)) composing all the available copper).[14,15] During this time, Fe(II) dominated the metalloprotein landscape, forming a variety of proteins that we still have today, which explains why very few copper proteins are utilized by anaerobic archaea till this day. During the great oxidation event, Fe(II) was more susceptible to oxidation, forming water-insoluble $Fe(OH)_3$ that pressured organisms to develop special accommodation, and accumulation/storage mechanisms to adopt their metabolic pathways. However, evolutionary pathway sequestered processes exploited the very soluble Cu(II) ion, leading to the emergence of copper-dependent proteins that were capable of carrying out many of the activities of their iron-containing relatives. The oxidation states accessible to copper under physiological conditions favor distinct ligands and geometry; however, copper proteins involved in electron transfer have adopted a geometrical requirement between the two-oxidation states

Table I-1: Common Geometries found in Cu(I) and Cu(II) proteins

Oxidation State	Coordination Number	Geometry
Cu(I)*	2	Linear
	3	Planar
	4	Tetrahedral
Cu(II)**	4	Square Planar
	4	Distorted Tetrahedral
	5	Square Pyramidal
	5	Trigonal Bipyramidal
	6	Axially Distorted Octahedral

* d^{10} metals have no preferences based on ligand field stabilization energies (LFSE)
**Geometric preference based on LFSE

known as an entatic state.[16,17] Therefore, each oxidation state can be stabilized when the preferred ligands, in the preferred geometry, are met. In this case, metalloproteins that stabilize one oxidation state of the metal are expected to only be used for storage/transport of copper or bind small molecules. However, redox-active enzymes that contain copper, or metals in general, require the particular arrangements of sidechains around the copper center to switch between Cu(I) and Cu(II) oxidation states during the catalytic cycle (Table I-1). Nature has satisfied this objective in active sites in two ways: 1) choosing ligands that favor the Cu(I) oxidation state or Cu(II) oxidation state, and 2) selecting metal-ligand geometries that are between those favored by either Cu(II) or Cu(I). These two factors predominantly determine the reduction potential of a copper active site. Regarding electronics of the sidechains and Hard-Soft Theory, stable complexes with Cu(I) tend to form in the ligands that are "softer" (*e.g.*, H–Cys, Cys^-, Met), while Cu(II) tends to form stable complexes with "harder" ligands (*e.g.*, Amide, Try, Tyr^-, Ser, His, Asp^-, Glu^-) (Figure I-1A).[16]

The redox couple for Cu(II)/Cu(I) in aqueous solution is E^o=+153 mV (SHE), while in copper proteins, the reduction potential ranges from +183 mV (hemocyanin) to +785 mV (SHE) (type 1 copper centers in laccase) depending on the copper binding site.[18] The potentials can be further modified by hydrophobic interactions around the primary coordination sphere and by rare copper cofactors that are found in a very small fraction of natural copper enzymes (Figure I-1B).[19]

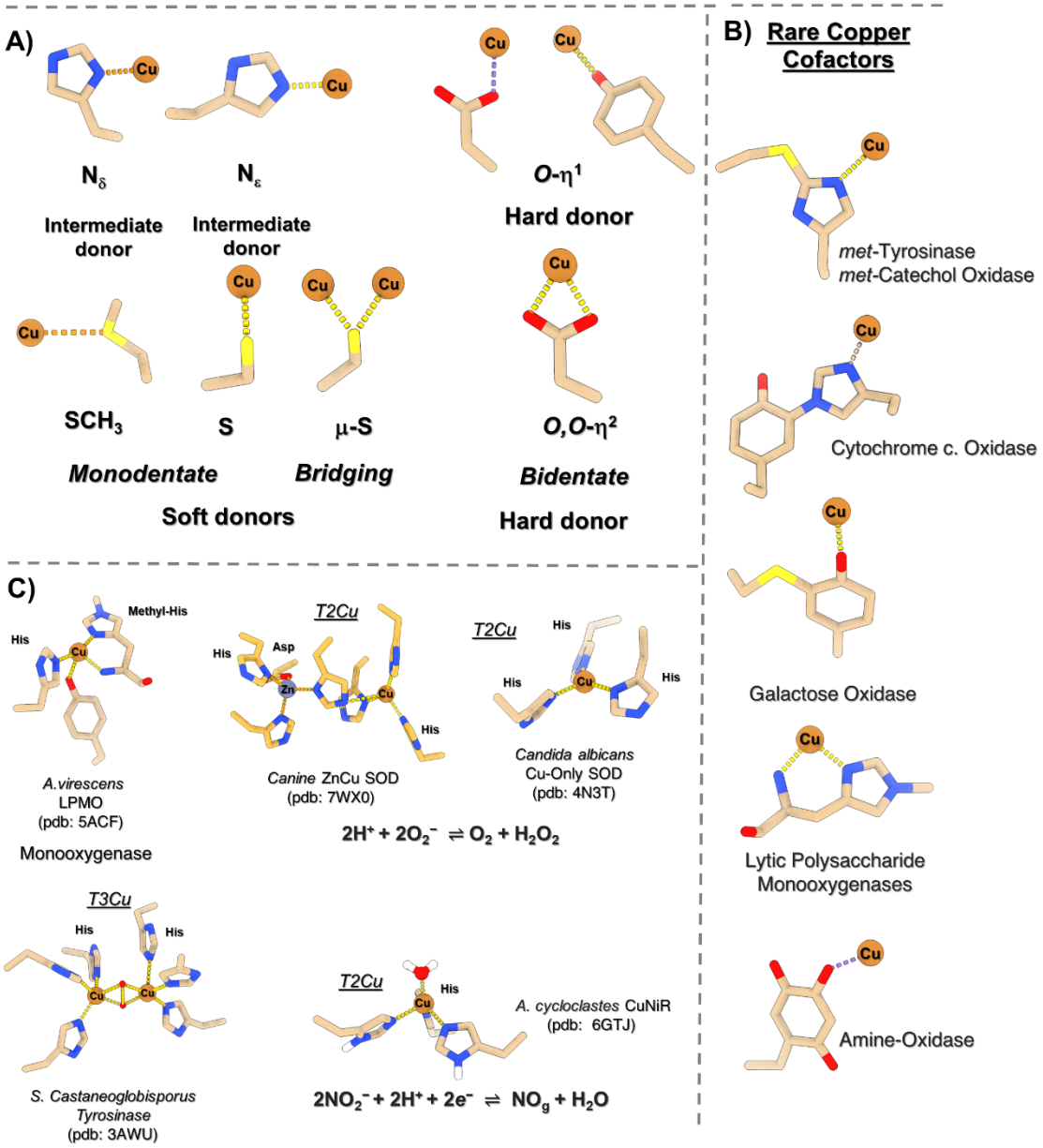


Figure I-1: The bioinorganic chemistry of the primary coordination sphere of copper: **A**) Summary of binding modes of Cu(II) and Cu(I) oxidation states, **B**) Copper bound to rare cofactors within metalloenzymes, highlighting nature's ability to finely tune active sites, and **C**) Examples of Type 2 copper centers and Type 3 copper center.

Copper proteins that catalyze reactions can be classified as either redox proteins or oxidoreductases, while non-catalytic centers are either electron or oxygen transport proteins (Figure I-1).[17] There are 7 types of copper proteins; Type 1 copper (T1Cu), Type 2 Copper (T2Cu), Type 3 copper (T3Cu), Trinuclear Centers, Cu_A-centers, Cu_B-Centers, and copper chaperone proteins (*e.g.*, CopC). As an example of a T3Cu center and a structurally important protein in the history of *de novo* designed metalloproteins, hemocyanin (Hc) is the extracellular O_2 transport protein in the circulator fluid in mollusk (*e.g.*, snails and squids) and arthropods (*e.g.*, spiders and scorpions) that binds O_2 at a pair of Cu(I) proteins that results in two Cu(II) centers that are EPR silent due to the antiferromagnetic coupling of the bridging oxygen atoms (Figure I-2A). Interestingly, both hemocyanin and the class of coupled binuclear polyphenol oxidases (CB-PPOs) are equipped with identical oxygen-binding copper centers and yet have very different functions.[20] As an example, tyrosinase (Ty), a monooxygenase, is the first step in the production of melanin, catalyzing *o*-hydroxylation of L-tyrosine to 3,4-dihydroxy-L-phenylalanine (L-DOPA) and the subsequent oxidation to L-DOPAquinone. In both proteins, two Cu(I) ions sit 4.6 Å (hemocyanin) and 3.4 Å (tyrosinase) apart from each other with three histidine coordinated to each copper, with two open coordinate sites for dioxygen binding. However, the active sites are in different positions within the respective proteins. The O_2 binding site in arthropod hemocyanin is situated in Domain 2 which is folded under Domain 3 that blocks access to substrates access to the copper site. This contrasts with the copper site in Ty which is not tucked under the C-terminal peptide (equivalent to domain 3) allowing solvent and substrate to enter. Unsurprisingly, at high substrate concentration, phenol-oxidase activity is observed in hemocyanin.[21] This example highlights one limitation in explaining the reactivity of different metalloproteins with only the primary coordination sphere and it validates the incremental steps that designers tend to employ when designing metalloenzyme. The structure of hemocyanin, with its di-copper $(His)_6$ site buried within an α-helical bundle, provided the template to design the $Zn(II)(His)_3$ site within a four-helix bundle, the first *de novo* metalloprotein (Figure I-2A-2C).[22] While no crystal structure of this

Zn(II)$(His)_3$ site has been reported, This structure shown in Figure I-2C is very similar to the first designed metalloprotein reported by Degrado *et al.*

In the context of T2Cu copper centers, the focus of this thesis, the similarity in the primary coordination of copper nitrite reductase (CuNiR) and Cu,Zn-superoxide dismutase (CuZn-SOD) and Cu-superoxide dismutase (CuSOD) raises the question of whether each of these enzymes could catalyze their counterpart's reaction (Figure I-1C). The reduction potential of the T2Cu center in *Ax*NiR is 250 mV (SHE) with SOD copper sites having a tightly controlled reduction potential of 360 mV (SHE), the midpoint potential between oxidation (-181 mV SHE) and reduction (910 mV SHE) of superoxide.[23] *Ax*NiR has ~56% of the SOD activity of bovine SOD, and a side-on

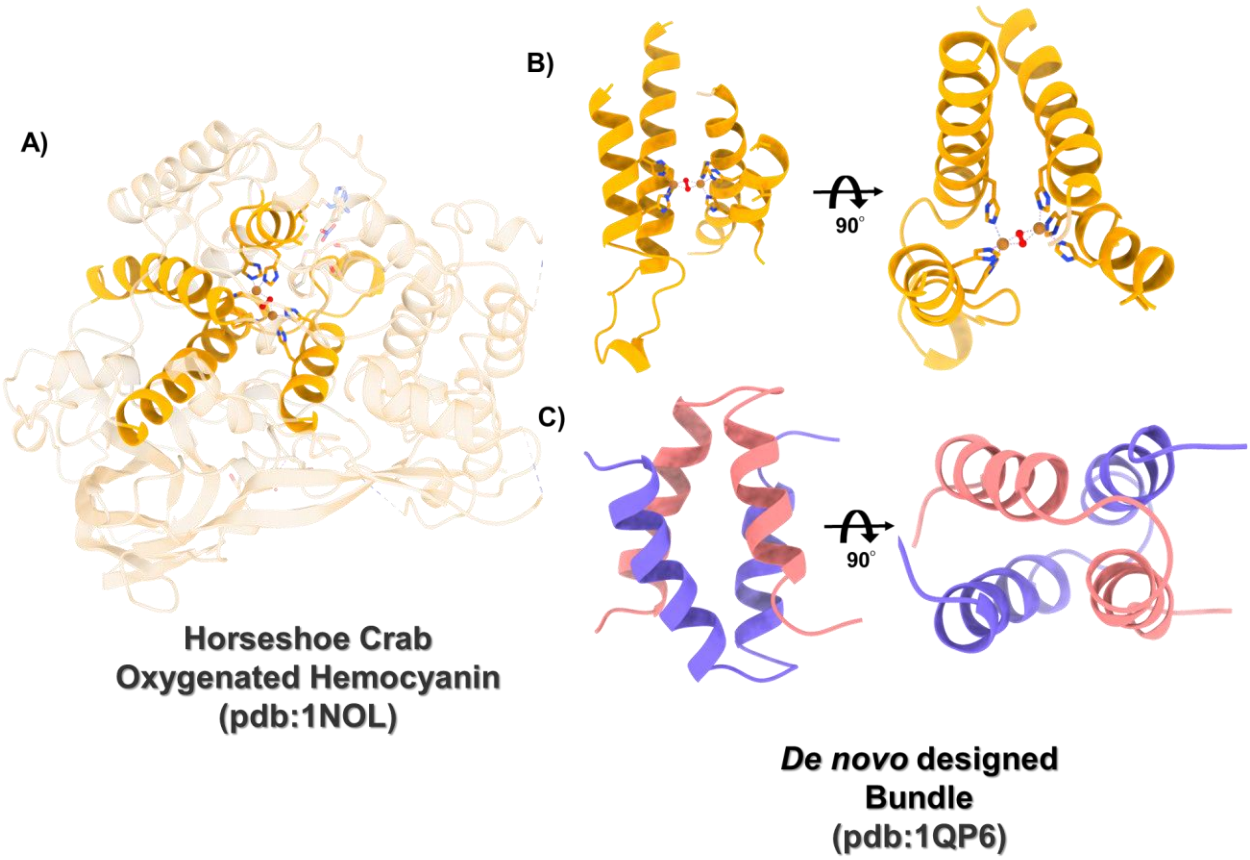


Figure I-2: An example of early protein design from horseshoe crab hemocyanin (pdb:1NOL): **A)** Crystal structure of horseshoe crab hemocyanin with the α-helix bundle highlighted (orange) (pdb:1NOL), **B)** α-helix bundle of hemocyanin positioned perpendicular to the supercoiled axis (left) and parallel to the super-coiled axis (right), and **C)** *de novo* designed four-helix bundle with similar topology as the di-copper site in hemocyanin, positioned perpendicular to the super-coiled axis (left) and parallel to the super-coiled axis (right) (pdb:1QP6). Ref. 22.

superoxide (or dioxygen) adduct has been reported, although is it possible that the T1Cu center may be able to catalyze this reaction.[24,25] Interestingly, no NiR activity was observed in bovine SOD, highlighting the specificity by which enzymes have evolved toward a particular chemical conversion. In the context of amino acids, the active sites of natural proteins are limited to a few amino acids that are able to bind to metals; however, nature has evolved strategies to adapt the primary coordination sphere in copper proteins with rare cofactors (Figure I-1B). These wide ranges of high reduction potentials allow copper to carry out various functions that include electron transport and reactions with dioxygen (O_2).

The primary coordination sphere of (T2Cu) is conserved to a lesser degree than either type 1 or type 3 copper centers. From a phylogenetic point of view, they share very little with one another in terms of their ligands, coordination geometries, or the protein tertiary structures in which they are found. Given this diverse landscape of structural types and environments, T2Cu centers include oxidases, dioxygenases, and oxidoreductases that metabolize reactive species. *This thesis involves designing a Copper Nitrite Reductase (CuNiR), an important enzyme in the bioenergetic pathways of denitrifying bacteria and fungi, that contains a specific CuN_3 example of a T2Cu center*.[26]

CuNiRs carry out the first committed step of denitrification with the conversion of NO_2^- to NO(g). Most CuNiRs are trimeric in symmetry with each monomer (~40 kDa) composed of two Cupredoxin (β-sandwich) domains with a C-terminal loop that wraps around an adjacent monomer to stabilize the trimeric oligomerization state (Figure I-3A). To date, all CuNiRs are composed of an electron transport T1Cu center (*i.e.*, green copper center) and a catalytic T2Cu center. The T1Cu center is coordinated by two histidines, one cysteine, and axial methionine in a distorted tetrahedral geometry, a geometry that is intermediary between the Cu(II) and Cu(I) preferred geometries (*i.e.*, entatic state) that allow for fast electron transport.[27,28] The unusual geometry and ligation give rise

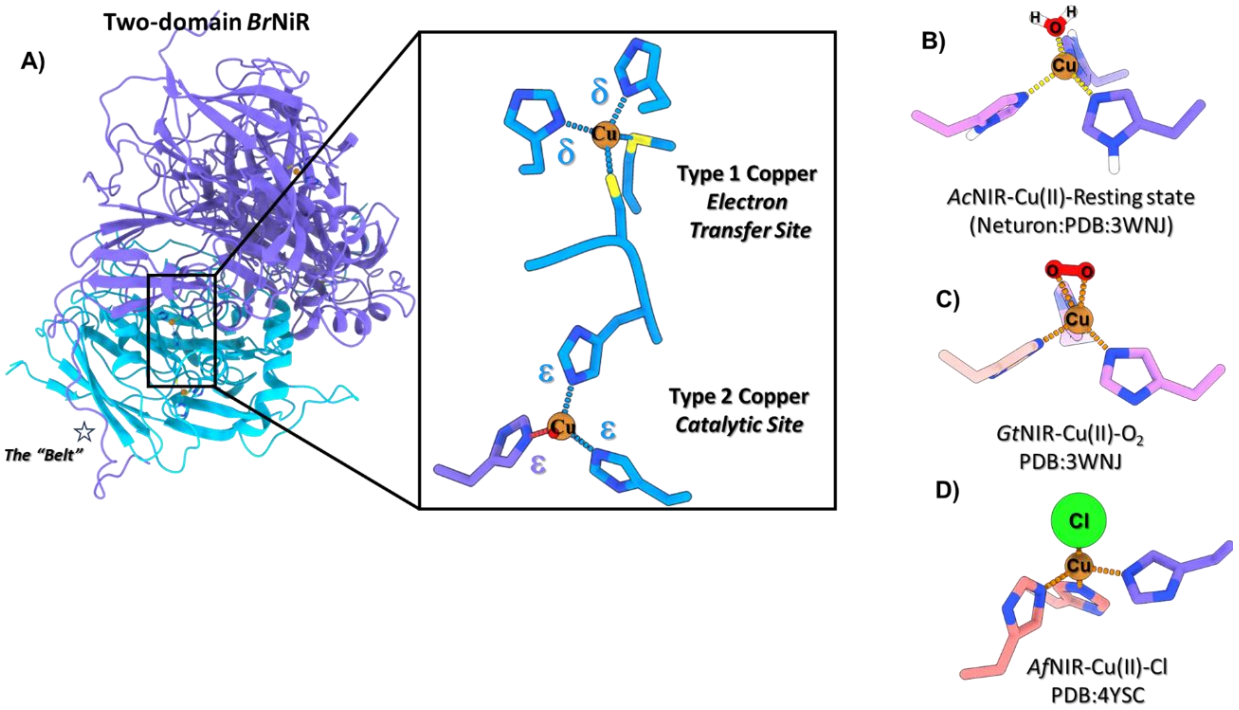


Figure I-3: Overview of the Type 1 and Type 2 Copper center: **A)** Overview of the Type 1 and Type 2 Copper center, **B**) Neutron-diffracted structure of the resting state of the $T2Cu_{Ox}$, **C)** X-ray structure of a dioxygen adduct of $T2Cu_{ox}$, and **D)** X-ray structure of the chloride adduct at the $T2Cu_{ox}$ Refs. 25,29.

to the unique spectral features of T1Cu copper centers.[17] In the resting state, the T2Cu site is composed of a single copper atom surrounded by three histidines and a H_2O [Cu(II)(His_3)-OH_2] with one of the three histidines extending from a neighboring monomer, making the C-terminal "belt" a very important structural feature (Figure I-3A). Although there are reports of X-ray crystal structure showing a $T2Cu_{ox}$ resting state with OH^- liganded [Cu(II)(His_3)-OH^-], 1.8 Å resolution neutron structure of per-deuterated CuNiR suggest a D_2O ligand (Figure I-3B).[29] In the oxidize form, the water is labile and easily displaced by nitrite , dioxygen[25] and chloride (Figure I-3C and D).[29]

There is a general consensus on the mechanism for two domain CuNiRs in which the resting state T2Cu binds NO_2^- in a *O,O*-bidentate fashion supported by EXAFS and X-ray crystallography. The binding of the NO_2^- lowers the reduction potential of the T2Cu center and

triggers the ET from the T1Cu center. It has been proposed that the electron travels through the Cys_{T1Cu}-His_{T2Cu} bridge, tunneling to the T2Cu center.[30] The secondary coordination sphere plays a vital role in supplying the two proton equivalents needed from the bulk solvent outside the protein surface in order to further activate the N–O bond and orient NO_2^- around the T2Cu site. Two highly conserved proton donors, His_{CAT} and Asp_{CAT}, are said to be involved in the rate determining proton-coupled electron-transfer (PCET) from the T1Cu to T2Cu, which is proposed to be part of a longer four-residue bridge that connects the T1Cu histidine ligands and Asp_{CAT} H-bonded to the water on $T2Cu_{ox}$ (the sensing loop).[31,32] In blue copper centers, the Cys_{T1Cu}-His_{T2Cu} bridge is the preferred ET path, while green CuNiRs exploit an additional pathway through the Cys_{T1Cu} amide H-bonded His_{T2Cu} that has been found to have an higher overall efficiency.[33] Density functional theory coupled to pH jump kinetics/spectroscopy have been interpreted to suggest that after substrate binding, the Asp_{CAT} transfers a proton to the NO_2^- followed by metal-ligand charge transfer from the $T2Cu_{red}$ d_x^2-$_y^2$ orbit to the N-OH σ* orbital.[34] However, there are currently conflicting reports on whether the Asp_{CAT} H^+ transfer takes place between a $T1Cu_{red}$-$T2Cu_{ox}$–NO_2^- unit or a $T1Cu_{ox}$-$T2Cu_{red}$–NO_2^- unit.[35,36] Leferink *et al*. demonstrated using a pH jump laser-flash photolysis experiment that protonation of NO_2^- triggers ET transfer from the T1Cu center, supporting Asp_{CAT} H^+ transfer to a $T1Cu_{red}$-$T2Cu_{ox}$–NO_2^-.[37] Historically, the binding of NO_2^- to $T2Cu_{ox}$ has been somewhat hard to nail down due in part to low resolution crystal structures and partial reductions during synchrotron data collection. The SR X-ray (SRX) and X-ray Free Electron Laser (XFEL) crystallography of *Br*CuNiR provide examples of the different orientations that NO_2^- binds to the $T2Cu_{ox}$ (Figure I-4).[38] There is agreement that NO_2^- chelates to the $T2Cu_{ox}$ through the oxygen atoms while small molecule mimics of CuNiR have shown the N-coordinated isomer to the Cu(I) oxidation state and the *O,O* bidentate binding mode to the Cu(II) oxidation state.[39–43] Currently, there are no crystal structures of authentic $T1Cu_{red}$- NO_2^- or electron damaged $T1Cu_{ox}$-NO_2^- centers which yield the N-coordinated monodentate mode observed in small molecule complexes. The highly conserved Ile_{CAT} plays a crucial steric role in orientating the

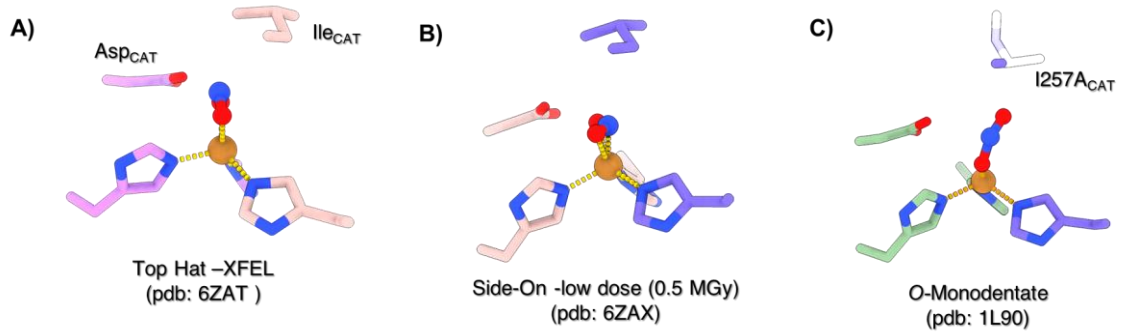


Figure I-4: Crystal Structure of various binding modes of nitrite to CuNiR**: A**) X-ray electron free laser structure of T1Cu$_{red}$-T2Cu$_{Ox}$-NO_2^- adduct, **B**) Low dose X-ray damaged side-on adduct, and **C**) X-ray structure of *O*-monodentate NO_2^- adduct. Refs. 38,43.

catalytically competent binding mode of NO_2^- which has been demonstrated in I257A and I257T mutants where the monodentate *O*-isomer is formed coupled with a factor of ~25 decrease in specific activity.[43] The *O,O* bidentate-coordinated mode observed in the I257V and I257L mutants, with only the I257V displaying a factor of 1.2 higher specific activity in *Af*CuNiR (Figure I-4C).[43] So far, the native CuNiRs of both *Bacillus stearothermophilus* and *Corynebacterium diphtheriae* have been identified to be the only native CuNiRs to have the Ile$_{CAT}$ replaced by Val$_{CAT}$.[44] It should be pointed out that up to this point in the mechanism, two pathways have been found to give a reduced T2Cu with nitrite bound (Figure I-5). The two different pathways hinge on whether the ET step occurs before NO_2^- binding (*i.e., reduction before binding* as proposed by Suzuki[45] or Hasnain[46]) or after binding (*i.e., binding before reduction* as proposed by Abraham[47] and Averill[48]). It appears that these two pathways can be in operation at the same time, with the non-physiological conditions of some kinetic assays (high NO_2^- concentration and high pH condition) contributing to the predominance of one mechanism over the other. By adding nitrite directly to reduced T2Cu *Ax*NiR, Hasnain *et al*. showed that NO(g) formation was eliminated, and argued that a three-coordinate reduced T2Cu center is an inactive form of the enzyme in the *reduction before binding*) route.[24] However, Canters *et al*. argued that a slow isomerization in *Af*CuNiR of Cu(His)$_3$-OH$_2$ T2Cu$_{red}$ to a Cu(His)3 site[an inactive form] is slower than nitrite displacing the H_2O ligand at $[NO_2^-]>K_{d,}^{red}$, a compatible step with the random-sequential mechanism proposed.[49]

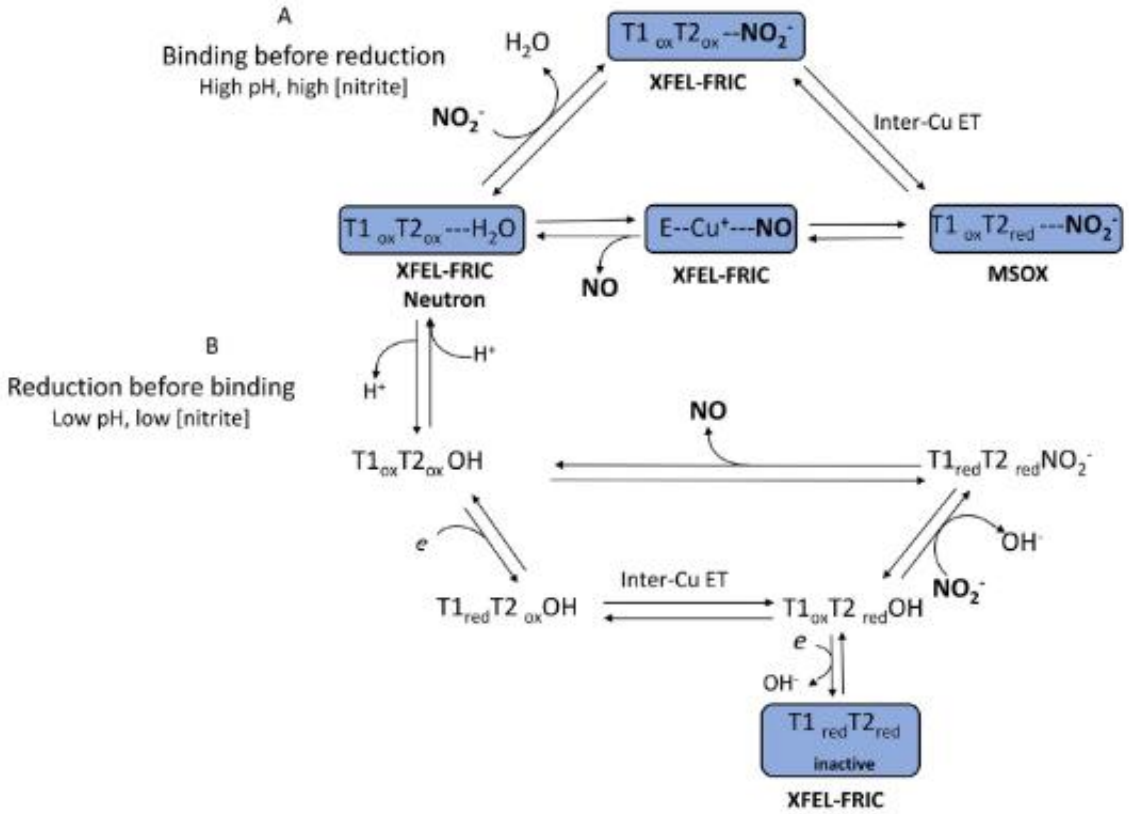


Figure I-5: CuNiR mechanism based on crystallography and kinetics in solution. Reprinted with permission of Ref. 60 Copyright 2022 Elsevier

Moreover, Canters *et al.* found fitting the steady state kinetics below pH 6.5, the rate of electron transfer was slower if NO_2^- displaces a H_2O on the $T2Cu_{ox}$ than replacing OH^- above pH 6.5. In other words, the ET rate constants to the $T2Cu_{ox}$ decreases in order $H_2O > NO_2^- > OH^-$. A single molecule solution study was conducted on *Af*CuNiR with an fluorescent dye close to the T1Cu center, resulting in spectral overlap with the broad absorption bands of the T1Cu center (450 nm and 590 nm) and allowing Forster resonance energy transfer to monitor the progress along the catalytic cycle.[50,51] Two different populations were observed under turnover conditions with 20-30 ms and 10 ms for the $T1Cu_{ox/red}$ ET with the concentration ratio dependent on $[NO_2^-]$ (5 μM to 5 mM).

T1Cu remained reduced for a long period of time in one population while the other population switched between the reduced and oxidized forms, suggesting a random-sequential mechanism

was operating. Interestingly, the kinetics also displayed features of an ordered mechanism in that any particular enzyme would remain in one pathway (once chosen) for a number of turnovers before switching to the other pathway, possibly explaining the appearance of randomness under non-physiological conditions during steady state kinetics.[52,53] A better description of the mechanism above would be an "alternate-route ordered mechanism." This is because the PCET dependence on the inter-ET from T1Cu to T2Cu is pH dependent and determines which route each molecule undergoes. The kinetic profile under this circumstance has been shown to follow a clear order in reactions step.[54]

The product of nitrite reduction by CuNiR, NO(g), has been the more controversial aspect of the mechanism, ranging from the binding geometry, the best description of the electronic valence structure [Cu(II)–NO^- vs. Cu(I)–$NO^\bullet$], or whether there is even a $\{CuNO\}^{10}$ complex at all. NO(g) is also a known inhibitor of CuNiRs.[26] The initial assignment of an NO(g) product was a side-on species Cu(II)–NO^- that was reported by Tocheva *et al*. using EPR of $T1Cu_{red}$ under excess exogenous NO(g).[55] This experiment confirmed the Cu(II) nature of the active site, which was also supported by a crystal structure under identical conditions with Cu-N and Cu-O bond distances of 2.09 Å and 1.99 Å, respectively.[55] Interestingly, this assignment was in complete opposition to all small $\{CuNO\}^{10}$ complexes that exhibited EPR spectra consistent with an end-on Cu(I)–$NO^\bullet$. This assignment has been challenged on the basis of MCD, EPR, ^1H and ^{15}N ENDOR that *Rs*NiR in the presence of excess NO(g) results in signatures identical to $T1Cu_{red}$-$T2Cu_{ox}$-NO_2^- enzyme form.[56] The Cu(I)-$NO^\bullet$ intermediate has been observed in *wt* CuNiR by EPR and ENDOR with 52% spin in 2p orbital on NO(g) nitrogen, 17% in Cu 3d and 4s orbitals, ~1% unpaired spin in the ENDOR being attributed to another exogenous nitrogen, likely a coordinated histidine.[56] The spin in the NO(g) showed dipolar interactions with the $C^{\delta 1}$ protons of Ile_{CAT}. The $\boldsymbol{g}$ and $\boldsymbol{A}$ tensors were fitted to a 160° Cu–N–O angle, confirming an end-on adduct. This data was collected using limited amounts of NO_2^- and limited amounts of biologically relevant reductant (NADH) in solution. Moreover, the Cu(I)–$NO^\bullet$ has been shown to convert to NO_2^- via a reductive coupling

N_2O intermediate that acts as a two electron sacrificial acceptor to oxidize the completely reduced enzyme and subsequent conversion to NO_2^- suggesting the NO(g) has to be end-on for this reaction to occur and CuNiR can catalyze the reverse reaction.[57,58] Correlating the structure of NO(g) intermediates between the spectroscopy in solution and the crystallography is currently a problem. The side-on geometry is executively seen in crystal structures of oxidized or reduced *Af*CuNiR is exposed to excess NO(g), which DFT suggests is best described as Cu(I)-NO$^\bullet$ (or could be a result of radiation damaged $\{CuNO\}^{11}$ configuration) while limited exposure of reduced *Af*CuNiR with NO(g) yields an end-on isomer and gives the same features as NO_2^- reacted with reduced CuNiR in solution.[59] DFT calculations suggest that a side-on $\{CuNO\}^{10}$ species hydrogen bonded to histidine ligands could be a viable intermediate, viewed as a $\{CuNO\}^{11}$–His$^\bullet$ antiferromagnetically coupled species, but in general, the protonation state of the Asp_{CAT} and His_{CAT} plays a critical role in the geometry of Cu ligand $\{CuNO\}^{10}$.[60] Moreover, Merkle and Lehnert *et al*. included the 2nd coordination sphere residues Asp_{CAT} and His_{CAT} in the DFT calculation and found that the side-on geometry is a *local* minimum while the end-on geometry is a *global* minimum.[61] Recently, high-resolution neutron crystallography has suggested that the $^-$OH-bound state forms after nitrite reduction, even at low pH, which the authors argue is evidence of not needing to invoke a $\{CuNO\}^{10}$ intermediate at all.[62]

Throughout this section above, CuNiR has been examined in terms of its structure and mechanism. The reaction is believed to follow an ordered mechanism that is best described as an alternate route ordered mechanism whereby nitrite can either bind to the Cu(I) or Cu(II) oxidation state before being reduced to NO(g). The secondary coordination sphere plays a crucial role in orienting the substrate to the copper site. In the next sections, the distinction between protein redesign and *de novo* design will be covered, highlighting the fundamental concepts of both fields and the historical aspects of *de novo* design, before discussing relevant examples of *de novo* metalloenzymes.

II: Native Protein Engineering and *de novo* Design:

2A: *The Engineer: Metalloproteins from a Synthetic Inorganic Chemist's Viewpoint*

In protein design, one explores the protein space by modifying either a natural sequence (protein redesign) or by designing a novel sequence from scratch (*de novo* design). When designing and engineering artificial metalloenzymes, the protein redesign strategy has been shown to be one of the most successful methods, in part due to the limitations of the predictive structure tools one would need to generate proteins from *ab initio* methods. In addition, redesigned native proteins often have more complex folds that allow for substrate binding, protein-protein interactions, and the presence of additional co-factors that are too complicated to design from first principles with our present understanding of protein folding. The ultimate objective of protein redesign is to acquire better and innovative features with the proteins that already have a function in nature, such as new activities, higher stereoselectivity, or new substrate specificity. By altering their structure to gain greater stability or change reactivity, metalloproteins can be redesigned to function better than their native enzyme. Many examples highlight the different approaches taken to design metalloproteins rationally (Figure I-6).[63] Developments in the field of protein chemistry have yielded new methods to incorporate non-coded amino acids, including native ligations, total synthesis, and synthetic tRNA/tRNA synthetase for *in vivo* incorporation, which has allowed designers to form narrower hypotheses about structure-function relationships within proteins.[64–70] However, challenges are associated with this set of techniques, including misincorporation of cofactors into recombinant proteins,[71] orthogonality with standard amino acids,[72] and installing multiple different non-coded amino acids into a protein.[73] By expressing a diverse gene library containing various protein mutants in an appropriate host organism, directed evolution has proven to be a powerful approach for redesigning natural metalloenzymes to catalyze novel reactions. [74]Subsequently, screening or selection techniques, which can range from colony activity screening to more sophisticated systems like yeast two-hybrid, phage display, mRNA display, and ribosome display, can be used to quickly create new functions in native proteins.[75] The selected proteins are those that best meet the criteria set for a specific function or trait; otherwise, additional rounds of cycles are done until the criteria are met. From their perspective, a key limitation of rational design

is the trickle down of information through scientific publications while the failures are not published.[76] Directed evolution faces constraints due to the exponential increase in possible evolutionary trajectories as mutations accumulate. This vast array of paths includes numerous neutral or deleterious steps that do not contribute to beneficial progress, essentially limiting directed evolution to follow a continuous uphill path in an adaptive walk.[77] Moreover, difficult-to-express proteins require resource-intensive and time consuming methods for iterative cycles of mutation, selections, and amplification. Despite these limitations, many successful protein systems have been evolved, and protein engineers are embracing directed evolution to produce new, useful proteins that catalyze novel reactions with high selectivity, high yields, and with large turnover numbers.[78–80] Machine-learning and deep learning have had impacts on the field of protein

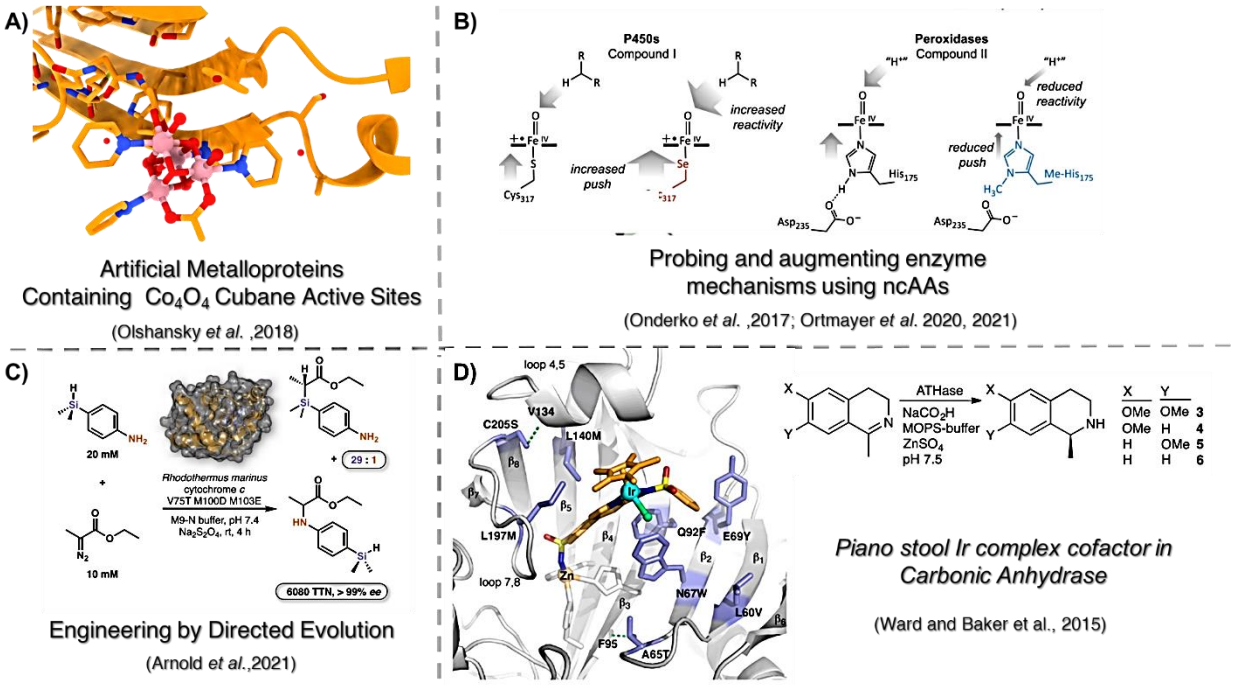


Figure I-6: Examples of *protein redesign*: **A**) Artificial metalloproteins (ArMs) containing Co_4O_4 cubane active site that was constructed via the biotin–streptavidin method, and **B**) Example of non-coded amino acids in selenocysteine or methyl-histidine ligated P450 compound I, demonstrating a clear connection between reactivity and electron donation, **C**) Example of directed evolution applied wild type Rma cytochrome c, yielding a heme enzyme that catalyzes Si−H insertion between 4-(dimethylsilyl)aniline and Me-EDA, and **D**) Model of Rosetta Design of an artificial hydrogenase based on crystal structure of complex [(h5-Cp*)Ir(pico)Cl] ⊂ WT hCA II (pdb: 3ZP9). Adapted with permissions of Ref. 87, Copyright 2018 American Chemical Society; Ref. 68 Copyright 2017 Nature Publishing Group; Ref. 69 Copyright 2020 American Chemical Society; Ref. 80 Copyright 2021 American Chemical Society; Ref. 63 Copyright 2020 American Chemical Society

engineering which includes predicting a metal-binding site,[81,82] predicting enzymes' mechanism,[83] and predicting enzymes' structure.[2,84] In contrast to redesign strategies that are very good at obtaining highly active catalysts of unique function, *de novo* design utilizes different strategies to address different questions that are either ignored or unanswerable using redesign.[68]

2B: *Applications of protein redesign to Cu enzyme*

Copper artificial metalloenzymes have been explored to catalyze a number of reactions with the aim of understanding metalloenzymes and for direct applications in industry.[85–87] Roelfes *et al*. retrofitted the 36 amino acid Bovine pancreatic polypeptide (bPP) with a copper-pyridine substitution, attempting to design a Cu(II)-(Pyridine)$_2$ at the dimer interface, which resulted in a chiral binding pocket (Figure I-7).[86] Naturally, bPP forms an antiparallel dimer between the polyproline helix (residues 1-8) and an α–helix (residues13-31).[63] Glutamate was mutated in the adjacent loop (D10E), which was in the vicinity of the active site, possibly chelating to Cu(II)-Pyridine, and an alanine was mutated into the loop interface to open the active site. The authors exploited solid-phase peptide synthesis to produce bPP and incorporate both L-3-Pyridylalanine (3'Pyridine) and L-4-Pyridylalanine (4'Pyridine) into the active site – a method that will be used in Chapters II-IV of this thesis.[88,89] The overall dimerization affinity, however, indicated that the peptide predominately existed in the monomeric form, even in the presence of Cu(II), following these mutations. In the absence of copper, the 4+2 cycloaddition between azachalcone and cyclopentadiene was not observed, while with only $CuSO_4$, product was formed but no enantioselectivity was observed.[86] The reaction does not involve a redox change in the copper

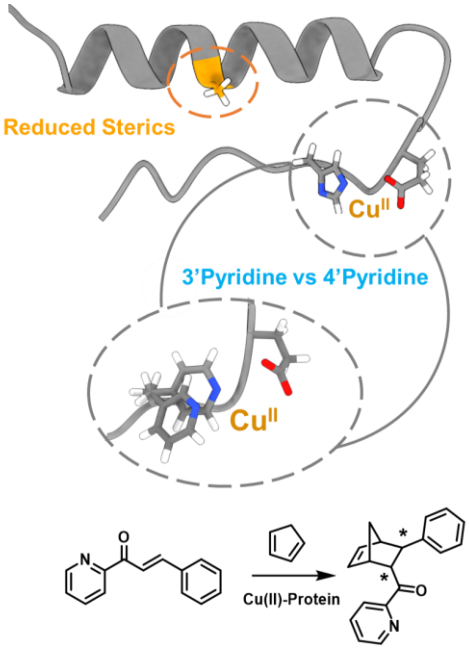


Figure I-7: Representation of monomeric bPP and the most active construct secondary mutations with putative 3'Pyridine and 4'Pyridine copper bind sites (pdb: 1BBA).

center and solely uses the Cu(II) center as a Lewis Acid catalysts. A strong dependence on the enantioselectivity between 3'Pyridine (80% *ee*) and 4'Pyridine (6% *ee*) was observed while also yielding similar conversation numbers. This points to the conclusion that the orientation of the copper in the active site plays a role in the selectivity throughout the reaction. Admittedly, the authors did not characterize the weakly bound Cu(II) sites in a matter that would give an indication of how the copper center interacts with either 3'Pyridine or 4'Pyridine, so the above comment would require further investigation to strongly support the role of the orientation of the pyridine ligands.

Metalloenzymes catalyze many different important reactions that are critical to industrial applications, most of which are engineered for high throughput under rigorous conditions.[90–92] Lytic polysaccharide monooxygenases (LPMO) is one of these examples that is widely used uniquely in several large-scale plants for the industrial production of lignocellulosic ethanol

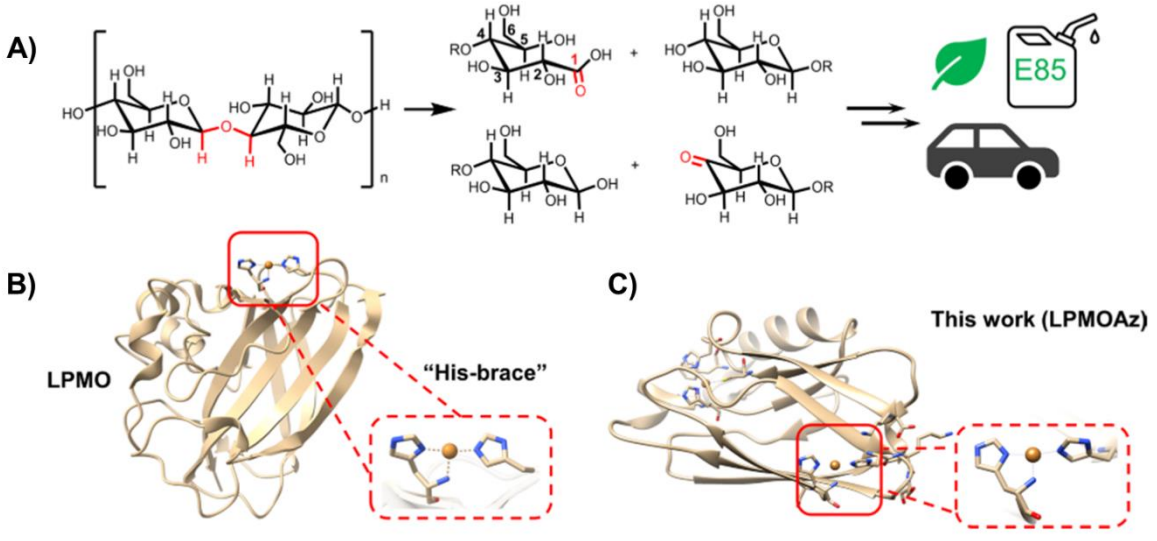


Figure I-8: Protein redesign of Lytic polysaccharide monooxygenases: **A)** LPMOs catalyze the oxidative breakdown of cellulose, resulting in the formation of oxidized ends at the C1 and/or C4 positions, a process that plays a crucial role in biofuel production. The carbon atoms in the pyranose ring are numerically labeled for clarity. **B)** The architecture of LPMO, showcasing the His-brace site where the substrate binds (pdb: 4ALR). **C)** The constructed model of LPMOAz presented in this study, with an emphasis on the specifically engineered His-brace site. Reprinted with permission of Ref. 96 Copyright 2023 PNAS.

(biomass conversion).[93] While LPMO is a recently discovered enzyme that can breakdown chitin and cellulose (ca. 2010), it has been demonstrated that LPMO suffers from inactivation from H_2O_2; however, this has not stopped its use in industry due to its ability to upcycle biomass into value-added products.[94,95] The active site is composed of two His residues near the enzyme surface, one of which is preserved as the N-terminus or His1. The backbone amine of His1 binds to copper in addition to the two imidazole side chains to form a tridentate site, also known as a "His-brace" site (Figure I-8). Recently, Lu *et al*. exploited *P. aeruginosa* azurin (LPMOAz) as a surrogate for the His-brace site near the surface of the type 1 protein.[96] Azurin was chosen because 1) the N-terminus is well-defined and relatively rigid, 2) it exhibits high stability towards copper-induced denaturation, and 3) it is straightforward to install a histidine at the N-terminus without disrupting the start codon upon bacterial expression. Moreover, azurin can be expressed in high yields, making this scaffold economically sustainable.[97] After T2Cu-ZnT1-LPMOAz was kept at 4°C for three months while 0.1 equivalents of extra CuSO4 were present, the UV-vis spectrum did not experience any notable spectral alterations, suggesting a stable scaffold. LPMO-like activity was observed up to 52 turnovers with the model substrate 4-nitrophenyl-D-glucopyranoside (4-NPGP) after optimizing the LPMOAz concentration, representing 9% of the activity of native LPMO under the same conditions. Furthermore, the authors discovered evidence of catalytic oxidative depolymerization for the polysaccharide substrate starch, showing a total turnover at C1 of 7.0, like what was observed with 4-NPGP under the same conditions (pH 6.3). The O_2 and H_2O_2 reactions indicate that LPMOAz, like native LPMOs, may activate both oxidants to carry out oxidative cleavage. Moreover, this provides an example of native LPMO activity being carried out in a slightly different fold in the presence of another metal binding site, which could be important for enzyme cascade processes in industry.[98]

Designing metalloproteins from native structures has been a hot area of research since the first engineered metalloprotein was published in 1956 by Akabori *et al*. where the complexation of silk fibroin fiber protein and $PdCl_2$ yielded an asymmetric hydrogenating catalyst capable of forming optically active amino acids from the appropriate precursors.[99] Since then, protein

redesign has expanded to the areas I have highlighted above (Figure I-6). The two examples directly discussed serve to highlight how orientation in non-redox active sites plays a role in catalysis in engineered proteins. Moreover, the adoption of a native scaffold that functions as an electron transfer protein can be transplanted with a catalytic active site (*i.e.*, "active-site transplant") to produce a more sustainable catalysis. In the next sections, I will focus on non-heme *de novo* designed proteins, with a focus on those designed within α-helical structures.

2C: Non-Heme *de novo* Design:

De novo design involves the development of sequences that can lead to desirable protein structures, including α-helical coiled coils or helical bundles, in contrast to techniques like directed evolution or protein re-engineering that alter naturally occurring protein scaffolds. One inherent advantage that *de novo* design has over protein redesign is that the protein chemical space expands immensely, leading to fold topologies and functions that are not found in native proteins. Within the context of protein evolution, a question that *de novo* designers are addressing is whether nature has sampled all the possible protein folds throughout the course of evolution or whether a large number of proton folds have yet to be explored.[100,101] Since the early 1990s, designed proteins have incorporated increasingly complex behaviors and functions, including generating membraneless organelles,[102] membrane transport proteins,[103,104] and allosteric cooperation.[105,106] Many *de novo* designed metalloproteins and metalloenzymes have also been published that contain both heme and non-heme metal centers, surveying a large space of functions and fold topologies.[107,108] Metalloproteins have been much harder to design, as they pose distinct challenges as one must consider the binding of a metal or metal cofactor. Therefore, one must consider not only the design of a binding pocket but potentially also the secondary coordination sphere that aids in substrate binding, substrate activation,[109] and intermediate stabilization.[110,111]

Non-heme active sites have held a privileged place in *de novo* design, as this type of active site tends to cover a wider range of chemistry but has offered unique challenges to designers. Early work with non-heme metalloproteins coincided with the design of heme proteins and has expanded

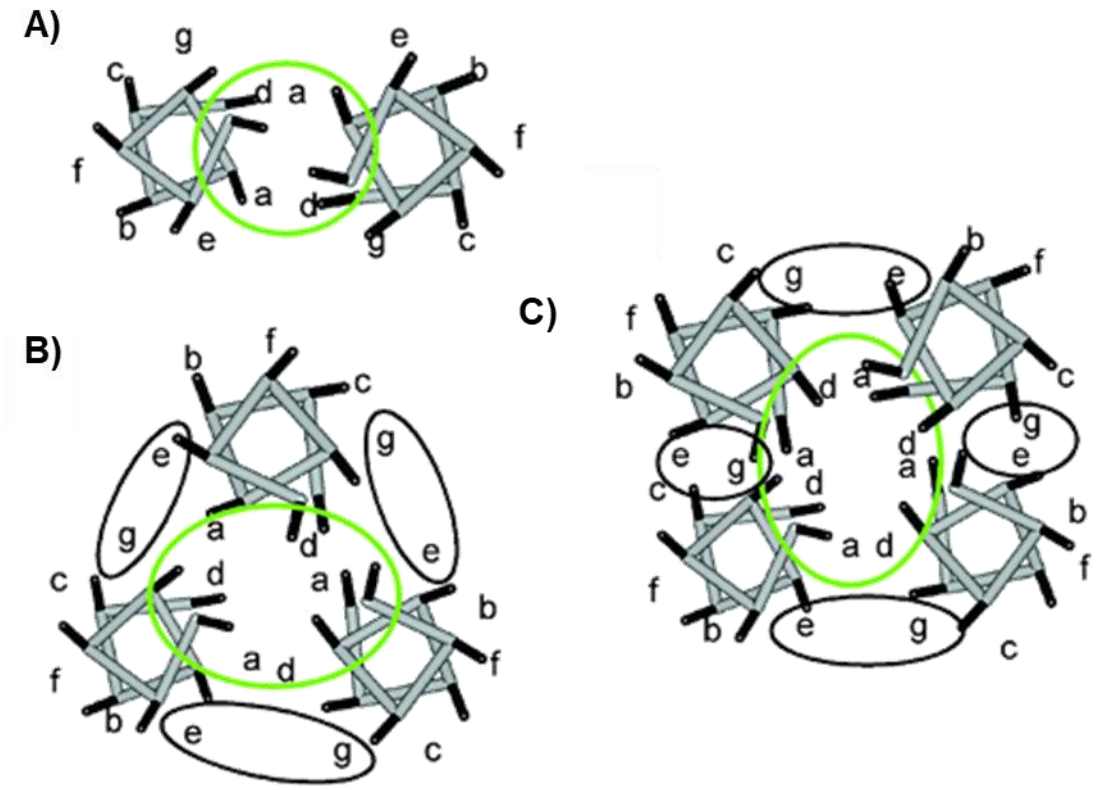
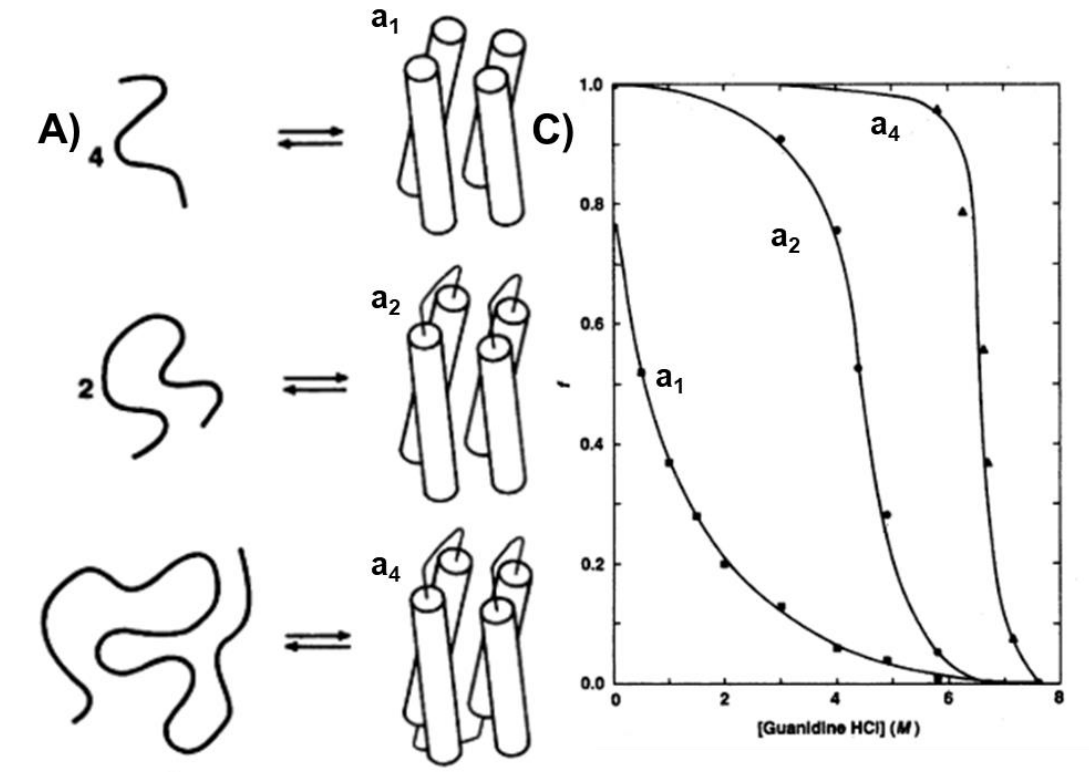


Figure I-9: Helical Wheel diagram different oligomerization states of parallel coiled coil: **A)** 2SCC, **B)**3SCC, and **C)** 4SCC. Reproduced with permission from Ref. 115, Copyright 2004 American Chemical Society.

to several metalloenzymes the past 40 years.[112] A variety ternary structures have been designed to include non-heme metal binding sites including coiled coils, dimeric 4-helix bundles, α-β folds, and β-sheets.[110] In this subsection, I will introduce a number of metalloenzymes that are relevant to the chapters that follow this introduction and will only mention and cite the remaining design strategies where appropriate. Throughout this thesis, α-helical coiled coil proteins are the central structure that this work is built around, and therefore these structures deserve special attention in terms of their properties and use in *de novo* design.[113] Coiled coil proteins are composed of α-helices (secondary structure) that form a quaternary structure with the addition of a number of α-helices around a central core.[114]

The basic design of a coiled coil is focused on a simple heptad repeat of hydrophobic and hydrophilic amino acids, which will assemble into different oligomerization states centered around

a hydrophobic core (Figure I-9).[115] A heptad sequence is composed of hydrophobic (*h*) and polar (*p*) side chains $(hpphppp)_n$ and is assigned a label based upon the position around the helical surface of the scaffold, $(abcdefg)_n$ where two distinct, core hydrophobic layers are formed in each heptad, ***a***-sites and ***d***-sites, and the ***e***-site and ***g***-sites are salt bridging residues that are solvent exposed and flank the hydrophobic core.[116,117] Arguably, Degrado *et al*. designed the first *de novo* protein and, in general, have designed *de novo* proteins containing α-helices including those of the



B)

Helix	-Gly-Glu-Leu-Glu-Glu-Leu-Leu-Lys-Lys-Leu-Lys-Glu-Leu-Leu-Lys-Gly-
Loop	-Pro-Arg-Arg-
α_1	Ac-Helix-$CONH_2$
α_2	Ac-Helix-Loop-Helix-$CONH_2$
α_4	Met-Helix-Loop-Helix-Loop-Helix-Loop-Helix-COOH

Figure I-10: First *de novo* design protein: **A)** Schematic of the interval changes made during the design process of a 4-helix bundle, **B)** The sequence and schematic illustrating the chain structure of each design, and **C)** Guanadium denaturation curves of each design protein, showing progressive increasing stability. Adapted with permission from Ref. 118, Copyright Science 1988.

CoilSer family, forming both parallel and antiparallel three stranded coiled coils (3SCC).[116,118] The first designed protein was a four helix bundle that spanned 12-16 amino acids per chain.[118] Helical bundles were fully characterized more than 65 years ago as a structure composed of simple, repeating heptads that, depending on their composition, could mediate different oligomerization states and traverse a range of thermodynamic stability.[115,119,120]

The design began from first principles by selecting and studying sequences that would self-assemble into α-helical terameters (α_1) (Figure I-10A). Then, two identical helices together formed dimers of dimers in solution (α_2) and translating this sequence to a continuous sequence resulted in the full-length 4-helix bundle (α_4). The helix loop in this design contained a single proline residue to terminate the α-helix and two arginine residues to promote chain inversion, while the α-helix was made up of heptad repeats with leucine lining the hydrophobic core (Figure I-10B). The stability of each iteration increased as a function of the number of cross-linked chains, both because of an entropic effect and the stabilization of the oligomerization state (Figure I-10C). Compared to natural α-helix-containing proteins, α_4 formed a stable protein under guanidinium chemical denaturation conditions with a $\Delta\Delta G^{H_2O}$ of –13 kcal mol^{-1} compared to lysozyme [$\Delta G^{H_2O}(a_4)$ [a] = –22.5 kcal mol^{-1} vs ΔG^{H_2O}(lysozyme) = –8.9 kcal mol^{-1}].[121,122] In general, the effect of increasing the number of heptad repeats within a coiled coil protein depends on the balance between enthalpic stabilization from the hydrophobic core residues and the entropic destabilization resulting from the increase in the number of amino acids. [123,124] However, the coiled coil proteins used in Chapters II-IV will be stabilized by increasing the number of heptad repeats. Since the start, designers have used rational protein design and natural proteins as a guide to help build new protein architectures. From this work, the first *de novo* designed metalloprotein was developed in α_2 and α_4 where a Zn(II) histidine site was built.[22] As mentioned earlier in *Section 1* of this introduction, the binuclear copper site in hemocyanin served to provide a template α_2 and α_4 with a binding site for Zn(II) near their surface, resulting in His residues projected into a tetrahedral or

[a] the free energy of folding in the absence of the guanidinium denaturant

octahedral geometry capable of binding Zn(II) in a Zn(II)$(His)_3$ site, similar to carbonic anhydrase (CA).[125] While helical bundles have a rich design history, the self-assembling coiled coil protein serves as a distinct class of protein design that needs special considerations for the overall oligomerization states and stability.

DeGrado and Pecoraro were some of the first to design the structure of coiled coil proteins, with the first family of scaffolds coined TRI. The heptad repeat of TRI is composed of three heptads of (LKALEEK) with the N-terminus and C-terminus terminated with acetylated glycine and amidated glycine, respectively. These modifications to each terminus align the dipole associated with the helical structure and aid in the formation of the coiled coil structure.[126–129] The oligomerization states of coiled coil proteins are controlled by factors that include the shape of the buried residues in the hydrophobic core and the composition of the amino acid sequence.[130,131] The helix orientation, namely whether the helices are parallel or anti-parallel, has been shown to influence interchain electrostatic interactions among the ***e***-site and ***g***-site positions in a number of coiled coil proteins.[132] Moreover, the ***e***-sites and ***g***-sites in TRI are occupied by lysine (Lys) and glutamate (Glu), respectively, and these residues give rise to the pH dependence of the 2SCC to 3SCC equilibrium that was observed with this sequence. At low pH (<5), the 2SCC form is the major species likely because of the lower surface-to-volume ratio of the dimer compared to the trimer which reduces the electrostatic repulsion between the positively charged Lys residues and the unfavored interaction between the neutral, protonated Glu residue and the hydrophobic ***a***-site and ***d***-site Leu side-chains.[127]

It was demonstrated early in the development of coiled coil proteins that a Leu layer can be substituted by metal binding side chains without causing the TRI scaffold to become unstable.[128,133–136] Some of the first lessons on how differential sidechain packing influenced metal binding were achieved with heavy metals binding to cystine in well-defined coiled coils. The unique aspect of coiled coil proteins is that the ***a***-sites and ***d***-sites sit differently within the hydrophobic core, providing two different ligand environments for metal binding and electronic

tuning. It was shown with ***a***-site cysteines that the preferred geometry of metals dictates the extent of rotations of the ***a***-site Cys_3 layer upon binding, not the size and charge of the metal.[133,136] To accommodate any metal in trigonal planar structures, a substantial rotation of the Cys ligands is required. On the other hand, when trigonal pyramidal ions adopt an endo conformation oriented toward the C-termini of the coiled coil, the cysteine environment is preorganized. The knob-into-hole packing between adjacent helices rotates the first ***a***-site 20° out of phase with respect to the next ***a***-site below.[119,137] *These aspects, which influence side chain orientation, will become especially important in Chapter IV when the addition of 3-residue inserts (i.e., stammer) are investigated.*

The organization of the cysteine sidechains proved to be critical in designing a two-site metalloprotein in $(TRIWL9CL23H)_3$ that resulted in a stable three-coordinate $Hg(II)S_3$ site in an ***a***-site penicillamine layer (a Cys analog) (Figure I-11B) and an ***a***-site $Zn(II)His_3$ (Figure I-11C) site in the crystallographic analog $[Hg(II)]_S[Zn(II)]_N(CSL9PenL23H)_3$.[138,139] Therefore, the $Hg(II)S_3$ site served as a structural site, and the $Zn(II)His_3$ served as a potential catalytic site. The Cys_3 layer has a relatively weak affinity for Zn(II) at pH 7.5 but favored tight binding at pH 9.0 ($K_{d,app}$~3-4 nM) suggesting a significant pH dependence, while the $K_{d,app}$ for Zn(II) at the His_3 site ranged from 0.22 μM (pH 9.5) to 0.8 μM (pH 7.5). These results highlight the importance of adding metals in order when assembling metalloproteins.

In addition to providing an excellent structural model for $Zn(His)_3$ protein sites as found in native Zn enzymes such as carbonic anhydrases (CA) and matrix metalloproteinases (MMP), this design provided a scaffold to test reactivity. Specifically, this site was poised to catalyze the hydratase reaction of $CO_2(g)$ into CO_3^{2-} and esterase activity using the model substrate para-nitrophenyl acetate (p-NPA), both hallmark reactions of CAs. This system was one of the first *de novo* designed enzymes to approach the rate constant of any wild-type enzyme, mimicking CA. The hydrolytic $ZnHis_3$ site in CA approaches diffusion-limited rate constants for the hydrolytic conversion of $CO_2(g)$ into CO_3^{2-}, with human CA isoform II (CA-II) being one of the fastest

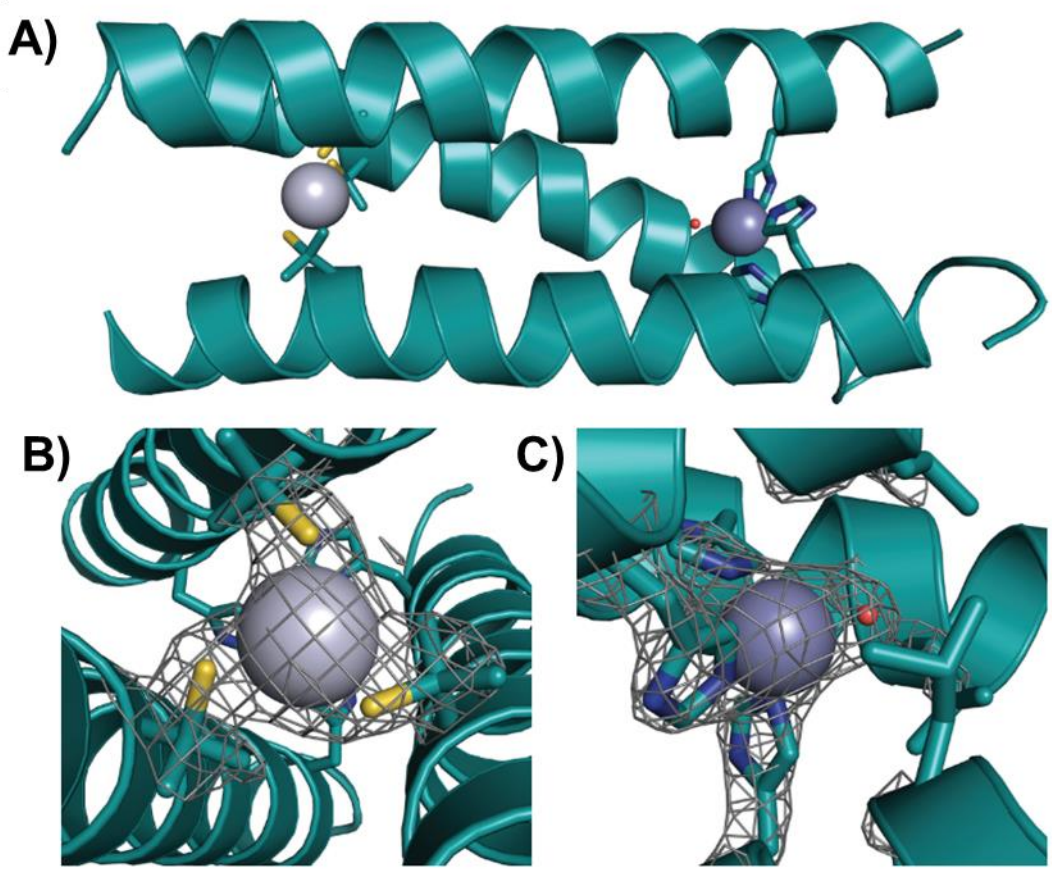


Figure I-11: Crystal Structure of $[Hg(II)]_S[Zn(II)]_N(CSL9PenL23H)_3$ (pdb:3PBJ): **A)** Overview, **B)** $Hg(II)(Cys)_3$ site, and **C)** $Zn(II)(His)_3$ site. Adapted from Ref. 236, Copyright, 2012 Nature Publishing.

enzymes currently known. From a *de novo* design perspective, two attractive aspects of CA-II are that zinc remains in one oxidation state through the catalytic cycle, and the WT enzymes contain a primary coordination sphere $Zn(II)His_3$ which could be recapitulated into a 3-fold symmetric scaffold.[140–142] In the $[Hg(II)]_S[Zn(II)]_N(CSL9PenL23H)_3$, Zn(II) is coordinated by H_2O/OH^- a three histidine, all coordinated with the ε nitrogen, while CA has a mixed structure with two εN and one δN histidine coordinated with a H_2O/OH^-. Furthermore, the crystal structure shows that the imidazole rings' overall orientations varied somewhat. With respect to catalysis, this scaffold catalyzed CO_2(g) hydration at pH 9.5 with a k_{cat}/K_m of 1.8 (±0.3) x 10^5 M^{-1} s^{-1}, which is ~500-fold from CA-II (9.2x10^7 M^{-1} s^{-1}) and within a factor of 50 of the catalytic efficiency of other native $Zn(His)_3$ enzymes. The major limitation of this Zn enzyme was that the activity occurred only at elevated pH. The fact that $[Zn(II)]_N[Hg(II)]_S(TRWIL9HL23C)_3$ catalyzed CO_2(g) hydration in

more basic media was primarily due to the increased pK_a of the Zn(II) bound water, which was recorded at roughly 2 pH units higher than CA-II (9.0 vs 6.8 for CA-II).[143] The modulation of this pK_a is a critical aspect of the mechanism of CA-II and, therefore, of any authentic CA mimic.[144,145] It was found that a larger substrate than CO_2(g) could be hydrolyzed, such as that with *p*-nitrophenyl acetate (*p*NPA) and displayed a catalytic efficiency that is 130-fold less than CA-II at pH 9.0 (Table I-2). The k_{cat} value associated with the designed scaffold is markedly lower than CA-II (1400x); however, the lower K_m value observed at pH 9 suggests easier access to the Zn(II)-OH^- than in CA-II. Interestingly, the K_m for CO_2(g) hydration (10 mM) was notably higher than pNPA (1.7 mM) which may suggest that K_m is not a reporter of enzyme-substrate complex K_d or that specific unknown interactions are at play. While the Hg(II) role is non-catalytic, the charge around the active site could impact the electronic environment around the Zn(II)-OH/H_2O, affecting the pK_a. Removal of the Hg(II)-$(Cys)_3$ layer $(TRIWL23H)_3$ did not result in a change in the steady state kinetic parameters or pK_a of the $Zn(His_3)OH_2$ species (9.2 ± 0.1), although the 3SCC became slightly destabilized. Exposing the $Zn(His)_3$ site to a more solvent accessible position near the N-terminus, $[Zn(II)]_N[Hg(II)]_S(TRIL9HL23C)_3$, lowered the Zn(II) affinity for the His_3 site by a factor of 4 at pH 9. The k_{cat} at this position was halved with respect to $[Hg(II)]_S[Zn(II)]_N(TRIWL9CL23H)_3$ while the K_m was relatively unchanged (Table I-2). The drop in k_{cat}/K_m from 23.3 ± 0.3 M^{-1} s^{-1} to 15.8 ± 1.1 M^{-1} s^{-1} in the flipped design suggests that a barrier to activation of a chemical step has increased. This barrier may be associated with the deprotonation of the solvent-exposed $Zn(His_3)OH_2$ as the kinetic pK_a increased by 0.2 units from the buried active site and the competitive $K_{i,acetate}$ of $[Zn(II)]_N[Hg(II)]_S(TRIWL9HL23C)_3$ (0.20 ± 0.01 M) is lower than $[Hg(II)]_S[Zn(II)]_N$ $(TRIWL9CL23H)_3$ (0.32 ± 0.01 M) which may suggest the substate is still too large to access the $Zn(His)_3OH_2$ site even in a more solvent exposed position.

It is worth mentioning that these designs have used an ***a***-site His, and the orientational distinctions between the ***a***-site and ***d***-site packing did not affect the pNPA activity to any reasonable degree (Table I-2).[139] Despite the changes made in the designed peptide above, little

has changed in terms of the kinetics of the enzyme. Cangelosi *et al*. designed a Zn(II)$(His)_3$ site into a single-stranded antiparallel three helix bundle.[146] The initial design was based on the 73 amino acid α_3D designed by DeGrado *et al*. and featured the $Zn(His)_3$ site near the N-terminal of the fold.[147] This parent scaffold yielded a $Zn(His)_3OH_2$ site that was more basic (kinetic pNPA pK_a=9.4) and catalyzed the hydrolysis of CO_2(g) with a k_{cat}/K_m that was 4.7 lower than $[Hg(II)]_S[Zn(II)]_N(TRIWL9CL23H)_3$. Design considerations have been focused solely on the primary coordination sphere thus far and has proven adequate in achieving catalytic efficiencies approaching those of the native enzyme (within 500x). This underscores the capacity of diverse protein structures and the primary coordination sphere to enable efficient catalytic turnover. In an attempt to retro-design the secondary coordination sphere of CAII, a threonine was mutated into the ***d***-site above the ***a***-site histidine $[Hg(II)]_S[Zn(II)]_N(TRIWL9CL19TL23H)_3$ which showed negligible saturation in the steady state kinetics with pNPA.[148] However, the substitution of Zn(II) for Co(II) in the His_3 site of TRIWL23H resulted in a doubling of the $k_{cat}/K_{m(max)}$ with respect to the *p*NPA hydrolysis.[149] It is tempting to attribute this increase to the differences in Lewis acidity. However, contrary to cases where Co(II) has been used as a faithful spectroscopic substitute for Zn(II) in hydrolytic metalloproteins, the geometry of the Co(II)-site is best described as CoN_3O_3

Table I-2: Kinetic parameters for hydrolysis of *p*NPA by Zn(II)-Peptides at pH 9.5

Enzyme	pK_a	k_{cat} (s^{-1})	K_m (mM)	k_{cat}/K_m (M^{-1} s^{-1})	$(k_{cat}/K_m)_{max}$ (M^{-1} s^{-1})
$[Hg(II)]_S(TRIWL9C)_3$ +Zn(II) (pH 9.0)		N/A	N/A	1.8 ± 0.2	N/A
$[Hg(II)]_S[Zn(II)]_N$ $(TRIWL9CL23H)_3$	~9.0	0.040 ± 0.012	1.7 ± 0.5	23.3 ± 0.3	31 ± 4
$Zn(II)(TRIWL23H)_3$	9.2 ± 0.1	0.033 ± 0.002	2.1 ± 0.2	15.5 ± 0.4	25 ± 2
$[Hg(II)]_S[Zn(II)]_N$ $(TRIWL9HL23C)_3$	9.2 ± 0.1	0.020 ± 0.002	1.2 ± 0.2	15.8 ± 1.1	24 ± 3
$[Hg(II)]_S[Zn(II)]_N$ $(TRIWL9CL19H)_3$	9.6 ± 0.1	0.035 ± 0.004	2.8 ± 0.4	12.4 ± 0.4	27 ± 5
CA-II (pH 9.0)	6.8	56 ± 10	23.9	2320	N/A

at pH 8.0 and CoN_3O_2 at pH 10.8 which is different from the tetrahedral ZnN_3O observed in $Zn(II)(TRIWL23H)_3$ within the same pH range.[150,151] The kinetic pK_a associated with *p*NPA hydrolysis increased in the Co(II) analog (10.32 ± 0.01) when compared to the Zn(II) site (9.2 ± 0.1) likely representing the geometry differences around the two metal sites and resulting Lewis acidity.[145,152] Despite this increase in pK_a, the Co(II) analog exhibited a 2x higher $k_{cat,max}$ value ($129 \times 10^{-3}\ s^{-1}$) signifying an increase in the chemical step(s) of the catalytic mechanism.

Other CA mimics have been designed that differ in the overall topology from the designs mentioned above. Two designs that I will briefly highlight are the works of the Kuhlman group and the Hilvert group to build a catalytic site at the interface between the assemblies' faces.[153,154] The metal-assisted helix-turn-helix design (MID1) is interesting because very little has been done in *de novo* design to build active sites at protein interfaces, and most designs feature active sites that are buried in folded scaffolds due to potential extra layers of interactions to facilitate the formation of protein interfaces.[155,156] Furthermore, the scaffold's design demonstrates how seemingly innocent residues located far from the active site can serve as design-points that produce catalytic activity exceeding that of the natural enzymes, CAII in this case. The solid-state structure of Zn(II)MID1 shows the Zn(II) ion is coordinated by three histidines $[Zn(N_\varepsilon)_2(N_\delta)]$ within a shallow, accessible opening at the interface which was hypothesized to support hydrolytic activity. This site catalyzed pNPA hydrolysis with a $k_{cat}/K_{m,\,(max)}$ 630 $M^{-1}\ s^{-1}$ with a pK_a of 8.2 ± 0.1 compared to the k_{cat}/K_m 23 $M^{-1}\ s^{-1}$ of $[Hg(II)]_S[Zn(II)]_N(TRIWL9CL23H)_3$ and 2550 $M^{-1}\ s^{-1}$ of CAII. [157,158] With this shallow, accessible opening in Zn(II)MID1, the K_m was 50x tighter than the native enzyme and may suggest the observed decrease in k_{cat} may be due to either a slowing of substrate activation or a lower substate recognition due to the lack of specific secondary sphere interactions as in the native enzyme.[159]

Studer *et al*. attempted to overcome this lack of specificity in Zn(II)MID1 by using a directed evolution whereby activity screening would guide the evolutionary selection process to the optimal secondary sphere interactions.[160] The associated dimer structure of Zn(II)MID1 was

linked into a single chain by a Gly-Ser loop, and the second Zn(II) site was deleted to form a more well-defined, stable structure *in vivo* (Zn(II)MID1sc).[160] After nine rounds of screening, the Zn binding site was altered by the swapping the His39 for the second strand's His35 in the primary coordination sphere, resulting in a less staggered dimer interface in the Zn(II)MID1sc9. It is noted by the authors that the His35 mutation was mutated mid-way through the evolutionary trajectory (after round #3), which prompted them to remove potential Zn(II) binding pockets around the new Zn(II). The resulting MID1sc10 design displayed esterase activity that was 10,000-fold greater than the MID1sc (k_{cat}/K_m =980,000 M^{-1} s^{-1}) and out competed human CAII in pNPA activity. The crystal structure of Zn(II)MID1sc10 reveals a crossover angle between two dimers of the helix turn helix portion that decreased to 47° (change of >30°) to a less staggered conformation which is still quite a bit larger than the 20° crossing angle observed in nominal four-helix bundles. Furthermore, this results in the switching of the primary histidine in Zn(II)MID1sc9 mentioned previously. In the case above, with the aid of directed evolution, an enzyme can be designed to yield a very efficient enzyme that outcompetes the native enzyme.[160] The key points from the above examples are that: i) catalytic activity can be obtained in a scaffold that is completely different from the natural enzyme's scaffold; ii) remarkable catalytic efficiencies can be achieved by designing around the primary coordination sphere, even if the C_3-symmetry of 3SCC limits their ability to fully include the secondary coordination sphere; and iii) residues that seem innocent can be leveraged to control how the primary coordinate sphere sits within the protein scaffold and control substrate access by opening up the active site. It should be noted that others, (*i.e.*, Tezcan's lab) have exploited symmetry to designed protein-metal interactions at interfaces to control assembly and catalysis; however, the reader is en.[153,156,161,162]

While there are many examples of *de novo* designed metalloenzymes that contain Zn(II), copper metalloenzymes are underrepresented among the metals. There are four types of examples of designed copper proteins which cover electron transfers in cupredoxins,[11,163] superoxide dismutase,[164] oxygen activating sites,[165] and copper nitrite reductase.[166–169] Pecoraro *et al*. set out to design a functional mimic of copper nitrite reductase in light of the 3-fold symmetry of the

active site, composed of three histidines chelated to the copper with the ε-N. The first design was based on the very scaffold that was used to design a functional carbonic anhydrase mimic; therefore, only switching the Zn(II)His_3 site to a $CuHis_3$ site may yield an active site that could reduce nitrite and thus reflect the design of a simple redox-active mono-copper center. From a more general standpoint, the transition from non-redox catalysis to redox catalysis represents a change in the basic design principles that needs to be considered between the two proteins. This is a meaningful designation because the active site must be finely tuned towards the appropriate geometry to accommodate two different oxidation states, ultimately controlling the reduction potential. The geometric preference for Cu(II) in a T2Cu center is distorted square planar, while Cu(I) in proteins tends to be found in tetrahedral or trigonal geometry.[170] Most of the evidence from numerous different spectroscopies of the T2Cu site in CuNiR suggests that at least one water or hydroxide ligand is bound in the resting Cu(II) oxidation state. Overlay of the crystal structure of CuNiR and $[Hg(II)]_S[Zn(II)]_N(CSL9CL23H)_3$ displays structural similarities between the two active sites, where the histidines are oriented in a different dihedral angle (Figure I-12A). Both Cu(II)/Cu(I) showed tight binding to the L23H ***a***-site position (TRIW-H) at pH 5.9, with the Cu(II) $K_{d,app}$ observed at 4.04×10^{-8} M and the Cu(I) binding at 3.09×10^{-12} M with a reduction potential of 400 mV SHE.[166] At physiological pH (7.4), TRIW-H binds more tightly to both oxidation states, with a reduction potential of 430 mV SHE. X-band EPR and Cu K-edge EXAFS of Cu(II)-TRIW-H suggest the active site is most consistent with a Cu(II)His_3 site with one or two bound waters, which matches the description of oxidized forms of native CuNiR's T2Cu center. The Cu(II)-TRIW-H is reduced by ascorbate at pH 5.8 with a pseudo 1st order rate constant of 5.2×10^{-4} s^{-1}. Upon reduction, one or two waters are lost to form a 3-cooridanate Cu(I) active site, and in the presence of substrate, NO_2^- is reduced to NO(g) with a pseudo 1st order rate constant of $4.6x10^{-4}$ s^{-1} (Table I-3). The production of N_2O(g) as an off-cycle product was monitored, revealing that Cu(I)-TRIW-H produced no observable N_2O(g) under pseudo-first-order conditions.[171,172] TRIW-H was the first to produce CuNiR activity in a non-native fold, despite the fact that a unphysiological pH (5.9) was necessary to achieve turnover and was significantly slower than

native CuNiR. As mentioned before, the secondary coordination sphere of all CuNiR feature conserved residues that serve a particular purpose: i) Asp_{CAT} (orients NO_2^- and activates the N–O bond through H-bonding),[60,173] and ii) Ile_{CAT} (orients NO_2^-).[174,175] The design of both steric or acid-base residues above and below the active site resulted in changes that suggested inherent limitations with the 3-fold symmetry of the 3SCC with respect to the Asp layer; however, the alanine layer turned out to be more interesting (Figure I-12B).[168] The pseudo first order rate constants increased by two orders of magnitude when the leucine layer above (L19) or below (L26) was mutated with either aspartate or alanine compared to TRW-H, while increased activity in these mutants was correlated with a blue shift in the 1s-4p edge shift in the Cu(I) XANES. The electronic structure and geometry of the Cu(I) site may be the cause of the increased activity, although the exact reason for this was unclear at the time. Remarkably, the addition of aspartate in close proximity to the substrate did not result in the expected enhancement of activity related to native CuNiR functional studies that mutated the acid-base residues out of the second coordination sphere.[176] Furthermore, alterations to the ***d***-site layers either above or below the active site (L19 vs. L26) yielded similar kinetics to one another, indicating that although the L26 layer is more C-terminally situated and solvent exposed, the overall impact on catalysis is relatively inert. According to earlier research using $Cd(II)(Cys)_3$ sites incorporated into 3SCC, changes in coordination number were caused by the relative steric packing above the metal site. As the alanine mutation just above the Cu(I) site (L19A) generates a $Cu(I)(His)_2$ site based on the XANES and EXAFS (ca. $Cu(I)–N_{His}$ 1.86 Å) from a $Cu(I)(His)_3$ site in TRIW-H, this work suggests that decreasing steric bulk in the layer towards the N-terminus of an ***a***-site metal might be a typical feature within 3SCCs that could be leveraged to perturb the active site design.[177]

To explore the perturbations caused by an Asp layer further, a His_3 site was designed into an antiparallel three helix bundle, GRWα_3D, which allowed the positioning of a single Asp near the active site (Figure I-12C).[178] Interestingly, placing one aspartate near the active site, GRWα_3D H_3D, decreased the CuNiR activity to that of GRWα_3D (18x decrease in *k*'). Moving the aspartate

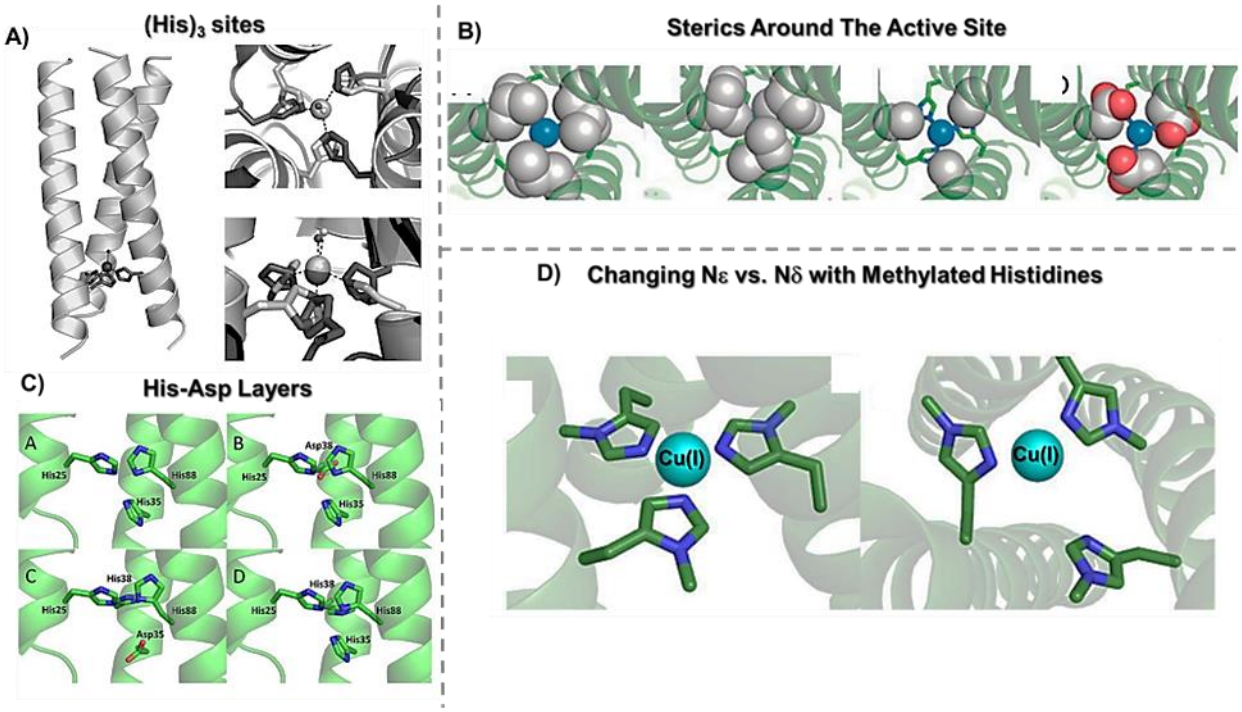


Figure I-12: Summary of *de novo* designed CuNiR within 3SCCs: **A)** TRIW-H overview (*left*) and overlay with native CuNiR showing the similarity of the designed active, **B)** PyMol models of TRIW-H L19I, L19D, L19A, and L19D (*left* to *right*) showing the change of steric packing around the active site, **C)** PyMol models of apo binding site within GRW-α_3D H_3 and GRWα_3D H_3 ***A***, GRWα_3D H_2DH ***B***, GRWα_3D H_3D ***C,*** GRWα_3D H_{4d},and **D)** Models of Cu(I)-TRIW-δ_mH (*left*) and Cu(I)-TRIW-ε_mH (*right*) based on EXAFS analysis. Adapted with permission from Ref. 166, Copyright 2012 PNAS; Adapted with permission from Ref. 168, Copyright 2018 Angewandte Chemie; Adapted with permission from Ref. 177, Copyright 2021 Springer Nature; Adapted with permission from Ref. 167, Copyright 2019 American Chemical Society.

slightly closer to the His_3 layer, GRWα_3D H_2DH resulted only in a 1.9x rate enhancement compared to GRWα_3D H_3 and 11x compared to GRWα_3D H_3D (Table I-3). Overall, the increase in the pseudo 1st order rate constants tended to be associated with shorter average Cu-N_{His} bond distances (1.87-1.89 Å) and two coordinate Cu$(His)_2$ sites. In comparison to the 3SCC, none of the GRWα_3D mutants competed with the simple design of TRIW-H L19A that displayed an increase in activity of 76x compared to TRIW-H and consists of a well-defined Cu(I)$(His)_2$ resting state (Cu-N_{His} 1.86 Å).

This switch in coordination mode towards Cu(I)$(His)_2$ will affect the reduction potentials of the copper center and could play a major role in priming the copper center to reduce nitrite.

With this in mind, mutations to the solvent exposed Lys22, Lys24, and Glu27 to neutral or negative charge side chains (maximum of Δ_{charge}= -12) resulted in T2Cu centers with reduction potentials that spanned ~100mV, and changed the Cu(I) $K_{d,app}$ by 2 orders of magnitude while not changing the Cu(II) $K_{d,app}$.[169] This +100 mV change in reduction potential only changed the CuNiR pseudo 1st order rate constants by a factor of 3.5x suggesting the change in reduction potential is not responsible for the change in reactivity with the Cu(I)$(His)_2$ sites. Of the design strategies employed, the CuNiR activity has increased 78x from the parent scaffold TRIW-H, with the fastest mimic simply employing a ***d***-site alanine layer above the active site TRIW-H. The alanine may add flexibility by disrupting the local packing directly above the active site slightly as previously shown in coiled coil proteins.[179] This relaxing likely results in the Cu(I) oxidation state preferring two-coordinate Cu(I)$(His)_2$ and results in a higher Debye–Waller factor compared to the Cu(I)$(His)_3$ structure of TRIW-H. As pointed out previously in this introduction chapter, the structure-function relationship involving T2Cu centers in N_ε or N_ε binding modes and their ability to undergo either catalysis or electron transfer processes has been a long-standing hypothesis in terms of the electronic and flexibility contributions during the respective function. Taking advantage of the well-defined scaffold of the TRIW-H family, both δN-methyl histidine and

Table I-3:Kinetic parameters of Pecoraro *et al*. designed CuNiRs.

Enzyme	k' (s^{-1})	k_{cat} (s^{-1})	K_m (M)	k_{cat}/K_m (M^{-1} s^{-1})
TRIW-H	4.6×10^{-4}	N/A	N/A	N/A
TRIW-H L19A	3.5×10^{-2}	0.23 (±0.03)	0.24 (±0.03)	1.0 (±0.3)
TRIW-H L19D	2.5×10^{-2}	N/A	N/A	N/A
TRIW-H L26A	2.2×10^{-2}	N/A	N/A	N/A
GRWα_3D-H_3	8.1×10^{-3}	N/A	N/A	N/A
GRWα_3D-H_2DH	4.8×10^{-3}	N/A	N/A	N/A
GRWα_3D-H_3D	4.6×10^{-4}	N/A	N/A	N/A
TRIW-δ_mH	0.12	1.5 (± 0.1)	0.18 (± 0.02)	8.2 (± 0.1)
TRIW-δ_mH L19A	0.30	1.5 (±0.1)	0.13 (±0.01)	11 (±0.1)
TRIW-ε_mH	4.1×10^{-3}	N/A	N/A	N/A

εN-methyl histidine were substituted for the His residues to determine the preferred binding mode for CuNiR activity (Figure I-12D).[167]

In accordance with the hypothesis that the N_ε is the preferred orientation for catalysis, the δNmethyl histidine (TRIW-δ_mH) resulted in a two order of magnitude increase in the pseudo first order rate constants compared to the parent TRIW-H design (0.12 s^{-1} vs. 4.6×10^{-4} s^{-1}), while the TRIW-ε_mH only increased the rate constant by a factor of 2.6. Again, the alanine in the ***d***-site above the Cu(I) site relaxed the more three coordination Cu(I) to the preferred two-coordination Cu(I)$(His)_2$ site, TRIW-δ_mH L19A, and increased the pseudo 1st order rate constant by 652x compared to the TRIW-H (Table I-3). The alanine layer only increased by a factor of 2.5x compared to the TRIW-δ_mH with the k_{cat} invariant, with only a small change in K_m contributing to the overall activity increase, suggesting that the pyridine-like character of the N_ε around the copper center is important in at least one chemical step in the mechanism. These designed CuNiR provide examples of the difficulty in recapitulating the redox active site into a totally different fold. Moreover, the lack of improvement on the activity may reflect a change in N_ε or N_δ binding modes that compose the $CuHis_3$ ($CuHis_2$) sites, for example, of the GRWα_3D series, where at 7.5, two electronically distinct mono-copper active sites were observed in the X-band EPR of Cu(II)-GRWα_3D H_3 and Cu(II)- GRWα_3D H_4 with $A_{||}$ values suggesting both N_δ and N_ε binding modes are present as greater than a 25% contribution to the spectra.[164] This has not been reported in the T2Cu site in native CuNiRs; however, speciation has been reported in native enzymes substituted with non-native metals into the active sites, for example, Co(II) substituted carbonic anhydrase.[180,181] In general, achieving a well-defined binding pocket has plagued quite a few *de novo* designed metalloproteins.[165,182,183]

When oxygen is used as an electron acceptor, it produces reactive intermediates like the superoxide radical [$O_2^{\bullet}$], which cause oxidative damage to organisms. To counteract these pathways, detoxification systems are required. [184,185] Native superoxide dismutase enzymes (SOD)

target superoxide in many organisms with four different redox metals cofactors (Fe, Mn, Ni, Cu) in relatively solvent-exposed active sites within a β-sheets fold.[23] All of these enzymes operate near diffusion limited rate constants and are appealing enzyme to target for *de novo* design, both testing our understanding of the protein-function relationship and designing therapeutic/diagnostic tools. The primary coordination sphere is quite diverse in the native enzymes ($MnHis_3Asp$, $FeHis_3Asp$, $NiHis_2Cys$, $CuHis_2$-His-$ZnHis_2$, and $CuHis_4$), but only one has been targeted for design so far.[23] From a design perspective, to simply design around the Cu-only SOD (CuSOD) is attractive given the relative symmetry of the binding site within CuSOD site.

The Pecoraro and Policar labs have explored the design of a CuSOD in a three helical bundle, $GR\alpha_3D$, to modulate the reactivity by changing the fourth ligand and reduction poteintals.[164] A small library of mutants was created: His_4 (H_4), His_3 (H_3), $His_2AspHis$ (H_2DH), and His_3Asp (H_3D), where the native primary coordination sphere was targeted (H_4) and mutants changed the position within the plane that the aspartate residue resides with respect to the His_3 ligands. The objective was to test the function of the aspartate location on catalysis (Figure I-12C). Based on XAS analysis, the Cu(II) average bond distances were slightly longer than those in the 3SCC peptide TRIW or GRW peptides (1.94-1.95 A at pH 7.5). All mutants in this library were found to have a coordination environment composed of Cu-His_3O_1 (Cu-His_4 for the mutant H_4). The aspartate's oxygen contribution in Cu(II)-H_2DH and Cu(II)-H_3D is unclear, as the oxygen could result from either H_2O or OH^-. Nevertheless, the H_2DH construct has a lower reduction potential than H_3 and H_4. An aspartate or OH^- may be bound to the Cu(II) oxidation state, as shown by the $K_{d,app}$ value, destabilizing the Cu(I) oxidation state. The reactivity toward superoxide was confined to a limited range (1.8-12.6 [$\times 10^6$] M^{-1} s^{-1}) with the activity correlating with the reduction potentials of each of the constructs. Although the secondary coordination sphere had little to no effect on activity, it is impossible to draw any firm conclusions about why the aspartate had minimal effect on catalysis because we do not know the structural details of the scaffolds.[186]

Copper enzymes are also able to carry out C-H bond abstraction reactions. All T2Cu copper monooxygenases and oxidases react with dioxygen at the Cu(I) oxidation state and form three proposed catalytically relevant Cu oxygen derived adducts that are responsible for oxidation of C-H bonds; 1) Cu(II)-superoxide adduct (Cu(II)-$OO^{-\bullet}$), 2) Cu(II)-hydroperoxide (Cu(II)-OOH),[187,188] and 3) Cu(II)-oxyl (Cu(III)-O^{2-}/Cu(II)-O^{-}, $[CuO]^{+}$).[189–191] The Cu(II)-superoxide adduct has been observed in the solid state adduct of peptidylglycine-α-hydroxylating monooxygenase (PHM).[192] Although to a lesser extent, designed proteins have also been explored in the context of O–O and O–H bond activation. Chakraborty *et al.* have recently reported a 3SCC, similar to those reported by Pecoraro *et al.*, with a monocopper $CuHis_3$ site (T2Cu) that had the

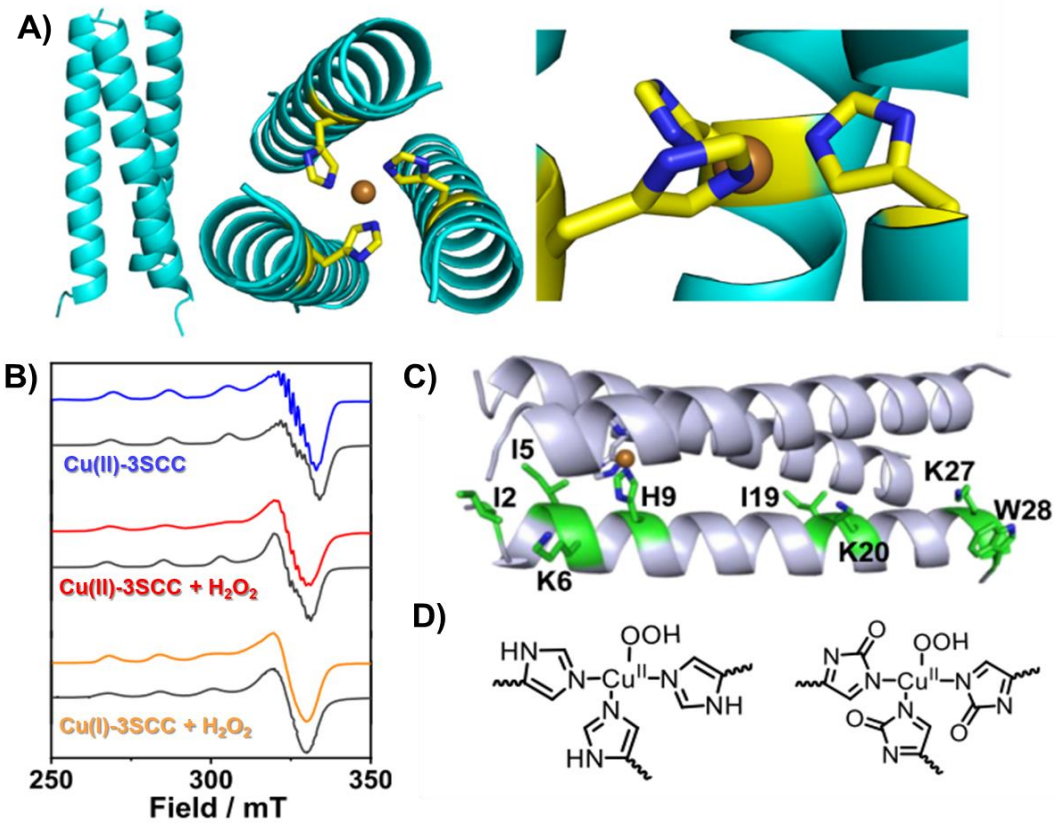


Figure I-13: X-ray structure of the Cu(II)-ArCuP (pdb:7L33): **A)** 1.45 Å X-ray structure of the Cu(II)-ArCuP (pdb:7L33), **B)** X-band EPR spectra of the ArCuP under different conditions at pH 7.5, **C)** Amino acid oxidation sites detected in LC−MS/MS shown as green, and **D)** Putative structure with Cu(II)-ArCuP having unoxidized His ligands (*left*) and with Cu(I)-peptide bound to 3-oxo His ligands (*right*) Only. Adapted with permission from Ref. 193 Copyright 2021 American Chemical Society.

capability of forming a long-lived Cu(II)-OOH intermediate upon the introduction of H_2O_2.[193] The crystal structure of the purported Cu(II) resting state revealed three histidines coordinated in the N_ε mode to copper with an average Cu(II)-N of 2.02 Å; however, the bond distances that the copper site exhibited might be the consequence of radiation damage. None-the-less, this report represents the first crystal structure of Cu adduct bound to histidine within a 3SCC (Figure I-13A). The design allowed for the immobilization of the Cu(II)-3SCC on a PGE electrode to characterize the redox behavior of the catalyzed H_2O_2 reduction (Figure I-14A). The artificial copper peptide (ArCuP) peroxide reduction activity was measured by the catalytic parameters k_{cat} and K_M. While the K_m of H_2O_2 reduction (3 mM) was only a factor of 2 lower than that of the highly active decaheme cytochrome MtrC, the k_{cat} (0.72 s^{-1}) was 7x slower.[194] In contrast to the benchmark enzyme, horseradish peroxidase (HRP) has a significantly lower K_m of 0.2 mM (Figure I-14B-D). During catalytic turnover, the Cu(II)-OOH unit was speculated to be responsible for the oxidation of the C1 position of the coordinated histidine, likely resulting in catalytic inactivation over time. Distant amino acids (5-28 Å from the Cu center) were also oxidized, specifically isoleucine, lysine, and tryptophan, which have also been reported in LMPO (Figure I-13C-D).[191] The oxidation of the histidine could be observed by the LC-MS spectra, and differences could be seen in the Cu(II) binding environment via the EPR/UV-Vis spectra of $[3SCC\text{-}Cu(I9H)_3]^{2+}$ + H_2O_2 vs. $[3SCC\text{-}Cu(I2H)^3]^+$ + H_2O_2 (Figure I-16B). Only in the reduced peptide is the oxidized His detected (Mass spec), which is the source of the spectrum differences of the Cu(II)−OOH species created with Cu(II) versus Cu(I) forms of the peptide. While monocopper sites are capable of producing strong oxidizing units with copper oxygen adducts, coupled binuclear copper sites also generate strong oxidizing copper units, such as those sites in polyphenol oxidases. Of this class of binuclear copper sites, tyrosinase and catechol oxidases are the most studied of the type 3 copper centers. Lombardi *et al*. recently

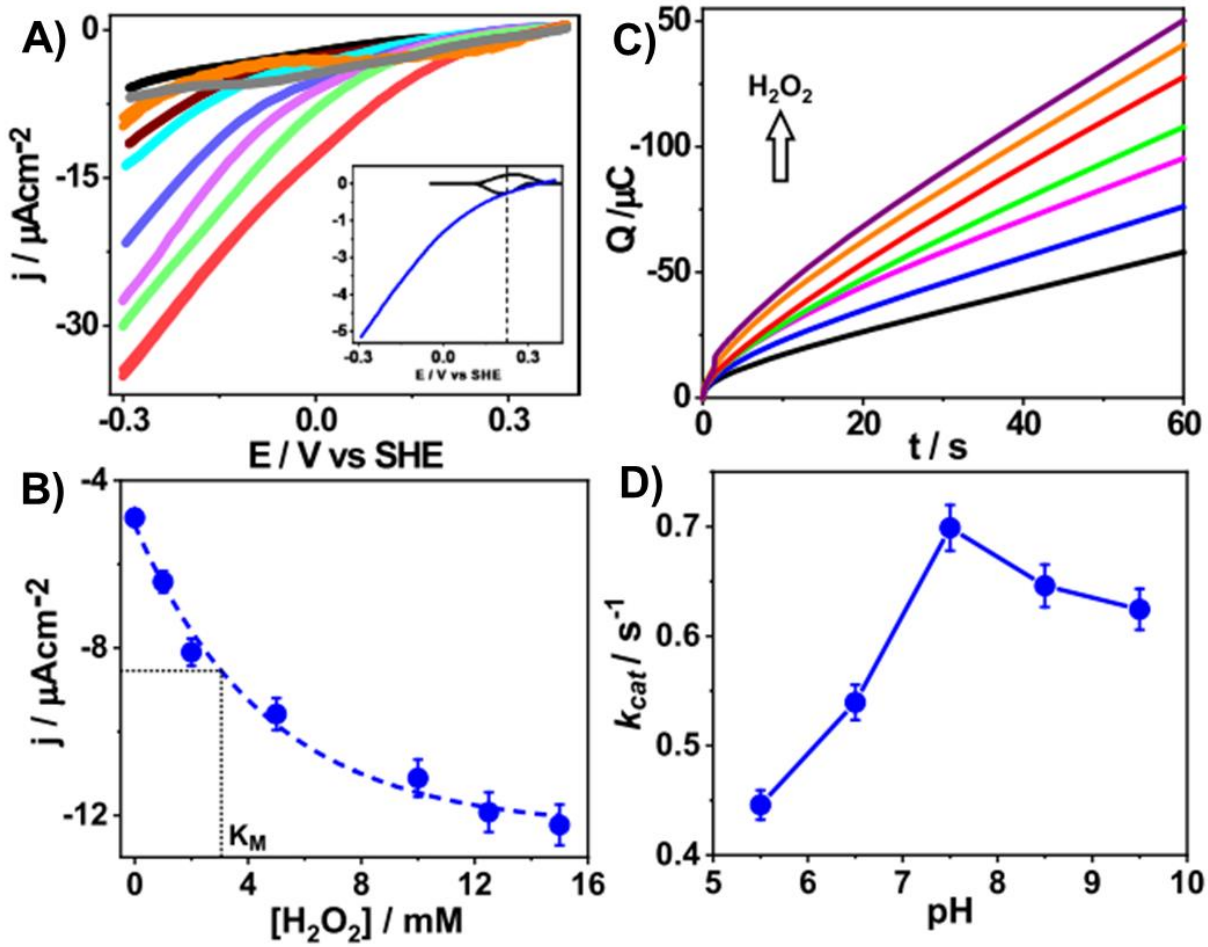


Figure I-14: A) LSVs of blank PGE in the absence (black trace) and presence of 1 mM H_2O_2 (wine trace), apo [3SCC-(I9H)$_3$] (cyan trace), free Cu(II) with 1 mM H_2O_2 (gray trace), and [3SCC-Cu(I9H)$_3$]$^{2+}$ films on PGE (blue trace) in the presence of 1 mM H2O2 in N2-saturated 80 mM mixed buffer at pH 7.5. Magenta, green, and red traces are LSVs in the presence of 2,5, and 10 mM H_2O_2. The orange trace is after the rinse test. The inset is an overlay of the noncatalytic redox peaks and the corresponding LSV with 1 mM H_2O_2 shown at a fourfold decreased scale to demonstrate that the catalytic H_2O_2 reduction is coupled to the reduction of Cu(II) to Cu(I). ν = 100 mV s^{-1}. The shaded regions represent error bars from three separate experiments of fresh protein films at each condition, **B)** Charge vs time traces from chronoamperometry experiments of Cu-peptide films on PGE at −0.3 V vs SHE in the presence of 0−15 mM H2O2 in 80 mM N_2-saturated mixed buffer at pH 7.5, **C)** Plot of the corresponding catalytic current densities vs H_2O_2 showing a KM of~3 mM, and **D)** Plot of k_{cat} vs pH at 12.5 mM H_2O_2. The error bars are from 2−3 independent measurements. Adapted with permission from Ref. 193 Copyright 2021 American Chemical Society.

designed a type 3 copper site in Due Rame 1 (DR1), a C_2 symmetric four helix bundle composed of two helix-loop-helix folds that, upon association, form a hydrophobic core.[165] This is an illustration of how to construct a flexible active site with a *de novo* metalloenzyme (Figure I-15A). The initial design started with the antiparallel four-helix bundles DF1, from Degrado's lab, that feature a di-iron $(Glu)_4$, $(His)_2$ metal binding site buried within the core.[195] The design strategies were composed of three categories: i) design the first coordination sphere to bind a di-copper site within the $(Glu)_4$, $(His)_2$ core via ***a***-sites and ***d***-sites; ii) redesign the H-bond network in the second coordination sphere to interact with the His ligands; and iii) create a substrate access channel around the active site. The original di-iron site was modified to closely align with several native T3Cu sites, resulting in His10, His32' (from the other symmetry-related helix-loop-helix), and His39 composing the copper triad (Figure I-15B and C). Furthermore, possible copper-binding side chains were removed to prevent adventitious binding. The second coordination sphere environment required the addition of salt-bridging residues to stabilize the N_δ-His mode to the copper through H-bonding to the N_ε (Figure I-15D-F). The substrate channel was formed by optimizing positions 9/9' and 13/13' towards both substate accessibility and protein stability which led to L9/L9 and A13/A13' as a balance between the two parameters (Figure I-15G-H).[108] The apo-protein folded as a homodimer, and the addition of $CuSO_4$ led to an overall change in the secondary structure, suggesting major changes around the active site upon the formation of the dinuclear Cu site. The $K_{d,app}$ for Cu(II) was reported to be 5μM for this dicopper site at pH 7.5, while native type 3 sites have an estimated $K_{d,app}$ of 10^{-15}.[196] Moreover, isothermal titration calorimetry shows that the binding of Cu(II) is an entropically driven process, suggesting that the active site of di-Cu(II)-DR1 is not predisposed for Cu(II) binding due to structural changes associated with copper binding.[196,197] However, the electronic structure of the di-copper site shows a weak d-d band (621 nm, ε=100 M^{-1} cm^{-1}) that is similar to those found in other type 3 copper centers, such as tyrosinase and catechol oxidases.[198,199] Upon the addition of 3,5-di-tert-butylcatechol (DTBC) to di-Cu(II)-DR1, 1 eqv. of the quinone 3,5-di-*tert*-butyl-o-benzoquinone (DTBQ) was exclusively detected as the electron-oxidized product, and upon the addition of

dioxygen, the oxidized *o*-quinone was detected, demonstrating diphenolase activity. The kinetics obeyed saturation kinetics with a k_{cat}/K_m value of 9.2 ($\pm$ 0.4) $\times$ 10^4 M^{-1} min^{-1} with a sub-millimolar K_m value of 0.7 ($\pm$ 0.06) mM. Saturation transfer difference NMR spectra are most consistent with DTBC orientating near the di-Cu(II) core, with DFT suggesting the *tert*-butyl (tBu) groups docked near the hydrophobic resides in the core, and the less sterically hindered oxygen is seated close to the di-Cu(II) core. A screen of different di-phenol substrates with steady state kinetics revealed that more hydrophobic substrates tended to have lower K_m, with the Hammett plot suggesting a positively charged transition date (ρ= −1.6) and the *t*Bu interacting with the hydrophobic core to orientate the substrate during catalysis. In closing, not only does this scaffold depict a properly designed primary coordination sphere to recapitulate a T3Cu site, but the interactions between the sculpted secondary spheres were found to be essential for substrate binding and recognition.

This section has covered relevant topics that will be necessary to understand the work in Chapters II–IV and their conclusions. The main points highlighted in this section emphasis the primary coordination sphere and the role that the secondary coordination sphere plays in modifying the primary coordination sphere and substate binding. The next section will describe non-heptad inserts to unwind and over-tighten coiled coil proteins around their superhelix axis, a unique feature of coiled coil proteins that will be explored to perturb the primary and secondary coordination spheres of 3SCC in Chapter IV.

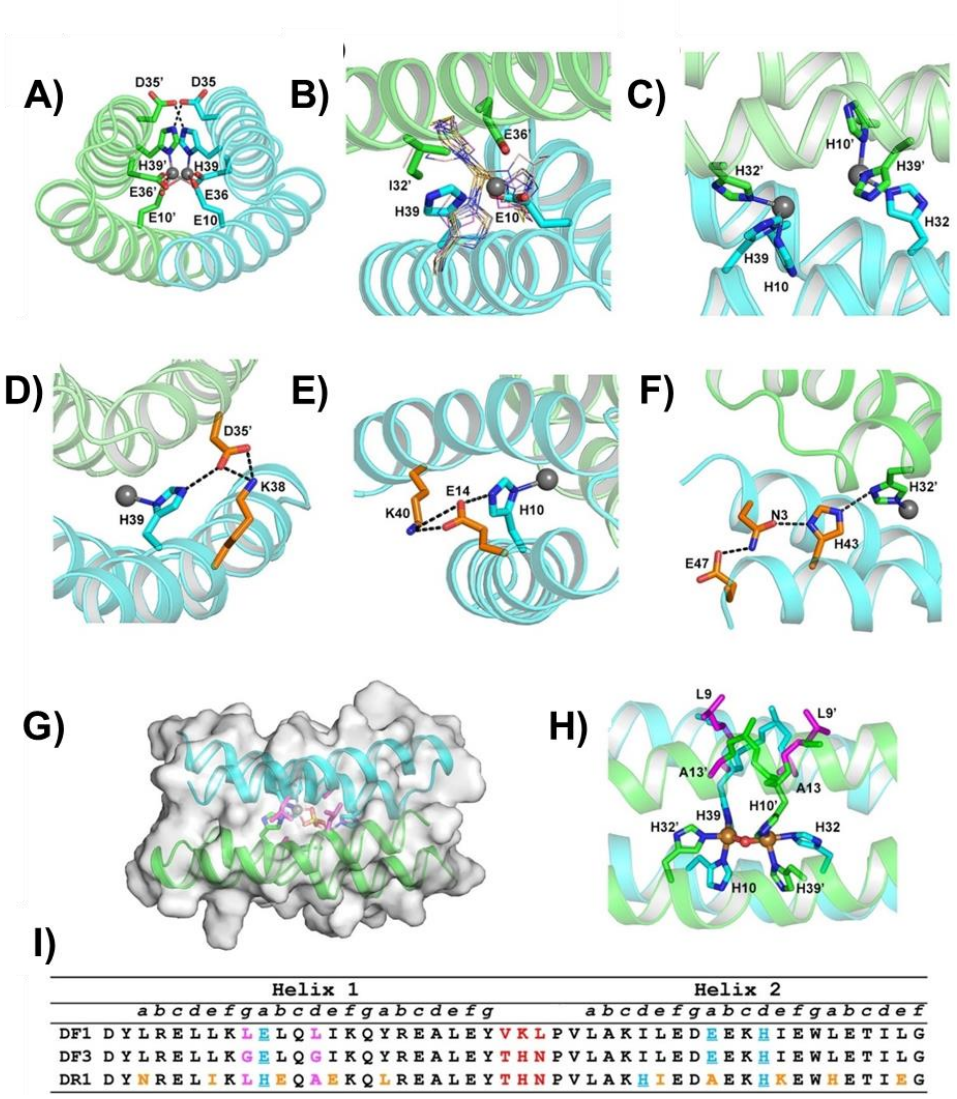


Figure I-15: Overview of the design of a type 3 copper site in Due Rame 1 (DR1): **A)** the active site of di-Zn(II)-DF1 (PDB ID: LEC5). **B)** superposition of the DF1 metal binding site, with one coordinating His triad from multiple T3 copper proteins and the emphasis of the **a** and **d** residues within 7 Å from a single Zn(II) ion. Sticks and spheres are used to symbolize side chains and the metal ion of DF1, respectively. The native proteins' triad sidechains and copper ion are shown as lines.; **C)** DR1 T3 di-copper site; **D)** H-bond network of His39; **E)** H-bond network of His10; **F)** H-bond network of His32; **G)** Centroid structure of the most abundant cluster determined on DR1 trajectory by cluster analysis (**H)** details from DFT calculations about the di-Cu(II)-DR1 active site. His coordinating residues are shown, along with Ala and Leu, who shaped the entrance cavity; **I)** alignment of the DR1 α2 motif peptide sequence with DF1 and DF3. Residues bordering the access site are given in magenta, loop residues in red, and coordinating residues are provided in cyan and underlined for every sequence. The other DR1 substitutions concerning DF1/DF3 are shown with orange underlining. For ease of viewing, the two symmetry-related α2 motifs are depicted as cartoons in cyan and green in each panel. The Zn(II) ions are grey spheres, and the Cu(II) ions are brown spheres. Reprinted with permission from Ref 165, Copyright 2023 Angewandte Chemie

III. Stammers and Stutters: A Twist on Protein Design

The α-helical coiled coil structure, previewed earlier in this thesis, is composed of two or more amphipathic α-helices that fold (or twist) around a supercoil axis, generating a hydrophobic core composed of hydrophobic residues, while residues exposed to solvents are often hydrophilic.[200] In the 1950's, Pauling, Corey and Crick laid out the bases for the mathematical description when they simultaneously hypothesized that α-keratins were in fact α-helical coiled coil.[120,201] Over 70 years later, the coiled coil structural motif has been found in 5% to 10% of natural proteins that have been structurally characterized and have been found to contribute to the assembly and dynamics of native proteins (*e.g.*, signal transduction and motors). William Astbury first systematically evaluated many protein fibers, including wool, native and denatured states, silk, and tendon. This resulted in the diffraction spectra falling into three categories: alpha-form (wool), beta-form (silk), and a "third form" (tendon). All displayed simple diffraction patterns observed with meridional arc spacing of 5.15 Å which arises from the diffraction caused by the reflexion of stacked planes, one upon the other, parallel to the orienting surface and indicating the repeating unit of the structure. A race between Bragg, Perutz, and Kendrew (Cambridge) and Pauling and Corey (Caltech) ensued to develop a structural model that would correctly predict the observed results of numerous hypothesized α-helix proteins. While Pauling and Corey won with their announcement of the mathematical model of the alpha-helix, their model did not predict the spacing periodicity of 5.15 Å that Astbury earlier observed in fibrous proteins, instead predicting 5.4 Å. Pauling and Corey argued that this model does in fact describe fiberous proteins, or at least the synthetic fiber, poly-gamma-methyl-L-glutamate, which was determined to have a periodicity of 5.4 Å, matching their predictions. However, both Pauling and Crick expanded the previous model by introducing packing-induced super-helical distortions in the native protein (Figure I-16A and B).[199]

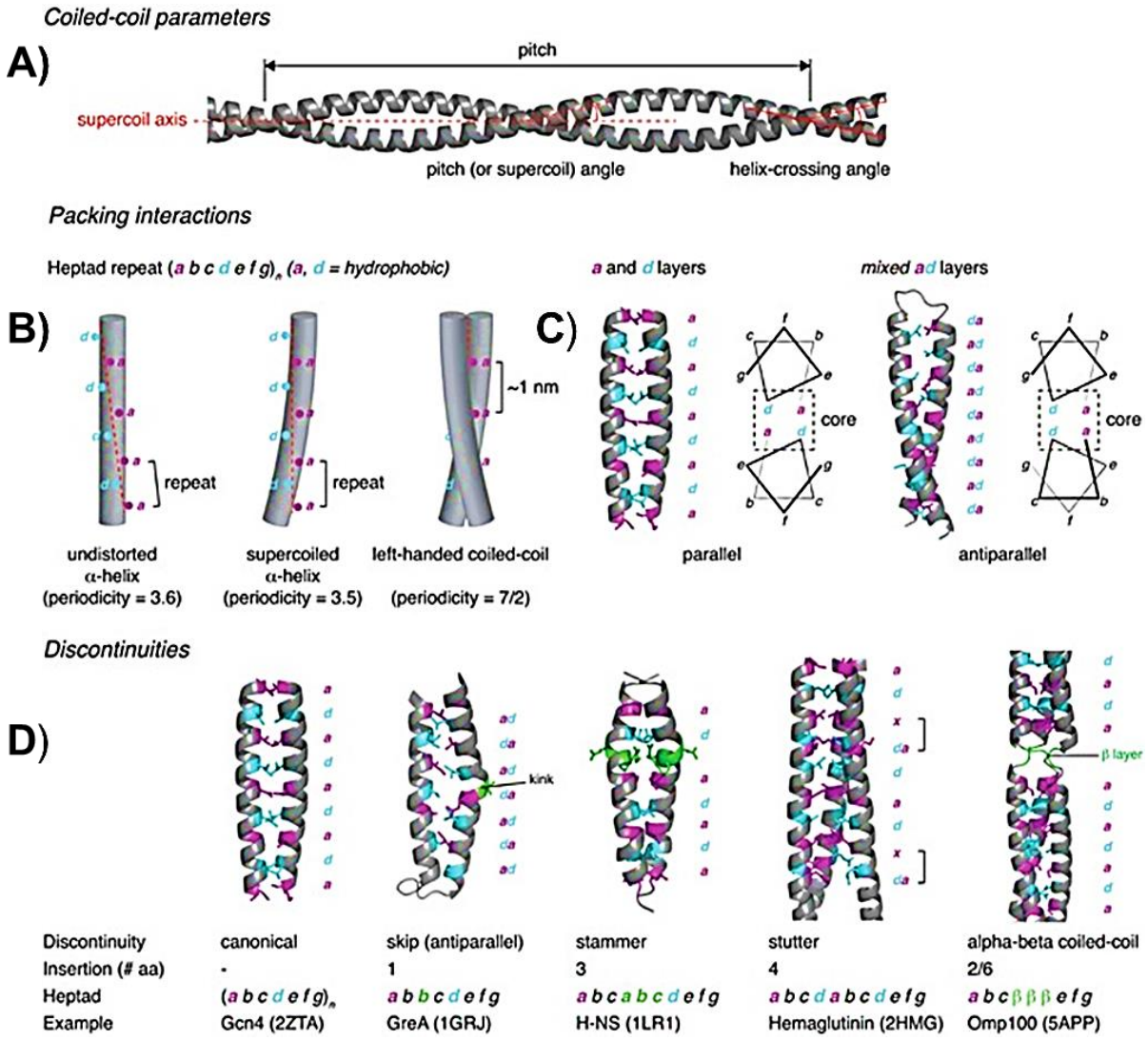


Figure I-16: Overview of the coiled coil architecture with stammers and stutter: **A)** Overview of the coiled coil architecture, **B**) Effect on the supercoiling on an undistorted helix leading to a decrease in periodicity, **C)** Packing within a parallel or antiparallel 2SCC, and **D)** Discontinuities effects on the layers in natural coiled coil proteins. Reprinted with permission from Ref. 202, Copyright 2016 BioEssays.

According to Pauling and Crick, the tight, precise packing of the core residues around a central axis is the basis for all of the common characteristics of the conventional left-handed coiled coils.[119] These internal residues pack in a knob-into-hole fashion, resulting in a periodicity of every seven residues over two turns of the helix (*i.e.*, the heptad repeat). Due to the limitations enforced by hydrogen bonds, the original helical periodicity cannot be altered. Consequently, the adjustment occurs through the intertwining of the helices, forming a supercoiled bundle.[202] Within this

configuration, the constituent α-helices maintain their natural periodicities; however, when observed for the basis of the bundle axis, the periodicity effectively decreases to 3.5, resulting in sidechains occupying structurally equivalent positions every 7 residues and slightly smaller than what is expected for undistorted helixes (3.63 residues per turn).[203] Henceforth, this adjusted periodicity will be termed "bundle periodicity" to prevent confusion with the helical periodicity (Figure I-16C and D). The bundle periodicity creates distinct layers throughout the coil coiled protein labeled (***abcdef***), where the ***a***-site and ***d***-site compose the hydrophobic core, the $\boldsymbol{g}_{i-1} \rightarrow \boldsymbol{e}_i$ form solvent-exposed salt bridges in parallel homomers, and the ***b***,***c***, and, ***f*** sites can fine-tune the stability of the scaffold.[204] While the 3.5 bundle periodicity makes up the majority of natural coiled coil segments in proteins, occasionally, one, three, or four residue inserts have been observed within natural coiled coil proteins (Figure I-17A). A number of x-ray crystallographically characterized systems have structurally defined stammers that behave by overwinding the helices around the bundle axis, resulting in a local periodicity of 10/3 = 3.33.[205,206] Considering 3.33 is less than a helical turn (*i.e.*, 3.5 residues/turn) and the minor helical frequency in a canonical coiled coil is 360°/3.5=102.86°/residue, the downstream residues are repacked with a 51° counterclockwise rotation (net helical phase) compared to the canonical coiled coil,

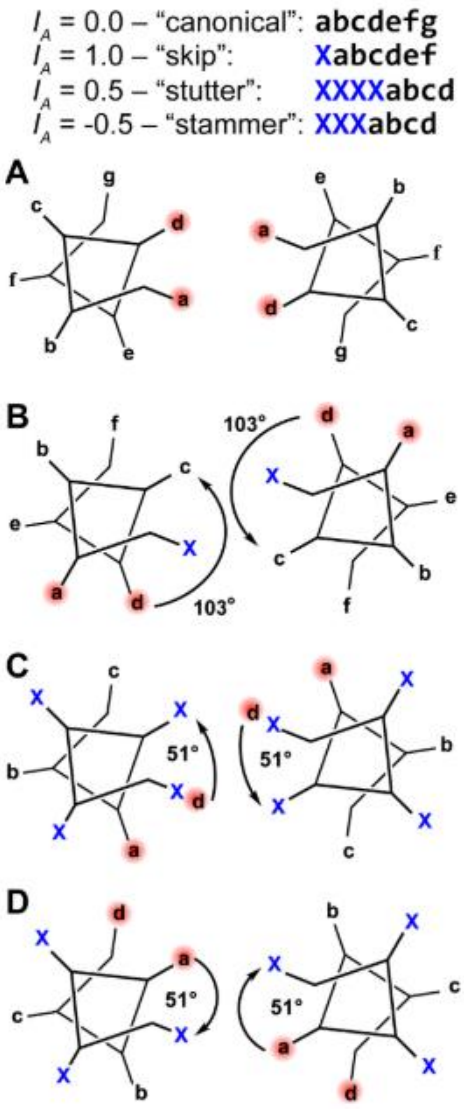


Figure I-17: Effects of heptad breaks on the packing of the α-carbons in a two-stranded coiled coil: **A)** Nominal 2SCC, **B**) Skip discontinuity **C**) Stutter discontinuity, and **D)** Stammer discontinuity. Angles are the net helical phase with respect to a nominal 2SCC Reprinted with permission from Ref. 220 Copyright 2017 Protein Science.

which results in a tightening of the left-handed supercoil (Figure I-17D). This is close to what is observed in 3_{10}-helix regions in proteins (3.36 residues/turn) and thus may be expected to be accompanied by a 3_{10}-helix segment.[207] A 4-residue insert (*i.e.*, stutter) represents more than a 3.5 residue/turn and results in a loosening of the supercoiling, leading to a 51° clockwise rotation of the preceding residues (Figure I-17C). These modifications result in a shift from knobs-to-hole to knobs-to-knobs interactions; however, they have different impacts on the residence of the parallel 3SCC. The addition of a stammer rotates the nominal ***a***-site to a more solvent-exposed, more ***g***-like position, forming a ***da***-layer with the ***g***-site. The ***d***-site moves more into the interior of the core, forming an *x*-layer. Stutters have the opposite effects on the core layers; where an ***a***-site packs into the core from an ***x***-layer, a ***d***-site will rotate to a more solvent-exposed position, forming a ***da***-layer (Figure I-17C). [205,208] Persistent stutters and stammers, extending beyond isolated disruptions, lead to deviations from the Crick model in coiled coils on a global scale. Initially, one skip, stammer, and stutter inserts were only thought to exist as an exception and viewed as discontinuities of the heptad repeat.[205] But as efforts were made to investigate their core residue packing effects and backbone conformation throughout the entire coiled coil region, this philosophy started to shift, giving rise to the theory that some discontinuities in coiled coils are better characterized over a larger span of residues than a heptad repeat. An example of the analysis is the work of McLachlax and Karn and their global perspective on the Myosin Rod coiled coil, which is in contrast to a local disruption model (π-turns**)** by Parry *et al*. [209,210] Although π-turns are known to be present in some coiled coil proteins near skips, the distinction mentioned above is significant because it explains the prevalence of very destabilizing skip insertions (local interpretation). A more comprehensive analysis indicates that skips are more accurately described as two stutters spaced about 18 residues apart, which allows the distortions to be accompanied over a larger number of residues and preserves some stability. [208,211] Within the heptad frame of reference, a skip is equivalent to two stutters, as eight residue inserts are equivalent to a heptad and *one* residue remainder. From a designer's perspective, we will treat these insertions as local disruptions in the sequence; however, it will be stated in Chapter IV of this thesis when that

viewpoint breaks down. Moreover, this thesis will only focus on stammers and stutters, in particular stammers, and readers are encouraged to explore skip inserts in the following references.[212–214]

These non-canonical modifications can have a profound impact on protein structure, leading to uniquely folded segments of coiled coils. An example of a novel segment has been found and subsequently explored in the trimeric autotransporter adhesins (TTA), which are fibrous proteins found on the surface of gram-negative bacteria (Figure I-18A).[215,216] TTAs are an interesting class of natural coiled coil proteins due to their segments that are composed of buried polar residues (typically asparagine) that coordinate anion (*e.g.*, nitrate and chloride) through hydrogen bonds. Chloride binding within coiled coil proteins is not uncommon, as the central Cl^- is stabilized by H-bonding interactions in fusion proteins, fibers, and *de novo* designed 3SCC.[217,218] Structurally, the basic composition of TTAs is an N-terminus head (adhesion and autoagglutination), the stalk, and a C-terminus anchor (aids in export function through adhesion), where binding of ions occurs in the trimeric coiled coil stalk portion. Woolfson and Lupas *et al*. studied the coiled coil regions of Salmonella TTA (*i.e.*,SadA) that are composed of IxxNTxx heptad repeat and demonstrated that even in the presence of different registers via an N-cap stammer and a C-cap stutter, the ***d***-site asparagine (N@d) layers remain folded in the interior of the core and retain their binding towards ions.[206] Due to the problematic expression of the isolated stalk domain, a sequence of 3 repeats of the IxxNTxx motif from the stalk domain of SadA was flanked by two copies of the trimeric form of the GCN4 leucine zipper (GCN4-pII), forming SadAK3 in the correct heptad frame of references (Figure I-18A). In SadAK3, two N@d layers in the stalk region retained their ability to hydrogen bond one Cl^- in a trigonal pyramid geometrical fashion (3.1 Å), similar to the way the other two N@d layers bind NO_3^- (Figure I-18D and E). Core-packed polar residues would be expected to lead to unstructured local folding of mature proteins; however, periodic, conserved layers of polar sidechains may reflect special folding requirements given that SadAK3 still unfolds at high temperatures and the binding anions that may help stabilize local segments of the 3SCC during export through the membrane periplasm in SadA.

To test the influence of stammers and stutters on the N@d layers, a stammer and a stutter were created at the GCN4-pII adaptor ends, encapsulating the region containing the four N@d layers. Due to the symmetry of the heptad reading frame, the deletion of the first four residues of the stalk motif (FDTN at the N-terminus cap) forms a stammer, and the addition of 4 residues at the C-terminus cap (ITTL) forms a stutter. As expected, the stammers introduced strain on an undistorted coiled coil in a heptad frame of reference, leading to an increase in supercoiling; however, the remaining strain is accommodated by the formation of a 3_{10}-helix segment in each individual α-helices near the insertion point (Figure I-19B). A 3_{10}-helix is characterized by a departure from the typical α-helical rise per residue of 1.5 A to 2 Å, and in the case of SadAK3b is very localized over 3 residues. In contrast, the stutter was accommodated over 11 residues in SadAK3b, a larger range from the abrupt changes of the stammer. The periodicity over this region was observed to be 3.6–3.7, consistent with a 4 residue insert (Figure I-19B). Interestingly, a second crystal was found under identical conditions to yield the stutter accompanied by over 18 residues while the stammer was unaffected, suggesting this heterogeneity points to the dynamical behavior of the stutter in solution, which is consistent with the stutter in the dimeric domain of vimentin.[219] These findings provide reasons why the addition of stammers and stutters can accommodate ions within the hydrophobic core and allow for the flexibility to sustain the binding of ions.

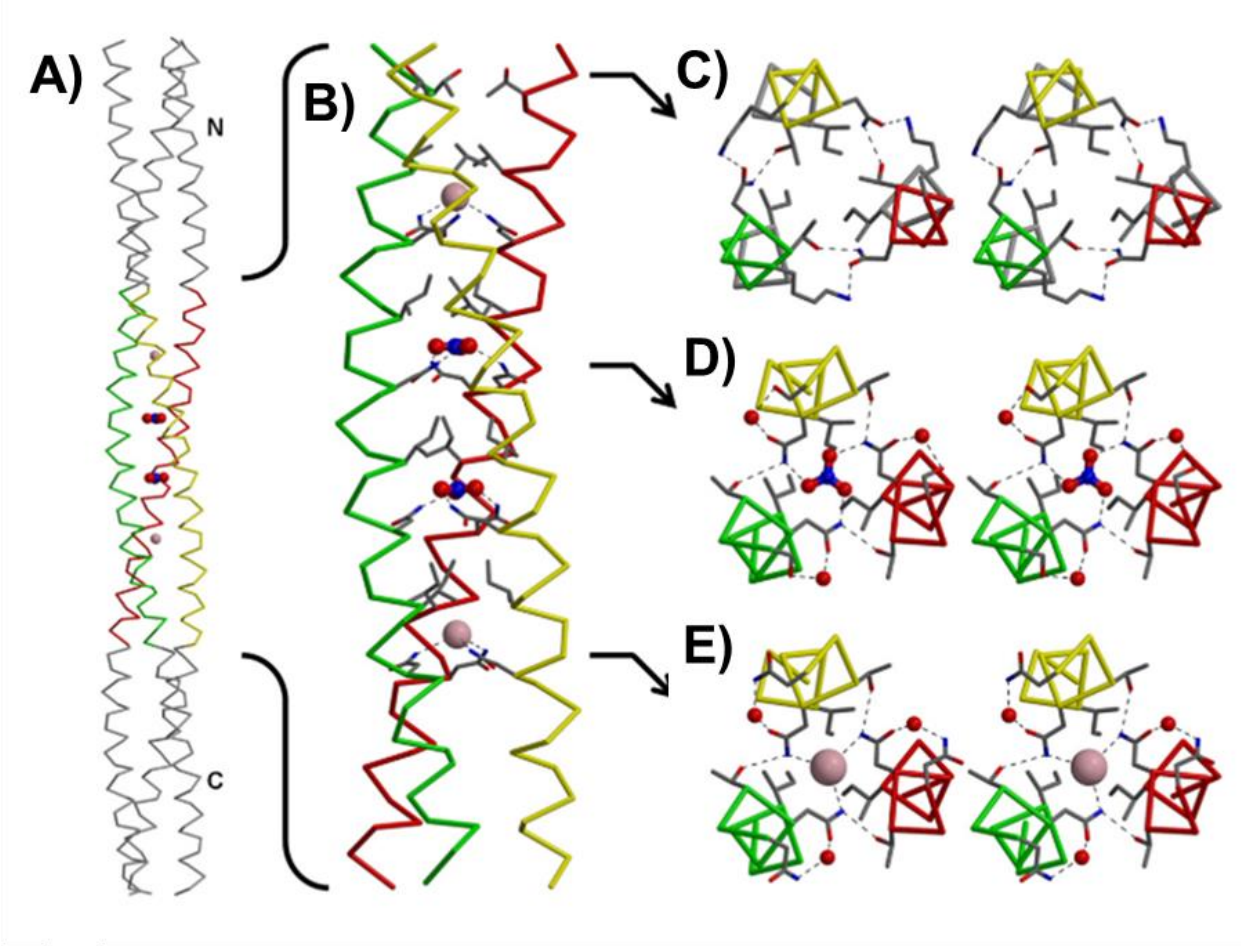


Figure I-18: Overview of discontinuities in SadAK3 protein: **A)** Structure of SadAK3, **B)** The whole crystal structure of SadAK3, including the GCN4-adaptors in gray and the 2 chloride and 2 nitrate anions trapped in the N@d layers, **C)** Close-up of the SadA insert. Residues in positions ***a*** and ***d*** of the N@d layers and the single T@d are shown as sticks. (**C**–**E**) Stereoview upstream of the helical bundle, showing I478, T481, N482, and K484 of the single T@d layer **D)**, I492, N495@d, T496, S498, and a bridging water coordinating nitrate, and **E)** I506, N509@d, T510, N512, and a bridging water coordinating chloride. Reprinted with permission from Ref. 200. Copyright 2009 PNAS.

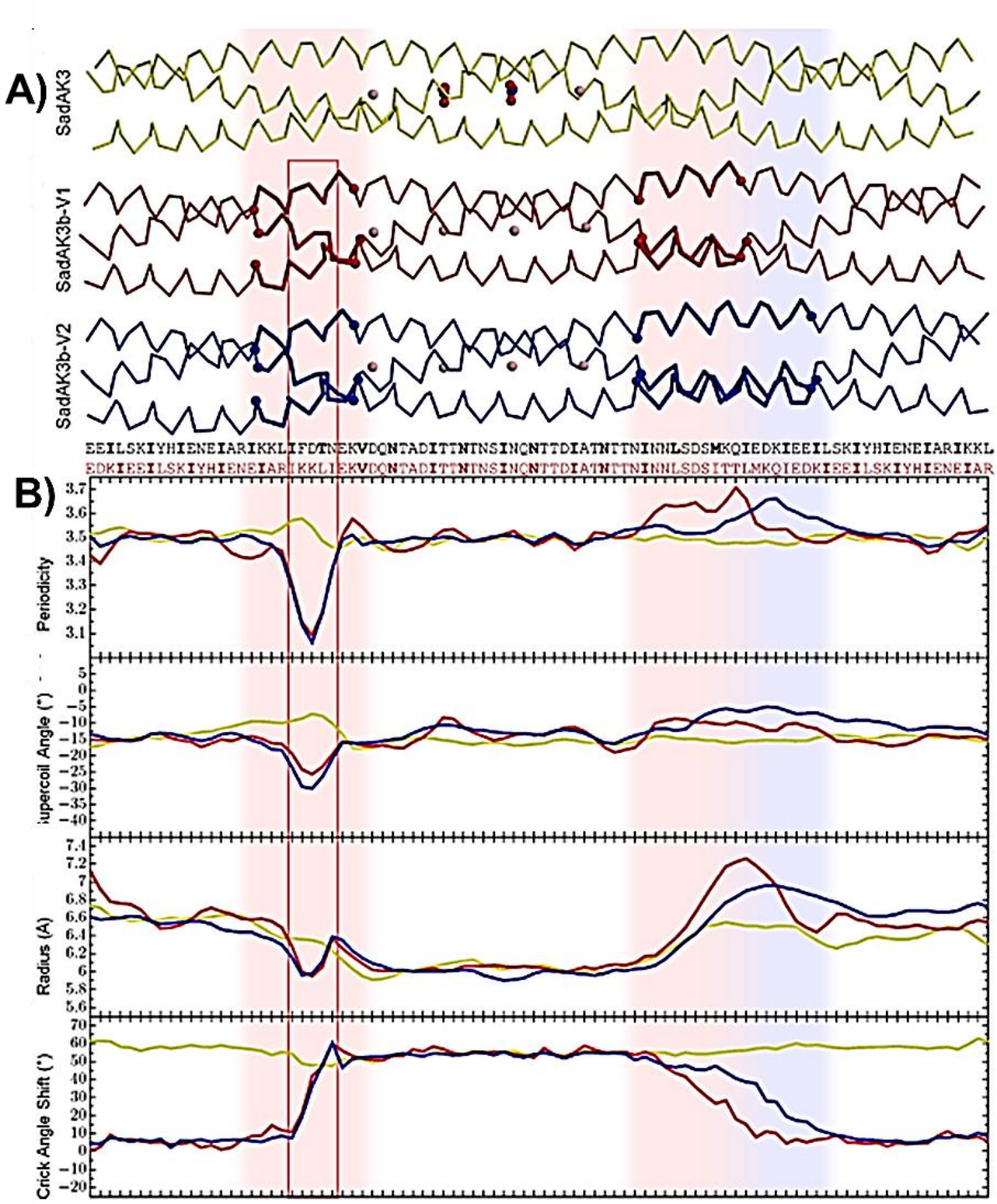


Figure I-19: SadAK3 sequences and plots of their coiled-coil parameters: **A)** The structures of SadAK3, SadAK3b-V1 (V1), and SadAK3b-V2 (V2) are depicted together with their sequences and plots of their coiled-coil parameters, and **B**) The discontinuities in the SadAK3b structures are highlighted by vertical shades throughout the figure, colored light red for V1, and additionally light blue for V2. The red box indicates the 3_{10} helix within the stammer. Because the alignment is based on the inserts, the Crick angle deviation for SadAK3 is constantly at the 3-maximum deviation of the SadAK3b structures. Reprinted with permission from Ref. 200. Copyright 2009 PNAS.

Naturally, the question arises of how these interruptions are tolerated downstream from their insertion point, resolving back to the nominal residue per turn over a course of residues. To get a general idea of the length needed to resolve the interruptions, DeGrado *et al*. used a number of experimentally determined coiled coils with well-defined insertion types to determine their accommodation length.[220] All three types of inserts showed notable differences in accommodation lengths. Interestingly, changes were even observed within a region of the same protein in a different signaling state (such as CpxA histidine kinase), which may indicate conformational flexibility, as seen in the stutter region in SadAK3 above. Within the two 3SCC proteins found containing stammers, the average accommodation length was calculated to be 5 residues (± ~2.5 residues), while the stutter inserts (n=13) were accommodated on average over 15 residues (± ~4 residues). Given that their dataset is small, this analysis should only be taken as indicative.

The effects of stammers and stutters on transition metals and how to use them to adjust catalysis are not well understood. Currently, only two examples explore the effects of heptads-break on metal binding and catalysis.[221] The large structures that heptad discontinuities typically occupy (*e.g.*, coiled coil domains) are unstable, difficult to express, and need incremental structural characterizations, which hinders research on how they can be used to finely tune active sites. With this in mind, *de novo* design has the advantage of studying these discontinuities in well-defined, stable constructions. ORF1p, an RNA chaperone that is coded within the Long interspersed nuclear elements (Line1) DNA sequence, is composed of a 3SCC N-terminal domain, an RNA recognition motif domain (RRM), and a C-terminal RNA binding domain.[222] Line1 make up ~20% of the genome of modern humans, and ORF1p plays the critial role of both n RNA-packing protein and a nucleic acid chaperone, with high affinity.[223,224] The ORF1p coiled coil domain contains two Cl^- binding sites interior to the hydrophobic core, one composed of a layer of asparagine and the other composed of a layer of arginine residues, and a stammer insert (MEL, residues 92-94) in the stalk.[225] Interestingly, metals such as nickel, cadmium, and mercury have a concentration-dependent increase in retrotransposition. [226,227] ORF1p contains highly conserved cysteine layers, [$(Cys)_3$-76, ***d***-site], [$(Cys)_3$-104, ***a***-site], [$(Cys)_3$-111, ***a***-site], which could bind heavy metals and

alter its function. $(Cys)_3$ layers in coiled coil proteins have been extensively investigated for their ability to form high affinity bindings sites for metals, but in particular heavy metals such as Pb(II), Hg(II), and Cd(II).[138,177,228–231] Pinter and Pecoraro *et al*. demonstrated Pb(II) binding to ORF1p and a *de novo* designed mimic of the ORF1p coiled coil stalk, $(GRCSL16CL23C)_3$, notability lacking the MEL stammer.[232] The apo-forms $(Cys)_3$ sites displayed structural similarities to $(Cys)_3$ sites previously characterized as preorganized towards Pb(II) binding, which have been investigated for their high affinity ($K_a>10^8$ M^{-1}).[136,233] The characteristic Pb(II)-S_{cys} ligand-metal charge transfer (LMCT) was observed upon the addition of Pb(II) up to 4 equivalence/trimer, 3 equivalent binding to the core $(Cys)_3$ layers, and 1 equivalent binding to the external cysteine (Cys86, ***g***-site), leading to precipitation due to aggregation between oligomers. $[Pb(II)]_3$-ORF1p molar extinction coefficient was 3x as large as previously recorded with single Pb(II) sites (λ_{max}=343 nm, ε_{343nm} =10,220 M^{-1} cm^{-1}).[234] $(GRCSL16CL23C)_3$ and because ORF1p binds both Pb(II) ions, it appears that the mutation in ORF1p does not prevent Pb(II) from binding. It appears that these *de novo* designed proteins are robust models of Pb(II) binding to the two ***a***-sites in ORF1pCCD because they overlay the native structure quite well (Figure I-20A and B). The SamCC-Turbo server program has also been used to examine the two crystal structures. Compared to ORF1pCCD, the apo-GRCSL16CL23C structure exhibits similar 3SCC radius, periodicity, and axial helical rotation (Figure I-20C-E). The use of *de novo* design proteins will surely be part of exploring the role of this stammer in ORF1p function and metal-dependent behavior *in vitro*.

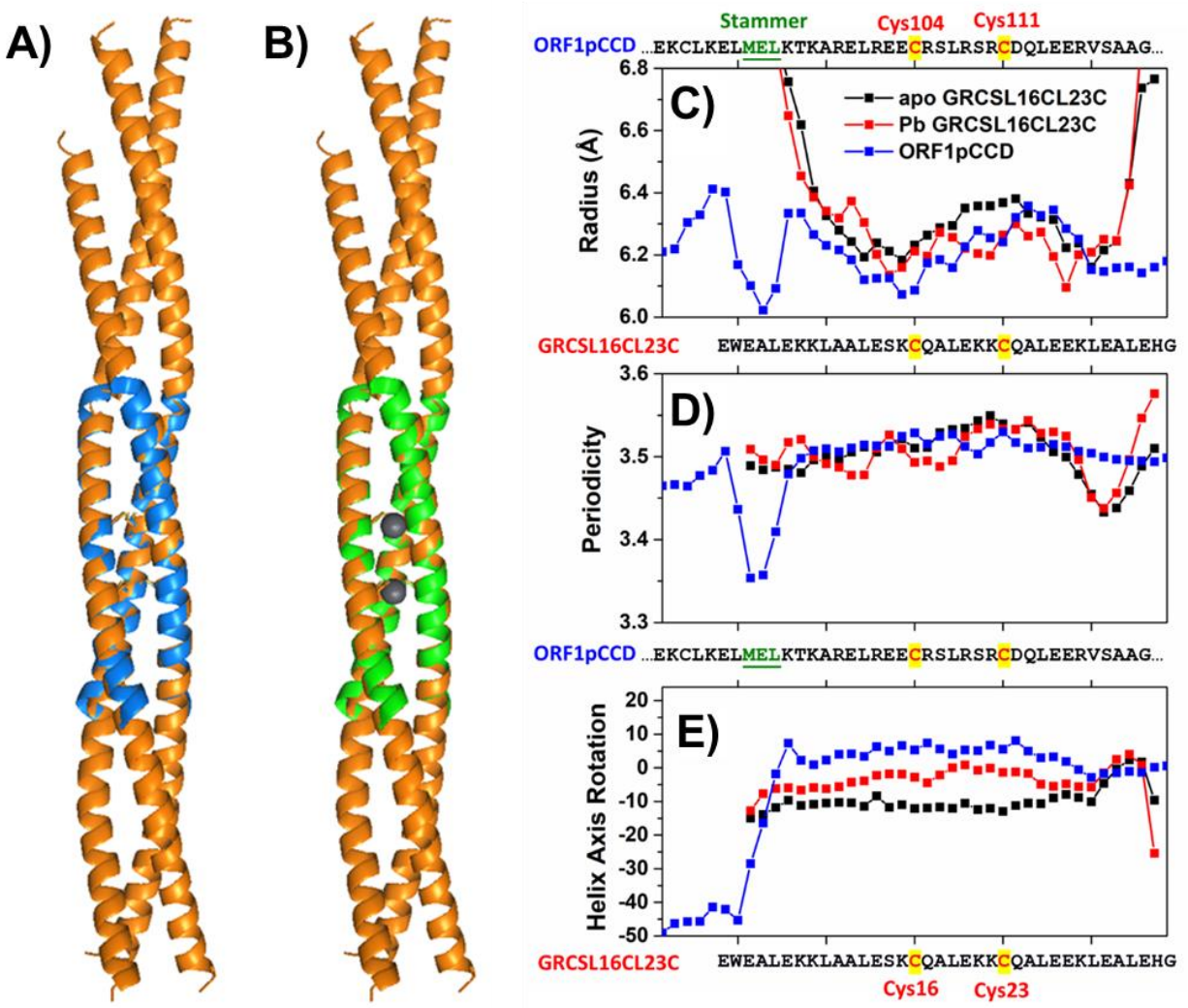


Figure I-20: Side-on view of superimpositions of the native ORF1pCCD (from residues 92Glu-155Glu) with *de novo* design proteins: **A)** apo-$(GRCSL16CL23C)_3$ and **B)** $Pb_2(GRCSL16CL23C)_3^{2-}$,and **(C-D)** Analysis of ORF1pCCD (blue), apo-$(GRCSL16CL23C)_3$ (black) and $Pb2(GRCSL16CL23C)_3^{2-}$ (red) geometries using the SamCC Turbo online server. Adapted with permission from Ref 232. Copyright 2021 American Chemical Society.

been reported.[221] Considering the extra heptad in GRW imposed more stability on the overall folding of the protein than did the TRI-family, the structure was incorporated into the GRAND (GRW) scaffold. This is due to the fact that stammers have a negative effect on protein folding stability by forming a 3_{10}-helix structure.[204,235] Specifically, the AEL stammer was directly inserted after the L26 ***d***-site, which was proposed to yield the most impact on the catalytic $(His)_3$ ***a***-site (L33H) by changing the relative position of the histidine to a more solvent-exposed ***g***-site, $GRW_{stam27(AEL)}L33H$ (Figure I-21). The AEL stammer minimally impacted the CD spectrum of

Apo-GRW$_{stam27(AEL)}$L33H and Zn(II)-GRW$_{stam27(AEL)}$L33H with well-defined minimums at 222 nm and 208 nm at pH 7.5, suggesting a relativity unperturbed secondary structure compared to the parent scaffolds. With the addition of the stammer, the apparent affinity for Zn(II) increased by 100x compared to Zn(II)-TRIW-H.[139] Moreover, the EXAFS of Zn(II)-GRW$_{stam27(AEL)}$L33H (pH 9.5) suggest that the tetrahedral geometry around the Zn(II) ion is retained from Zn(II)-TRIWL30-H and Zn(II)-GRW-H (ZnHis$_3$O). However, the pseudo first order esterase activity towards pNPA was reduced to nearly background level hydrolysis of pNPA, while both Zn(II)-TRIWL30-H and Zn(II)-GRW-H have background-corrected rate constants of 22 × 10^{-4} s^{-1} and 52 × 10^{-4} s^{-1}, respectively (Table I-4). Clearly, the modification associated with the stammer had an impact on the Zn(II) ability to catalyze the hydrolysis of pNPA. While puzzling, it should be cautioned that the Zn(II) EXAFS, while quite similar between the parent proteins, is limited to only identifying vastly different ligands and the Zn(II)-O scatter between the parent scaffolds and Zn(II)-GRW$_{stam27(AEL)}$L33H could be the result of an unknown oxygen doner (*i.e.*, Glu), impacting the catalytic site. Moreover, the stammer could perturb the sterics near the Zn(II)His$_3$ site resulting in an active site less accessible to the substrate. The CuNiR activity with Cu-GRW$_{stam27(AEL)}$L33H is 4x higher than Cu-GRWL30H and 24x higher than Cu-TRIW-H. The authors speculated that the size difference between pNPA and NO_2^- may explain the divergence in reactivity. The Cu(I)-GRW$_{stam27(AEL)}$L33H site was best modeled as a Cu(I)-His$_2$, likely adopting a linear geometry similar to Cu(I)-TRIW-H L19A, the fastest CuNiR designed proteins currently reported with histidine in the active site.[168] (Table I-4)

Table I-4: Key parameters for CuNiR (pH 5.8) and Zn-pNPA hydrolysis (pH 9.5)

Enzyme	k' (s^{-1}) CuNiR	k' (s^{-1}) pNPA esterase	Zn(II) $K_{d,app}$ (M)	Cu(I) $K_{d,app}$ (M)	Cu(II) $K_{d,app}$ (M)
TRIW-H	4.6×10^{-4}	22×10^{-4}	0.6×10^{-6} (± 0.1)	3.1×10^{-9} (± 0.7)	4.0×10^{-8} (± 0.8)
TRIW-H L19A	3.5×10^{-2}	N/A	N/A	2.3×10^{-12} (± 0.7)	1.3×10^{-5} (± 0.2)
GRW-H	28×10^{-4}	52×10^{-4}	N/A	N/A	N/A
$GRW_{stam27AEL}$L33-H	112×10^{-4}	3.5×10^{-4}	4.2×10^{-9} (± 0.1)	15×10^{-8} (± 3)	7.5×10^{-7} (± 0.4)

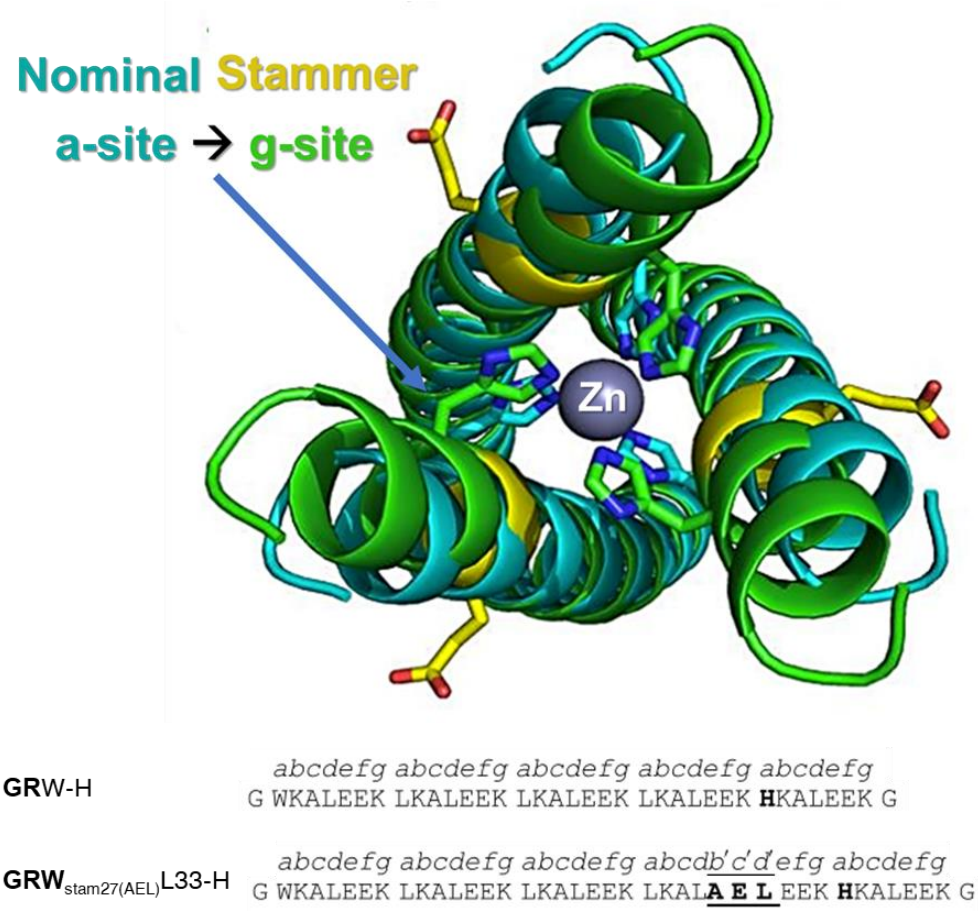


Figure I-21: Model of $GRW_{stam27(AEL)}$L33H (green) overlayed with GRCSL16CL30H (blue) modelled with a diamagnetic Zn(II). The stammer was created using the stammer (residue 91-93) ORF1p CDD (pdb:6FIA) and inserting it into 5KB0 structure of GRCSL16CL30H with GRWL30H and $GRW_{stam27(AEL)}$L33H sequences.

Throughout this subchapter, the basis of the assignment of stammers and stutters within the context of nominal coiled coil proteins has been discussed. The insertion type led to relative changes in their position with respect to the hydrophobic core, leading to both flexibility and different accommodation downstream from their insertion point. Stammers and stutters do not fully disrupt the hydrophobic core, both in the absence and presence of a metal, as highlighted by the stammers and stutters mentioned above. Importantly, Pecoraro *et al*. showed that a simple stammer discontinuity can influence the catalytic cycle of both redox and non-redox designed metalloenzymes. Combined, these key takeaways will be important in Chapter IV of this thesis, where both stammers and stutters are explored to tune catalysis.

IV. Thesis outline:

This thesis investigates the structure-function of a CuNiR by utilizing non-coded amino acids and non-canonical sequence discontinuities (*i.e.*, stammer) in a highly-defined *de novo* 3SCC. Throughout this thesis, this approach allows for precise control of the electronics and structure of the primary coordination sphere of an unnatural T2Cu copper center, and I describe in detail the synthesis, spectroscopy, and kinetics to evaluate their impact on nitrite reduction. In Chapter II and Chapter III, I will show that the sterics of the secondary coordination sphere above the active site are responsible for changing the coordination number at the reduced copper center and results in tighter nitrite binding at the coordinatively unsaturated Cu(I) enzyme form. It will also be shown that a highly reactive Cu(I)-NO_2 enzyme substrate complex forms during catalytic cycle. In Chapter IV, non-canonical sequence discontinuities stammers will be used to generate both 2- and 3-coordinate Cu(I) in a unique manner compared to simply modifying the secondary coordination sphere. The structure and kinetics of each of these designs will be reported, highlighting the distinguishing features from designs in Chapter II.

In Chapter II, I describe the design and characterization of a three stranded coiled coil *de novo* protein containing a T2Cu composed of 6-membered ring N-heterocycles. This design yields the most active homogenous CuNiR mimic in water. I achieved this result by controlling three

factors. First, previous studies with N_δ and N_ε-Methyl Histidine had indicated that a ligand providing pyridine-like electronic character to the copper site was superior to a pyrrole-like donor for nitrite reduction. By substitution of the parent histidine with the non-coded amino acids pyridyl alanine (3'-Pyridine [3'Py] vs 4'-Pyridine [4'Py]), an authentic pyridine donor was employed without the complications of electronic and steric effects with the tautomerization of histidine or methylated histidine. Second, by changing the position of the nitrogen atom within the active site (4'-Pyridine vs. 3'Pyridine) a doubling of the enzyme's catalytic efficiency resulted. This effect was driven exclusively by substrate binding to the copper site. Third, I replaced the leucine layer adjacent to the active site with an alanine, and the disparity between the 3'Py and 4'Py became more apparent. The decreased steric bulk engendered by the smaller alanine minimally impacted the 3'Py derivative; however, the 4'Py K_m decreased by an order of magnitude (600 mM to 50 mM), resulting in a 40-fold enhancement in the k_{cat}/K_m compared to the analogue histidine site and a 1500-fold improvement compared with the initially reported CuNiR catalyst of this family, TRIW-H. When combined with XANES/EXAFS, the relaxing of the Cu(I) site to a more 2-coordinate Cu(I) like structure in the resting state appears to be the major factor that increases the overall catalytic efficiency of nitrite reduction via the lowering of K_m. This study illustrates how by combining advanced spectroscopic methods, detailed kinetic analysis, and a broad toolbox of amino acid side chain functionality, one can rationally design systems that optimize biomimetic catalysis.

In Chapter III, I investigate substrate binding to the preferred oxidation state of the enzymes described in Chapter II and explain the trend in K_m values using detailed analysis of Cl^- inhibition kinetics and spectroscopic techniques. From Chapter II, the geometry of the Cu(I) enzyme played a critial role in determining the catalytic efficiency of nitrite reduction by altering the K_m values toward tighter substrate binding with the removal of the sterically demanding leucine layer above the active site. I first demonstrate that Cl^- competitively inhibits nitrite reduction using Michaelis-Menten kinetics, suggesting that NO_2^- binds to the same enzyme form as the Cl^- ion, with the

K_{i,Cl^-} ranging from 30-70 mM. I explore this further by characterizing each oxidation state in the presence of Cl^-. Using Cu K-edge XAS, the Cu(I) enzymes are characterized in the presence of chloride, confirming that chloride forms an adduct with the Cu(I) oxidation state under catalytic conditions. The overall analysis suggests that the chloride species only forms a 3-coordinate adduct (*i.e.*, $Cu(I)N_{2Py}Cl$), independent of the initial coordination number of the Cu(I) resting enzyme. The coordination number of the enzyme substrate is best described as a 3-coordinate Cu(I) intermediate which sheds new light on the structure-function relationship observed in Chapter II and in previously designed CuNiR mimics composed of natural histidine active sites. The data presented in this chapter will motivate a different approach to generate 2-coordinate Cu(I) enzymes in Chapter IV while simultaneously generating a secondary coordination sphere that is unique compared to Chapter II.

In Chapter IV, I combine what has been learned in Chapters II and III and design 3 residue inserts (*i.e.*, stammer) into the sequence to modify the supercoil (*i.e.*, overtighten) of the coiled coil to alter which ligands bind to the copper center (due to changes in the orientation of the first coordination ligands and the sterics surrounding the metal binding site), and this will be reflected in the function of the designed metalloenzyme by i) altering the coordination number of the Cu(I) oxidation state and ii) altering the sterics around the active site for better substrate access. The two design strategies I use in this chapter to accomplish this are 1) coupling ***a***-site ligands (Histidine, 3'Pyridine, 4'Pyridine) with ***d***-site stammers (AEL, AEA) or designing each active site into the stammer (AEX_{ligand}) to maximize the effect of the stammer on the active site. The stability and folding of each scaffold are screened, along with the full characterization of both the reduced and oxidized enzyme forms. Next, detailed Michaelis-Menten kinetics are performed to relate structural changes to alterations in the steps of the mechanism. Taken together, the data suggests stammers near the active site can alter the primary coordination sphere structure of Cu(I) and Cu(II) bound to both histidine and pyridine, and mechanistic insights can be gained from the resulting increase and decrease in CuNiR activity. This chapter provides the first in-depth study of stammers' impact on transition metal catalysis. In Chapter V, I conclude with major takeaways

from this thesis and propose future directions for this project and implications for other designed proteins.

References:

(1) Jumper, J.; Evans, R.; Pritzel, A.; Green, T.; Figurnov, M.; Ronneberger, O.; Tunyasuvunakool, K.; Bates, R.; Žídek, A.; Potapenko, A.; Bridgland, A.; Meyer, C.; Kohl, S. A. A.; Ballard, A. J.; Cowie, A.; Romera-Paredes, B.; Nikolov, S.; Jain, R.; Adler, J.; Back, T.; Petersen, S.; Reiman, D.; Clancy, E.; Zielinski, M.; Steinegger, M.; Pacholska, M.; Berghammer, T.; Bodenstein, S.; Silver, D.; Vinyals, O.; Senior, A. W.; Kavukcuoglu, K.; Kohli, P.; Hassabis, D. Highly Accurate Protein Structure Prediction with AlphaFold. *Nature* **2021**, *596* (7873), 583–589.

(2) Baek, M.; DiMaio, F.; Anishchenko, I.; Dauparas, J.; Ovchinnikov, S.; Lee, G. R.; Wang, J.; Cong, Q.; Kinch, L. N.; Dustin Schaeffer, R.; Millán, C.; Park, H.; Adams, C.; Glassman, C. R.; DeGiovanni, A.; Pereira, J. H.; Rodrigues, A. V; Van Dijk, A. A.; Ebrecht, A. C.; Opperman, D. J.; Sagmeister, T.; Buhlheller, C.; Pavkov-Keller, T.; Rathinaswamy, M. K.; Dalwadi, U.; Yip, C. K.; Burke, J. E.; Christopher Garcia, K.; Grishin, N. V.; Adams, P. D.; Read, R. J.; Baker, D. Accurate Prediction of Protein Structures and Interactions Using a Three-Track Neural Network. *Science (80-.).* **2021**, *373* (6557), 871–876.

(3) Lin, Z.; Akin, H.; Rao, R.; Hie, B.; Zhu, Z.; Lu, W.; Smetanin, N.; Verkuil, R.; Kabeli, O.; Shmueli, Y.; dos Santos Costa, A.; Fazel-Zarandi, M.; Sercu, T.; Candido, S.; Rives, A. Evolutionary-Scale Prediction of Atomic-Level Protein Structure with a Language Model. *Science (80-.).* **2023**, *379* (6637), 1123–1130.

(4) Fujisawa, K.; Tanaka, M.; Moro-oka, Y.; Kitajima, N. A Monomeric Side-On Superoxocopper(II) Complex: Cu(O2)(HB(3-TBu-5-IPrpz)3). *J. Am. Chem. Soc.* **1994**, *116* (26), 12079–12080.

(5) Wasbotten, I. H.; Ghosh, A. Modeling Side-on NO Coordination to Type 2 Copper in Nitrite Reductase: Structures, Energetics, and Bonding. *J. Am. Chem. Soc.* **2005**, *127* (44), 15384–15385.

(6) Chino, M.; Leone, L.; Maglio, O.; D'Alonzo, D.; Pirro, F.; Pavone, V.; Nastri, F.; Lombardi, A. A De Novo Heterodimeric Due Ferri Protein Minimizes the Release of Reactive Intermediates in Dioxygen-Dependent Oxidation. *Angew. Chemie - Int. Ed.* **2017**, *56* (49), 15580–15583.

(7) Roy, A.; Sommer, D. J.; Schmitz, R. A.; Brown, C. L.; Gust, D.; Astashkin, A.; Ghirlanda, G. A de Novo Designed 2[4Fe-4S] Ferredoxin Mimic Mediates Electron Transfer. *J. Am. Chem. Soc.* **2014**, *136* (49), 17343–17349.

(8) Grzyb, J.; Xu, F.; Weiner, L.; Reijerse, E. J.; Lubitz, W.; Nanda, V.; Noy, D. De Novo Design of a Non-Natural Fold for an Iron-Sulfur Protein: Alpha-Helical Coiled-Coil with a Four-Iron Four-Sulfur Cluster Binding Site in Its Central Core. *Biochim. Biophys. Acta - Bioenerg.* **2010**, *1797* (3), 406–413.

(9) Tebo, A. G.; Pinter, T. B. J.; García-Serres, R.; Speelman, A. L.; Tard, C.; Sénéque, O.; Blondin, G.; Latour, J. M.; Penner-Hahn, J.; Lehnert, N.; Pecoraro, V. L. Development of a Rubredoxin-Type Center Embedded in a de Dovo -Designed Three-Helix Bundle. *Biochemistry* **2018**, *57* (16), 2308–2316.

(10) Chino, M.; Di Costanzo, L. F.; Leone, L.; La Gatta, S.; Famulari, A.; Chiesa, M.; Lombardi, A.; Pavone, V. Designed Rubredoxin Miniature in a Fully Artificial Electron Chain Triggered by Visible Light. *Nat. Commun.* **2023**, *14* (1), 1–11.

(11) Koebke, K. J.; Alfaro, V. S.; Pinter, T. B. J.; Deb, A.; Lehnert, N.; Tard, C.; Penner-Hahn, J. E.; Pecoraro, V. L. Traversing the Red-Green-Blue Color Spectrum in Rationally Designed Cupredoxins. *J. Am. Chem. Soc.* **2020**, *142* (36), 15282–15294.

(12) Plegaria, J. S.; Duca, M.; Tard, C.; Friedlander, T. J.; Deb, A.; Penner-Hahn, J. E.; Pecoraro, V. L. De Novo Design and Characterization of Copper Metallopeptides Inspired by Native Cupredoxins. *Inorg. Chem.* **2015**, *54* (19), 9470–9482.
(13) Shiga, D.; Nakane, D.; Inomata, T.; Funahashi, Y.; Masuda, H.; Kikuchi, A.; Oda, M.; Noda, M.; Uchiyama, S.; Fukui, K.; Kanaori, K.; Tajima, K.; Takano, Y.; Nakamura, H.; Tanaka, T. Creation of a Type 1 Blue Copper Site within a de Novo Coiled-Coil Protein Scaffold. *J. Am. Chem. Soc.* **2010**, *132* (51), 18191–18198.
(14) Holland, H. D. The Oxygenation of the Atmosphere and Oceans. *Philosophical Transactions of the Royal Society B: Biological Sciences*. Royal Society 2006, pp 903–915.
(15) Ochiai, E. I. Copper and the Biological Evolution. *BioSystems* **1983**, *16* (2), 81–86.
(16) Zong, C.; Wilson, C. J.; Shen, T.; Wittung-Stafshede, P.; Mayo, S. L.; Wolynes, P. G. Establishing the Entatic State in Folding Metallated Pseudomonas Aeruginosa Azurin. *Proc. Natl. Acad. Sci. U. S. A.* **2007**, *104* (9), 3159–3164.
(17) Penfield, K. W.; Gewirth, A. A.; Solomon, E. I. Electronic Structure and Bonding of the Blue Copper Site in Plastocyanin. *J. Am. Chem. Soc* **1985**, *107*, 4519–4529.
(18) Solomon, E. I.; Heppner, D. E.; Johnston, E. M.; Ginsbach, J. W.; Cirera, J.; Qayyum, M.; Kieber-Emmons, M. T.; Kjaergaard, C. H.; Hadt, R. G.; Tian, L. Copper Active Sites in Biology. *Chem. Rev.* **2014**, *114* (7), 3659–3853.
(19) Hosseinzadeh, P.; Lu, Y. Design and Fine-Tuning Redox Potentials of Metalloproteins Involved in Electron Transfer in Bioenergetics. *Biochim. Biophys. Acta - Bioenerg.* **2016**, *1857* (5), 557–581.
(20) Yoon, J.; Fujii, S.; Solomon, E. I. Geometric and Electronic Structure Differences between the Type 3 Copper Sites of the Multicopper Oxidases and Hemocyanin/Tyrosinase. *Proc. Natl. Acad. Sci. U. S. A.* **2009**, *106* (16), 6585–6590.
(21) Jaenicke, E.; Decker, H. Kinetic Properties of Catecholoxidase Activity of Tarantula Hemocyanin. *FEBS J.* **2008**, *275* (7), 1518–1528.
(22) Regan, L.; Degrado, W. F.; Wasserman, Z. R.; Lear, J. D.; Ho, S. P.; Eriksson, A. E.; Jones, T. A.; Liljas, A.; Volbeda, A.; Hoi, W. G. J.; Hoi, W. G.; Salemme, F. R.; Ghadiri, M. R.; Choi, C. J. De Novo Design of a Zn2+-Binding Protein Helix 2-CONH2 H3tt2: *J. Am. Chem. Soc* **1990**, *112* (2), 1630–1632.
(23) Sheng, Y.; Abreu, I. A.; Cabelli, D. E.; Maroney, M. J.; Miller, A. F.; Teixeira, M.; Valentine, J. S. Superoxide Dismutases and Superoxide Reductases. *Chemical Reviews*. 2014, pp 3854–3918.
(24) Strange, R. W.; Murphy, L. M.; Dodd, F. E.; Abraham, Z. H. L.; Eady, R. R.; Smith, B. E.; Hasnain, S. S. Structural and Kinetic Evidence for an Ordered Mechanism of Copper Nitrite Reductase. *J. Mol. Biol.* **1999**, *287* (5), 1001–1009.
(25) Fukuda, Y.; Tse, K. M.; Kado, Y.; Mizohata, E.; Matsumura, H.; Inoue, T. Insights into Unknown Foreign Ligand in Copper Nitrite Reductase. *Biochem. Biophys. Res. Commun.* **2015**, *464* (2), 622–628.
(26) Zumft, W. G. Cell Biology and Molecular Basis of Denitrification. *Microbiol. Mol. Biol. Rev.* **1997**, *61* (4), 533–616.
(27) Solomon, E. I. Spectroscopic Methods in Bioinorganic Chemistry: Blue to Green to Red Copper Sites. *Inorganic Chemistry*. Wiley 2006, pp 8012–8025.
(28) Marcus, R. A. On the Theory of Electron-Transfer Reactions. VI. Unified Treatment for Homogeneous and Electrode Reactions. *J. Chem. Phys.* **1965**, *43* (2), 679–701.
(29) Fukuda, Y.; Tse, K. M.; Nakane, T.; Nakatsu, T.; Suzuki, M.; Sugahara, M.; Inoue, S.;

Masuda, T.; Yumoto, F.; Matsugaki, N.; Nango, E.; Tono, K.; Joti, Y.; Kameshima, T.; Song, C.; Hatsui, T.; Yabashi, M.; Nureki, O.; Murphy, M. E. P.; Inoue, T.; Iwatae, S.; Mizohata, E. Redox-Coupled Proton Transfer Mechanism in Nitrite Reductase Revealed by Femtosecond Crystallography. *Proc. Natl. Acad. Sci. U. S. A.* **2016**, *113* (11), 2928–2933.

(30) Cristaldi, J. C.; Gómez, M. C.; González, P. J.; Ferroni, F. M.; Dalosto, S. D.; Rizzi, A. C.; Rivas, M. G.; Brondino, C. D. Study of the Cys-His Bridge Electron Transfer Pathway in a Copper-Containing Nitrite Reductase by Site-Directed Mutagenesis, Spectroscopic, and Computational Methods. *Biochim. Biophys. Acta - Gen. Subj.* **2018**, *1862* (3), 752–760.

(31) Brenner, S.; Heyes, D. J.; Hay, S.; Hough, M. A.; Eady, R. R.; Hasnain, S. S.; Scrutton, N. S. Demonstration of Proton-Coupled Electron Transfer in the Copper-Containing Nitrite Reductases. *J. Biol. Chem.* **2009**, *284* (38), 25973–25983.

(32) Kohzuma, T.; Kikuchi, M.; Horikoshi, N.; Nagatomo, S.; Kitagawa, T.; Czernuszewicz, R. S. Intersite Structural Rearrangement of the Blue Copper Site Induced by Substrate Binding: Spectroscopic Studies of a Copper-Containing Nitrite Reductase from Alcaligenes Xylosoxidans NCIMB 11015. *Inorg. Chem.* **2006**, *45* (21), 8474–8476.

(33) Hadt, R. G.; Gorelsky, S. I.; Solomon, E. I. Anisotropic Covalency Contributions to Superexchange Pathways in Type One Copper Active Sites. *J. Am. Chem. Soc.* **2014**, *136* (42), 15034–15045.

(34) Ghosh, S.; Dey, A.; Sun, Y.; Scholes, C. P.; Solomon, E. I. Spectroscopic and Computational Studies of Nitrite Reductase: Proton Induced Electron Transfer and Backbonding Contributions to Reactivity. *J. Am. Chem. Soc.* **2009**, *131* (1), 277–288.

(35) Lintuluoto, M.; Lintuluoto, J. M. DFT Study on Enzyme Turnover Including Proton and Electron Transfers of Copper-Containing Nitrite Reductase. *Biochemistry* **2016**, *55* (33), 4697–4707.

(36) Leferink, N. G. H.; Eady, R. R.; Hasnain, S. S.; Scrutton, N. S. Laser-Flash Photolysis Indicates That Internal Electron Transfer Is Triggered by Proton Uptake by Alcaligenes Xylosoxidans Copper-Dependent Nitrite Reductase. *FEBS J.* **2012**, *279* (12), 2174–2181.

(37) Leferink, N. G. H.; Han, C.; Antonyuk, S. V.; Heyes, D. J.; Rigby, S. E. J.; Hough, M. A.; Eady, R. R.; Scrutton, N. S.; Hasnain, S. S. Proton-Coupled Electron Transfer in the Catalytic Cycle of Alcaligenes Xylosoxidans Copper-Dependent Nitrite Reductase. *Biochemistry* **2011**, *50* (19), 4121–4131.

(38) Rose, S. L.; Antonyuk, S. V.; Sasaki, D.; Yamashita, K.; Hirata, K.; Ueno, G.; Ago, H.; Eady, R. R.; Tosha, T.; Yamamoto, M.; Samar Hasnain, S. An Unprecedented Insight into the Catalytic Mechanism of Copper Nitrite Reductase from Atomic-Resolution and Damage-Free Structures. *Sci. Adv.* **2021**, *7* (1).

(39) Kumar, M.; Dixon, N. A.; Merkle, A. C.; Zeller, M.; Lehnert, N.; Papish, E. T. Hydrotris(Triazolyl)Borate Complexes as Functional Models for Cu Nitrite Reductase: The Electronic Influence of Distal Nitrogens. *Inorg. Chem.* **2012**, *51* (13), 7004–7006.

(40) Halfen, J. A.; Mahapatra, S.; Wilkinson, E. C.; Gengenbach, A. J.; Young, V. G.; Que Jnr, L.; Tolman, W. B. Synthetic Modeling of Nitrite Binding and Activation by Reduced Copper Proteins. Characterization of Copper(I)-Nitrite Complexes That Evolve Nitric Oxide. *J. Am. Chem. Soc.* **1996**, *118* (4), 763–776.

(41) Hsu, S. C. N.; Chang, Y. L.; Chuang, W. J.; Chen, H. Y.; Lin, I. J.; Chiang, M. Y.; Kao, C. L.; Chen, H. Y. Copper(I) Nitro Complex with an Anionic [HB(3,5-Me2Pz) 3]- Ligand: A Synthetic Model for the Copper Nitrite Reductase Active Site. *Inorg. Chem.* **2012**, *51* (17), 9297–9308.

(42) Merkle, A. C.; Lehnert, N. Binding and Activation of Nitrite and Nitric Oxide by Copper Nitrite Reductase and Corresponding Model Complexes. *Dalton Transactions*. 2012, pp 3355–3368.
(43) Boulanger, M. J.; Murphy, M. E. P. Directing the Mode of Nitrite Binding to a Copper-containing Nitrite Reductase from Alcaligenes Faecalis S-6: Characterization of an Active Site Isoleucine. *Protein Sci.* **2003**, *12* (2), 248–256.
(44) Boulanger, M. J.; Kukimoto, M.; Nishiyama, M.; Horinouchi, S.; Murphy, M. E. P. Catalytic Roles for Two Water Bridged Residues (Asp-98 and His-255) in the Active Site of Copper-Containing Nitrite Reductase. *J. Biol. Chem.* **2000**, *275* (31), 23957–23964.
(45) Suzuki, S.; Deligeer; Yamaguchi, K.; Kataoka, K.; Kobayashi, K.; Tagawa, S.; Kohzuma, T.; Shidara, S.; Iwasaki, H. Spectroscopic Characterization and Intramolecular Electron Transfer Processes of Native and Type 2 Cu-Depleted Nitrite Reductases. *J. Biol. Inorg. Chem.* **1997**, *2* (2), 265–274.
(46) Antonyuk, S. V.; Strange, R. W.; Sawers, G.; Eady, R. R.; Hasnain, S. S. Atomic Resolution Structures of Resting-State, Substrate- and Product-Complexed Cu-Nitrite Reductase Provide Insight into Catalytic Mechanism. *Proc. Natl. Acad. Sci. U. S. A.* **2005**, *102* (34), 12041–12046.
(47) Abraham, Z. H. L.; Smith, B. E.; Howes, B. D.; Lowe, D. J.; Eady, R. R. PH-Dependence for Binding a Single Nitrite Ion to Each Type-2 Copper Centre in the Copper-Containing Nitrite Reductase of Alcaligenes Xylosoxidans. *Biochem. J.* **1997**, *324* (2), 511–516.
(48) Averill, B. A. Dissimilatory Nitrite and Nitric Oxide Reductases. *Chem. Rev.* **1996**, *96* (7), 2951–2964.
(49) Wijma, H. J.; Jeuken, L. J. C.; Verbeet, M. P.; Armstrong, F. A.; Canters, G. W. A Random-Sequential Mechanism for Nitrite Binding and Active Site Reduction in Copper-Containing Nitrite Reductase. *J. Biol. Chem.* **2006**, *281* (24), 16340–16346.
(50) Kuznetsova, S.; Zauner, G.; Aartsma, T. J.; Engelkamp, H.; Hatzakis, N.; Rowan, A. E.; Nolte, R. J. M.; Christianen, P. C. M.; Canters, G. W. The Enzyme Mechanism of Nitrite Reductase Studied at Single-Molecule Level. *Proc. Natl. Acad. Sci. U. S. A.* **2008**, *105* (9), 3250–3255.
(51) Tabares, L. C.; Kostrz, D.; Elmalk, A.; Andreoni, A.; Dennison, C.; Aartsma, T. J.; Canters, G. W. Fluorescence Lifetime Analysis of Nitrite Reductase from Alcaligenes Xylosoxidans at the Single-Molecule Level Reveals the Enzyme Mechanism. *Chem. - A Eur. J.* **2011**, *17* (43), 12015–12019.
(52) Edman, L.; Rigler, R. Memory Landscapes of Single-Enzyme Molecules. *Proc. Natl. Acad. Sci. U. S. A.* **2000**, *97* (15), 8266–8271.
(53) Lu, H. P. Single-Molecule Enzymatic Dynamics. *Science (80-.).* **1998**, *282* (5395), 1877–1882.
(54) Leferink, N. G. H.; Eady, R. R.; Hasnain, S. S.; Scrutton, N. S. Laser-Flash Photolysis Indicates That Internal Electron Transfer Is Triggered by Proton Uptake by Alcaligenes Xylosoxidans Copper-Dependent Nitrite Reductase. *FEBS J.* **2012**, *279* (12), 2174–2181.
(55) Tocheva, E. I.; Rosell, F. I.; Mauk, A. G.; Murphy, M. E. P. Side-On Copper-Nitrosyl Coordination by Nitrite Reductase. *Science (80-.).* **2004**, *304* (5672), 867–870.
(56) Usov, O. M.; Sun, Y.; Grigoryants, V. M.; Shapleigh, J. P.; Scholes, C. P. EPR-ENDOR of the Cu(I)NO Complex of Nitrite Reductase. *J. Am. Chem. Soc.* **2006**, *128* (40), 13102–13111.
(57) Ghosh, S.; Dey, A.; Usov, O. M.; Sun, Y.; Grigoryants, V. M.; Scholes, C. P.; Solomon, E.

I. Resolution of the Spectroscopy versus Crystallography Issue for NO Intermediates of Nitrite Reductase from Rhodobacter Sphaeroides. *J. Am. Chem. Soc.* **2007**, *129* (34), 10310–10311.

(58) Ruggiero, C. E.; Carrier, S. M.; Tolman, W. B. Reductive Disproportionation of NO Mediated by Copper Complexes: Modeling N2O Generation by Copper Proteins and Heterogeneous Catalysts. *Angew. Chemie Int. Ed. English* **1994**, *33* (8), 895–897.

(59) Hough, M. A.; Conradie, J.; Strange, R. W.; Antonyuk, S. V; Eady, R. R.; Ghosh, A.; Hasnain, S. S. Nature of the Copper-Nitrosyl Intermediates of Copper Nitrite Reductases during Catalysis. *Chem. Sci.* **2020**, *11* (46), 12485–12492.

(60) Eady, R. R.; Samar Hasnain, S. New Horizons in Structure-Function Studies of Copper Nitrite Reductase. *Coordination Chemistry Reviews*. 2022.

(61) Merkle, A. C.; Lehnert, N. The Side-on Copper(I) Nitrosyl Geometry in Copper Nitrite Reductase Is Due to Steric Interactions with Isoleucine-257. *Inorg. Chem.* **2009**, *48* (24), 11504–11506.

(62) Fukuda, Y.; Hirano, Y.; Kusaka, K.; Inoue, T.; Tamada, T. High-Resolution Neutron Crystallography Visualizes an OH-Bound Resting State of a Copper-Containing Nitrite Reductase. *Proc. Natl. Acad. Sci. U. S. A.* **2020**, *117* (8), 4071–4077.

(63) Heinisch, T.; Pellizzoni, M.; Dürrenberger, M.; Tinberg, C. E.; Köhler, V.; Klehr, J.; Häussinger, D.; Baker, D.; Ward, T. R. Improving the Catalytic Performance of an Artificial Metalloenzyme by Computational Design. *J. Am. Chem. Soc.* **2015**, *137* (32), 10414–10419.

(64) Kent, S. B. H. Total Chemical Synthesis of Proteins. *Chem. Soc. Rev.* **2009**, *38* (2), 338–351.

(65) Dawson, P. E.; Muir, T. W.; Clark-Lewis, I.; Kent, S. B. H. Synthesis of Proteins by Native Chemical Ligation. *Science (80-.).* **1994**, *266* (5186), 776–779.

(66) Wang, L.; Brock, A.; Herberich, B.; Schultz, P. G. Expanding the Genetic Code of Escherichia Coli. *Science (80-.).* **2001**, *292* (5516), 498–500.

(67) Hohsaka, T.; Sisido, M. Incorporation of Non-Natural Amino Acids into Proteins. *Current Opinion in Chemical Biology*. December 2002, pp 809–815.

(68) Onderko, E. L.; Silakov, A.; Yosca, T. H.; Green, M. T. Characterization of a Selenocysteine-Ligated P450 Compound I Reveals Direct Link between Electron Donation and Reactivity. *Nat. Chem.* **2017**, *9* (7), 623–628.

(69) Ortmayer, M.; Fisher, K.; Basran, J.; Wolde-Michael, E. M.; Heyes, D. J.; Levy, C.; Lovelock, S. L.; Anderson, J. L. R.; Raven, E. L.; Hay, S.; Rigby, S. E. J.; Green, A. P. Rewiring the "Push-Pull" Catalytic Machinery of a Heme Enzyme Using an Expanded Genetic Code. *ACS Catal.* **2020**, *10* (4), 2735–2746.

(70) Lee, J.; Yang, M.; Song, W. J. The Expanded Landscape of Metalloproteins by Genetic Incorporation of Noncanonical Amino Acids. *Bulletin of the Korean Chemical Society*. John Wiley & Sons, Ltd January 1, 2023, pp 23–34.

(71) Wang, Y.; Zhang, J.; Han, B.; Tan, L.; Cai, W.; Li, Y.; Su, Y.; Yu, Y.; Wang, X.; Duan, X.; Wang, H.; Shi, X.; Wang, J.; Yang, X.; Liu, T. Noncanonical Amino Acids as Doubly Bio-Orthogonal Handles for One-Pot Preparation of Protein Multiconjugates. *Nat. Commun.* **2023**, *14* (1), 248–253.

(72) Wang, Y.; Zhang, J.; Han, B.; Tan, L.; Cai, W.; Li, Y.; Su, Y.; Yu, Y.; Wang, X.; Duan, X.; Wang, H.; Shi, X.; Wang, J.; Yang, X.; Liu, T. Noncanonical Amino Acids as Doubly Bio-Orthogonal Handles for One-Pot Preparation of Protein Multiconjugates. *Nat. Commun.* **2023**, *14* (1), 1–16.

(73) Quast, R. B.; Mrusek, D.; Hoffmeister, C.; Sonnabend, A.; Kubick, S. Cotranslational Incorporation of Non-Standard Amino Acids Using Cell-Free Protein Synthesis. *FEBS Letters*. 2015, pp 1703–1712.
(74) Hill, E. A.; Weitz, A. C.; Onderko, E.; Romero-rivera, A.; Guo, Y.; Swart, M.; Bominaar, E. L.; Green, M. T.; Hendrich, M. P.; Lacy, D. C.; Borovik, A. S. Reactivity of an Fe IV - Oxo Complex with Protons and Oxidants. **2016**, 2–5.
(75) Kai Johnsson; Susanne Brakmann; Schuster, P.; Hilvert, D.; Taylor, S. V.; Kast, P.; Daniel, R.; Soumillion, P.; Fastrez, J.; Wittrup, D.; Carter, B. T.; Lin, H.; Cornish, V. W.; Schwienhorst, A.; Benkovic, S. J.; Lutz, S.; Arnold, F. H.; Cirino, P. C.; Jaeger, K.-E.; Reetz, M. T.; Davidson, J. F.; Anderson, J.; Guo, H.; Landis, D.; Loeb, L. A.; Lanio, T.; Jeltsch, A.; Pingoud, A.; Bornscheuer, U. T. *Directed Molecular Evolution of Proteins*; Wiley, 2002.
(76) Arnold, F. H. Design by Directed Evolution. *Acc. Chem. Res.* **1998**, *31* (3), 125–131.
(77) Romero, P. A.; Arnold, F. H. Exploring Protein Fitness Landscapes by Directed Evolution. *Nature Reviews Molecular Cell Biology*. Nature Publishing Group December 2009, pp 866–876.
(78) Schnettler, J. D.; Klein, O. J.; Kaminski, T. S.; Colin, P. Y.; Hollfelder, F. Ultrahigh-Throughput Directed Evolution of a Metal-Free α/β-Hydrolase with a Cys-His-Asp Triad into an Efficient Phosphotriesterase. *J. Am. Chem. Soc.* **2023**, *145* (2), 1083–1096.
(79) Markel, U.; Sauer, D. F.; Schiffels, J.; Okuda, J.; Schwaneberg, U. Towards the Evolution of Artificial Metalloenzymes—A Protein Engineer's Perspective. *Angewandte Chemie - International Edition*. John Wiley & Sons, Ltd March 26, 2019, pp 4454–4464.
(80) Sarai, N. S.; Levin, B. J.; Roberts, J. M.; Katsoulis, D. E.; Arnold, F. H. Biocatalytic Transformations of Silicon - The Other Group 14 Element. *ACS Central Science*. 2021, pp 944–953.
(81) Passerini, A.; Frasconi, P. Learning to Discriminate between Ligand-Bound and Disulfide-Bound Cysteines. *Protein Eng. Des. Sel.* **2004**, *17* (4), 367–373.
(82) Dürr, S. L.; Levy, A.; Rothlisberger, U. Metal3D: A General Deep Learning Framework for Accurate Metal Ion Location Prediction in Proteins. *Nat. Commun.* **2023**, *14* (1), 1–14.
(83) De Ferrari, L.; Mitchell, J. B. O. From Sequence to Enzyme Mechanism Using Multi-Label Machine Learning. *BMC Bioinformatics* **2014**, *15* (1), 1–13.
(84) van Breugel, M.; Rosa e Silva, I.; Andreeva, A. Structural Validation and Assessment of AlphaFold2 Predictions for Centrosomal and Centriolar Proteins and Their Complexes. *Commun. Biol.* **2022**, *5* (1), 1–10.
(85) Drienovská, I.; Rioz-Martínez, A.; Draksharapu, A.; Roelfes, G. Novel Artificial Metalloenzymes by in Vivo Incorporation of Metal-Binding Unnatural Amino Acids. *Chem. Sci.* **2015**, *6* (1), 770–776.
(86) Coquière, D.; Bos, J.; Beld, J.; Roelfes, G. Enantioselective Artificial Metalloenzymes Based on a Bovine Pancreatic Polypeptide Scaffold. *Angew. Chemie - Int. Ed.* **2009**, *48* (28), 5159–5162.
(87) Olshansky, L.; Huerta-Lavorie, R.; Nguyen, A. I.; Vallapurackal, J.; Furst, A.; Tilley, T. D.; Borovik, A. S. Artificial Metalloproteins Containing Co4O4 Cubane Active Sites. *J. Am. Chem. Soc.* **2018**, *140* (8), 2739–2742.
(88) Guzmán, F.; Aróstica, M.; Román, T.; Beltrán, D.; Gauna, A.; Albericio, F.; Cárdenas, C. Peptides, Solid-Phase Synthesis and Characterization: Tailor-Made Methodologies. *Electron. J. Biotechnol.* **2023**, *64*, 27–33.

(89) Palomo, J. M. Solid-Phase Peptide Synthesis: An Overview Focused on the Preparation of Biologically Relevant Peptides. *RSC Advances*. 2014, pp 32658–32672.
(90) Ortega-Requena, S.; Montiel, C.; Máximo, F.; Gómez, M.; Murcia, M. D.; Bastida, J. Esters in the Food and Cosmetic Industries: An Overview of the Reactors Used in Their Biocatalytic Synthesis. *Materials (Basel).* **2024**, *17* (1), 268.
(91) Milczek, E. M. Commercial Applications for Enzyme-Mediated Protein Conjugation: New Developments in Enzymatic Processes to Deliver Functionalized Proteins on the Commercial Scale. *Chemical Reviews*. American Chemical Society January 10, 2018, pp 119–141.
(92) Schrittwieser, J. H.; Velikogne, S.; Hall, M.; Kroutil, W. Artificial Biocatalytic Linear Cascades for Preparation of Organic Molecules. *Chemical Reviews*. American Chemical Society January 10, 2018, pp 270–348.
(93) Johansen, K. S. Discovery and Industrial Applications of Lytic Polysaccharide Mono-Oxygenases. *Biochem. Soc. Trans.* **2016**, *44*, 143–149.
(94) Kuusk, S.; Eijsink, V. G. H.; Väljamäe, P. The "Life-Span" of Lytic Polysaccharide Monooxygenases (LPMOs) Correlates to the Number of Turnovers in the Reductant Peroxidase Reaction. *J. Biol. Chem.* **2023**, *299* (9).
(95) Haddad Momeni, M.; Fredslund, F.; Bissaro, B.; Raji, O.; Vuong, T. V.; Meier, S.; Nielsen, T. S.; Lombard, V.; Guigliarelli, B.; Biaso, F.; Haon, M.; Grisel, S.; Henrissat, B.; Welner, D. H.; Master, E. R.; Berrin, J. G.; Abou Hachem, M. Discovery of Fungal Oligosaccharide-Oxidising Flavo-Enzymes with Previously Unknown Substrates, Redox-Activity Profiles and Interplay with LPMOs. *Nat. Commun.* **2021**, *12* (1), 1–13.
(96) Liu, Y.; Harnden, K. A.; Van Stappen, C.; Dikanov, S. A.; Lu, Y. A Designed Copper Histidine-Brace Enzyme for Oxidative Depolymerization of Polysaccharides as a Model of Lytic Polysaccharide Monooxygenase. *Proc. Natl. Acad. Sci. U. S. A.* **2023**, *120* (43).
(97) Karlsson, B. G.; Pascher, T.; Nordling, M.; Arvidsson, R. H. A.; Lundberg, L. G. Expression of the Blue Copper Protein Azurin from Pseudomonas Aeruginosa in Escherichia Coli. *FEBS Lett.* **1989**, *246* (1–2), 211–217.
(98) Nazor, J.; Liu, J.; Huisman, G. Enzyme Evolution for Industrial Biocatalytic Cascades. *Current Opinion in Biotechnology*. 2021, pp 182–190.
(99) Akabori, S.; Sakurai, S.; Izumi, Y.; Fujii, Y. An Asymmetric Catalyst. *Nature*. Nature Publishing Group 1956, pp 323–324.
(100) Taylor, W. R.; Chelliah, V.; Hollup, S. M.; MacDonald, J. T.; Jonassen, I. Probing the "Dark Matter" of Protein Fold Space. *Structure* **2009**, *17* (9), 1244–1252.
(101) Cossio, P.; Trovato, A.; Pietrucci, F.; Seno, F.; Maritan, A.; Laio, A. Exploring the Universe of Protein Structures beyond the Protein Data Bank. *PLoS Comput. Biol.* **2010**, *6* (11), 1000957.
(102) Hilditch, A. T.; Romanyuk, A.; Cross, S. J.; Obexer, R.; McManus, J. J.; Woolfson, D. N. Assembling Membraneless Organelles from de Novo Designed Proteins. *Nat. Chem.* **2023**, *16* (1), 89–97.
(103) Scott, A. J.; Niitsu, A.; Kratochvil, H. T.; Lang, E. J. M.; Sengel, J. T.; Dawson, W. M.; Mahendran, K. R.; Mravic, M.; Thomson, A. R.; Brady, R. L.; Liu, L.; Mulholland, A. J.; Bayley, H.; DeGrado, W. F.; Wallace, M. I.; Woolfson, D. N. Constructing Ion Channels from Water-Soluble α-Helical Barrels. *Nat. Chem.* **2021**, *13* (7), 643–650.
(104) Xu, C.; Lu, P.; Gamal El-Din, T. M.; Pei, X. Y.; Johnson, M. C.; Uyeda, A.; Bick, M. J.; Xu, Q.; Jiang, D.; Bai, H.; Reggiano, G.; Hsia, Y.; Brunette, T. J.; Dou, J.; Ma, D.; Lynch,

E. M.; Boyken, S. E.; Huang, P. S.; Stewart, L.; DiMaio, F.; Kollman, J. M.; Luisi, B. F.; Matsuura, T.; Catterall, W. A.; Baker, D. Computational Design of Transmembrane Pores. *Nature* **2020**, *585* (7823), 129–134.

(105) Pirro, F.; Schmidt, N.; Lincoff, J.; Widel, Z. X.; Polizzi, N. F.; Liu, L.; Therien, M. J.; Grabe, M.; Chino, M.; Lombardi, A.; DeGrado, W. F. Allosteric Cooperation in a de Novo-Designed Two-Domain Protein. *Proc. Natl. Acad. Sci. U. S. A.* **2020**, *117* (52), 33246–33253.

(106) Kosugi, T.; Iida, T.; Tanabe, M.; Iino, R.; Koga, N. Design of Allosteric Sites into Rotary Motor V1-ATPase by Restoring Lost Function of Pseudo-Active Sites. *Nat. Chem.* **2023**, *15* (11), 1591–1598.

(107) Chalkley, M. J.; Mann, S. I.; DeGrado, W. F. De Novo Metalloprotein Design. *Nature Reviews Chemistry*. Nature Publishing Group December 6, 2022, pp 31–50.

(108) Lombardi, A.; Pirro, F.; Maglio, O.; Chino, M.; DeGrado, W. F. De Novo Design of Four-Helix Bundle Metalloproteins: One Scaffold, Diverse Reactivities. *Acc. Chem. Res.* **2019**, *52* (5), 1148–1159.

(109) Kalvet, I.; Ortmayer, M.; Zhao, J.; Crawshaw, R.; Ennist, N. M.; Levy, C.; Roy, A.; Green, A. P.; Baker, D. Design of Heme Enzymes with a Tunable Substrate Binding Pocket Adjacent to an Open Metal Coordination Site. *J. Am. Chem. Soc.* **2023**, *145* (26), 14307–14315.

(110) Pinter, T. B. J.; Koebke, K. J.; Pecoraro, V. L. Catalysis and Electron Transfer in De Novo Designed Helical Scaffolds. *Angewandte Chemie - International Edition*. 2020, pp 7678–7699.

(111) Mann, S. I.; Nayak, A.; Gassner, G. T.; Therien, M. J.; Degrado, W. F. De Novo Design, Solution Characterization, and Crystallographic Structure of an Abiological Mn-Porphyrin-Binding Protein Capable of Stabilizing a Mn(V) Species. *J. Am. Chem. Soc.* **2021**, *143* (1), 252–259.

(112) DeGrado, W. F.; Summa, C. M.; Pavone, V.; Nastri, F.; Lombardi, A. De Novo Design and Structural Characterization of Proteins and Metalloproteins. *Annual Review of Biochemistry*. 1999, pp 779–819.

(113) Schneider, J. P.; Lombardi, A.; DeGrado, W. F. Analysis and Design of Three-Stranded Coiled Coils and Three-Helix Bundles. *Fold. Des.* **1998**, *3* (2).

(114) Cohen, C.; Parry, D. A. D. A-Helical Coiled Coils and Bundles: How to Design an A-helical Protein. *Proteins: Structure, Function, and Bioinformatics*. 1990, pp 1–15.

(115) Ghosh, D.; Pecoraro, V. L. Understanding Metalloprotein Folding Using a de Novo Design Strategy. *Inorganic Chemistry*. 2004, pp 7902–7915.

(116) Ogihara, N. L.; Weiss, M. S.; Degrado, W. F.; Eisenberg, D. The Crystal Structure of the Designed Trimeric Coiled Coil Coil- V(a)L(d): Implications for Engineering Crystals and Supramolecular Assemblies. *Protein Sci.* **1997**, *6* (1), 80–88.

(117) McLachlan, A. D.; Stewart, M. Tropomyosin Coiled-Coil Interactions: Evidence for an Unstaggered Structure. *J. Mol. Biol.* **1975**, *98* (2), 293–304.

(118) Regan, L.; Degrado, W. F. Characterization of a Helical Protein Designed from First Principles. *Science (80-.).* **1988**, *241* (4868), 976–978.

(119) Crick, F. H. C. Is α-Keratin a Coiled Coil? *Nature* **1952**, *170* (4334), 882–883.

(120) Crick, F. H. C. The Fourier Transform of a Coiled-Coil. *Acta Crystallogr.* **1953**, *6* (8), 685–689.

(121) Macdonald, R. D.; Khajehpour, M. Effects of the Protein Denaturant Guanidinium Chloride

on Aqueous Hydrophobic Contact-Pair Interactions. *Biophys. Chem.* **2015**, *196*, 25–32.
(122) Biswas, B.; Muttathukattil, A. N.; Reddy, G.; Singh, P. C. Contrasting Effects of Guanidinium Chloride and Urea on the Activity and Unfolding of Lysozyme. *ACS Omega* **2018**, *3* (10), 14119–14126.
(123) Zhu, B. -Y; Zhou, M. E.; Kay, C. M.; Hodges, R. S. Packing and Hydrophobicity Effects on Protein Folding and Stability: Effects of B-branched Amino Acids, Valine and Isoleucine, on the Formation and Stability of Two-stranded A-helical Coiled Coils/Leucine Zippers. *Protein Sci.* **1993**, *2* (3), 383–394.
(124) Kwok, S. C.; Hodges, R. S. Effect of Chain Length on Coiled-Coil Stability: Decreasing Stability with Increasing Chain Length. *Biopolym. - Pept. Sci. Sect.* **2004**, *76* (5), 378–390.
(125) Avvaru, B. S.; Kim, C. U.; Sippel, K. H.; Gruner, S. M.; Agbandje-McKenna, M.; Silverman, D. N.; McKenna, R. A Short, Strong Hydrogen Bond in the Active Site of Human Carbonic Anhydrase II. *Biochemistry* **2010**, *49* (2), 249–251.
(126) Dieckmann, G. R.; McRorie, D. K.; Tierney, D. L.; Utschig, L. M.; Singer, C. P.; O, T. V; Penner-Hahn, J. E.; DeGrado, W. F.; Pecoraro, V. L. De Novo Design of Mercury-Binding Two- and Three-Helical Bundles. *J. Am. Chem. Soc* **1997**, *261* (1), 6195–6196.
(127) Dieckmann, G. R.; McRorie, D. K.; Lear, J. D.; Sharp, K. A.; DeGrado, W. F.; Pecoraro, V. L. The Role of Protonation and Metal Chelation Preferences in Defining the Properties of Mercury-Binding Coiled Coils. *J. Mol. Biol.* **1998**, *280* (5), 897–912.
(128) Peacock, A. F. A.; Iranzo, O.; Pecoraro, V. L. Harnessing Natures Ability to Control Metal Ion Coordination Geometry Using de Novo Designed Peptides. *Dalt. Trans.* **2009**, No. 13, 2271–2280.
(129) Van Damme, P.; Lasa, M.; Polevoda, B.; Gazquez, C.; Elosegui-Artola, A.; Kim, D. S.; De Juan-Pardo, E.; Demeyer, K.; Hole, K.; Larrea, E.; Timmerman, E.; Prieto, J.; Arnesen, T.; Sherman, F.; Gevaert, K.; Aldabe, R. N-Terminal Acetylome Analyses and Functional Insights of the N-Terminal Acetyltransferase NatB. *Proc. Natl. Acad. Sci. U. S. A.* **2012**, *109* (31), 12449–12454.
(130) Woolfson, D. N.; Alber, T. Predicting Oligomerization States of Coiled Coils. *Protein Sci.* **1995**, *4* (8), 1596–1607.
(131) Harbury, P. B.; Zhang, T.; Kim, P. S.; Alber, T. A Switch between Two-, Three-, and Four-Stranded Coiled Coils in GCN4 Leucine Zipper Mutants. *Science (80-.).* **1993**, *262* (5138), 1401–1407.
(132) Monera, O. D.; Zhou, N. E.; Kay, C. M.; Hodges, R. S. Comparison of Antiparallel and Parallel Two-Stranded α-Helical Coiled- Coils. Design, Synthesis, and Characterization. *J. Biol. Chem.* **1993**, *268* (26), 19218–19227.
(133) Matzapetakis, M.; Farrer, B. T.; Weng, T. C.; Hemmingsen, L.; Penner-Hahn, J. E.; Pecoraro, V. L. Comparison of the Binding of Cadmium(II), Mercury(II) and Arsenic(III) to the de Novo Designed Peptides TRI L12C and TRI L16C. *J. Am. Chem. Soc.* **2002**, *124* (27), 8042–8054.
(134) Chakraborty, S.; Touw, D. S.; Peacock, A. F. A.; Stuckey, J.; Pecoraro, V. L. Structural Comparisons of Apo-and Metalated Three-Stranded Coiled Coils Clarify Metal Binding Determinants in Thiolate Containing Designed Peptides. *J. Am. Chem. Soc.* **2010**, *132* (38), 13240–13250.
(135) Touw, D. S.; Nordman, C. E.; Stuckey, J. A.; Pecoraro, V. L. Identifying Important Structural Characteristics of Arsenic Resistance Proteins by Using Designed Three-Stranded Coiled Coils. *Proc. Natl. Acad. Sci. U. S. A.* **2007**, *104* (29), 11969–11974.

(136) Ruckthong, L.; Zastrow, M. L.; Stuckey, J. A.; Pecoraro, V. L. A Crystallographic Examination of Predisposition versus Preorganization in de Novo Designed Metalloproteins. *J. Am. Chem. Soc.* **2016**, *138* (36), 11979–11988.
(137) Lupas, A. N.; Bassler, J. Coiled Coils – A Model System for the 21st Century. *Trends in Biochemical Sciences*. Elsevier Ltd February 1, 2017, pp 130–140.
(138) Farrer, B. T.; Pecoraro, V. L. Hg(II) Binding to a Weakly Associated Coiled Coil Nucleates an Encoded Metalloprotein Fold: A Kinetic Analysis. *Proc. Natl. Acad. Sci. U. S. A.* **2003**, *100* (7), 3760–3765.
(139) Zastrow, M. L.; Pecoraro, V. L. Influence of Active Site Location on Catalytic Activity in de Novo-Designed Zinc Metalloenzymes. *J. Am. Chem. Soc.* **2013**, *135* (15), 5895–5903.
(140) Chen, X.; Tu, C.; LoGrasso, P. V; Laipis, P. J.; Silverman, D. N. Interaction and Influence of Phenylalanine-198 and Threonine-199 on Catalysis by Human Carbonic Anhydrase III. *Biochemistry* **1993**, *32* (31), 7861–7865.
(141) Lindskog, S.; Coleman, J. E. The Catalytic Mechanism of Carbonic Anhydrase. *Proc. Natl. Acad. Sci. U. S. A.* **1973**, *70* (9), 2505–2508.
(142) Lindskog, S. Structure and Mechanism of Carbonic Anhydrase. *Pharmacology and Therapeutics*. 1997, pp 1–20.
(143) Jackman, J. E.; Merz, K. M.; Fierke, C. A. Disruption of the Active Site Solvent Network in Carbonic Anhydrase II Decreases the Efficiency of Proton Transfer. *Biochemistry* **1996**, *35* (51), 16421–16428.
(144) Bertini, I.; Luchinat, C.; Rosi, M.; Sgamellotti, A.; Tarantelli, F. *PKaof Zinc-Bound Water and Nucleophilicity of Hydroxo-Containing Species. Ab Initio Calculations on Models for Zinc Enzymes*; 1990; Vol. 29.
(145) Linder, D. P.; Baker, B. E.; Rodgers, K. R. [(H2o)Zn (Imidazole)n]2+: The Vital Roles of Coordination Number and Geometry in Zn-OH2 Acidity and Catalytic Hydrolysis. *Phys. Chem. Chem. Phys.* **2018**, *20* (38), 24979–24991.
(146) Cangelosi, V. M.; Deb, A.; Penner-Hahn, J. E.; Pecoraro, V. L. A de Novo Designed Metalloenzyme for the Hydration of CO2. *Angew. Chemie - Int. Ed.* **2014**, *53* (30), 7900–7903.
(147) Walsh, S. T. R.; Sukharev, V. I.; Betz, S. F.; Vekshin, N. L.; DeGrado, W. F. Hydrophobic Core Malleability of a de Novo Designed Three-Helix Bundle Protein. *J. Mol. Biol.* **2001**, *305* (2), 361–373.
(148) Melissa L. Zastrow. De Novo Designed Metalloenzymes: Structural Stabilization and Hydrolytic Catalysis in a Family of -Helical Coiled Coils, University of Michigan, 2013.
(149) Borghesani, V.; Zastrow, M. L.; Tolbert, A. E.; Deb, A.; Penner-Hahn, J. E.; Pecoraro, V. L. Co(II) Substitution Enhances the Esterase Activity of a de Novo Designed Zn(II) Carbonic Anhydrase. *Chem. - A Eur. J.* **2024**, e202304367.
(150) Hakansson, K.; Wehnert, A.; Liljas, A. X-Ray Analysis of Metal-Substituted Human Carbonic Anhydrase II Derivatives. *Acta Crystallogr. Sect. D Biol. Crystallogr.* **1994**, *50* (1), 93–100.
(151) Kogut, K. A.; Rowlett, R. S. A Comparison of the Mechanisms of CO2 Hydration by Native and Co2+-Substituted Carbonic Anhydrase II. *J. Biol. Chem.* **1987**, *262* (34), 16417–16424.
(152) Mock, W. L.; Freeman, D. J.; Aksamawati, M. Fluxionate Lewis Acidity of the Zn2+ Ion in Carboxypeptidase A. *Biochem. J.* **1993**, *289* (1), 185–193.
(153) Song, W. J.; Tezcan, F. A. A Designed Supramolecular Protein Assembly with in Vivo Enzymatic Activity. *Science (80-.).* **2014**, *346* (6216), 1525–1528.

(154) Rufo, C. M.; Moroz, Y. S.; Moroz, O. V; Stöhr, J.; Smith, T. A.; Hu, X.; Degrado, W. F.; Korendovych, I. V. Short Peptides Self-Assemble to Produce Catalytic Amyloids. *Nat. Chem.* **2014**, *6* (4), 303–309.
(155) Der, B. S.; Edwards, D. R.; Kuhlman, B. Catalysis by a de Novo Zinc-Mediated Protein Interface: Implications for Natural Enzyme Evolution and Rational Enzyme Engineering. *Biochemistry* **2012**, *51* (18), 3933–3940.
(156) Salgado, E. N.; Faraone-Mennella, J.; Tezcan, F. A. Controlling Protein-Protein Interactions through Metal Coordination: Assembly of a 16-Helix Bundle Protein. *J. Am. Chem. Soc.* **2007**, *129* (44), 13374–13375.
(157) Verpoorte, J. A.; Mehta, S.; Edsall, J. T. *Esterase Activities of Human Carbonic Anhydrases B and C.*; 1967; Vol. 242.
(158) LIANG, Z.; XUE, Y.; BEHRAVAN, G.; JONSSON, B. -H; LINDSKOG, S. Importance of the Conserved Active-site Residues Try7, Glu106 and Thr199 for the Catalytic Function of Human Carbonic Anhydrase II. *Eur. J. Biochem.* **1993**, *211* (3), 821–827.
(159) Babtie, A.; Tokuriki, N.; Hollfelder, F. What Makes an Enzyme Promiscuous? *Current Opinion in Chemical Biology*. 2010, pp 200–207.
(160) Studer, S.; Hansen, D. A.; Pianowski, Z. L.; Mittl, P. R. E.; Debon, A.; Guffy, S. L.; Der, B. S.; Kuhlman, B.; Hilvert, D. Evolution of a Highly Active and Enantiospecific Metalloenzyme from Short Peptides. *Science (80-.).* **2018**, *362* (6420), 1285–1288.
(161) Choi, T. S.; Tezcan, F. A. Design of a Flexible, Zn-Selective Protein Scaffold That Displays Anti-Irving-Williams Behavior. *J. Am. Chem. Soc.* **2022**, *144* (39), 18090–18100.
(162) Han, K.; Na, Y.; Zhang, L.; Tezcan, F. A. Dynamic, Polymer-Integrated Crystals for Efficient, Reversible Protein Encapsulation. *J. Am. Chem. Soc.* **2022**, *144* (23), 10139–10144.
(163) Koebke, K. J.; Ruckthong, L.; Meagher, J. L.; Mathieu, E.; Harland, J.; Deb, A.; Lehnert, N.; Policar, C.; Tard, C.; Penner-Hahn, J. E.; Stuckey, J. A.; Pecoraro, V. L. Clarifying the Copper Coordination Environment in a de Novo Designed Red Copper Protein. *Inorg. Chem.* **2018**, *57* (19), 12291–12302.
(164) Mathieu, E.; Tolbert, A. E.; Koebke, K. J.; Tard, C.; Iranzo, O.; Penner-Hahn, J. E.; Policar, C.; Pecoraro, V. Rational De Novo Design of a Cu Metalloenzyme for Superoxide Dismutation. *Chem. - A Eur. J.* **2020**, *26* (1), 249–258.
(165) Pirro, F.; La Gatta, S.; Arrigoni, F.; Famulari, A.; Maglio, O.; Del Vecchio, P.; Chiesa, M.; De Gioia, L.; Bertini, L.; Chino, M.; Nastri, F.; Lombardi, A. A De Novo-Designed Type 3 Copper Protein Tunes Catechol Substrate Recognition and Reactivity. *Angew. Chemie - Int. Ed.* **2023**, *62* (1), e202211552.
(166) Tegoni, M.; Yu, F.; Bersellini, M.; Penner-Hahn, J. E.; Pecoraro, V. L. Designing a Functional Type 2 Copper Center That Has Nitrite Reductase Activity within α-Helical Coiled Coils. *Proc. Natl. Acad. Sci. U. S. A.* **2012**, *109* (52), 21234–21239.
(167) Koebke, K. J.; Yu, F.; Van Stappen, C.; Pinter, T. B. J.; Deb, A.; Penner-Hahn, J. E.; Pecoraro, V. L. Methylated Histidines Alter Tautomeric Preferences That Influence the Rates of Cu Nitrite Reductase Catalysis in Designed Peptides. *J. Am. Chem. Soc.* **2019**, *141* (19), 7765–7775.
(168) Koebke, K. J.; Yu, F.; Salerno, E.; Van Stappen, C.; Tebo, A. G.; Penner-Hahn, J. E.; Pecoraro, V. L. Modifying the Steric Properties in the Second Coordination Sphere of Designed Peptides Leads to Enhancement of Nitrite Reductase Activity. *Angew. Chemie* **2018**, *130* (15), 4018–4021.

(169) Yu, F.; Penner-Hahn, J. E.; Pecoraro, V. L. De Novo-Designed Metallopeptides with Type 2 Copper Centers: Modulation of Reduction Potentials and Nitrite Reductase Activities. *J. Am. Chem. Soc.* **2013**, *135* (48), 18096–18107.
(170) Rubino, J. T.; Franz, K. J. Coordination Chemistry of Copper Proteins: How Nature Handles a Toxic Cargo for Essential Function. *Journal of Inorganic Biochemistry*. Elsevier February 1, 2012, pp 129–143.
(171) Jackson, M. A.; Tiedje, J. M.; Averill, B. A. Evidence for an NO-Rebound, Mechanism for Production of N2O from Nitrite by the Copper-Containing Nitrite Reductase from Achromobacter Cycloclastes. *FEBS Lett.* **1991**, *291* (1), 41–44.
(172) Yang, R.; Yuan, L. jiang; Wang, R.; Wang, G.; Zhu, M. Role of Nitrite Reductase in N2O Production under Aerobic Conditions: An Index for Predicting the Intensity of N2O Production. *Biochem. Eng. J.* **2022**, *177*, 1369–1703.
(173) Murphy, M. E. P.; Turley, S.; Adman, E. T. Structure of Nitrite Bound to Copper-Containing Nitrite Reductase from Alcaligenes Faecalis: Mechanistic Implications. *J. Biol. Chem.* **1997**, *272* (45), 28455–28460.
(174) Leferink, N. G. H.; Antonyuk, S. V.; Houwman, J. A.; Scrutton, N. S.; Eady, R. R.; Hasnain, S. S. Impact of Residues Remote from the Catalytic Centre on Enzyme Catalysis of Copper Nitrite Reductase. *Nat. Commun.* **2014**, *5*, 1–8.
(175) Adhikari, U. K.; Rahman, M. M. Comparative Analysis of Amino Acid Composition in the Active Site of Nirk Gene Encoding Copper-Containing Nitrite Reductase (CuNiR) in Bacterial Spp. *Comput. Biol. Chem.* **2017**, *67*, 102–113.
(176) Kataoka, K.; Furusawa, H.; Takagi, K.; Yamaguchi, K.; Suzuki, S. Functional Analysis of Conserved Aspartate and Histidine Residues Located around the Type 2 Copper Site of Copper-Containing Nitrite Reductase. *J. Biochem.* **2000**, *127* (2), 345–350.
(177) Ruckthong, L.; Deb, A.; Hemmingsen, L.; Penner-Hahn, J. E.; Pecoraro, V. L. Incorporation of Second Coordination Sphere D-Amino Acids Alters Cd(II) Geometries in Designed Thiolate-Rich Proteins. *J. Biol. Inorg. Chem.* **2018**, *23* (1), 123–135.
(178) Koebke, K. J.; Tebo, A. G.; Manickas, E. C.; Deb, A.; Penner-Hahn, J. E.; Pecoraro, V. L. Nitrite Reductase Activity within an Antiparallel de Novo Scaffold. *J. Biol. Inorg. Chem.* **2021**, *26* (7), 855–862.
(179) Röder, K. The Effects of Glycine to Alanine Mutations on the Structure of GPO Collagen Model Peptides. *Phys. Chem. Chem. Phys.* **2022**, *24* (3), 1610–1619.
(180) Bertini, I.; Luchinat, C. Cobalt(II) as a Probe of the Structure and Function of Carbonic Anhydrase. *Acc. Chem. Res.* **1983**, *16* (8), 272–279.
(181) Haffner, P. H.; Coleman, J. E. High Spin and Low Spin Forms of Co(II) Carbonic Anhydrase. *J. Biol. Chem.* **1973**, *248* (19), 6630–6636.
(182) Mills, J. H.; Sheffler, W.; Ener, M. E.; Almhjell, P. J.; Oberdorfer, G.; Pereira, J. H.; Parmeggiani, F.; Sankaran, B.; Zwart, P. H.; Baker, D. Computational Design of a Homotrimeric Metalloprotein with a Trisbipyridyl Core. *Proc. Natl. Acad. Sci. U. S. A.* **2016**, *113* (52), 15012–15017.
(183) Zastrow, M. L.; Peacock, A. F. A.; Stuckey, J. A.; Pecoraro, V. L. Hydrolytic Catalysis and Structural Stabilization in a Designed Metalloprotein. *Nat. Chem.* **2012**, *4* (2), 118–123.
(184) O'Brien, E. M.; Dirmeier, R.; Engle, M.; Poyton, R. O. Mitochondrial Protein Oxidation in Yeast Mutants Lacking Manganese- (MnSOD) or Copper- and Zinc-Containing Superoxide Dismutase (CuZnSOD): Evidence That Mnsod and Cuznsod Have Both Unique and Overlapping Functions in Protecting Mitochondrial Proteins From. *J. Biol. Chem.* **2004**, *279*

(50), 51817–51827.
(185) Bahadorani, S.; Mukai, S. T.; Rabie, J.; Beckman, J. S.; Phillips, J. P.; Hilliker, A. J. Expression of Zinc-Deficient Human Superoxide Dismutase in Drosophila Neurons Produces a Locomotor Defect Linked to Mitochondrial Dysfunction. *Neurobiol. Aging* **2013**, *34* (10), 2322–2330.
(186) Valentino, R. B. The Structure–Function Relationships and Physiological Roles of MnSOD Mutants. *Bioscience Reports*. 2022, p 20220202.
(187) Meliá, C.; Ferrer, S.; Řezáč, J.; Parisel, O.; Reinaud, O.; Moliner, V.; De La Lande, A. Investigation of the Hydroxylation Mechanism of Noncoupled Copper Oxygenases by Ab Initio Molecular Dynamics Simulations. *Chem. - A Eur. J.* **2013**, *19* (51), 17328–17337.
(188) Chen, P.; Bell, J.; Eipper, B. A.; Solomon, E. I. Oxygen Activation by the Noncoupled Binuclear Copper Site in Peptidylglycine α-Hydroxylating Monooxygenase. Spectroscopic Definition of the Resting Sites and the Putative CuIIM-OOH Intermediate. *Biochemistry* **2004**, *43* (19), 5735–5747.
(189) Rezabal, E.; Gauss, J.; Matxain, J. M.; Berger, R.; Diefenbach, M.; Holthausen, M. C. Quantum Chemical Assessment of the Binding Energy of CuO+. *J. Chem. Phys.* **2011**, *134* (6), 64304.
(190) Kamachi, T.; Kihara, N.; Shiota, Y.; Yoshizawa, K. Computational Exploration of the Catalytic Mechanism of Dopamine β-Monooxygenase: Modeling of Its Mononuclear Copper Active Sites. *Inorg. Chem.* **2005**, *44* (12), 4226–4236.
(191) Yoshizawa, K.; Kihara, N.; Kamachi, T.; Shiota, Y. Catalytic Mechanism of Dopamine-Monooxygenase Mediated by Cu(III)−Oxo. **2006**.
(192) Prigge, S. T.; Eipper, B. A.; Mains, R. E.; Amzel, L. M. Dioxygen Binds End-On to Mononuclear Copper in a Precatalytic Enzyme Complex. *Science (80-.).* **2004**, *304* (5672), 864–867.
(193) Mitra, S.; Prakash, D.; Rajabimoghadam, K.; Wawrzak, Z.; Prasad, P.; Wu, T.; Misra, S. K.; Sharp, J. S.; Garcia-Bosch, I.; Chakraborty, S. De Novo Design of a Self-Assembled Artificial Copper Peptide That Activates and Reduces Peroxide. *ACS Catal.* **2021**, *11*, 10267–10278.
(194) Reuillard, B.; Ly, K. H.; Hildebrandt, P.; Jeuken, L. J. C.; Butt, J. N.; Reisner, E. High Performance Reduction of H2O2 with an Electron Transport Decaheme Cytochrome on a Porous ITO Electrode. *J. Am. Chem. Soc.* **2017**, *139* (9), 3324–3327.
(195) Pasternak, A.; Kaplan, J.; Lear, J. D.; Degrado, W. F. Proton and Metal Ion-dependent Assembly of a Model Diiron Protein. *Protein Sci.* **2001**, *10* (5), 958–969.
(196) Kidani, Y.; Ohkuma, K.; Hirose, J.; Noji, M. Coordination Chemical Studies on Metalloenzymes. Measurement of Binding Constant between Apo-Tyrosinase and Copper Ion. *Arch. Biochem. Biophys.* **1980**, *200* (2), 452–460.
(197) Kertesz, D.; Rotilio, G.; Brunori, M.; Zito, R.; Antonini, E. Kinetics of Reconstitution of Polyphenoloxidase from Apoenzyme and Copper. *Biochem. Biophys. Res. Commun.* **1972**, *49* (5), 1208–1215.
(198) Solomon, E. I.; Baldwin, M. J.; Lowery, M. D. Electronic Structures of Active Sites in Copper Proteins: Contributions to Reactivity. *Chem. Rev.* **1992**, *92* (4), 521–542.
(199) Yoon, J.; Fujii, S.; Solomon, E. I. Geometric and Electronic Structure Differences between the Type 3 Copper Sites of the Multicopper Oxidases and Hemocyanin/Tyrosinase. *Proc. Natl. Acad. Sci. U. S. A.* **2009**, *106* (16), 6585–6590.
(200) Woolfson, D. N. Understanding a Protein Fold: The Physics, Chemistry, and Biology of α-

Helical Coiled Coils. *Journal of Biological Chemistry*. 2023.
(201) LINUs PAULING, B.; CoREY, R. B. *CONFIGURATIONS OF POLYPEPTIDE CHAINS WITH FAVORED ORIENTATIONS AROUND SINGLE BONDS: TWO NEW PLEATED SHEETS*; 1951.
(202) Truebestein, L.; Leonard, T. A. Coiled-Coils: The Long and Short of It. *BioEssays* **2016**, *38* (9), 903–916.
(203) Crick, F. H. C. The Packing of A-Helices: Simple Coiled-Coils. *Acta Cryst.* **1953**, *6*, 689.
(204) Drobnak, I.; Gradišar, H.; Ljubetič, A.; Merljak, E.; Jerala, R. Modulation of Coiled-Coil Dimer Stability through Surface Residues While Preserving Pairing Specificity. *J. Am. Chem. Soc.* **2017**, *139* (24), 8229–8236.
(205) Brown, J. H.; Cohen, C.; Parry, D. A. D. Heptad Breaks in α-Helical Coiled Coils: Stutters and Stammers. *Proteins Struct. Funct. Genet.* **1996**, *26* (2), 134–145.
(206) Hartmann, M. D.; Ridderbusch, O.; Zeth, K.; Albrecht, R.; Testa, O.; Woolfson, D. N.; Sauer, G.; Dunin-Horkawicz, S.; Lupas, A. N.; Alvarez, B. H. A Coiled-Coil Motif That Sequesters Ions to the Hydrophobic Core. *Proc. Natl. Acad. Sci. U. S. A.* **2009**, *106* (40), 16950–16955.
(207) Dunin-Horkawicz, S.; Lupas, A. N. Measuring the Conformational Space of Square Four-Helical Bundles with the Program SamCC. *J. Struct. Biol.* **2010**, *170* (2), 226–235.
(208) Lupas, A.; Muüller, S.; Goldie, K.; Engel, A. M.; Engel, A.; Baumeister, W. Model Structure of the Ompα Rod, a Parallel Four-Stranded Coiled Coil from the Hyperthermophilic EubacteriumThermotoga Maritima. *J. Mol. Biol.* **1995**, *248* (1), 180–189.
(209) McLachlan, A. D.; Karn, J. Periodic Features in the Amino Acid Sequence of Nematode Myosin Rod. *J. Mol. Biol.* **1983**, *164* (4), 605–626.
(210) Parry, D. A. D. Structure of Rabbit Skeletal Myosin. Analysis of the Amino Acid Sequences of Two Fragments from the Rod Region. *J. Mol. Biol.* **1981**, *153* (2), 459–464.
(211) Lupas, A. Coiled Coils: New Structures and New Functions. *Trends in Biochemical Sciences*. 1996, pp 375–382.
(212) Taylor, K. C.; Buvoli, M.; Korkmaz, E. N.; Buvoli, A.; Zheng, Y.; Heinze, N. T.; Cui, Q.; Leinwand, L. A.; Rayment, I. Skip Residues Modulate the Structural Properties of the Myosin Rod and Guide Thick Filament Assembly. *Proc. Natl. Acad. Sci. U. S. A.* **2015**, *112* (29), E3806–E3815.
(213) Offer, G. Skip Residues Correlate with Bends in the Myosin Tail. *J. Mol. Biol.* **1990**, *216* (2), 213–218.
(214) Apostolovic, B.; Danial, M.; Klok, H. A. Coiled Coils: Attractive Protein Folding Motifs for the Fabrication of Self-Assembled, Responsive and Bioactive Materials. *Chem. Soc. Rev.* **2010**, *39* (9), 3541–3575.
(215) Hoiczyk, E.; Roggenkamp, A.; Reichenbecher, M.; Lupas, A.; Heesemann, J. Structure and Sequence Analysis of Yersinia YadA and Moraxella UspAs Reveal a Novel Class of Adhesins. *EMBO J.* **2000**, *19* (22), 5989–5999.
(216) Hartmann, M. D.; Grin, I.; Dunin-Horkawicz, S.; Deiss, S.; Linke, D.; Lupas, A. N.; Hernandez Alvarez, B. Complete Fiber Structures of Complex Trimeric Autotransporter Adhesins Conserved in Enterobacteria. *Proc. Natl. Acad. Sci. U. S. A.* **2012**, *109* (51), 20907–20912.
(217) Park, E.; Mackinnon, R. Structure of the CLC-1 Chloride Channel from Homo Sapiens. *Elife* **2018**, *7*.

(218) Rudresh; Ramakumar, S.; Ramagopal, U. A.; Inai, Y.; Goel, S.; Sahal, D.; Chauhan, V. S. De Novo Design and Characterization of a Helical Hairpin Eicosapeptide: Emergence of an Anion Receptor in the Linker Region. *Structure* **2004**, *12* (3), 389–396.
(219) Ackbarow, T.; Buehler, M. J. Molecular Mechanics of Stutter Defects in Vimentin Intermediate Filaments. *Exp. Mech.* **2009**, *49* (1), 79–89.
(220) Schmidt, N. W.; Grigoryan, G.; DeGrado, W. F. The Accommodation Index Measures the Perturbation Associated with Insertions and Deletions in Coiled-Coils: Application to Understand Signaling in Histidine Kinases. *Protein Science*. Blackwell Publishing Ltd March 1, 2017, pp 414–435.
(221) Pinter, T. B. J.; Manickas, E. C.; Tolbert, A. E.; Koebke, K. J.; Deb, A.; Penner-Hahn, J. E.; Pecoraro, V. L. Making or Breaking Metal-Dependent Catalytic Activity: The Role of Stammers in Designed Three-Stranded Coiled Coils. *Angew. Chemie Int. Ed.* **2020**, *59* (46), 20445–20449.
(222) Briggs, E. M.; Ha, S.; Mita, P.; Brittingham, G.; Sciamanna, I.; Spadafora, C.; Logan, S. K. Long Interspersed Nuclear Element-1 Expression and Retrotransposition in Prostate Cancer Cells. *Mob. DNA* **2018**, *9* (1), 1–9.
(223) Kolosha, V. O.; Martin, S. L. In Vitro Properties of the First ORF Protein from Mouse LINE-1 Support Its Role in Ribonucleoprotein Particle Formation during Retrotransposition. *Proc. Natl. Acad. Sci. U. S. A.* **1997**, *94* (19), 10155–10160.
(224) Hohjoh, H.; Singer, M. F. Sequence-Specific Single-Strand RNA Binding Protein Encoded by the Human LINE-1 Retrotransposon. *EMBO J.* **1997**, *16* (19), 6034–6043.
(225) Khazina, E.; Truffault, V.; Büttner, R.; Schmidt, S.; Coles, M.; Weichenrieder, O. Trimeric Structure and Flexibility of the L1ORF1 Protein in Human L1 Retrotransposition. *Nat. Struct. Mol. Biol.* **2011**, *18* (9), 1006–1014.
(226) Kale, S. P.; Moore, L.; Deininger, P. L.; Roy-Engel, A. M. Heavy Metals Stimulate Human LINE-1 Retrotransposition. In *International Journal of Environmental Research and Public Health*; Molecular Diversity Preservation International, 2005; Vol. 2, pp 14–23.
(227) Sato, S.; Gillette, M.; de Santiago, P. R.; Kuhn, E.; Burgess, M.; Doucette, K.; Feng, Y.; Mendez-Dorantes, C.; Ippoliti, P. J.; Hobday, S.; Mitchell, M. A.; Doberstein, K.; Gysler, S. M.; Hirsch, M. S.; Schwartz, L.; Birrer, M. J.; Skates, S. J.; Burns, K. H.; Carr, S. A.; Drapkin, R. LINE-1 ORF1p as a Candidate Biomarker in High Grade Serous Ovarian Carcinoma. *Sci. Rep.* **2023**, *13* (1), 1–15.
(228) Ruckthong, L.; Peacock, A. F. A.; Pascoe, C. E.; Hemmingsen, L.; Stuckey, J. A.; Pecoraro, V. L. D-Cysteine Ligands Control Metal Geometries within De Novo Designed Three-Stranded Coiled Coils. *Chem. - A Eur. J.* **2017**, *23* (34), 8232–8243.
(229) Tolbert, A. E.; Ervin, C. S.; Ruckthong, L.; Paul, T. J.; Jayasinghe-Arachchige, V. M.; Neupane, K. P.; Stuckey, J. A.; Prabhakar, R.; Pecoraro, V. L. Heteromeric Three-Stranded Coiled Coils Designed Using a Pb(Ii)(Cys)3 Template Mediated Strategy. *Nat. Chem.* **2020**, *12* (4), 405–411.
(230) Touw, D. S.; Nordman, C. E.; Stuckey, J. A.; Pecoraro, V. L. Identifying Important Structural Characteristics of Arsenic Resistance Proteins by Using Designed Three-Stranded Coiled Coils. *Proc. Natl. Acad. Sci. U. S. A.* **2007**, *104* (29), 11969–11974.
(231) Peacock, A. F. A.; Stuckey, J. A.; Pecoraro, V. L. Switching the Chirality of the Metal Environment Alters the Coordination Mode in Designed Peptides. *Angew. Chemie - Int. Ed.* **2009**, *48* (40), 7371–7374.
(232) Pinter, T. B. J.; Ruckthong, L.; Stuckey, J. A.; Deb, A.; Penner-Hahn, J. E.; Pecoraro, V. L.

Open Reading Frame 1 Protein of the Human Long Interspersed Nuclear Element 1 Retrotransposon Binds Multiple Equivalents of Lead. *J. Am. Chem. Soc.* **2021**, *143* (37), 15271–15278.

(233) Zampella, G.; Neupane, K. P.; De Gioia, L.; Pecoraro, V. L. The Importance of Stereochemically Active Lone Pairs for Influencing PbII and AsIII Protein Binding. *Chem. - A Eur. J.* **2012**, *18* (7), 2040–2050.

(234) Matzapetakis, M.; Ghosh, D.; Weng, T. C.; Penner-Hahn, J. E.; Pecoraro, V. L. Peptidic Models for the Binding of Pb(II), Bi(III) and Cd(II) to Mononuclear Thiolate Binding Sites. *J. Biol. Inorg. Chem.* **2006**, *11* (7), 876–890.

(235) Tripet, B.; Wagschal, K.; Lavigne, P.; Mant, C. T.; Hodges, R. S. Effects of Side-Chain Characteristics on Stability and Oligomerization State of a de Novo-Designed Model Coiled-Coil: 20 Amino Acid Substitutions in Position "D." *J. Mol. Biol.* **2000**, *300* (2), 377–402.

(236) Zastrow, M. L.; Peacock, A. F. A.; Stuckey, J. A.; Pecoraro, V. L. Hydrolytic Catalysis and Structural Stabilization in a Designed Metalloprotein. *Nat. Chem.* **2012**, *4* (2), 118–123.

Chapter II

Exploiting Non-Coded Amino Acids to Enhance the Activity of Designed Copper Nitrite Reductases.

Introduction:

Metalloenzymes are workhorses of the cell and rely on metal cofactors that are primed toward a particular reaction pathway via the ligand environment surrounding a transition metal cofactor. However, only a very small fraction of the naturally occurring amino acids are able to chelate metals. In principle, designing metalloproteins from the ground up allows one to simplify metalloenzyme's structure and yet capture important properties of the native enzyme such as those around the first and second coordination sphere. Modifying the primary coordination sphere in artificial, redox-active metalloenzymes with unnatural heterocycles have be exploited to make new biologically inspired catalysts and to learn more about existing enzymes.[1–9] A key goal of *de novo* metalloprotein design is building protein models that share a similar metal environment of a native enzyme in a very dissimilar scaffold, removing any evolutionary baggage that is unnecessary for catalysis.[10–12] Evolution has selected different N-isomers of histidine to bind copper depending on the function of the protein. While there are rare exceptions, Cu–N_{ε}His sites typically catalyze oxidase or oxygenase reactions while Cu–N_{δ}His sites participate in electron transfer.[13–17]

Copper nitrite reductase is a key enzyme in many different denitrifying fungi and bacteria that catalyzes the reduction of nitrite to nitric oxide, which is partly responsible for maintaining the balance of nitrogen content in the nitrogen cycle.[18] The first *de novo* designed CuNiR mimic was a 3SCC, TRIW-H, which was able to complete over 1000 turnovers without a detectable decrease in activity and demonstrated that CuNiR activity could be achieved in a non-native fold by simply replicating the primary coordination sphere around the copper site.[19] However, the

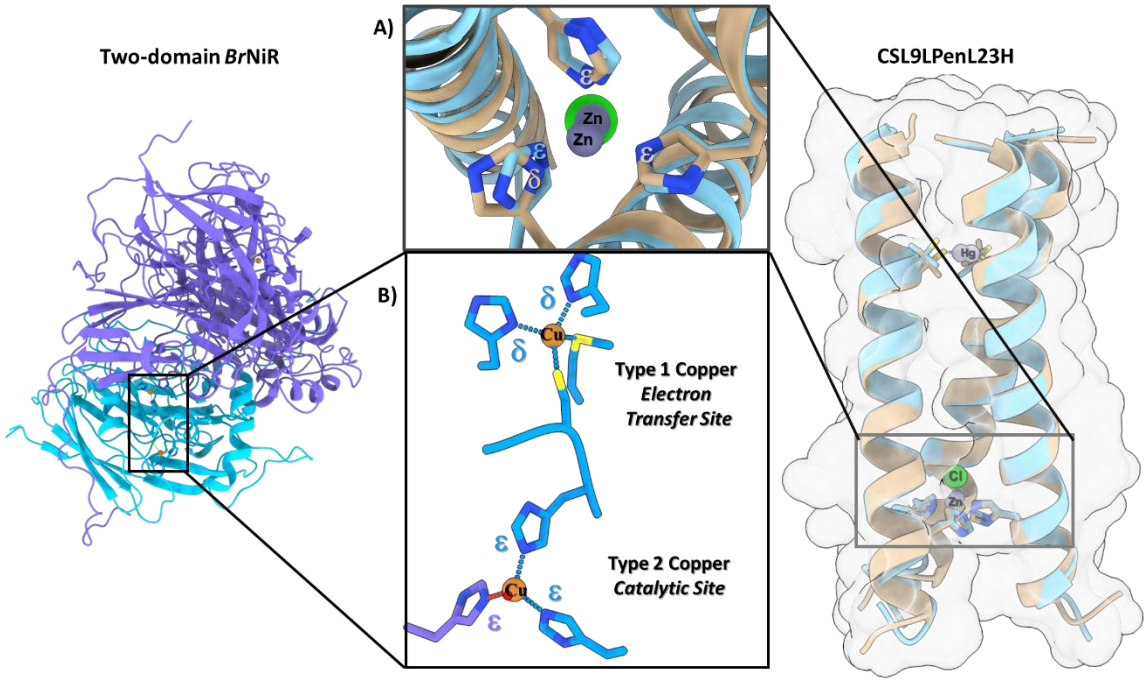
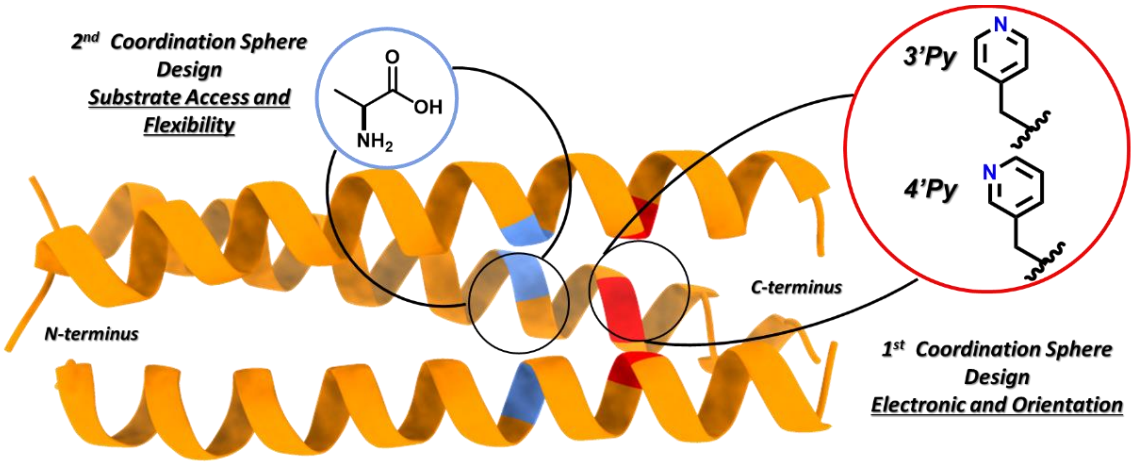


Figure II-1: Comparison of 3SCC (pdb: 3PBJ) with two-domain CuNiR from *Bradyrhizobium* (pdb:6THF): **A)** Overlay of the two 3SCC in the asymmetric unit cells of $[Hg^{II}]_S[Zn^{II}(H_2O/OH^-)]_N(CSL9PenL23H)_3^{n+}$ (PDB:3PBJ), each with a different coordination mode to the Zn(II) ion. **B)** Primary coordination sphere of the Type 2 copper site and Type 1 copper site in the two-domain CuNiR from *Bradyrhizobium* (pdb:6THF) highlighting the coordination modes of the histidines to each copper site.

activity was enhanced up to three orders of magnitude compared to the originally designed TRIW-H by opening the 2nd coordination sphere with less bulky mutations (*i.e.*, alanine) giving the first hint that limited substrate access could be hindering the designed enzyme's activity.[20] The two nitrogens on histidine are electronically different in that the N_ε is pyridine-like with a pK_a of 6.12 while the N_δ is more electron donating with a pK_a of 6.73.[21] Previous studies with δ_m-His and ε_m-His derivatives indicated that the peptide using the N_ε of histidine to bind copper was the most active.[22] Based on this observation we chose to make derivatives utilizing pyridyl alanine derivatives instead of histidine to enhance catalytic efficiency. Based on numerous spectroscopic techniques, it has been argued that the pyridine-like N_ε in TRIW-H is bound to the copper center in both oxidation states, and recently a solid state structure of the Cu(II) bound to the N_ε in an ***a***-site histidine pocket within a 3SCC was published, supporting these spectroscopic

interpretations.[22–24] However, the asymmetric unit of the analogous Zn(II)-His_3 contains two different Zn sites, one favoring a $Zn(N_\varepsilon)_3$ coordination mode while a $Zn(N_\varepsilon)_2(N_\delta)$ coordination mode is favored in the presence of a fourth chloride ligand (Figure II-1).[11] *Moreover, the influence of the ligand orientation around the Cu(II)/Cu(I) site cannot be probed with methyl-histidine derivatives without simultaneously altering the donor properties of the N_ε vs. N_δ nitrogens.* For this reason, I set out to design a novel active site that was composed entirely of pyridine ligands while modifying the ligand geometries with respect to the backbone of the scaffold. Pyridine is distinct from imidazole, both in terms of its electronic and steric properties, all of which can influence the geometry and ligand field around the copper active site. Pyridine is a slightly weaker σ-donor than the ε-nitrogen of histidine which is reflected in the experimental pK_as of their conjugate acids (5.22 and 6.12, respectively).[21,25] Furthermore, the pyridine nitrogen orientation is expected to deviate from histidine, possibly resulting in active site structural changes. Unlike imidazole, which can be deprotonated to form an imidazolate or engage in H-bonding, pyridine is always neutral and cannot be influenced by local proton acceptors. With these differences and



	1 2	9	16 19	23	30
TRIW:	Ac-GWKALEEK	LKALEEK	LKALEEK	LKALEEK	G-NH_2
TRIW-x'Py:	Ac-GWKALEEK	LKALEEK	LKALEEK	x_{Py}KALEEK	G-NH_2
TRIW-x'Py L19A:	Ac-GWKALEEK	LKALEEK	LKAAEEK	x_{Py}KALEEK	G-NH_2
			a b c d e f g		

Figure II-2: Overview of chemical structures of N-heterocycles discussed in relation to the position in the 3SCC. The protein abbreviation, along with their corresponding amino acid sequences, are provided.

similarities in mind, I explored how an ***a***-site pyridine influenced nitrite reduction. I have altered the orientation of the Cu-active site by incorporating two different pyridine ligands into a simple parallel 3SCC composed of the repeating heptad [Ac-G($L_aK_bA_cL_dE_eE_fK_g$)$_4$G-NH_2)] (TRIW) to explore the NiR activity of unnatural T2Cu centers (Figure II-2).[26]

Materials and Methods:

General Methods:

Most reagents were purchased from Sigma-Aldrich and Fisher Scientific and used as supplied unless otherwise indicated. All samples containing Cu(I) were prepared in a $N_{2(g)}$ glove box <1.5ppm O_2. Both Fmoc-3-(3'-pyridyl)-L-alanine and Fmoc-3-(4'-pyridyl)-L-alanine were purchased from Chem-Impex International, Inc or Aapptec and used without any further purification. Metal concentration was determined by inductively coupled plasma mass spectrometry using 1000ppm Cu standard. Concentrations of sodium nitrite and sodium ascorbate were determined by UV-VIS at 360 nm (ε =21.88 M^{-1} cm^{-1})[27] and 251nm (ε=8250 M^{-1} cm^{-1} at pH 5.9)[28], respectively.

Synthesis and purification of peptides:

Peptides were synthesized using standard Fmoc chemistry solid phase peptide synthesis on a Rink Amide Methylbenzhydrylamine (MBHA) resin with a Biotage Initiator+Alstra microwave synthesizer following previously reported procedures.[20] Some proteins in this chapter were synthesized on a Liberty Blue 2.0 using diisopropylcarbodiimide (DIC) as the coupling reagent and OxymaPure as an additive for the inhibition of racemization. Deprotection steps were carried out for 90 seconds at 90°C using 10% Piperidine/DMF (v/v) and each coupling step was carried out at 90°C for 2 minutes. The crude peptide was simultaneously cleaved and deprotected using a cleavage cocktail consisting of trifluoroacetic acid (TFA), ethanedithiol, anisole, and thioanisole (90:3:2:5). The peptide was precipitated with cold diethyl ether, recovered by vacuum filtration, dissolved in 50% acetonitrile in double distilled H_2O (ddH_2O) and lyophilized to dryness. The

lyophilized crude product was then redissolved in 10% acetic acid in ddH_2O and loaded onto a 300 mm x 50 mm DeltaPAK preparative C18 column using a Waters 600 HPLC system with the following parameters: flow rate: 20 mL/min, solvent A: 0.1% TFA in water, solvent B: 0.1% TFA in (90:10) CH3CN:H2O, linear gradient: 100:0 (A:B) increasing to 20:80 over 50 minutes and fractions containing pure peptide were combined and lyophilized to yield pure, white powder. The powder was redissolved in ddH_2O and lyophilized once again to remove any remaining acetonitrile after HPLC purification (confirmed by ^{1}H NMR). The dried peptide was stored at 0°C until use. Purity and identity were confirmed using an Agilent Q-TOF ESI-MS operated in positive ion mode.

Spectroscopy:

UV visible absorption data were collected with a Cary 100 spectrometer at room temperature in 10 mm quartz cuvettes. CD data were collected on a Jasco J-1500 CD spectropolarimeter at a trimer concertation of 3 μM in MES Buffer pH 5.9 (T=25°C). Electron paramagnetic resonance spectral data were collected using a Bruker EMXE 200 EPR spectrometer on solutions containing 1.5 mM peptide, 1 mM $CuSO_4$, 30% glycerol, and 50 mM MES at pH 5.9. The EPR spectra were processed using the *MATLAB* ver. R2020b and EasySpin.[29] Simulations were also performed using EasySpin to determine the g_z, g_y, g_x, $A_{\|}$, and $A_{\perp}$ values.

Guanidinium Denaturation Titration:

Guanidinium-HCl denaturation titrations were carried out using Jasco J-1500 CD spectropolarimeter with Hellma Quartz 1mm 0.4mL cuvettes. Before use, guanidinium HCl was added to a round bottom flask and heated overnight at 60°C under high vac (50 mtorr) to remove excess water before weighing. Two 5mL stock solutions were used, one containing 8 M Gdn-HCl and the other containing 0 M Gdn-HCl, and each was prepared as follows: Stock 1 contained 8 M Gdn-HCl, 10 mM Phosphate buffer, and 40μM Pep_3 (pH'd to 5.9), and stock 2 contained only 10 mM Phosphate buffer and 40μM Pep_3. These stocks were mixed into appropriate ratios in

Eppendorf tube that represent each individual point collected during the titrations (V_{tot}=200µL). Titrations were fit using Equation II-1 where MRE is the mean residue ellipticity (MRE), MRE_f and MRE_u are the *y*-axis intercepts of the folded and unfolded regions' baseline, respectively, and M_f and M_u are the slope of the baseline in the fold and unfolded regions, respectively. The m-value is derived from an analysis of Gdn-HC1-induced denaturation curves and is a measure of the difference in the accessibility of the folded versus the unfolded states of a protein to the denaturant with units of kcal $M^{-1}mol^{-1}$. The gas constant (R) used was 0.0199 kcal mol^{-1} K^{-1} yielding the ΔG (G) in kcal mol^{-1} at T=298 K.

$$MRE = \left(MRE_f + M_f \times [Gdn]\right) + \left(MRE_u + M_u \times [Gdn]\right) \times \frac{e^{\frac{(m\times[Gdn]-G)}{R\times T}}}{1+\ e^{\frac{(m\times[Gdn]-G)}{R\times T}}} \quad \text{Eq. II-1}$$

Temperature Dependent Denaturation:

Temperature Dependent titrations were carried out using Jasco J-1500 CD spectropolarimeter with Hellma Quartz 1mm 0.4mL cuvettes. The temperature range explored was 10-100°C at 5°C intervals. The temperature ramp speed was set to 1°C/min with a one min equilibration time between each temperature recorded. Eq. II-2 was used to fit the denaturation data where T is the temperature (in K), and T_m is the temperature at the mid-point transition between folded (*f*) and unfolded (*u*) regions. The gas constant (R) used was 0.0199 kcal mol^{-1} K^{-1} yielding the enthalpy (H) in kcal mol^{-1}.

$$MRE = \left[(MRE_u + M_u \times T) + \left(MRE_f + M_f \times T\right)\right] \times \frac{e^{-\left(\frac{1}{T_m}-\frac{1}{T}\right)\times\frac{H}{R}}}{1 + e^{-\left(\frac{1}{T_m}-\frac{1}{T}\right)\times\frac{H}{R}}} \quad \text{Eq. II-2}$$

Protein Nuclear Magnetic Resonance Spectroscopy:

Protein NMR experiments were conducted on a Burker 800 MHz equipped with a 5 mm triple resonance inverse detection TCI cryoprobe. Sodium trimethylsilylpropanesulfonate (DSS) was used as the ^1H reference (F2 axis) at a concentration of 0.25 mM in double-distilled H_2O. All

samples were prepared in 50 mM phosphate and 0.25 mM DSS which were subsequently loaded into a coaxial tube with the inner tube containing D_2O. ^1H NMR was collected at 25°C using the pulse program zgesgp which features gradient-based 1D excitation sculpting to eliminate the water peak at ~4.7ppm (*this was calibrated for each sample*). $^1H/^{13}C$ Heteronuclear Single Quantum Correlation (HSQC) experiments were conducted using the hsqcedetgp pulse sequence using ~36 scans in the ^1H axis (F2) and ~200 scans in the ^{13}C axis (F1).[30] This method yields the relationship between the chemical shifts of carbon and protons through one-bond *J*-coupling which featured echo-antiecho "et" to improve sensitivity. The "ed" was used to filter specific protons (CH vs CH_2 or CH_3).The ^1H FIDs were collected with ^{13}C decoupling. With CH and CH_3 having the same phase and CH_2 having the opposite phase, it can be easily used to distinguish between C-H protons from others. Cu(I) titrations were conducted using ~1-3 mM Pep_3 and were carried out in a glovebox. To avoid the formation of a Cu(I)-acetonitrile adduct within the active site using tetrakis(acetonitrile)copper(I) tetrafluoroborate, titrations were done by forming the oxidized enzyme (using $CuSO_4$) and subsequently reducing this complex with 10 eqv. sodium ascorbate to yield the reduced form of the enzyme. Careful attention was given to both the pH changes and loss of volume during these experiments. Each data set was subsequently processed and analyzed in either Bruker Topspin or MestReNova. The spectra were baseline corrected, referenced to 0 ppm (DSS), and normalized at 0 ppm. The ^{13}C axis was calibrated directly using the ^1H reference and the method outlined in Harris *et al.*[31]

Cu(I) X-ray absorption spectroscopy (XANES/EXAFS):

Samples with final concentrations of 1 mM $CuSO_4$, 1.5 mM 3SCC, 50 mM MES, and 30 % glycerol (as a glassing agent) were prepared, pH adjusted, loaded into an XAS sample cell, and frozen in liquid nitrogen for transport and analysis. Although multiple attempts to collect XAS on the Cu(II) forms were done, the enzymes underwent photo-reduction during collection. Sub-stoichiometric concentrations of metal were used to ensure limited amounts of non-peptide associated metal. All XAS measurements were performed at Stanford Synchrotron Radiation

Lightsource (SSRL) Beam line 9-3. A Si(220) double crystal monochromator was utilized, with a flat Rh-coated vertically collimating harmonic rejection monochromator. The X-ray energy was calibrated by collecting the absorption spectrum of a reference metal foil, placed between two ionization chambers situated behind the sample, at the same time as the fluorescence data were collected, with the first inflection point of the foil assigned as 8980.29 eV for Cu. The samples were maintained at a temperature of ~4-10 K during data acquisition using a liquid helium cryostat, and the data were measured in fluorescence mode with a 100-element energy resolving Ge detector. The data were collected using 0.25 eV steps in the XANES region (1 sec. integration time), and 0.05 $Å^{-1}$ increments for the extended X-ray absorption fine structure (EXAFS) region up to k=15 $Å^{-1}$, with an integration time of 1-20 s (k^3 weighted) in the EXAFS region. The maximum incident count rate for the channel with the highest counts was kept below 10,000 to avoid detector saturation. XANES data were normalized with Athena[32] and processed with a threshold energy (E_0) of 8990 eV for Cu and the background was removed using a 3-region cubic spline. The EXAFS data were analyzed using Artemis[33], and the Cu-Pyridine EXAFS model was derived from a single Cu-Pyridine unit from the crystal structure of a tetrakis(pyridine)-copper(I) oxalate complex reported by Royappa *et al*.[34] The Cu-N_{Py} bond distance was modified to 1.95 Å before generating the scattering paths by FeFF 6 lite in Artemis. The models were fit with ΔE fixed to $\Delta E_0 = -5$ eV which was determined by aligning the Feff6 theoretical k^3-space for the Cu-Pyridine model with the experimental k^3-space in Athena, which resulted in a relative −5 eV shift. The Debye-Waller factors were estimated from Zn-Histidine paths reported by Bunker *et al*. and fitted by freely floating the Cu-N_{py} Debye-Waller factors, linking the remaining paths to the Cu-N_{py} to maintain a constant ratio to the original values throughout the fit.[35] The goodness of fit employed in EXAFSPak for the histidine active sites was the F-Value which is the sum of the squares of the difference between experimental and calculated curves. While Pitts *et al.* employed a fitting error equation, this thesis will use a modified version to take into account changes in the number of fitting variables associated with additional coordination shells in some designs, and changes in the range of k^3-space in subsequent chapters. In Eq. II-3, x_i^{measured} equals the measured

i^{th} data point value in *k*-space and $x_i^{\ model}$ equals the i^{th} theoretical point of the fitted model and is summed over 3-13.1 $Å^{-1}$ k^3-space. The N_{idp} represents an upper bound number of independent parameters that can be extracted for a given data range in the EXAFS and is given in Eq. II-4 from Stern *et al*.[36] N_{fit} is the number of data points that composed the fitting range and N_{vary} is the number of parameters varied during the fitting process. Below, the experimental data is presented in the normalized E-space (XANES and EXAFS regions), *k*-space (weighted by k^3), and the Fourier Transform of k^3-space with the appropriate fits are overlayed with their experimental data.

$$< x^2 f >= \frac{\frac{N_{idp}}{N_{fit}} \sum_i k_i^3 \left[\chi(k)_i^{measured} - \chi(k)_i^{model}\right]^2}{N_{idp} - N_{Vary}} \quad \text{Eq. II-3}$$

$$N_{idp} \approx \frac{2\Delta k \Delta R}{\pi} \quad \text{Eq. II-4}$$

Cu(II)-Pep$_3$ $K_{d,app}$ determinations and fitting:

Cu(II) dissociation constants were determined by tryptophan fluorescence quenching in 50 mM MES) at pH 5.9 (T=25^{o}C). The quenching curve was fitted to a 1-to-1 isothermal binding curve (Eq. II-5) where I_z=Final Intensity, I_o=Initial Intensity, $[Pep]_{3,total}$= total trimer concentration, $[Cu(II)]_{total}$=total $CuSO_4$ concentration, and K_d=apparent dissociation constant. The I_z,I_o and $[Pep]_{3,total}$ parameters were fixed while the $[Cu(II)]_{total}$ and K_d parameters were allowed to float during the calculation.

$$I = \left(\frac{I_o - (I_o - I_z)}{2 \times [Pep]_{3,tot}}\right) \times \left(([Cu]_{tot} + [Pep]_{3,tot} + K_d) - \left(\sqrt{([Cu]_{tot} + [Pep]_{3,tot} + K_d)^2 - 4 \times [Pep]_{3,tot} \times [Cu]_{tot}}\right)\right) \quad \text{Eq. II-5}$$

CuNiR Kinetics:

Background corrected CuNiR activity was measured by UV-Visible spectroscopy using previously published procedures by monitoring ascorbate oxidation and using $CuSO_4$ as the copper salt.[19] Pseudo first order rate constants were determined in solutions containing 50 mM sodium phosphate buffer, 30 mM sodium nitrite, 1.5 mM ascorbate and varying the enzyme concentration at pH 5.9 while maintaining an 8:1 3SCC:Cu(II) ratio to ensure Cu(II)/Cu(I) is completely bound to the 3SCC. The background reactions were determined at each enzyme concentration containing 50 mM sodium phosphate buffer, 1.5mM ascorbate, and 30 mM $NaNO_2$ with 7 eqv. apo-3SCC. Steady State kinetics were conducted by varying the $NaNO_2$ concentration over a range of 50 mM-600 mM with 1 μM of Cu(II)-3SCC and 8μM apo-3SCC and the steady state background reaction was treated at each substrate concentration with 50 mM Phosphate buffer, 1.5 mM ascorbate, and 7 eqv. apo-3SCC. The steady state curves were fitted using Eq. II- 6 where k_{sp} is the k_{cat}/K_m (M^{-1} s^{-1}). These experiments were conducted in triplicates.

$$\frac{\nu_{obs}}{E_T} = \frac{\left(k_{sp} \times [NO_2^-]\right)}{\left(1 + \frac{\left(k_{sp} \times [NO_2^-]\right)}{(k_{cat})}\right)} \quad \text{Eq. II-6}$$

Results:

Contributions to this chapter:

I would like to thank Dr. Aniruddha Deb for helping with the collection of the XAS data at beamline 9-3 at Stanford Synchrotron Radiation Lightsource (SSRL). I would also like to thank Gretchen Stemmler, who contributed jointly to the synthesis and purification of the enzymes at different times during this project. Gretchen also conducted the Cu(II) titration spectra of TRIW-4'Py L19A. Thank you for the many hours you spent in the lab helping with this chapter!

CD Spectroscopy of Apo and Cu(II) Proteins:

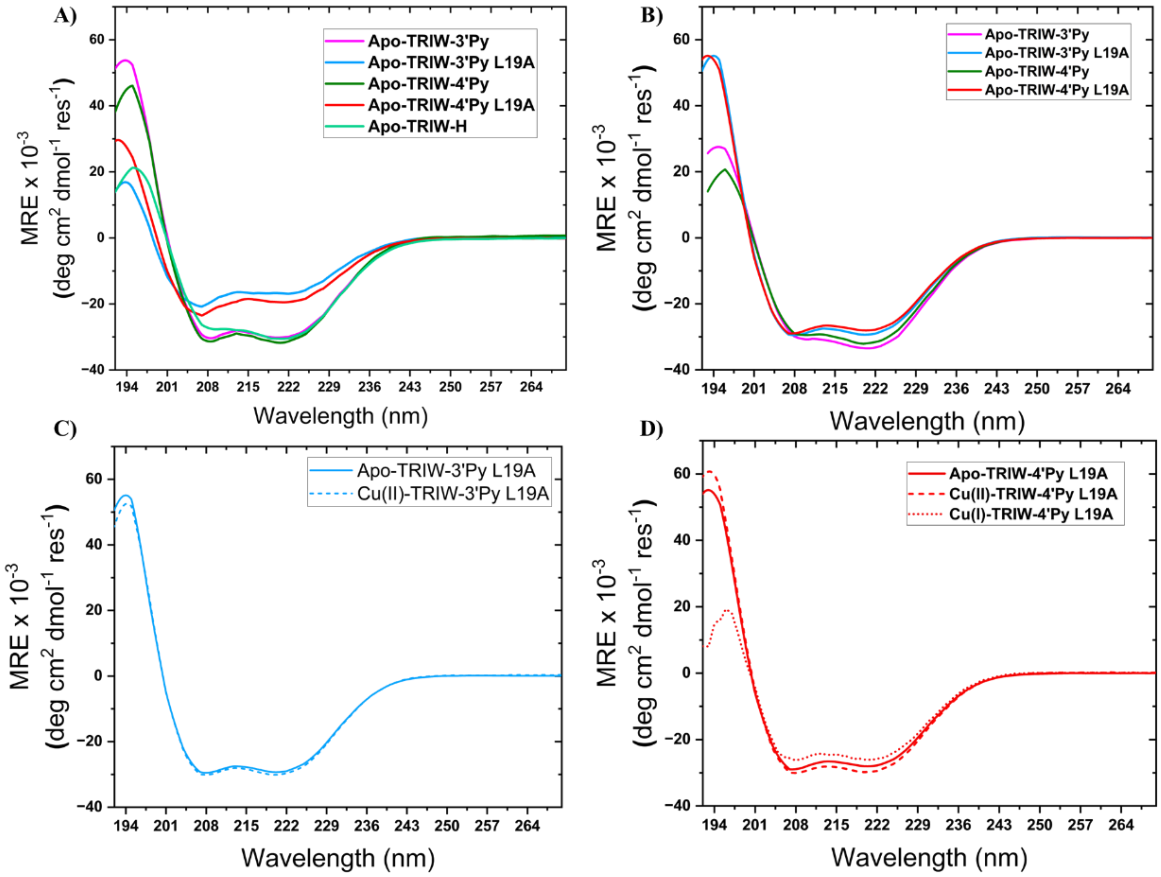


Figure II-3: CD spectra of apo, Cu(II), and Cu(I) designed enzymes: **A**) CD spectra of each apo-protein at 3μM trimer at pH 5.9 at 25°C **B**) CD spectra of each apo-protein at 30 μM trimer at pH 5.9 **C**) CD spectra of apo-TRIW-3'Py L19A and 1.1eqv Cu^{II} holo form at 30 μM trimer (pH 5.9), **D**) CD spectra of apo-TRIW-4'Py L19A and 1.1eqv Cu^{II} and Cu(I) holo forms at 30

The CD spectrum of each apo-protein yielded the characteristics double well features at 222nm and 208nm which are hallmarks of α-helical characteristics within the coiled coil protein (Figure II-3A).[41,42] There is a concentration dependence on the peptide folding with slight changes that are observed going from 3 μM to 30 μM trimer at pH 5.9 with TRIW-3'Py L19A and TRIW-4'Py L19A (Figure II-3 A and B). The molar ellipticity of the TRIW series at 222 nm is -30,000 deg cm^2 $dmol^{-1}$ res^{-1}, except in the cases where alanine was mutated in the ***d***-site at 3 μM trimmer, where the molar ellipticity observed is -19,000 deg cm^2 $dmol^{-1}$ res^{-1}.

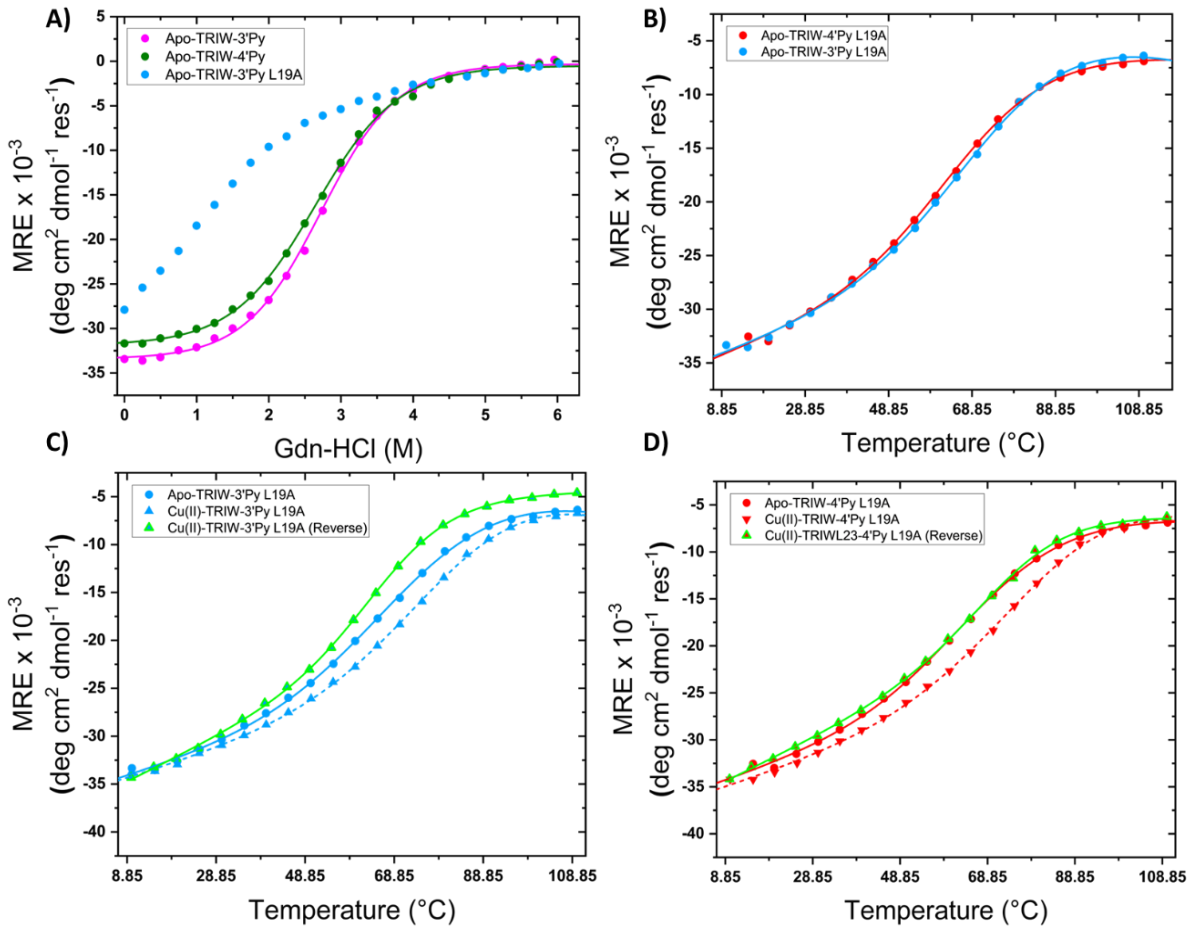


Figure II-4: Chemical and thermal denaturation of designed T2Cu centers: **A)** Chemical denaturation titrations of 30 μM trimer with Guanidinium Hydrochloride at 25°C (pH 5.9) (solid lines-fits), **B)** Thermal denaturation of alanine mutants at 30 μM trimer at pH 5.9 (solid lines-fits). **C-D**) Thermal denaturation of alanine mutants in the absences and presence of 1.1 eqv. $CuSO_4$. Monitored at 222 nm.

Table II-1: Stability parameters determined from the chemical denaturation curves in Figure II-4A

Enzyme	**m** **(kcal M^{-1}_{GdnHCl} mol^{-1})**	**$[Gdn\text{-}HCl]_{1/2}$** **(M)**	**ΔG_u° (H_2O)** **kcal mol^{-1}**	**MRE** **(30μM Trimer)** **(deg cm^2 $dmol^{-1}$ res^{-1})**
Apo-TRIW-4'Py	1.3	2.7	3.4	-31789 (90% Folded)
Apo-TRIW-3'Py	1.4	2.8	4.0	-33466 (94% Folded)

Table II-2: Stability parameters determined from the thermal denaturation curves in Figure II-4B-D

Enzyme	T_m (°C)	ΔH (kcal mol^{-1})	MRE (30μM Trimer) (deg cm^2 $dmol^{-1}$ res^{-1})
Apo-TRIW-4'Py L19A	69	18.0	-27945 (79% Folded)
Cu(II)-TRIW-4'Py L19A	88	16.6	-29597 (83% Folded)
Apo-TRIW-3'Py L19A	76	16.5	-29155 (82% Folded)
Cu(II)-TRIW-3'Py L19A	86	17.7	-29832 (84% Folded)

The stability of the apo-proteins was determined using guanidinium hydrochloride (Gdn-HCl) at pH 5.9 which was fitted to a two-state unfolding model (Figure II-4A, Table II-1). Unlike the leucine parent protein, the alanine mutants' mid-point transition occurred much earlier which hindered the fitting process due to the lack of pre-transition region between 0-0.5 M Gdn-HCl. While this suggests the loss of stability with the substitution of the leucine layer with an alanine layer, the thermal denaturation (Figure II-4B) still follows a two-state unfolding model with a T_m of 76 °C and 64 °C of TRIW-3'Py L19A and TRIW-4'Py L19A, respectively. Upon the addition of 1.1eqv $CuSO_4$ to each of the alanine designs, no changes were observed in the CD spectra that would suggest a large change in secondary structure and suggest a metal independent folding of the design (Figure II-4 C-D). Moreover, the binding of Cu^{II} to the pyridine site stabilizes the overall fold of both alanine constructs as determined by thermal denaturation (Table II-2). The refolding of each Cu(II)-protein does not follow the same temperature dependence as the forward denaturation curve. While Cu(II) did not result in changes in the apo CD spectra, reducing the

Cu(II) to Cu(I) in TRIW-4'Py L19A resulted in a slight decrease in the MRE at 222 nm with a more noticeable decrease in the 190 nm region.

Characterization of Cu(II) Form:

Oligomerization State in the Holo Form:

To determine the number of monomers that composed the active site of these designed constructs, small volumes representing sub-equivalences of $CuSO_4$ (0.1eqv intervals, ~1 μL $CuSO_4$) were added to 300 μM apo-trimer and the absorbance of the d-d transitions associated with the Cu^{II} were monitored and plotted against the ratio of the concentration of $CuSO_4$ to the concentration of apo-

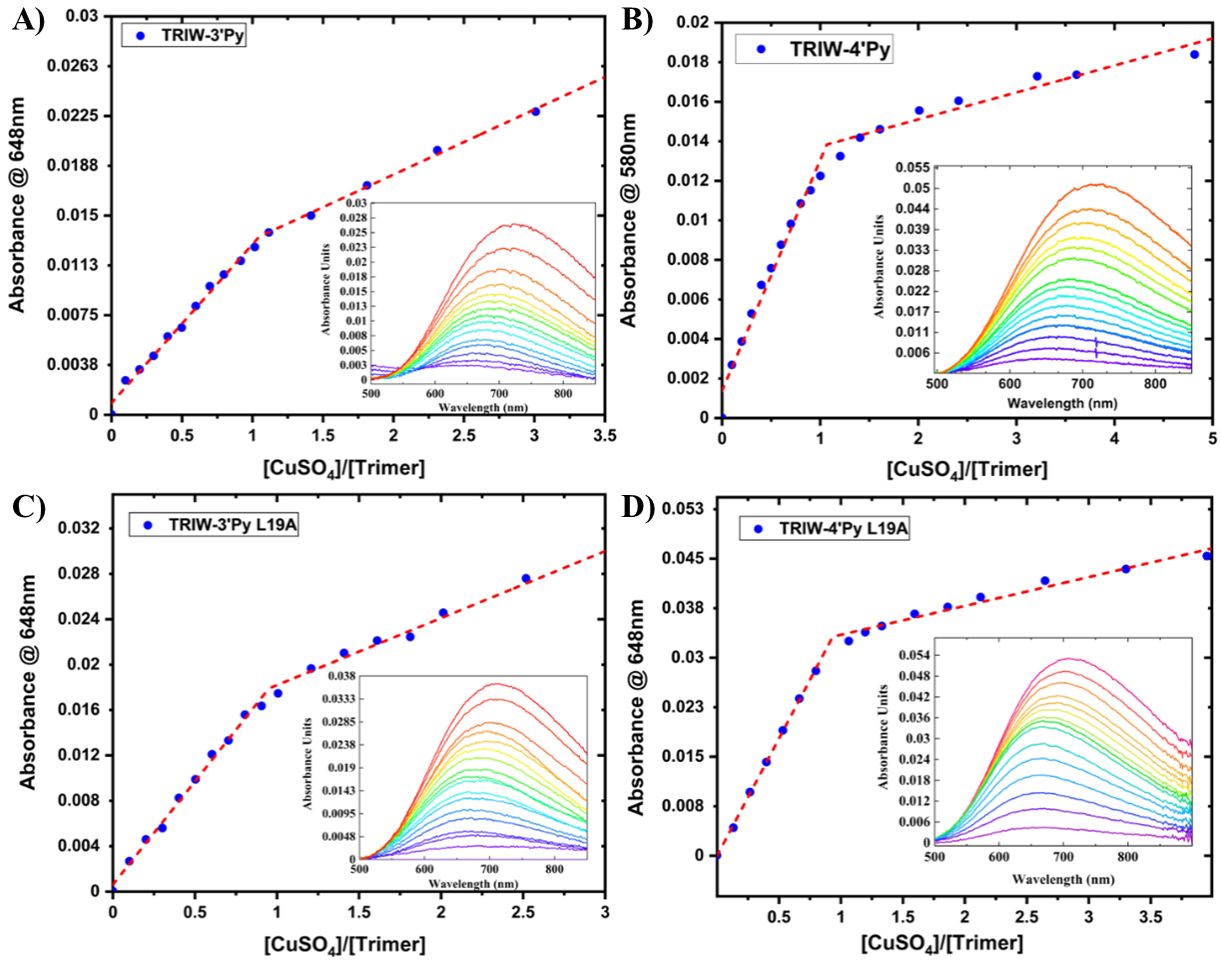


Figure II-5: Cu(II) UV-VIS titration confirming a Cu(II)/Trimer ratio of 1 to1: **A)** TRIW-3'Py, **B)** TRIW-4'Py, **C)** TRIW-3'Py L19A, and **D)** TRIW-4'Py L19A.

trimer. (Figure II-5) while maintaining a pH range of 5.89-5.91 throughout the experiment. With each protein, the absorption of the d-d band increased upon the addition of each aliquot up to a ratio of 1 with the subsequence aliquots resulting in a change in slope up to a ratio of 4, suggesting that three monomers are need for the formation of the final Cu(II) form. Non-specific binding of the $CuSO_4$ to exterior glutamates on the scaffold cannot be ruled out with this experiment alone, which may explain the increase in the absorption past the [$CuSO_4$]/[Trimer]=1 ratio. The molar absorbance coefficient associated with the species after [$CuSO_4$]/[Trimer]=1 is ~21 M^{-1} cm^{-1} which is consistent with the appearance of a high symmetry Cu(II) site.

Determination of Cu(II) $K_{d,app}$ Constants:

The $K_{d,app}$ was determined using fluorescence spectroscopy to monitor the paramagnetic fluorescence quenching of the tryptophan's (in position 2 near the N-terminus) signal (excitation 280 nm) upon the addition of $CuSO_4$ to 100 nM concentration of apo-trimer (Figure II-6). The emission of this band was observed at 350 nm, suggesting the tryptophan is not buried in the hydrophobic core as one would expect a more blue shifted emission band if this were the environment.[37] The dissociation constants were obtained by fitting the resulting curves to a 1-to-1 binding isotherm (Eq. II-4) that yield dissociation constants in the range of 0.13-1.7 μM.

Table II-3: Dissociation constants based on fluorescence tryptophan quenching experiments at pH 5.9. UV-VIS and EPR parameters of Cu(II) forms of protein.

[a] Units: λ_{max} nm, ε_λ M^{-1} cm^{-1} , A_{II} ($A_{II}\times10^{-4}$) cm^{-1}

Enzyme	Cu(II) $K_{d,app}$ (μM)	λ_{max} [a] $[\varepsilon_\lambda]$ [a]	g_z	g_y	g_x	A_{II} [a]
TRIW-4'Py	0.13 ± (0.01)	685 [73]	2.27	2.03	2.03	170
TRIW-4'Py L19A	2.0 ± (0.1)	673 [116]	2.28	2.04	2.04	169
TRIW-3'Py	1.0 ± (0.4	670 [52]	2.29	2.04	2.04	168
TRIW-3'Py L19A	1.7 ± (0.2)	680 [60]	2.29	2.05	2.04	170

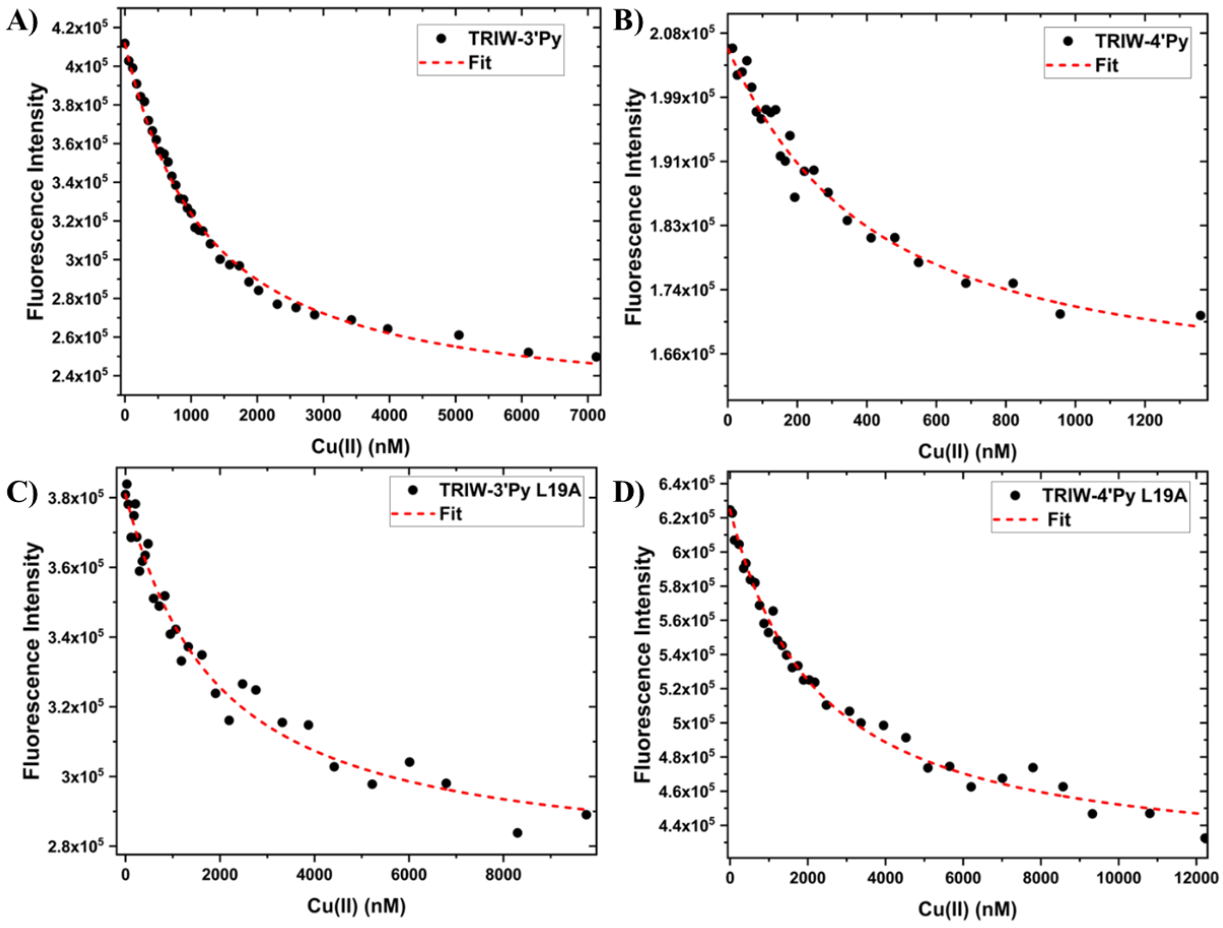


Figure II-6: Fluorescence quenching of the N-terminal tryptophan as a function of $CuSO_4$: **A)** TRIW-3'Py, **B)** TRIW-4'Py, **C)** TRIW-3'Py L19A, **D)** TRIW-4'Py L19A.

UV-VIS and EPR of Cu(II) Forms:

The UV-Vis spectra showed a narrow range of λ_{max} between 670 (14925 cm^{-1}) to 685 nm (14599 cm^{-1}) for all the mutates studied (Figure II-7A). It should be noted that $CuSO_4 \times (H_2O)_6$ absorbs at 810 nm with an ε_{810nm}=15 M^{-1} cm^{-1}.[38] The Cu(II)-TRIW-4'Py L19A displayed a much larger molar absorptivity coefficient (117 M^{-1} cm^{-1}) than the other oxidized enzymes (~50-60 M^{-1} cm^{-1}) which suggests the Cu(II) is in a relatively different environment/geometry. All oxidized forms resulted in axial X-band EPR spectra with $A_{\|}$ values that are suggestive of a T2Cu center ($A_{\|}$ >150×10^{-4} cm^{-1}) (Figure II-7B, Table II-3).

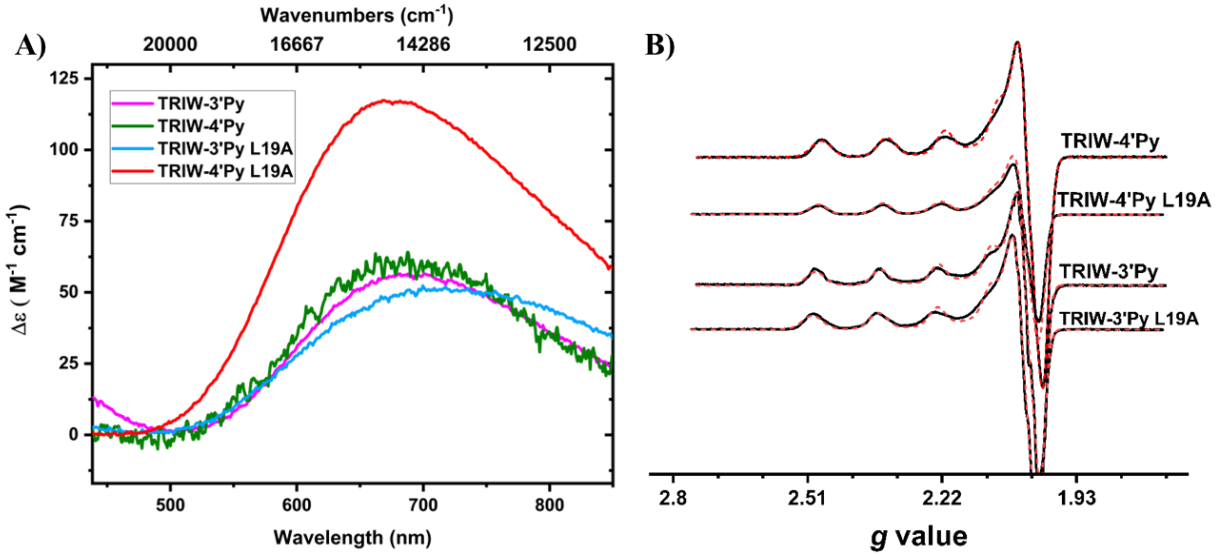


Figure II-7: UV-VIS and EPR of oxidized designed T2Cu centers: **A)** UV-VIS of Cu(II) proteins at pH 5.9, **B)** X-Band EPR at 90K of the Cu(II) proteins at 1mM Cu(II) and 1.5mM Trimer (Dotted curves-simulated fits).

Characterization of Cu(I) Form:

Cu(I) NMR Titrations:

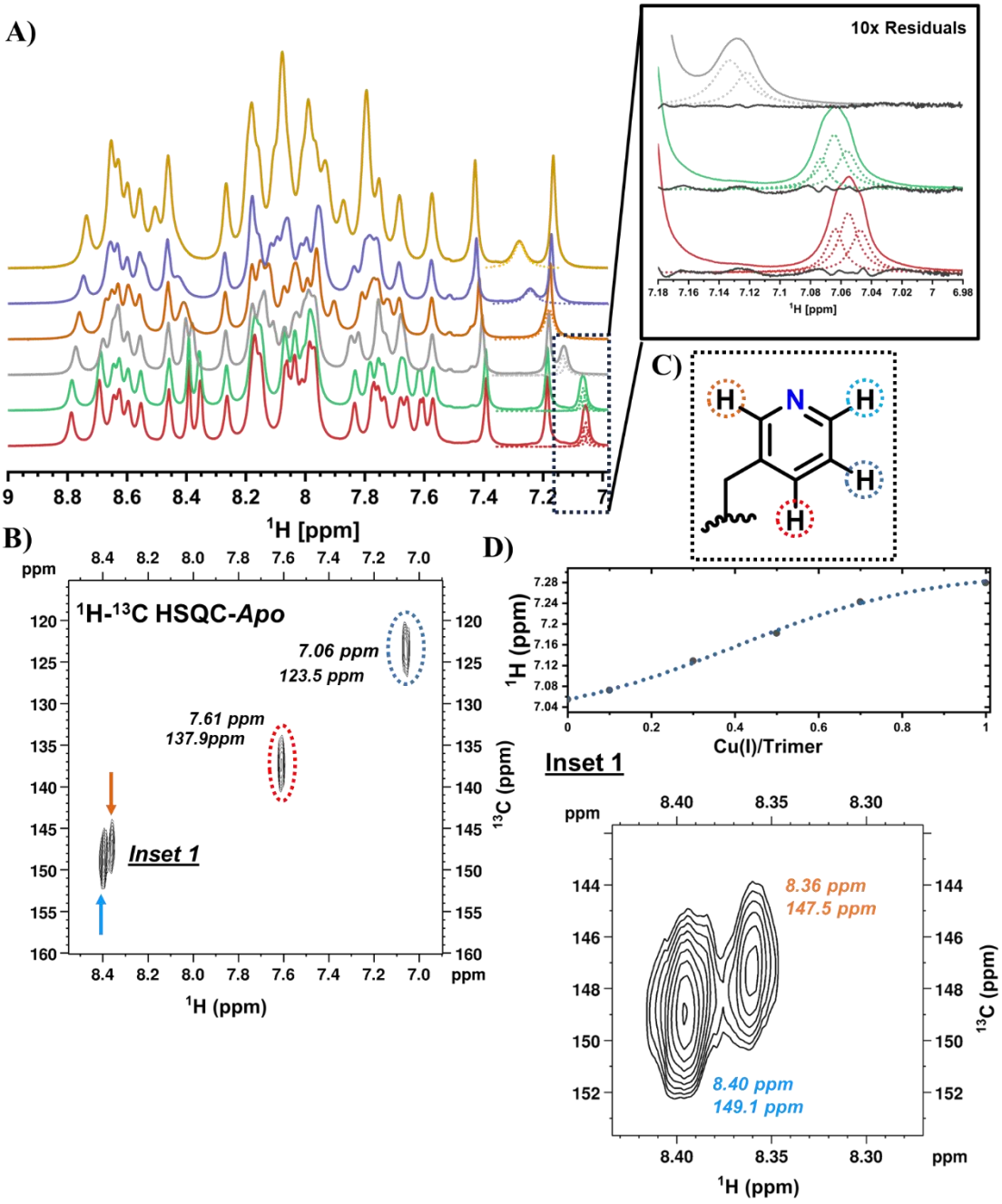


Figure II-8: NMR Cu(I) Titration of TRI-3'Py (pH 5.9, 298 K): **A**) 800 MHz ^{1}H NMR spectra upon increasing concentrations of Cu(I). Also shown is the magnified apo, 0.1 eqv. and 0.3 eqv Cu(I) addition along with the carefully chosen peak fittings (Residual are the solid black line), **B**) ^{1}H-^{13}C HSQC of apo-TRI-3'Py showing the chemical shift of C-H protons on 3'Pyridine, **C**) 3'Pyridine ChemDraw highlighting the expected protons in the NMR, and **D**) Titration plot following the meta protons upon the addition of Cu(I).

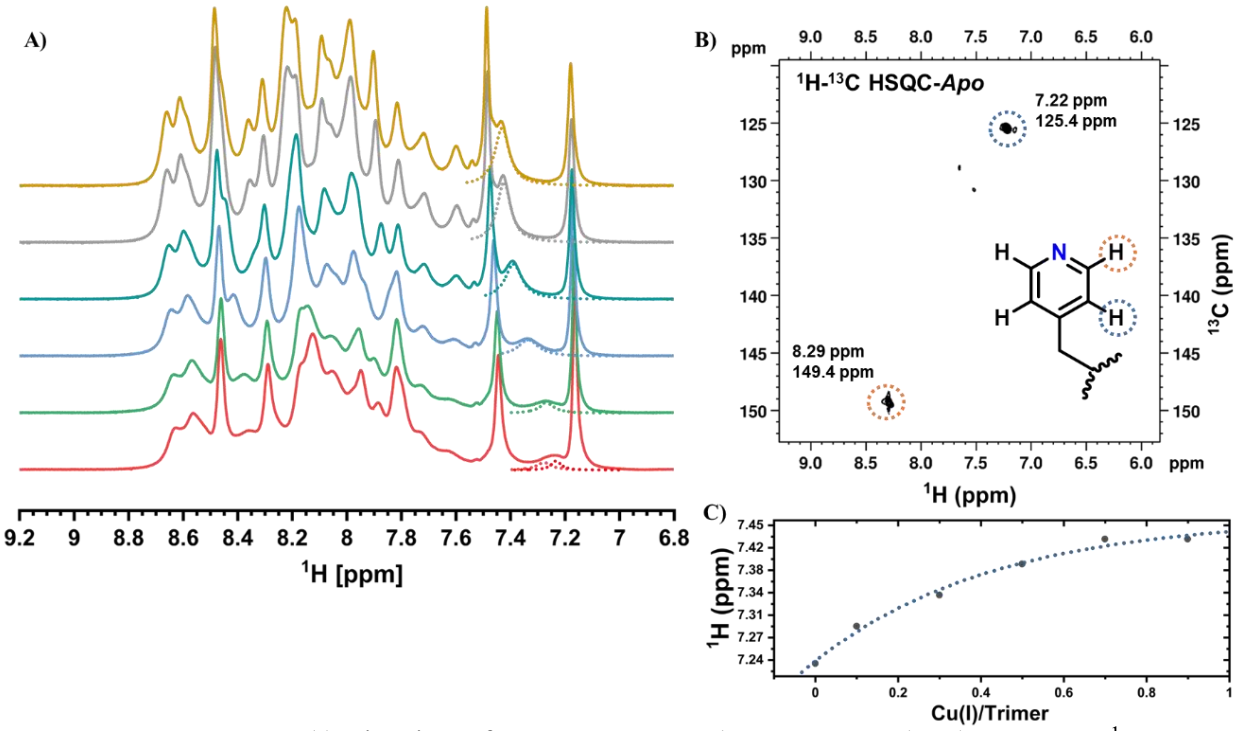


Figure II-9: NMR Cu(I) Titration of TRI-4'Py L19A (pH 5.9, 298 K): **A**) 800 MHz ^{1}H NMR spectra upon increasing the concentration of Cu(I) (- - - peak fittings), **B**) ^{1}H-^{13}C HSQC of apo-TRI-4'Py showing the chemical shift of C-H protons on 4'Pyridine, and **C**) Titration plot following the meta protons upon the addition of Cu(I).

The binding of Cu(I) to both TRI-3'Py and TRI-4'Py L19A was studied using one-dimensional and two-dimensional NMR spectroscopy (Figure II-8A and Figure II-9A). First, to distinguish between the C-H protons attributed to the pyridyl active and the amide backbone protons, (Figure II-8A, Figure II-9A), a ^{1}H-^{13}C Heteronuclear Single Quantum Coherence (HQSC) experiment was used to detect only those protons and carbons associated through one-bond *J*-coupling within the pyridine ring in the aromatic region . This was the clearest method to observe this proton in the absence of tryptophan in the Leu 2 position. As predicted, 4 C-H protons were detected in the apo-TRI-3'Py HSQC spectrum, with the 2 orthro protons shifted to within 0.04 ppm of each other and within 1.6 ppm of their respective ^{13}C spectra (Figure II-8B, *inset 1*). While the active site of apo TRI-3'Py was well resolved in the HSQC, the TRI-4'Py L19A suffered from a low S/N ratio which precluded the unambiguous assignment of the ortho and meta protons in the HSQC (data not shown). These two different C-H pyridyl protons are identical to those in apo

TRI-4'Py HSQC at pH 5.9 and allowed for the assignment of L19A protons peaks in the ^{1}H spectrum (Figure II-9B). The low intensity of these protons in the L19A mutant may be a result of disorder associated with the introduction of the alanine above the apo active site and will be further expanded upon in the discussion section. The incremental introduction of Cu(I) to both proteins, up to 1 eqv. Cu(I) with respect to trimer, resulted in a steady upfield shift of the meta-protons, where it leveled off to the holo form of the enzyme (Figure II-8D, Figure II-9C). These relative shifts and positions are consistent with the reported ^{1}H NMR of Cu(I)-Bipyridyl complexes.[39] The lack of an apo-protein signal during the titration indicates a rapid exchange process between bound and free Cu(I) on the NMR time scale, indicating a greater k_{off} value than the difference in chemical shift between the apo and holo proteins (> 0.184 s^{-1}).[40] The meta-protons were chosen due to their relative ease in following their perturbations upon the addition of Cu(I). While peak fitting analysis of the meta-protons in apo TRI-3'Py yielded 3 peaks, careful consideration of the concentration of the protons against the reference suggests this likely does not arise from coupling with the adjacent protons. This will be briefly discussed in the discussion section.

X-Ray Absorption Spectroscopy of the Cu(I) Protein:

The coordination of Cu(I) to each pyridine active site was investigated by X-ray absorption spectroscopy. Cu(I) complexes feature a resolved band at ca 8983 eV that is associated with a core electron from the 1s orbital to the 4p orbital where the intensity is governed by the amount of the surrounding ligand's orbital character mixing into the empty 4p orbital of Cu(I).[41,42] Kau et al. developed a methodology based on the empirical analysis of this edge structure of a large collection of Cu(I) and Cu(II) small molecule complexes to differentiate between coordination number where two-coordinate Cu(I) complexes exhibit the highest normalized absorption amplitudes, three-coordinate Cu(I) complexes exhibit moderately intense normalized absorption amplitudes, and four-coordinate Cu(I) complexes yield the lowest absorption amplitude which is accompanied by a blue shift in the edge energy to ~8984-8986 eV.[42] This semiempirical ligand field analysis was subsequently employed to assign the coordination number around the dinuclear

type III copper site in type 2 copper depleted laccase. The 1s-4p transition energy associated with these designed pyridines active site are ~ 8984 eV and feature a pre-edge at slightly lower energy than the parent transition as seen more clearly in the first derivative spectra (Figure II-10B), which is predominantly absent in the edge structure of exclusively histidine containing Cu^{I} active sites.[41] This has been observed experimentally and computationally in Cu(I) pyridine complexes.[43–45]

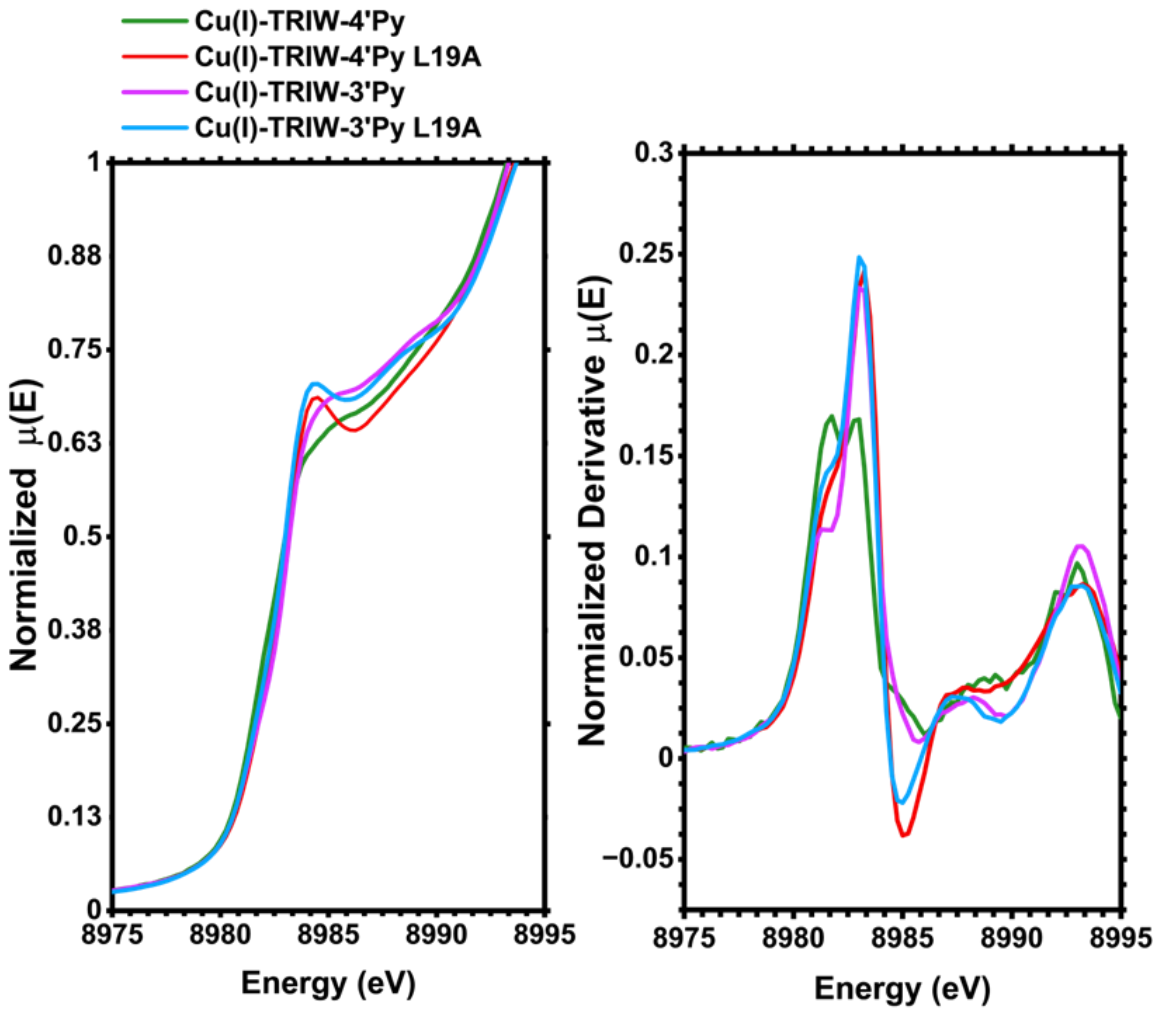


Figure II-10: K-edge Cu(I) XANES of designed T2Cu Centers at pH 5.9:**A)** Cu(I) XANES at pH 5.8/5.9 comparing the different pyridine designs and **B)** First derivative of E-space.

Table II-4: Structural parameters of the best fits to the Cu(I) EXAFS. The E_0 was assigned the value of 8990 eV and ΔE was fixed to – 5 eV.

Enzyme	Best Model	Cu(I)-N	Cu(I)-N $\sigma^2 \times 10^{-3}$	Bond Valance Sum	$\langle \chi^2 f \rangle \times 10^{-4}$
TRIW-4'Py	$CuPy_2$	1.97 Å	3.17 $Å^2$	0.78	23
	$CuPy_3$	1.97 Å	5.26 $Å^2$	1.05	19
TRIW-3'Py	$CuPy_2$	1.96 Å	2.94 $Å^2$	0.80	14
	$CuPy_3$	1.97 Å	5.17 $Å^2$	1.08	16
TRIW-4'Py L19A	$CuPy_2$	1.94 Å	3.31 $Å^2$	0.85	18
	$CuPy_3$	1.94 Å	5.60 $Å^2$	1.14	19
TRIW-3'Py L19A	$CuPy_2$	1.95 Å	4.31 $Å^2$	0.83	16
	$CuPy_3$	1.95 Å	6.96 $Å^2$	1.10	17

The observation is explained as either resulting from distortions towards a trigonal pyramidal structure for a primarily two coordinate environment or pseudotetrahedral for a three-coordinate geometry[41]. Alternatively, it may result from a 1s orbital to a low lying π^* orbital MLCT transition of the pyridine, which gains intensity by mixing in $4p_z$ character. [43,44] However, polarized single-crystal X-ray absorption experiments calls into question these assignment in Cu(I) Bis-2,2'-bipyridine as truly not MLCT but rather the intensity is conferred through a minor amount of metal 4p mixing, without charge separation, into otherwise ligand-dominated acceptor molecular orbitals.[45]

The extended X-ray absorption fine structure (EXAFS) region shows one peak at ~2 Å which is the first shell scatter associated with a nearest neighbor atom bonded to the Cu(I) and longer-range scatters between 2-5 Å (multiple scatter region) that is constant with the binding of a pyridine (Figure II-11). The multiple scattering region of the Cu(I) proteins was modeled quite well with at least two pyridine ligands while only varying the $Cu–N_{py}$ bond distance and the Cu–N

Debye-Weller factor[a] reported by Bunker *et al.* for $Zn–N_{imidzole}$ (0.00265 $Å^2$).[35] The average $Cu–N_{Py}$ bond distances observed range from 1.94 Å to 1.97 Å with the alanine constructs tending to have a smaller average $Cu–N_{Py}$ distance (Table II-4). Both two and three pyridines modeled the Cu(I) sites well, making it difficult to distinguish between two-coordinate and three-coordinate geometries.

[a] The modeling of all Debye-Weller factors for the pyridine model is discussed in the material and methods sections for Chapter II.

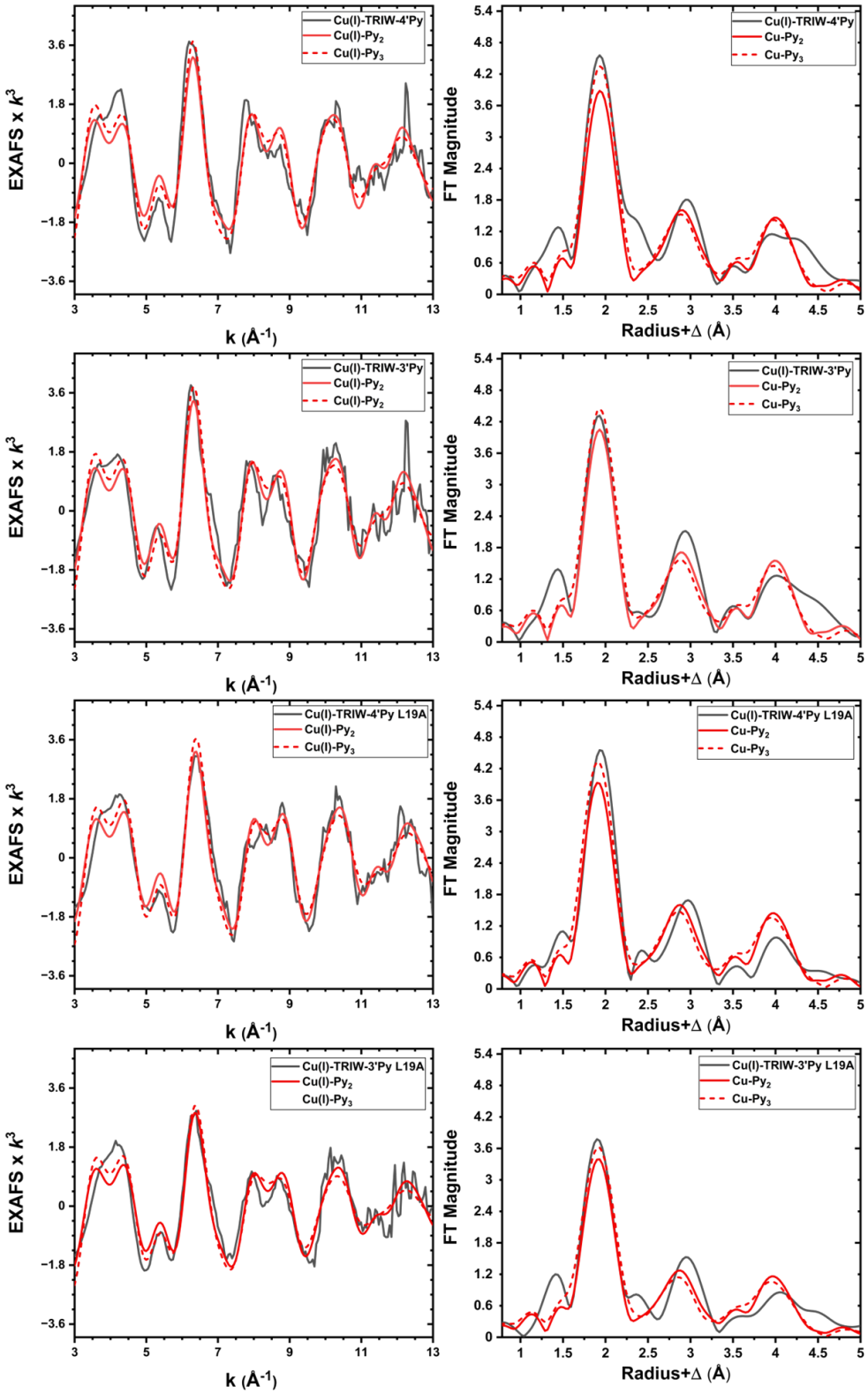


Figure II-11: EXAFS of Cu(I) designed T2Cu centers at pH 5.9: **Left**: k^3-Space (3-13.1 Å^{-1}) of the each of the Cu(I) proteins. **Right**: The corresponding Fourier transform of each of the k^3-spaces. Fits are included in each space, even if the fitting process was conducted in k^3-space.

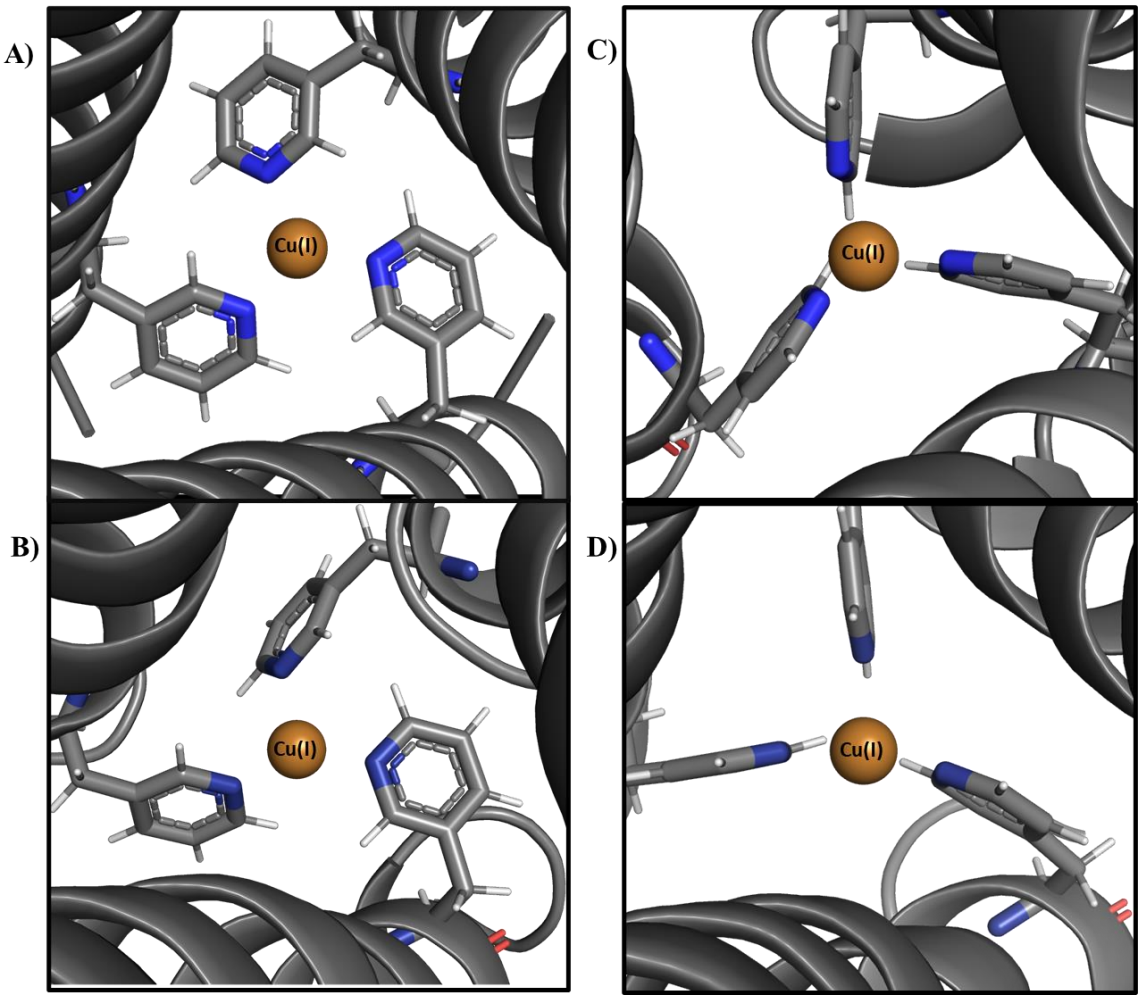
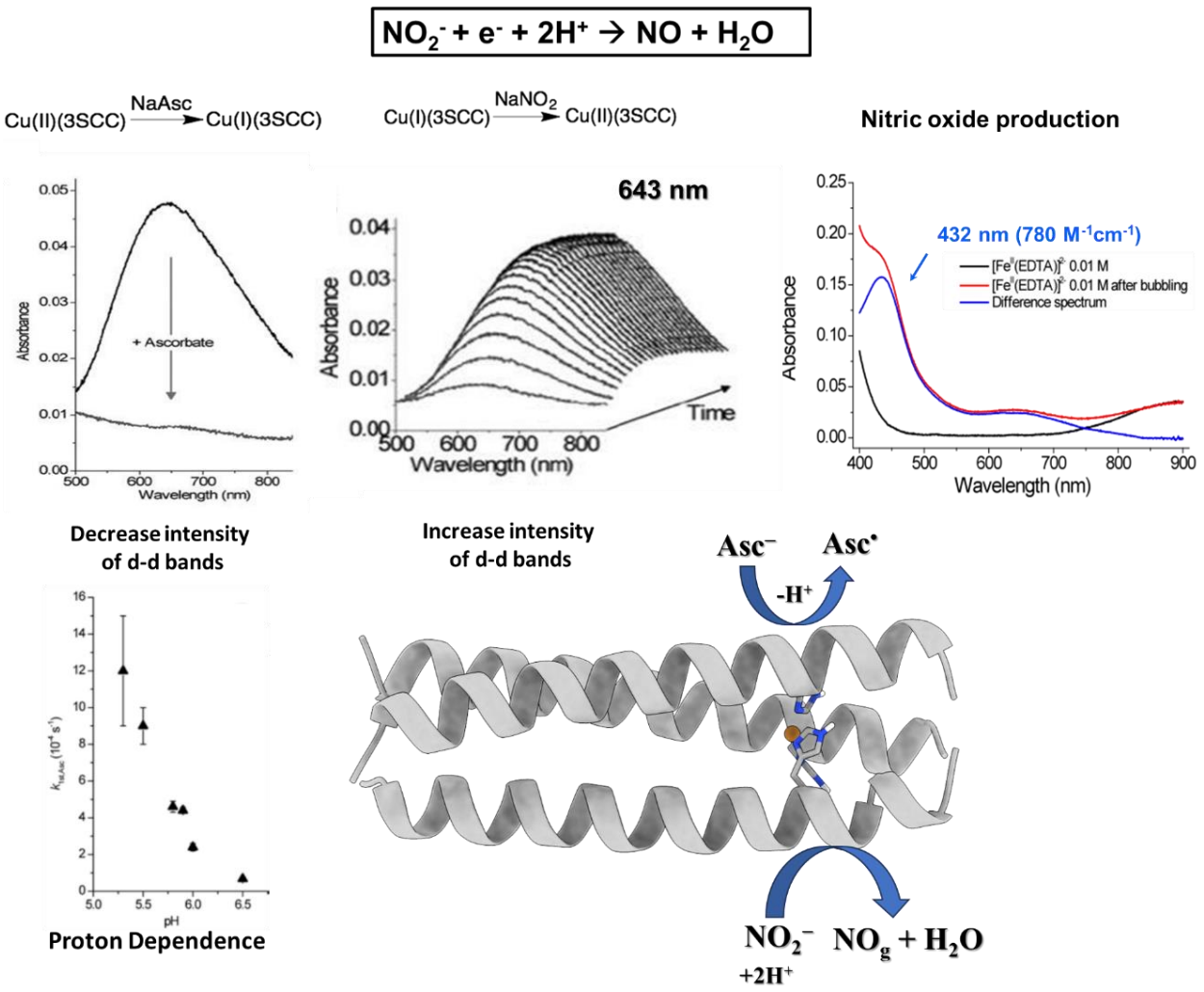


Figure II-12: Models of the metal binding sites of designed Cu(I) proteins: **A)** Cu(I)-TRIW-3'Py, **B)** Cu(I)-TRIW-3'Py L19A, **C)** Cu(I)-TRIW-4'Py and **D)** Cu(I)-TRIW-4'Py L19A. Models were made using the program Pymol and based on the AlphaFold of the apo-trimer with a phenylalanine active site, and spectroscopic analysis of the Cu(I) XANES/EXAFS at pH 5.9.

Copper Nitrite Reductase Kinetics:

The ability of these unnatural type 2 copper centers to catalyze the reduction of nitrite was investigated by monitoring the oxidation of sodium ascorbate (sacrificial donor) in the presence of enzyme and substate. The sodium ascorbate acts as a sacrificial donor to reduce the Cu(II)-form of the 3SCC to the catalytic active Cu(I)-form of the 3SCC.[19] In the presence of sodium nitrite, Cu(I)-3SCC catalyzes the conversion of sodium nitrite and two protons to NO(g) and water. It has already been shown by Yu *et al*. that nitrite can oxidize Cu(I)-TRIW-H with the reappearance of



Scheme II-1: CuNiR kinetics steady state kinetics associated with TRIW peptides. Figures modified from Ref. 19 Copyright 2012 PNAS.

the Cu(II)-3SCC d-d bands at pH 5.8, with a recovery of 77% yield of the original signal (Scheme II-1).[19] It is known that sodium ascorbate catalyzes the reduction of NO_2^- in the absence of a catalysis; however, in the presence of a catalyst, these rates are not competitive within the range of 20-600 mM $NaNO_2$ (Figure II-13).[46] Given this, a control experiment was conducted each time which contained 7 eqv. apo-peptide, 1.5 mM sodium ascorbate, and appropriate amount of sodium nitrite which was subsequently subtracted from the rate of the catalytic experiment to ensure that the background reaction did not contribute to the reactivity reported. The reactivity was first explored under pseudo first order conditions with respect to the $NaNO_2$ (30 mM $NaNO_2$), where rate constants were calculated from the slope of the plot observed rate (ν_{obs}) vs. $NaNO_2$

concentration (Figure II-14). Under first order conditions, all peptides behaved linearly when the catalyst was varied in concentration. This has two implications; a) this process reflects a true biomolecular reaction that has a second order rate constant associated with this process, b) the catalyst does not change form (*i.e.*, change in the equilibrium between oligomerization states) over this concentration range. The TRIW-4'Py L19A construct was an outlier with the largest rate constant (1.4 s^{-1}) suggesting this scaffold has the highest activity among the designed proteins. Interestingly, this was not likely due to the alanine sterics but is, in part, an effect of the orientation differences between 3'Pyridine and 4'Pyridine in the active site, as the TRIW-3'Py L19A catalyzes the reaction with a lower rate constant (Table II-5). To investigate this further, Michaelis-Menten kinetics were conducted to examine the steady state of the enzyme at various substate concentrations to understand the changes associated with each of these design strategies. All of the enzymes studied exhibited saturation kinetics in the concentration range from 50-600mM $NaNO_2$ at pH 5.9 at a saturating concentration of sodium ascorbate (1.5 mM) (Figure II-15) when subtracting the initial rates from the background reaction at each concentration of substrate. For the first time, the Michaelis-Menten kinetics of parent design, TRIW-H, that mimic the primary coordination sphere the closest were collected revealing a comparatively low k_{cat} (0.032 s^{-1}) and a

Table II-5: Nitrite reduction kinetics parameters fitted at pH 5.9.
N/A: Enzyme activity was too low to conduct Michaelis–Menten kinetics k_{cat} and K_m could not be reliably determined from the Michaelis–Menten kinetics, only the linear portion at low substrate concentration could be fitted to yield an accurate k_{cat}/K_m.
[a] The pseudo 1st order rate constant of TRIW-ε_MH L19A was determined by Dr. Karl Koebke.

Enzyme	k' (s^{-1})	k_{cat} (s^{-1})	K_m (M)	k_{cat}/K_m (M^{-1} s^{-1})
TRIW-H	4.6×10^{-4}	0.032 (±0.016)	1.2 (± 0.9)	0.026 (±0.005)
TRIW-ε_mH L19A [a]	3.8×10^{-2}	N/A	N/A	0.14 (±0.01)
TRIW-3'Py	0.30	3.0 (±0.1)	0.28 (±0.03)	11 (± 1)
TRIW-3'Py L19A	0.51	2.8 (±0.3)	0.19 (±0.06)	15 (± 3)
TRIW-4'Py	0.11	2.9 (±1)	0.60 (±0.26)	5 (± 1)
TRIW-4'Py L19A	1.4	1.9 (±0.1)	0.05 (±0.01)	39 (± 3)

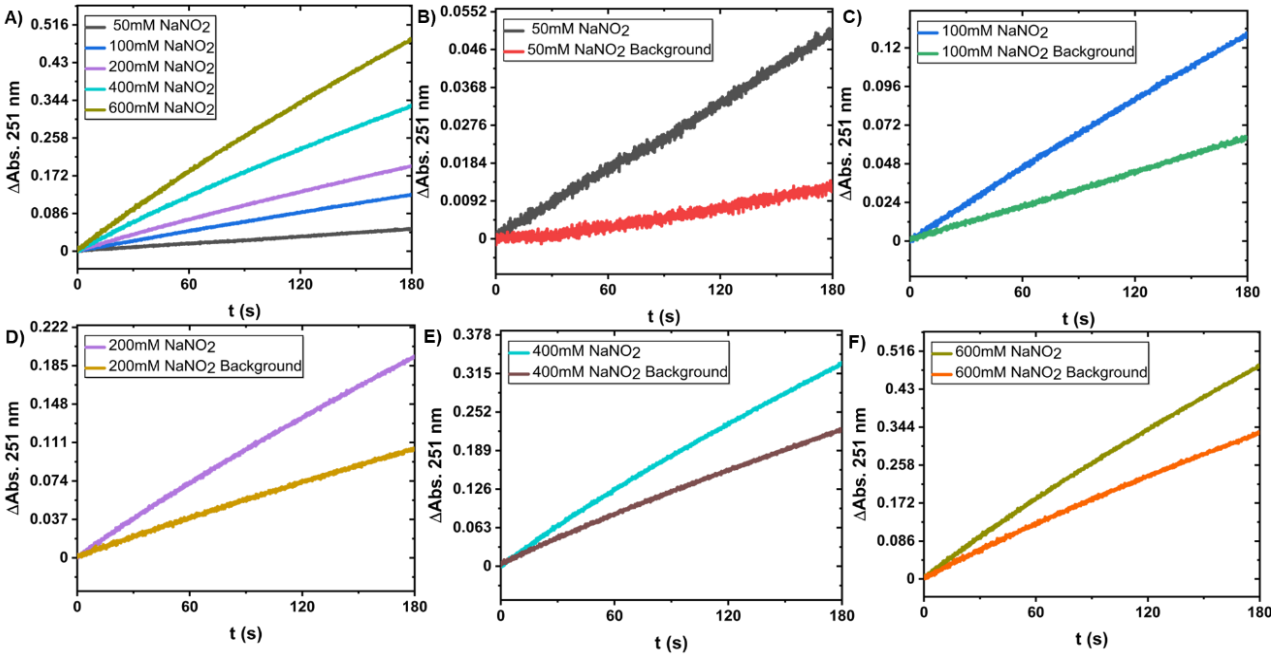


Figure II-13: Kinetics progress curves of nitrite reductase assay at pH 5.9: **A)** Example of ΔAbs_{251nm} vs time progress curves of the consumption of 1.5mM sodium ascorbate in the presence of 1μM Cu-TRIW-3'Py and varying $NaNO_2$ concentrations, **B-F:** Progress curves for each substrate concentration in the presence of 1μM Cu-TRIW-3'Py and the respective control (0 μM copper loading).

sluggish k_{cat}/K_m (0.026 $M^{-1}s^{-1}$) value that yields an estimated K_m value of 1.2 M. The low activity enzymes studied exhibited saturation kinetics in the concentration range from 50-600mM $NaNO_2$ at pH 5.9 at a saturating concentration of sodium ascorbate (1.5 mM) (Figure II-15) when subtracting the initial rates from the background reaction at each concentration of substrate. For the first time, the Michaelis-Menten kinetics of parent design, TRIW-H, that mimic the primary coordination sphere the closest were collected revealing a comparatively low k_{cat} (0.032 s^{-1}) and a sluggish k_{cat}/K_m (0.026 $M^{-1}s^{-1}$) value that yields an estimated K_m value of 1.2 M. The low activity of this enzyme limited the substrate concentration range below 600 mM as the background reaction rate outcompeted the enzymic reaction above 600 mM $NaNO_2$. Therefore, both the fitted k_{cat} value and derived K_m values are estimated. Invoking negative design to model an enzyme with the enforcement of the N_δ-coordinated with the alanine layer design resulted in an elevated k_{cat}/K_m

value, with respect to TRIW-H, of 0.14 (± 0.01) $M^{-1}s^{-1}$.[b] While the factor of 5 increase in k_{cat}/K_m is apparent in kinetics, the k_{cat} nor the K_m value could be determined due to the extremely high values likely associated with this construct. Incorporating the pyridine ligand into the ***a***-site yielded k_{cat} values that are independent of the ***d***-site design with the alanine or the primary coordination sphere orientation between 3'Pyridine and 4'Pyridine (~3.0 s^{-1}). However, both design strategies influenced the K_m values which is most apparent in TRIW-4'Py and TRIW-4'Py L19A design (600 mM and 50 mM, respectively).

[b] Dr. Karl Koebke collected the pseudo 1st order rate constant for TRIW-ε_MH L19A

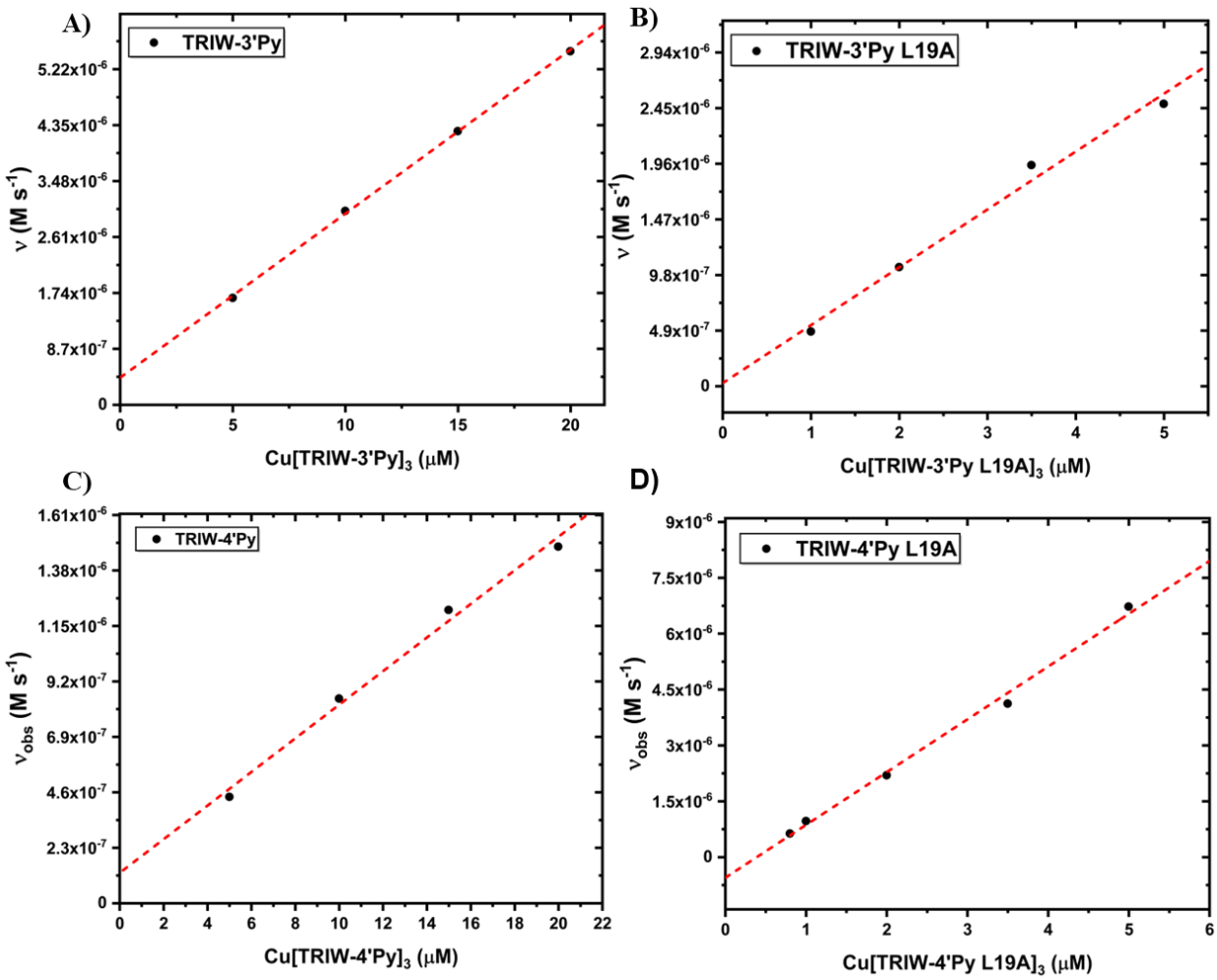


Figure II-14: Nitrite reduction pseudo first-order rate plots at pH 5.9: **A)** Fitted observed velocity vs. catalyst concentration plots to determine the pseudo first-order rate constant of each enzyme: **A)** TRIW-3'Py, **B)** TRIW-3'Py L19A, **C)** TRIW-4'PY, and **D)** TRIW-4'Py L19A.

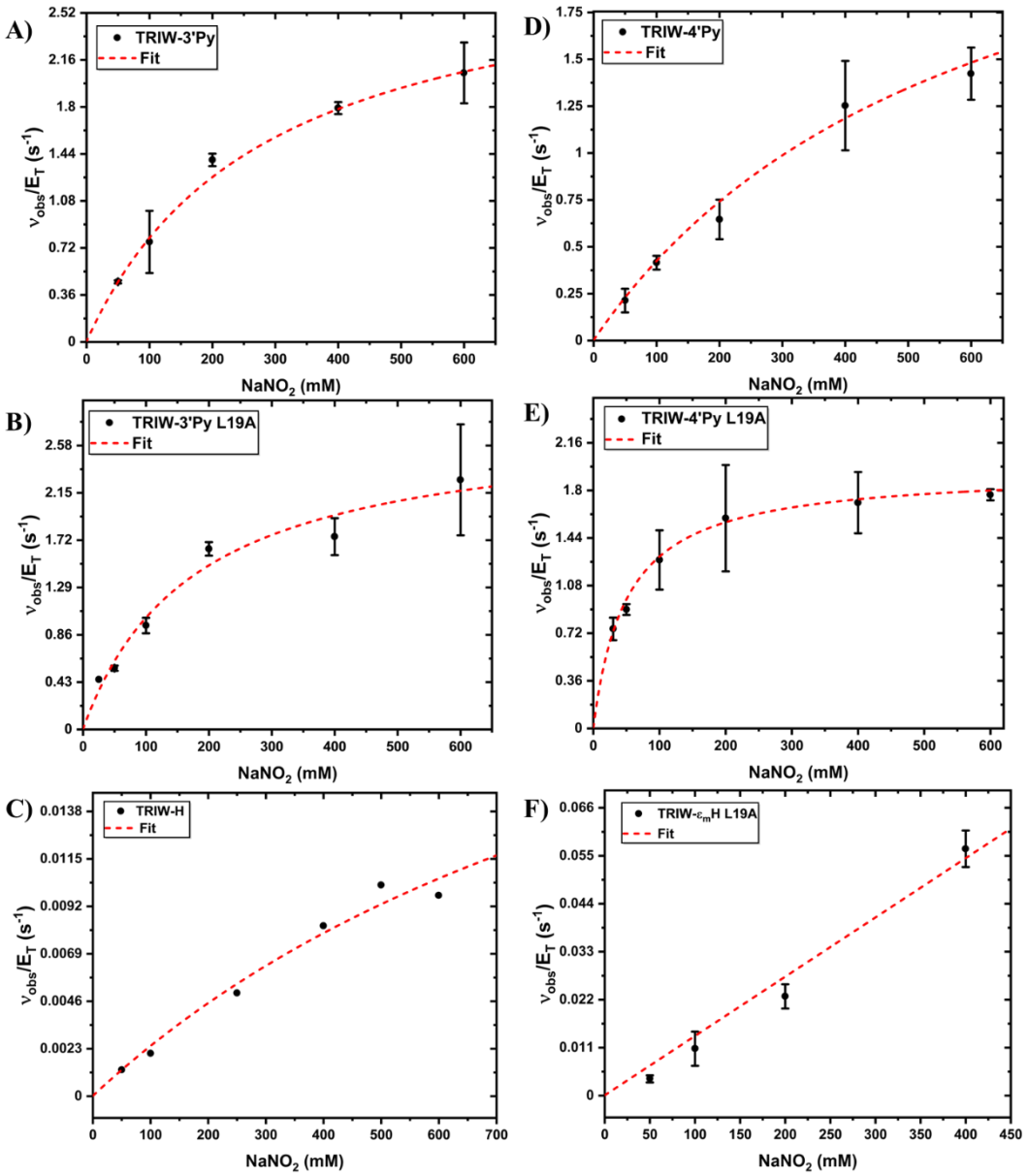


Figure II-15: CuNiR Michaelis-Menten kinetics curves at pH 5.9: **A)** TRIW-3'Py, **B)** TRIW-3'Py L19A, **C)** TRIW-H, **D)** TRIW-4'Py, **E)** TRIW-4'Py, and **F)** TRIW-ε_mH L19A. (Dotted curves represent fits to the Michaelis-Menten equation Eq II-5.).

Discussion:

Designing 3'Py or 4'Py into the TRIW scaffold results in well-folded 3SCCs for (TRIW-3'Py)$_3$[c] and (TRIW-4'Py)$_3$[d], respectively (Figure II-3). Additionally, the mutation of the leucine layer above the active site with alanine (L19A) leads to a slight unwinding of the apo-3SCC as noticed in the CD spectra; however, all remained a 3SCC in the presence of Cu(II) (Figure II-5). The three slightly different meta-protons observed in apo TRI-3'Py may result from different stable conformers the pyridine adopts in the absence of the metal which as previously seen with cysteine and the cysteine analog in 3SCCs (Table II-6).[47] However, up to 0.5 equivalents of Cu(I) were needed to bring each of the three 3'pyridyl sidechains into a single magnetic environment, whose ^{13}C chemical shifts are consistent with Cu(I) Bipyridyl complexes. (Table II-7). Substituting the ***d***-site leucine layer with an alanine layer will locally disrupt the knob-into-hole packing above the active site leading to a decrease in stability of the construct, as clearly seen in the chemical Gdn-HCl denaturation titration (Figure II-4A).[48] The midpoint of unfolding of the alanine mutants were noticeably below the lowest concentration of Gdn-HCl point which allowed for the temperature dependent unfolding to be monitored, unlike most well-designed coiled coil proteins which display a strong resistance to unfold even when subjected to temperatures above 100°C.[49,50] The Cu(II) was noticeably more resistant to thermal unfolding than the apo-forms; however, no changes were observed in the CD spectrum upon the addition of Cu(II). No large structural rearrangements are expected to occur upon metal binding, as opposed to recently reported *de novo* coiled coil and helix bundle proteins which display a strong metal dependence on folding.[10,51] However, given the broad signals observed for the pyridyl protons and low chemical dispersion observed with the backbone amide protons in apo TRI-4'Py L19A, the introduction of the alanine above the active site introduced some disorder to the structure, making the protein more molten globular-like, resolving to a more ordered structure upon the addition of Cu(I) as indicated by the

[c] Sequence of the monomers of TRIW-3'Py Ac-GWKALEEK LKALEEK LKALEEK (3-Py) KALEEK G-NH_2

[d] Sequence of the monomers of TRIW-4'Py: Ac-GWKALEEK LKALEEK LKALEEK (4-Py) KALEEK G-NH_2

Table II-6: ^{1}H and ^{13}C shifts for TRI-3'Py and TRI-4'Py L19A during the Cu(I) titration. [a] shift values are those from the fitted ^{1}H NMR

Equivalents Cu(I)/Trimer	TRI-3'Py Meta ^{1}H (ppm)[a]	^{1}H-^{13}C HSQC (ppm) (^{13}C)	TRI-4'Py L19A Meta ^{1}H (ppm)[a]	^{1}H-^{13}C HSQC (ppm) (^{13}C)
Apo	7.046 7.054 7.063	7.04 (123.5) 7.06 (123.5)	7.233	7.22 (125.4)
0.1 eqv.	7.055 7.063 7.072	--	7.267	--
0.3 eqv.	7.121 7.133	7.12 (123.6) 7.13 (123.8)	7.335	7.34 (125.7)
0.5 eqv.	7.182	7.18 (124.1)	7.389	--
0.7 eqv.	7.242	--	7.424	7.42 (126.1)
1.0 eqv.	7.279	7.28 (124.9)	7.431	--

amide protons' chemical dispersion (Figure II-9A).[52–54] Compared to apo TRI-4'Py L19A, the one-dimensional ^{1}H NMR spectra of TRI-3'Py exhibit significantly more dispersion in the amide region as Cu(I) is incrementally added, which is in line with its stronger CD single at 222 nm (Figure II-3B). Overall, it is clear from the CD spectra, but clearer in the NMR spectra, that Cu(I) slightly alters the overall structure of the apo proteins.

The UV-Vis spectra of the Cu(II) complexes showed a narrow range of λ_{max} between 670 (14,930 cm^{-1}) to 685 nm (14,600 cm^{-1}) (Figure II-5 and Table II-7) for all the mutations studied. This is indicative of an N_2O_2 or N_3O_1 type environment which absorbs at ~690 nm and is consistent with the blue-shifted spectra of other histidine containing Cu(II)-3SCCs, as pyridine is

Table II-7: UV-VIS and EPR parameters of relevant designed Cu(II)-proteins and Cu(II) model complexes.
[a] Units λ_{max} nm, ε_λ M^{-1} cm^{-1} , A_{II} ($A_{II} \times 10^{-4}$) cm^{-1}

Enzyme	λ_{max} [a] $[\varepsilon_\lambda]$ [a]	g_z	g_y	g_x	A_{II} [a]	Solvent [pH]	Ref.
TRIW-4'Py	685 [73]	2.27	2.03	2.03	170	H_2O [5.9]	--
TRIW-4'Py L19A	673 [116]	2.28	2.04	2.04	169	H_2O [5.9]	--
TRIW-3'Py	670 [52]	2.29	2.04	2.04	168	H_2O [5.9]	--
TRIW-3'Py L19A	680 [60]	2.29	2.05	2.04	170	H_2O [5.9]	--
TRIW-H	643 [135]	2.27	2.03	2.06	167	H_2O [5.8]	19
TRIW-δ_mH	670 [67]	2.28	2.05	2.05	167	H_2O [5.8]	22
TRIW-ε_mH	689 [71]	2.30	2.03	2.05	151	H_2O [5.8]	22
[3SCC-Cu(I9H)$_3$]$^{2+}$	590 [78]	2.25	2.05	2.05	189	H_2O [7.5]	56
***Sm*CuNiR**	[n/a]	2.30	2.053	2.05	151	H_2O [7.1]	57
(Cu[26]py$_2$N$_4$)$^{2+}$	660 [n/a]	2.24	2.08	2.05	180	H_2O:DMSO (1:1)	58
Peptidylglycine α-Hydroxylating Monooxygenase	[n/a]	2.29	2.06	2.05	157	H_2O [6.0]	59
[Cu(tpy)(H_2O)(ClO_4)]ClO_4	693 [65]	2.28	2.067	2.07	178	Methanol [n/a]	60

a slightly weaker sigma donor than imidazole.[22,55] All enzymes display axial EPR spectra at pH 5.9 and have A_{II} values that are consistent with these copper active sites being classified as T2Cu centers. Moreover, the A_{II} values for these pyridine-containing sites closely match those of our previously reported Cu(II)-TRIW-H and Cu(II)-TRIW-δ_mH systems where the N_ε nitrogens (*e.g.*, the pyridine-like nitrogen) are coordinated around a Cu(II)N_3O center based on EXAFS.[61–63]

Taken together, these data indicate that while the oxidized copper pyridyl site shares some similarities with the histidine designs, the environment of the copper centers is distinct from native histidine.[19,22,23,57,58,60,64,65]

Although Cu(I) spectroscopy is more limited than Cu(II), X-ray absorption spectroscopy (XAS) provided valuable structural insights for the active sites of the various peptide modifications. The intensity of the pre-edge, 1s−4p transition (ca. 8984 eV), serves as a useful measure of the coordination number around Cu(I), and has previously allowed for Cu(I)-TRIW-H L19A and Cu(I)-TRIW-H to be assigned as 2-coordinate and 3-coordinate histidine sites, respectively.[42,66] These assignments agree with the fitting of their EXAFS regions (Figure II-16

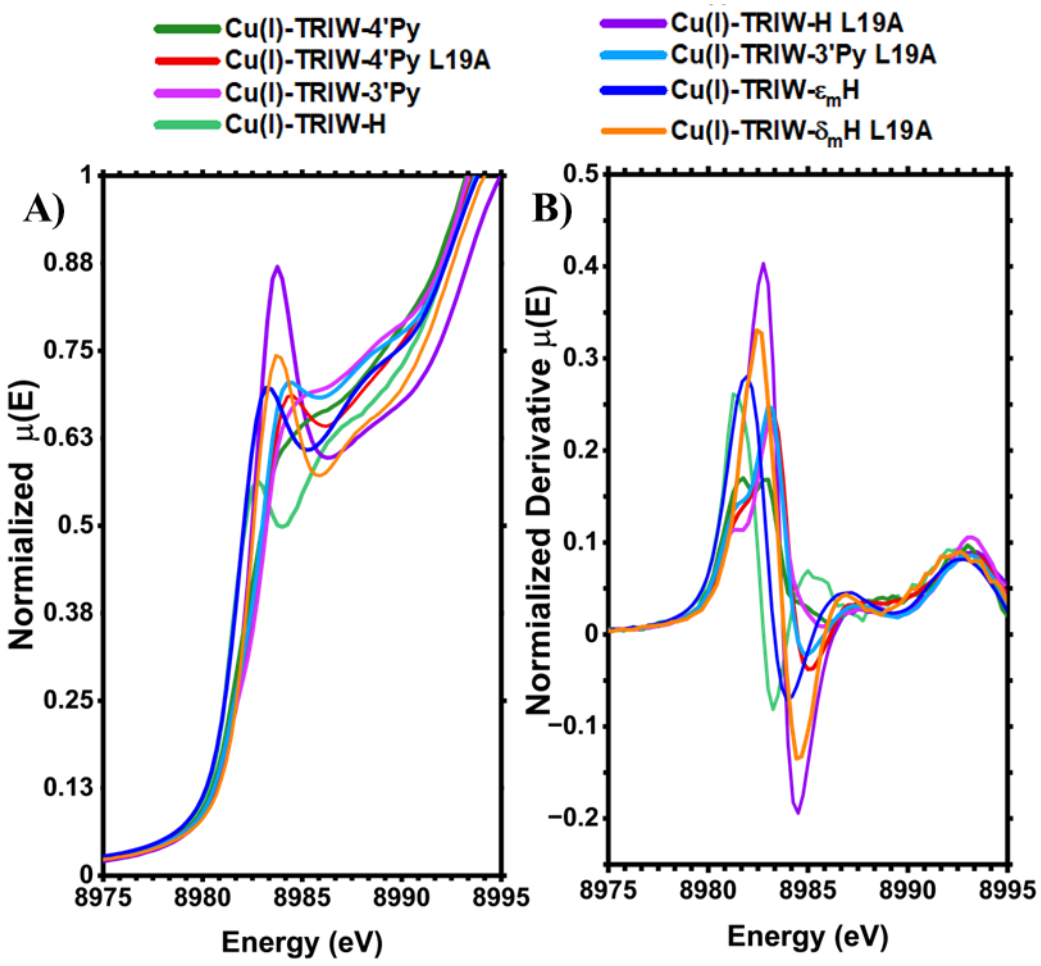


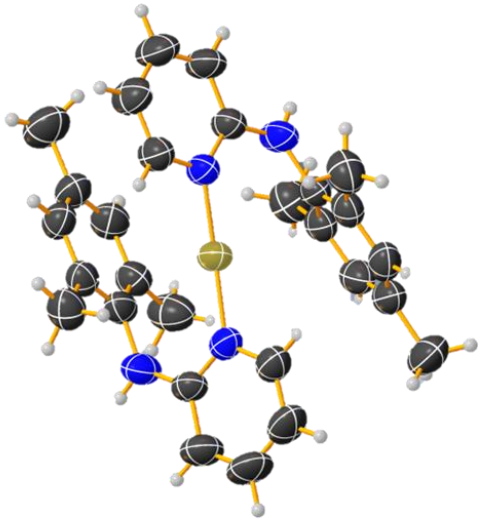
Figure II-16: Cu(I) XANES at pH 5.8/5.9 comparing the pyridine constructs with histidine active sites: (Inset) first derivative of E-space (*Left*). The XANES for *all histidine and methyl histidine Cu(I)-proteins were collected by Dr. Fangting Yu or Dr. Karl Koebke.*

and Table II-9).[19,22] The Cu(I) pyridine active sites, notably, have a split pre-edge (ca. 8981 eV and 8983 eV) and are blue shifted by 1.9 eV relative to the Cu(I)-TRIWL23-H (Figure II-16B). This blue shift and splitting in these transitions has been attributed to low-lying unoccupied ligand molecular orbitals (MO) (π*) mixing into the unoccupied Cu p_z orbital (perpendicular to the bonding axis), splitting the peak into two bands.[41–43,67] This observation may suggest that the Cu(I) is in a more T-shape geometry than trigonal planar.[43] This feature is likely unresolved at the imidazole site due to its π-acceptor capability and the resolution of Cu K-Edge.[43] Overall, the pyridine sites are of intermediate intensity between these two histidine sites, and the distinction between 2 and 3-coordinate geometries is not as clear. This is consistent with the fitting of the EXAFS where either Cu(I)$(Pyridine)_2$ or Cu(I)$(Pyridine)_3$ gave comparable fits to the data. The EXAFS of this protein is not easy to interpret unambiguously, but this observation suggests the Cu(I) may sit in an active site that has distorted bond distances or there exists an equilibrium between 2-coordinate and 3-coordinate structures that is averaged during the experiment. Moreover, these fits can be influenced by static disorder in first-shell Cu(I)–N_{His} bond, leading to the coordination number being unassignable while still giving well resolved and accurate bond distances (Table II-8).[68] Cu(I)-TRIW-H has previously been assigned to Cu(I)-His with an average Cu-N bond length of 1.93 Å at pH 5.8 and pH 7.9, which is in contrast to the Cu(I)-TRIW-H L19A where the steric bulk is removed and relaxes the active site to a more preferred 2-coordinate Cu(I)$(His)_2$ structure with an average Cu–N_{His} distance of 1.86 Å.[19,20] The pyridine ligands form longer Cu(I)–N_{py} bonds than histidine in these scaffolds (Table II-8). Crystal structures of synthetic 2-coordinate and 3-coordinate pyridine complexes have Cu(I)–N_{Py} bond distances that range from 1.91-1.94 Å for 2-coordinate complexes and 1.97-1.99 Å for 3-coordinate complexes (Figure II-17).[69–72] The alanine mutation relaxes the more 3-coordinate Cu(I)-TRIW-4'Py to a more 2-coordinate Cu(I)-TRIW-4'Py L19A which in turns decrease the Cu–N_{Py} bond distance from 1.97 Å to 1.94 Å, respectively (Table II-8). This was observed to a lesser degree with the 3'Py active site, but in both cases, the edge intensity increases with the alanine mutation and toward a more 2-coordinate geometry. Given these differences in both the electronics and structure of the Cu(I)

active site when bound to histidine or pyridine, I sought to explore nitrite reduction with this novel active site.[20,22,73]

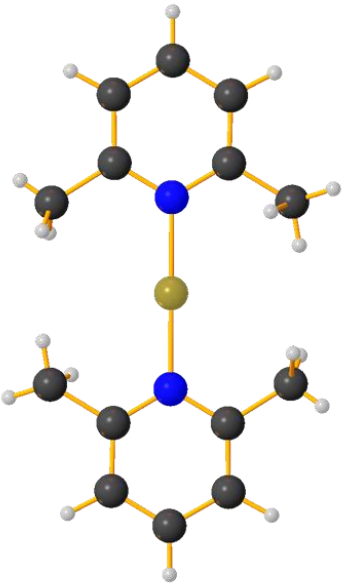
Table II-8: Summary of bonding parameters of Cu(I) pyridine and histidine complexes.
[a] E_0 was set to 8990 eV and $\Delta E = -5$ eV was fixed during the fitting process
[b] Average bond distances are calculated for these complexes.

Enzyme	Best Model	Cu(I)-N	Cu(I)-N $\sigma^2 \times 10^{-3}$	Bond Valance Sum	Solvent [pH]	Ref.
TRIW-4'Py	$CuPy_2$	1.97 Å	3.17 $Å^2$	0.78	H_2O [5.9]	--
	$CuPy_3$	1.97 Å	5.26 $Å^2$	1.05		
TRIW-3'Py	$CuPy_2$	1.96 Å	2.94 $Å^2$	0.80	H_2O [5.9]	--
	$CuPy_3$	1.97 Å	5.17 $Å^2$	1.08		
TRIW-4'Py L19A	$CuPy_2$	1.94 Å	3.31 $Å^2$	0.85	H_2O [5.9]	--
	$CuPy_3$	1.94 Å	5.60 $Å^2$	1.14		
TRIW-3'Py L19A	$CuPy_2$	1.95 Å	4.31 $Å^2$	0.83	H_2O [5.9]	--
	$CuPy_3$	1.95 Å	6.96 $Å^2$	1.10		
Cu(I)-TRIW-H	$CuHis_3$	1.93 Å	9.0 $Å^2$	1.17	H_2O [5.8]	19
Cu(I)-TRIW-H L19A	$CuHis_2$	1.86 Å	8.0 $Å^2$	1.05	H_2O [5.8]	20
	$CuHis_3$	1.86 Å	9.7 $Å^2$	1.42		--
Cu(I)-TRIW-δ_mH L19A	$CuHis_2$	1.89 Å	8.1 $Å^2$	0.97	H_2O [5.8]	22
	$CuHis_3$	1.89 Å	10.4 $Å^2$	1.30		--
Reduced *ps*AO	$CuHis_3$	1.94 Å	6.1 $Å^2$	1.14	H_2O [n/a]	73
Cu(I)-bis(N-(2,4,6-Trimethyl)phenyl-N-(2-pyridyl)amine)) (BF_4)[b]	$CuPy_2$	1.91 Å	[n/a]	0.92	MeOH	72
Cu(I)-Bis(2,6-Dimethylpyridine)(ClO_4)[b]	$CuPy_2$	1.94 Å	[n/a]	0.85	Acetonitrile	71
Cu(I)-Tris(2-methylpyridine)(PF_6)[b]	$CuPy_3$	1.98 Å	[n/a]	1.02	Acetonitrile	69
Cu(I)-Tris(3,5-Dimethylpyridine)(PF_6)[b]	$CuPy_3$	1.99 Å	[n/a]	1.00	Acetonitrile	69



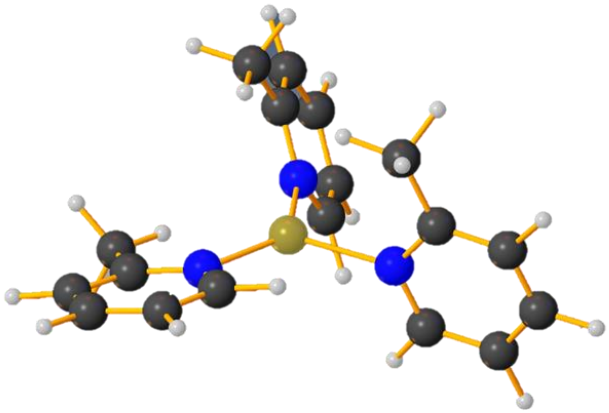
Cu(I)-bis(N-(2,4,6-Trimethyl)phenyl-N-(2-pyridyl)amine))

Avg. Cu^{I}-N 1.91 Å



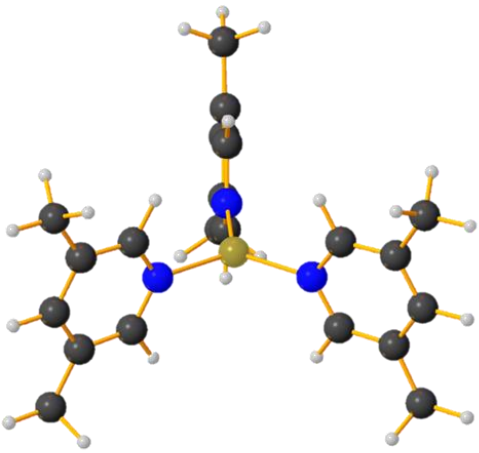
Cu(I)-Bis(2,6-Dimethylpyridine)

Avg. Cu^{I}-N 1.94 Å



Cu(I)-Tris(2-methylpyridine)

Avg. Cu^{I}-N 1.98 Å



Cu(I)-Tris(3,5-Dimethylpyridine)

Avg. Cu^{I}-N 1.99 Å

Figure II-17: X-ray structures of model Cu(I)-pyridine complexes in Table II-8.

Initially, I probed these catalysts under pseudo first order conditions at 30 mM $NaNO_2$.[19] All pyridyl derivatives have markedly higher rate constants than those of Cu-TRIW-H and Cu-TRIW-H L19A (Table II-9). This observation supports the proposal that the primary reason that the Nε with the δ_m-His in the active site is more catalytically active is that it more closely resembles the pyridine donor type. This is not to say that the different chelate rings formed by N_δ or N_ε

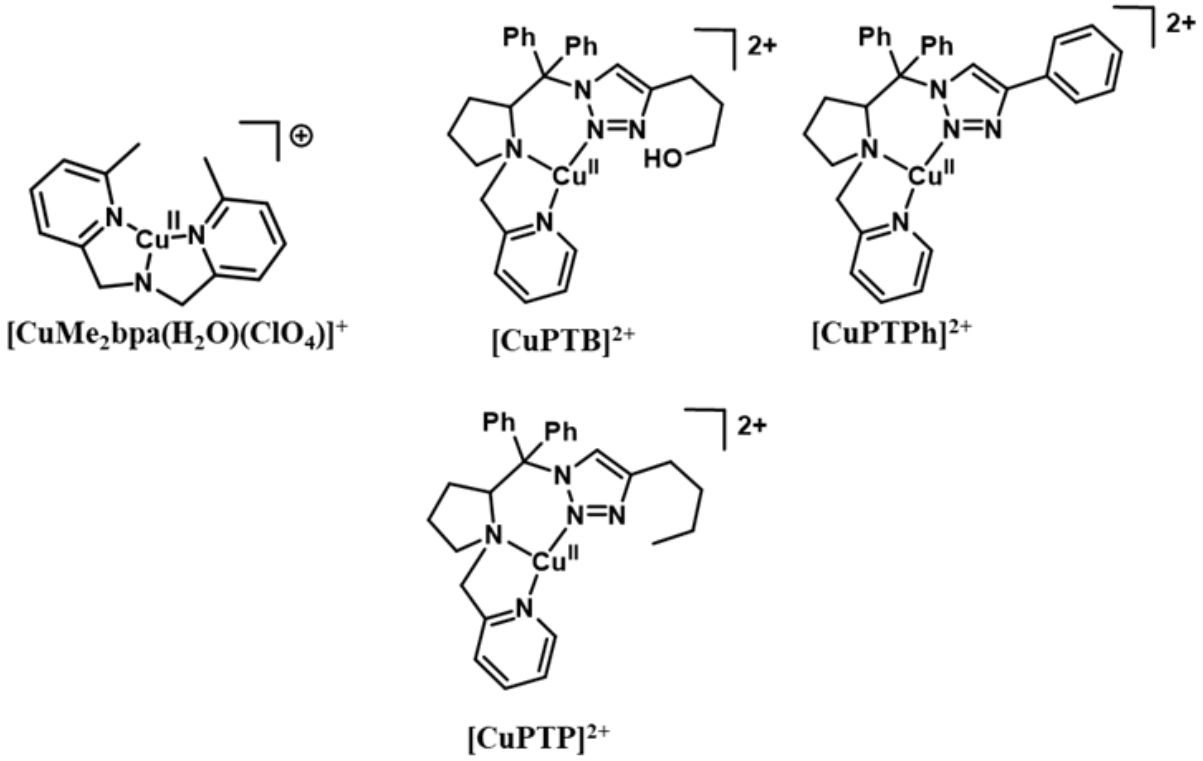
chelation is unimportant, but that the electronic donor capacity of the N confers the proper Cu electronegativity to facilitate catalysis. The N_δ in the ε_m-His active sites, which are more electron donating, are an order of magnitude lower activity. While these rate constants suggest the pyridyl active sites have increased activity, the pseudo 1st order rate constants are calculated at fixed NO_2^- concentration, which can hinder an accurate comparison if substrate affinity varies between these derivatives. I set out to understand these catalysts further by performing steady state kinetics which revealed how both histidine and different orientations of the pyridine ligands influence nitrite reduction (Figure II-12).

Since the catalytic conditions for the nitrite reduction assay maintain the Cu(I) resting state of these designed enzymes it is important to understand substrate binding to this reduced center. Firstly, given the overall similarities in the primary coordination sphere to native CuNiR (Table II-9), it is surprising that Cu-TRIW-H catalyzes nitrite reduction with the slowest effective 2nd order rate constant (k_{cat}/K_m) to the point that acquiring a full steady state curve was difficult. This construct has the lowest nitrite affinity, with a K_m > 400 mM and a very low k_{cat}. Cu-TRIW-H L19A lowered the K_m to 240 mM, supporting the idea that substrate binding is critical to the catalytic efficiency. Both Cu-TRIW-ε_mH and Cu-TRIW-ε_mH L19A had sluggish kinetics, and only some of the Michaelis-Menten parameters could be reported (Table II-9). This is not surprising as the N_δ is not coordinated in *wt* CuNiRs and is unfavored toward NO_2^- reduction. The k_{cat} values associated with the pyridyl maximize at ~3 s^{-1}, which is a factor of 250 greater than histidine. It is currently unclear whether pyridine increases these k_{cat} values because of the enhancement of the proton transfer step, N–O bond cleavage, product release or a combination of these factors.

However, it is clear that nature's preference to enforce the N_ε coordination is, at least partially due to an electronic preference for this N donor type, which is supported by the leveling off of the k_{cat} values across all pyridyl derivatives. While the k_{cat} values have saturated with the pyridine and δ_m-His sites, one can further attempt to increase catalytic efficiency by changing the way in which the Cu(I) sits within the 3SCC. This orientational control is achieved by simply using the 3'Py vs 4'Py ligands (Figure II-12).

Table II-9: Kinetic parameters for native, small molecule and designed NIRs.
N/A: Enzyme activity was too low to conduct Michaelis–Menten kinetics
[a] k_{cat} and K_m could not be reliably determined from the Michaelis–Menten kinetics, only the linear portion at low substrate concentration could be fitted to yield the accurate k_{cat}/K_m
[b] part of the original work within this thesis
ChemDraw of synthetic models in Table II-9 are shown in Scheme II-2

Enzyme	k' (s^{-1})	k_{cat} (s^{-1})	K_m (M)	k_{cat}/K_m (M^{-1} s^{-1})	Ref.
AfCuNiR pH 6.5	--	620	1.5×10^{-4}	4.1×10^{6}	74
$[CuMe_2bpa(H_2O)(ClO_4)]^+$ (in water pH 5.5)	--	5.3×10^{-5}	0.0025	0.021	75
$[CuMe_2bpa(H_2O)(ClO_4)]^+$ (on electrode pH 5.5)	--	0.063	0.0015	42	75
$[CuPTB]^{2+}$ (*MeOH*)	--	3.04	0.0117	259.8	76
$[CuPTPh]^{2+}$ (*MeOH*)	--	5.08	0.00786	646.3	76
$[CuPTP]^{2+}$ (*MeOH*)	--	4.92	0.00487	1010.2	76
TRIW-H	4.6×10^{-4}	0.032 (±0.016)	1.2 (± 0.9)	0.026 (±0.005)	19
TRIW-H L19A	3.5×10^{-2}	0.23 (±0.03)	0.24 (±0.03)	1.0 (±0.3)	20,22
TRIW-δ_mH	0.12	1.5 (± 0.1)	0.18 (± 0.02)	8.2 (± 0.1)	22
TRIW-δ_mH L19A	0.30	1.5 (±0.1)	0.13 (±0.01)	11 (±0.1)	22
TRIW-ε_mH[a]	4.1×10^{-3}	N/A	N/A	N/A	22
TRIW-ε_mH L19A[a]	3.8×10^{-2}	N/A	N/A	0.14 (±0.01)[b]	22
TRIW-3'Py	0.30	3.0 (±0.1)	0.28 (±0.03)	11 (± 1)	--
TRIW-3'Py L19A	0.51	2.8 (±0.3)	0.19 (±0.06)	15 (± 3)	--
TRIW-4'Py	0.11	2.9 (±1)	0.60 (±0.26)	5 (± 1)	--
TRIW-4'Py L19A	1.4	1.9 (±0.1)	0.05 (±0.01)	39 (± 3)	--



Scheme II-2

While this did not impact the coordination number of the reduced enzyme (*i.e.*, 3-coordinate Cu(I)), this modification perturbed the k_{cat}/K_m values and shifted the K_m value from 600 mM (Cu-TRIW-4'Py) to 260 mM (Cu-TRIW-3'Py), without perturbing their respective k_{cat} values (Table II-9). This suggests that while all steps after N–O bond cleavage are unaffected (*i.e.*, no change in k_{cat}), the relative orientation of the ligands plays a role in tuning the catalytic mechanism before or during N–O bond cleavage.[77] This was further enhanced by the L19A mutants. While there is only a slight decrease in K_m (factor of 1.4) between Cu-TRIW-3'Py L19A and Cu-TRIW-3'Py, the 4'Pyridine showed a much greater disparity between K_m values, with Cu-TRIW-4'Py L19A having the tightest K_m (50 mM). Again, since the k_{cat} values level off at ~ 3 s^{-1}, the primary driver for the increased catalytic efficiencies is a tighter K_m and is likely a consequence of both the coordination environment of the reduced enzyme and a likely increase in substate access to the copper center via the less sterically demanding alanine layer. Both the 1s–4p edge and EXAFS bond distances suggest that the resting state for 4'Py-alanine mutant converted to a more 2-coordinate Cu(I)

geometry compared to the 4'Py-leucine mutant, and it is likely then that the substrate benefits from the lower coordination number of 4'Py-alanine mutant due in part to the removal of a sterically impending pyridine ligand. TRIW-4'Py has a very high K_m value (600 mM), comparable to that of TRIW-H (> 400 mM). This value is likely attributed to the more 3-coordinate nature of the reduced enzyme. This 3-coordiante reduced state in native CuNiR has been observed in single-shot diffraction experiments under similar catalytic conditions where one water is lost from the oxidized T2Cu center and is subsequently reduced to a Cu(I)–$(His)_3$.[78] Moreover, it has been shown that this intermediate, in *Ax*CuNiR, yields a Cu(I)–$(His)_3$ that is catalytically inactive towards nitrite reduction.[79,80]

The fastest aqueous CuNiR small molecule mimic ($[CuMe_2bpa(H_2O)(ClO_4)]^+$, designed by Yamaguchi and Isoda, has catalytic efficiencies inferior to the present peptides.[81] This complex is electron transfer limited in solution and most efficiently undergoes nitrite reduction when physisorbed onto an electrode surface where electron transfer is unlikely to be rate-limiting. This conclusion is reflected in the increase of k_{cat} on the electrode versus off the electrode, 0.063 s^{-1} and 5.3 x 10^{-5} s^{-1}, respectively (Table II-9). Despite these low k_{cat} values of the heterogeneous catalyst, the k_{cat}/K_m of the physisorbed catalyst is comparable to the designed enzymes because of the much lower K_m, a likely result of the unencumbered access of nitrite to the Cu complex. The designed enzymes discussed herein are likely not electron transfer limited under the conditions of the kinetics experiments because the electron transfer between $Cu(II)(Pep)_3$ and ascorbate has been shown to be very fast, and ascorbate is at saturating concentrations.[19] Therefore, even the poorest designed scaffold is comparable to the efficiency of the small molecule in solution which was measured at pH 5.5 where the activity should be significantly enhanced, while the best Cu-TRIW-4'Py L19A at pH 5.9 is a nearly 200 more efficient catalyst. Recently, Ferreira *et al.* synthesized three new tridentate ligands that feature an L-proline attachment point that provides a pyridine, triazole, and pyrrole nitrogen, with pendant groups that are designed to interact with the substrate, similarly to how native CuNiRs exploit secondary coordination sphere residues (Scheme II-2).[75] The catalyst efficiency of the best complex, $Cu[PTP]^{2+}$, approaches 1010.2 M^{-1} s^{-1} in methanol.

From a structural and kinetic perspective, it is surprising that Cu[PTP]$^{2+}$ complex resulted in the highest K_m. The secondary coordination sphere H-bond donor may have been expected to help stabilize the Cu–NO_2 intermediate based the function of the Asp_{CAT} residue in native CuNiR; however, this illustrates the overarching point in this chapter and thesis, that designing native active sites within a non-native scaffold requires an understanding of the factors that tune reactivity within the limits of *that non-native scaffold* as opposed to only fully replicating the primary and secondary coordination sphere of the native enzyme. More to this point, the n-butyl and phenyl pendant groups resulted in inhibition at high substrate concentrations, which has been reported in *AfCu*NiR.[76,82–87] In the TRIW design and the native CuNiR, only one nitrite binds to the Cu(I) resting state. *I will demonstrate this explicitly in Chapter III for the pyridyl active site*. The other possibility is that at high NO_2^- concentrations, nitrite can bind to the Cu(I) catalysts rather than the oxidized Cu(II) complex, which has been reported to result in lower turnover numbers in WT CuNiR where a random-sequential mechanism is thought to operate under high, non-physiology concentrations of NO_2^-.[87] It is important to point out that the primary and secondary coordination sphere modifications made above may act together to enhance the catalytic efficiency via effects that cannot be interpreted using only the steady state parameters above. The alanine mutation likely provides more substrate access to the copper center by reducing the sterics in the substrate cavity above the active site and providing addition space in the primary coordination sphere by relaxing the primary coordination sphere to the preferred 2-coordinate geometry. Moreover, it is clear that the pyridine ligands themselves provide an enhancement through an electronic effect in the catalytic pathway.

Conclusion:

In summary, I have built a novel, unnatural active site made of entirely pyridine ligands within a *de novo* designed protein that creates a type 2 copper center capable of catalyzing NO_2^- reduction faster than any water-soluble CuNiR mimic reported. Compared to the more native active site composed of histidines, pyridine enhances the chemical step preceding substrate binding (k_{cat} values), and the large disparity between substrate binding between 3'Py and 4'Py active sites with and without alanine indicates that the 4'Py complex likely benefited from more than just extra space and flexibility but led to a coordination number shift in the Cu(I) oxidation state. These observations emphasize the role that flexibility plays in the control of the primary coordination sphere when engineering new proteins for enzymatic reactivity. While I have designed the fastest CuNiR mimic yet in water, our construct remains a factor of 10^5 lower in terms of catalytic efficiency than the native enzyme in *Alcaligenes faecalis* NiR (*Af*CuNiR) and 10^3 worse in terms of K_m, possibly reflecting that the native system binds nitrite using the Cu(II) oxidation state while the designed system engenders catalysis with nitrite coordinating to Cu(I).[74] Future designs should focus on exploring strategies to shift the equilibrium of the resting state of our designed system to be at the Cu(II) redox level, a shift that is anticipated to lead to much more efficient substrate binding, lower K_m values, and even greater catalytic efficiencies. Moreover, the installation of a proton accept/donor side chain (*i.e.*, aspartate or glutamate) within the secondary sphere active site could aid in exploring the role of a possible rate limiting proton transfer during the catalytic cycle. The next chapter of this thesis sheds light on the catalytic cycle using both spectroscopy and steady state kinetics to explore substrate binding to reduced form of the enzyme.

References:

(1) Yu, Y.; Lv, X.; Li, J.; Zhou, Q.; Cui, C.; Hosseinzadeh, P.; Mukherjee, A.; Nilges, M. J.; Wang, J.; Lu, Y. Defining the Role of Tyrosine and Rational Tuning of Oxidase Activity by Genetic Incorporation of Unnatural Tyrosine Analogs. *J. Am. Chem. Soc.* **2015**, *137* (14), 4594–4597.

(2) Mills, J. H.; Sheffler, W.; Ener, M. E.; Almhjell, P. J.; Oberdorfer, G.; Pereira, J. H.; Parmeggiani, F.; Sankaran, B.; Zwart, P. H.; Baker, D. Computational Design of a Homotrimeric Metalloprotein with a Trisbipyridyl Core. *Proc. Natl. Acad. Sci. U. S. A.* **2016**, *113* (52), 15012–15017.

(3) Planchestainer, M.; Segaud, N.; Shanmugam, M.; McMaster, J.; Paradisi, F.; Albrecht, M. Carbene in Cupredoxin Protein Scaffolds: Replacement of a Histidine Ligand in the Active Site Substantially Alters Copper Redox Properties. *Angew. Chemie - Int. Ed.* **2018**, *57* (33), 10677–10682.

(4) McAllister, K. A.; Zou, H.; Cochran, F. V; Bender, G. M.; Senes, A.; Fry, H. C.; Nanda, V.; Keenan, P. A.; Lear, J. D.; Saven, J. G.; Therien, M. J.; Blasie, J. K.; DeGrado, W. F. Using α-Helical Coiled-Coils to Design Nanostructured Metalloporphyrin Arrays. *J. Am. Chem. Soc.* **2008**, *130* (36), 11921–11927.

(5) Drienovská, I.; Rioz-Martínez, A.; Draksharapu, A.; Roelfes, G. Novel Artificial Metalloenzymes by in Vivo Incorporation of Metal-Binding Unnatural Amino Acids. *Chem. Sci.* **2015**, *6* (1), 770–776.

(6) Pott, M.; Hayashi, T.; Mori, T.; Mittl, P. R. E.; Green, A. P.; Hilvert, D. A Noncanonical Proximal Heme Ligand Affords an Efficient Peroxidase in a Globin Fold. *J. Am. Chem. Soc.* **2018**, *140* (4), 1535–1543.

(7) Pott, M.; Tinzl, M.; Hayashi, T.; Ota, Y.; Dunkelmann, D.; Mittl, P. R. E.; Hilvert, D. Noncanonical Heme Ligands Steer Carbene Transfer Reactivity in an Artificial Metalloenzyme. *Angew. Chemie - Int. Ed.* **2021**, *60* (27), 15063–15068.

(8) Moore, E. J.; Fasan, R. Effect of Proximal Ligand Substitutions on the Carbene and Nitrene Transferase Activity of Myoglobin. *Tetrahedron* **2019**, *75* (16), 2357–2363.

(9) Koebke, K. J.; Pinter, T. B. J.; Pitts, W. C.; Pecoraro, V. L. Catalysis and Electron Transfer in De Novo Designed Metalloproteins. *Chemical Reviews*. 2022, pp 12046–12109.

(10) Pirro, F.; La Gatta, S.; Arrigoni, F.; Famulari, A.; Maglio, O.; Del Vecchio, P.; Chiesa, M.; De Gioia, L.; Bertini, L.; Chino, M.; Nastri, F.; Lombardi, A. A De Novo-Designed Type 3 Copper Protein Tunes Catechol Substrate Recognition and Reactivity. *Angew. Chemie - Int. Ed.* **2023**, *62* (1), e202211552.

(11) Zastrow, M. L.; Peacock, A. F. A.; Stuckey, J. A.; Pecoraro, V. L. Hydrolytic Catalysis and Structural Stabilization in a Designed Metalloprotein. *Nat. Chem.* **2012**, *4* (2), 118–123.

(12) Mathieu, E.; Tolbert, A. E.; Koebke, K. J.; Tard, C.; Iranzo, O.; Penner-Hahn, J. E.; Policar, C.; Pecoraro, V. Rational De Novo Design of a Cu Metalloenzyme for Superoxide Dismutation. *Chem. - A Eur. J.* **2020**, *26* (1), 249–258.

(13) Klabunde, T.; Eicken, C.; Sacchettini, J. C.; Krebs, B. Crystal Structure of a Plant Catechol Oxidase Containing a Dicopper Center. *Nature Structural Biology*. Nature Publishing Group December 1998, pp 1084–1090.

(14) Iwata, S.; Ostermeier, C.; Ludwig, B.; Michel, H. Structure at 2.8 Å Resolution of Cytochrome c Oxidase from Paracoccus Denitrificans. *Nature* **1995**, *376* (6542), 660–669.

(15) Fusetti, F.; Schröter, K. H.; Steiner, R. A.; Van Noort, P. I.; Pijning, T.; Rozeboom, H. J.;

Kalk, K. H.; Egmond, M. R.; Dijkstra, B. W. Crystal Structure of the Copper-Containing Quercetin 2,3-Dioxygenase from Aspergillus Japonicus. *Structure* **2002**, *10* (2), 259–268.
(16) Guo, J.; Fisher, O. S. Orchestrating Copper Binding: Structure and Variations on the Cupredoxin Fold. *Journal of Biological Inorganic Chemistry*. Springer August 22, 2022, pp 529–540.
(17) Sukumar, N.; Chen, Z. W.; Ferrari, D.; Merli, A.; Rossi, G. L.; Bellamy, H. D.; Chistoserdov, A.; Davidson, V. L.; Mathews, F. S. Crystal Structure of an Electron Transfer Complex between Aromatic Amine Dehydrogenase and Azurin from Alcaligenes Faecalis. *Biochemistry* **2006**, *45* (45), 13500–13510.
(18) Hauck, R. D. Atmospheric Nitrogen. Chemistry, Nitrification, Denitrification, and Their Interrelationships. In *Handbook of Environmental Chemistry*; Springer Verlag, 1984; Vol. 1, pp 105–125.
(19) Tegoni, M.; Yu, F.; Bersellini, M.; Penner-Hahn, J. E.; Pecoraro, V. L. Designing a Functional Type 2 Copper Center That Has Nitrite Reductase Activity within α-Helical Coiled Coils. *Proc. Natl. Acad. Sci. U. S. A.* **2012**, *109* (52), 21234–21239.
(20) Koebke, K. J.; Yu, F.; Salerno, E.; Van Stappen, C.; Tebo, A. G.; Penner-Hahn, J. E.; Pecoraro, V. L. Modifying the Steric Properties in the Second Coordination Sphere of Designed Peptides Leads to Enhancement of Nitrite Reductase Activity. *Angew. Chemie* **2018**, *130* (15), 4018–4021.
(21) Tanokura, M. 1H-NMR Study on the Tautomerism of the Imidazole Ring of Histidine Residues. I. Microscopic PK Values and Molar Ratios of Tautomers in Histidine-Containing Peptides. *Biochim. Biophys. Acta (BBA)/Protein Struct. Mol.* **1983**, *742* (3), 576–585.
(22) Koebke, K. J.; Yu, F.; Van Stappen, C.; Pinter, T. B. J.; Deb, A.; Penner-Hahn, J. E.; Pecoraro, V. L. Methylated Histidines Alter Tautomeric Preferences That Influence the Rates of Cu Nitrite Reductase Catalysis in Designed Peptides. *J. Am. Chem. Soc.* **2019**, *141* (19), 7765–7775.
(23) Mitra, S.; Prakash, D.; Rajabimoghadam, K.; Wawrzak, Z.; Prasad, P.; Wu, T.; Misra, S. K.; Sharp, J. S.; Garcia-Bosch, I.; Chakraborty, S. De Novo Design of a Self-Assembled Artificial Copper Peptide That Activates and Reduces Peroxide. *ACS Catal.* **2021**, *11*, 10267–10278.
(24) Ross, M. R.; White, A. M.; Yu, F.; King, J. T.; Pecoraro, V. L.; Kubarych, K. J. Histidine Orientation Modulates the Structure and Dynamics of a de Novo Metalloenzyme Active Site. *J. Am. Chem. Soc.* **2015**, *137* (32), 10164–10176.
(25) Andon, R. J. L.; Cox, J. D.; Herington, E. F. G. The Ultra-Violet Absorption Spectra and Dissociation Constants of Certain Pyridine Bases in Aqueous Solution. *Trans. Faraday Soc.* **1954**, *50*, 918–927.
(26) Pitts, W. C.; Deb, A.; Penner-Hahn, J. E.; Pecoraro, V. L. Revving up a Designed Copper Nitrite Reductase Using Noncoded Active Site Ligands. *ACS Catal.* **2024**, *14* (6), 4362–4368.
(27) Zuo, Y.; Deng, Y. The Near-UV Absorption Constants for Nitrite Ion in Aqueous Solution. *Chemosphere* **1998**, *36* (1), 181–188.
(28) Wagner, B. A.; Buettner, G. R. Stability of Aqueous Solutions of Ascorbate for Basic Research and for Intravenous Administration. *Adv. Redox Res.* **2023**, *9*, 100077.
(29) Stoll, S.; Schweiger, A. EasySpin, a Comprehensive Software Package for Spectral Simulation and Analysis in EPR. **2005**.

(30) Willker, W.; Leibfritz, D.; Kerssebaum, R.; Bermel, W. Gradient Selection in Inverse Heteronuclear Correlation Spectroscopy. *Magn. Reson. Chem.* **1993**, *31* (3), 287–292.
(31) Harris, R. K.; Becker, E. D.; de Menezes, S. M. C.; Goodfellow, R.; Granger, P. Nuclear Spin Properties and Conventions for Chemical Shifts (IUPAC Recommendations 2001†). *eMagRes* **2007**, *2007* (11), 1795–1818.
(32) Weng, T. C.; Waldo, G. S.; Penner-Hahn, J. E. A Method for Normalization of X-Ray Absorption Spectra. In *Journal of Synchrotron Radiation*; 2005; Vol. 12, pp 506–510.
(33) Ravel, B.; Newville, M. ATHENA, ARTEMIS, HEPHAESTUS: Data Analysis for X-Ray Absorption Spectroscopy Using IFEFFIT. In *Journal of Synchrotron Radiation*; 2005; Vol. 12, pp 537–541.
(34) Royappa, A. T.; Royappa, A. D.; Moral, R. F.; Rheingold, A. L.; Papoular, R. J.; Blum, D. M.; Duong, T. Q.; Stepherson, J. R.; Vu, O. D.; Chen, B.; Suchomel, M. R.; Golen, J. A.; André, G.; Kourkoumelis, N.; Mercer, A. D.; Pekarek, A. M.; Kelly, D. C. Copper(I) Oxalate Complexes: Synthesis, Structures and Surprises. *Polyhedron* **2016**, *119*, 563–574.
(35) Dimakis, N.; Bunker, G. XAFS Debye-Waller Factors for Zn Metalloproteins. *Phys. Rev. B - Condens. Matter Mater. Phys.* **2004**, *70* (19), 1–12.
(36) Stern, E. A. Number of Relevant Independent Points in X-Ray-Absorption Fine-Structure Spectra. *Phys. Rev. B* **1993**, *48* (13), 9825–9827.
(37) Vivian, J. T.; Callis, P. R. Mechanisms of Tryptophan Fluorescence Shifts in Proteins. *Biophys. J.* **2001**, *80* (5), 2093–2109.
(38) Wu, H.; Tian, C.; Zhang, Y.; Yang, C.; Zhang, S.; Jiang, Z. Stereoselective Assembly of Amino Acid-Based Metal-Biomolecule Nanofibers. *Chem. Commun.* **2015**, *51* (29), 6329–6332.
(39) Kitagawa, S.; Munakata, M.; Miyaji, N. New Mixed-Ligand Copper(I) Complexes with 2,2′-Bipyridine and Their NMR Spectra. *Inorg. Chem.* **1982**, *21* (10), 3842–3843.
(40) Maity, S.; Gundampati, R. K.; Kumar, T. K. S. NMR Methods to Characterize Protein-Ligand Interactions. *Natural Product Communications*. Natural Product Incorporation May 1, 2019.
(41) Blackburn, N. J.; Strange, R. W.; Reedijk, J.; Volbeda, A.; Farooq, A.; Zubieta, J.; Karlin, K. D. X-Ray Absorption Edge Spectroscopy of Copper(I) Complexes. Coordination Geometry of Copper(I) in the Reduced Forms of Copper Proteins and Their Derivatives with Carbon Monoxide. *Inorg. Chem.* **1989**, *28* (7), 1349–1357.
(42) Kau, L. shan; Spira-solomon, D. J.; Penner-Hahn, J. E.; Hodgson, K. O.; Solomon, E. I. X-Ray Absorption Edge Determination of the Oxidation State and Coordination Number of Copper: Application to the Type 3 Site in Rhus Vernicifera Laccase and Its Reaction with Oxygen. *J. Am. Chem. Soc.* **1987**, *109* (21), 6433–6442.
(43) Rudolph, J.; Jacob, C. R. Revisiting the Dependence of Cu K-Edge X-Ray Absorption Spectra on Oxidation State and Coordination Environment. *Inorg. Chem.* **2018**, *57* (17), 10591–10607.
(44) Walroth, R. C.; Uebler, J. W. H.; Lancaster, K. M. Probing Cu I in Homogeneous Catalysis Using High-Energy-Resolution Fluorescence-Detected X-Ray Absorption Spectroscopy. *Chem. Commun.* **2015**, *51* (48), 9864–9867.
(45) DiMucci, I. M.; MacMillan, S. N.; Walroth, R. C.; Lancaster, K. M. Scrutinizing "Ligand Bands" via Polarized Single-Crystal X-Ray Absorption Spectra of Copper(I) and Copper(II) Bis-2,2′-Bipyridine Species. *Inorg. Chem.* **2020**, *59* (18), 13416–13426.
(46) Myshkin, A. E.; Konyaeva, V. S.; Gumargalieva, K. Z.; Moiseev, Y. V. Oxidation of

Ascorbic Acid in the Presence of Nitrites. *J. Agric. Food Chem.* **1996**, *44* (10), 2948–2950.
(47) Ruckthong, L.; Peacock, A. F. A.; Pascoe, C. E.; Hemmingsen, L.; Stuckey, J. A.; Pecoraro, V. L. D-Cysteine Ligands Control Metal Geometries within De Novo Designed Three-Stranded Coiled Coils. *Chem. - A Eur. J.* **2017**, *23* (34), 8232–8243.
(48) Offer, G.; Sessions, R. Computer Modelling of the α-Helical Coiled Coil: Packing of Side-Chains in the Inner Core. *J. Mol. Biol.* **1995**, *249* (5), 967–987.
(49) Polizzi, N. F.; Wu, Y.; Lemmin, T.; Maxwell, A. M.; Zhang, S. Q.; Rawson, J.; Beratan, D. N.; Therien, M. J.; DeGrado, W. F. De Novo Design of a Hyperstable Non-Natural Protein-Ligand Complex with Sub-Å Accuracy. *Nat. Chem.* **2017**, *9* (12), 1157–1164.
(50) Zhu, B. -Y; Zhou, M. E.; Kay, C. M.; Hodges, R. S. Packing and Hydrophobicity Effects on Protein Folding and Stability: Effects of B-branched Amino Acids, Valine and Isoleucine, on the Formation and Stability of Two-stranded A-helical Coiled Coils/Leucine Zippers. *Protein Sci.* **1993**, *2* (3), 383–394.
(51) Boyle, A. L.; Rabe, M.; Crone, N. S. A.; Rhys, G. G.; Soler, N.; Voskamp, P.; Pannu, N. S.; Kros, A. Selective Coordination of Three Transition Metal Ions within a Coiled-Coil Peptide Scaffold. *Chem. Sci.* **2019**, *10* (31), 7456–7465.
(52) Bryson, J. W.; Desjarlais, J. R.; Handel, T. M.; DeGrado, W. F. From Coiled Coils to Small Globular Proteins: Design of a Native-like Three-Helix Bundle. *Protein Sci.* **1998**, *7* (6), 1404–1414.
(53) Redfield, C. NMR Studies of Partially Folded Molten-Globule States. *Methods Mol. Biol.* **2004**, *278*, 233–254.
(54) Betz, S. F.; Raleigh, D. P.; DeGrado, W. F.; Lovejoy, B.; Anderson, D.; Ogihara, N.; Eisenberg, D. Crystallization of a Designed Peptide from a Molten Globule Ensemble. *Fold. Des.* **1996**, *1* (1), 57–64.
(55) Prenesti, E.; Daniele, P. G.; Berto, S.; Toso, S. Spectrum-Structure Correlation for Visible Absorption Spectra of Copper(II) Complexes Showing Axial Co-Ordination in Aqueous Solution. *Polyhedron* **2006**, *25* (15), 2815–2823.
(56) Mitra, S.; Prakash, D.; Rajabimoghadam, K.; Wawrzak, Z.; Prasad, P.; Wu, T.; Misra, S. K.; Sharp, J. S.; Garcia-Bosch, I.; Chakraborty, S. De Novo Design of a Self-Assembled Artificial Copper Peptide That Activates and Reduces Peroxide. *ACS Catal.* **2021**, *11*, 10267–10278.
(57) Ferroni, F. M.; Guerrero, S. A.; Rizzi, A. C.; Brondino, C. D. Overexpression, Purification, and Biochemical and Spectroscopic Characterization of Copper-Containing Nitrite Reductase from Sinorhizobium Meliloti 2011. Study of the Interaction of the Catalytic Copper Center with Nitrite and NO. *J. Inorg. Biochem.* **2012**, *114*, 8–14.
(58) Li, F.; Delgado, R.; Costa, J.; Drew, M. G. B.; Félix, V. Ditopic Hexaazamacrocycles Containing Pyridine: Synthesis, Protonation and Complexation Studies. *Dalt. Trans.* **2005**, No. 1, 82–91.
(59) Chen, P.; Bell, J.; Eipper, B. A.; Solomon, E. I. Oxygen Activation by the Noncoupled Binuclear Copper Site in Peptidylglycine α-Hydroxylating Monooxygenase. Spectroscopic Definition of the Resting Sites and the Putative CuIIM-OOH Intermediate. *Biochemistry* **2004**, *43* (19), 5735–5747.
(60) Sant'Ana, A. C.; Alves, W. A.; Santos, R. H. A.; Ferreira, A. M. D.; Temperini, M. L. A. The Adsorption of 2,2′:6′,2″-Terpyridine, 4′-(5-Mercaptopentyl)-2,2′:6′,2″-Terpyridinyl, and Perchlorate on Silver and Copper Surfaces Monitored by SERS. *Polyhedron* **2003**, *22* (13), 1673–1682.

(61) Jeschke, G. Structure Characterization of the Copper(II) Complex of Poly(4-Vinylpyridine) by a Combination of EPR, ENDOR, and Molecular Modeling Techniques. *J. Phys. Chem. B* **2000**, *104* (35), 8382–8390.
(62) Scholl, H. J.; Hüttermann, J. ESR and ENDOR of Cu(II) Complexes with Nitrogen Donors: Probing Parameters for Prosthetic Group Modeling of Superoxide Dismutase. *J. Phys. Chem.* **1992**, *96* (24), 9684–9691.
(63) Yu, F.; Penner-Hahn, J. E.; Pecoraro, V. L. De Novo-Designed Metallopeptides with Type 2 Copper Centers: Modulation of Reduction Potentials and Nitrite Reductase Activities. *J. Am. Chem. Soc.* **2013**, *135* (48), 18096–18107.
(64) Chen, P.; Bell, J.; Eipper, B. A.; Solomon, E. I. Oxygen Activation by the Noncoupled Binuclear Copper Site in Peptidylglycine α-Hydroxylating Monooxygenase. Spectroscopic Definition of the Resting Sites and the Putative CuIIM-OOH Intermediate. *Biochemistry* **2004**, *43* (19), 5735–5747.
(65) Ross, M. O.; MacMillan, F.; Wang, J.; Nisthal, A.; Lawton, T. J.; Olafson, B. D.; Mayo, S. L.; Rosenzweig, A. C.; Hoffman, B. M. Particulate Methane Monooxygenase Contains Only Mononuclear Copper Centers. *Science (80-.).* **2019**, *364* (6440), 566–570.
(66) Solomon, E. I.; Heppner, D. E.; Johnston, E. M.; Ginsbach, J. W.; Cirera, J.; Qayyum, M.; Kieber-Emmons, M. T.; Kjaergaard, C. H.; Hadt, R. G.; Tian, L. Copper Active Sites in Biology. *Chem. Rev.* **2014**, *114* (7), 3659–3853.
(67) Lukens, J. T.; DiMucci, I. M.; Kurogi, T.; Mindiola, D. J.; Lancaster, K. M. Scrutinizing Metal–Ligand Covalency and Redox Non-Innocence via Nitrogen K-Edge X-Ray Absorption Spectroscopy. *Chem. Sci.* **2019**, *10* (19), 5044–5055.
(68) Blackburn, N. J.; Hasnain, S. S.; Knowles, P. F. EXAFS Studies of Non-Blue Copper Proteins: Superoxide Dimutase, Dopamine-Monooxygenase and Monoamine Oxidase; Springer, Berlin, Heidelberg, 1984; pp 124–129.
(69) Habiyakare, A.; Lucken, E. A. C.; Bernardinelli, G. Nuclear Quadrupole Resonance and Crystallographic Studies of Three-Co-Ordinated Copper(I) Cations with Alkylpyridine Ligands. *J. Chem. Soc. Dalt. Trans.* **1992**, No. 17, 2591–2599.
(70) Engelhardt, L. M.; Pakawatchai, C.; White, A. H.; Healy, P. C. Lewis-Base Adducts of Group 1B Metal(I) Compounds. Part 12. Structural Studies of Some Bis(Methyl-Substituted Pyridine)-Copper(I) and -Silver(I) Nitrates and Perchlorates. *J. Chem. Soc. Dalt. Trans.* **1985**, No. 1, 117–123.
(71) Habiyakare, A.; Lucken, E. A. C.; Bernardinelli, G. Crystallographic and Copper-63,65 Nuclear Quadrupole Resonance Study of Two-Co-Ordinated Copper(I) Cations with Hindered Substituted Pyridine Ligands. *J. Chem. Soc. Dalt. Trans.* **1991**, No. 9, 2269–2273.
(72) Allen, J. J.; Hamilton, C. E.; Barron, A. R. Molecular Structures of RN(H)Py (R = 2,4,6-Me3C 6H2, 2,6-Et2C6H3, Ph 3C), and the Copper Complex [Cu{(2,4,6-Me3C 6H2)N(H)Py}2]BF4. *J. Chem. Crystallogr.* **2009**, *39* (8), 573–580.
(73) Dooley, D. M.; Scott, R. A.; Knowles, P. F.; Colangelo, C. M.; McGuirl, M. A.; Brown, D. E. Structures of the Cu(I) and Cu(II) Forms of Amine Oxidases from X-Ray Absorption Spectroscopy. *J. Am. Chem. Soc.* **1998**, *120* (11), 2599–2605.
(74) Tocheva, E. I.; Eltis, L. D.; Murphy, M. E. P. Conserved Active Site Residues Limit Inhibition of a Copper-Containing Nitrite Reductase by Small Molecules. *Biochemistry* **2008**, *47* (15), 4452–4460.
(75) Ferreira, M. P.; Castro, C. B.; Honorato, J.; He, S.; Gonçalves Guimarães Júnior, W.; Esmieu, C.; Castellano, E. E.; de Moura, A. F.; Truzzi, D. R.; Nascimento, O. R.;

Simonneau, A.; Marques Netto, C. G. C. Biomimetic Catalysis of Nitrite Reductase Enzyme Using Copper Complexes in Chemical and Electrochemical Reduction of Nitrite. *Dalt. Trans.* **2023**, *52* (32), 11254–11264.

(76) Boulanger, M. J.; Murphy, M. E. P. Directing the Mode of Nitrite Binding to a Copper-containing Nitrite Reductase from Alcaligenes Faecalis S-6: Characterization of an Active Site Isoleucine. *Protein Sci.* **2003**, *12* (2), 248–256.

(77) Park, C. Visual Interpretation of the Meaning of Kcat/ KMin Enzyme Kinetics. *J. Chem. Educ.* **2022**, *99* (7), 2556–2562.

(78) Murphy, M. E. P.; Turley, S.; Adman, E. T. Structure of Nitrite Bound to Copper-Containing Nitrite Reductase from Alcaligenes Faecalis: Mechanistic Implications. *J. Biol. Chem.* **1997**, *272* (45), 28455–28460.

(79) Strange, R. W.; Murphy, L. M.; Dodd, F. E.; Abraham, Z. H. L.; Eady, R. R.; Smith, B. E.; Hasnain, S. S. Structural and Kinetic Evidence for an Ordered Mechanism of Copper Nitrite Reductase. *J. Mol. Biol.* **1999**, *287* (5), 1001–1009.

(80) Krzemiński, Ł.; Ndamba, L.; Canters, G. W.; Aartsma, T. J.; Evans, S. D.; Jeuken, L. J. C. Spectroelectrochemical Investigation of Intramolecular and Interfacial Electron-Transfer Rates Reveals Differences between Nitrite Reductase at Rest and during Turnover. *J. Am. Chem. Soc.* **2011**, *133* (38), 15085–15093.

(81) Isoda, N.; Yokoyama, H.; Nojiri, M.; Suzuki, S.; Yamaguchi, K. Electroreduction of Nitrite to Nitrogen Oxide by a Copper-Containing Nitrite Reductase Model Complex Incorporated into Collagen Film. *Bioelectrochemistry* **2010**, *77* (2), 82–88.

(82) Adman, E. T.; Godden, J. W.; Turley, S. The Structure of Copper-Nitrite Reductase from Achromobacter Cycloclastes at Five PH Values, with NO2- Bound and with Type II Copper Depleted. *J. Biol. Chem.* **1995**, *270* (46), 27458–27474.

(83) Dodd, F. E.; Hasnain, S. S.; Abraham, Z. H. L.; Eady, R. R.; Smith, B. E. Structures of a Blue-Copper Nitrite Reductase and Its Substrate-Bound Complex. *Acta Crystallogr. Sect. D Biol. Crystallogr.* **1997**, *53* (4), 406–418.

(84) Dodd, F. E.; Van Beeumen, J.; Eady, R. R.; Hasnain, S. S. X-Ray Structure of a Blue-Copper Nitrite Reductase in Two Crystal Forms. The Nature of the Copper Sites, Mode of Substrate Binding and Recognition by Redox Partner. *J. Mol. Biol.* **1998**, *282* (2), 369–382.

(85) Tocheva, E. I.; Rosell, F. I.; Mauk, A. G.; Murphy, M. E. P. Side-On Copper-Nitrosyl Coordination by Nitrite Reductase. *Science (80-.).* **2004**, *304* (5672), 867–870.

(86) Antonyuk, S. V.; Strange, R. W.; Sawers, G.; Eady, R. R.; Hasnain, S. S. Atomic Resolution Structures of Resting-State, Substrate- and Product-Complexed Cu-Nitrite Reductase Provide Insight into Catalytic Mechanism. *Proc. Natl. Acad. Sci. U. S. A.* **2005**, *102* (34), 12041–12046.

(87) Wijma, H. J.; Jeuken, L. J. C.; Verbeet, M. P.; Armstrong, F. A.; Canters, G. W. A Random-Sequential Mechanism for Nitrite Binding and Active Site Reduction in Copper-Containing Nitrite Reductase. *J. Biol. Chem.* **2006**, *281* (24), 16340–16346.

Chapter III

Exploring Nitrite Binding at Both the Oxidized and Reduced Enzyme Form in *de novo* Designed CuNiRs.

Introduction:

As seen in the previous chapter, steady-state kinetics and Michaelis-Menten analysis allow for the investigation of enzymes and the assessment of the effects of mutations on the catalytic mechanism. Moreover, steady-state kinetics allow one to deduce the kinetic mechanisms of complex multi-substrate enzymes and study inhibitor effects by hiding the complexity of individual rate constants and equilibrium constants in steady-state kinetic parameters. However, by doing so, it becomes difficult to discern chemical complexity, which is more appropriately investigated using transient kinetics or a combination of both.[1,2] For the purpose of this chapter's aims, inhibition kinetics under conditions favoring binding to the reduced enzyme form will be used to aid in exploring substrate binding to the reduced copper center during catalytic turnover at 2- and 3-coordinate Cu(I) geometries designed in Chapter II.

Inhibitors are classified as i) *competitive* if only a slope-dependence is observed in the reciprocal plot; ii) *uncompetitive* if only a $1/v$–axis intercept-dependence is observed in the reciprocal plot; iii) *mixed* inhibitors if both are affected as the inhibitor is introduced to the enzyme and iv) *noncompetitive* is a species case of mixed inhibition where the K_d's values for both E/ES and E/EI are the same (Figure III-1).[3–5] The slope of the reciprocal plot will vary if changing the inhibitor concentration changes the ability to capture the varied substrate, establishing that there is a reversible step(s) connecting the substrate and inhibitor. If there is a change, the intercept of the reciprocal plots will vary if the inhibitor and substrate bind to different enzyme forms. These patterns allow for the exploration of the mechanisms of a metalloenzyme using small inhibitors that report on the equilibrium between enzyme forms. At the mechanistic level, substrate binding

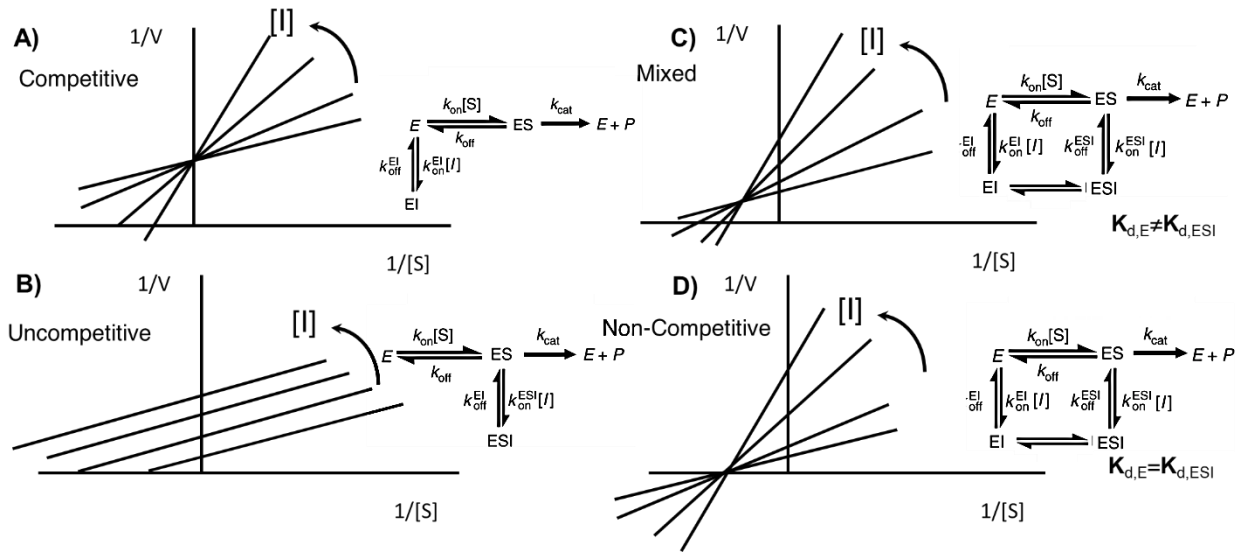


Figure III-1: Inhibition patterns and reaction schemes: **A)** Competitive inhibition, **B)** Uncompetitive inhibition, **C)** Mixed inhibition, and **D)** Non-Competitive inhibition.

to specific oxidation states is both a consequence of differences in the discrete protein structure between oxidized and reduced forms and built-in gate-keeping events (*e.g.*, negative design) that prevent the binding events leading to deactivated forms of the enzyme.[6,7] As previously covered in the introduction of this thesis, the second coordination sphere residues of CuNiR have not only evolved to transfer protons to the substate (*i.e.*, Asp_{CAT} and His_{CAT}) and orient the substate in the proper coordination mode, but Ile_{CAT} and Asp_{CAT} have been implicated in preventing exogenous anions from binding to the T2Cu. This has be suspected to cause inappropriate enzymes forms that inhibit nitrite reduction.[8,9] Small-molecule inhibitors highlight how crucial the protein environment is for tuning the T2Cu site in CuNiR toward selectively binding and orientating the nitrite during the catalytic cycle. Small molecules such as azide, formate, acetate, and nitrate have been observed to inhibit the dithionite-dependent reduction of nitrite in native *Af*CuNiR with mixed inhibition observed for acetate and formate while nitrate uncompetitively inhibits *Af*CuNiR at pH 6.5.[8] The competitive component of the mixed inhibition is explained by the formation of an acetate or formate adduct to the $T2Cu_{ox}$ site which competes with the substrate for the $T2Cu_{ox}$ center. Their respective crystal structures indicated one additional binding partner at the entry channel of the $T2Cu_{ox}$ center, which is consistent with the uncompetitive component of the mixed

inhibition observed. Significantly, the only anion that exhibited a competitive inhibition pattern against nitrite was azide. T1Cu_{red}-T2Cu_{ox} azide-soaked crystals demonstrated that azide binds to the T2Cu_{ox} centers in both *Af*CuNiR and *Ax*CuNiR in an *N*-monodentate mode, closely resembling the azide-T2Cu_{ox} adduct in Bovine Cu,Zn-SOD where it functions as a binding analog of dioxygen.[10,11] All of these observations point to nitrite binding to at least the T2Cu_{ox} form. Nitrite binding to the T2Cu_{red} form cannot be ruled out as that would have required the authors to show azide binding to the T2Cu_{red} form in the absence of nitrite to be able to affect the 1/V vs. [NO_2^-] plot at different concentrations of azide. Unsurprisingly, *Af*CuNiR had a greater specificity for the natural substrate (K_m=150 μM) than azide (K_i=2.0 mM).[12] While there are many polyatomic anions that bind to T2Cu_{ox} centers, monoatomic anions (*e.g.*, halides) would be expected to bind to histidine-containing copper centers in general, considering azide is a pseudohalide. In the context of metalloproteins, Cl^- has been observed binding to the T2C_{ox} and T2Cu_{red} in Cu,ZnSOD and the T2Cu_{ox} form in CuNiR.[11,13,14] A large amount of work has been dedicated to Cl^- binding to the T2Cu_{ox} center in LPMOs, where it is considered a binding analog of O_2 in the equatorial plane of the square pyramidal Cu-site and may be required for the oxidized enzyme to bind the amino nitrogen during a maturation step.[15–17] In the context of copper enzymes, halide inhibition has been extensively studied in tyrosinase where halides show competitive inhibition in the conversion of L-DOPA when it binds to the oxidized enzyme (*i.e.*, F^- and Cl^-) and non-competitive inhibition (*i.e.*, Br^- and I^-) when binding is occurs at the reduced enzyme.[18] These examples demonstrate the importance of exogenous ligands binding to Cu-sites and their use in understanding particular steps in the mechanism of metalloenzymes.

In Chapter II, modifications to both the primiary (*i.e.*, the orientation of 3'Pyridine and 4'Pyridine) and the secondary coordination spheres (*i.e.*, the layer above the metal binding site) were found to increase the k_{cat}/K_m. This trend was closely associated with the K_m and the coordination number of the Cu(I) oxidation state. Moreover, it has been previously shown that NO_2^- influences the EPR spectrum of the designed Cu(II)His_3 site in Cu(II)-TRIW-H,

demonstrating substrate binding to the oxidized form of the enzyme.[19] However, it has been challenging to demonstrate nitrite binding to the reduced form in both native CuNiRs and designed protein mimics because the reactivity of the Cu(I)-NO_2^- complex in the presence of a proton source (*i.e.*, water) requires ultra-fast freezing methods to isolate and structurally characterize such an intermediate.[20,21] Therefore, to demonstrate that Cu(I) is a catalytically relevant binding state, additional kinetic experiments are required. Herein, I demonstrate NO_2^- binding to the oxidized form of the enzyme under non-catalytic conditions, and I will describe a series of experiments that allow for the invesigation of substrate binding at the reduced enzyme during the catalytic cycle.

Materials and Methods:

General Methods:

Most reagents were purchased from Sigma-Aldrich and Fisher Scientific and used as supplied, unless otherwise indicated. All samples containing Cu(I) were prepared in a $N_{2(g)}$ glove box <1.5ppm O_2. Both Fmoc-3-(3'-pyridyl)-L-alanine and Fmoc-3-(4'-pyridyl)-L-alanine were purchased from Chem-Impex International, Inc. or Aapptec and used without any further purification. Metal concentration was determined by inductively coupled plasma (ICP) mass spectrometry using a 1000 ppm Cu standard. Concentrations of sodium nitrite and sodium ascorbate were determined by UV-VIS at 360 nm (ε =21.88 M^{-1} cm^{-1})[22] and 251 nm (ε=8250 M^{-1} cm^{-1} at pH 5.9)[23], respectively.

Synthesis and purification of peptides:

Peptides were synthesized using standard Fmoc chemistry solid phase peptide synthesis on a Rink Amide Methylbenzhydrylamine (MBHA) resin with a Biotage Initiator+Alstra microwave synthesizer following previously reported procedures.[24] The crude peptide was simultaneously cleaved and deprotected using a cleavage cocktail consisting of trifluoroacetic acid (TFA), ethanedithiol, anisole, and thioanisole (90:3:2:5). The peptide was precipitated with cold diethyl ether, recovered by vacuum filtration, dissolved in 50% acetonitrile in double distilled H_2O

(ddH_2O) and lyophilized to dryness. The lyophilized crude product was then redissolved in 10% acetic acid in ddH_2O and loaded onto a 300 mm x 50 mm DeltaPAK preparative C18 column using a Waters 600 HPLC system with the following parameters: flow rate: 20 mL/min, solvent A: 0.1% TFA in water, solvent B: 0.1% TFA in (90:10) CH3CN:H2O, linear gradient: 100:0 (A:B) increasing to 20:80 over 50 minutes and fractions containing pure peptide were combined and lyophilized to yield pure, white powder. The powder was redissolved in ddH_2O and lyophilized once again to remove any remaining acetonitrile after HPLC purification (confirmed by ^{1}H NMR). The dried peptide was stored at 0°C until use. Purity and identity of the samples were confirmed using an Agilent Q-TOF ESI-MS operated in positive ion mode.

Spectroscopy:

UV visible absorption data were collected with a Cary 100 spectrophotometer at room temperature in 10 mm quartz cuvettes. Electron paramagnetic resonance spectral data were collected using a Bruker EMXE 200 EPR spectrometer on solutions containing 1.5 mM peptide, 1 mM $CuSO_4$, 30% glycerol, and 50 mM MES at pH 5.9. The EPR spectra were processed using the *MATLAB* ver. R2020b and EasySpin.[25] Simulations were also performed using EasySpin to determine the $g_{\parallel}$, $g_{\perp}$, $A_{\parallel}$, and $A_{\perp}$ values.

EPR and UV-VIS spectra at pH 5.9:

Nitrite and chloride X-Band EPR samples were prepared at a concentration of 1 mM $CuSO_4$ and 1.5 mM Trimer, in 50 mM MES Buffer (pH 5.9) and 30% glycerol (v/v). Each sample was pH-checked before transferring them to the EPR tube. The NaCl solid was dried at 70^{o}C under high vac (<50 mtor) overnight to remove excess water which ensured the proper weight was collected.

Cu(I) X-ray absorption spectroscopy (XANES/EXAFS):

Samples with final concentrations of 1 mM $CuSO_4$, 1.5 mM 3SCC , 50 mM MES, and 50% glycerol (as a glassing agent) were prepared, pH adjusted, loaded into an XAS sample cell, and frozen in liquid nitrogen for transport and analysis. *Although multiple attempts to collect XAS on the Cu(II) forms were made, the enzymes underwent photo-reduction during collection and are not included in this chapter.* Sub-stoichiometric concentrations of metal were used to ensure limited amounts of non-peptide associated metal. All XAS measurements were performed at Stanford Synchrotron Radiation Lightsource (SSRL) Beam line 9-3. A Si(220) double crystal monochromator was utilized, with a flat Rh-coated vertically collimating harmonic rejection monochromator. The X-ray energy was calibrated by collecting the absorption spectrum of a reference metal foil, placed between two ionization chambers situated behind the sample, at the same time as the fluorescence data were collected, with the first inflection point of the foil assigned as 8980.3 eV for Cu. The samples were maintained at a temperature of ~7-10 K during data acquisition using a liquid helium cryostat, and the data were measured in fluorescence mode with a 100-element energy resolving Ge detector. The data were collected using 0.25 eV steps in the XANES region (1 sec. integration time), and 0.05 $Å^{-1}$ increments for the extended X-ray absorption fine structure (EXAFS) region up to k=15 $Å^{-1}$, with an integration time of 1-20 s in the EXAFS region. The maximum incident count rate for the channel with the highest counts was kept below 10,000 to avoid detector saturation. XANES data were normalized with Athena[26] and processed with a threshold energy of E_0 8990 eV for Cu and the background was removed using a 3-region cubic spline. The EXAFS data were analyzed using Artemis[27], and the Cu-Pyridine EXAFS model was derived from a single Cu-Pyridine unit from the crystal structure of a tetrakis(pyridine)-copper(I) oxalate complex reported by Royappa *et al.*[28] The Cu–N_{Py} bond distance was modified to 1.95 Å and one chloride atoms was added at a Cu(I) –Cl distance of 2.30 Å before generating the scattering paths by FeFF 6 lite in Artemis. The models were fit with ΔE fixed to $\Delta E_0 = -5$ eV which was determined by aligning the Feff6 theoretical k^3-space for the Cu-Pyridine unit with the experimental k^3-space in Athena, which resulted in a relative –5 eV. The Debye-Waller factors

(DW-Factors) were estimated from the Zn-Histidine paths reported by Bunker *et al*. and fitted by freely floating the Cu–N_{Py} Debye-Waller factors and linking the remaining paths to the Cu–N_{Py} DW-factor and scaling by the ratio of change of the Cu–N_{Py}.[29] While traditionally the F-Factor has been used as a metric for relative fits, I have attempted to produce a better quantity that reflects a more normalized approach across the different ranges of *k*-space that were used to fit the Cu(I) peptides by to take into account changes in the number of fitting variables associated with additional coordination shells in some designs, and changes in the range of k^3-space in subsequent chapters. In Eq. III-1, $x_i^{measured}$ equals the measured i^{th} data point value in *k*-space and x_i^{model} equals the i^{th} theoretical point of the fitted model and is summed over 3-13.1 $Å^{-1}$ k^3-space. The N_{idp} represents an upper bound number of independent parameters that can be extracted for a given data range in the EXAFS and is given in Eq. II-4 from Stern *et al*.[30] N_{fit} is the number of data points that composed the fitting range and N_{vary} is the number of parameters varied during the fitting process. Below, the experimental data is presented in the normalized E-space (XANES and EXAFS regions), *k*-space (weighted by k^3), and the Fourier Transform of k^3-space along with the appropriate fits are overlayed with their experimental data.

$$< x^2 f >= \frac{\frac{N_{idp}}{N_{fit}} \sum_i k_i^3 \left[\chi(k)_i^{measured} - \chi(k)_i^{model}\right]^2}{N_{idp} - N_{Vary}} \quad \text{Eq. III-1}$$

$$N_{idp} \approx \frac{2\Delta k \Delta R}{\pi} \quad \text{Eq. III-2}$$

CuNiR Inhibition Kinetics:

Background corrected CuNiR activity was measured by monitoring ascorbate oxidation at 251 nm via UV-Visible spectroscopy using previously published procedures with $CuSO_4$ as the copper salt.[31] Pseudo-first order rate constants were determined in solutions containing 50 mM sodium phosphate buffer, 30 mM sodium nitrite and 1.5 mM ascorbate. The enzyme concentration was varied at pH 5.9 while maintaining an 8:1 3SCC:Cu(II) ratio to ensure that the Cu(II)/Cu(I) was completely bound to the 3SCC. The background reactions were determined at each enzyme concentration containing 50 mM sodium phosphate buffer, 1.5 mM ascorbate, and 30 mM $NaNO_2$ with 7 eqv. apo-3SCC. Steady-state kinetics were conducted by varying the $NaNO_2$ concentration over a range of 50-600 mM with 1 μM of Cu(II)-3SCC and 8μM apo-3SCC and the steady state background reaction was treated at each substrate concentration with 50 mM sodium phosphate buffer, 1.5 mM ascorbate, and 7 eqv. apo-3SCC. This was repeated for each Cl^- concentration between 0 mM to 100 mM to derive the K_i value by using Eq. III-3. These experiments were conducted in at least triplicates.

Detemintion of K_i using v_{obs}/E_t vs. NO_2^- plots at different chloride concentrations:

$$\frac{v_{obs}}{E_T} = \frac{(k_{cat} \times [NO_2^-])}{\left(K_m \times \left(1 + \frac{[I]}{K_i}\right) + [NO_2^-]\right)} \quad \text{Eq. III-3}$$

Detemintion of pure vs. partial competitive inhibition:

$$\frac{v_{obs}}{E_T} = \frac{(k_{cat} \times [NO_2^-])}{\left(K_m \times \left(\frac{\left(1 + \frac{[I]}{K_i}\right)}{\left(1 + \frac{[I]}{\alpha K_i}\right)}\right) + [NO_2^-]\right)} \quad \text{Eq. III-4}$$

Results:

Contributions to this chapter:

I would like to thank Dr. Aniruddha Deb for helping with the collection of the XAS data at beamline 9-3 at Stanford Synchrotron Radiation Lightsource (SSRL).

X-Ray Absorption Spectroscopy of Cu(I)-Cl adducts:

Table III-1: Summary of each Cu(I)-Cl adduct's fits at pH 5.9: $\Delta E_0 = -5$ eV was used throughout each fit with $E_0 = 8990$ eV

Enzyme	Best Model	Cu(I)-N	Cu(I)-N $\sigma^2 \times 10^{-3}$	Cu(I)-Cl	Cu(I)-Cl $\sigma^2 \times 10^{-3}$	Bond Valence Sum	$\langle \chi^2 f \rangle \times 10^{-4}$
TRIW-4'Py	$CuPy_1Cl$	1.97 Å	1.81 Å^2	2.23 Å	4.71 Å^2	0.73	17
	$CuPy_2Cl$	**1.98 Å**	**4.87 Å^2**	**2.24 Å**	**5.09 Å^2**	1.03	18
	$CuPy_3Cl$	1.98 Å	8.02 Å^2	2.24 Å	5.99 Å^2	1.23	28
TRIW-4'Py L19A	$CuPy_1Cl$	1.97 Å	1.91 Å^2	2.26 Å	6.82 Å^2	0.70	17
	$CuPy_2Cl$	1.97 Å	4.82 Å^2	2.27 Å	6.38 Å^2	1.02	30
	$CuPy_3Cl$	1.98 Å	7.86 Å^2	2.28 Å	6.61 Å^2	1.20	48
TRIW-3'Py	$CuPy_1Cl$	1.96 Å	1.15 Å^2	2.25 Å	5.36 Å^2	0.72	17
	$CuPy_2Cl$	**1.96 Å**	**4.11 Å^2**	**2.26 Å**	**4.95 Å^2**	1.05	22
	$CuPy_3Cl$	1.97 Å	7.03 Å^2	2.27 Å	5.20 Å^2	1.23	38
TRIW-3'Py L19A	$CuPy_1Cl$	1.96 Å	1.31 Å^2	2.25 Å	7.68 Å^2	0.72	16
	$CuPy_2Cl$	**1.96 Å**	**4.50 Å^2**	**2.26 Å**	**7.54 Å^2**	1.05	19
	$CuPy_3Cl$	1.97 Å	7.56 Å^2	2.27 Å	8.18 Å^2	1.23	32

Upon incubation of 400mM NaCl, the EXAFS of each of the enzymes in Chapter II showed an intense peak in the Fourier Transform at ~2.3 Å, and this peak was reasonably accounted for by adding a chloride ligand to the pyridine-model used in Chapter II (Figure III-2–Figure III-6). The addition of oxygen atoms, as opposed to chloride, resulted in large unphysical DW-Factors.[18] With the sequential addition of pyridine ligands to the model, the Cu(I)–N_{Py} distances increased by 0.01 Å (Table III-1). Overall, the Cu(I)–N_{Py} distances are in the range of those reported in Chapter II, ranging from 1.94-1.97 Å and were not perturbed by the addition of a primary coordination sphere

chloride ligand. The Cu(I)–Cl distances of the best fits (~2.25 Å) are in the range of those typically found within Cu(I)–Cl complexes with DW-Factors ranging from 5.0-7.8×10^{-3}Å^2. The static disorder in the chloride ligand for the L19A designs was slightly higher than that of the leucine, as seen in the DW-Factors (Table III-1). The addition of three pyridine ligands did not result in a better fit and the best-fit structures agreed with the bond distances expected from Cu(I)-Cl model complexes. Valance bond sum analysis ensured agreement between the oxidation state of the Cu(I) and the relative coordination number and bond distances (Table III-1).[32,33] It should be noted that the fit values (<$\chi^2 f$>) for the chloride adducts of both Cu(I) TRIW-3'Py and Cu(I) TRIW-4'Py L19A favored a 2-coordinate $CuPy_1Cl$ over the 3- or 4-coordiate structure. While a linear structure is possible, the Cu(I)-N_{Py}/Cu(I)-Cl bond distances and the valence bond sum analysis tend to support a predominantly 3-coordinate complex, and the lower <$\chi^2 f$> values for the $CuPy_1Cl$ centers likely reflects the tendency to for the weighted fitting to over emphasize the amplified noise in the k^3 weighted *k*-space (Table III-1).[34–37]

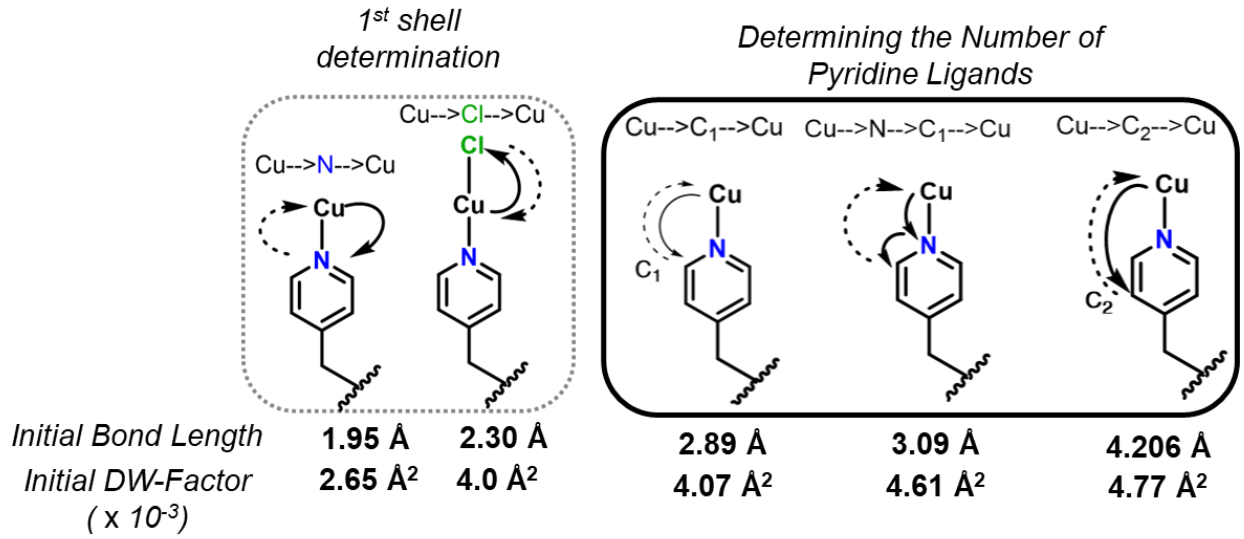


Figure III-2: Simple scheme highlighting the scattering paths, and their associated initial parameters used to fit k^3-space .

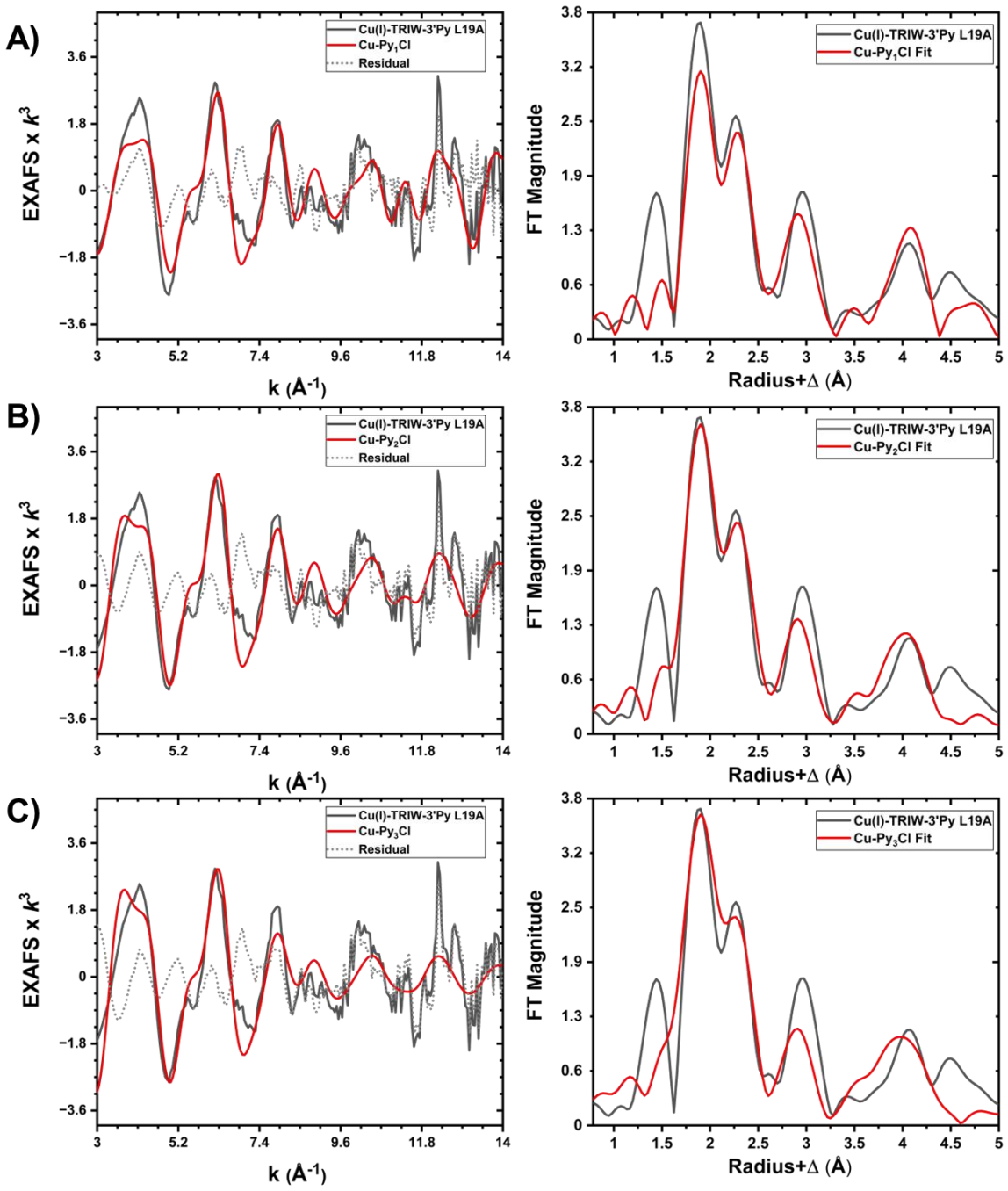


Figure III-3: *k*-space weighted by k^3 (*left*) and associated Fourier Transform (*right*) of Cu(I)-TRIW-3'Py L19A (400 mM NaCl) fits: **A)** $CuPy_1Cl$, **B)** $CuPy_2Cl$, and **C)** $CuPy_3Cl$.

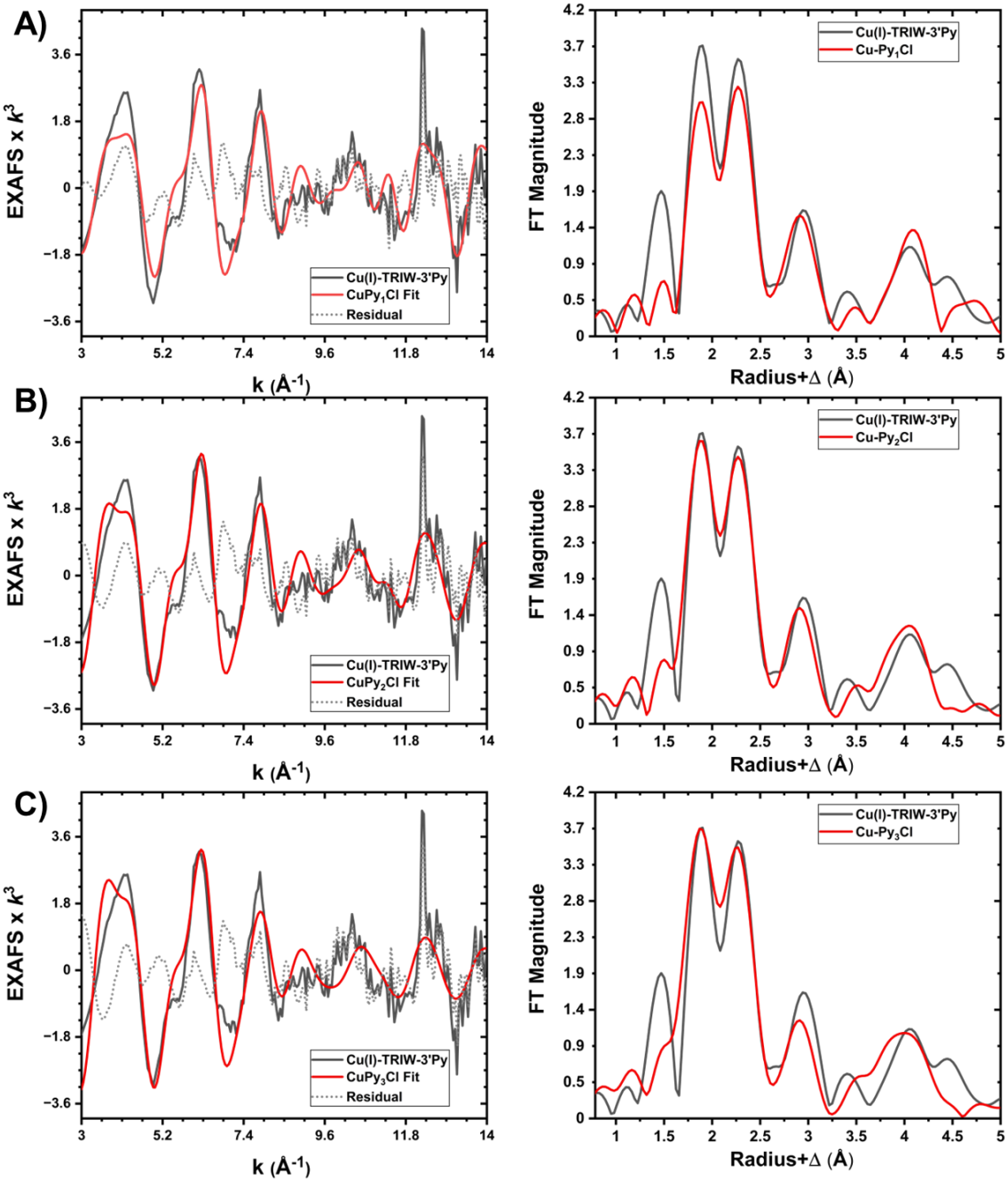


Figure III-4: *k*-space weighted by k^3 (*left*) and associated Fourier Transform (*right*) of Cu(I)-TRIW-3'Py (400 mM NaCl) fits: **A)** $CuPy_1Cl$ **B)** $CuPy_2Cl$ **C)** $CuPy_3Cl$.

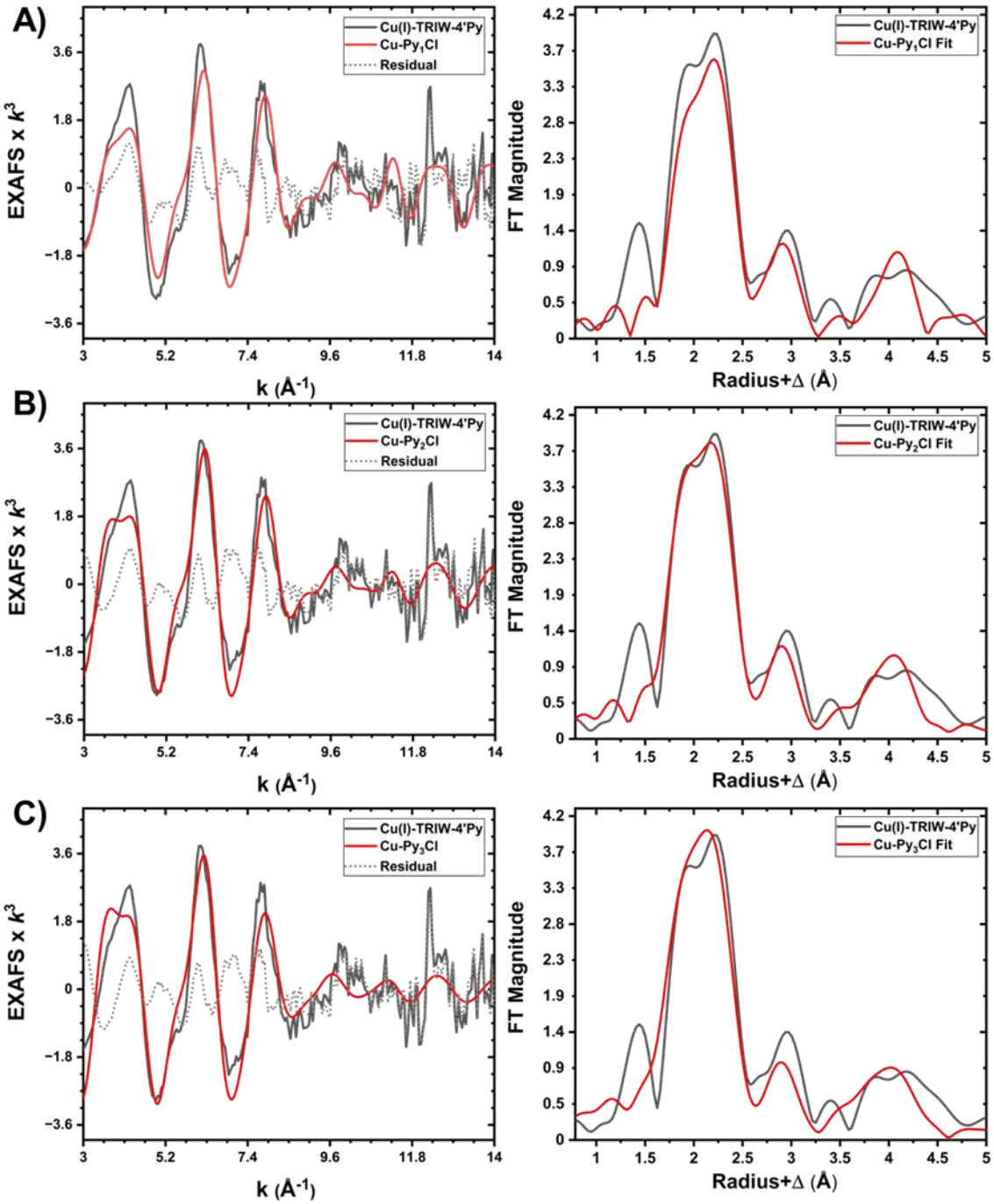


Figure III-5: *k*-space weighted by k^3 (*left*) and associated Fourier Transform (*right*) of Cu(I)-TRIW-4'Py (400 mM NaCl) fits:**A)** $CuPy_1Cl$, **B)** $CuPy_2Cl$, and **C)** $CuPy_3Cl$.

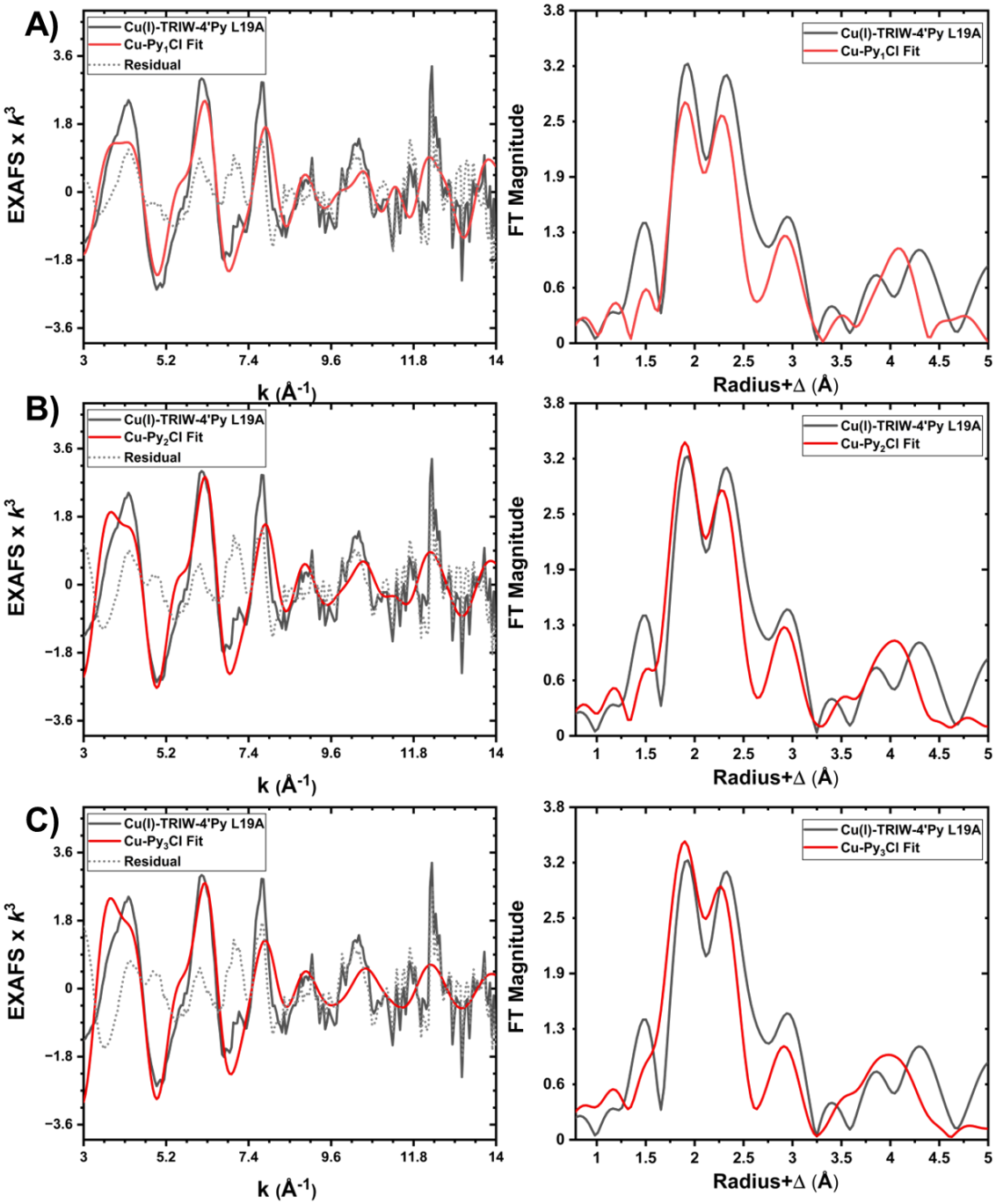


Figure III-6: *k*-space weighted by k^3 (*left*) and associated Fourier Transform (*right*) of Cu(I)-TRIW-4'Py L19A (400 mM NaCl) modeled by **A)** $CuPy_1Cl$, **B)** $CuPy_2Cl$, and **C)** $CuPy_3Cl$.

The XANES spectra of each chloride adduct featured pre-edge peaks between ~ 8983-8984 eV, consistent with reported Cu(I) complexes bearing transitions arising predominately from Cu 1s–4p transitions (Figure III-7, Figure III-8).[38] The normalized intensities of the dominate pre-edge transition (ca. 8983-8984 eV) are slightly increased and sharper in the chloro-adducts compared the chloride free forms and are more 3- or slightly pseudo 4-coordinate than a pure 2-coordinate structure. As discussed in Chapter II, the pre-edge is split into a doublet pattern between 8980-8984 eV in their respective derivative spectrum which constitutes a weak shoulder at ~8981-8982 eV and main pre-edge feature at 8983-8984 eV.[39,40] Admittedly, the formation of a 2-coordinate complex ($CuPy_1Cl$) cannot be completely ruled out from the EXAFS alone as the chloride adducts of both Cu(I)-TRIW-3'Py and Cu(I)-TRIW-4'Py L19A have a slightly better fitting parameter ($<\chi^2 f>$) for a $CuPy_1Cl$ type structure (Table III-1). However, all the pre-edge transition associated with the chloro-adducts (*i.e.*, large dip in derivative spectra at ~8983-8984 eV), with the exception of Cu(I) TRIW-4'Py L19A, are slightly shifted to lower energies compared the chloride free samples which suggest the chloro-adducts are likely more 3-coordinate rather than 2- or 4-coordinate.[38,41] I should stress that any interpretation of absorption edge features must be tentative due to the impact of scattering and modified covalency of the complexes, and therefore a holistic approach is used.

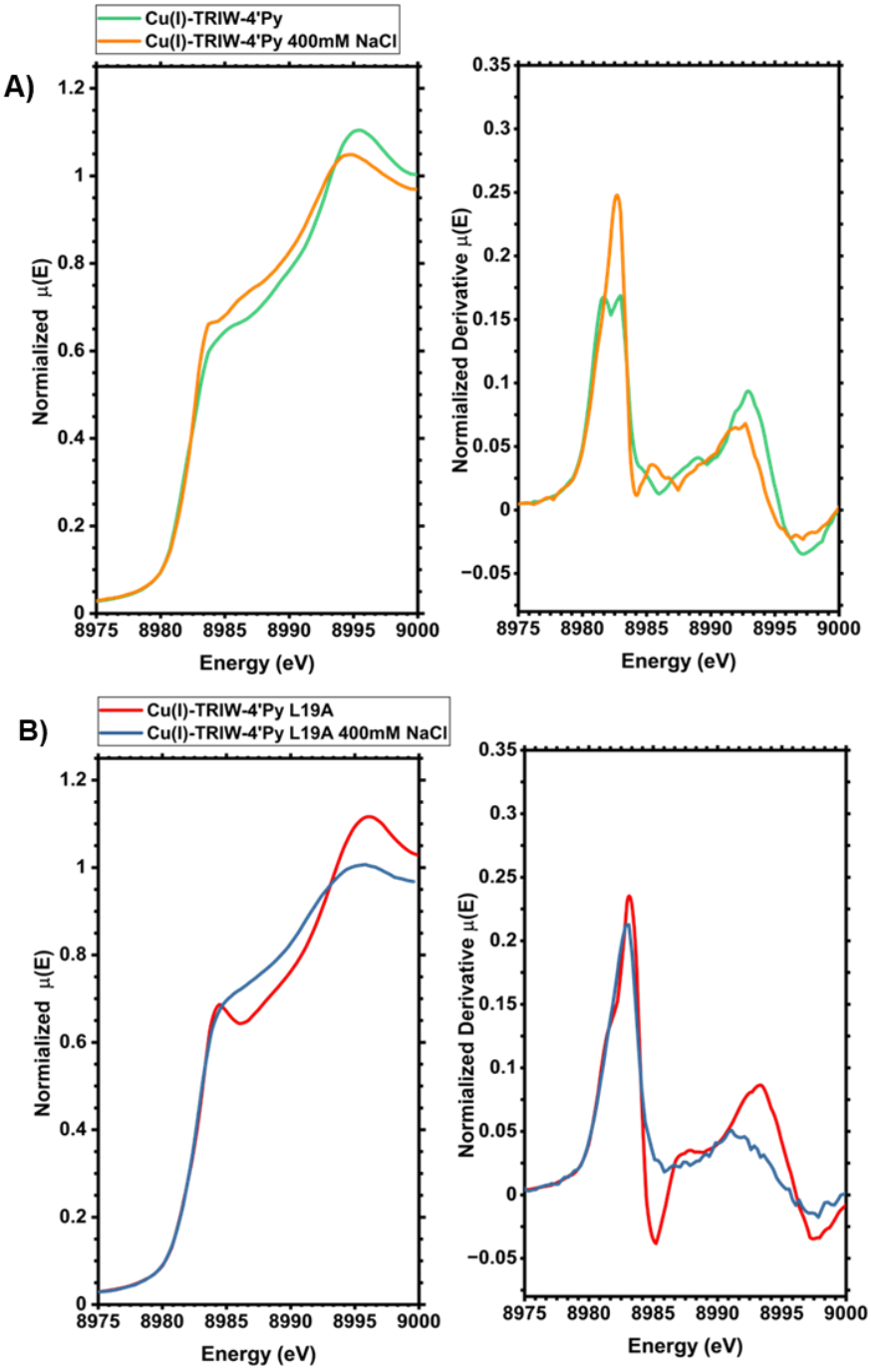


Figure III-7: XANES (derivative, *right*) comparison between the reduced enzyme with 4'Py sites in the presence and absence of NaCl: **A**) Cu(I)-TRIW-4'Py, and **B**) Cu(I)-TRIW-4'Py L19A

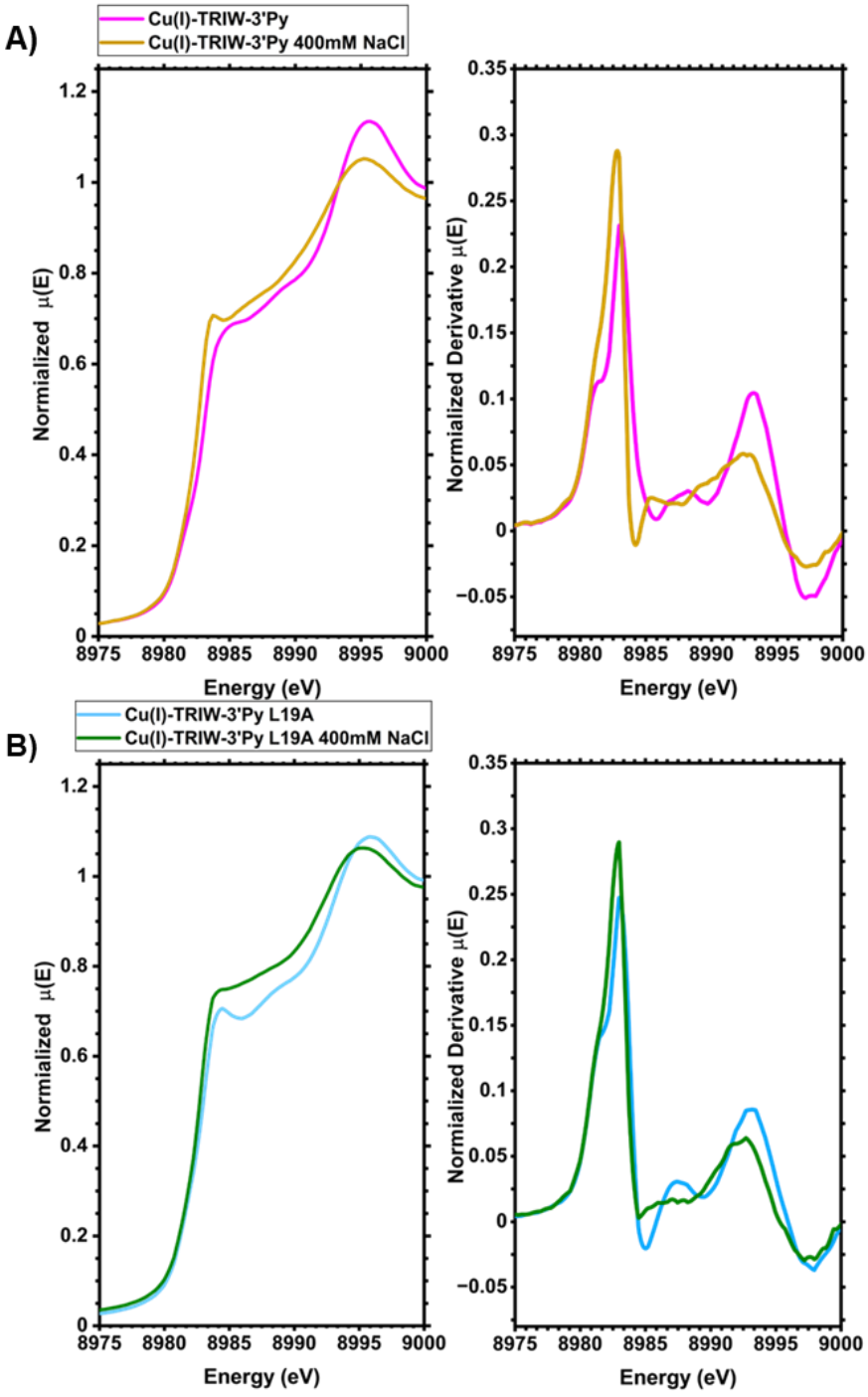


Figure III-8: XANES **(**derivative, *right***)** comparison between the reduced enzyme with 3'Py sites in the presence and absence of NaCl: **A)** Cu(I)-TRIW-3'Py **B)** Cu(I)-TRIW-3'Py L19A

Nitrite and Chloride binding to the Cu(II)-Oxidation state:

Table III-2: X-Band EPR parameters of oxidized forms with 50 eqv. $NaNO_2$ at pH 5.9.
[a] g-values are $g_{\|}$ and $g_{\perp}$, respectively (TRIW-H collected by Dr. Fangting Yu)

Enzyme	g_z	g_y	g_x	$A_{\|}$ ($\times 10^{-4}$ cm^{-1})
Cu(II)-TRIW-4'Py L19A	2.28	2.04	2.04	169
50 eqv. $NaNO_2^-$				
Cu(II) Species #1 [32%]	2.268	2.027	2.053	178.5
Cu(II) Species #2 [68%]	2.282	2.039	2.039	158.5
Cu(II)-TRIW-3'Py	2.29	2.04	2.04	168
50 eqv. $NaNO_2^-$				
Cu(II) Species #1 [62%]	2.263	2.052	2.036	177.4
Cu(II) Species #2 [38%]	2.295	2.041	2.039	161.0
Cu(II)-TRIW-3'Py L19A	2.29	2.05	2.04	170
50 eqv. $NaNO_2^-$				
Cu(II) Species #1 [70%]	2.269	2.040	2.036	162.2
Cu(II) Species #2 [30%]	2.302	2.044	2.038	156.7
Cu(II)-TRIW-H[a]				
50 eqv. $NaNO_2^-$	2.270	2.050		197.1
	2.282	2.034		174.7

The EPR spectra of each enzyme was collected after flash freezing with 50 eqv. $NaNO_2$ at pH 5.9 to observe NO_2^- binding to the Cu(II)-form (Figure III-9–Figure III-12).[*] This was carried out with 30% glycerol in 50 mM MES buffer at 90 K. In every case, two species are observed under these conditions which were carefully fitted to account for correlated variables and physical reasonableness of the fitted values based on numerous literature examples of $T2Cu_{ox}$ EPR in the presence of nitrite (Table III-2).[42–46] Interestingly, neither adducts match the nitrite free form of the enzyme. Both species are best described as having predominantly d_x^2-$_y^2$ ground state character (*i.e.*, $g_z > g_x = g_y$), with the minor copper adduct of TRW-4Py L19A and TRIW-3'Py displaying

[*] Cu(II)-TRIW-4'Py (w/ 50 eqv. NO_2) was excluded as this design was unable to be probed with the current assay due to its high K_m.

rhombic character in the g_x and g_y regions ($g_x \neq g_y$) signifying a mixture of d_z^2 ground state. In all cases, the major population has a lower $A_{\|}$ than the nitrite free spectrum and the minor population has a higher $A_{\|}$ value than the nitrite free spectrum (Table III-2).

The room temperature UV-Vis spectra of the oxidized copper center were unperturbed upon the addition of sodium chloride up to 250 mM (Figure III-12A-C). Similar, the addition of Cl^- has been shown to alter the EPR spectra of Cu(II) proteins when directly binding to the copper center.[47] However, adding 400 mM NaCl to the most efficient CuNiR mimic, TRIW-4'Py L19A, resulted in minor changes in the EPR parameters compared to those under Cl^- free conditions (Figure III-9–Figure III-11).

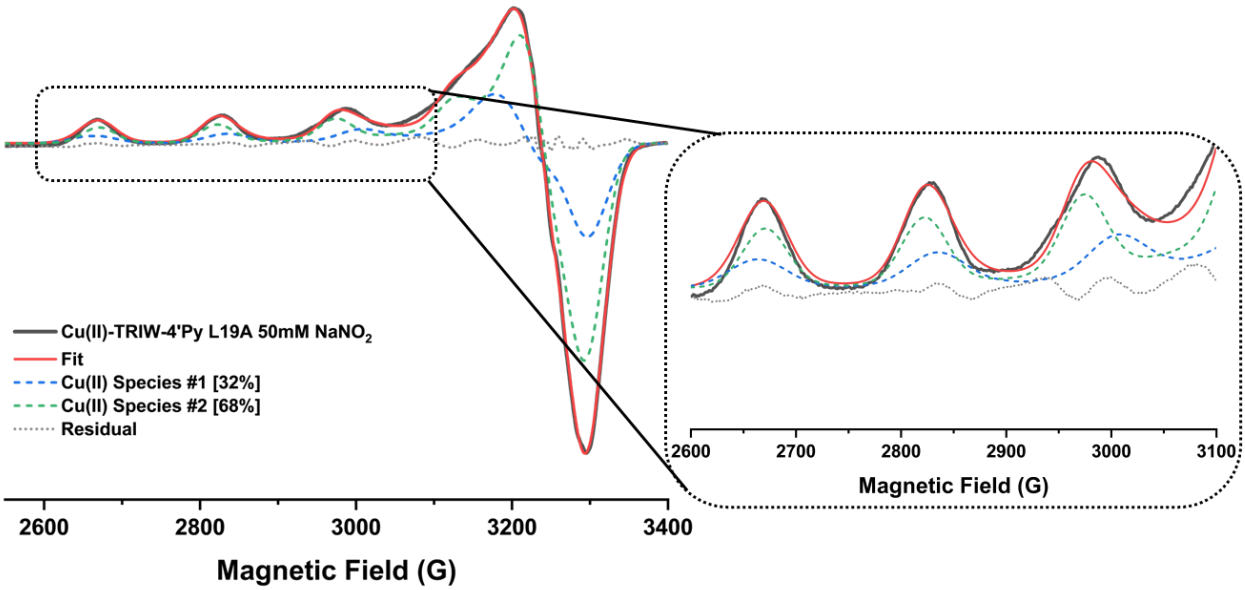


Figure III-9: X-band EPR of Cu(II)-TRIW-4'Py L19A in the presence of 50 eqv. $NaNO_2$ (50 mM) at 90 K.

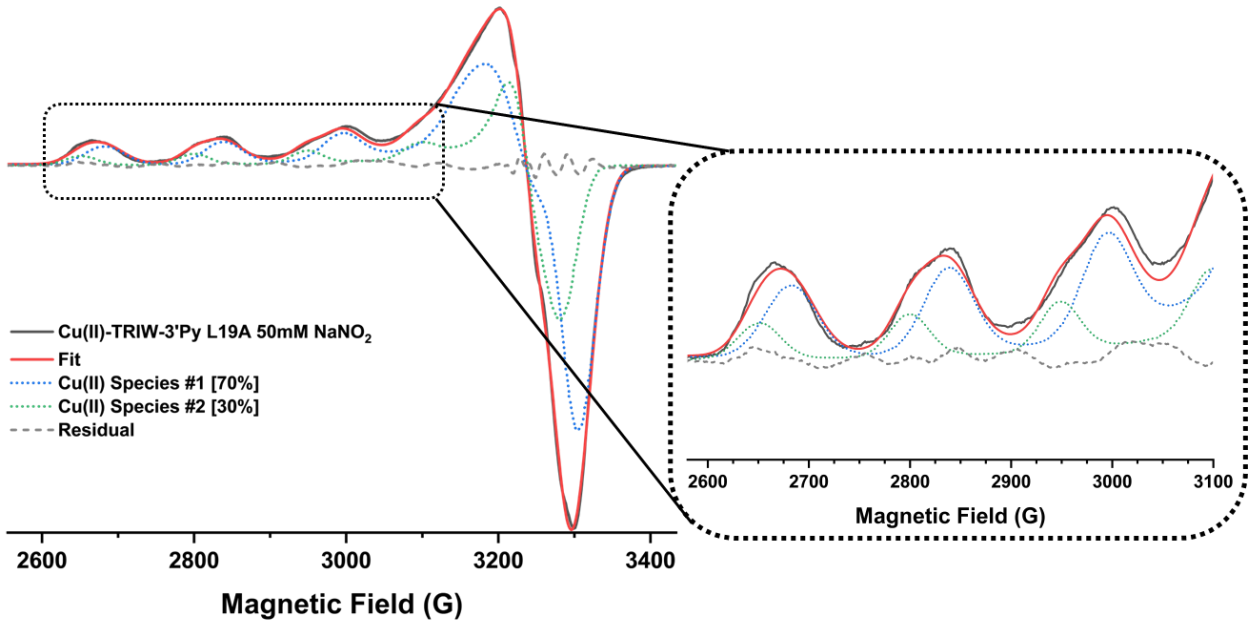


Figure III-10: X-band EPR of Cu(II)-TRIW-3'Py L19A in the presence of 50 eqv. $NaNO_2$ (50 mM) at 90 K.

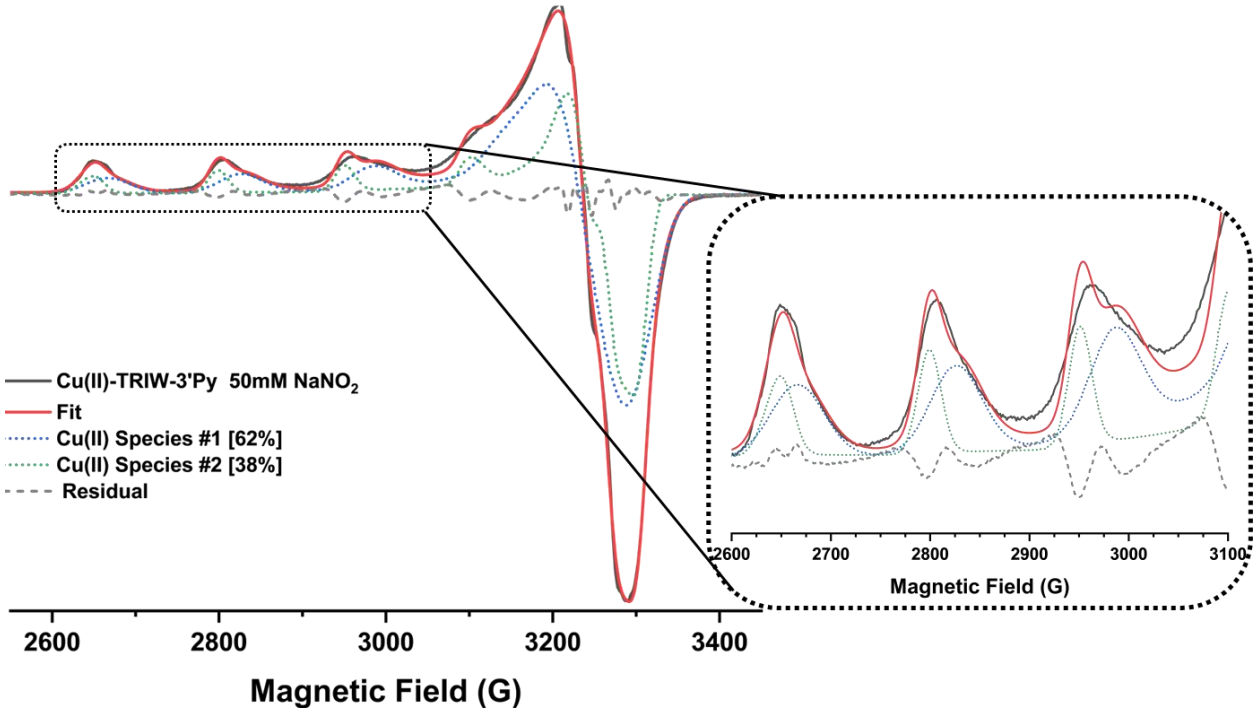


Figure III-11: X-band EPR of Cu(II)-TRIW-3'Py in the presence of 50 eqv. $NaNO_2$ (50 mM) at 90 K.

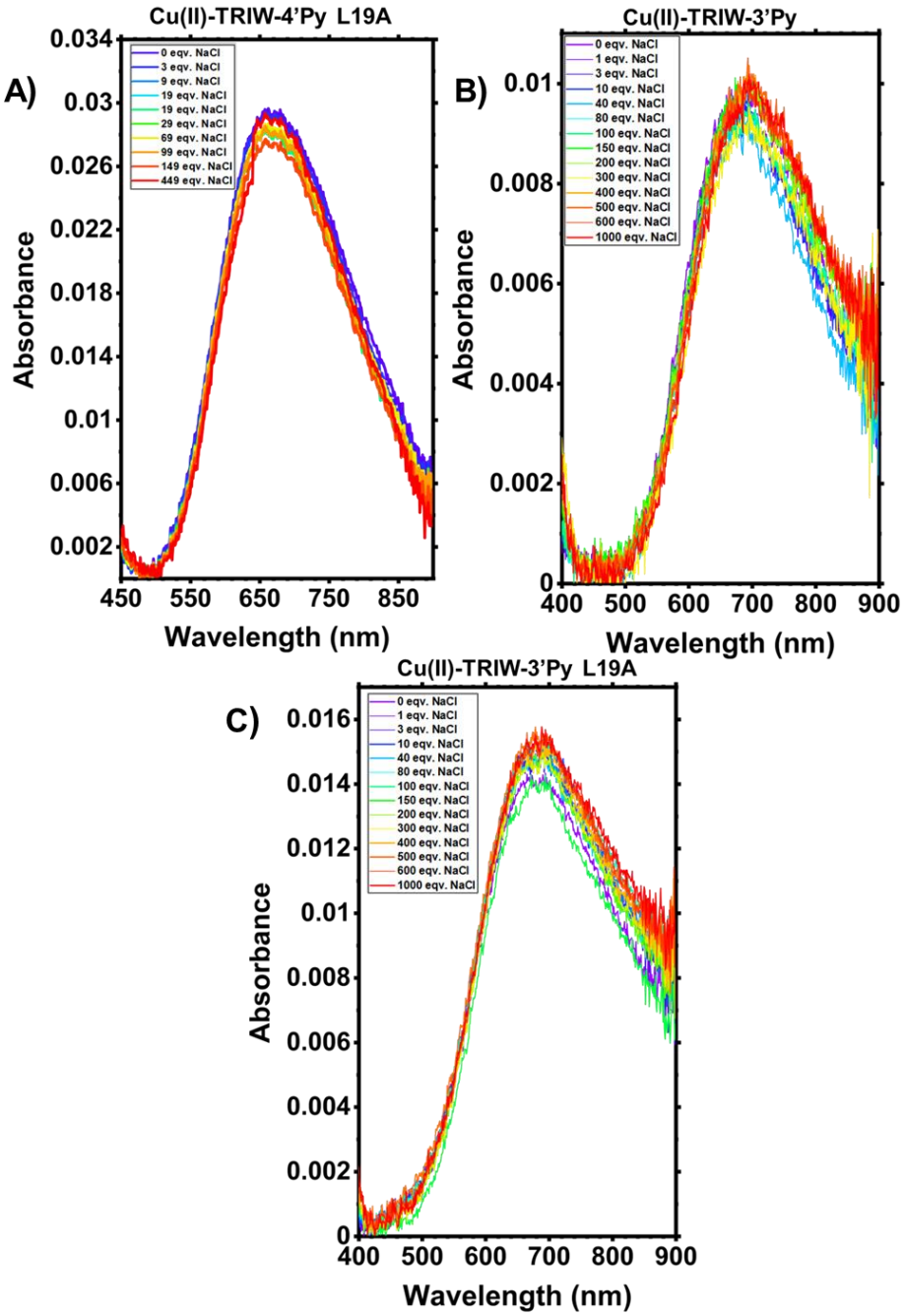


Figure III-12: UV-Vis spectra (d-d region) in the presence of increasing equivalents of NaCl (0 mM-279 mM) and 250 μM Cu(II)-Trimers: **A**) TRIW-4'Py L19A, **B**) TRIW-3'Py, and **C**) TRIW-3'Py L19A. *(Each absorption spectrum was correct for dilution volume)*

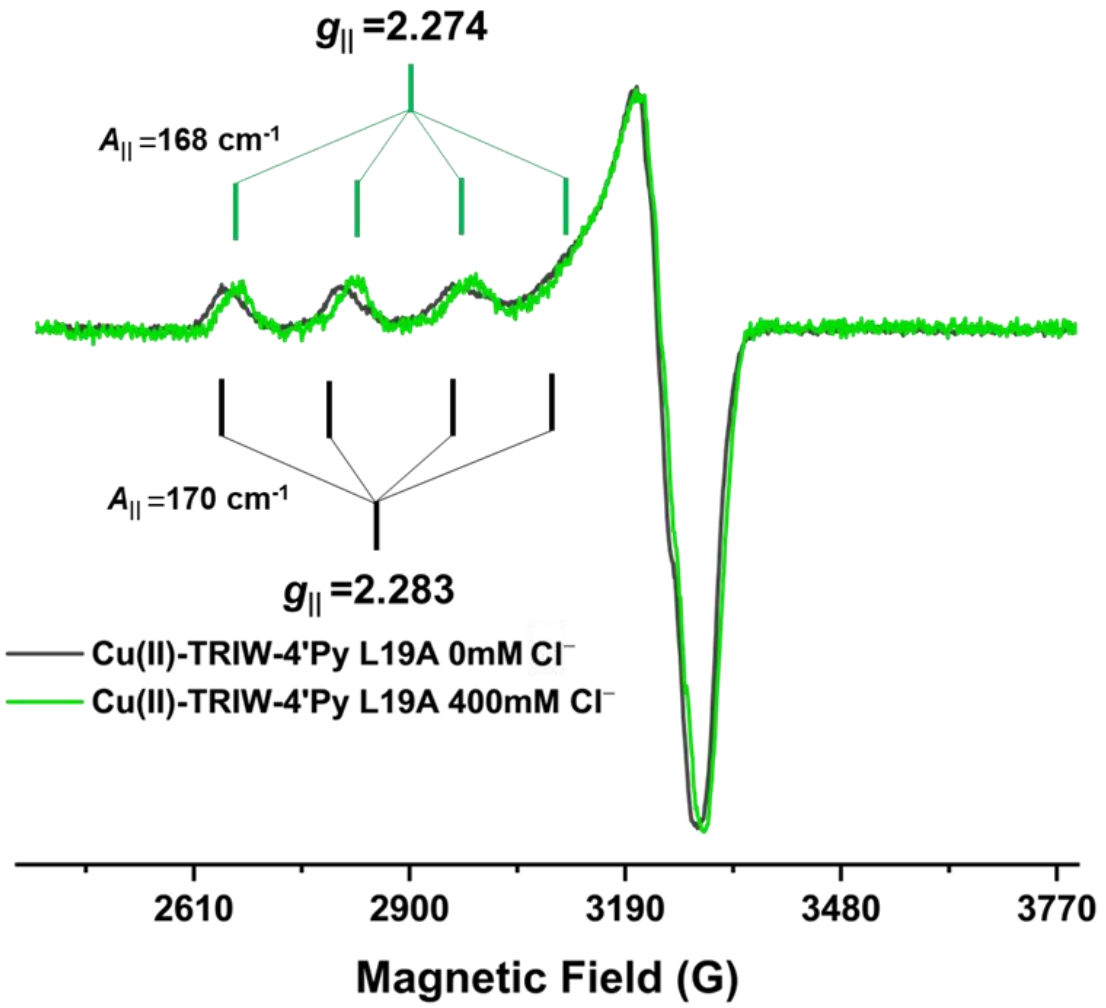


Figure III-13: X-band EPR of Cu(II)-TRIW-4'Py L1A in absence (*black*) and presence of 400 eqv. (400 mM) NaCl at 95 K (*green*).

Chloride Steady State Inhibition Kinetics:

Table III-3. Summary K_{i,Cl^-} values for each enzyme and their steady state parameters resulting from each method used. [a]Values from Chapter II, [b]Global fitting parameters that were held constant.

Enzyme	K_{i,Cl^-} (mM)	k_{cat} (s^{-1})	K_m (M)	k_{cat}/K_m (M^{-1} s^{-1})
TRIW-3'Py[a]	--	3.0 (±0.1)	0.28 (±0.03)	11 (± 1)
Method #1	67 (±20)	3.4 (±0.3)	0.35 (±0.08)	9.7 (± 2.4)
Method #2		2.9 (±0.3)	0.280[b]	11[b]
TRIW-3'Py L19A[a]	--	2.8 (±0.3)	0.19 (±0.06)	15 (± 3)
Method #1	33 (±6)	2.8 (±0.2)	0.170 (±0.03)	16.5 (±3.1)
Method #2		3.2 (±0.1)	0.190[b]	16.8[b]
TRIW-4'Py L19A[a]	--	1.9 (±0.1)	0.05 (±0.01)	39 (± 3)
Method #1	18 (±4)	1.9 (±0.1)	0.04 (±0.01)	47.5 (±12.1)
Method #2		2.0 (±0.2)	0.05[b]	40[b]

The background reaction between sodium ascorbate and $NaNO_2$ was not inhibited by the addition of Cl^- within the ranges used in these experiments (Figure III-14). *The high K_m value (600 mM NO_2^-) of uninhibited TRIW-4'Py and the deadtime limit to collect data on a conventional UV-Vis spectrometer precluded this enzyme from being investigated using the current assay because the initial rates of the background reaction are greater than the enzyme reaction above 800 mM $NaNO_2$.* The Cl^- inhibition kinetics with TRIW-3'Py, TRIW-3'Py L19A, and TRIW-4'Py L19A all display competitive inhibition between the concentration range of 0-120 mM NaCl and 50-600 mM $NaNO_2$ (Figure III-15–Figure-III-17). The $K_{i,Cl}$ for each design was calculated by plotting the v_{obs}/E_t vs. $NaNO_2$ curves at different chloride concentrations and global fitting each to Eq. III-3 which describes a competitive inhibition mechanism.[†] With this method, the k_{cat} value from each enzyme was within error to those under Cl^- free conditions in Chapter II, which ruled out the possibility of Cl^- forming an irreversible dead-end enzyme which would lower the kcat values

[†] All methods can be found in Segel *et al*. in Ref. [62]

with increasing Cl^- concentration. Similarly, while $K_{m,app}$ changed as expected for a competitive inhibitor, the K_m was allowed to vary during the fit and each time converged to within error to those in Chapter II (Table III-3). It is clear from the Lineweaver-Burk plot that the chloride inhibits in a competitive fashion as the line intercepts at a single value on the y-axis (Figure III-15B-16B). The possibility that a partial competitive inhibition could explain the data was investigated (Equation III-4). The coefficient α in the slope factor treats partial and pure competitive inhibition on a spectrum, effectively "mixing" the two types of inhibition to determine how much of the ESI complex goes on to form product. Since the ESI complex can catalyze the chemical conversion to product, it is expected that an excess amount of inhibitor would not be expected to drive the $V_{max,app}$ to 0 M^{-1} s^{-1} at any particular concentration of $NaNO_2$. In every case, α approached ∞ (ca. $>1\times10^{24}$), suggesting a pure, competitive inhibition as opposed to partial competitive inhibition within the kinetic error of the experiments. The $K_{i,Cl}$ for TRIW-3'Py L19A and TRIW-4'Py L19A were

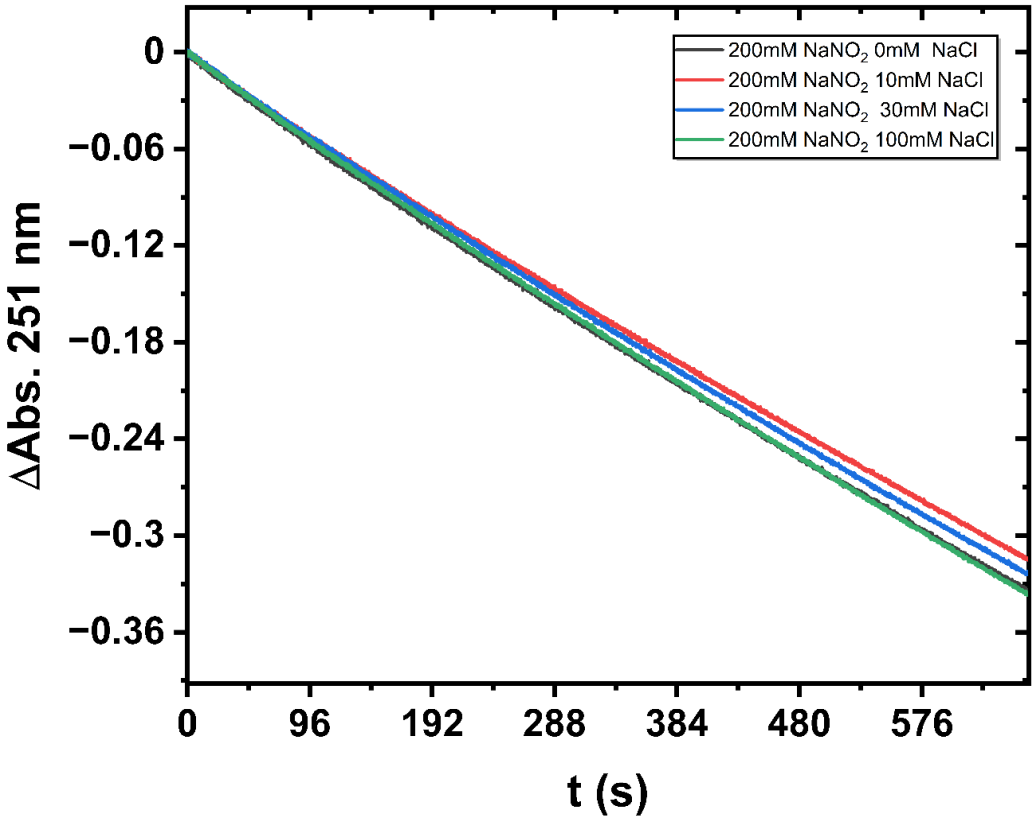


Figure III-14: Progress curves of the background reaction between nitrite and sodium ascorbate at various NaCl concentrations (200 mM $NaNO_2$, 1.5 mM NaAsc). This demonstrate that the background reaction is independent of Cl^-.

calculated to be in the range of 33 mM (±6) and 18 mM (±4), respectively. The Cl^- associated with TRIW-3'Py design with a higher $K_{i,Cl}$ 67 (±20) mM, despite the larger error with these averages.

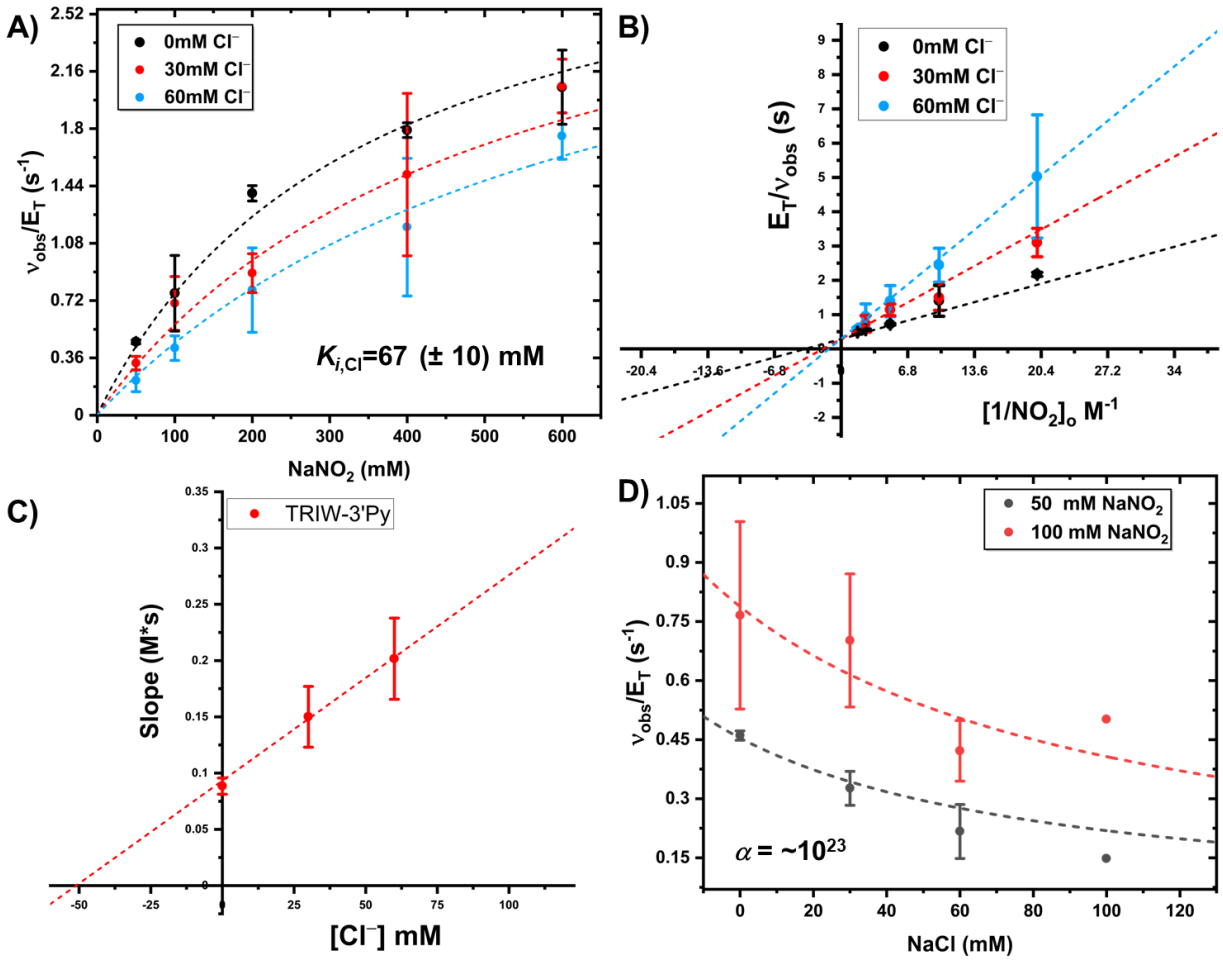


Figure III-15: Steady-state plots showing competitive inhibition of TRIW-3'Py by Cl^-: **A)** v_{obs}/E_t vs. $NaNO_2$ plot and fitting based on *method #1*, **B)** Lineweaver-Burk plotting of the kinetic data showing a competitive inhibition pattern, **C)** Replot of the slopes fitted from the Lineweaver-Burk plot against $[Cl^-]$, highlighting that only one chloride binds during inhibition, **D)** v_{obs}/E_t vs. $[Cl^-]$ plot used to determine the α to distinguish between a pure competitive inhibition mechanism and partial competitive inhibition mechanism. (---- Fitted Curve)

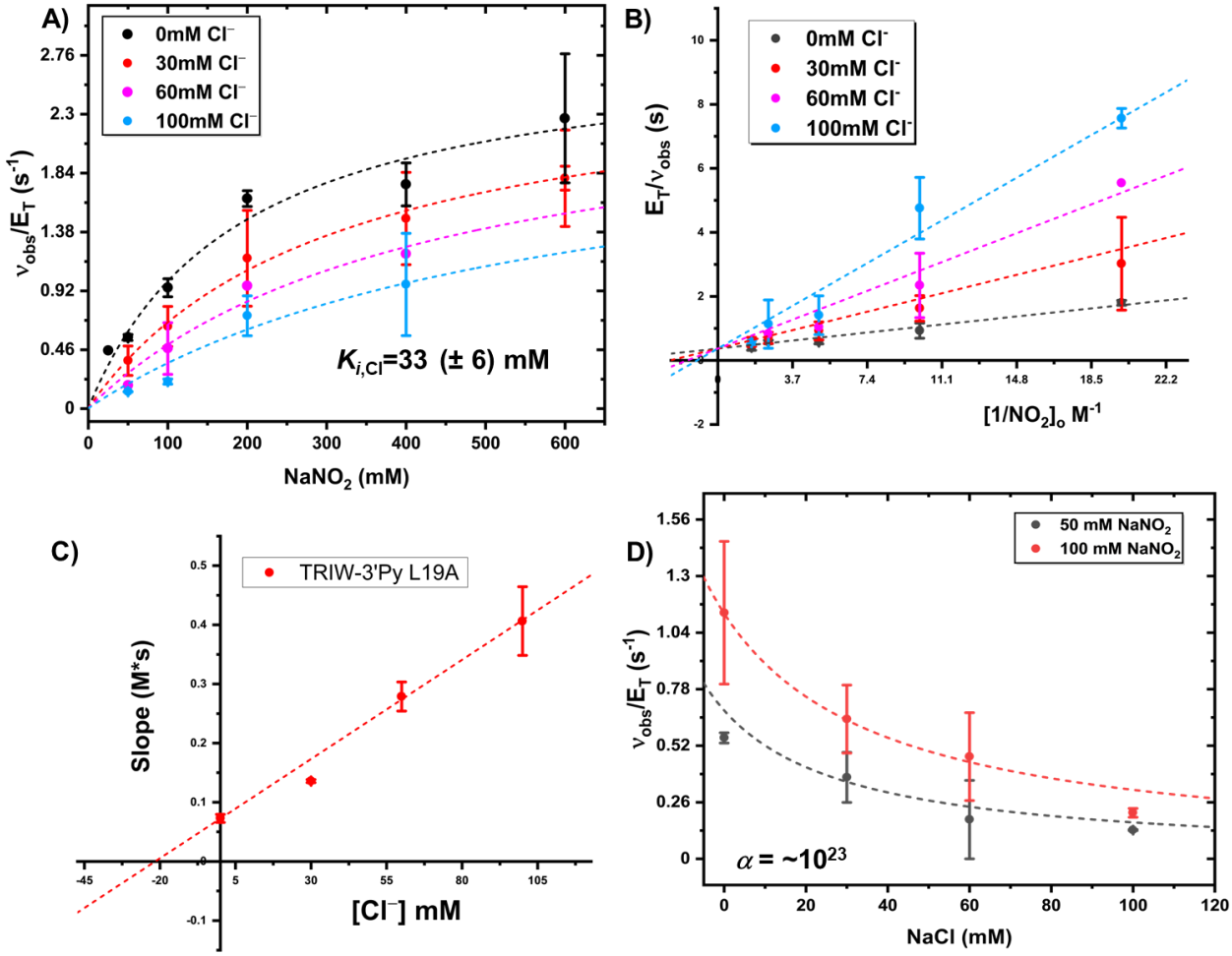


Figure III-16: Steady-state plots showing competitive inhibition of TRIW-3'Py L19A by Cl^-: **A)** v_{obs}/E_t vs. $NaNO_2$ plot and fitting based on *method #1*, **B)** Lineweaver-Burk plotting of the kinetic data showing a competitive inhibition pattern, **C)** Replot of the slopes fitted from the Lineweaver-Burk plot against [Cl^-], highlighting that only one chloride binds during inhibition, **D)** v_{obs}/E_t vs. [Cl^-] plot used to determine the α to distinguish between a pure competitive inhibition mechanism and partial competitive inhibition mechanism. (---- Fitted Curve)

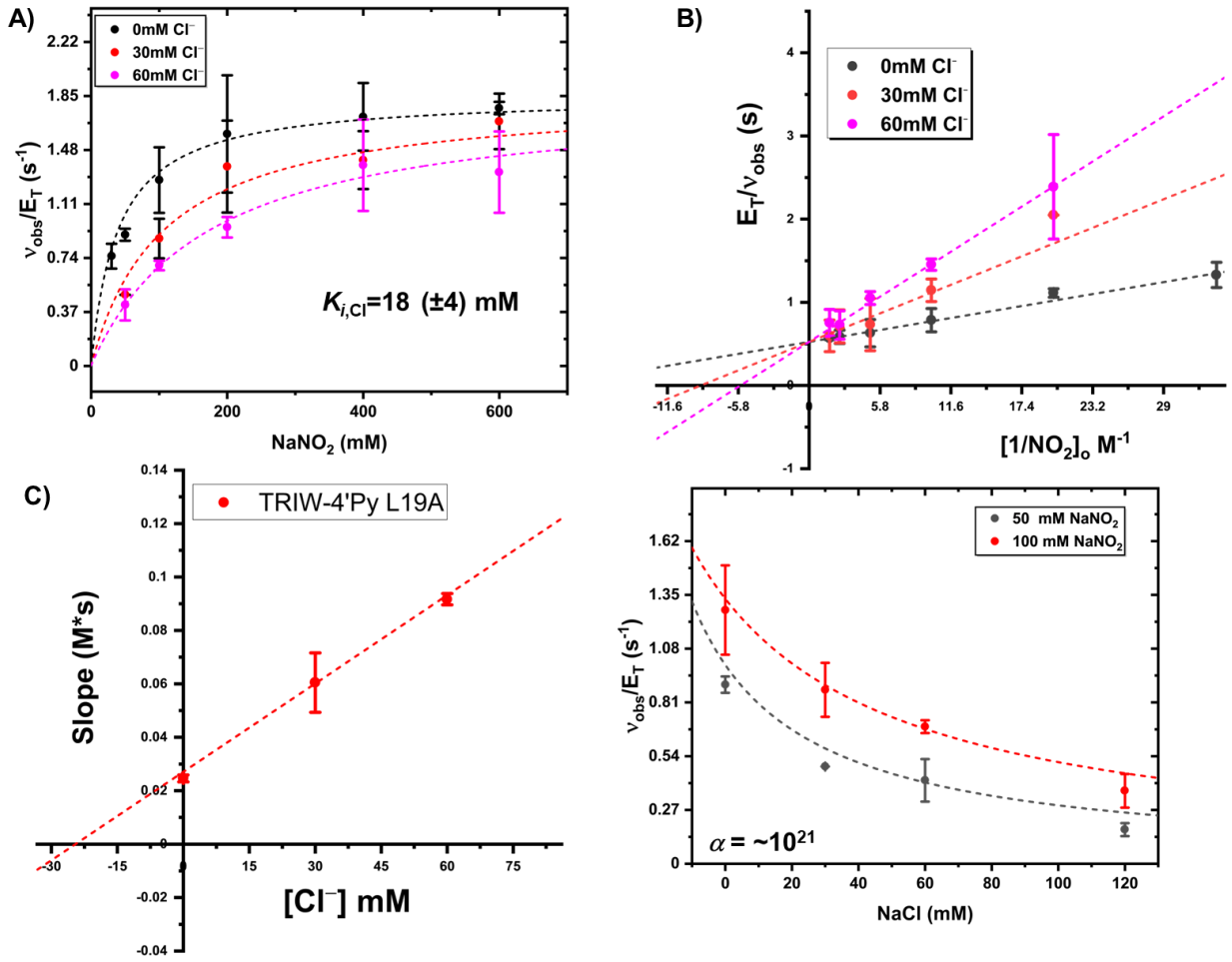


Figure III-17: Steady-state plots showing competitive inhibition of TRIW-4'Py L19A by Cl^- **A)** v_{obs}/E_t vs. $NaNO_2$ plot and fitting based on *method #1*, **B)** Lineweaver-Burk plotting of the kinetic data showing a competitive inhibition pattern, **C)** Replot of the slopes fitted from the Lineweaver-Burk plot against [Cl^-], highlighting that only one chloride binds during inhibition , **D)** v_{obs}/E_t vs. [Cl^-] plot used to determine the α to distinguish between a pure competitive inhibition mechanism and partial competitive inhibition mechanism. (---- Fitted Curve)

Discussion:

As emphasized previously, the oxidized enzyme in native CuNiRs binds nitrite before the electron is transfer from the T1Cu center which defines the "*binding before electron transfer*" and in primarily enforced by the outer sphere Asp_{CAT} and Ile_{CAT} residues to H-bond and align NO_2^-, yielding a rate limiting electron transfer step in order that nitrite binds directly to the CuNiR center.[48] The "*binding after electron transfer*" pathway has indirectly been investigated and shown to catalyze nitrite reduction; however, it has also been said to be an inactive enzyme form. [10,49] Others have claimed that this pathway is able to turnover NO_2^-. In the absence of the Asp_{CAT} redox gating mechanism in 3SCC CuNiR mimic to direct nitrite binding, previous designs with histidine have suffered from low catalytic efficiencies and high K_m values. The TRIW-H and TRIW-H L19A designs were studied under the assumption that the alanine mutation provided greater substrate access to the copper center and lowered the Cu(I) coordination number to yield a linear 2-coordinate reduced enzyme which was tentatively thought to provide alternate NO_2^- binding modes to the copper center that were more favorable to undergo reduction.[24] This interpretation was made in the context of parallel studies with the Cu(I)–CO adducts where it was discovered dependence of the first coordination sphere in altering the potential energy surface of a bound substrate using 2D FT-IR and QM/MM calculations. This suggest that ligand orientation may play a role in catalytic activity.[50] Furthermore, XANES data demonstrated that all elevated rate constructs had a similar 1 eV blue shift in their edge transition energies, highlighting that this enhancement is probably substantial for the Cu(I) species.(cite) The δ-methyl histidine and ε-methyl histidine analogs were shown to direct Cu(II) and Cu(I) coordination modes, binding affinities, and reduction potential. The switch from N_ε and N_δ coordinative nitrogen resulted in an oxidized enzyme that is best described as a $CuHis_2O_2$ site which contrasts with the CuN_3O with the Cu(II) TRIW-δ_mH designed. In native CuNiR, the coordination of an additional H_2O or ^-OH ligand to the resting Cu(II)$(His)_3H_2O$ T2Cu center has been shown to limit the rate of nitrite reduction.[51] The native reduced enzyme's coordination environment has not been explored in the

context of the influence of coordination number on nitrite reduction; however, the methylated histidine designs above suggest that the electronics, namely pyridyl character of the δ_m-Histidine, is critical to achieve high activity (k'_{1st} = 1.2 × 10^{-3} s^{-1} vs. k'_{1st} =0.12 s^{-1}), especially when coupled to a shift to a 2-coordinate geometry of the reduced enzyme with the L19A mutation.[52] The latter mutation resulted in a 10x increase in catalytic efficiency when comparing the TRIW-δ_mH L19A vs. TRIW-H L19A (k_{cat}/K_m = 11.3 M^{-1} s^{-1} vs. 1.0 M^{-1} s^{-1}, respectively) stemming from this electronic effect of the coordinated ε-nitrogen (8x increase in k_{cat}) and with a slight decrease in K_m due to greater substrate access to the copper center (0.24 ± 0.05 mM vs. 0.13 ± 0.01), respectively. Collectively, these studies have given rise to a model that invokes ligand electronics and substrate access to the copper center as the primary driver of the observed increase in nitrite reduction. Moreover, modifications of the Cu(I) oxidation state (coordination number and electronics) have closely followed the increase in CuNiR activity over these studies, leading to the speculation that it was particularly important in the catalytic cycle. It is difficult to establish substrate binding to the Cu(I) oxidation state using traditional spectroscopy, as the Cu(I)–NO_2 intermediate is quite unstable in the presence of a proton source, decomposing rapidly into NO(g) and H_2O.[53] This chapter investigates the K_m effects at the reduced enzyme during the catalytic cycle using chloride as an inhibitor and will explore the structure of this adduct using XAS spectroscopy. These simple experiments will provide models that attempt to explain the observations in Chapter II and offer a slightly different interpretation of the effects steric modifications play in these coiled coil proteins.

The relative binding of chloride to the oxidized and reduced enzyme forms can be examined in the context of spectroscopy under non-turnover conditions. The reduced copper center was first explored in the presence of the inhibitor using XAS spectroscopy to determine the structure. The addition of excess NaCl (400 mM) to the reduced enzymes results in the formation of a new species that is best described as a Cu(I)Py_2Cl structure as opposed to favoring a 2-coordinate Cu(I)Py_1Cl or 4-coordinate Cu(I)Py_3Cl structure. Admittedly, the formation of a 2-coordinate complex ($CuPy_1Cl$) or 4-coordinate complex ($CuPy_3Cl$) cannot be completely ruled out from the EXAFS alone as the chloride adducts of both Cu(I)-TRIW-3'Py and Cu(I)-TRIW-4'Py L19A have a slightly better fitting parameter ($<\chi^2 f>$) for a linear $CuPy_1Cl$ structure (Table III-4). The Cu(I)–N_{Py} bond distances fall within 2- and 3-coordinate Cuprous-Pyridyl complexes (1.94-2.00 Å), while the Cu(I)–Cl bond distances are in between 2- and 4-coordinate Cuprous-Chloro-Pyridyl complexes (Table III-4, Scheme III-1).[36,54–57] However, the bond valence sum analysis tends to favor a more 3-coordinate cuprous complexes.[35,58] The Cu(I) XANES region is more sensitive to the coordination number of the copper center and the energy of the Cu(I) 1s-4p edge transitions are indicative of a 2- or 3-coordinate Cu(I), as 4-coordinate typically exhibit a main peak at ~8986 eV, while 2- and 3-coordinate complexes exhibit a positive peak between ~8983-8984 eV.[38] In the cupric state, a single chloride has been observed to bind to native $T2Cu_{ox}$, displacing a coordinated water to form a distorted tetrahedral.[42,59] However, no EPR or K_d has been reported for this chloride adduct or other halogens adduct with native CuNiRs. The addition of chloride to the oxidized enzyme does not result in spectral changes in the EPR or UV-Vis which

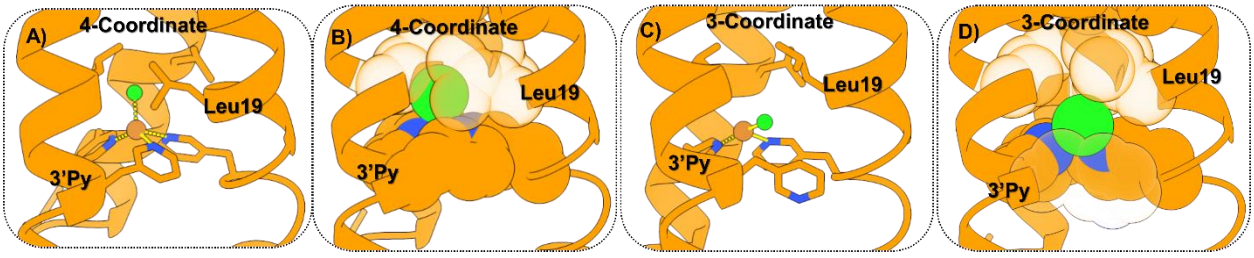


Figure III-18: Models highlighting 3-coordinate adduct less sterics interactions than a 4-coordinate tetrahedral adduct: **A**) 4-coordinate chloride adduct in Cu(I) TRIW-3'Py, **B**) the respective space-filling model, **C**) 3-coordinate chloride adduct in Cu(I) TRIW-3'Py, and **D**) the respective space-filling model.

suggests: a) the chloride does not interact with the copper center; or b) it binds weakly to the oxidized enzyme (*i.e.*, $K_{d,app}$. >>400 mM) (Figure III-9–Figure-III-12). I favor (a), but I cannot rule (b). According to hard/soft theory, chloride is a hard base that would be expected to form more covalent-like bonds with hard acids (*i.e.*, Cu(II)) and more ionic-like bonds with soft acids (*i.e.*, Cu(I)).[60] However, cupric complexes tend to require a higher coordination number (*i.e.*, 4 to 6-coordinated ligands) which could sterically disfavor the formation of a Cu(II)-Cl adduct with the 6-membered heterocycles composing the primary coordination sphere and without a large structural change in the protein. The lower coordination number observed in most Cu(I) complexes may play a selective role in binding chloride over Cu(II).

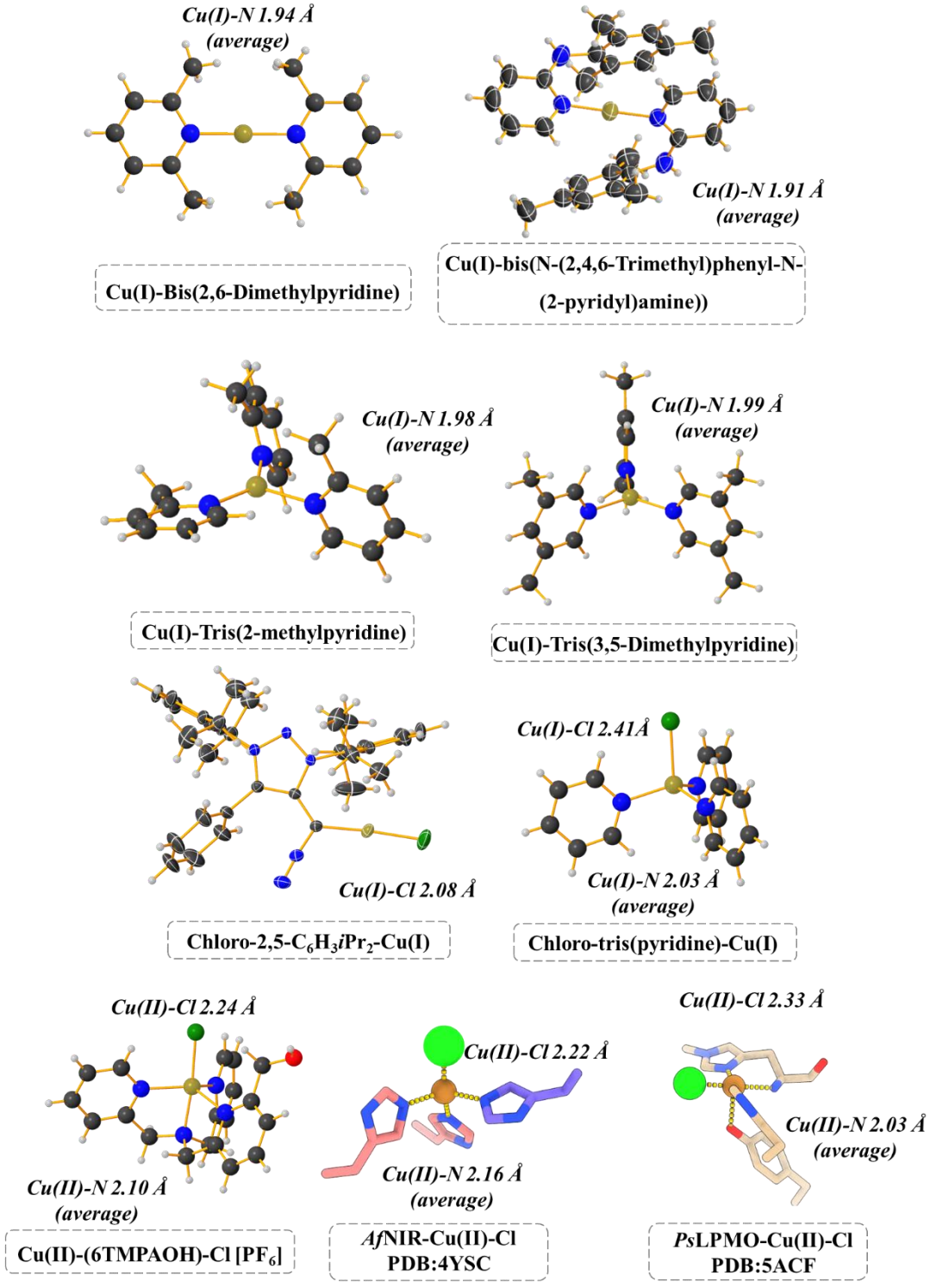
The binding of Cl^- to only the reduced form would raise the possibility of interrogating substrate binding to the active catalyst during turnover. It should be emphasized that while nitrite binds to the oxidized copper center under non-turnover conditions, chloride would not report on the *binding before reduction*. It is unlikely that NO_2^- binding to the oxidized form occurs under turnover conditions as the rate of electron transfer exceed the rate of substrate binding to the oxidized form, and the conditions reported in the EPR experiment (which is an equilibrium condition) would not be relevant during turnover. Therefore, it predicted that NO_2^- never interacts with the Cu(II) form.[61] While keeping in mind that Cl^- binds to the reduced form of the enzyme, I explored the chloride inhibition kinetics, which resulted in a few interesting conclusions about the nature of the mechanism under conditions in which electron transfer is not limited. From the kinetics, the Cu(I)Py_2Cl form is not an irreversible dead-end complex as the $V_{max,app}$ is not driven to zero as the inhibitor concentration is increased, suggesting the chloride is a reversible inhibitor that can be displaced at high concentrations of substrate. Therefore, the addition of excess Cl^- does not dramatically destabilize the Cu(I)-Cl adduct which would result in the demetallation and precipitation of the Cu(I) form of the enzyme.

Table III-4: Summary of relevant distances in Cu(I) complexes.

Cu(I)/Cu(II) Complexes	Best Model	Cu(I)-N	Cu(I)-N $\sigma^2 \times 10^{-3}$	Cu(I)-Cl	Cu(I)-Cl $\sigma^2 \times 10^{-3}$	Bond Valence Sum	Ref.
Cu(I)-TRIW-4'Py	$CuPy_2$	1.97 Å	3.17 $Å^2$	--	--	0.78	--
	$CuPy_3$	1.97 Å	5.26 $Å^2$	--	--	1.05	--
	$CuPy_2Cl$	1.98 Å	4.87 $Å^2$	2.24 Å	5.09 $Å^2$	1.03	--
Cu(I)-TRIW-3'Py	$CuPy_2$	1.96 Å	2.94 $Å^2$	--	--	0.80	--
	$CuPy_3$	1.97 Å	5.17 $Å^2$	--	--	1.08	--
	$CuPy_2Cl$	1.96 Å	4.11 $Å^2$	2.26 Å	4.95 $Å^2$	1.05	--
Cu(I)-TRIW-4'Py L19A	$CuPy_2$	1.94 Å	3.31 $Å^2$	--	--	0.85	--
	$CuPy_3$	1.94 Å	5.60 $Å^2$	--	--	1.14	--
	$CuPy_2Cl$	1.97 Å	4.82 $Å^2$	2.27 Å	6.38 $Å^2$	1.02	--
Cu(I)-TRIW-3'Py L19A	$CuPy_2$	1.95 Å	4.31 $Å^2$			0.83	--
	$CuPy_3$	1.95 Å	6.96 $Å^2$			1.10	--
	$CuPy_2Cl$	1.96 Å	4.50 $Å^2$	2.26 Å	7.54 $Å^2$	1.05	--
Cu(I)-Bis(2,6-Dimethylpyridine)	$CuPy_2$	1.94 Å	--	--	--	0.85	36
Cu(I)-bis(N-(2,4,6-Trimethyl)phenyl-N-(2-pyridyl)amine	$CuPy_2$	1.91 Å	--	--	--	0.92	57
Cu(I)-Tris(2-methylpyridine)	$CuPy_3$	1.98 Å	--	--	--	1.02	54
Cu(I)-Tris(3,5-Dimethylpyridine)	$CuPy_3$	1.99 Å	--	--	--	1.00	54
Cu(I)-Chloro-2,5-C_6H_3*i*Pr_2	CuCCl	1.86 Å	--	2.08 Å	--	1.19	55
Cu(I)-Chloro-tris(pyridine)	$CuPy_3Cl$	2.03 Å	--	2.41 Å	--	1.00	33
Cu(II)-(6TMPAOH)-Cl [PF_6]	$CuPy_3N'Cl$	2.10 Å	--	2.24 Å	--	1.90	56
Cu(II)-*Af*NIR-Cl	$CuHis_3Cl$	2.16 Å	--	2.22 Å	--	1.69	59
Cu(II)-*Ps*LPMO-Cl	$CuN_2N'OCl$	2.03 Å	--	2.33 Å	--	1.77	47

The crystal structures in **Scheme III-1** are those referenced in the **Table III-4**

Scheme III-1



Inspection of the Lineweaver-Burk plots show inhibition patterns that is most consistent with Cl^- behaving as a competitive type of inhibitor with respect to NO_2^-, suggesting Cl^- binds to the same enzyme form as the substrate during the catalytic cycle (Figure III-15B–Figure-III-17B). While nitrite binds to the oxidized form under non-turnover conditions, this is not consistent with the inhibition kinetic patterns observed under catalytic relevant conditions. Certainly, the affinity for nitrite to the Cu(II) form of histidine containing designs is much stronger than would be expected by the K_m values for the Cu(I)His_3 site (K_d for nitrite binding ~2 mM for Cu(II) TRIW-H whereas the K_m is > 400 mM), again suggesting the relevant interaction is at the Cu(I) oxidation level.[19]

Table III-5: Relevant NiR activity comparisons between CuNiR mimics.

Enzyme	k' (s^{-1})	k_{cat} (s^{-1})	K_m (M) ($K_{i,Cl}$-)[b]	k_{cat}/K_m (M^{-1} s^{-1})	Ref.
***Af*CuNiR pH 6.5**	--	620	1.5×10^{-4}	4.1×10^{6}	8
TRIW-H[a]	4.6×10^{-4}	0.032 (±0.016)	1.2 (± 0.9)	0.026 (±0.005)	[31]
TRIW-H L19A[a]	3.5×10^{-2}	0.23 (±0.03)	0.24 (±0.03)	1.0 (±0.3)	24
TRIW-δ_mH[a]	0.12	1.5 (± 0.1)	0.18 (± 0.02)	8.2 (± 0.1)	[52]
TRIW-δ_mH L19A[a]	0.30	1.5 (±0.1)	0.13 (±0.01)	11 (±0.1)	[52]
TRIW-ε_mH[a]	4.1×10^{-3}	N/A	N/A	N/A	[52]
TRIW-ε_mH L19A[a]	3.8×10^{-2}	N/A	N/A	0.14 (±0.01)	[52]
TRIW-3'Py	0.30	3.0 (±0.1)	0.28 (±0.03) *0.067 (±0.020)*	11 (± 1)	--
TRIW-3'Py L19A	0.51	2.8 (±0.3)	0.19 (±0.06) *0.033 (±0.006)*	15 (± 3)	--
TRIW-4'Py	0.11	2.9 (±1)	0.60 (±0.26) *N/A*	5 (± 1)	--
TRIW-4'Py L19A	1.4	1.9 (±0.1)	0.05 (±0.01) *0.018 (±0.004)*	39 (± 3)	--

[a] CuNiR kinetics carried out at pH 5.8.
[b] $K_{i,Cl}$- values were calculated using Equation #1.
N/A: The kinetic parameter could not be obtained.

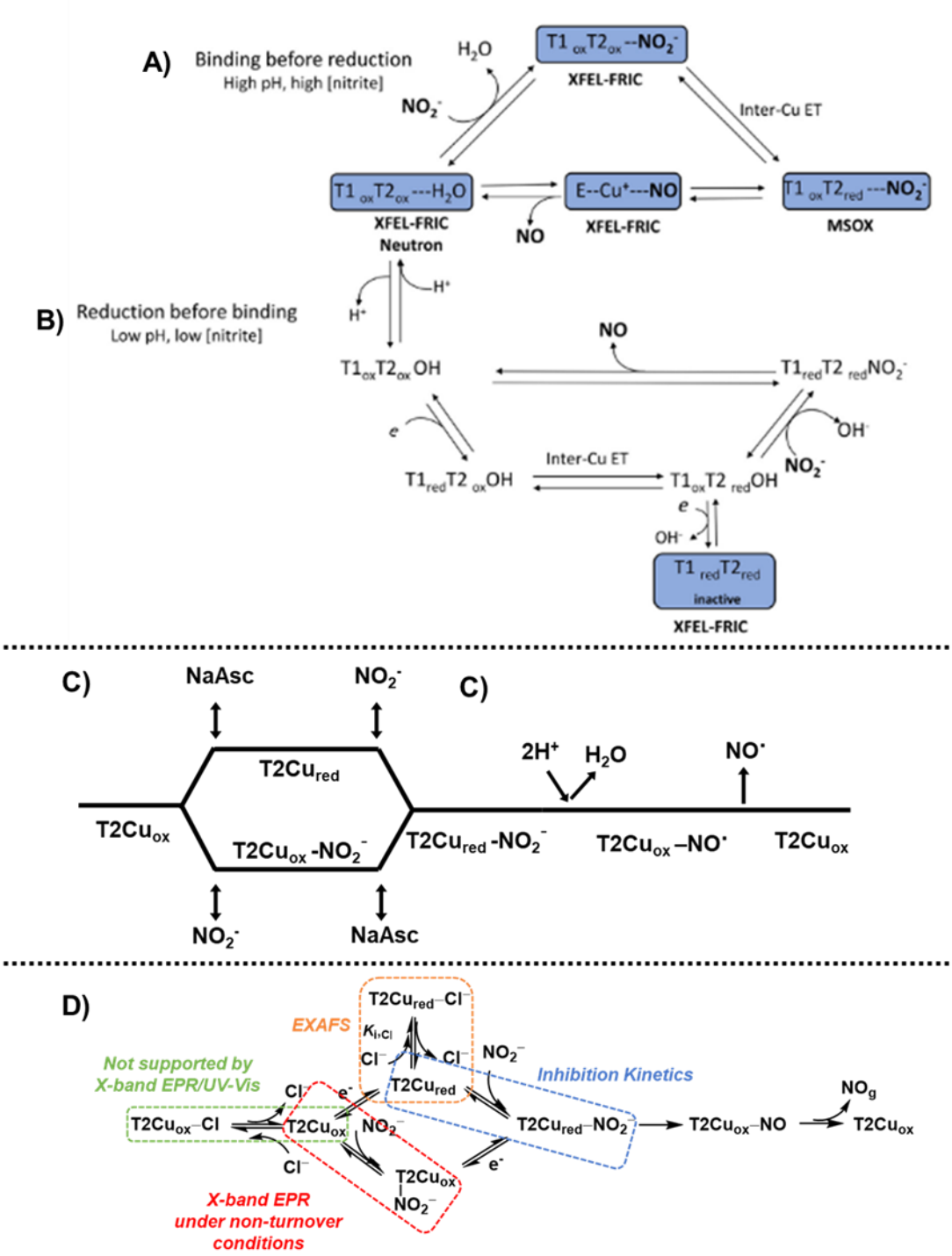


Figure III-19: Mechanism in native and designed CuNiRs, highlighting the *binding before reduction* pathway (**A**), and the *reduction before binding* pathway (**B**) (*Reproduced with permission from Ref.* [48] *Copyright 2022 Elsevier B.V.*), **C**) Cleland diagram of the proposed mechanisms of nitrite reduction to NO(g) by TRIW, and **D**) The proposed substrate binding events during the catalytic mechanism of *de novo* designed CuNiRs based on the experiments in Chapter III.

The reduction of the Cu TRIW-H is reported to be ~ 400 mV (SHE) at pH 5.9 and therefore strongly favor the reduced form of the enzyme.[31] Both the XAS structure and the inhibition pattern suggest the Cl^- and NO_2^- compete for the Cu(I)-pyridyl sites. The linearity of this secondary plot also suggests that only one Cl^- anion binds to the Cu(I) active site as two Cl^- binding would yield a parabolic dependence on $[Cl^-]$ which cannot be distinguished from the (E_t/ν_{obs}) vs. $1/[NO_2^-]$ plot; however, the velocity equation that would model this modified catalytic cycle would have a $[Cl^-]^2$ dependence on the $(1/k_{cat})^{App}$ and $(K_m/k_{cat})^{App}$ terms which would result in the $slope_{1/S}$ vs. $[Cl^-]$ secondary plot having a hyperbolic shape and not a linear one as is observed (*See Segel pg. 467*).[62] With these in mind, the adduct observed in the EXAFS above likely represents the species captured during the catalytic cycle under turnover conditions. Admittedly, it is possible that nitrite could form an adduct with $Cu(I)Py_2Cl$ (*i.e.*, EIS complex), resulting in product formation with equal or less propensity than the enzyme-substrate complex (ES), which is dissimilar to a non-competitive mechanism. This cannot be distinguished from the (E_t/ν_{obs}) vs. $1/[NO_2^-]$ curves (*i.e.*, one-site partial competitive mechanism vs. one-site pure competitive mechanism).[62] If a $Cu(I)Py_2Cl$-(NO_2^-) was catalytically active, then at any particular $[NO_2^-]$ concentration, the addition of infinite $[Cl^-]$ would drive all enzyme forms to $Cu(I)Py_2Cl$ and $Cu(I)Py_2Cl$-NO_2^-, where the latter would be able to turnover to product (*i.e.*, one-site partial competitive mechanism vs. one-site pure competitive mechanism).[62] In other words, the ν vs. $[Cl^-]$ plot at fixed $[NO_2^-]$ would not be driven to $V_{max}=0$ M s^{-1} at high chloride concentrations. In practice this can be difficult to assess with the same level of confidence as, for example, determining the number of chloride binding sites. However, based on the fittings using equation III-4, this pathway is unlikely to occur . I have previously demonstrated in Chapter II that the alanine residues in the secondary coordination sphere relax the mostly 3-coordinate reduced enzyme to a more 2-coordinate form which coincides with a drop in the K_m values and constant k_{cat} values (Table III-5). While no structure has been reported of a the fully reduced T2Cu center bound to nitrite, the majority of Cu(I)-NO_2^- small molecule complexes have been described as N-bound nitrites (η^1-N mode), suggesting that the energy of this form is relatively low and likely the correct binding isomer in these designs, as

well.[43,63,64] However, it cannot be ruled out that the Cu(I)- η^1-O isomer is the important intermediate as Cu(I)-η^1-N and Cu(I)-η^1-O linkage isomers have been observed to co-crystallize in synthesized complexes, which is consistent with the conclusions of DFT calculation suggesting the relative energies are similar. These results indicate that the energies of these two isomers are similar, but the η^1–N linkage appears to be slightly more stable.

In case of a pure competitive mechanism, the $K_{i,Cl}$ values reflect a true dissociation constant of the chloride to the reduced form. The relative drop in $K_{i,Cl}$ and K_m values may reflect a structural analogy between chloride and nitrite during the catalytic cycle. Using this model, the trend in the chloride $K_{i,Cl}$ values for the 3'Py sites ($K_{i,Cl,Leu}$=67 (±20) mM to $K_{i,Cl,L1A}$=33 (±6) mM) reflects the steric constraints that the substrate experiences during the catalytic cycle. The relative changes in the K_m values between the designs with 2- and 3-coordinate geometry reflect nitrite's access to a less sterically crowded primary coordination sphere, where nitrite is more easily accommodated to promote catalysis. This is consistent with the original proposal that substrate access is one of the limiting factors in this coiled coil design. Moreover, this $K_{i,Cl}$ was similar to the most active TRIW-4'Py L19A which suggests this is likely a universal among the alanine derivatives. Under this model both a 2- or 3-coordinate resting state are catalytically competent, which is opposed to

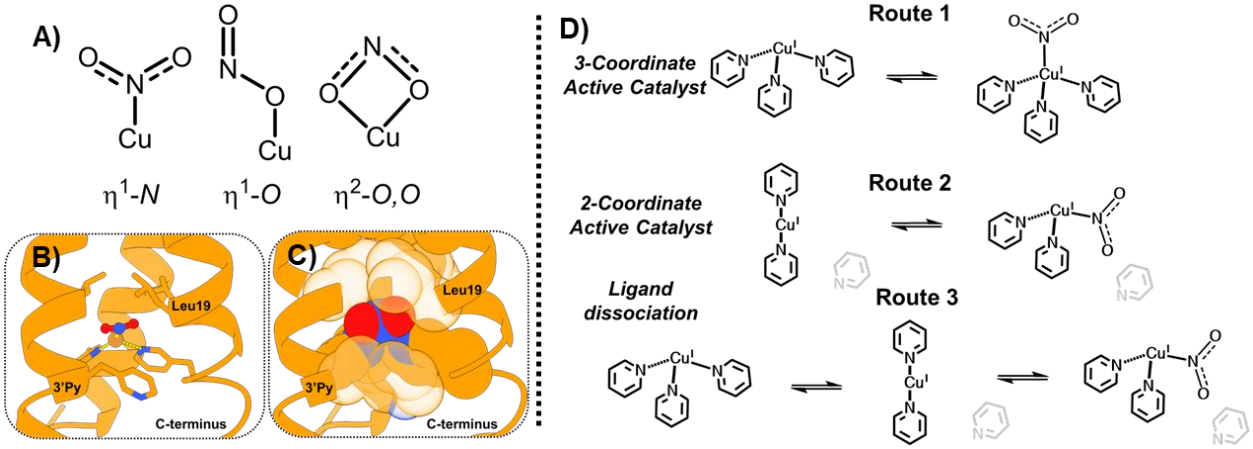


Figure III-20: Binding isomers to the Cu(I) enzyme and proposed enzyme substrate complex: **A**) Nitrite binding isomers to copper, **B**) model proposed nitrite binding in a proposed η^1-N fashion to Cu(I)-TRIW-3'Py, **C**) space-filling model highlighting the reduced steric in 3-coordinate Cu(I)-nitrite adduct in (**B**), and **D**) Simple scheme of possible nitrite binding pathways to the reduce enzyme substrate complex.(Grayed out pyridine represent the non-chelated pyridine.)

a thermodynamically inactive 3-coordinate reduced enzyme (nitrite does not bind to the Cu(I)$(His)_3$) that have been reported in *wt* CuNiRs.[46] To this point, the gradual isomerization of $Cu(His_3)$-OH_2 T2Cu_{red} to a $Cu(His)_3$ in *Af*CuNiR [the inactive form], according to Canters *et al.*, is in agreement with the suggested random-sequential mechanism since it occurs more slowly than nitrite displacing the H_2O ligand at $[NO_2^-]>K_{d,red}$ (Figure III-19A-B).[49,48] This specific isomerization is likely not operating in these mimics since the copper EXAFS of the reduced enzymes are reasonably accounted for without the need to invoke a disordered $^-OH/H_2O$ in the primary coordination sphere in the reduced enzyme.[65,52] Depending on the binding mode of nitrite and the coordination number of the resting enzyme, the enzyme-substrate complex could be between 3- to 5-coordinate geometry, assuming the reduced enzyme at most forms a 3-coordinate resting enzyme (Figure III-20A-B). This is best described by *Route 1* and *Route 2*, where the lower energy Cu(I)-η^1-N adduct is predicted to form (Figure III-20D). If *Route 1* or *Route 2* were the preferred pathway for TRIW-X and TRIW-X L19A, respectively, then the k_{cat} may have been expected to change between the two design families, as the metal-to-ligand charge transfer from the Cu(I) to the N–O bond during the N–O bond cleaving step) is sensitive to both orbital energy

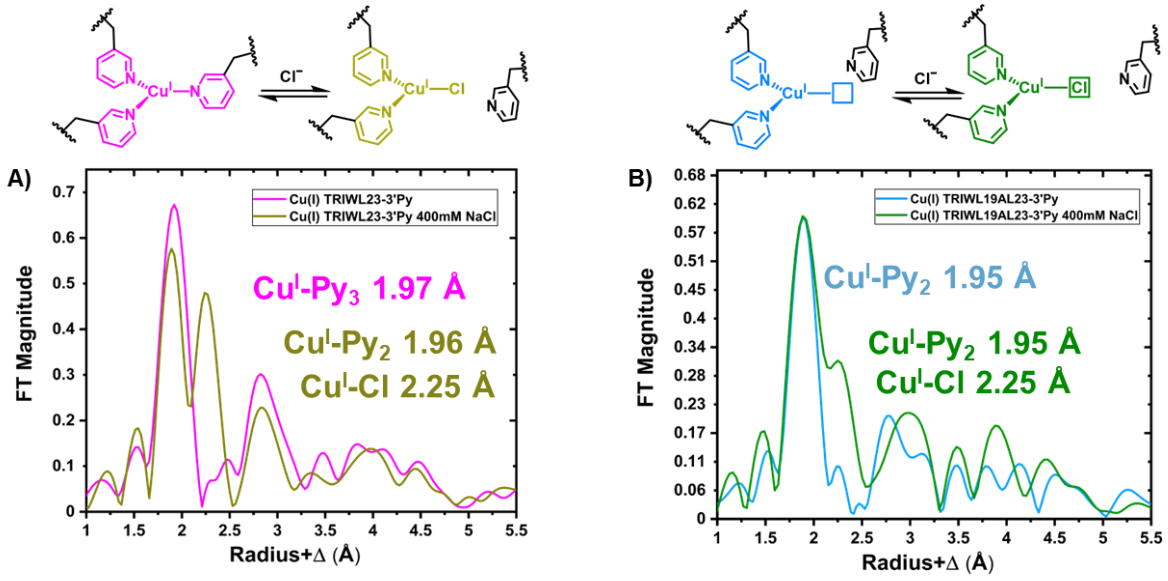


Figure III-21: Fourier Transform of 3'Py sites with and without Cl^-: **A)** Cu(I)-TRIW-3'Py with a proposed binding equilibrium and **B)** Cu(I)-TRIW-3'Py L19A with a proposed binding equilibrium during catalysis.

and orientation.[64,66] This is not consistent with the constant k_{cat} values reported in Chapter II nor the methyl-histidine analogs.

A slightly different interpretation is the steric constraints of the bulky leucine layer, and the 3 pyridine ligands hinder the formation of the 4-coordinate enzyme substrate complex. This reconciles *Route 1* and *Route 2* with the kinetics observed in Chapter II and Chapter III. Interestingly, the chloride adducts all resemble 3-coordinate complexes, irrespective of the starting geometry of the resting enzyme (Figure III-21). The removal of a pyridine ligand in favor of a nitrite ligand from the primary coordination sphere may be caused, from a structural perspective, by the steric crowding from the pyridine ligands coupled with bulky leucine residues above the copper center (Figure III-18B and D). This step would be expected to occur before nitrite reduction and therefore would influence the k_{cat}/K_m and K_m values, while the k_{cat} values would remain constant (Figure III-20, *Route 3*). The TRIW-X'Py 19A designs not only benefited from their 2-coordinate geometry to yield an accessible copper center without the need to lose a pyridine ligand, but also provided the required space above for the unbound pyridine to access without imposing a steric penalty on the nearby residues (Figure III-20B). It is also possible the unbound pyridine points down towards the more open C-terminus rather than pointing towards the active site above, which would result in greater access to the 2-coordinate complex. Before these results, the observed decrease in the K_m values associated with the alanine mutants may have been interpreted in terms of more space above the active site or, in other words, to imply that a substrate binding cavity was blocked by the leucine layer and limiting substrate access.[24] This can be seen in the TRIW-δ_mH L19A and TRIW-δ_mH designs where only the K_m changes and very presumably TRIW-ε_mH L19A and TRIW-ε_mH (Table III-5). Simply considering substrate access in this way is likely not sufficient as an explanation for the increase in the k_{cat}/K_m observed in Chapter II and among the histidine analogs. The increase in CuNiR activity upon the addition of the L19A layer above the Cu(I)His_3 center (*e.g.*, TRIW-H L19A) was speculated to be due to nitrite accessing the substrate binding pocket.[24] This design likely benefits from just more than substrate access as the increase in k_{cat}/K_m is coupled to an increase in k_{cat}, which the substrate association step cannot not

perturb, even when it's the highest transition state in the catalytic cycle (*i.e.*, the rate limiting step).[67] In this case, it cannot rule out that *Route 1* governs the substrate binding steps in Cu(I) TRIW-H or *Route 2* from governing that of Cu(I) TRIW-H L19A, separately(Figure III-20D)[24,52] However, the binding pathway in *Route 3* alone would not be expected to explain the increase in k_{cat} without considering the consequences of this route on the steps after the binding of nitrite (*e.g.*, change in substrate's binding isomer preference, H^+ transfer, or rate of product release).

There clearly are limitations of this peptide system to mimic the native CuNiR. These limitations range from the lack of incorporation of proton-donor/acceptor residues for accelerated substrate activation to the enforcement of the reduced enzyme's authentic coordination number as in native CuNiRs. Therefore, these designed peptides could not replicate key features of the proposed mechanism of native CuNiR such as the rate-limiting electron transfer step for turnover in CuNiR which controls the substrate binding predominantly to the oxidized T2Cu center. What has yet to be demonstrated during *wt* CuNiRs' "*binding after electron transfer"* pathway (under turnover conditions), is the coordination number of the reduced enzyme-substrate complex which is likely a function of the positions of both Asp_{CAT} and Ile_{CAT} residues during the pathway.[10,68] This residues are critical, only activating the substrate at the reduced T2Cu center, but orientating the substrate to the oxidized form governing. However, it has been shown that substrate binds to oxidized form of Cu(II) TRIW-H with a $K_{d,app}$ ~1.5-2.1 mM, resulting in a decrease in the $A_{\|}$ from 197 to 174 ($\times 10^{-4}$ cm^{-1}) and a slight increase in the g_z value to 2.282 from 2.270 (at 50 eqv. NO_2^-).[61] In the case of the pyridyl active sites, the addition of 50 eqv. NO_2^-, two sets of Cu(II) hyperfine couplings in the g_z region are observed and fitted (Table III-2). Admittingly, little structural information can be concluded from only the X-band EPR spectra of these two species; however, that does not mean there is nothing that can be concluded about these copper centers. For Cu(II) complexes, the electronic ground state depends on the ligand field experienced by the Cu(II) ion. Specifically, the ground state is $d_{x^2-y^2}$ ($g_z > g_y > g_x > 2.0023$) for coordination geometries corresponding to either Jahn-Teller axial elongated octahedral, square pyramidal (C_{4v}), or square planar, while the ground state is d_{z^2} ($g_\perp > g_\| = 2.0023$) when the coordination around the copper

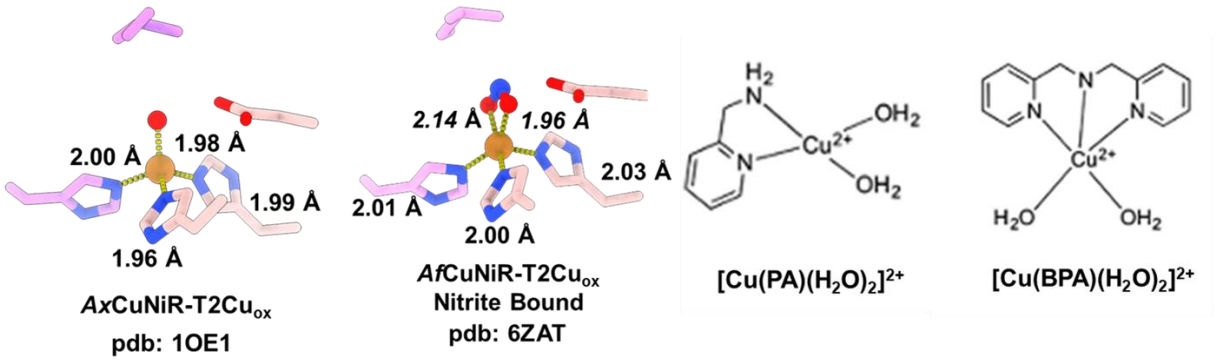
ion is a trigonal bipyramid (D_{3h}) or a compressed octahedron (D_{4h}).[69,70] The simulated EPR parameters in Chapter II suggest these new species are distinct from the nitrite-free form (Table III-6).[65] Moreover, all are consistent with a $d_{x^2-y^2}$ ground state (($g_z>g_y>g_x>2.0023$) within a 4-coordiante ($CuN_{Py3}O/CuN_{Py2}O_2$) or 5-coordinate ($CuN_{Py3}O/CuN_{Py2}O_2$) ligand field (Table III-6).[71–73] Any structural model of the nitrite adduct must have a $d_{x^2-y^2}$ ground state (better described as $d_{x^2-y^2}/d_{xy}$ for lower than ideal symmetry), and *this requirement limits the possible geometry of the ligand field around the nitrite adduct* (Figure III-22). In general, 5-coordinate d^9 configuration exists either as trigonal bipyramids or square pyramids with distortions in-between that define the Berry pseudorotation pathway. However, a small amount of d_{z^2} will is likely needed to account for the slight rhombic character between the g_x and g_y values observed for the higher $A_{\|}$ species in TRIW-4'Py L19A and TRIW-3'Py adducts which could be a result of a distortion or binding along the axial axis (Table III-6, Figure III-22C). To this point, an example of a structure not possible would be a tetragonally elongated D_{2d} tetrahedron which would have predominantly d_{z^2} ground state character, which would produce a rhombic splitting that is not observed.[74,75] On the other hand, if nitrite forms a 5-coordinate adduct with the copper center, it will likely have structural parameters between trigonal bipyramidal (D_{3h}) and square pyramidal (C_{4v}). It will be closer to the latter in the Berry pseudorotation pathway due to its predominantly $d_{x^2-y^2}$ ground state with a small amount of mixture from d_{z^2} character between the two structure ($105°<\theta<120°$ and $150°<\phi<180°$) (Figure III-22C).[76] It is possible that an axial elongated trigonal bipyramidal ligand field can produce the required $d_{x^2-y^2}$ ground state (Figure III-22D).[69] With 4-coordinate geometry, a square planar or distorted square planar structure may also be a possible structure (Scheme III-2, $[Cu(PA)(H_2O)_2]_2^+$).[72,74,77,78] All major species have a lower $A_{\|}$ species relative to the nitrite free form, which is characteristic binding of the nitrite based on studies with native $T2Cu_{ox}$-NO_2 and the behavior of Cu(II) TRIW-H under these conditions (Table III-6).[44,66,79] This shift to a smaller spin density on the copper center hints that the SOMO has moved onto the nitrite ligand via σ or π bonding with the Cu(II) center in the bidentate mode.[80] However, the higher value suggests a less covalent interaction between copper and nitrite than observed in *Ax*CuNiR-NO_2^- (pH 7.0).

Table III-6: Relevant Cu(II) EPR comparisons [a]Data collected by Dr. Fangting Yu

Enzyme	g_z	g_y	g_x	$A_{\parallel}$ ($\times 10^{-4}$ cm^{-1})	Ref.
***Ax*CuNiR pH 7.0**	2.35	2.087	2.021	110	66
***Ax*CuNiR-NO_2^- pH 7.0**	2.29	2.045	2.023	123.4	81
***Ax*CuNiR-NO_2^- pH 5.5**	2.345	2.162	2.04	120	66
$[Cu(BPA)(H_2O)_2]^{2+}$	2.262	2.065	2.062	185	72
$[Cu(PA)(H_2O)_2]^{2+}$	2.303	2.071	2.061	178	72
Cu(II)-TRIW-4'Py L19A	2.28	2.04	2.04	169	--
50 eqv. NO_2^- **Cu(II) Species #1 [32%]** **Cu(II) Species #2 [68%]**	2.268 2.282	2.027 2.039	2.053 2.039	178.5 158.5	--
Cu(II)-TRIW-3'Py	2.29	2.04	2.04	168	
50 eqv. NO_2^- **Cu(II) Species #1 [62%]** **Cu(II) Species #2 [38%]**	2.263 2.295	2.052 2.041	2.036 2.039	177.4 161.0	--
Cu(II)-TRIW-3'Py L19A	2.29	2.05	2.04	170	--
50 eqv. NO_2^- **Cu(II) Species #1 [70%]** **Cu(II) Species #2 [30%]**	2.269 2.302	2.040 2.044	2.036 2.038	162.2 156.7	--
Cu(II)-TRIW-H[a] **50 eqv. NO_2^-**	2.270 2.282	2.050 2.034		197.1 174.7	--

The crystal structures in **Scheme III-2** are those referenced in the **Table III-6**

Scheme III-2



This suggest a structural modified adduct possibly resulting from an isomer other than the η^2-O,O,but one that is less π-acidic (*i.e.*, η^1-O, η^1-N).[81] The adduct with the higher $A_{\|}$ values and lower g_z values suggest a stronger equatorial ligand field than the nitrite-free enzyme. However, ESEEM and ENDOR spectroscopy would be required to experimentally verify the nature of the SOMO in the bidentate mode.[44] Given the results in the EPR, the relative binding preference for nitrite in the absence of the Asp_{CAT} and Ile_{CAT} residues is uncertain given the two species observed in the EPR with the pyridyl site.

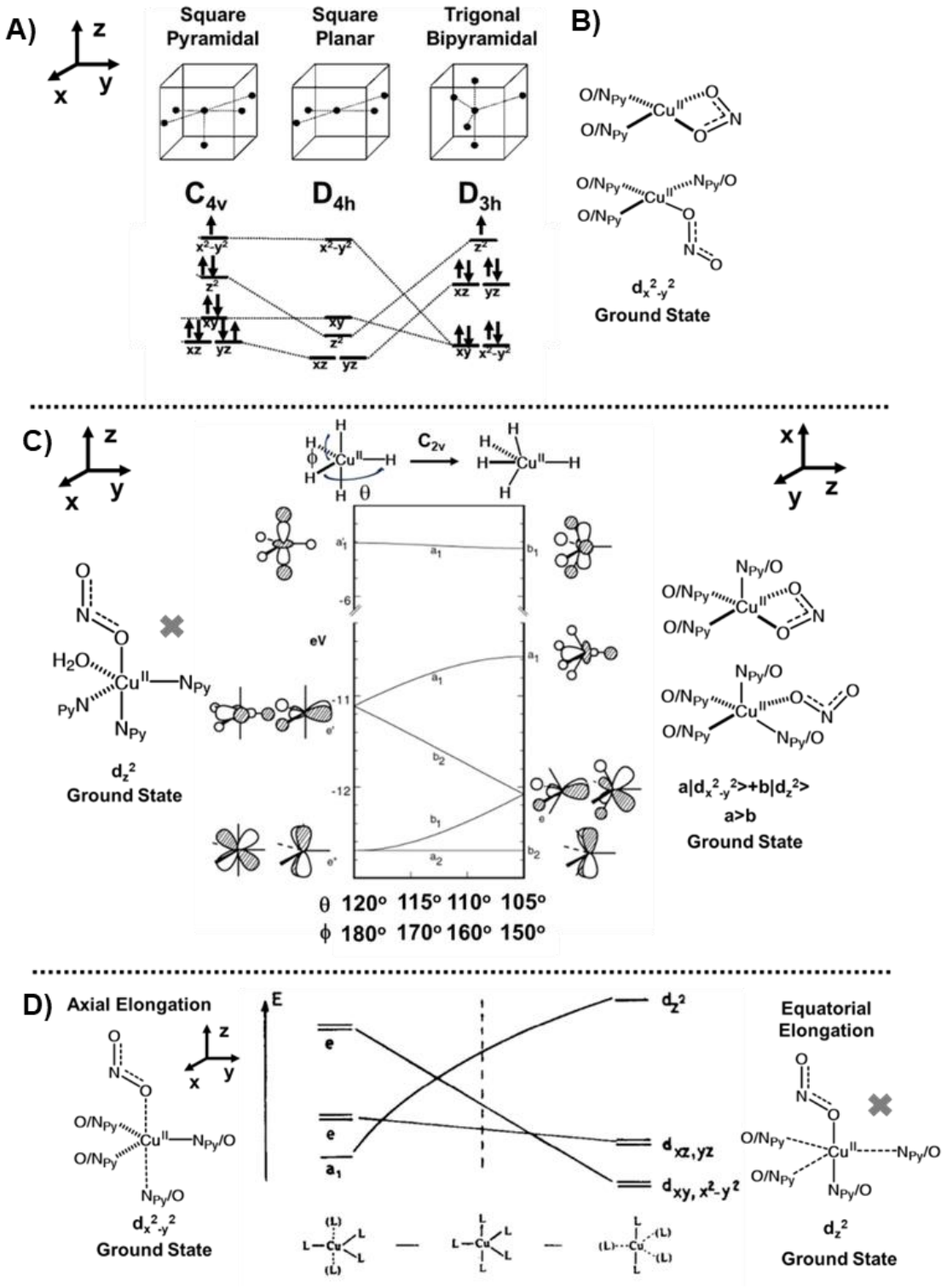


Figure III-22: Possible Cu(II) nitrite adducts consistent with the X-Band EPR: **A)** Simple ligand field splitting for Cu(II) in 4 and 5-coordinate geometry, **B)** Possible models with square planar adduct, **C**) Berry Pseudorotation correlation diagram highlighting the different ground state adducts in the 5-coordinate geometry (*note the change in coordinate axis in square bipyramidal structure*), and **D**) Correlation diagram highlighting the rational for a axial elongated trigonal bipyramidal (TP) geometry as opposed to a equatorial elongated TP.

Conclusion:

Chapter III goes through a series of experiments that investigate substrate binding to the oxidized and reduced enzyme forms to understand the high K_m values from Chapter II and previous designs. The oxidized form of the enzyme produced two electrically inequivalent copper forms in the presence of 50 eqv. nitrite, signifying nitrite binding in two non-specific isomers to the copper center. Furthermore, the type of nitrite bound was dependent on the steric bulk present in the layer close to the T2Cu site. However, given this and the conditions of the assay in Chapter II, the nature of the Cu(I) form was expected to influence the K_m and k_{cat}/K_m value. Therefore, an excess concentration of the electron donor was used which allowed for the study of this *binding after reduction* pathway. This pathway was probed using Cl^- which generates a species that is best described as a $Cu(I)Py_2Cl$ structure upon the addition of excess NaCl (400 mM). From this and examining the Lineweaver-Burk plot, Cl^- binds to the same enzyme form as the substrate during the catalytic cycle, exhibiting an inhibitory pattern that is most consistent with Cl^- acting as a competitive type of inhibitor with respect to NO_2^- at the reduced enzyme form. The linearity of the secondary plot further indicates only one Cl^- anion binds to the Cu(I) active site during the mechanism which supports the XAS measurement. Therefore, the Cl^- adduct observed in the EXAFS is likely the same adduct observed during catalytic turnover in the presence of Cl^-. The $K_{i,Cl}$ values suggested a few possible mechanisms; However, one was more consistent with the data in Chapter II and suggested that the L19A designs (including methyl-histidine and likely the histidine design) not only benefit from addition space above the active site, but also benefit from their 2-coordinate geometry to yield a more accessible reduced copper center. In the next chapter, I combine what I have learned in Chapters II and Chapter III to design heptad discontinuities and modify the supercoil of the coiled coil to alter the ligands around the copper center.

References:

(1) Cleland, W. W. Kinetic Competence of Enzymic Intermediates: Fact or Fiction? *Biochemistry* **1990**, *29* (13), 3194–3197.

(2) Palfey, B. A. New Approaches for Flavin Catalysis. *Methods Enzymol.* **2019**, *620*, 2–544.

(3) Lineweaver, H.; Burk, D. The Determination of Enzyme Dissociation Constants. *J. Am. Chem. Soc.* **1934**, *56* (3), 658–666.

(4) Janson, C. A.; Cleland, W. W. The Kinetic Mechanism of Glycerokinase. *J. Biol. Chem.* **1974**, *249* (8), 2562–2566.

(5) Cleland, W. W. The Kinetics of Enzyme-Catalyzed Reactions with Two or More Substrates or Products. II. Inhibition: Nomenclature and Theory. *BBA - Biochim. Biophys. Acta* **1963**, *67* (C), 173–187.

(6) Fukuda, Y.; Tse, K. M.; Lintuluoto, M.; Fukunishi, Y.; Mizohata, E.; Matsumura, H.; Takami, H.; Nojiri, M.; Inoue, T. Structural Insights into the Function of a Thermostable Copper-Containing Nitrite Reductase. *J. Biochem.* **2014**, *155* (2), 123–135.

(7) Hedison, T. M.; Shenoy, R. T.; Iorgu, A. I.; Heyes, D. J.; Fisher, K.; Wright, G. S. A.; Hay, S.; Eady, R. R.; Antonyuk, S. V; Hasnain, S. S.; Scrutton, N. S. Unexpected Roles of a Tether Harboring a Tyrosine Gatekeeper Residue in Modular Nitrite Reductase Catalysis. *ACS Catal.* **2019**, *9* (7), 6087–6099.

(8) Tocheva, E. I.; Eltis, L. D.; Murphy, M. E. P. Conserved Active Site Residues Limit Inhibition of a Copper-Containing Nitrite Reductase by Small Molecules. *Biochemistry* **2008**, *47* (15), 4452–4460.

(9) Sen, K.; Hough, M. A.; Strange, R. W.; Yong, C. W.; Keal, T. W. A QM/MM Study of Nitrite Binding Modes in a Three-Domain Heme-Cu Nitrite Reductase. *Molecules* **2018**, *23* (11), 2997.

(10) Strange, R. W.; Murphy, L. M.; Dodd, F. E.; Abraham, Z. H. L.; Eady, R. R.; Smith, B. E.; Hasnain, S. S. Structural and Kinetic Evidence for an Ordered Mechanism of Copper Nitrite Reductase. *J. Mol. Biol.* **1999**, *287* (5), 1001–1009.

(11) Hart, P. J.; Balbirnie, M. M.; Ogihara, N. L.; Nersissian, A. M.; Weiss, M. S.; Valentine, J. S.; Eisenberg, D. A Structure-Based Mechanism for Copper-Zinc Superoxide Dismutase. *Biochemistry* **1999**, *38* (7), 2167–2178.

(12) Abraham, Z. H. L.; Smith, B. E.; Howes, B. D.; Lowe, D. J.; Eady, R. R. PH-Dependence for Binding a Single Nitrite Ion to Each Type-2 Copper Centre in the Copper-Containing Nitrite Reductase of Alcaligenes Xylosoxidans. *Biochem. J.* **1997**, *324* (2), 511–516.

(13) Antonyuk, S. V.; Strange, R. W.; Sawers, G.; Eady, R. R.; Hasnain, S. S. Atomic Resolution Structures of Resting-State, Substrate- and Product-Complexed Cu-Nitrite Reductase Provide Insight into Catalytic Mechanism. *Proc. Natl. Acad. Sci. U. S. A.* **2005**, *102* (34), 12041–12046.

(14) Fee, J. A.; Ward, R. L. Evidence for a Coordination Position Available to Solute Molecules on One of the Metals at the Active Center of Reduced Bovine Superoxide Dismutase. *Biochem. Biophys. Res. Commun.* **1976**, *71* (2), 427–437.

(15) Tandrup, T.; Muderspach, S. J.; Banerjee, S.; Santoni, G.; Ipsen, J.; Hernández-Rollán, C.; Nørholm, M. H. H.; Johansen, K. S.; Meilleur, F.; Lo Leggio, L.; Moffat, K. Changes in Active-Site Geometry on X-Ray Photoreduction of a Lytic Polysaccharide Monooxygenase Active-Site Copper and Saccharide Binding. *IUCrJ* **2022**, *9* (Pt 5), 666–681.

(16) Walton, P. H.; Davies, G. J. On the Catalytic Mechanisms of Lytic Polysaccharide Monooxygenases. *Current Opinion in Chemical Biology*. 2016, pp 195–207.

(17) Wang, B.; Walton, P. H.; Rovira, C. Molecular Mechanisms of Oxygen Activation and Hydrogen Peroxide Formation in Lytic Polysaccharide Monooxygenases. *ACS Catal.* **2019**, *9* (6), 4958–4969.
(18) Tepper, A. W. J. W. Structure and Mechanism of the Type-3 Copper Protein Tyrosinase, Leiden, Universiteit, 2005.
(19) Yu, F. De Novo Designed Metallopeptides with a Type 2 Copper Center : A Structural and Functional Model for Copper Nitrite Reductase By, University of Michigan, 2014.
(20) Halfen, J. A.; Mahapatra, S.; Wilkinson, E. C.; Gengenbach, A. J.; Young, V. G.; Que Jnr, L.; Tolman, W. B. Synthetic Modeling of Nitrite Binding and Activation by Reduced Copper Proteins. Characterization of Copper(I)-Nitrite Complexes That Evolve Nitric Oxide. *J. Am. Chem. Soc.* **1996**, *118* (4), 763–776.
(21) Kumar, M.; Dixon, N. A.; Merkle, A. C.; Zeller, M.; Lehnert, N.; Papish, E. T. Hydrotris(Triazolyl)Borate Complexes as Functional Models for Cu Nitrite Reductase: The Electronic Influence of Distal Nitrogens. *Inorg. Chem.* **2012**, *51* (13), 7004–7006.
(22) Zuo, Y.; Deng, Y. The Near-UV Absorption Constants for Nitrite Ion in Aqueous Solution. *Chemosphere* **1998**, *36* (1), 181–188.
(23) Wagner, B. A.; Buettner, G. R. Stability of Aqueous Solutions of Ascorbate for Basic Research and for Intravenous Administration. *Adv. Redox Res.* **2023**, *9*, 100077.
(24) Koebke, K. J.; Yu, F.; Salerno, E.; Van Stappen, C.; Tebo, A. G.; Penner-Hahn, J. E.; Pecoraro, V. L. Modifying the Steric Properties in the Second Coordination Sphere of Designed Peptides Leads to Enhancement of Nitrite Reductase Activity. *Angew. Chemie* **2018**, *130* (15), 4018–4021.
(25) Stoll, S.; Schweiger, A. EasySpin, a Comprehensive Software Package for Spectral Simulation and Analysis in EPR. **2005**.
(26) Weng, T. C.; Waldo, G. S.; Penner-Hahn, J. E. A Method for Normalization of X-Ray Absorption Spectra. In *Journal of Synchrotron Radiation*; 2005; Vol. 12, pp 506–510.
(27) Ravel, B.; Newville, M. ATHENA, ARTEMIS, HEPHAESTUS: Data Analysis for X-Ray Absorption Spectroscopy Using IFEFFIT. In *Journal of Synchrotron Radiation*; 2005; Vol. 12, pp 537–541.
(28) Royappa, A. T.; Royappa, A. D.; Moral, R. F.; Rheingold, A. L.; Papoular, R. J.; Blum, D. M.; Duong, T. Q.; Stepherson, J. R.; Vu, O. D.; Chen, B.; Suchomel, M. R.; Golen, J. A.; André, G.; Kourkoumelis, N.; Mercer, A. D.; Pekarek, A. M.; Kelly, D. C. Copper(I) Oxalate Complexes: Synthesis, Structures and Surprises. *Polyhedron* **2016**, *119*, 563–574.
(29) Dimakis, N.; Bunker, G. XAFS Debye-Waller Factors for Zn Metalloproteins. *Phys. Rev. B - Condens. Matter Mater. Phys.* **2004**, *70* (19), 1–12.
(30) Stern, E. A. Number of Relevant Independent Points in X-Ray-Absorption Fine-Structure Spectra. *Phys. Rev. B* **1993**, *48* (13), 9825–9827.
(31) Tegoni, M.; Yu, F.; Bersellini, M.; Penner-Hahn, J. E.; Pecoraro, V. L. Designing a Functional Type 2 Copper Center That Has Nitrite Reductase Activity within α-Helical Coiled Coils. *Proc. Natl. Acad. Sci. U. S. A.* **2012**, *109* (52), 21234–21239.
(32) Brown, I. D.; Altermatt, D. Bond-valence Parameters Obtained from a Systematic Analysis of the Inorganic Crystal Structure Database. *Acta Crystallogr. Sect. B* **1985**, *41* (4), 244–247.
(33) Balamurugan, R.; Palaniandavar, M.; Srinivasa Gopalan, R. Trigonal Planar Copper(I) Complex: Synthesis, Structure, and Spectra of a Redox Pair of Novel Copper(II/I) Complexes of Tridentate Bis(Benzimidazol-2′-Yl) Ligand Framework as Models for

Electron-Transfer Copper Proteins. *Inorg. Chem.* **2001**, *40* (10), 2246–2255.
(34) Scholz, S.; Lerner, H.-W.; Bolte, M. Chlorotripyridinecopper(I). *Acta Crystallogr. Sect. E Struct. Reports Online* **2002**, *58* (2), m72–m73.
(35) Ozutsumi, K.; Kawashima, T. Exafs and Spectrophotometric Studies on the Structure of Pyridine Complexes with Copper(II) and Copper(I) Ions in Aqueous Solution. *Polyhedron* **1992**, *11* (2), 169–175.
(36) Habiyakare, A.; Lucken, E. A. C.; Bernardinelli, G. Crystallographic and Copper-63,65 Nuclear Quadrupole Resonance Study of Two-Co-Ordinated Copper(I) Cations with Hindered Substituted Pyridine Ligands. *J. Chem. Soc. Dalt. Trans.* **1991**, No. 9, 2269–2273.
(37) Periyannan, G. R.; Costello, A. L.; Tierney, D. L.; Yang, K.-W.; Bennett, B.; Crowder, M. W. Sequential Binding of Cobalt(II) to Metallo-Lactamase CcrA †. *Biochemistry* **2006**, *45*.
(38) Kau, L. shan; Spira-solomon, D. J.; Penner-Hahn, J. E.; Hodgson, K. O.; Solomon, E. I. X-Ray Absorption Edge Determination of the Oxidation State and Coordination Number of Copper: Application to the Type 3 Site in Rhus Vernicifera Laccase and Its Reaction with Oxygen. *J. Am. Chem. Soc.* **1987**, *109* (21), 6433–6442.
(39) Blackburn, N. J.; Strange, R. W.; Reedijk, J.; Volbeda, A.; Farooq, A.; Zubieta, J.; Karlin, K. D. X-Ray Absorption Edge Spectroscopy of Copper(I) Complexes. Coordination Geometry of Copper(I) in the Reduced Forms of Copper Proteins and Their Derivatives with Carbon Monoxide. *Inorg. Chem.* **1989**, *28* (7), 1349–1357.
(40) Rudolph, J.; Jacob, C. R. Revisiting the Dependence of Cu K-Edge X-Ray Absorption Spectra on Oxidation State and Coordination Environment. *Inorg. Chem.* **2018**, *57* (17), 10591–10607.
(41) Walroth, R. C.; Uebler, J. W. H.; Lancaster, K. M. Probing Cu I in Homogeneous Catalysis Using High-Energy-Resolution Fluorescence-Detected X-Ray Absorption Spectroscopy. *Chem. Commun.* **2015**, *51* (48), 9864–9867.
(42) Fittipaldi, M.; Wijma, H. J.; Verbeet, M. P.; Canters, G. W.; Huber, M. Electronic Structure of the Two Copper Sites in Nitrite Reductase by 9 and 95 GHz EPR on Cavity Mutants. *Appl. Magn. Reson.* **2006**, *30* (3–4), 417–426.
(43) Chandra Maji, R.; Mishra, S.; Bhandari, A.; Singh, R.; Olmstead, M. M.; Patra, A. K. A Copper(II) Nitrite That Exhibits Change of Nitrite Binding Mode and Formation of Copper(II) Nitrosyl Prior to Nitric Oxide Evolution. *Inorg. Chem.* **2018**, *57* (3), 1550–1561.
(44) Fittipaldi, M.; Wijma, H. J.; Verbeet, M. P.; Canters, G. W.; Groenen, E. J. J.; Huber, M. The Substrate-Bound Type 2 Copper Site of Nitrite Reductase: The Nitrogen Hyperfine Coupling of Nitrite Revealed by Pulsed EPR. *Biochemistry* **2005**, *44* (46), 15193–15202.
(45) Lehnert, N.; Cornelissen, U.; Neese, F.; Ono, T.; Noguchi, Y.; Okamoto, K. I.; Fujisawa, K. Synthesis and Spectroscopic Characterization of Copper(II)-Nitrito Complexes with Hydrotris(Pyrazolyl)Borate and Related Coligands. *Inorg. Chem.* **2007**, *46* (10), 3916–3933.
(46) Howes, B. D.; Abraham, Z. H. L.; Lowe, D. J.; Brüser, T.; Eady, R. R.; Smith, B. E. EPR and Electron Nuclear Double Resonance (ENDOR) Studies Show Nitrite Binding to the Type 2 Copper Centers of the Dissimilatory Nitrite Reductase of Alcaligenes Xylosoxidans (NCIMB 11015). *Biochemistry* **1994**, *33* (11), 3171–3177.
(47) Frandsen, K. E. H.; Simmons, T. J.; Dupree, P.; Poulsen, J. C. N.; Hemsworth, G. R.; Ciano, L.; Johnston, E. M.; Tovborg, M.; Johansen, K. S.; Von Freiesleben, P.; Marmuse, L.; Fort, S.; Cottaz, S.; Driguez, H.; Henrissat, B.; Lenfant, N.; Tuna, F.; Baldansuren, A.; Davies, G. J.; Lo Leggio, L.; Walton, P. H. The Molecular Basis of Polysaccharide Cleavage by

Lytic Polysaccharide Monooxygenases. *Nat. Chem. Biol.* **2016**, *12* (4), 298–303.
(48) Eady, R. R.; Samar Hasnain, S. New Horizons in Structure-Function Studies of Copper Nitrite Reductase. *Coordination Chemistry Reviews*. 2022.
(49) Wijma, H. J.; Jeuken, L. J. C.; Verbeet, M. P.; Armstrong, F. A.; Canters, G. W. A Random-Sequential Mechanism for Nitrite Binding and Active Site Reduction in Copper-Containing Nitrite Reductase. *J. Biol. Chem.* **2006**, *281* (24), 16340–16346.
(50) Ross, M. R.; White, A. M.; Yu, F.; King, J. T.; Pecoraro, V. L.; Kubarych, K. J. Histidine Orientation Modulates the Structure and Dynamics of a de Novo Metalloenzyme Active Site. *J. Am. Chem. Soc.* **2015**, *137* (32), 10164–10176.
(51) Fukuda, Y.; Hirano, Y.; Kusaka, K.; Inoue, T.; Tamada, T. High-Resolution Neutron Crystallography Visualizes an OH-Bound Resting State of a Copper-Containing Nitrite Reductase. *Proc. Natl. Acad. Sci. U. S. A.* **2020**, *117* (8), 4071–4077.
(52) Koebke, K. J.; Yu, F.; Van Stappen, C.; Pinter, T. B. J.; Deb, A.; Penner-Hahn, J. E.; Pecoraro, V. L. Methylated Histidines Alter Tautomeric Preferences That Influence the Rates of Cu Nitrite Reductase Catalysis in Designed Peptides. *J. Am. Chem. Soc.* **2019**, *141* (19), 7765–7775.
(53) Krzemiński, Ł.; Ndamba, L.; Canters, G. W.; Aartsma, T. J.; Evans, S. D.; Jeuken, L. J. C. Spectroelectrochemical Investigation of Intramolecular and Interfacial Electron-Transfer Rates Reveals Differences between Nitrite Reductase at Rest and during Turnover. *J. Am. Chem. Soc.* **2011**, *133* (38), 15085–15093.
(54) Habiyakare, A.; Lucken, E. A. C.; Bernardinelli, G. Nuclear Quadrupole Resonance and Crystallographic Studies of Three-Co-Ordinated Copper(I) Cations with Alkylpyridine Ligands. *J. Chem. Soc. Dalt. Trans.* **1992**, No. 17, 2591–2599.
(55) Kooij, B.; Varava, P.; Fadaei-Tirani, F.; Scopelliti, R.; Pantazis, D. A.; Van Trieste, G. P.; Powers, D. C.; Severin, K. Copper Complexes with Diazoolefin Ligands and Their Photochemical Conversion into Alkenylidene Complexes. *Angew. Chemie - Int. Ed.* **2023**, *62* (4), e202214899.
(56) Lucchese, B.; Humphreys, K. J.; Lee, D. H.; Incarvito, C. D.; Sommer, R. D.; Rheingold, A. L.; Karlin, K. D. Mono-, Bi-, and Trinuclear CuII-Cl Containing Products Based on the Tris(2-Pyridylmethyl)Amine Chelate Derived from Copper(I) Complex Dechlorination Reactions of Chloroform. *Inorg. Chem.* **2004**, *43* (19), 5987–5998.
(57) Allen, J. J.; Hamilton, C. E.; Barron, A. R. Molecular Structures of RN(H)Py (R = 2,4,6-Me3C 6H2, 2,6-Et2C6H3, Ph 3C), and the Copper Complex [Cu{(2,4,6-Me3C 6H2)N(H)Py}2]BF4. *J. Chem. Crystallogr.* **2009**, *39* (8), 573–580.
(58) Thorp, H. H. Bond Valence Sum Analysis of Metal-Ligand Bond Lengths in Metalloenzymes and Model Complexes. *Inorg. Chem.* **1992**, *31* (9), 1585–1588.
(59) Fukuda, Y.; Tse, K. M.; Nakane, T.; Nakatsu, T.; Suzuki, M.; Sugahara, M.; Inoue, S.; Masuda, T.; Yumoto, F.; Matsugaki, N.; Nango, E.; Tono, K.; Joti, Y.; Kameshima, T.; Song, C.; Hatsui, T.; Yabashi, M.; Nureki, O.; Murphy, M. E. P.; Inoue, T.; Iwatae, S.; Mizohata, E. Redox-Coupled Proton Transfer Mechanism in Nitrite Reductase Revealed by Femtosecond Crystallography. *Proc. Natl. Acad. Sci. U. S. A.* **2016**, *113* (11), 2928–2933.
(60) Reed, J. L. Hard and Soft Acids and Bases: Atoms and Atomic Ions. *Inorg. Chem.* **2008**, *47* (13), 5591–5600.
(61) Yu, F.; Penner-Hahn, J. E.; Pecoraro, V. L. De Novo-Designed Metallopeptides with Type 2 Copper Centers: Modulation of Reduction Potentials and Nitrite Reductase Activities. *J. Am. Chem. Soc.* **2013**, *135* (48), 18096–18107.

(62) Irwin H. Segel. *Enzyme Kinetics: Behavior and Analysis of Rapid Equilibrium and Steady-State Enzyme Systems*, Wiley Clas.; Wiley, 1993.
(63) van Langevelde, P. H.; Engbers, S.; Buda, F.; Hetterscheid, D. G. H. Elucidation of the Electrocatalytic Nitrite Reduction Mechanism by Bio-Inspired Copper Complexes. *ACS Catal.* **2023**, *13* (15), 10094–10103.
(64) Kujime, M.; Izumi, C.; Tomura, M.; Hada, M.; Fujii, H. Effect of a Tridentate Ligand on the Structure, Electronic Structure, and Reactivity of the Copper(I) Nitrite Complex: Role of the Conserved Three-Histidine Ligand Environment of the Type-2 Copper Site in Copper-Containing Nitrite Reductases. *J. Am. Chem. Soc.* **2008**, *130* (19), 6088–6098.
(65) Pitts, W. C.; Deb, A.; Penner-Hahn, J. E.; Pecoraro, V. L. Revving up a Designed Copper Nitrite Reductase Using Noncoded Active Site Ligands. *ACS Catal.* **2024**, *14* (6), 4362–4368.
(66) Ghosh, S.; Dey, A.; Sun, Y.; Scholes, C. P.; Solomon, E. I. Spectroscopic and Computational Studies of Nitrite Reductase: Proton Induced Electron Transfer and Backbonding Contributions to Reactivity. *J. Am. Chem. Soc.* **2009**, *131* (1), 277–288.
(67) Cleland, W. W.; Northrop, D. B. Energetics of Substrate Binding, Catalysis, and Product Release. *Methods Enzymol.* **1999**, *308*, 3–27.
(68) Wijma, H. J.; Jeuken, L. J. C.; Verbeet, M. P.; Armstrong, F. A.; Canters, G. W. A Random-Sequential Mechanism for Nitrite Binding and Active Site Reduction in Copper-Containing Nitrite Reductase. *J. Biol. Chem.* **2006**, *281* (24), 16340–16346.
(69) Reinen, D.; Friebel, C. Copper(2+) in 5-Coordination: A Case of a Second-Order Jahn-Teller Effect. 2. Pentachlorocuprate(3-) and Other CuIIL5 Complexes: Trigonal Bipyramid or Square Pyramid? *Inorg. Chem.* **1984**, *23* (7), 791–798.
(70) Goodman, B. A.; Raynor, J. B. Electron Spin Resonance of Transition Metal Complexes. *Adv. Inorg. Chem. Radiochem.* **1970**, *13* (C), 135–362.
(71) Solomon, E. I.; Szilagyi, R. K.; DeBeer George, S.; Basumallick, L. Electronic Structures of Metal Sites in Proteins and Models: Contributions to Function in Blue Copper Proteins. *Chemical Reviews*. 2004, pp 419–458.
(72) Spencer, J.; Stevens, J.; Perry, C.; Murphy, D. M. An EPR Investigation of Binding Environments by N-Donor Chelating Exchange Resins for Cu Extraction from Aqueous Media. *Inorg. Chem.* **2018**, *57* (17), 10857–10866.
(73) Hoffmann, S.; Szpakowska, M.; Uruska, I. EPR Study of Cu(II)Carboxylate Complexes with Pyridine Derivatives. *J. Magn. Reson.* **1986**, *68* (3), 490–498.
(74) Hoffmann, S. K.; Goslar, J. Crystal Field Theory and EPR Parameters in D2d and C2v Distorted Tetrahedral Copper(II) Complexes. *J. Solid State Chem.* **1982**, *44* (3), 343–353.
(75) Ziegler, T.; Jan Linderberg; John Scales Avery; Avery, J. E.; Sutcliffe, B. T.; McCaffery, A. J.; Mihail Atanasov, Dmitry Ganyushin, Kantharuban Sivalingam, F. N.; R. Stephen Berry, B. M. S. *Molecular Electronic Structures of Transition Metal Complexes II*, 1st ed.; Mingos, D. M. P., Day, P., Dahl, J. P., Eds.; Structure and Bonding; Springer Berlin Heidelberg: Berlin, Heidelberg, 2014; Vol. 58.
(76) Albright, T. A.; Burdett, J. K.; Whangbo, M. H. *Orbital Interactions in Chemistry: Second Edition*; 2013.
(77) Batra, G.; Mathur, P. Tetrahedrally Distorted Tetragonal Copper Complexes of a Tridentate Ligand. *Inorg. Chem.* **1992**, *31* (9), 1575–1580.
(78) Chen, P.; Bell, J.; Eipper, B. A.; Solomon, E. I. Oxygen Activation by the Noncoupled Binuclear Copper Site in Peptidylglycine α-Hydroxylating Monooxygenase. Spectroscopic

Definition of the Resting Sites and the Putative CuIIM-OOH Intermediate. *Biochemistry* **2004**, *43* (19), 5735–5747.
(79) Suzuki, S.; Deligeer; Yamaguchi, K.; Kataoka, K.; Kobayashi, K.; Tagawa, S.; Kohzuma, T.; Shidara, S.; Iwasaki, H. Spectroscopic Characterization and Intramolecular Electron Transfer Processes of Native and Type 2 Cu-Depleted Nitrite Reductases. *J. Biol. Inorg. Chem.* **1997**, *2* (2), 265–274.
(80) Michel Schosseler Dipl Chem ETH, P. Electron Paramagnetic Resonance Study of the Copper(Ll) Complexation with Carbonate Ligands in Aqueous Solution and at Calcium Carbonate Surface, ETH Zürich, 1969.
(81) Hedison, T. M.; Shanmugam, M.; Heyes, D. J.; Edge, R.; Scrutton, N. S. Active Intermediates in Copper Nitrite Reductase Reactions Probed by a Cryotrapping-Electron Paramagnetic Resonance Approach. *Angew. Chemie* **2020**, *132* (33), 14040–14044.

Chapter IV

Stretch, Twist, and Switch: *de novo* Designed Copper Nitrite Reductase Mimics with Sequence Discontinuities.

Introduction:

Local transitions away from the nominal heptad periodicity of 3.5 residues per turn are found in many naturally occurring coiled coils proteins (cc proteins), leading to a departure from Crick's "perfect" coiled-coil knob-into-hole packing model.[1] This results in either a local tightening or loosening of the 3SCC around the supercoil axis by locally adding or subtracting resides per turn. To better understand the implications of these transitions in periodicity, it is important to know that the periodicity of an un-supercoiled cc protein is not ideal for the minimization of steric interactions along the interfaces of multiple helices. To compensate, the vast majority of those found in nature form a twist along the central α-helix coils to form *knobs-into-hole* packing along this seam, forming the classic cc protein (*e.g.*, nominal cc proteins) that is characterized by a slight left-handed twist about the supercoil axis that distributes seven residues over two turns (3.5 residue/turn).[2] Along the sequence, the mean hydrophobicity of each position displays a seven-residue pattern, with the most hydrophobic residues occupying the core. Noticeably, this is not always observed when analyzing the sidechain angles (in reference to the α-carbon) in natural cc proteins. While this chapter focuses on discontinuities in terms of catalysis and metal binding, stammers and stutters have broad significance in cc proteins.[3,4] An important example of this is the Influenza hemagglutinin protein which is a homotrimeric glycoprotein found on the surface of influenza viruses and is integral to its infectivity. Moreover, the functions may help this virus outlive defense mechanism by rescuing replication early in the viral entry process in the current outbreak of "Bird flu" and responsible for the recent reports of human infections.[5]

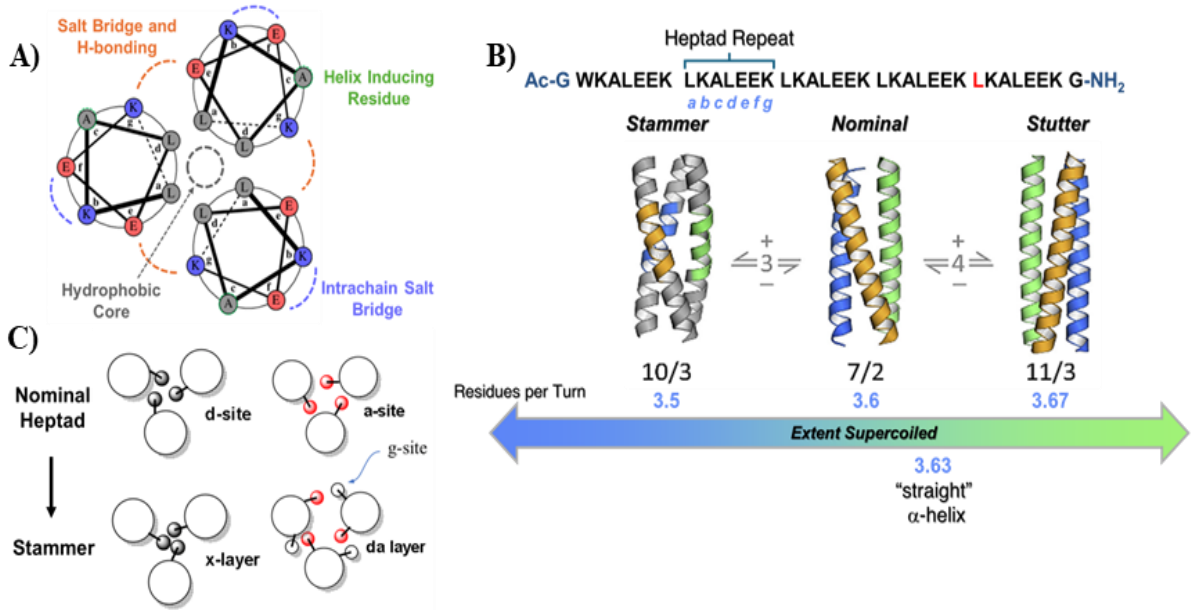


Figure IV-1: Summary of impacts of stammer inserts on 3SCC: **A**) Helical wheel of 3SCC of sequence used in this work highlights the geometry of the ***a***-site and ***d***-site residues' α-carbon and interactions associated with the coiled coil protein, **B**) **S**cheme highlighting the effects of stammer and stutter discontinues on the supercoiling, and **C**) The effects on adjacent ***a***-site and ***d***-site α-carbons directly below a stammer form distinct layers from numerous crystallographic studies.

The stutter has been implicated in mediating pH-dependent conformational effects leading to the speculation this is critical to its function.[6,7] Moreover, stammers are found in Long interspersed element 1 (LINE-1) open reading frame 1 protein (ORF1p) which is a nucleic acid chaperone responsible for L1 retrotransposition activity. L1 retrotransposition responsible for millions of years of ongoing genetic mutation, and implicated in neurologic diseases such as Rett's syndrome.[8–11]

The insertion of both 3-residues (*e.g.*, stammer) and 4-residues (*e.g.*, stutter) inserts into the coiled coil represents a less than a heptad motif, repacking the distinct sites (*e.g.*, ***a-g*** sites) into alternative positions downstream from this insertion.[4,12] The delocalization of these inserts can occur over multiple heptads which is thought to allow coiled coil proteins to accommodate multiple inserts without much loss in the stability of the protein. This is particularly important in transitions such as a skip (1-residue insert), where within a single heptad perspective, it would lead to periodicities of 2.66 or 4.0. The further a periodicity is from 3.63 residues per turn (*e.g.* an

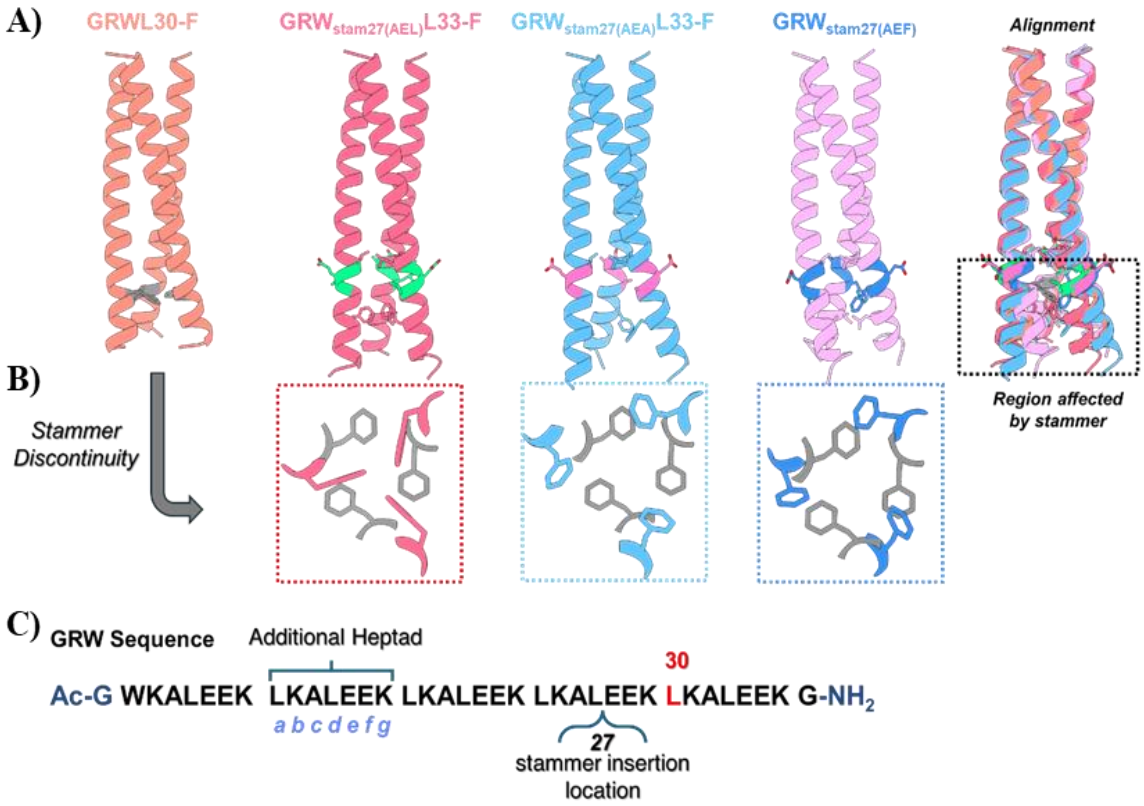


Figure IV-2: Overview of the design process of stammers into the GRAND scaffold: **A**) AlphaFold models of the nominal design (*e.g.*, GRW-F) and stammer design with phenylalanine as a steric substitute in the apo-form, **B**) **S**cheme highlighting the effects of stammer discontinues on the metal binding region, **C**) Sequence of the design used in this chapter (*e.g.*, GRW) that highlights the basic design elements in the scaffold.

undistorted helix), the tighter (lower number) or looser (higher number) the supercoiling of the coiled coil protein (Figure IV-1B). However, both 2.66 and 4.0 periodicities are outside the possible range that can be accommodated within a coiled coil protein. This accommodation over multiple heptads moves away from the notion of local discontinuities and treats these departures from the coiled coil from a more global perspective.

Despite extensive computational and crystallographic assessment, there remains virtually no information on the impact of such discontinuities on metal binding sites within cc proteins. The Pecoraro lab has investigated metal binding to ORF1p protein which contains one (MEL) stammer within the coiled coil domain. While only recently a structure has been solved of the three distinct domains of ORF1p, heavy metal-dependent activation of ORF1p *in vivo* has been

known but unexplained.[13] Pinter *et al*. demonstrated that the stammer did not exclude Pb(II) binding to $(Cys)_3$ layers found upstream or downstream of the MEL stammer within the ORF1p coiled coil domain (ORF1pCCD) which precipitated after 4 eqv. Pb(II).[14] Other metal structural motifs are thought to be able to form within the $(Cys)_3$ layers of ORF1pCCD. For example, Pinter *et al*. demonstrated that a Cu(I) binuclear Cu_2S_2 cluster could form within an analogous $(Cys)_3$ ***a***-site in TRIWL16C.[15] Although the structure of TRIWL16C and the MEL stammer analog were similar, the formation of Cu_2S_2 was observed to be less cooperative within the same pH range (*unpublished*). In contrast to Pb(II) or Cd(II), Cu(I) binds with a pH-dependent stoichiometry, likely forming binuclear centers at low pH levels. At pH 9, on the other hand, a deformed three coordinate Cu(I) center occurs prior to the appearance of the Cu_2 complex.

The impact on the catalytic activity of stammer containing peptides was previously reported for both hydrolytic and redox enzymes containing Zn(II) and Cu, respectively. The catalytic $(His)_3$ ***a***-site (L33H) was predicted to be most affected by the direct insertion of the (AEL) immediately after the L26 ***d***-site, since this insertion alters the relative position of the histidine to a more solvent-exposed ***g***-site, $GRW_{stam27AEL}L33H$.[16] When comparing the pseudo first order rate constants for Cu-$GRW_{stam27AEL}$L33H to Cu-GRW-H and Cu-TRIW-H, the copper nitrite reductase (CuNiR) activity is 4 times higher. In contrast, Zn(II)-TRIW-H and Zn(II)-GRW-H have background adjusted rate constants of 22×10^{-4} s^{-1} and 52×10^{-4} s^{-1}, respectively, whilst the pseudo first order esterase activity towards *para*-Nitrophenyl acetate (*p*-NPA) for the (AEL) stammer was lowered to almost background level hydrolysis of *p*-NPA. The authors speculated that the size difference between pNPA and NO_2^- may explain the divergence in reactivity. Zn(II)'s ability to catalyze the hydrolysis of *p*-NPA was obviously affected by the stammer modification. However, despite this, it is important to note that Zn(II) EXAFS, although remarkably similar between the parent proteins, is only capable of identifying different ligands with significantly different metal binding atoms (*e.g*., N vs S). Thus, nearly identical EXAFS might be obtained if a bound water is replaced by a coordinated carboxylate (such as Glutamate influencing the catalytic site).

Given that the orientation of the nitrogen on the active site pyridine ligands was essential to its success as the most efficient CuNiR enzyme in water, it is the goal of this chapter to modify the active site further by introducing the non-coded amino acids 3'Py and 4'Py near stammer inserts to influence the electronics of the copper center and CuNiR activity. Similar to naturally occurring cc proteins, sequence discontinuities change the orientation of a ligand's α-carbon, which can result in a minor but significant reorientation of the side chain inside the core of 3SCC (Figure IV-2).[8,9]. We can now examine 3'Py vs. 4'Py derivatives that present an electronically similar pyridyl nitrogen at different orientations and observe how the overwinding, conferred by a stammer, perturbs the kinetics either by changing the metal-coordination geometry or forming a more solvent-exposed environment.

Materials and Methods:

General Methods:

Most reagents were purchased from Sigma-Aldrich and Fisher Scientific and used as supplied unless otherwise indicated. All samples were prepared in doubled distilled water. All samples containing Cu(I) were prepared in a $N_{2(g)}$ glove box <1.5ppm O_2. Both Fmoc-3-(3'-pyridyl)-L-alanine and Fmoc-3-(4'-pyridyl)-L-alanine were purchased from Chem-Impex International, Inc or Aapptec and used without any further purification. Metal concentration was determined by inductively coupled plasma mass spectrometry using 1000ppm Cu standard. Concentrations of sodium nitrite and sodium ascorbate were determined by UV-VIS at 360 nm (ε =21.88 M^{-1} cm^{-1}) [17] and 251 nm (ε=8250 M^{-1} cm^{-1} at pH 5.9) [18], respectively.

Synthesis and purification of peptides:

Peptides were synthesized using standard Fmoc chemistry solid phase peptide synthesis on a Rink Amide Methylbenzhydrylamine (MBHA) resin with a Biotage Initiator+Alstra microwave synthesizer following previously reported procedures.[19] Some proteins in this chapter were synthesized on a Liberty Blue 2.0 using diisopropylcarbodiimide (DIC) as the coupling reagent

and OxymaPure as an additive for the inhibition of racemization. Deprotection steps were carried out for 90 seconds at 90°C using 10% Piperidine/DMF (v/v) and each coupling step was carried out at 90°C for 2 minutes. The crude peptide was simultaneously cleaved and deprotected using a cleavage cocktail consisting of trifluoroacetic acid (TFA), ethanedithiol, anisole, and thioanisole (90:3:2:5). The peptide was precipitated with cold diethyl ether, recovered by vacuum filtration, dissolved in 50% acetonitrile in double distilled H_2O (ddH_2O) and lyophilized to dryness. The lyophilized crude product was then redissolved in 10% acetic acid in ddH_2O and loaded onto a 300 mm x 50 mm DeltaPAK preparative C18 column using a Waters 600 HPLC system with the following parameters: flow rate: 20 mL/min, solvent A: 0.1% TFA in water, solvent B: 0.1% TFA in (90:10) CH_3CN:H_2O, linear gradient: 100:0 (A:B) increasing to 20:80 over 50 minutes and fractions containing pure peptide were combined and lyophilized to yield pure, white powder. The powder was redissolved in ddH_2O and lyophilized once again to remove any remaining acetonitrile after HPLC purification (confirmed by ^1H NMR). The dried peptide was stored at 0°C until use. Purity and identity were confirmed using an Agilent Q-TOF ESI-MS operated in positive ion mode.

Spectroscopy:

UV visible absorption data were collected with a Cary 100 spectrometer at room temperature in 10 mm quartz cuvettes. CD data were collected on a Jasco J-1500 CD spectropolarimeter at a trimer concertation of 3 µM in MES Buffer pH 5.9 (T=25°C). Electron paramagnetic resonance spectral data were collected using a Bruker EMXE 200 EPR spectrometer on solutions containing 1.5 mM peptide, 1 mM $CuSO_4$, 30% glycerol, and 50 mM MES at pH 5.9. The EPR spectra were processed using the *MATLAB* ver. R2020b and EasySpin.[20] Simulations were also performed using EasySpin to determine the g_z, g_y, g_x, $A_{||}$, and $A_{\perp}$ values.

Guanidinium Denaturation Titration:

Guanidinium-HCl denaturation titrations were carried out using Jasco J-1500 CD spectropolarimeter with Hellma Quartz 1mm 0.4mL cuvettes. Before use, guanidinium HCl was added to a round bottom flask and heated overnight at 60°C under high vac (50 mtorr) to remove excess water before weighing and using.

$$MRE = \left(MRE_f + M_f \times [Gdn]\right) + \left(MRE_u + M_u \times [Gdn]\right) \times \frac{e^{\frac{(m\times[Gdn]-G)}{R\times T}}}{1 + e^{\frac{(m\times[Gdn]-G)}{R\times T}}} \quad \text{Eq. IV-1}$$

Cu(I) X-ray absorption spectroscopy (XANES/EXAFS):

Samples with final concentrations of 1 mM $CuSO_4$, 1.5 mM 3SCC, 50 mM MES, and 30 % glycerol (as a glassing agent) were prepared, pH adjusted, loaded into an XAS sample cell, and frozen in liquid nitrogen for transport and analysis. Although multiple attempts to collect XAS on the Cu(II) forms were done, the enzymes underwent photo-reduction during collection. Sub-stoichiometric concentrations of metal were used to ensure limited amounts of non-peptide associated metal. All XAS measurements were performed at Stanford Synchrotron Radiation Lightsource (SSRL) Beam line 9-3. A Si(220) double crystal monochromator was utilized, with a flat Rh-coated vertically collimating harmonic rejection monochromator. The X-ray energy was calibrated by collecting the absorption spectrum of a reference metal foil, placed between two ionization chambers situated behind the sample, at the same time as the fluorescence data were collected, with the first inflection point of the foil assigned as 8980.29 eV for Cu. The samples were maintained at a temperature of ~4-10 K during data acquisition using a liquid helium cryostat, and the data were measured in fluorescence mode with a 100-element energy resolving Ge detector. The data were collected using 0.25 eV steps in the XANES region (1 sec. integration time), and 0.05 $Å^{-1}$ increments for the extended X-ray absorption fine structure (EXAFS) region up to k=15 $Å^{-1}$, with an integration time of 1-20 s (k^3 weighted) in the EXAFS region. The maximum incident count rate for the channel with the highest counts was kept below 10,000 to

avoid detector saturation. XANES data were normalized with Athena[21] and processed with a threshold energy of E_0 8990 eV for Cu and the background was removed using a 3-region cubic spline. The EXAFS data were analyzed using Artemis[22], and the Cu-Pyridine EXAFS model was derived from a single Cu-Pyridine unit from the crystal structure of a tetrakis(pyridine)-copper(I) oxalate complex reported by Royappa *et al*.[23] The Cu-N_{Py} bond distance was modified to 1.95 Å before generating the scattering paths by FeFF 6 lite in Artemis. The models were fit with ΔE fixed to $\Delta E_0 = -5$ eV which was determined by aligning the Feff6 theoretical k^3-space for the Cu-Pyridine unit with the experimental k^3-space in Athena, which resulted in a relative -5 eV shift the needed to be accounted for within the fit. The Debye-Waller factors were estimated from Zn-Histidine paths reported by Bunker *et al*. and fitted by freely floating the Cu-N_{py} Debye-Waller factors, linking the remaining paths to the Cu-N_{py} to maintain a constant ratio to the original values throughout the fit.[24] The goodness of fit employed in EXAFSPak for the histidine active sites was the F-Value which is the sum of the squares of the difference between experimental and calculated curves. While Pitts *et al.* employed a fitting error equation, this thesis will use a modified version to take into account changes in the number of fitting variables associated with additional coordination shells in some designs, and changes in the range of k^3-space in subsequent chapters. In Eq. IV-2, x_i^{measured} equals the measured i^{th} data point value in *k*-space and x_i^{model} equals the i^{th} theoretical point of the fitted model and is summed over 3-13.1 $Å^{-1}$ k^3-space. The N_{idp} represents an upper bound number of independent parameters that can be extracted for a given data range in the EXAFS and is given in Eq. IV-3 from Stern *et al*.[25] N_{fit} is the number of data points that composed the fitting range and N_{vary} is the number of parameters varied during the fitting process. Below, the experimental data is presented in the normalized E-space (XANES and

EXAFS regions), *k*-space (weighted by k^3), and the Fourier Transform of k^3-space along with the appropriate fits are overlayed with their experimental data.

$$< x^2 f >= \frac{\frac{N_{idp}}{N_{fit}} \sum_i k_i^3 \left[\chi(k)_i^{measured} - \chi(k)_i^{model}\right]^2}{N_{idp} - N_{Vary}} \quad \text{Eq. IV-2}$$

$$N_{idp} \approx \frac{2\Delta k \Delta R}{\pi} \quad \text{Eq. IV-3}$$

Cu(II)-Pep$_3$ $K_{d,app}$ determinations and fitting:

Cu(II) dissociation constants were determined by tryptophan fluorescence quenching in 50 mM MES) at pH 5.9 (T=25^{o}C). The quenching curve was fitted to a 1-to-1 isothermal binding curve (Eq. IV-4) where I_z=Final Intensity, I_o=Initial Intensity, $[Pep]_{3,total}$= total trimer concentration, $[Cu(II)]_{total}$=total $CuSO_4$ concentration, and K_d=apparent dissociation constant. The I_z,I_o and $[Pep]_{3,total}$ parameters were fixed while the $[Cu(II)]_{total}$ and K_d parameters were allowed to float during the calculation.

$$I = \left(\frac{I_o - (I_o - I_z)}{2 \times [Pep]_{3,tot}}\right) \times \left(([Cu]_{tot} + [Pep]_{3,tot} + K_d) - \left(\sqrt{([Cu]_{tot} + [Pep]_{3,tot} + K_d)^2 - 4 \times [Pep]_{3,tot} \times [Cu]_{tot}}\right)\right) \quad \text{Eq. IV-4}$$

CuNiR Kinetics:

Background corrected CuNiR activity was measured by UV-Visible spectroscopy using previously published procedures by monitoring ascorbate oxidation and using $CuSO_4$ as the copper salt.[26] Pseudo first order rate constants were determined in solutions containing 50 mM sodium phosphate buffer, 30 mM sodium nitrite, 1.5 mM ascorbate and varying the enzyme concentration at pH 5.9 while maintaining an 8:1 3SCC:Cu(II) ratio to ensure Cu(II)/Cu(I) is completely bound to the 3SCC. The background reactions were determined at each enzyme concentration containing 50 mM sodium phosphate buffer, 1.5mM ascorbate, and 30 mM $NaNO_2$ with 7 eqv. apo-3SCC. Steady State kinetics were conducted by varying the $NaNO_2$ concentration over a range of 50 mM-600 mM with 1 μM of Cu(II)-3SCC and 8μM apo-3SCC and the steady state background reaction

was treated at each substrate concentration with 50 mM Phosphate buffer, 1.5 mM ascorbate, and 7 eqv. apo-3SCC. The steady state curves were fitted using Eq. IV-5 where K_{sp} is the k_{cat}/K_m (M^{-1} s^{-1}). These experiments were conducted in triplicates.

$$\frac{v_{obs}}{E_T} = \frac{\left(k_{sp} * [NO_2^-]\right)}{\left(1 + \frac{\left(k_{sp} * [NO_2^-]\right)}{(k_{cat})}\right)} \quad \text{Eq. IV-5}$$

Results:

Contributions to this chapter:

Gretchen Stemmler and Marla Muter contributed jointly to the synthesis and purification of the enzymes at different times during this project. Marla collected the UV-VIS data of the oxidized enzymes, while Gretchen collected the steady state kinetics for GRW-H, $GRW_{stam27AEL}$L33H, GRW-3'Py, $GRW_{stam27(AEL)}$L33-3'Py and contributed to the overall design of the AEL and AEA stammer with the 3'Py active site.

Circular Dichroism Spectroscopy of Apo Proteins:

Table IV-1: Stability parameters determined from the chemical denaturation curves.

Enzyme	m (kcal M^{-1}_{GdnHCl} mol^{-1})	$[Gdn\text{-}HCl]_{1/2}$ (M)	ΔG_u° (H_2O) kcal mol^{-1}	MRE (30mM Trimer) (deg cm^2 $dmol^{-1}$ res^{-1})
TRIW-4'Py	1.3	2.7	3.4	-31789 (90% Folded)
TRIW-3'Py	1.4	2.8	4.0	-33466 (94% Folded)
GRW-3'Py	1.8	5.1	9.1	-31659 (89% Folded)
GRW-4'Py	1.6	5.1	8.4	-34405 (97% Folded)
$GRW_{stam27(AEA)}$L33-4'Py	1.5	4.8	7.2	-31681 (89% Folded)
$GRW_{stam27(AE3'Py)}$	1.3	4.8	6.4	-29512 (83% Folded)
$GRW_{stam27(AEH)}$	--	--	--	-26795 (75% Folded)

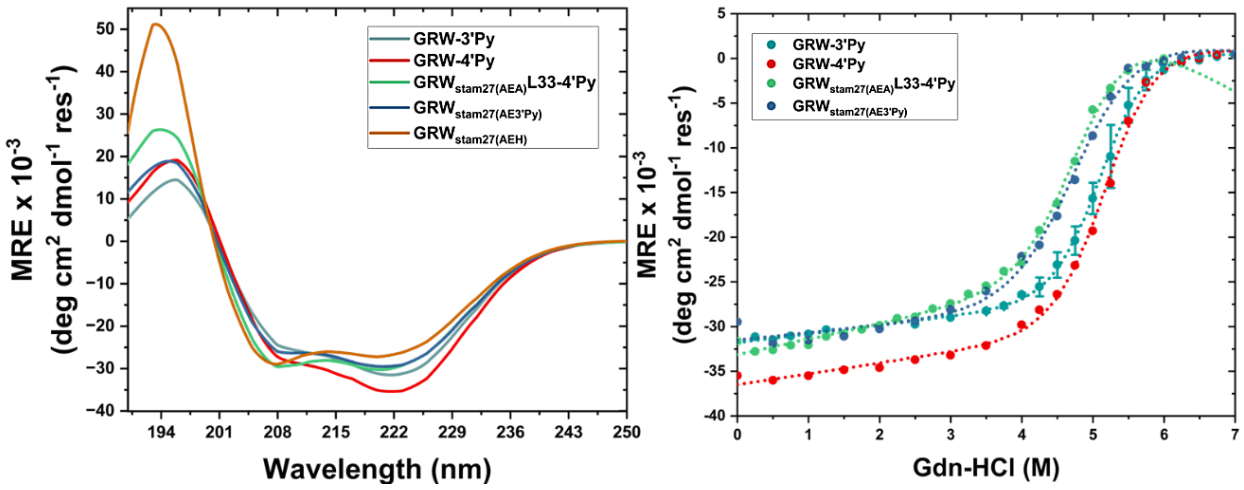


Figure IV-3: CD and chemical denaturation of designed proteins: **A)** CD spectra of each apo-protein at 30μM trimer at pH 5.9 at 25°C and **B)** Chemical denaturation titrations of 30 μM trimer with Guanidinium Hydrochloride at 25°C (pH 5.9) (solid lines-fits)

The degree of folding and the free energy of folding (reflecting the aggregate stability) of the designed proteins in this chapter were investigated using circular dichroism spectroscopy. All designed scaffolds were well folded, forming classic double-well minimums at 222 nm and 208 nm (at pH 5.9), indicating a composition of mostly α-helical secondary structure in the overall protein fold (Figure IV-3). The GRW sequence was not significantly destabilized across the categories of mutations that were adopted in this chapter. The additional heptad (LKALEEK) in TRIW-3'Py and TRIW-4'Py did not result in a noticeable change in folding; however, the stability increased by ~5 kcal mol^{-1}, as the extra heptad provides additional hydrophobic contacts and salt bridge interactions that stabilize the system. These and other favorable helix-propensity effects contribute to the higher stability under Guanadium hydrochloride desaturations (Table IV-1).[27] The addition of a stammer near the center of the sequence (below the L26 ***d***-site) resulted in a slight decrease of the 222 nm band (*e.g.*, $GRW_{stam27(AEA)}$L33-4'Py vs. GRW-4'py), indicating a change in the structure of the coiled coil with minimal loss in aggregate stability compared to the parent design ($\Delta G_u^\circ(H_2O)$=8.4 kcal mol^{-1} to $\Delta G_u^\circ(H_2O)$=7.2 kcal mol^{-1}).

Characterization of Cu(II) Enzymes:

Determination of Cu(II) $K_{d,app}$ Constants:

The apparent dissociation constants ($K_{d,app}$) were determined using fluorescence spectroscopy to monitor the parametric fluorescence quenching of the tryptophan's (in position 2 near the N-terminus) signal (excitation 280 nm) upon the addition of $CuSO_4$ to 80-500 nM concentrations of apo-trimer protein (Figure II-6). As with the TRIW sequence in Chapter II, the emission band of this band was observed at 350 nm suggesting that the majority of the tryptophan residues are not buried in the hydrophobic core, as one would expect a more blue-shifted emission band if this were the environment.[28] The dissociation constants were obtained by fitting the resulting curves to a 1-to-1 binding isotherm (Eq. IV-3) that yielded apparent dissociation constants in the range of 7-750 nM. [29]

Table IV-2: Apparent dissociation constants based on fluorescence tryptophan quenching experiments at pH 5.9.

Enzyme	Cu(II) $K_{d,app}$ (nM)	Ref.
TRIW-H	40 (±1)	26
$GRW_{stam27(AEL)}$L33-H	750 (±1)	16
GRW-3'Py	30 (±1)	--
GRW-4'Py	7 (±1)	--
$GRW_{stam27(AEL)}$L33-3'Py	746 (±60)	--
$GRW_{stam27(AE3'Py)}$	10 (±4)	--
$GRW_{stam27(AEA)}$L33-4'Py	11 (±6)	--

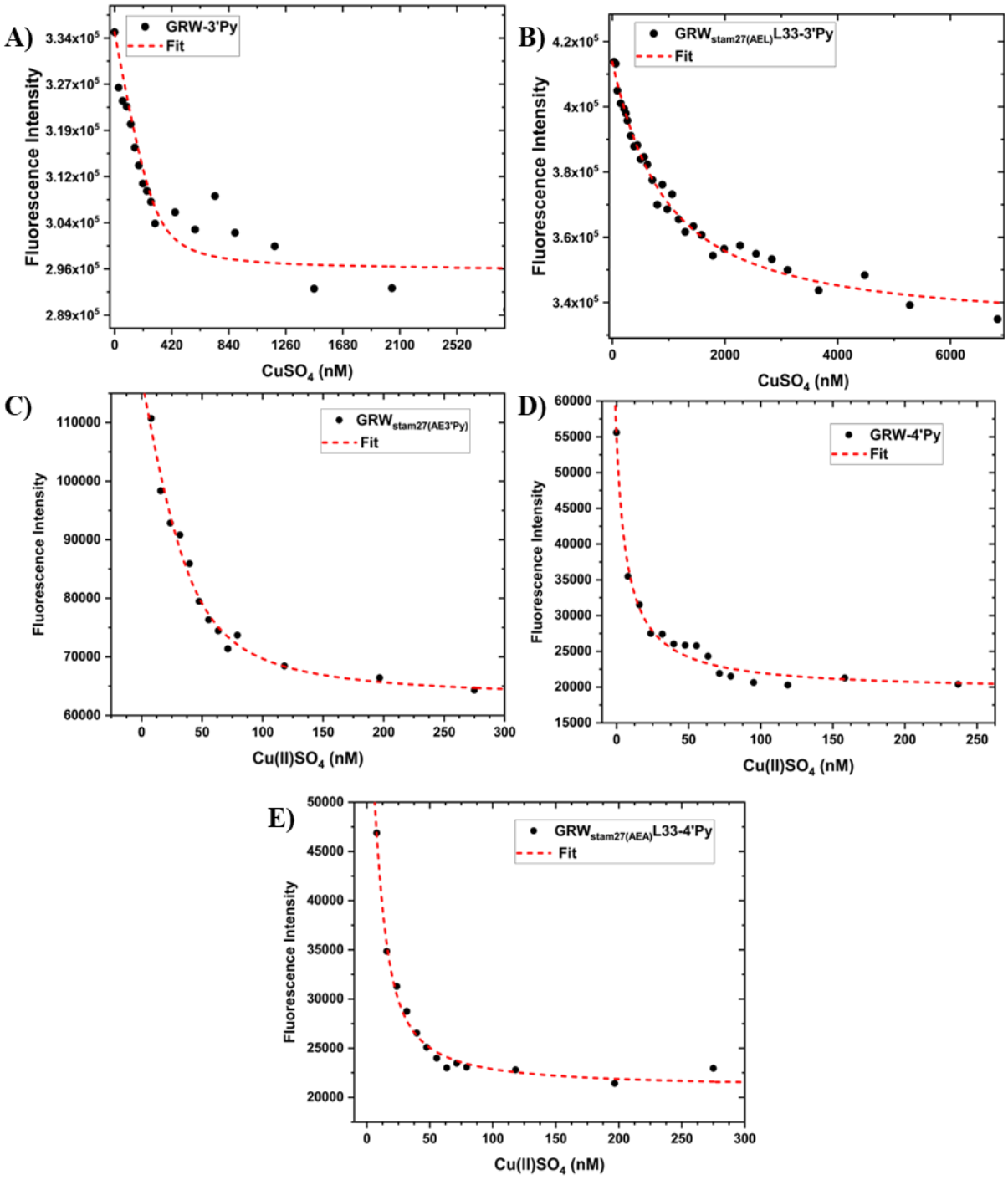


Figure IV-4: Fluorescence quenching curves of the N-terminal tryptophan as a function of $CuSO_4$: **A**) GRW-3'Py, **B**) $GRW_{stam27(AEL)}$L33-3'Py, **C**) $GRW_{stam27(AE3'Py)}$, **D**) GRW-4'Py, and **E**) $GRW_{stam27(AEA)}$L33-4'Py.

UV-VIS and EPR of the Oxidized Forms:

The UV-vis of the oxidized form of the enzymes displayed d-d transitions between the wavelengths of 600-730 nm at pH 5.9 with the molar absorptivity coefficient ranging between 40-110 M^{-1} cm^{-1}. These observed spectra are not consistent with unbound Cu(II) which has an absorption band at 800 nm (ε =14 M^{-1} cm^{-1}) in 50 mM MES buffer. The X-band EPR spectra were recorded at 90 K for Cu(II)-GRW-3'Py and Cu(II)-$GRW_{stam27(AEL)}$L33-3'Py as each UV-Vis spectrum suggested a rearrangement of the active site (Figure IV-5). Both oxidized enzymes were T2Cu copper centers (e.g., $A_{\|}$>150 × 10^{-4} cm^{-1}); however, the AEL stammer resulted in a slight increase in rhombicity of the g_x and g_y values with a lower $A_{\|}$ compared to GRW-3'Py (159 × 10^{-4} cm^{-1} vs. 169× 10^{-4} cm^{-1}) (Table IV-3). From a structural perspective of model complexes, the changes in the UV-vis and EPR tend to supports either the addition or perturbation of the axial ligand in the AEL stammer when compared to the Cu(II)-GRW-3'Py.[30,31]

Table IV-3: X-band EPR parameters of the oxidized enzyme at pH 5.9 (T=90-100 K).

Enzyme	g_z	g_y	g_x	$A_{\|}$ (x 10^{-4} cm^{-1})	Ref.
TRIW-H	2.271	2.028	2.064	167	26
$GRW_{stam27(AEL)}$L33-H	2.280	2.045	2.045	173	--
TRIW-ε_mH	2.30	2.03	2.05	151	29
TIRW-3'Py	2.29	2.04	2.04	168	--
GRW-3'Py	2.280	2.035	2.035	169	--
$GRW_{stam27(AEL)}$L33-3'Py	2.276	2.026	2.038	159	--

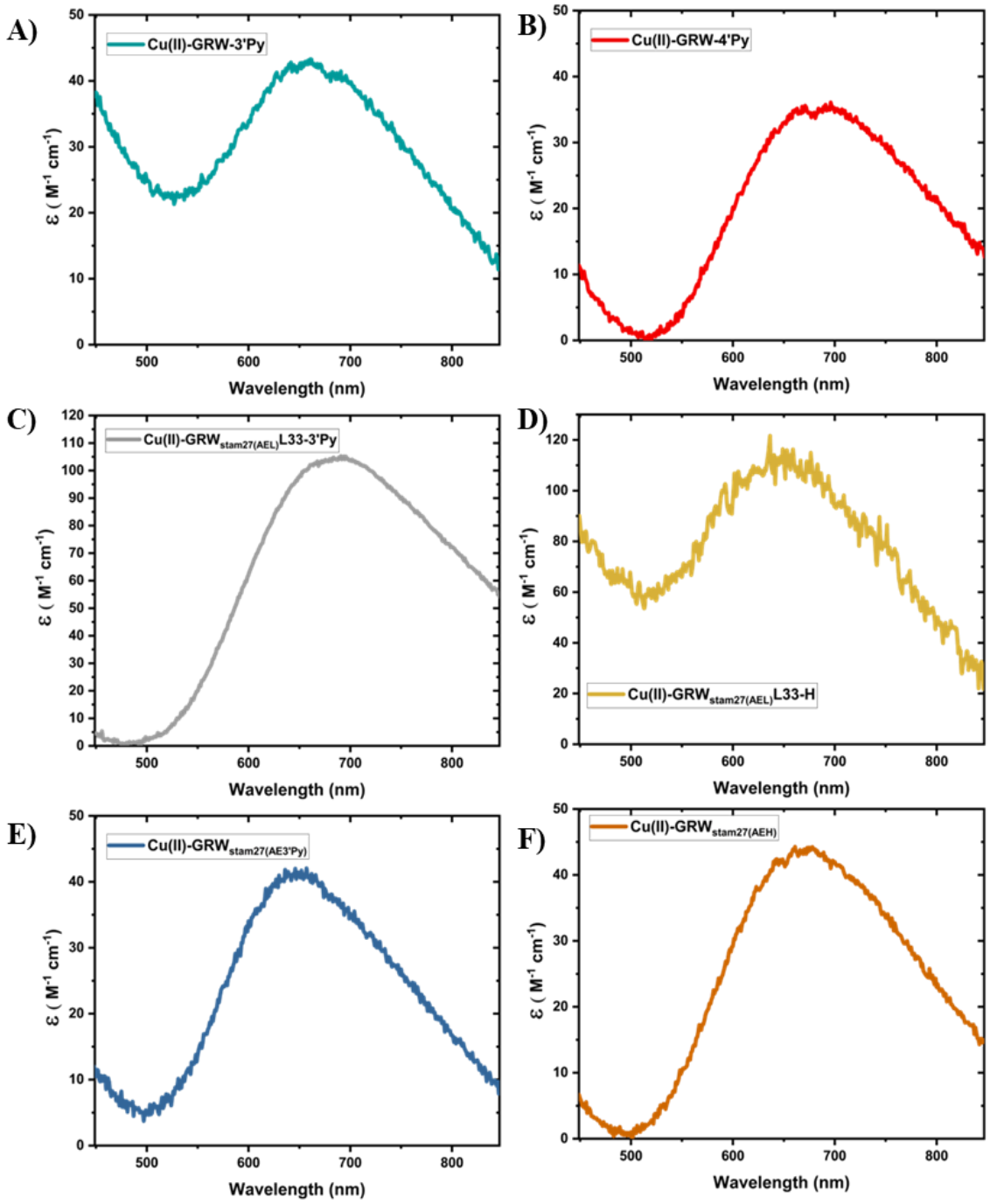


Figure IV-5: UV-Vis spectra of the oxidized enzyme at pH 5.9: **A**) Cu(II)-GRW-3'Py, **B**) Cu(II)-GRW-4'Py, **C**) Cu(II)-GRW$_{stam27(AEL)}$L33-3'Py, **D**) Cu(II)-GRW$_{stam27(AEL)}$L33-H, **E**) Cu(II)-GRW$_{stam27(AE3'Py)}$, and **F**) Cu(II)-GRW$_{stam27(AEH)}$.

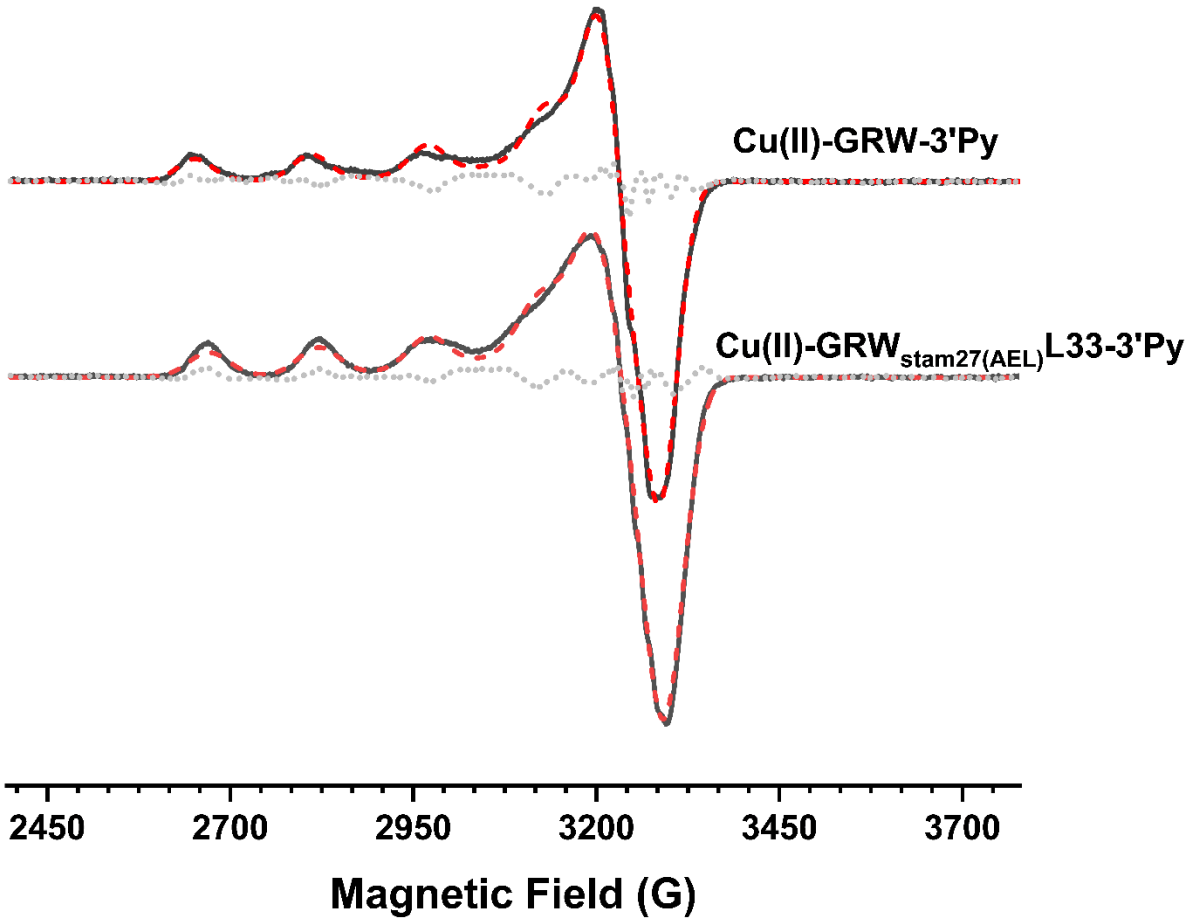


Figure IV-6: EPR spectra of the oxidized forms at pH 5.9 Cu(II)-GRW-3'Py and Cu(II)-$GRW_{stam27(AEL)}$L33-3'Py. Fits are dashed red lines and residuals are the dotted gray lines.

Characterizing the Cu(I) Enzyme Form:

X-Ray Absorption Spectroscopy of the Cu(I) Protein:

Table IV-4: Summary of EXAFS fits for reduced pyridine and histidine designs. The E_0 was assigned 8990 eV and ΔE was fixed to – 5 eV.

Enzyme	Best Model	Cu(I)-N	Cu(I)-N $\sigma^2 \times 10^{-3}$	Cu(I)-O	Cu(I)-O $\sigma^2 \times 10^{-3}$	Bond Valence Sum	$\langle\chi^2 f\rangle \times 10^{-4}$
Cu(I)-GRW$_{stam27(AEH)}$	$CuHis_2$	1.90 Å	5.16 Å^2	--	--	0.95	16
	$CuHis_3$	1.90 Å	8.18 Å^2	--	--	1.27	21
Cu(I)-GRW-3'Py	$CuPy_2$	1.97 Å	4.56 Å^2	--	--	0.78	25
	$CuPy_3$	1.97 Å	7.39 Å^2	--	--	1.05	19
Cu(I)-GRW-4'Py	$CuPy_2$	1.97Å	2.44 Å^2	--	--	0.78	37
	$CuPy_3$	1.97 Å	4.66 Å^2	--	--	1.05	30
Cu(I)-GRW$_{stam27(AEL)}$L33-3'Py	$CuPy_2$	1.97 Å	1.99 Å^2	--	--	0.78	19
	$CuPy_3$	1.97 Å	4.23 Å^2	--	--	1.05	27
	$CuPy_2O$	1.98 Å	1.99 Å^2	1.89 Å	10.00 Å^2	1.11	16
	$CuPy_3O$	1.98 Å	3.66 Å^2	1.82 Å	9.79 Å^2	1.36	27
Cu(I)-GRW$_{stam27(AEA)}$L33-3'Py	$CuPy_2$	1.97 Å	2.39 Å^2	--	--	0.78	18
	$CuPy_3$	1.98 Å	4.59 Å^2	--	--	1.02	24
	$CuPy_2O$	1.97 Å	2.63 Å^2	1.95 Å	14.61 Å^2	1.07	15
	$CuPy_3O$	1.98 Å	4.38 Å^2	1.81 Å	20.94 Å^2	1.34	17
Cu(I)-GRW$_{stam27(AE3'Py)}$	$CuPy_2$	1.94 Å	3.88 Å^2	--	--	0.85	12
	$CuPy_3$	1.95 Å	6.66 Å^2	--	--	1.11	19
Cu(I)-GRW$_{stam27(AEA)}$L33-4'Py	$CuPy_2$	1.94 Å	3.50 Å^2	--	--	0.85	18
	$CuPy_3$	1.95 Å	6.10 Å^2	--	--	1.11	22

The coordination and electronic environments around the catalytic copper in the reduced enzymes were examined using X-ray absorption spectroscopy, as it has previously provided valuable insights into these copper enzymes. Cu(I) complexes featured a resolved band at *ca.* 8983 eV that is associated with a core electron from the 1s orbital to the 4p orbital, where the intensity is governed by the amount of the surrounding ligand's orbital character mixing into the empty 4p orbital of Cu(I).[32,33] First, the EXAFS of both Cu(I)-GRW-3'Py and Cu(I)-GRW-4'Py suggest that the Cu(I) is best described as a 3-coordinate pyridine with an average Cu(I)–N_{Py} bond distance of

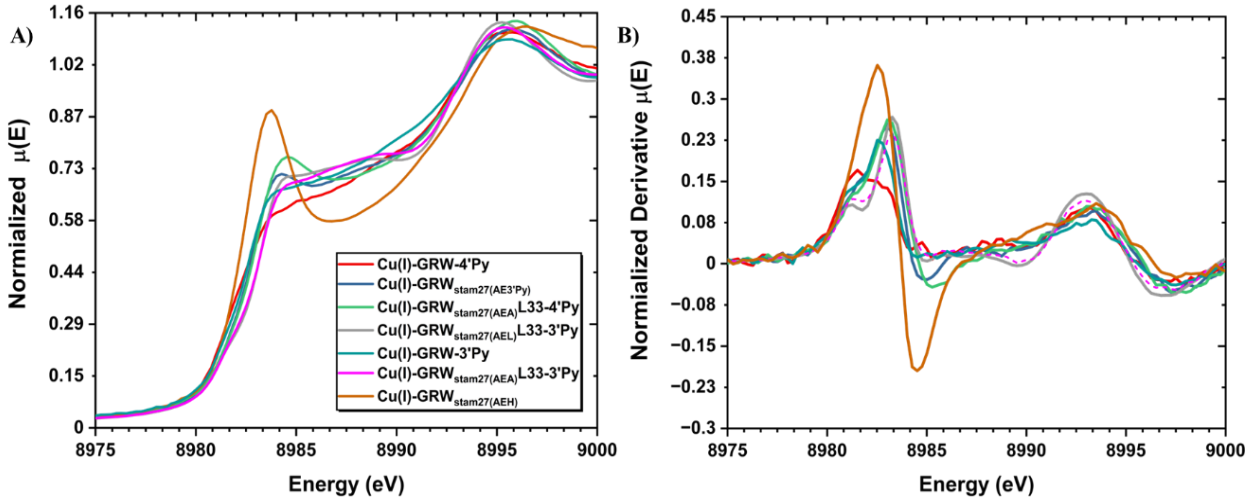


Figure IV-7: XANES comparison between the reduced enzyme resting state at pH 5.9: **B)** Derivatives of spectra in (**A**) which highlight the subtle electronic and structural changes in the Cu(I) oxidation state.

1.97 Å and 1.97 Å, respectively. The bonding parameters are identical to TRW-3'Py and TRW-4'Py, observed in Chapter II (Figure IV-9). Moreover, the Cu(I) ion likely adopts an almost identical geometry with respect to the TRW design, as reflected in the similarity of the analogous XANES (Table IV-4 and Figure IV-7). Both the nominal and stammer peptides investigated in this chapter displayed a unique perturbation of the XANES features compared to those discussed with the alanine mutation in Chapter II of this thesis. The addition of either the (AEL) or (AEA) ***d***-site stammer above the 3'Py site resulted in negligible changes in the intensity in the Cu(I) edge compared to GRW-3'Py; however, the effect of the stammer blue shifts the Cu(I) edge by the ~0.75 eV. The coordination number for these two stammers are more ambiguous with their average Cu(I)-N bond distance laying closer to a coordination number of 3; however, each best-fit parameter is lowest with only 2 coordination numbers. These two designs will be represented as 3-coordinate Cu(I) active sites given their bond distances with the condition that stammer may lengthen the bond distances associated with a hypothetical 2-coordinate Cu(I) in an ***a***-site. The addition of the oxygen donor to the primary coordination sphere results in a better normalized fit error while being physically unrealistic in terms of the Cu(I)–O bond distance (*ca*. 1.80-1.90 Å). However, the EXAFS fittings are unable to distinguish between nitrogen and oxygen atoms and, therefore, this assignment is tentative. Placing the 3'Py ligand directly into the stammer (*e.g.*,

$GRW_{stam27(AE3'Py)}$) resulted in a more 2-coordinate site with a corresponding decrease in the average Cu(I)–N_{Py} distance (1.94 Å) and a slight increase in the 1s-4p edge intensity; however, a mix of 3-coordinate Cu(I) cannot be ruled out. Interestingly, the addition of the (AEA) stammer to GRW-4'Py (*e.g.*, Cu(I)-$GRW_{stam27(AEA)}$L33-4'Py) resulted in a less ambiguous 2-coordinate structure compared to the nominal heptad design, GRW-4'Py (Figure IV-12A-B). The Cu(I)-$GRW_{stam27(AEH)}$ design displays an intense edge strongly supporting the assignment of the Cu(I) site as a 2-coordinate with a Cu(I)–N_{His} of 1.89 Å falling within range of a Cu(I) bis-histidine site previously reported in Cu(I)-TRIW-H L19A and Cu(I)-$GRW_{stam27(AEL)}$L33-H.[16,19]

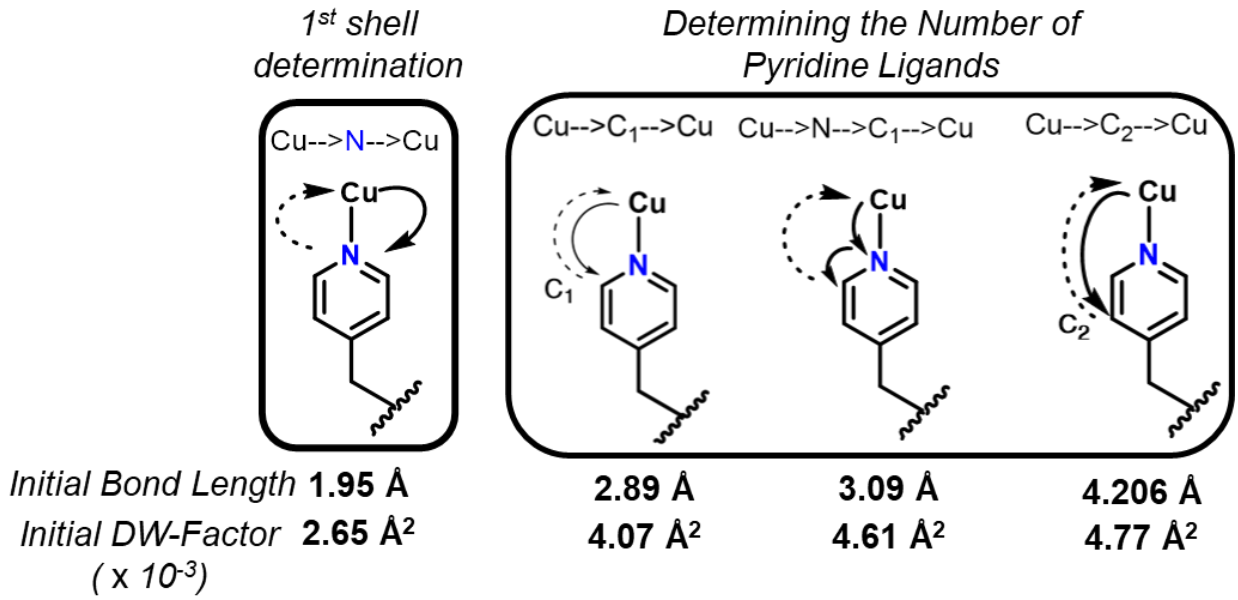


Figure IV-8: Simple scheme highlighting scattering paths, and their associated initial parameters used to the fit k^3-space .

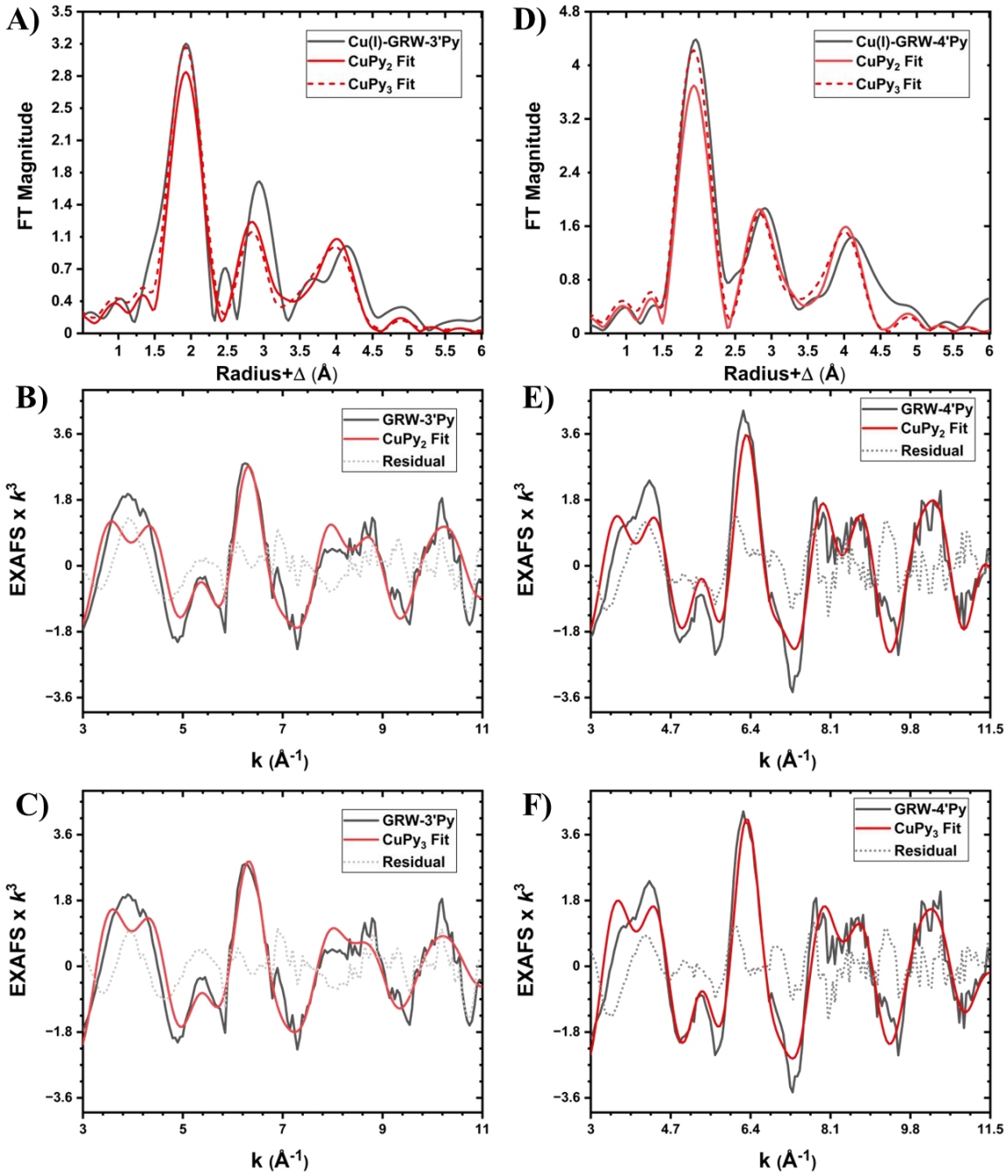


Figure IV-9: EXAFS fits of Cu(I)-GRW-3'Py (*left* **A**-**C**) and Cu(I)-GRW-4'Py (*right* **D**-**F**): Fourier Transform (*top*) and associated *k*-space weighted by k^3 (*bottom*) of Cu-Py_2 (**B**-**C**)and Cu-Py_3 (**E**-**F**) models.

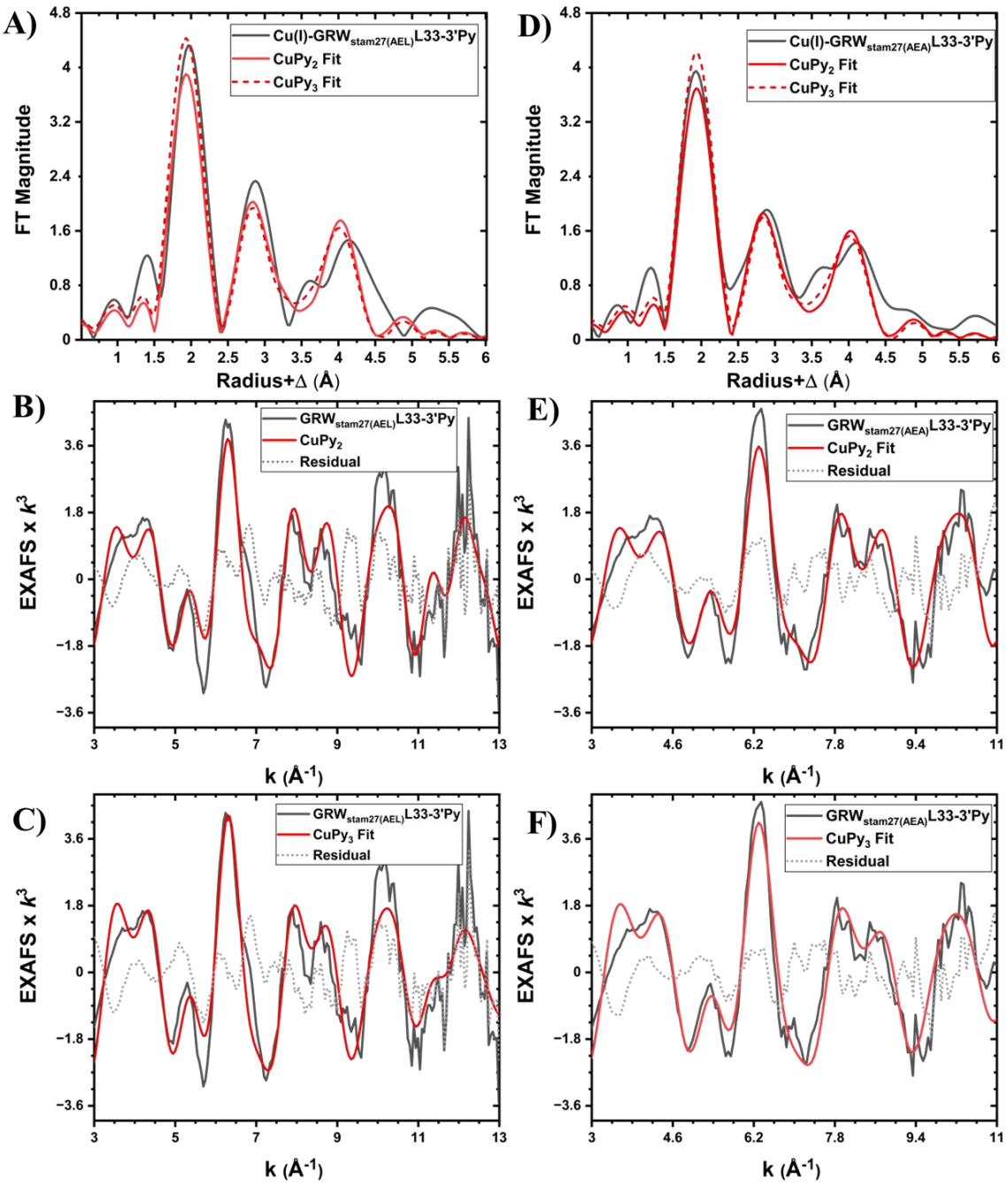


Figure IV-10: EXAFS fits of Cu(I)-GRW$_{stam27(AEL)}$L33-3'Py (*left* **A**-**C**) and Cu(I)-GRW$_{stam27(AEA)}$L33-3'Py (*right* **D**-**F**): Fourier Transform (*top*) and associated *k*-space weighted by k^3 (*bottom*) of Cu-Py$_2$ (**B**-**C**)and Cu-Py$_3$ (**E**-**F**) models.

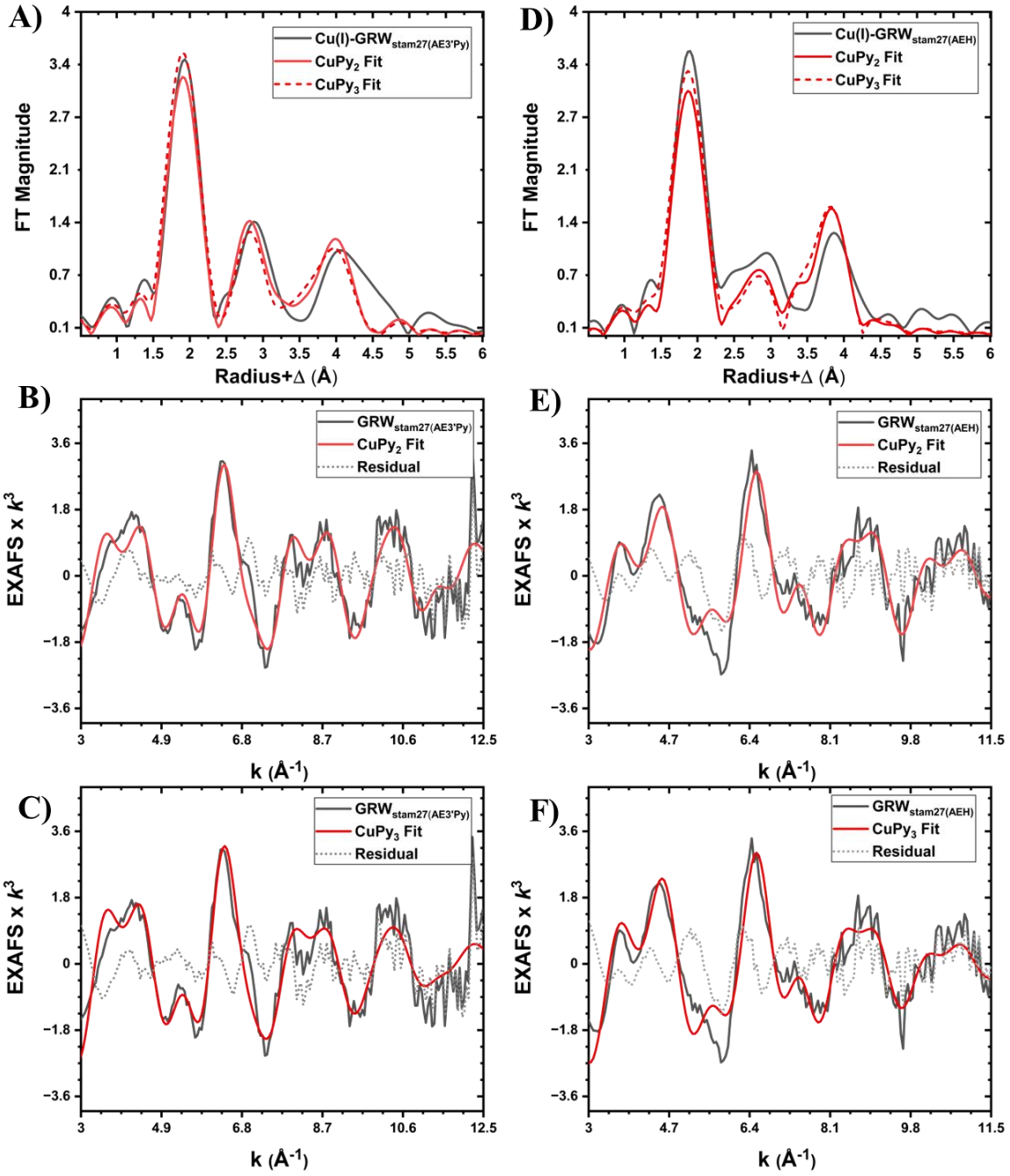


Figure IV-11: EXAFS fits of Cu(I)-GRW$_{stam27(AE3'Py)}$ (*left* **A**-**C**) and Cu(I)-GRW$_{stam27(AEH)}$ (*right* **D**-**F**): Fourier Transform (*top*) and associated *k*-space weighted by k^3 (*bottom*) of Cu-Py2 (**B**-**C**)and Cu-Py$_3$ (**E**-**F**) models.

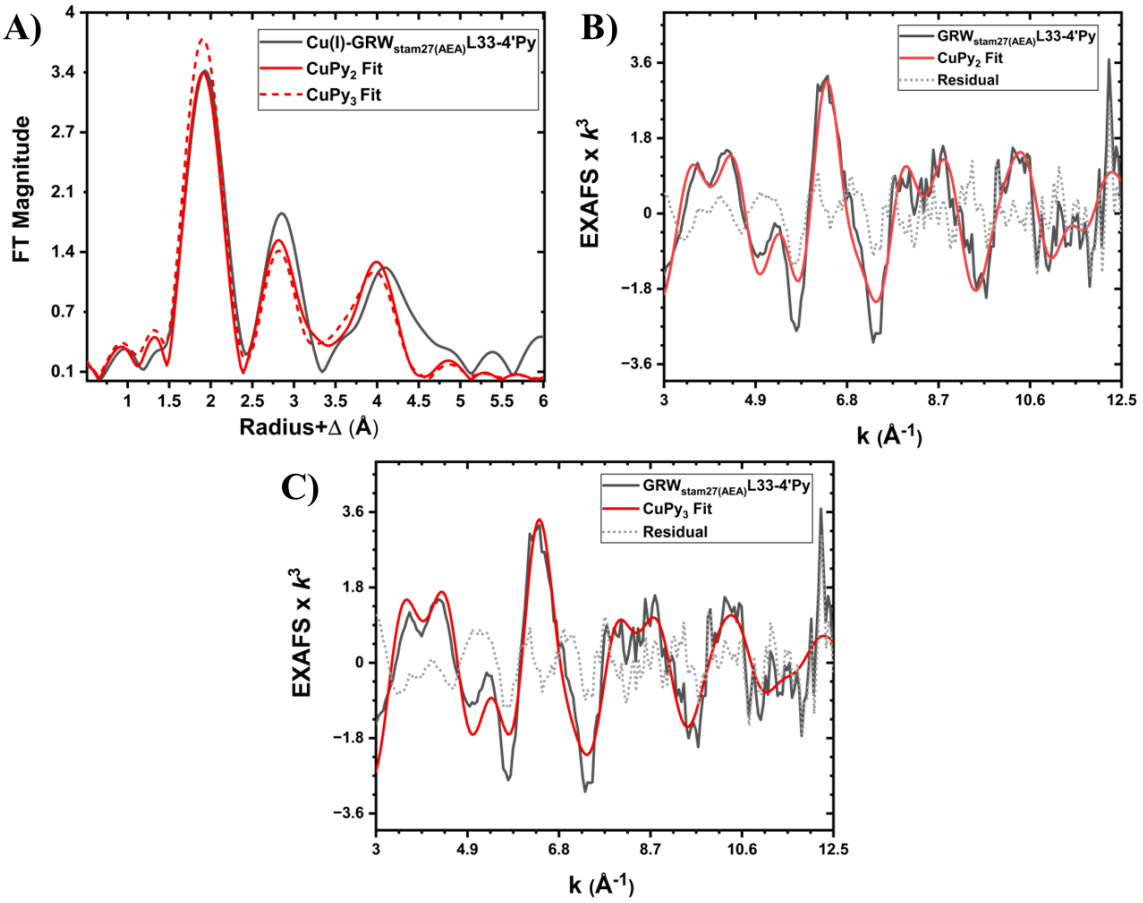


Figure IV-12: EXAFS fits of Cu(I)-GRW$_{stam27(AEA)}$L33-4'Py: Fourier Transform (**A**) and *k*-space weighted by k^3 and the associated Cu-Py$_2$ (**B**)and Cu-Py$_3$ (**C**) fits.

CuNiR Steady-State Kinetics:

Table IV-5: Nitrite reduction kinetics at pH 5.9.

Enzyme	k_{cat} (s^{-1})	K_m (M)	k_{cat}/K_m (M^{-1} s^{-1})
GRW-3'Py	4.0 (± 0.5)	0.37 (± 0.1)	11.0 (± 1.8)
GRW-4'Py	N/A	N/A	2.9 (± 1.3)
$GRW_{stam27(AEL)}$L33-3'Py	2.3 (± 0.1)	0.16 (± 0.02)	15.3 (± 1.7)
$GRW_{stam27(AEA)}$L33-3'Py	2.4 (± 0.5)	0.43 (± 0.17)	5.5 (± 1.2)
$GRW_{stam27(AE3'Py)}$	2.2 (± 0.4)	0.13 (± 0.08)	17 (± 8)
$GRW_{stam27(AEA)}$L33-4'Py	2.6 (± 0.3)	0.29 (± 0.08)	9.5 (± 1.6)
$GRW_{stam27(AEH)}$	N/A	N/A	0.25 (± 0.03)
GRW-H	N/A	N/A	0.96 (± 0.4)
$GRW_{stam27(AEL)}$L33-H	N/A	N/A	0.17 ± (0.02)

N/A: k_{cat} and K_m could not be reliably determined from the Michaelis–Menten kinetics, only the linear portion at low substrate concentration could be fitted to yield an accurate k_{cat}/K_m.

Michaelis-Menten kinetics were conducted to examine the steady state reactivity of the enzyme at various substate concentrations to understand the changes associated with each of these design strategies. With the exception of GRW-H, $GRW_{stam27(AEL)}$L33-H, and $GRW_{stam27(AEH)}$, all of the enzymes studied exhibited saturation kinetics in the concentration range of 50-600 mM $NaNO_2$ at pH 5.9. While the histidine and the GRW-4'Py designs proved to be difficult to collect the k_{cat} and K_m Michaelis-Menten kinetics parameters, the k_{cat}/K_m was obtained from the linear portion of the curve which yielded a reliable value. Both AEL and AEH stammers slightly decreased the k_{cat}/K_m compared to the GRW-H (Table IV-5); however, the order of magnitude increase in the catalytic efficiency between histidine and pyridine follows the results in Chapter II. The addition of the (AEL) stammer to GRW-3'Py resulted in a slight decrease in K_m value, resulting in only a marginal increase in the catalytic efficiency (11.0 M^{-1} s^{-1} vs. 15.3 M^{-1} s^{-1}).

Depending on the orientation of the ligand (3'Py vs. 4'Py), the (AEA) stammer affects reductase activity differently where (AEA) stammer decreases the catalytic efficiency (5.5 M^{-1} s^{-1}). However, the effect of the (AEA) stammer on GRW-4'Py (e.g., $GRW_{stam27(AEA)}$L33-4'Py) slightly increased the k_{cat}/K_m (9.5 M^{-1} s^{-1}) compared to GRW-4'Py (2.9 M^{-1} s^{-1}). The design that placed the 3'Py into the AEL stammer (*e.g.*, $GRW_{stam27(AE3'Py)}$) did not significantly perturb the kinetics compared to GRW-3'Py or (AEL)/(AEA) site stammers. The k_{cat} values with the pyridine active sites with stammers were not perturbed compared to the TRIW series.

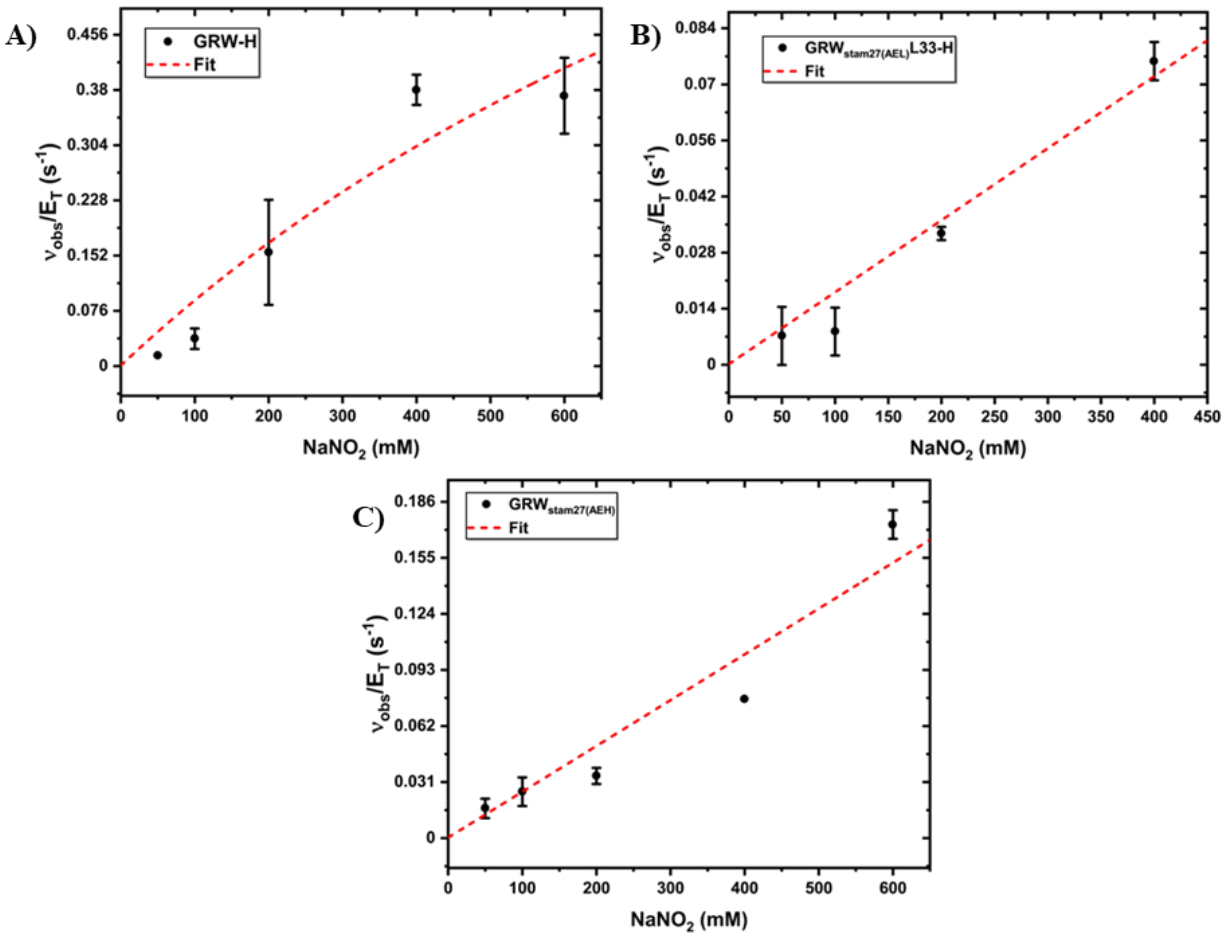


Figure IV-13: CuNiR Michaelis-Menten kinetics of designed histidine sites: **A**) GRW-H, **B**) $GRW_{stam27(AEL)}$L33-H, and **C**) $GRW_{stam27(AEH)}$. Dotted curves represent fits to the Michaelis-Menten equation (Eq. IV-5).

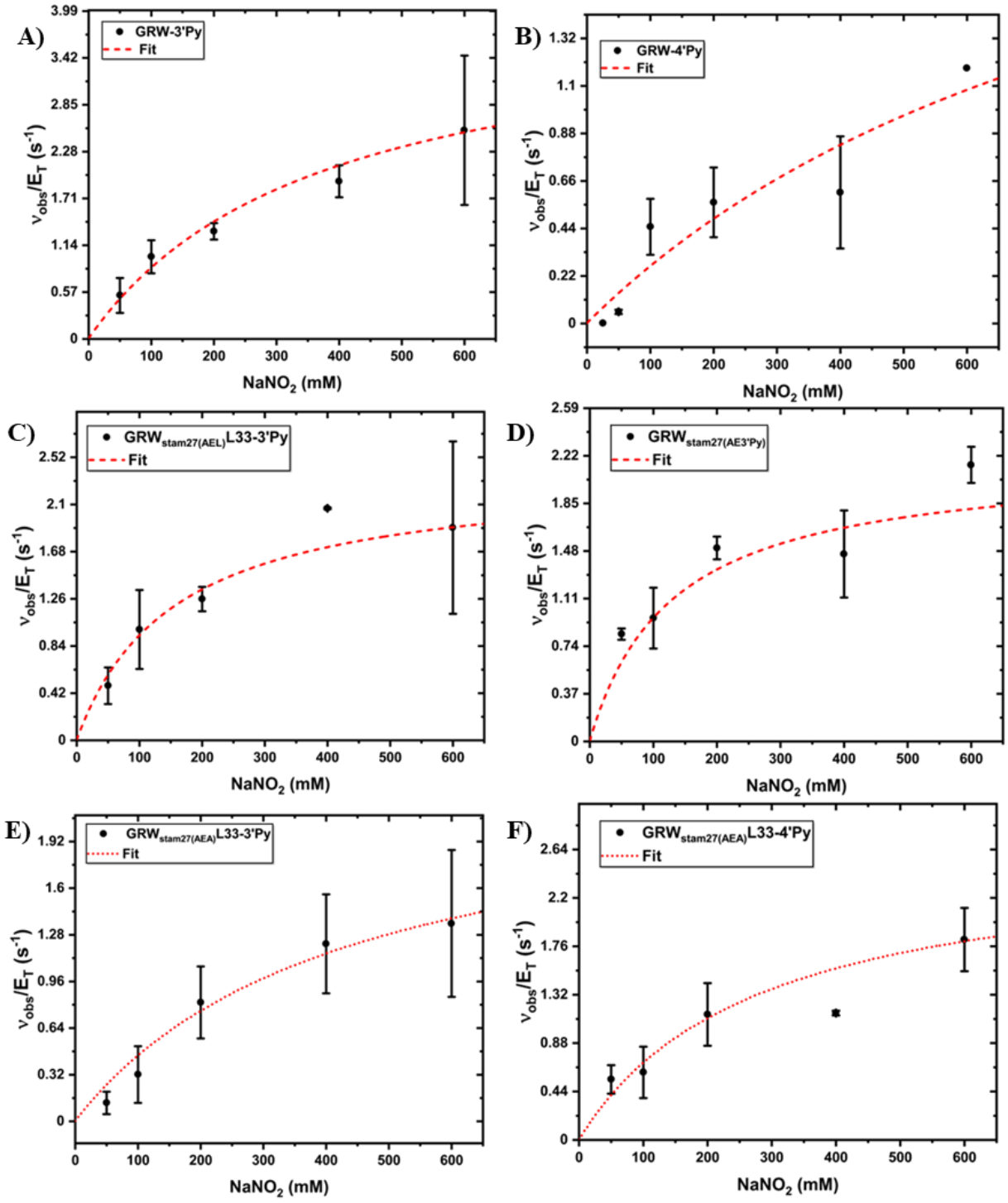


Figure IV-14: CuNiR Michaelis-Menten kinetics of pyridine sites with and without stammers: **A**) GRW-3'Py, **B**) GRW-4'Py, **C**) GRWstam27(AEL)L33-3'Py, **D**) GRWstam27(AE3'Py), **E**) GRWstam27(AEA)L33-3'Py, and **F**) GRWstam27(AEA)L33-4'Py. Dotted curves represent fits to the Michaelis-Menten equation Eq.IV-5).

Discussion:

This chapter aims to assess if three amino acid discontinuities (*e.g.*, stammers) introduced inside nominal coiled coil sequences can alter the overall structure of Cu active sites and whether these modifications can result in significant changes in the kinetic parameters of the designed CuNiR. It is predicted that these insertions will cause the helical assembly to overwind, which will alter the orientation of primary coordination sphere ligands and potentially lead to structural or functional deviations from the canonical assemblies. Furthermore, pyridyl ligands at alternate orientations are investigated to determine whether the presence of a stammer impacts the steady state kinetics from Chapter II. The histidine analogs will also be briefly explored.

As discussed previously in Chapter II, the chemical step after substrate binding is enhanced when pyridine is adopted as the primary coordination sphere ligand as opposed to histidine.[29,34] The large disparity between substrate binding between 3'Py and 4'Py ligands with and without alanine indicates that the 4'Py design likely benefited from more than just extra space with the L19A mutation. A coordination number shift in the Cu(I) oxidation state provided additional space

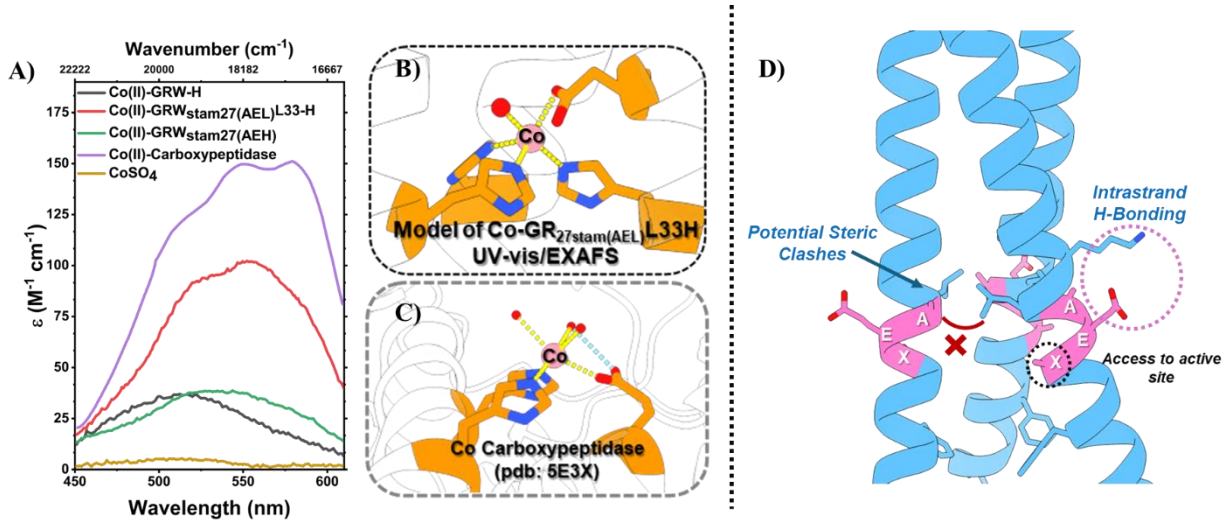


Figure IV-15: A case of asymmetry in the primary coordination induced with the Co(II) (AEL) stammer **A)** UV-Vis of Co(II) peptides where stammer design yields a similar spectrum to Carboxypeptidase, **B**) Model of Co(II)-GRW$_{stam27(AEL)}$L33-H, **C**) Crystal structure of Co(II) substituted Carboxypeptidase, and **D)** The stammers were designed to yield the maximum possible stabilization based on coiled coil design principles. The "x" layer was mutated to either leucine, alanine, or to metal binding ligands (*e.g.*,3'Pyridine or Histidine). (*UV-Vis spectra are courtesy of Dr. Salvatore La Gatta*)

Table IV-6: Summary of Nitrite Reduction kinetics in 3SCC.

Enzyme	k_{cat} (s^{-1})	K_m (M)	k_{cat}/K_m (M^{-1} s^{-1})	Ref.
TRIW-H	0.032 (±0.016)	1.2 (± 0.9)	0.026 (±0.005)	--
TRIW-H L19A	0.23 (±0.03)	0.24 (±0.03)	1.0 (±0.3)	29
TRIW-δ_mH L19A	1.5 (±0.1)	0.13 (±0.01)	11 (±0.1)	29
TRIW-ε_mH L19A	N/A	N/A	0.14 (±0.01)	--
GRW-H	N/A	N/A	0.96 (± 0.4)	--
GRW$_{stam27(AEL)}$L33-H	N/A	N/A	0.17 ± (0.02)	--
GRW$_{stam27(AEH)}$	N/A	N/A	0.25 (± 0.03)	--
TRIW-3'Py	3.0 (±0.1)	0.28 (±0.03)	11 (± 1)	--
TRIW-3'Py L19A	2.8 (±0.3)	0.19 (±0.06)	15 (± 3)	--
TRIW-4'Py	2.9 (±1)	0.60 (±0.26)	5 (± 1)	--
TRIW-4'Py L19A	1.9 (±0.1)	0.05 (±0.01)	39 (± 3)	--
GRW-3'Py	4.0 (± 0.5)	0.37 (± 0.1)	11.0 (± 1.8)	--
GRW-4'Py	N/A	N/A	2.9 (± 1.3)	--
GRW$_{stam27(AEL)}$L33-3'Py	2.3 (± 0.1)	0.16 (± 0.02)	15.3 (± 1.7)	--
GRW$_{stam27(AEA)}$L33-3'Py	2.4 (± 0.5)	0.43 (± 0.17)	5.5 (± 1.2)	--
GRW$_{stam27(AE3'Py)}$	2.2 (± 0.4)	0.13 (± 0.08)	17 (± 8)	--
GRW$_{stam27(AEA)}$L33-4'Py	2.6 (± 0.3)	0.29 (± 0.08)	9.5 (± 1.6)	--

at the copper center itself. Despite extensive computational and crystallographic assessment, there remains virtually no information on the impact of such discontinuities on metal binding sites within coiled coils. The native histidine site Zn(II) catalyzed pNPA hydrolysis and nitrite reduction at a mono copper center have previously been demonstrated to be in opposition to each other by the (AEL) stammer.[16] In other words, in comparison to the parent design (i.e., GRW-H), the rate of hydrolysis is lowered close to background levels while the rate of nitrite reduction appears to

Table IV-7: Summary of EXAFS fits for Cu(I) pyridine and histidine enzymes

Enzyme	Best Model	Cu(I)-N	Cu(I)-N $\sigma^2 \times 10^{-3}$	Ref.
Cu(I)-TRIW-H	$CuHis_3$	1.93 Å	9.0 $Å^2$	26
Cu(I)-TRIW-H L19A	$CuHis_2$	1.86 Å	8.0 $Å^2$	19
	$CuHis_3$	1.86 Å	9.7 $Å^2$	--
Cu(I)-TRIW-δ_mH L19A	$CuHis_2$	1.89 Å	8.1 $Å^2$	29
	$CuHis_3$	1.89 Å	10.4 $Å^2$	--
Cu(I)-GRW$_{stam27(AEL)}$L33-H	$CuHis_2$	1.89 Å	7.5 $Å^2$	16
Cu(I)-GRW$_{stam27(AEH)}$	$CuHis_2$	1.90 Å	5.16 $Å^2$	--
	$CuHis_3$	1.90 Å	8.18 $Å^2$	--
Cu(I)-TRIW-3'Py	$CuPy_2$	1.96 Å	2.94 $Å^2$	--
	$CuPy_3$	1.97 Å	5.17 $Å^2$	--
Cu(I)-TRIW-4'Py	$CuPy_2$	1.97 Å	3.17 $Å^2$	--
	$CuPy_3$	1.97 Å	5.26 $Å^2$	--
Cu(I)-TRIW-3'Py L19A	$CuPy_2$	1.95 Å	4.31 $Å^2$	--
	$CuPy_3$	1.95 Å	6.96 $Å^2$	--
Cu(I)-TRIW-4'Py L19A	$CuPy_2$	1.94 Å	3.31 $Å^2$	--
	$CuPy_3$	1.94 Å	5.60 $Å^2$	--
Cu(I)-GRW-3'Py	$CuPy_2$	1.97 Å	4.56 $Å^2$	--
	$CuPy_3$	1.97 Å	7.39 $Å^2$	--
Cu(I)-GRW-4'Py	$CuPy_2$	1.97Å	2.44 $Å^2$	--
	$CuPy_3$	1.97 Å	4.66 $Å^2$	--
Cu(I)-GRW$_{stam27(AEL)}$L33-3'Py	$CuPy_2$	1.97 Å	1.99 $Å^2$	--
	$CuPy_3$	1.97 Å	4.23 $Å^2$	--
Cu(I)-GRW$_{stam27(AEA)}$L33-3'Py	$CuPy_2$	1.97 Å	2.39 $Å^2$	--
	$CuPy_3$	1.98 Å	4.59 $Å^2$	--
Cu(I)-GRW$_{stam27(AE3'Py)}$	$CuPy_2$	1.94 Å	3.88 $Å^2$	--
	$CuPy_3$	1.95 Å	6.66 $Å^2$	--
Cu(I)-GRW$_{stam27(AEA)}$L33-4'Py	$CuPy_2$	1.94 Å	3.50 $Å^2$	--
	$CuPy_3$	1.95 Å	6.10 $Å^2$	--

increase by a factor of 7. Apo-GRW$_{stam27(AEL)}$L33-H, the (AEL) stammer in the apo structure, was predicted by AlphaFold3[35] and Rosetta Relax[36] to repack the two flanking ***e***-site Glu layers to core positions that sandwiched the $(His)_3$ site. This could imply that the oxygen of $ZnHis_3O$ site determined by EXAFS, is a Glu residue rather than water (Figure IV-15A and 15B). An analogous UV-Vis signature to that of Co(II) substituted carboxypeptidase was produced by the Co(II) substituted enzyme (Figure IV-15A). Given these modifications with Zinc and Cobalt, the copper geometry and possibly the CuNiR activity are expected to be modified.

The addition of a 3-residue insert has the potential to destabilize the local structure of the 3SCC by, for example, forming a 3_{10}-helix.[8,37,38] The addition of one additional heptad (LKALEEK) to the TRIW sequence resulted in the stabilization of the GRW-3'Py and GRW-4'Py by 5.0 kcal mol^{-1} compared to the analogues TRIW-3'Py and TRW-4'Py under guanidinium chloride denaturation conditions (Table IV-1). Despite the noticeable differences in the stabilities between GRW and TRIW peptides and between GRW-3'Py and were peptides, similar CuNiR kinetics were observed for all derivatives. The addition of an extra heptad to the TRIW designs yielded similar XANES/EXAFS, EPR parameters, and kinetics, suggesting that the oxidized and reduced copper sites are the same between the two designs (Table IV-3 and Table IV-6). Therefore, the GRW scaffold offers a more stable scaffold to explore the effects of stammers without substantially altering the metal binding site from those in Chapter II.

The GRW-4'Py design resulted in presumably a weak K_m value (>600 mM) similar to TRIW-4'Py. However, taking the design approach from what has been learned in Chapter II and Chapter III, the predicted perturbation of an ***a***-site 4'Py to a more ***g***-like position by incorporating a ***d***-site stammer would be predicted to yield a 2-coordinate Cu(I) structure based on the extensive computational and crystallographic assessments of non-metal binding native cc proteins (Figure IV-2, Figure IV-15D).[4,39] This conversion from 2- to 3-coordinate is predicted to allow for tighter substrate binding based on Chapter III. The sequence identity for the stammer was chosen to be AEA because: i) the first alanine would avoid steric clashes with the leucine layer directly above the metal binding site; ii) the glutamate would serve to stabilize the structure through hydrogen

bonding and salt bridge interactions with the neighboring lysine residue on adjacent helices; and iii) the terminating alanine would play a similar role in the secondary coordination sphere as in Cu(I)-TRIW-4'Py L19A (Figure IV-15).

Incorporating the AEA stammer into GRW-4'Py (*e.g.*, $GRW_{stam27(AEA)}$L33-4'Py) resulted in a slight decrease in the stability of the $\Delta\Delta G_u^{\circ}$ (H_2O) < 5.0 kcal mol^{-1}.[40] It is worth pointing out here that the impact on the folding observed in the (AEA) stammer is minimal compared to the ***d***-site alanine substitution made in Chapter II in TRIW-4'Py (*e.g.*, TRIW-4'Py L19A), which produced a noticeable decrease in folding. This may reflect the stabilization afforded by the additional heptad, lessening the impact of the alanine layers on the overall fold of the AEA stammer design. In other words, the structure of GRW is less sensitive to mutation than the TRIW scaffold.[27] As predicted, a 2-coordinate Cu(I) geometry is observed that is best modeled as a $Cu(I)Py_2$ site with $Cu–N_{Py}$ bond distances of 1.94 Å (Table IV-7). This represents a shortening of

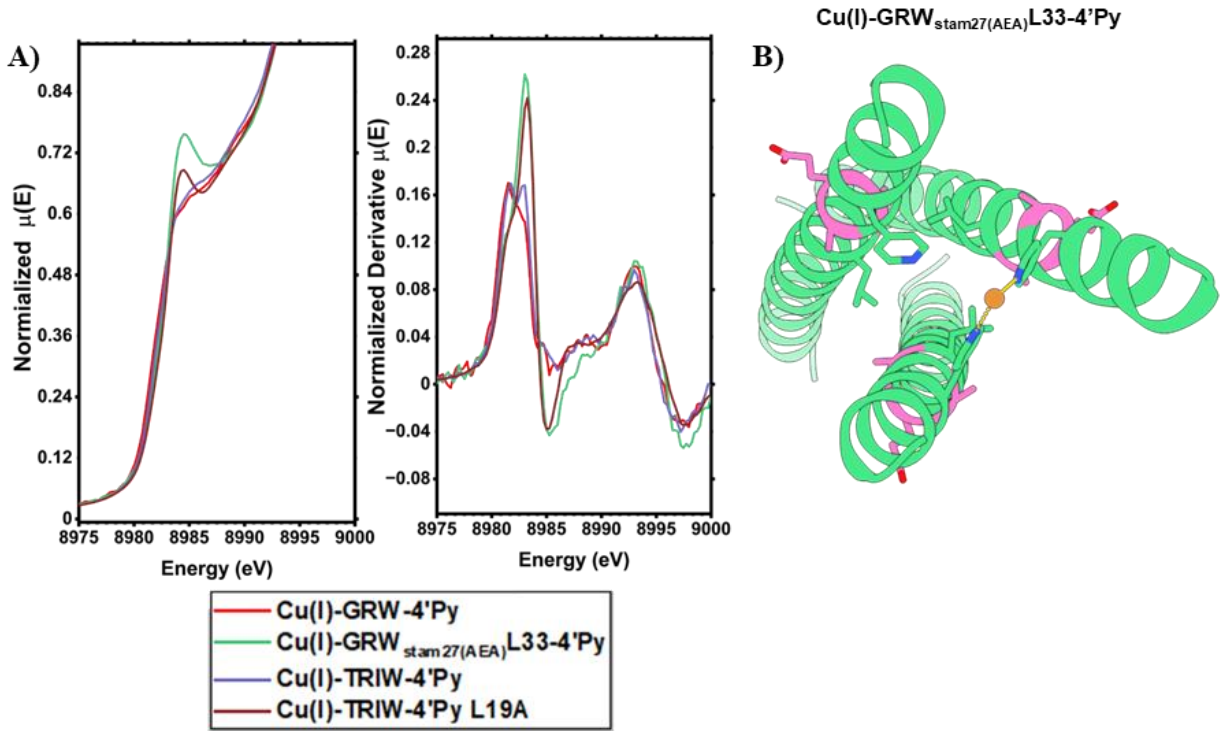


Figure IV-16: Cu(I) XANES comparison of TRIW and GRAND-stammer designs with 4'Py sites: **A)** XANES spectra of reduced enzymes in TRIW and GRW sequences with 4'Py active site (derivative plot [left]), and **B)** AlphaFold assisted modeling of the reduced enzyme of $GRW_{stam27(AEA)}$L33-4'Py.

the average bond distances compared to the 1.97 Å Cu–N_{Py} distance of the 3-coordinate Cu(I)-GRW-4'Py. However, 1.94 Å is still a distance than might be expected for a pure 2-coordinate copper site (*e.g.*, Cu(I)-TRIW-H L19A (1.86 Å Cu(I)–N) but is within range of the 2-coordiante Cu(I)–Pyridine complexes introduced in Chapter II.[41]

Given that modeling the EXAFS cannot with certainty distinguish between 2-coordinate and 3-coordinate complexes due to parameter correlation, their respective rising edges in the XANES regions further supports the assignments as the relative changes observed with the ***d***-site alanine from Chapter II match that of the (AEA) stammer (Figure IV-16). Moreover, comparing the XANES of Cu(I) model complexes from Karlin *et al.* suggests the dip in the derivative spectrum at ~8984 eV is closely associated with 2-coordinate complexes, which corresponds to the intensity of the inflection point at the 1s-4p Cu(I) transition and supports this assignment further. (Figure IV-18).[32] Generating this 2-coordinate Cu(I) resting state is predicted to be more catalytically active, but interestingly, the CuNiR activity only marginally increases with respect to the k_{cat}/K_m (9.5 ± (1.6) M^{-1} s^{-1} vs. 2.6 ± (0.3) M^{-1} s^{-1}, respectively). This design displayed a tighter K_m value (0.29 ± (0.08) M) compared to the GRW-4'Py, which is admittedly undefined within the concentration limits of the CuNiR assay. As with the ***d***-site alanine mutation in Chapter II which relaxes 3-coordinate geometries to more 2-coordinate geometries, the (AEA) stammer provides an alternative method to tune the coordination number around the copper site in 3SCC, albeit utilizing a more complex design that cannot be understood in the context of the strategies developed in Chapter II.

The orientation of the ligand within the core plays a critical role in tuning CuNiR activity. This is most clearly demonstrated in comparing the 3'Py and 4'Py designs in Chapter II (Table IV-6). The ***d***-site alanine mutation (L19A) in TRIW-3'Py exerted a less notable impact on the Cu(I) coordination number and the K_m and k_{cat}/K_m of nitrite reduction compared to the 4'Py ligand. To explore stammer inserts further, along with the AEA stammer, one slightly different stammer (AEL) was introduced in the ***d***-site above the 3'Py site to investigate its influence on the structure of the protein (*e.g.*, $GRW_{stam27(AEL)}$L33-3'Py). The introduction of the AEL stammer into the ***d***-site

above GRW-3'Py did not result in a noticeable change in the 3-coordinate nature of the reduced enzyme compared to Cu(I)-GRW-3'Py; however, the 29th residue influences the fine-structure of the copper center according to the XANES of the AEA stammer (Figure IV-17)[32,42] In Cu(I)-GRW-3'Py, the decrease in intensity and relative red shift of the 8984 eV peak compared to the AEL stammer resemble the XANES of the Cu(I) model $[Cu_2(N_4Py_2)][ClO_4]_2$, reported by Karlin *et al.*, where perchlorate was reasoned to weakly bind to the CuN_3 center, although a crystal

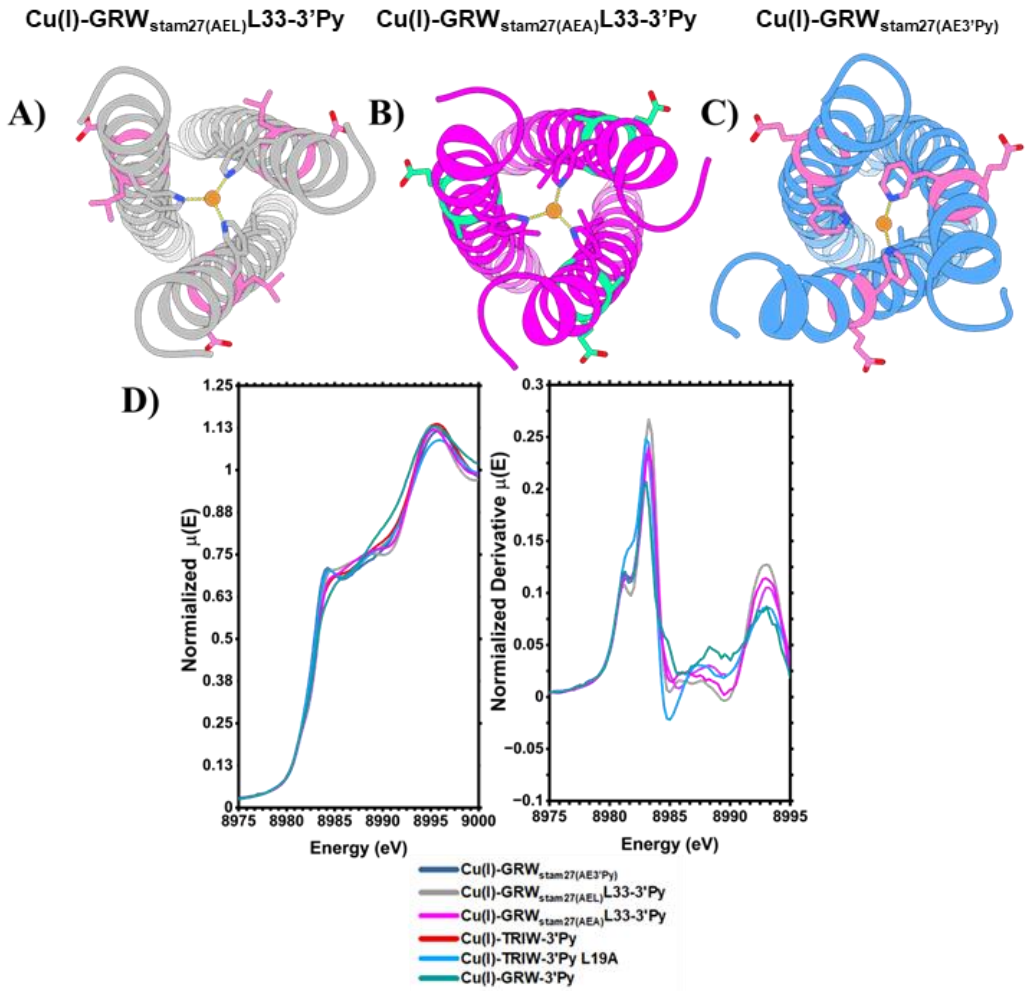


Figure IV-17: Cu(I) XANES comparison of TRIW and GRAND-stammer designs with 3'Py sites and AlphaFold assisted modeling of the reduced enzyme: **A**) Cu(I)-$GRW_{stam27(AEL)}$L33-3'Py, **B)** Cu(I)-$GRW_{stam27(AEA)}$L33-3'Py, **C)** Cu(I)-$GRW_{stam27(AE3'Py)}$, and **D)** XANES spectra of reduced enzymes in TRIW and GRW sequences with 3'Py active site (derivative plot [*right*])**.**

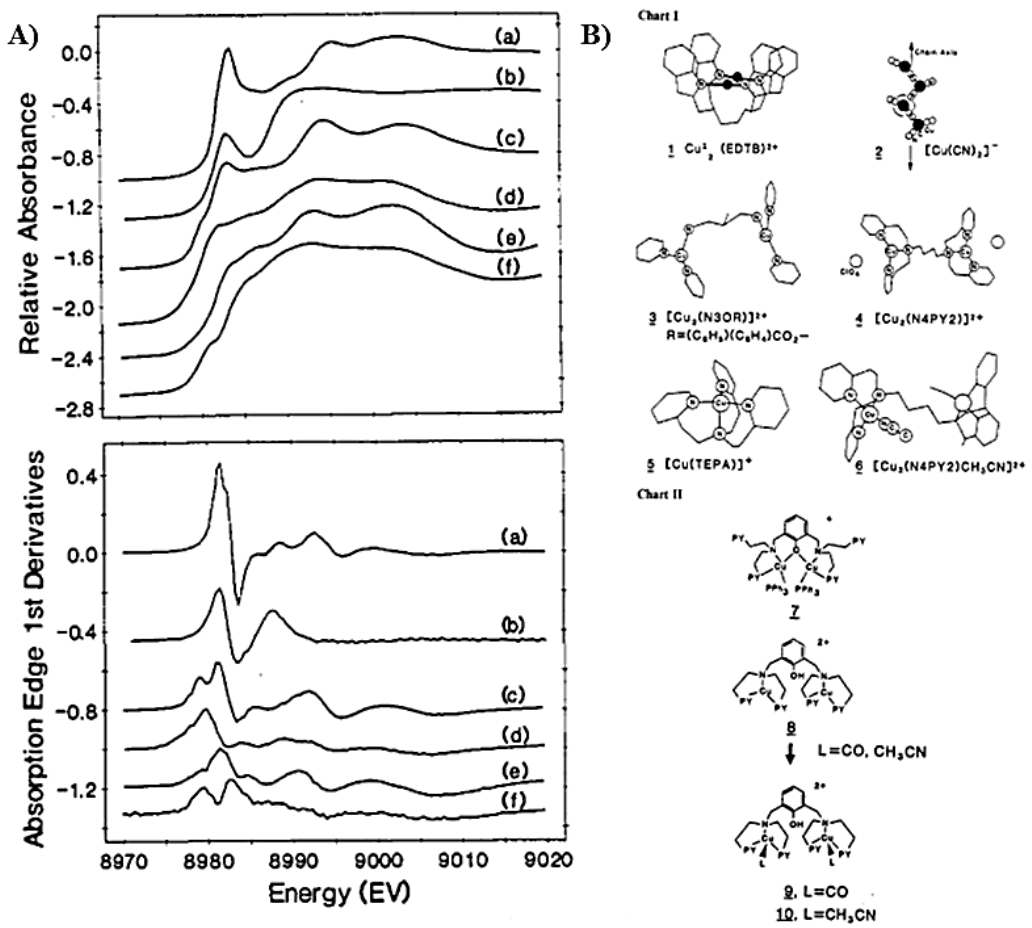


Figure IV-18: XANES of Cu(I) in 2-, 3-, and 4-coordinate pyridine complexes: **A**) X-Ray absorption Cu(I) K-edges (*top*) and their associated first derivative (*bottom*) of Cu(I) model complexes in (**B**). *Note: spectra **(a)-(f)** in **(A)** refer to the complexes 1-6 in **(B)**, respectively.* Reprinted (adapted) with permission from Ref. 32. Copyright 1989 American Chemical Society.

structure was not published. (Figure IV-18).[a] [32] The slight increase in the average Cu–N_{Py} bond distance supports the idea that an additional fourth weak ligand may compose the active site of Cu(I)-GRW-3'Py; however, it is likely not fully occupying this site as the DW-Factor is relatively large for a well-defined primary coordinative ligand (Table IV-7). The derivative spectrum of Cu(I)-$GRW_{stam27(AEL)}$L33-3'Py closely matches the features observed with complex *3*, supporting the assignment of a 3-coordinate geometry than a pure 4-coordinate geometry (Figure IV-18A,

[a] Karlin *et.al* calibrated the Cu Foil to 8982 eV, while the Cu Foil in this thesis are calibrated to 8980.29 eV.

spectrum *c*). A slight tightening of the K_m (0.16 ± (0.02) M vs. 0.37 ± (0.1) M) is observed, and between these two designs, the Cu(II) apparent K_d are thermodynamically different. Considering the differences in their respective EPR and UV-Vis spectra, the AEL stammer may alter the local core packing to yield electronically distinct Cu(II) binding sites. In the context of the CuNiR kinetics, these observations may suggest the CuNiR activity can be modified by altering the active site in the oxidized enzyme rather than with the reduced enzyme, as we have seen in the previous chapters.

The trends in the steady state kinetics of TRIW-3'Py, $GRW_{stam27(AEL)}$L33-3'Py, and $GRW_{stam27(AEA)}$L33-4'Py at least suggest that removing the sterically cumbersome leucine with the (AEA) stammer does not change the preferred coordination number of Cu(I), and therefore, any subsequent increase the catalytic efficiency (via a lowering of K_m). The (AEA) stammer lowered the k_{cat}/K_m with respect to the (AEL) stammer (k_{cat}/K_m=5.5 ± (1.2) M^{-1} s^{-1} vs. 15.3 ± (1.7) M^{-1} s^{-1}, respectively). However, the A29 layer in this stammer (*i.e.*, $A_{27}E_{28}A_{29}$) is solvent exposed rather than tucked away in the core in a similar manner to the L19A layer in Chapter II. Therefore, the extent of substrate access to the 2-coordinate Cu(I) site is likely different, especially given the possibility that at least one ***g***-site glutamate residue (E30) moves into the core and bind to the Cu(II) form. In the absence of a crystal structure of either the apo or holo forms, AlphaFold's and Rosetta's relaxed structure of the apo-$GRW_{27stamAEA}$L33-F places the A29 in an ***e***-like position that is more excluded from the hydrophobic core (Figure IV-15D). This would allow for a new copper site to be generated by restricting the ability for a third pyridine ligand to compose the primary coordination sphere with at 3'Py active site (Figure IV-15D).[43] In other words, the design strategy was to rotate the pyridine slightly outside the hydrophobic core in order that only two pyridines on adjacent helixes could reasonably chelate Cu(I) to form two-coordinate Cu(I). This configuration would be predicted to enhance CuNiR activity via a lower K_m effect. As predicted, the $GRW_{stam27(AE3'Py)}$ forms what is best described as a 2-coordinate Cu(I) complex with an average Cu–N_{Py} bond distance of 1.94 Å which is the most 2-coordinate Cu(I) structure of any 3'Py active sites designed in this thesis, according to the XANES (Figure IV-17D).[34] Considering the error

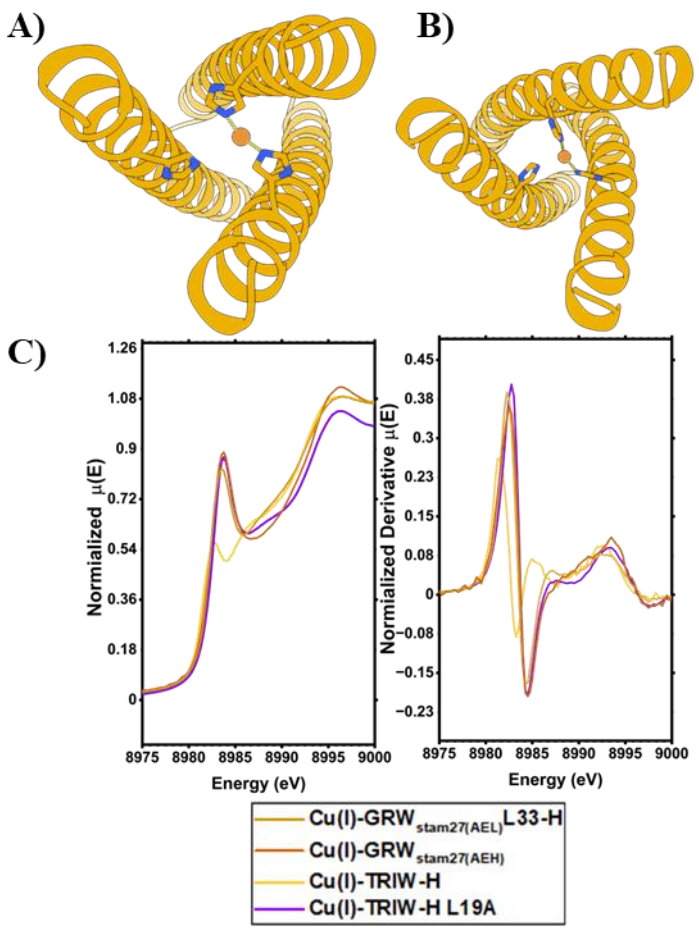


Figure IV-19: Cu(I) XANES comparison of TRIW and GRAND-stammer designs with histidine sites and AlphaFold assisted modeling of the reduced enzyme: **A**) $GRW_{stam27(AEL)}$L33-H, **B)** $GRW_{stam27(AEH)}$, and **C)** XANES spectra of reduced enzymes in TRIW and GRW sequences with histidine active sites (derivative plot [*left*])**.**

associated with the kinetics, there is little change in the k_{cat}/K_m compared to the parent design GRW-3'Py (17.0 ± (8) M^{-1} s^{-1} vs. 11.0 ± (1.8) M^{-1} s^{-1}) but with a slightly tighter NO_2^- affinity for the active site (K_m=0.13 ± (0.08) M vs 0.37 ± (0.1) M, respectively). Thus, the strategy to design a 2-coordinate reduced copper site using the A29 mutation was successful, however, the kinetic parameters were closely similar to the (AEL) stammer, indicating that the 2-coordinate nature of the reduced enzyme is alone not sufficient to engender better catalytic efficiency. Given the similar orientations between the ε-nitrogen in histidine and the nitrogen in 3'pyridine when bound to a metal within the hydrophobic core, a histidine layer was designed into the stammer in a way analogous to the AE3'Py stammer in order to determine if a similar 2-coordinate Cu(I) complex

to the Cu(I)-GRW$_{stam27(AEL)}$L33-H would yield a change in CuNiR in a slightly different environment.[16] First, the addition of the ***d***-site AEL or AEH stammers resulted in a decreased catalytical efficiency compared to the parent design, GRW-H (Table IV-6). Similar to TRIW-H in Chapter II, the K_m is significantly higher than any of the designs featuring a pyridine active site and was not accessible in a reasonable range of $NaNO_2$. Interestingly, the oxidized enzymes of GRW$_{stam27(AEL)}$L33-H and GRW$_{stam27(AEH)}$ are relatively different as judged by their UV-Vis spectrum which is similar to the relationship between their 3'Py analogs (ε = 115 M^{-1} cm^{-1} vs. 45 M^{-1} cm^{-1}, respectively) (Figure IV-5). However, the impact of their reduced forms is dependent on the identity of the ligand, where the histidine designs are best described as both 2-coordinate Cu(I) bis-His sites, and the reduced 3'Py analogs are coordinatively different from one another (Table IV-7). Another question that was addressed is whether inserting the metal binding residue within the stammer insert led to behavior different from locating the active site one heptad below the stammer. As previously mentioned, studies using Co(II) suggest that the binding mode is quite different between two such positions, with the histidine in the 33-position, possibility leading to at least one carboxylate bound to the Co(II) center, whereas a histidine placed in the 29-position yielded a Co(II) center that was perturbed further. Therefore, these two are quite distinct from one another. For the copper derivative, only a marginal improvement is achieved by moving the histidine into the stammer compared to GRW$_{stam27(AEL)}$L33-H, and the k_{cat} values cannot be reasonably fitted, making the small improvement difficult to interpret considering the changes in coordination number between the two oxidation states (Table IV-6). However, it is not unreasonable to speculate that the k_{cat} values are lower than the pyridine active

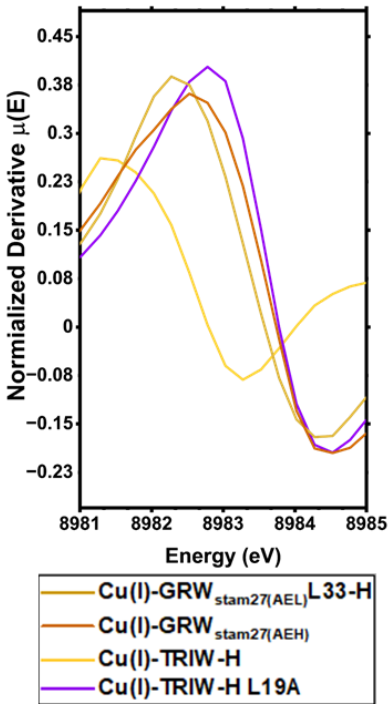


Figure IV-20: XANES derivative spectra of the reduced copper-histidine enzymes.

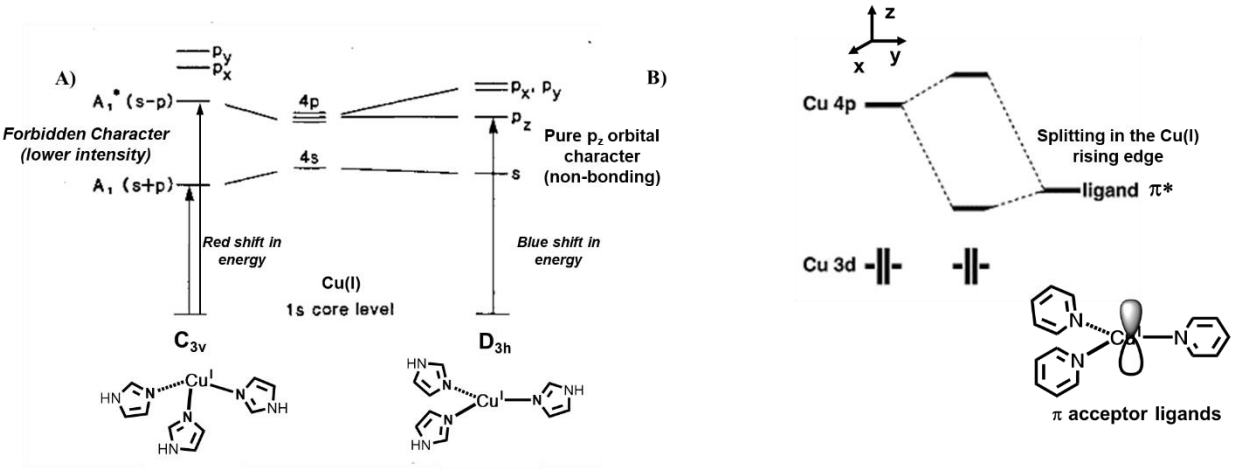


Figure IV-21: Summary of orbital interactions of the Cu(I) XANES: **A**) Orbital diagram highlighting the C_{3v} to D_{3h} distortion in 3-coordinate Cu(I), and **B)** Orbital diagram highlighting a π-acceptor ligands effects on Cu(I) 4p orbital. (**A**) was adapted with permission from Ref. 32, Copyright 1989 American Chemical Society.

sites, given the relative velocities observed in their CuNiR kinetics (Table IV-6). The XANES suggest that the 2-coordinate reduced enzymes are, however, electronically different, as the 3'Py pre-edge is shifted by ~ +0.79 eV compared to the histidine ligand. This feature has been a common occurrence among both histidine and pyridine active sites, whether a stammer is present or not. It has previously been speculated that, within the histidine family of peptides, higher CuNiR activity also exhibits a slight increase in the peak energy of this feature, and this trend is maintained once more, with the $GRW_{stam27(AEH)}$ displaying a shift to higher energy than TRIW-H in agreement with TRIW-H L19A and a higher intensity, which is more suggestive of a 2-coordinate species (Figure IV-20).[16,19] This observation within the histidine family may stem from the more 2-coordinate nature of the most efficient enzymes in their reduced state or could reflect a distortion to more D_{3h} symmetry (Figure IV-21A).[33] The pyridine ligand blue shifts this transition, independent of the coordination number, compared to the histidine and may reflect the more π-acid character of the pyridine ligands to alter the reduced enzyme electronics and effect the chemical step after binding (*e.g.*, an increase in k_{cat}) and substrate binding (Figure IV-21B).[44,45] With respect to k_{cat}/K_m values, admittedly, $GRW_{stam27(AEL)}$L33-H did not have the expected CuNiR activity (4x) to that of GRW-H based on the pseudo 1st order rate constants (k'=112 × 10^{-4} s^{-1} vs.

k=28 × 10^{-4} s^{-1}, respectively).[16] Future experiments will likely have to take into account the differences in catalyst concentration between both experiments (20-200 μM vs. 1 μM, respectively) to resolve the seemingly contradictory relationship between the two parameters.

Conclusion:

In this chapter, I have presented sequence modifications that alter the preferred packing of the interfacial residues in the proximity of various mono-copper binding sites. Compared to the changes in the catalytic efficiencies in Chapter II, the stammers explored in this chapter did not rival TRIW-4'Py L19A. The details of the atomic-level changes in the second coordination sphere and the overall structure are not fully understood and will require crystallographic characterization of the apo and holo forms to generalize this approach to different designed scaffolds. However, there are conclusions that can be used to optimize the design of metalloenzymes that can be drawn based on the current understanding gained from this chapter: i) the addition of a single stammer led to minimal destabilization of the GRW scaffold which yielded well-folded and stable proteins even when the active site was built within the stammer; ii) these mutations did not *interfere* with metal binding to the active sites; and iii) the alterations of the metal coordination number and CuNiR activity are dependent not only on the stammer's sequence but also on the orientation of the ligand within the active site.

The insertion of an additional heptad to the sequence introduced in Chapter II did not play a role in influencing CuNiR activity. However, over the course of this thesis and this chapter, the Cu(I) oxidation state and its primary coordination sphere play a vital role in determining the rate of nitrite reduction within these designed monocopper active sites. Interestingly, the (AEL) stammer changed the geometry around the Cu(II) oxidation state while minimally impacting the reduced enzyme geometry. Overall, this work suggests that sequence discontinuities within coiled coil topologies are another tool for designers to control catalytic centers to achieve a targeted response and influence the rate of catalysis.

References:

(1) Lupas, A. N.; Gruber, M. The Structure of α-Helical Coiled Coils. *Adv. Protein Chem.* **2005**, *70*, 37–38.

(2) Crick, F. H. C. The Packing of A-Helices: Simple Coiled-Coils. *Acta Cryst.* **1953**, *6*, 689.

(3) Carr, C. M.; Chaudhry, C.; Kim, P. S. Influenza Hemagglutinin Is Spring-Loaded by a Metastable Native Conformation. *Proc. Natl. Acad. Sci. U. S. A.* **1997**, *94* (26), 14306–14313.

(4) Brown, J. H.; Cohen, C.; Parry, D. A. D. Heptad Breaks in α-Helical Coiled Coils: Stutters and Stammers. *Proteins Struct. Funct. Genet.* **1996**, *26* (2), 134–145.

(5) Xing, X.; Shi, J.; Cui, P.; Yan, C.; Zhang, Y.; Zhang, Y.; Wang, C.; Chen, Y.; Zeng, X.; Tian, G.; Liu, L.; Guan, Y.; Li, C.; Suzuki, Y.; Deng, G.; Chen, H. Evolution and Biological Characterization of H5N1 Influenza Viruses Bearing the Clade 2.3.2.1 Hemagglutinin Gene. *Emerg. Microbes Infect.* **2024**, *13* (1).

(6) Higgins, C. D.; Malashkevich, V. N.; Almo, S. C.; Lai, J. R. Influence of a Heptad Repeat Stutter on the PH-Dependent Conformational Behavior of the Central Coiled-Coil from Influenza Hemagglutinin HA2. *Proteins Struct. Funct. Bioinforma.* **2014**, *82* (9), 2220–2228.

(7) Reed, M. L.; Bridges, O. A.; Seiler, P.; Kim, J.-K.; Yen, H.-L.; Salomon, R.; Govorkova, E. A.; Webster, R. G.; Russell, C. J. The PH of Activation of the Hemagglutinin Protein Regulates H5N1 Influenza Virus Pathogenicity and Transmissibility in Ducks. *J. Virol.* **2010**, *84* (3), 1527–1535.

(8) Hartmann, M. D.; Ridderbusch, O.; Zeth, K.; Albrecht, R.; Testa, O.; Woolfson, D. N.; Sauer, G.; Dunin-Horkawicz, S.; Lupas, A. N.; Alvarez, B. H. A Coiled-Coil Motif That Sequesters Ions to the Hydrophobic Core. *Proc. Natl. Acad. Sci. U. S. A.* **2009**, *106* (40), 16950–16955.

(9) Hartmann, M. D.; Mendler, C. T.; Bassler, J.; Karamichali, I.; Ridderbusch, O.; Lupas, A. N.; Hernandez Alvarez, B. α/β Coiled Coils. *Elife* **2016**, *5*.

(10) Martin, S. L. Nucleic Acid Chaperone Properties of ORF1p from the Non-LTR Retrotransposon, LINE-1. *RNA Biology*. Taylor and Francis Inc. November 28, 2010, pp 706–711.

(11) Thomas, C. A.; Paquola, A. C. M.; Muotri, A. R. LINE-1 Retrotransposition in the Nervous System. *Annual Review of Cell and Developmental Biology*. 2012, pp 555–573.

(12) Gruber, M.; Lupas, A. N. Historical Review: Another 50th Anniversary - New Periodicities in Coiled Coils. *Trends in Biochemical Sciences*. 2003, pp 679–685.

(13) Kale, S. P.; Moore, L.; Deininger, P. L.; Roy-Engel, A. M. Heavy Metals Stimulate Human LINE-1 Retrotransposition. In *International Journal of Environmental Research and Public Health*; Molecular Diversity Preservation International, 2005; Vol. 2, pp 14–23.

(14) Pinter, T. B. J.; Ruckthong, L.; Stuckey, J. A.; Deb, A.; Penner-Hahn, J. E.; Pecoraro, V. L. Open Reading Frame 1 Protein of the Human Long Interspersed Nuclear Element 1 Retrotransposon Binds Multiple Equivalents of Lead. *J. Am. Chem. Soc.* **2021**, *143* (37), 15271–15278.

(15) Pinter, T. B. J.; Ervin, C. S.; Deb, A.; Penner-Hahn, J. E.; Pecoraro, V. L. Cu(I) Binding to Designed Proteins Reveals a Putative Copper Binding Site of the Human Line1 Retrotransposon Protein ORF1p. *Inorg. Chem.* **2022**, *61* (12), 5084–5091.

(16) Pinter, T. B. J.; Manickas, E. C.; Tolbert, A. E.; Koebke, K. J.; Deb, A.; Penner-Hahn, J. E.;

Pecoraro, V. L. Making or Breaking Metal-Dependent Catalytic Activity: The Role of Stammers in Designed Three-Stranded Coiled Coils. *Angew. Chemie Int. Ed.* **2020**, *59* (46), 20445–20449.
(17) Zuo, Y.; Deng, Y. The Near-UV Absorption Constants for Nitrite Ion in Aqueous Solution. *Chemosphere* **1998**, *36* (1), 181–188.
(18) Wagner, B. A.; Buettner, G. R. Stability of Aqueous Solutions of Ascorbate for Basic Research and for Intravenous Administration. *Adv. Redox Res.* **2023**, *9*, 100077.
(19) Koebke, K. J.; Yu, F.; Salerno, E.; Van Stappen, C.; Tebo, A. G.; Penner-Hahn, J. E.; Pecoraro, V. L. Modifying the Steric Properties in the Second Coordination Sphere of Designed Peptides Leads to Enhancement of Nitrite Reductase Activity. *Angew. Chemie* **2018**, *130* (15), 4018–4021.
(20) Stoll, S.; Schweiger, A. EasySpin, a Comprehensive Software Package for Spectral Simulation and Analysis in EPR. **2005**.
(21) Weng, T. C.; Waldo, G. S.; Penner-Hahn, J. E. A Method for Normalization of X-Ray Absorption Spectra. In *Journal of Synchrotron Radiation*; 2005; Vol. 12, pp 506–510.
(22) Ravel, B.; Newville, M. ATHENA, ARTEMIS, HEPHAESTUS: Data Analysis for X-Ray Absorption Spectroscopy Using IFEFFIT. In *Journal of Synchrotron Radiation*; 2005; Vol. 12, pp 537–541.
(23) Royappa, A. T.; Royappa, A. D.; Moral, R. F.; Rheingold, A. L.; Papoular, R. J.; Blum, D. M.; Duong, T. Q.; Stepherson, J. R.; Vu, O. D.; Chen, B.; Suchomel, M. R.; Golen, J. A.; André, G.; Kourkoumelis, N.; Mercer, A. D.; Pekarek, A. M.; Kelly, D. C. Copper(I) Oxalate Complexes: Synthesis, Structures and Surprises. *Polyhedron* **2016**, *119*, 563–574.
(24) Dimakis, N.; Bunker, G. XAFS Debye-Waller Factors for Zn Metalloproteins. *Phys. Rev. B - Condens. Matter Mater. Phys.* **2004**, *70* (19), 1–12.
(25) Stern, E. A. Number of Relevant Independent Points in X-Ray-Absorption Fine-Structure Spectra. *Phys. Rev. B* **1993**, *48* (13), 9825–9827.
(26) Tegoni, M.; Yu, F.; Bersellini, M.; Penner-Hahn, J. E.; Pecoraro, V. L. Designing a Functional Type 2 Copper Center That Has Nitrite Reductase Activity within α-Helical Coiled Coils. *Proc. Natl. Acad. Sci. U. S. A.* **2012**, *109* (52), 21234–21239.
(27) Kwok, S. C.; Hodges, R. S. Effect of Chain Length on Coiled-Coil Stability: Decreasing Stability with Increasing Chain Length. *Biopolym. - Pept. Sci. Sect.* **2004**, *76* (5), 378–390.
(28) Vivian, J. T.; Callis, P. R. Mechanisms of Tryptophan Fluorescence Shifts in Proteins. *Biophys. J.* **2001**, *80* (5), 2093–2109.
(29) Koebke, K. J.; Yu, F.; Van Stappen, C.; Pinter, T. B. J.; Deb, A.; Penner-Hahn, J. E.; Pecoraro, V. L. Methylated Histidines Alter Tautomeric Preferences That Influence the Rates of Cu Nitrite Reductase Catalysis in Designed Peptides. *J. Am. Chem. Soc.* **2019**, *141* (19), 7765–7775.
(30) Tabbì, G.; Giuffrida, A.; Bonomo, R. P. Determination of Formal Redox Potentials in Aqueous Solution of Copper(II) Complexes with Ligands Having Nitrogen and Oxygen Donor Atoms and Comparison with Their EPR and UV-Vis Spectral Features. *J. Inorg. Biochem.* **2013**, *128*, 137–145.
(31) Neese, F. Theoretical Study of Ligand Superhyperfine Structure. Application to Cu(II) Complexes. *J. Phys. Chem. A* **2001**, *105* (17), 4290–4299.
(32) Blackburn, N. J.; Strange, R. W.; Reedijk, J.; Volbeda, A.; Farooq, A.; Zubieta, J.; Karlin, K. D. X-Ray Absorption Edge Spectroscopy of Copper(I) Complexes. Coordination Geometry of Copper(I) in the Reduced Forms of Copper Proteins and Their Derivatives

with Carbon Monoxide. *Inorg. Chem.* **1989**, *28* (7), 1349–1357.
(33) Kau, L. shan; Spira-solomon, D. J.; Penner-Hahn, J. E.; Hodgson, K. O.; Solomon, E. I. X-Ray Absorption Edge Determination of the Oxidation State and Coordination Number of Copper: Application to the Type 3 Site in Rhus Vernicifera Laccase and Its Reaction with Oxygen. *J. Am. Chem. Soc.* **1987**, *109* (21), 6433–6442.
(34) Pitts, W. C.; Deb, A.; Penner-Hahn, J. E.; Pecoraro, V. L. Revving up a Designed Copper Nitrite Reductase Using Noncoded Active Site Ligands. *ACS Catal.* **2024**, *14* (6), 4362–4368.
(35) Abramson, J.; Adler, J.; Dunger, J.; Evans, R.; Green, T.; Pritzel, A.; Ronneberger, O.; Willmore, L.; Ballard, A. J.; Bambrick, J.; Bodenstein, S. W.; Evans, D. A.; Hung, C. C.; O'Neill, M.; Reiman, D.; Tunyasuvunakool, K.; Wu, Z.; Žemgulytė, A.; Arvaniti, E.; Beattie, C.; Bertolli, O.; Bridgland, A.; Cherepanov, A.; Congreve, M.; Cowen-Rivers, A. I.; Cowie, A.; Figurnov, M.; Fuchs, F. B.; Gladman, H.; Jain, R.; Khan, Y. A.; Low, C. M. R.; Perlin, K.; Potapenko, A.; Savy, P.; Singh, S.; Stecula, A.; Thillaisundaram, A.; Tong, C.; Yakneen, S.; Zhong, E. D.; Zielinski, M.; Žídek, A.; Bapst, V.; Kohli, P.; Jaderberg, M.; Hassabis, D.; Jumper, J. M. Accurate Structure Prediction of Biomolecular Interactions with AlphaFold 3. *Nature* **2024**, *630* (8016), 493–500.
(36) Conway, P.; Tyka, M. D.; DiMaio, F.; Konerding, D. E.; Baker, D. Relaxation of Backbone Bond Geometry Improves Protein Energy Landscape Modeling. *Protein Sci.* **2014**, *23* (1), 47–55.
(37) Woolfson, D. N. Coiled-Coil Design: Updated and Upgraded. *Subcell. Biochem.* **2017**, *82*, 35–61.
(38) Bottorf, L.; Rafferty, S.; Sahu, I. D.; McCarrick, R. M.; Lorigan, G. A. Utilizing Electron Spin Echo Envelope Modulation to Distinguish between the Local Secondary Structures of an α-Helix and an Amphipathic 310-Helical Peptide. *J. Phys. Chem. B* **2017**, *121* (14), 2961–2967.
(39) Schmidt, N. W.; Grigoryan, G.; DeGrado, W. F. The Accommodation Index Measures the Perturbation Associated with Insertions and Deletions in Coiled-Coils: Application to Understand Signaling in Histidine Kinases. *Protein Science*. 2017, pp 414–435.
(40) Hicks, M. R.; Holberton, D. V; Kowalczyk, C.; Woolfson, D. N. Coiled-Coil Assembly by Peptides with Non-Heptad Sequence Motifs. *Fold. Des.* **1997**, *2* (3), 149–158.
(41) Habiyakare, A.; Lucken, E. A. C.; Bernardinelli, G. Crystallographic and Copper-63,65 Nuclear Quadrupole Resonance Study of Two-Co-Ordinated Copper(I) Cations with Hindered Substituted Pyridine Ligands. *J. Chem. Soc. Dalt. Trans.* **1991**, No. 9, 2269–2273.
(42) Zhang, R.; McEwen, J. S. Local Environment Sensitivity of the Cu K-Edge XANES Features in Cu-SSZ-13: Analysis from First-Principles. *J. Phys. Chem. Lett.* **2018**, *9* (11), 3035–3042.
(43) Jumper, J.; Evans, R.; Pritzel, A.; Green, T.; Figurnov, M.; Ronneberger, O.; Tunyasuvunakool, K.; Bates, R.; Žídek, A.; Potapenko, A.; Bridgland, A.; Meyer, C.; Kohl, S. A. A.; Ballard, A. J.; Cowie, A.; Romera-Paredes, B.; Nikolov, S.; Jain, R.; Adler, J.; Back, T.; Petersen, S.; Reiman, D.; Clancy, E.; Zielinski, M.; Steinegger, M.; Pacholska, M.; Berghammer, T.; Bodenstein, S.; Silver, D.; Vinyals, O.; Senior, A. W.; Kavukcuoglu, K.; Kohli, P.; Hassabis, D. Highly Accurate Protein Structure Prediction with AlphaFold. *Nature* **2021**, *596* (7873), 583–589.
(44) Habiyakare, A.; Lucken, E. A. C. The 63, 65Cu NQR Spectra of Di-Coordinated CuI Cations with 2-Substituted Pyridine Ligands. *Zeitschrift fur Naturforsch. - Sect. A J. Phys.*

Sci. **1990**, *45* (3–4), 224–228.
(45) Rudolph, J.; Jacob, C. R. Revisiting the Dependence of Cu K-Edge X-Ray Absorption Spectra on Oxidation State and Coordination Environment. *Inorg. Chem.* **2018**, *57* (17), 10591–10607.

Chapter V
Conclusions and Future Directions.

While the designed copper centers discussed herein are embedded in an α-helical coiled coil, a scaffold completely different from that in native copper nitrite reductase (CuNiR), a certain degree of structural integrity and reactivity is still present inherent to the non-natural copper-pyridine centers. In Chapter II, I designed novel, unnatural active sites composed entirely of pyridine ligands within a *de novo* designed protein. These copper proteins formed type 2 copper centers (T2Cu) capable of catalyzing NO_2^- reduction faster than any water-soluble homogeneous CuNiR mimic reported. It is clear that pyridine enhances a chemical step that follows substrate binding in comparison to the more native active site that contains histidines (larger k_{cat} values). Additionally, the substantial disparity in substrate binding between the 3'Pyridine (3'Py) and 4'Pyridine (4'Py) active sites, with and without alanine, suggests that the 4'Py site likely benefited from more than just extra space and flexibility, as it also resulted in a coordination number shift in the Cu(I) oxidation state. These observations emphasize the role that the secondary coordination sphere plays in the control of the primary coordination sphere when engineering new proteins for enzymatic reactivity. The invariance of the k_{cat} values from enzymes reported in Chapter II and Chapter IV suggests that either N–O bond activation or proton transfer is unchanged during the catalytic cycle. Furthermore, it was discovered in Chapter III that the reduced enzyme is essential for binding NO_2^- during catalysis. From Chapter IV, the addition of a heptad to the sequence described in Chapter II did not significantly impact CuNiR activity but resulted in changes in the geometry of the copper in oxidized and reduced enzymes. Furthermore, CuNiR activity remained unchanged within the GRW-X'Py and TRIW-X'Py design families, indicating the possibility that some design elements could be shared by the pyridine-containing GRW and TRIW families of

enzymes. Overall, this thesis has shown that, rather than relying solely on a secondary coordination sphere effect to remove steric interactions, the degree of nitrite reduction activity within these engineered monocopper active sites is primarily dependent on the Cu(I) oxidation state and its primary coordination sphere ligands which, in turn, influences K_m values. *Based on the conclusions in this thesis, a few elements should be considered to further improve the CuNiR rates.*

V.1: Designing 3SCC with features important to catalysis.

In bioinorganic chemistry, nature's capacity to distinguish between metal complexation at various binding sites is fundamental. The histidine brace motif, for example, serves an important role in binding copper within copper chaperone proteins such as CopC (*i.e., Cu(I)/*Cu(II)) while also composing the active site of an enzyme such as lytic polysaccharide monooxygenases (*i.e.*, Cu(I)/Cu(II)), exemplifying an active site motif that serves two different functions that are finely tuned by the primary coordination and local folding.[1–4] The design strategies implemented herein focused on controlling the electronics and coordination number within the primary coordination sphere, and in particular, the ***a***-site was used to explore the effects on CuNiR activity from this above modification. However, the ***d***-sites are projected more interiorly than the ***a***-sites which offers a completely different design space to leverage.[5] Moving the binding site along the coiled coil towards the N-terminus, either in an ***a***-site or ***d***-site, offers a different design space to explore to modify metal binding and k_{cat} and K_m. This design is motivated by the CuNiR activity of the 3'Py and 4'Py analogs, whereby the differing orientations of the nitrogen shifted the k_{cat}/K_m from 5 M^{-1} s^{-1} (TRIW-4'Py) to 11 M^{-1} s^{-1} (TRIW-3'Py).[6] While this efficiency change is only a slight increase, a point to consider is the design of the primary coordination sphere in a ***d***-site to stabilize different oxidation states and the investigation of the secondary coordination sphere within the ***a***-sites which has yet to be explored. For example, a critial residue in native CuNiRs is the Asp_{CAT} which is responsible for proton-coupled electron-transfer and activating the substrate at the T2Cu center.[7] The lack of the Asp_{CAT} and/or His_{CAT} motifs within this design is likely partially, if not entirely, responsible for the factor of 10^3 K_m difference between native CuNiR and the 3-fold

symmetric scaffolds herein. The proposal that the secondary coordination sphere is a limiting factor in designing a CuNiR currently is further supported by the fact that the introduction of only the primary coordination sphere of CuNiR (*i.e.*, $CuHis_3$) within the electron transfer protein, azurin, produced similar K_m (~30 mM) and k_{cat} (~9 s^{-1}) values as the scaffolds reported in Chapter II.[8] It was previously demonstrated in TRIW-H, however, that the incorporation of a ***d***-site Asp layer above or below the ***a***-site $(His)_3$ yielded only marginal increases in the pseudo first-order rate constants and was comparable to that of a non-proton donor such as alanine ($k'_{L19D}=2.4 \times 10^{-2}$ s^{-1} vs. $k'_{L19A}=3.5 \times 10^{-2}$ s^{-1}, respectively).[9] The close proximity of the negative charges could result in the possible exclusion of the Asp residues from the core. In contrast, ***a***-sites are in a more "open" configuration, potentially providing the space needed to adopt favorable conformations within the core.[10] One of the key elements defining site selectivity and the preferred binding modes of particular metals to these cysteine ***a*** and ***d***-sites is the varied orientations of Leu layers above and below them which suggest that any secondary coordination sphere modifications should be explored both above and below the active sites.[5]

An important avenue to investigate is the transition from the 3-fold symmetric design and explore CuNiR activity within an asymmetric scaffold. An example of where the foundation has previously been explored is the A_2B heterotrimer reported by Dr. Audrey Tolbert.[11] The selectivity in the GRW scaffold results from the ability of a ***d***-site layer of Pb(II)-binding cysteines to hydrogen bond with a core water that is controlled by the steric packing of the ***a***-site leucine above. To achieve the desired A_2B constructs, an energetic competition must be waged between the best possible packing of hydrophobes (*e.g.*, Leu), the stability that results from water access to the hydrophobic cavity formed by Ala, and the subsequent hydrogen-bond formed to one of the cysteine sulfur atoms coordinated to Pb(II). The minimum requirement that provided additional space for one water was an $(Ala^a)(Leu^a)_2$ layer which was subsequently demonstrated not to impact metal binding to an ***a***-site $(His)_3$ site, allowing the design of a catalyst with an asymmetric secondary coordination sphere. Specifically, the first design would involve the placement of a $(Leu^d)_2(Asp^d)$ layer directly above an ***a***-site histidine or pyridyl active site to first test the

involvement for substrate stabilization and proton transfer (Figure V-1F&1G). This design has already enhanced copper-only superoxide dismutase (CuSOD) activity by ~4x compared to the parent design using the Fridovich assay (k_{McF}=2.7 × 10^7 M^{-1} s^{-1} vs. k_{McF}=0.67 × 10^7 M^{-1} s^{-1}, respectively) which motivates this use of the strategy further to improve CuNiR activity.[12] One limitation of the A_2B design with Cys^d site is the 7.5–9.5 pH range at which full selectivity is observed (*unpublished data*).[12] This is because the Pb(II)-Scys bonds are protonated under acidic conditions. However, structural analysis has demonstrated that As(III), which has a larger positive charge than Pb(II), produces an identical MS_3 core while retaining its cysteine bonds all the way down to pH 2.[13] As(III) may be identified by ESI-MS and exhibits a high preference for cysteine over His or carboxylates. As(III) heterotrimer will therefore enable investigation into the desired CuNiR.[14] Moreover, CuNiR activity has been studied at more acidic pH values than 7.5 (*e.g.*, pH 5.8-5.9) due to the very sluggish catalytic efficiency of TRIW-H (k_{cat}/K_m= 0.026 M^{-1} s^{-1}). However, the pyridyl active sites explored in Chapter II result in far superior catalytic efficiency, with TRIW-3'Py striking a balance between catalytic efficiency and a parent design that can be readily used for comparison at pH 7.5. Another limitation of this design stems from a possible preference of the Asp sidechain to act as a primary coordination ligand and bind to the Cu(II) site, yielding either one or two Cu(II)-O bonds rather than a proton donor above the active site.[15] The Co(II) analog, which tends to be more sensitive to electronic transitions from the primary coordination sphere, yields similar UV-Vis and EPR spectra to that of Co(II) substituted carboxypeptidase which contains an active site composed of $(His)_2(Asp)$ (Figure V-1B and 1D).[16–18] While a different metal than Cu(II), this suggests the distances between the ***d***-site and ***a***-site do not restrict this adduct from forming. To restrict this distance and to design a second generation of heterotrimers, a negative design approach should be taken to incorporate the unnatural amino acid, 2-amino-propanedioic acid, which shortens the Asp residue by one methylene group and prevents the formation of a carboxylate-copper bond (Figure V-1H). The ligand to metal charge transfer from Cu(I) to NO_2^- is energetically unfavorable without proton transfer to the Cu(I)-NO_2^-, according to a two-dimensional potential energy surface based on a synthetic small molecule model.[19] In Chapter III,

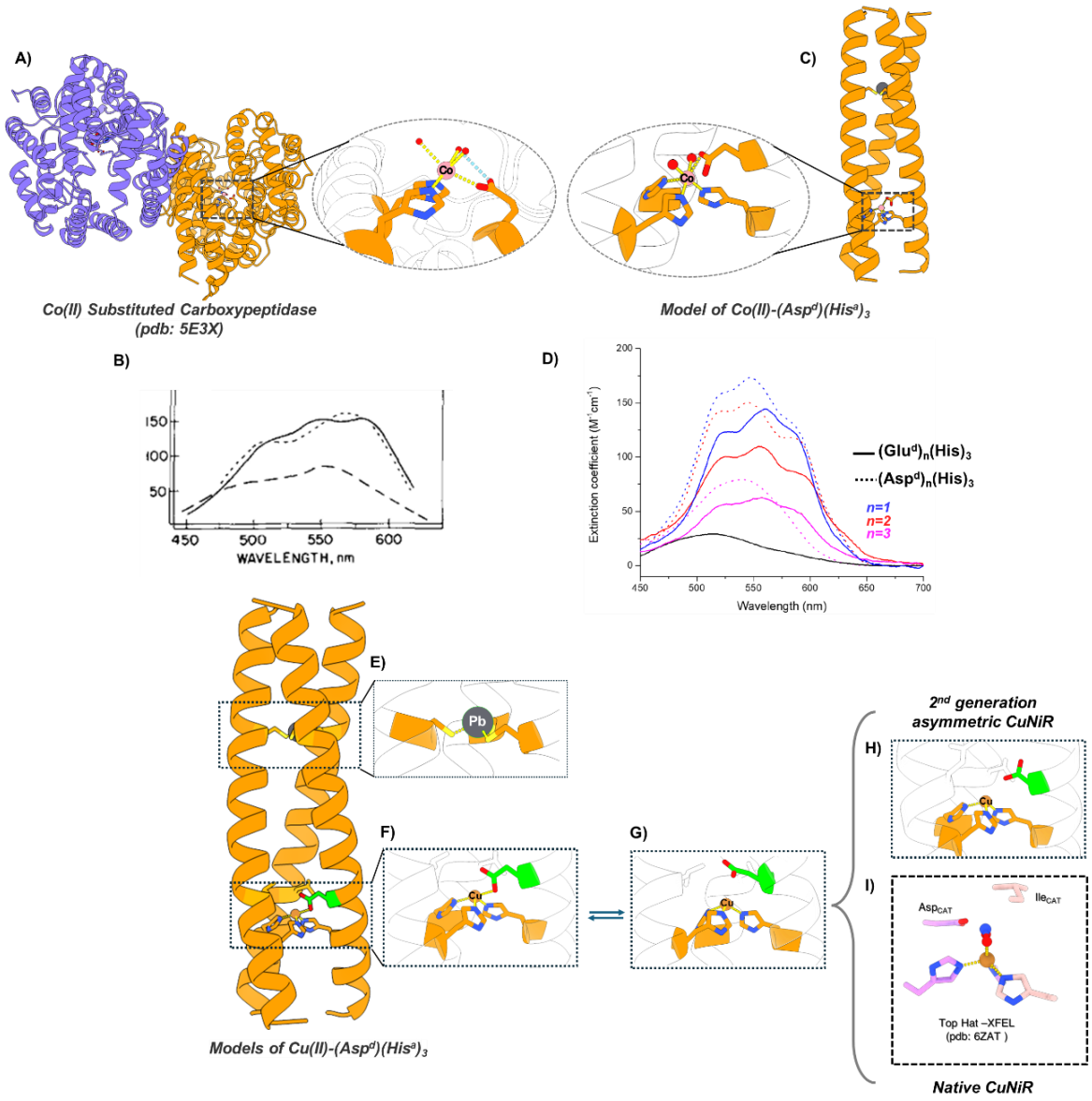


Figure V-1: Limitations of the Asp^d design with Cu(II) by highlighting Asp. binding within Co(II) heterotrimer: **A**) Crystal structure of Co(II) substituted carboxypeptidase highlighting the active site containing an Asp residue (pH 7.5), **B)** UV-Vis spectra of Co(II) substituted carboxypeptidase (pH 7.5) [*Modified with Permission of Ref. 16*], **C)** Model of Pb(II)^{Cys} Co(II)-GRWL16C (Asp^d)$_1$(His^a)$_3$ based on-Vis spectroscopy (*note: the number of bound waters may vary*), **D)** UV-Vis of both Pb(II)^{Cys}Co(II)-GRWL16C (Asp^d)$_n$(His^a)$_3$ and Pb(II)^{Cys}Co(II)-GRWL16C (Glu^d)$_n$(His^a)$_3$ designs at pH 7.5 highlighting the similarities in carboxypeptidase spectra (**B**), **E-G)** Model of Pb(II)^{Cys}Cu(II)-GRWL16C (Asp^d)$_1$(His^a)$_3$ highlighting the Cys^d Pb(II) site (**E**), Cu(II) site without waters added highlighting the possible negative impact of installing an Asp residue (**F**&**G**), Cu(II) site with the incorporation of 2-amino-propanedioic acid in place of Asp (**H**) and highlighting the design to the native active site (**I**). [***Note**: all Asp data were acquired by Dr. Mocny and all Glu data was collected by Dr. Tolbert and is distributed within their respective thesis*]

the EPR suggested that the pyridyl active sites formed a mixture of two different binding isomers of nitrite, with their $A_{\parallel}$ values in the range of those isomers reported in *wt* CuNiR and mutated CuNiR.[20–23] With this in mind, the addition of this proton donor and acceptor will serve to stabilize the Cu(II)-NO_2^- in the proper orientation and assist in proton transfer from the exterior solvent.

V.2: Further investigation into the mechanism underlying CuNiR activity in 3SCCs.

In Chapter III, I laid out the argument that nitrite binds to the reduced enzyme within the pyridyl active sites using a combination of X-ray absorption spectroscopy and chloride inhibition kinetics. Under non-catalytic conditions, the EPR of the oxidized form in the presence of nitrite results in at least two different binding modes of the nitrite. Chloride inhibition proved very informative in determining nitrite binding to the Cu(I) form; however, the EPR suggested that Cl^- likely does not have an affinity for the oxidized enzyme, which hinders the investigation of substrate binding to the oxidized form. However, there are small anions that have affinity for the

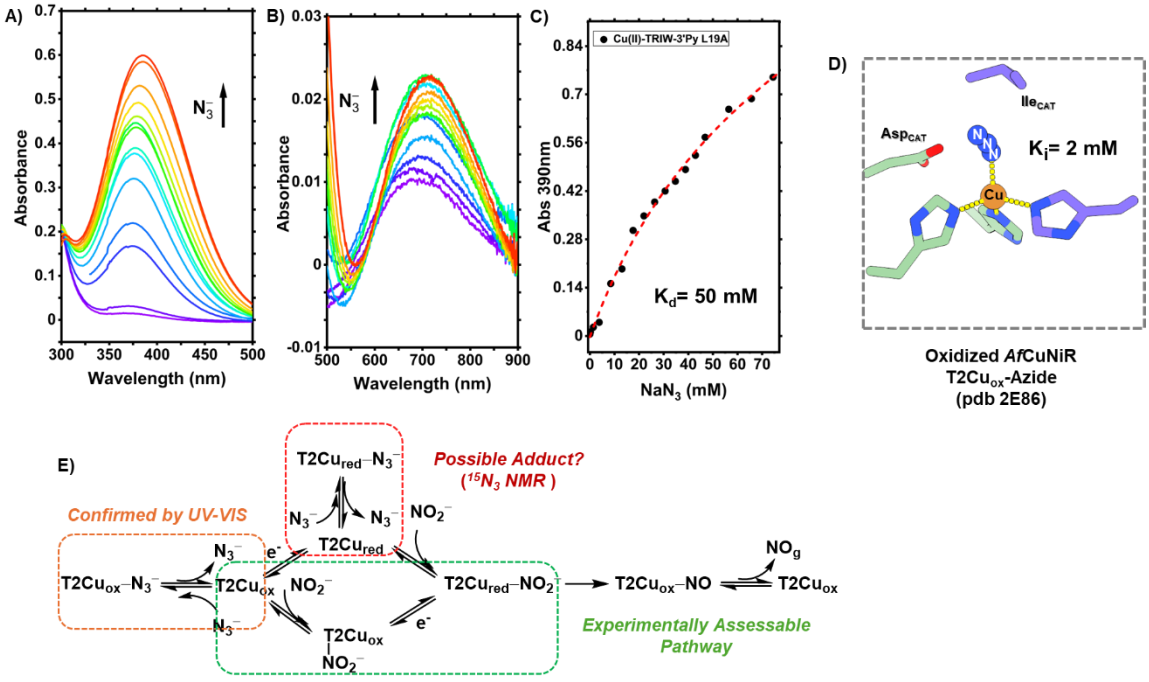


Figure V-2: Cu(II)-TRIW-3'Py L19A azide titration at pH 5.9, demonstrating binding in the (**A**) charge transfer region and (**B**) in the d-d transitions region, **C**) Fitting of the CT band (390 nm) resulting in an apparent K_d =50 mM, **D**) Azide adduct crystallized in native *Af*CuNiR demonstrating the nature of the reported competitive inhibition kinetics (pdb: 2E86), and **E**) Schematic highlighting of the binding events of substrate and azide during the catalytic cycle.

oxidized enzyme to investigate nitrite binding during the catalytic cycle further.[24] Azide, for example, has been shown to form adducts to the oxidized form of both histidine and pyridine-containing active sites in this thesis and has been reported in $T2Cu_{ox}$ of *wt* CuNiR where this adduct competitively inhibits nitrite reduction with respect to nitrite (Figure V-2A-2D).[8,25] A few routes can be realized from this situation: i) if nitrite binds only to the reduced enzyme, while N_3^- only binds to the oxidized enzyme (*i.e.*, N_3^- does not bind to the reduced form), then N_3^- will produce an *uncompetitive inhibition pattern* with respect to NO_2^-; ii) if NO_2^- binds to both forms of the enzymes, while N_3^- only binds to the oxidized form, then N_3^- will produce a *competitive inhibition pattern*; and iii) if NO_2^- and N_3^- bind to both enzyme forms, then N_3^- will produce a more complicated inhibition pattern (Figure V-2E).[26,27] The latter situation would yield a *competitive inhibition pattern* in the $1/v$ vs. $1/[NO_2^-]$ under non-saturating conditions of sodium ascorbate (*i.e.*, electron donor e^-); however, the slope replots would yield a parabolic dependence on $[N_3^-]$ because azide combines at two points that are reversibly connected in the mechanism, and both points result in slope effects.[27] The results of these experiments would offer insights into the direct binding of substrate to either oxidation state and yield key insights important to designing a more authentic model of CuNiR.

V.3: Expanding on stammers and stutters within GRAND homotrimers.

In Chapter IV, the addition of sequence discontinuities within designed 3SCCs allowed for the alteration of the coordination number and electronics at both the oxidized and reduced enzyme forms. Even though the specific stammers discussed in Chapter IV did not significantly affect activity, they did cause anticipated coordination number shifts in the reduced enzymes, and more importantly, there are functionalities that are still unexplored. The position of the sequence discontinuities in natural coiled coil proteins has been observed to vary along the structure; hence, the positioning of these discontinuities should be examined in relation to catalysis.[28] Copper-only superoxide dismutase (CuSOD) activity in homotrimeric 3SCC has been shown to be influenced by the stammer's location in conjunction with the active site's location (unpublished data).[29]

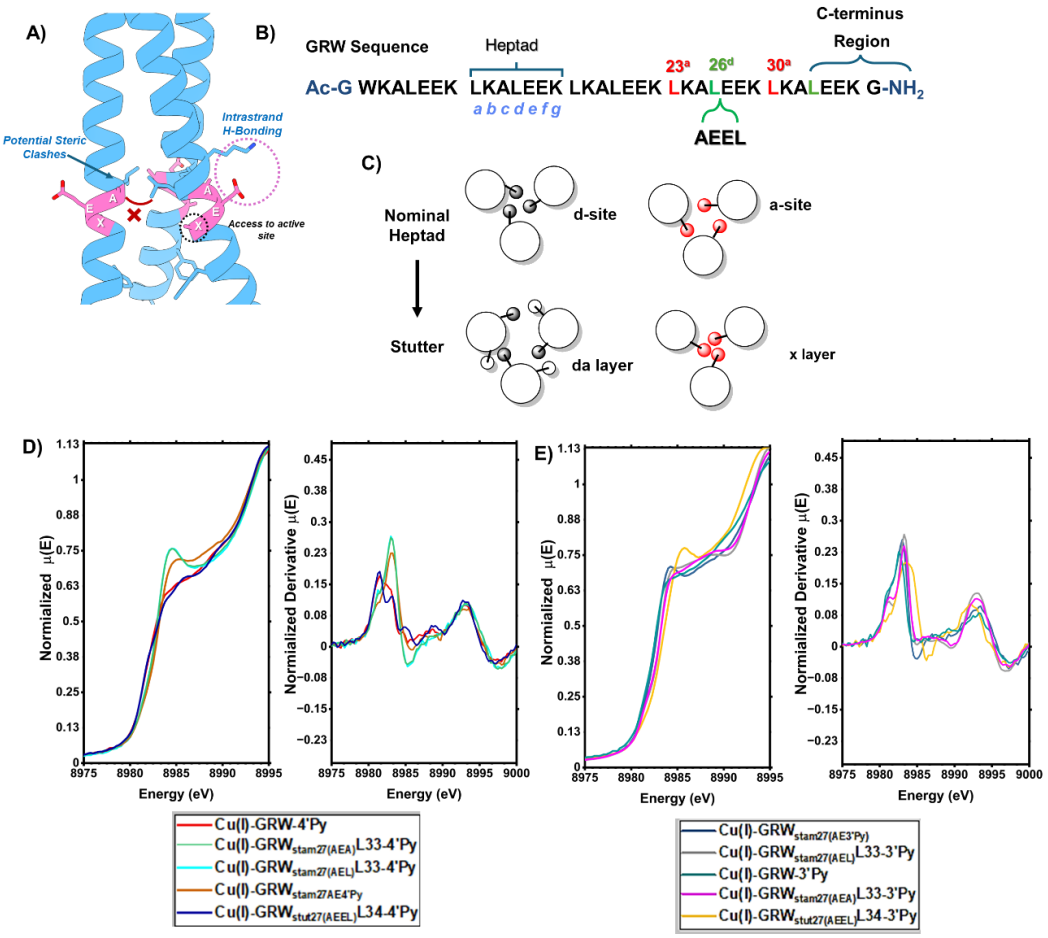


Figure V-3: Summary of stutter peptides: **A)** Local considerations of the discontinuities' sequence within the specific 3SCC in this thesis, **B)** GRW sequence highlighting potential targets of active sites and the initial stutter with preliminary data**,** and **D)** XANES spectra of Cu(I)-GRW$_{stut27(AEEL)}$L34-4'Py and previously characterized 4'Py sites (derivative plot [*Right*])**,** and **E)** XANES spectra of Cu(I)-GRW$_{stut27(AEEL)}$L34-3'Py and previously characterized 3'Py sites.

Table V-1: First-shell EXAFS fits of stutter sites: (*Data treated as pervious chapters*)

Enzyme	Best Model	Cu(I)-N	Cu(I)-N $\sigma^2 \times 10^{-3}$	$\langle \chi^2 f \rangle$ 10^{-4}
GRW$_{stut27(AEEL)}$L34-3'PY	$CuPy_2$	2.02 Å	2.68 Å^2	47
	$CuPy_3$	2.02 Å	4.81 Å^2	39
GRW$_{stut27(AEEL)}$L34-4'PY	$CuPy_2$	1.97 Å	2.84 Å^2	26
	CuPy3	1.98 Å	4.92 Å^2	28

In particular, a ~3x increase in CuSOD activity was observed in moving the ***a***-site His layer (k_{McF}=3.6 × 10^6 M^{-1} s^{-1}) to the above ***d***-site (k_{McF}=9.9 × 10^6 M^{-1} s^{-1}), both with a preceding AEL stammer (*unpublished*).* The ***d***-site design selectively destabilized the Cu(II) oxidation state while maintaining the reduced enzymes $K_{d,app}$, leading to a +48 mV increase in the reduction potential. There is a noticeable lack of change in the reduction potential in the absence of the AEL stammer, where copper $(His^d)_3$ and $(His^a)_3$ sites both have high reduction potential (~530 mV). Interestingly, the metal-dependent changes observed in Chapter IV with the pyridyl active sites at pH 5.9 further support the proposal that stammers can selectively change the electronics and geometry of each oxidation state. From a structural perspective, the AEL and AEA stammer did have a small impact on the Cu(I) electronics, even when changing the orientation of the pyridine (3'Py vs. 4'Py). However, catalysis was not greatly perturbed which may suggest that the position is relatively unimportant in altering the ligand packing around the reduced enzyme (Figure V-3E&F). An important strategy examined in Chapter IV was that incorporating the active site within the stammer has the most impact on the reduced enzyme form. The XANES was noticeably perturbed in the AE4'Py stammer, where the perturbation were primarily in the 8880-8884eV area which has been explained in terms of ligand field theory and mean displacement of the Cu(I) from the N_3 plane (Figure V-3D).[30]

Future design efforts should also investigate stutters (*e.g.*, AEEL) above both ***a***-site and ***d***-site active sites, as the unique sidechain repacking could result in changes in coordination numbers around both the oxidized and reduced forms. The addition of a stutter is predicted to lead to the underwinding of the helices around the 3-fold axis which is opposite to the stammer motif on the core residues within the 3SCC (Figure V-3A). More specifically, the addition of a stutter alters a nominal ***a***-site into the core, resulting in an ***x***-layer, while a nominal ***d***-sites will yield a more solvent-exposed ***da***-layer, similar to a nominal ***a***-site (Figure V-3C). To differentiate this from the stammer work, an analogous ***d***-site stutter was designed above both an ***a***-site 3'Py and 4'Py

*All SOD data with proteins containing stammers and stutters were collected by Dr. Jean Bouvet.

($GRW_{stut27(AEEL)}$L34-X'Py) and the Cu(I) XANES were collected. Interestingly, the stutter resulted in noticeable changes within their respective XANES in comparison with previous designs examined so far (Figure V-3D&E). Two effects are observed in the Cu(I) XANES that are different from those observed in this thesis: i) The 4'Py resulted in a more pronounced shoulder at ~8980 eV compared to other reduced 4'Py sites; and ii) the edge shifts by +1.4 eV in the reduced 3'Py site compared to the parent design (Cu(I)-GRW-3'Py) (Figure V-3E, Table V-1). The shoulder at ~8980 eV is reminiscent of the recently examined Cu 1s to pyridine ligand π* transition and may suggest the pyridyl ligands have rotated about the copper to allow for sufficient orbital overlap.[31] Additionally, it should be noted that any assignments made to absorption edge features are tentative due to the effects of multiple scattering and enhanced covalency of the complexes. Both structures deviate from the analogous stammer design which motivates further investigation into stutters as distinct design motifs.

As was said at the outset from Chapter I, it is crucial to keep in mind that there have been reports of notable differences in the accommodation lengths of all three kinds of inserts. The average accommodation length of the two 3SCC proteins that were discovered to include stammers was determined to be 5 residues (± ~2.5 residues), whereas the stutter inserts were accommodated on average over 15 residues (± ~4 residues) to fully resolve back to the nominal packing. This thesis' findings about stammers suggest that to impose the discontinuities' impact on the copper center fully, future designs should consider locating the active site inside the stammer or stutter (*e.g.*, AEEX). Lastly, care should be taken when designing sequence discontinuities to ensure that the structural changes only occur within the context of a 3SCC and do not disrupt the oligomerization state due to steric clashing in the core or breaking of stabilized interhelical salt bridges.[10,32]

With the goal of achieving native-like reactivity within a minimal construct, the studies included in this thesis show that precisely identifying the primary coordination sphere is crucial to achieving superior redox catalytic activity. This project progresses from designing the first coordination sphere to the systematic modifications of the second coordination sphere, and some

of these constructs show the best catalytic efficiency among the CuNiR models under homogeneous aqueous conditions reported in the literature.

This thesis focused on the molecular effects of ligand identity and coordination number on the efficiency of nitrite reduction in a 3-stranded coiled coil (3SCC) with an unnatural T2Cu center. The design strategies employed have contributed to a better understanding of the structure-function relationship of a redox-active metal center. A basis for modifying the catalytic activity of metalloenzymes in a nonnative fold is laid out in my doctoral work, which can also be used as a basis to compare and design native reactivity within non-native scaffolds. This allows for the enhancement of catalytic activity through the creation of scaffold-specific features.

References:

(1) Frandsen, K. E. H.; Simmons, T. J.; Dupree, P.; Poulsen, J. C. N.; Hemsworth, G. R.; Ciano, L.; Johnston, E. M.; Tovborg, M.; Johansen, K. S.; Von Freiesleben, P.; Marmuse, L.; Fort, S.; Cottaz, S.; Driguez, H.; Henrissat, B.; Lenfant, N.; Tuna, F.; Baldansuren, A.; Davies, G. J.; Lo Leggio, L.; Walton, P. H. The Molecular Basis of Polysaccharide Cleavage by Lytic Polysaccharide Monooxygenases. *Nat. Chem. Biol.* **2016**, *12* (4), 298–303.

(2) Walton, P. H.; Davies, G. J.; Diaz, D. E.; Franco-Cairo, J. P. The Histidine Brace: Nature's Copper Alternative to Haem? *FEBS Letters*. John Wiley & Sons, Ltd February 1, 2023, pp 485–494.

(3) Ciano, L.; Davies, G. J.; Tolman, W. B.; Walton, P. H. Bracing Copper for the Catalytic Oxidation of C–H Bonds. *Nat. Catal.* **2018**, *1* (8), 571–577.

(4) Guo, J.; Fisher, O. S. Orchestrating Copper Binding: Structure and Variations on the Cupredoxin Fold. *Journal of Biological Inorganic Chemistry*. Springer August 22, 2022, pp 529–540.

(5) Chakraborty, S.; Touw, D. S.; Peacock, A. F. A.; Stuckey, J.; Pecoraro, V. L. Structural Comparisons of Apo-and Metalated Three-Stranded Coiled Coils Clarify Metal Binding Determinants in Thiolate Containing Designed Peptides. *J. Am. Chem. Soc.* **2010**, *132* (38), 13240–13250.

(6) Pitts, W. C.; Deb, A.; Penner-Hahn, J. E.; Pecoraro, V. L. Revving up a Designed Copper Nitrite Reductase Using Noncoded Active Site Ligands. *ACS Catal.* **2024**, *14* (6), 4362–4368.

(7) Brenner, S.; Heyes, D. J.; Hay, S.; Hough, M. A.; Eady, R. R.; Hasnain, S. S.; Scrutton, N. S. Demonstration of Proton-Coupled Electron Transfer in the Copper-Containing Nitrite Reductases. *J. Biol. Chem.* **2009**, *284* (38), 25973–25983.

(8) Berry, S. M.; Strange, J. N.; Bladholm, E. L.; Khatiwada, B.; Hedstrom, C. G.; Sauer, A. M. Nitrite Reductase Activity in Engineered Azurin Variants. *Inorg. Chem.* **2016**, *55* (9), 4233–4247.

(9) Koebke, K. J.; Yu, F.; Salerno, E.; Van Stappen, C.; Tebo, A. G.; Penner-Hahn, J. E.; Pecoraro, V. L. Modifying the Steric Properties in the Second Coordination Sphere of Designed Peptides Leads to Enhancement of Nitrite Reductase Activity. *Angew. Chemie* **2018**, *130* (15), 4018–4021.

(10) Woolfson, D. N. The Design of Coiled-Coil Structures and Assemblies. *Adv. Protein Chem.* **2005**, *70*, 79–112.

(11) Tolbert, A. E.; Ervin, C. S.; Ruckthong, L.; Paul, T. J.; Jayasinghe-Arachchige, V. M.; Neupane, K. P.; Stuckey, J. A.; Prabhakar, R.; Pecoraro, V. L. Heteromeric Three-Stranded Coiled Coils Designed Using a Pb(Ii)(Cys)3 Template Mediated Strategy. *Nat. Chem.* **2020**, *12* (4), 405–411.

(12) Tolbert, A. Fully Selective Pb(II) Templated Heterotrimeric Redox and Hydrolytic Metalloenzymes, University of Michigan, 2021.

(13) Touw, D. S.; Nordman, C. E.; Stuckey, J. A.; Pecoraro, V. L. Identifying Important Structural Characteristics of Arsenic Resistance Proteins by Using Designed Three-Stranded Coiled Coils. *Proc. Natl. Acad. Sci. U. S. A.* **2007**, *104* (29), 11969–11974.

(14) Matzapetakis, M.; Farrer, B. T.; Weng, T. C.; Hemmingsen, L.; Penner-Hahn, J. E.; Pecoraro, V. L. Comparison of the Binding of Cadmium(II), Mercury(II) and Arsenic(III) to the de Novo Designed Peptides TRI L12C and TRI L16C. *J. Am. Chem. Soc.* **2002**, *124* (27), 8042–8054.

(15) Mocny, C. S. Examining the Metal Selectivity of Thiol Rich de Novo Designed Peptides as a Strategy to Make Asymmetric Alpha-Helical Protein Assemblies., Universtiy of Michigan, 2016.
(16) Kaden, T. A.; Holmquist, B.; Vallee, B. L. Magnetic Circular Dichroism of Cobalt Metalloenzyme Derivatives. *Biochem. Biophys. Res. Commun.* **1972**, *46* (4), 1654–1659.
(17) Martinelli, R. A.; Hanson, G. R.; Thompson, J. S.; Holmquist, B.; Pilbrow, J. R.; Auld, D. S.; Vallee, B. L. Characterization of the Inhibitor Complexes of Cobalt Carboxypeptidase A by Electron Paramagnetic Resonance Spectroscopy. *Biochemistry* **1989**, *28* (5), 2251–2258.
(18) Lee, Y. J.; Dhanasingh, I.; Ahn, J. S.; Jin, H. S.; Choi, J. M.; Lee, S. H.; Lee, D. W. Biochemical and Structural Characterization of a Keratin-Degrading M32 Carboxypeptidase from Fervidobacterium Islandicum AW-1. *Biochem. Biophys. Res. Commun.* **2015**, *468* (4), 927–933.
(19) Ghosh, S.; Dey, A.; Sun, Y.; Scholes, C. P.; Solomon, E. I. Spectroscopic and Computational Studies of Nitrite Reductase: Proton Induced Electron Transfer and Backbonding Contributions to Reactivity. *J. Am. Chem. Soc.* **2009**, *131* (1), 277–288.
(20) Pinho, D.; Besson, S.; Brondino, C. D.; De Castro, B.; Moura, I. Copper-Containing Nitrite Reductase from Pseudomonas Chlororaphis DSM 50135: Evidence for Modulation of the Rate of Intramolecular Electron Transfer through Nitrite Binding to the Type 2 Copper Center. *Eur. J. Biochem.* **2004**, *271* (12), 2361–2369.
(21) Howes, B. D.; Abraham, Z. H. L.; Lowe, D. J.; Brüser, T.; Eady, R. R.; Smith, B. E. EPR and Electron Nuclear Double Resonance (ENDOR) Studies Show Nitrite Binding to the Type 2 Copper Centers of the Dissimilatory Nitrite Reductase of Alcaligenes Xylosoxidans (NCIMB 11015). *Biochemistry* **1994**, *33* (11), 3171–3177.
(22) Olesen, K.; Veselov, A.; Zhao, Y.; Wang, Y.; Danner, B.; Scholes, C. P.; Shapleigh, J. P. Spectroscopic, Kinetic, and Electrochemical Characterization of Heterologously Expressed Wild-Type and Mutant Forms of Copper-Containing Nitrite Reductase from Rhodobacter Sphaeroides 2.4.3. *Biochemistry* **1998**, *37* (17), 6086–6094.
(23) Boulanger, M. J.; Murphy, M. E. P. Directing the Mode of Nitrite Binding to a Copper-containing Nitrite Reductase from Alcaligenes Faecalis S-6: Characterization of an Active Site Isoleucine. *Protein Sci.* **2003**, *12* (2), 248–256.
(24) Valles, M.; Kamaruddin, A. F.; Wong, L. S.; Blanford, C. F. Inhibition in Multicopper Oxidases: A Critical Review. *Catalysis Science and Technology*. 2020, pp 5386–5410.
(25) Tocheva, E. I.; Eltis, L. D.; Murphy, M. E. P. Conserved Active Site Residues Limit Inhibition of a Copper-Containing Nitrite Reductase by Small Molecules. *Biochemistry* **2008**, *47* (15), 4452–4460.
(26) Tepper, A. W. J. W. Structure and Mechanism of the Type-3 Copper Protein Tyrosinase, Leiden, Universiteit, 2005.
(27) Irwin H. Segel. *Enzyme Kinetics: Behavior and Analysis of Rapid Equilibrium and Steady-State Enzyme Systems*, Wiley Clas.; Wiley, 1993.
(28) Schmidt, N. W.; Grigoryan, G.; DeGrado, W. F. The Accommodation Index Measures the Perturbation Associated with Insertions and Deletions in Coiled-Coils: Application to Understand Signaling in Histidine Kinases. *Protein Science*. 2017, pp 414–435.
(29) Bouvet, J. Superoxide Dismutase Mimics : An Integrated Approach from Chemical Design to Bioactivity in Cells : Mimes de Superoxyde Dismutase : Une Approche Intégrée de La Conception Chimique à La Bio-Activité Cellulaire, Ecole Normale Supérieure de Paris,

2023.
(30) Blackburn, N. J.; Strange, R. W.; Reedijk, J.; Volbeda, A.; Farooq, A.; Zubieta, J.; Karlin, K. D. X-Ray Absorption Edge Spectroscopy of Copper(I) Complexes. Coordination Geometry of Copper(I) in the Reduced Forms of Copper Proteins and Their Derivatives with Carbon Monoxide. *Inorg. Chem.* **1989**, *28* (7), 1349–1357.
(31) DiMucci, I. M.; MacMillan, S. N.; Walroth, R. C.; Lancaster, K. M. Scrutinizing "Ligand Bands" via Polarized Single-Crystal X-Ray Absorption Spectra of Copper(I) and Copper(II) Bis-2,2′-Bipyridine Species. *Inorg. Chem.* **2020**, *59* (18), 13416–13426.
(32) Schneider, J. P.; Lombardi, A.; DeGrado, W. F. Analysis and Design of Three-Stranded Coiled Coils and Three-Helix Bundles. *Fold. Des.* **1998**, *3* (2).

Appendix A

High Resolution Nuclear Magnetic Resonance Spectra of *de novo* Designed Apo-3SCC and Copper(I)/(II)-3SCC.

Introduction:

This appendix is a collection of high resolution nuclear magnetic resonance spectra of proteins in their apo and holo forms. The raw and processed data is archived in digital format on the Pecoraro's lab research drive under Winston Pitts' lab folder (\Lab\NMR\Protein_NMR\800mHz_NMR\). Where appropriate, comments are made about the experiments (*e.g.*, interpretation, suggestions, and important references) near their corresponding spectrum. The reader will find useful 2D NMR of copper(I) complexes in Refs. 1,2 (including the supplementary information). All data can be requested by emailing Prof. Vincent L. Pecoraro at vlpec@umich.edu.

Methods:

^{1}H NMR Experiments:

Protein NMR experiments were conducted on a Burker 800 MHz equipped with a 5 mm triple resonance inverse detection TCI cryoprobe. Sodium trimethylsilylpropanesulfonate (DSS) was used as the ^{1}H reference (f2 axis) at a concentration of 0.25 mM in double-distilled H_2O. All samples were prepared in 50 mM phosphate and 0.25 mM DSS which were subsequently loaded into a coaxial tube with the inner tube containing D_2O, unless otherwise mentioned. ^{1}H NMR was collected at 25°C using the pulse program zgesgp which features gradient-based 1D excitation sculpting to eliminate the water peak at ~4.7ppm (*this was calibrated for each sample*). Cu(I)

titrations were conducted using ~1-3 mM Pep_3 and were carried out in a glovebox. To avoid the formation of a Cu(I)-acetonitrile adduct within the active site using tetrakis(acetonitrile)copper(I) tetrafluoroborate, titrations were done by forming the oxidized enzyme (using $CuSO_4$) and subsequently reducing this complex with 10 eqv. sodium ascorbate to yield the reduced form of the enzyme. Although, tetrakis(acetonitrile)copper(I) tetrafluoroborate was in as a Cu(I) source in some experiments (which will be highlighted in the figure captions below). Careful attention was given to both the pH changes and loss of volume during these experiments. Each data set was subsequently processed and analyzed in either Bruker Topspin 4.2.0 or MestReNova. Each spectrum was baseline corrected, referenced to 0 ppm (DSS), and a simple normalization at 0 ppm to a value of 1 which allowed for the comparison of different spectra during the progress of the titration NMR experiments. The ^{13}C axis was calibrated directly using the ^{1}H reference and the method outlined in Harris *et al.*[3]

^{1}H-^{13}C Heteronuclear Single Quantum Correlation Experiments:

$^{1}H/^{13}C$ Heteronuclear Single Quantum Correlation (HSQC) experiments were conducted using the "hsqcedetgp" pulse sequence using ~36 scans in the ^{1}H axis (F2) and ~200 scans in the ^{13}C axis (F1).[4] The 2D H/C correlation is accomplished via double insensitive nuclei enhancement by polarization transfer (inept transfer), which is phase sensitive using Echo/Antiecho-TPPI gradient selection with decoupling during acquisition using trim pulses in inept transfer using f3 channel. This method yields the relationship between the chemical shifts of carbon and protons through one-bond *J*-coupling which featured echo-antiecho "et" to improve sensitivity. The "ed" was used to filter specific protons (CH vs CH_2 or CH_3). CH and CH_3 groups will have positive phases (black contours) and CH_2 have negative phases (blue contours) due to the delay. With CH and CH_3 having the same phase and CH_2 having the opposite phase, it can be easily used to distinguish between C–H protons from others. This was accomplished by setting the delay double inept transfer constant to the inverse of the J_{CH} constant of the interested C-H bond of interest (175 Hz). The following parameters were used for the ^{1}H-^{13}C HSQC: for ^{1}H dimension (at 800 MHz), 14.2 ppm spectrum width (SW), 4000 points (TD), 176 ms AQ, resulted in 5.7 Hz digital resolution

(FIDRES); for ^{13}C dimension, 100 ppm SW, sufficient points to resolve nitrogen signals (300 increments and 56 number of scans were used). The ^{1}H axis was calibrated using a ^{1}H experiment collected directly before the HSQC experiments. The ^{13}C axis was calibrated directly using the ^{1}H reference and the method outlined in Harris *et al.*[3] An Excel spreadsheet is stored in the NMR directory mentioned above to assist in referencing spectra.

^{1}H-^{1}H and ^{1}H-^{15}N Nuclear Overhauser Effect Spectroscopy (NOESY) Experiments:

Samples were prepared in a glovebox to avoid dissolved oxygen suppressing NOESY signals. ^{1}H-^{15}N HSQC-NOESY were collected using the "hsqcetf3gpno" pulse program with 2D H-1/X correlation accomplished via double insensitive nuclei enhancement by polarization transfer (inept transfer), which is phase sensitive using Echo/Antiecho-TPPI gradient selection with decoupling during acquisition using trim pulses in inept transfer using f3 channel. The mixing time used was 200 ms.[5] Correlation via dipolar coupling dipolar coupling may be due to NOE or chemical exchange. ^{1}H-^{1}H NOESY were collected with the pulse program "noesyesgpph" with 2D homonuclear correlation via dipolar coupling and water suppression using excitation sculpting with gradients (use parameterset NOESYESGPPH) (Phase-sensitive 2D NOESY with excitation sculpting). The best results were collected using a mixing time of 100 ms. The following parameters were used for the ^{1}H-^{1}H HSQC-NOESY : for ^{1}H dimension (at 800 MHz), 15.6 ppm spectrum width (SW), 2048 points (TD), 8.1 ms AQ, resulted in 12 Hz digital resolution (FIDRES); for ^{15}H dimension, 15.6 ppm SW, sufficient points to resolve nitrogen signals (512 increments and 64 number of scans were used). The following parameters were used for the ^{1}H-^{1}H HSQC-NOESY : for ^{1}H dimension (at 800 MHz), 14.2 ppm spectrum width (SW), 2048 points (TD), 9,0 ms AQ, resulted in 11 Hz digital resolution (FIDRES); for the ^{15}N dimension, 100 ppm SW, sufficient points to resolve nitrogen signals (200 increments and 200 number of scans were used). The ^{1}H axis was calibrated using a ^{1}H experiment collected directly before the NOESY experiments. The ^{15}N axis was calibrated directly using the ^{1}H reference and the method outlined

in Harris *et al.*[3] An Excel spreadsheet is stored in the NMR directory mentioned above to assist in referencing spectra.

^{1}H-^{15}N HMBC Heteronuclear Multiple Bond Correlation Experiments:

This experiment allowed for the through bond correlation of the ^{15}N and ^{1}H nuclei that are separated by two-three bonds, unlike the HSQC experiments above. The hmbcndprqf pulse program was used with 2D H-1/X correlation via heteronuclear zero and double quantum and is optimized for long range couplings.[6] A delay of $1/(2*J_{XH})$ is implemented with this pulse sequence where the J_{XH} of coupling constant of the interested system. The scalar J_{XH} value used herein is 10.76 Hz (*i.e.*, −10.76 Hz) which corresponds to the ^{15}N-$^{1}H_{othro}$ of pyridine.[7] The following parameters are used for ^{1}H dimension (at 800 MHz); 4.3 ppm spectrum width (SW), 4096 points (TD) or 12018 complex points, 2.0 s AQ, resulted in 0.5 Hz digital resolution (FIDRES); for ^{15}N dimension, 200 ppm SW, sufficient points to resolve nitrogen signals (200 increments and 70 number of scans were used). The ^{1}H axis was calibrated using a ^{1}H experiment collected directly before the NOESY experiments. The ^{15}N axis was calibrated directly using the ^{1}H reference and the method outlined in Harris *et al.*[3]

A.1 Chapter II Nuclear Magnetic Resonance Data (TRI and TRIW Proteins)

Protein: TRIW-H

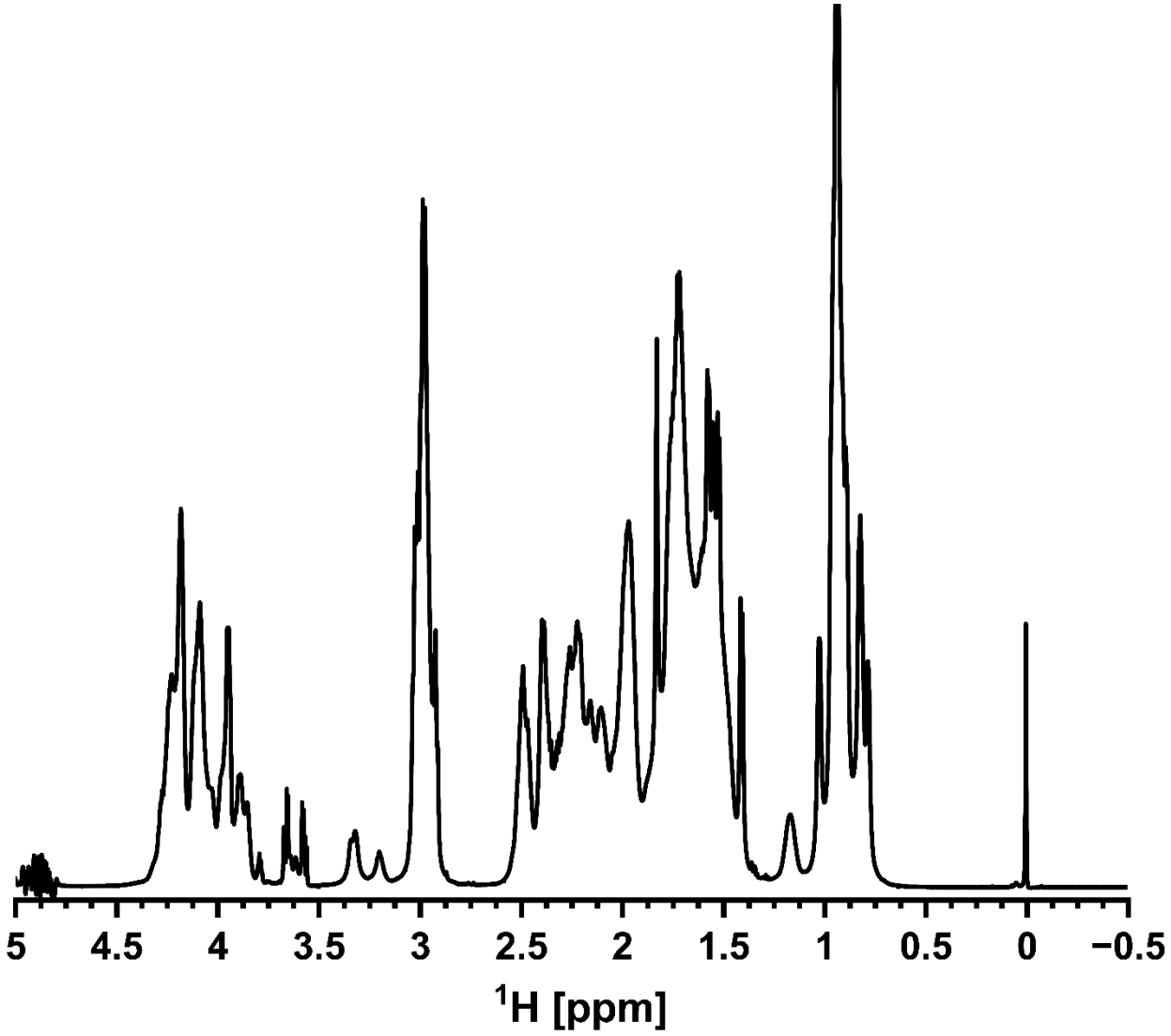


Figure A-1: ^{1}H-NMR of apo-TRIW-4'Py at pH 5.88 (Region: Aliphatic): *(file name: wcp4_123_TRIWL23_H_090523 [Spectrum 2]).*

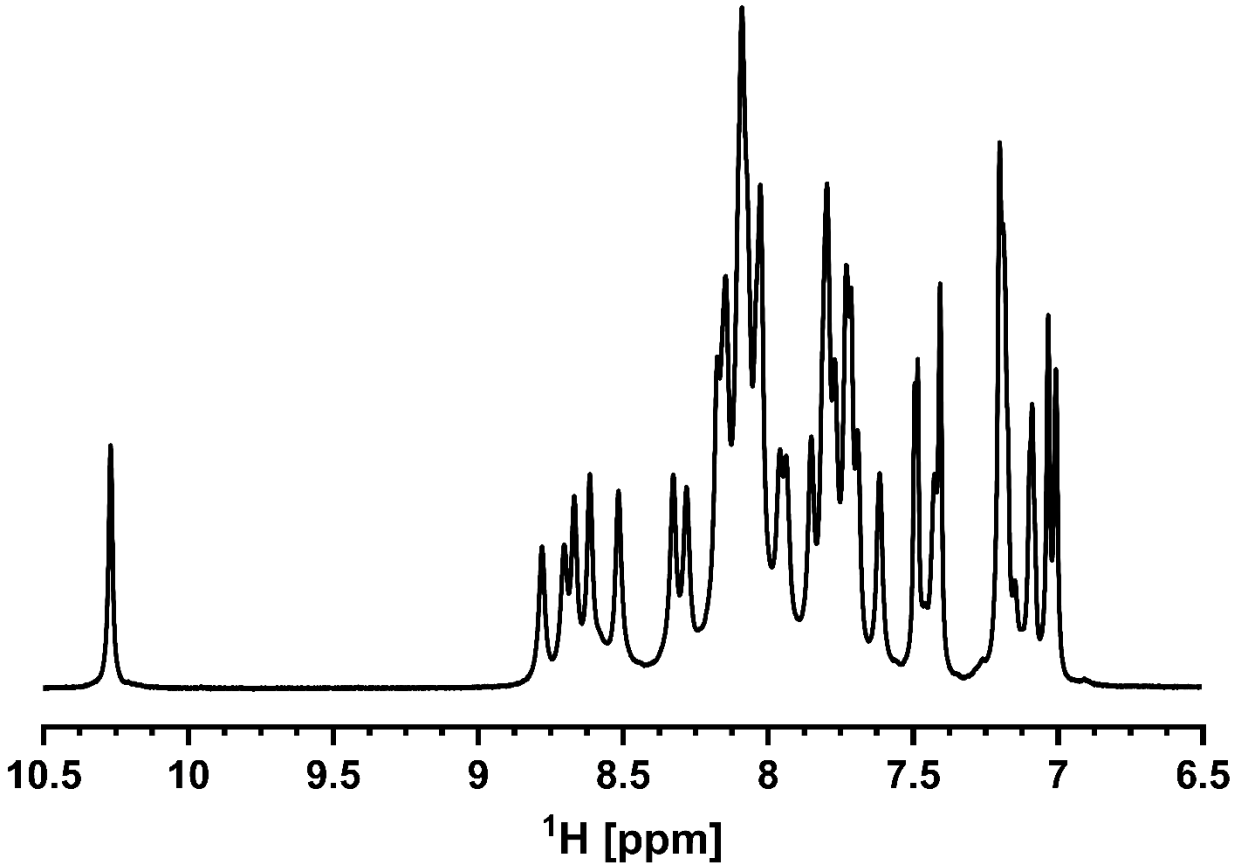


Figure A-2: ^{1}H-NMR of apo-TRIW-4'Py at pH 5.88 (Region: Aromatic/Amide): *(file name: wcp4_123_TRIWL23_H_090523 [Spectrum 2]).*

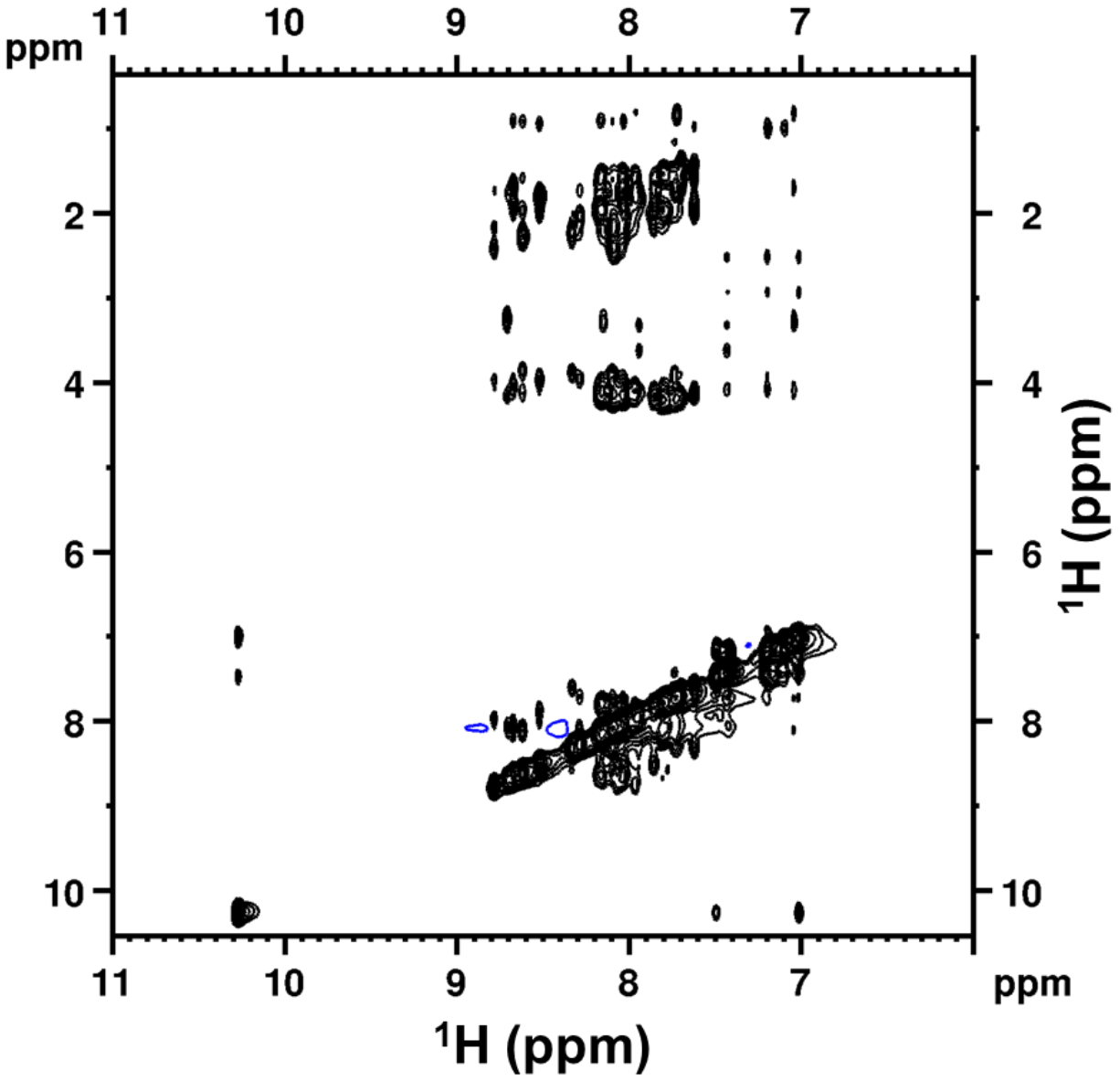


Figure A-3: ^{1}H-^{1}H NOESY of apo-TRIW-H pH 5.86 (Region: Aromatic/Amide): mixing time=100 ms *(file name: wcp4_123_TRIWL23_H_090523 [Spectrum 3]).*

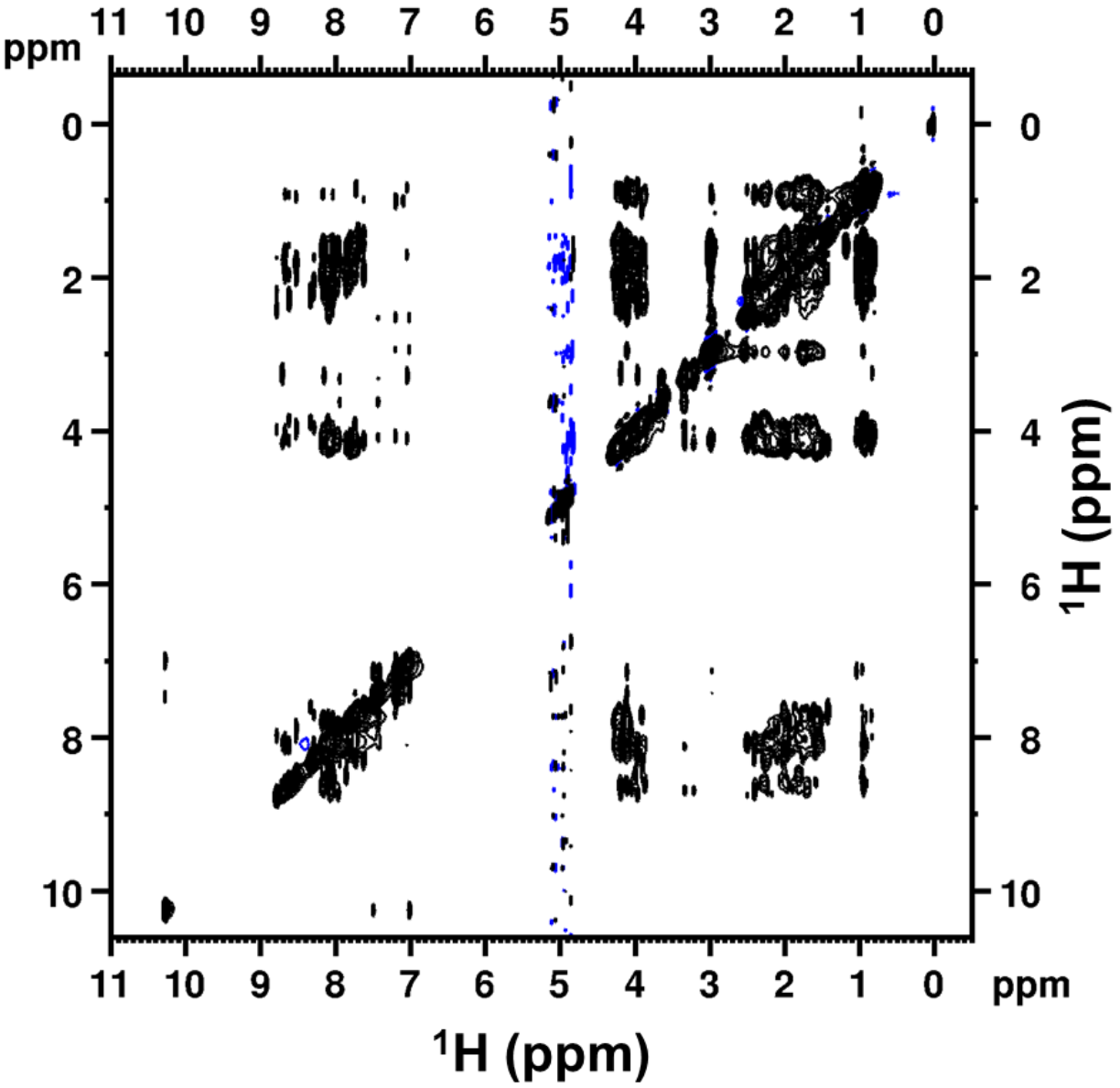


Figure A-4: ^{1}H-^{1}H NOESY of apo-TRIW-H pH 5.86 (Region: Overview): mixing time=100 ms *(file name: wcp4_123_TRIWL23_H_090523 [Spectrum 3])*.

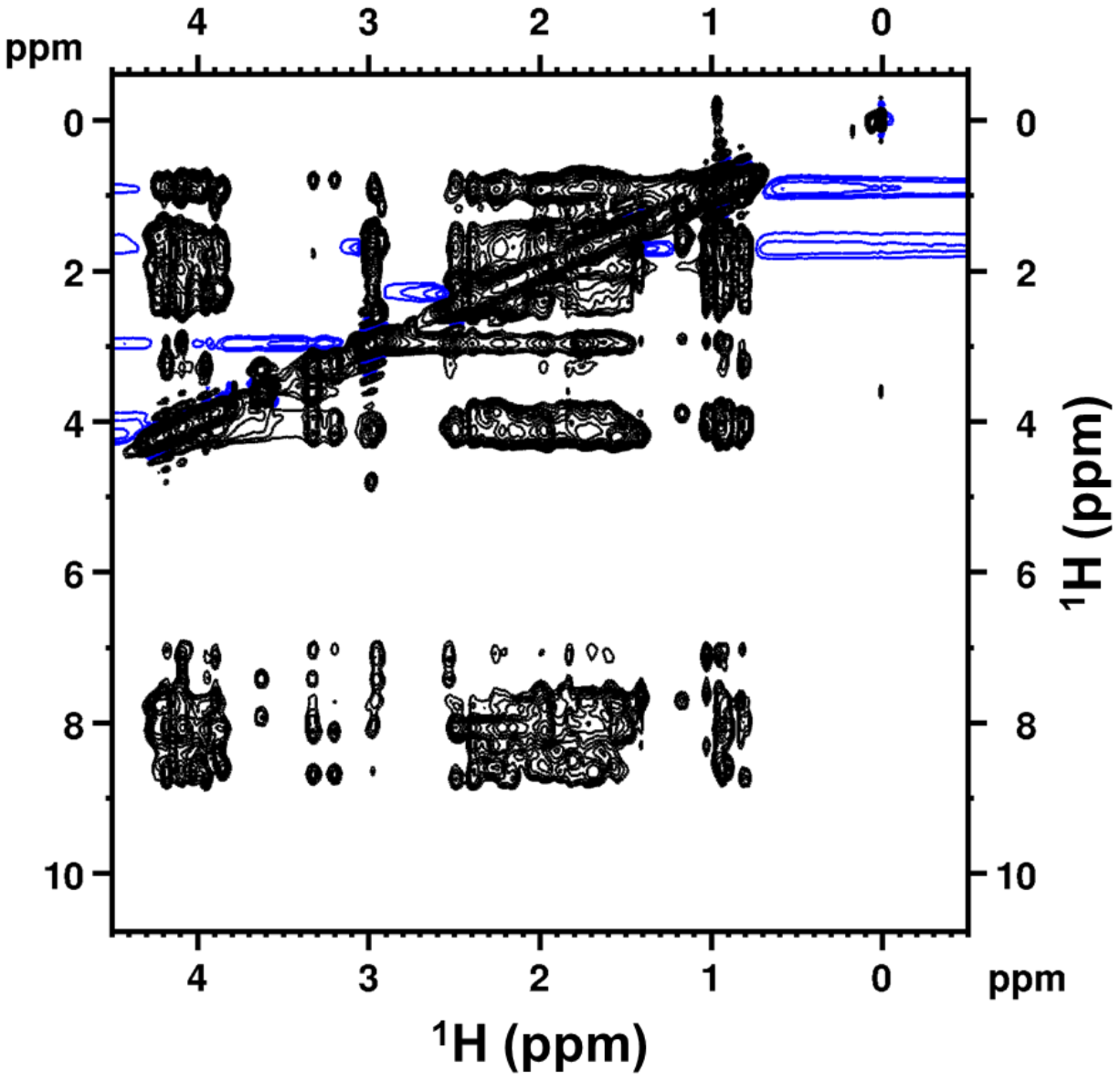


Figure A-5: ^{1}H-^{1}H NOESY of apo-TRIW-H pH 5.86 (Region: Aliphatic): mixing time=100 ms *(file name: wcp4_123_TRIWL23_H_090523 [Spectrum 3]).*

Protein:TRI-4'Py and TRIW-4'Py

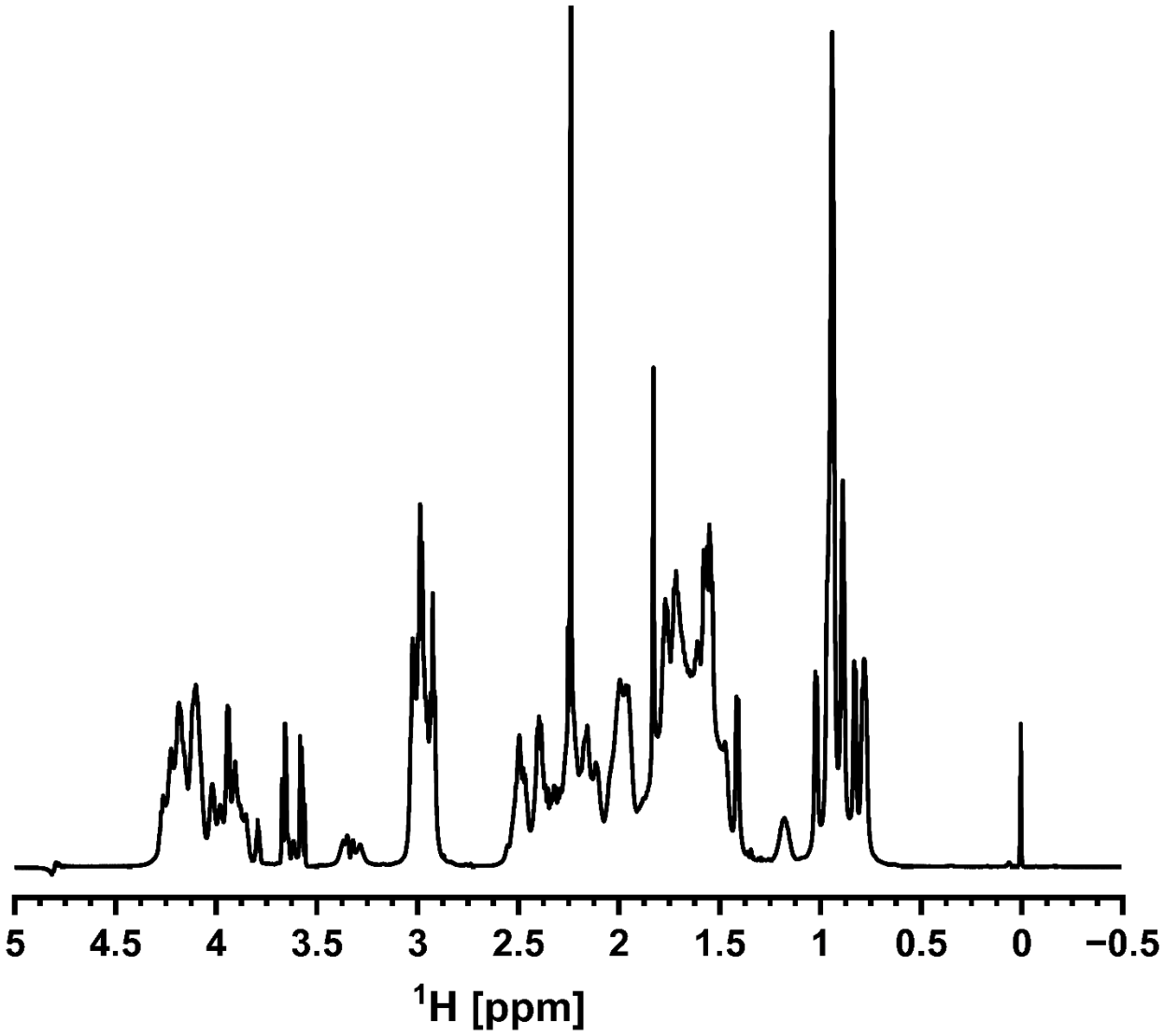


Figure A-6: ^{1}H-NMR of apo-TRIW-4'Py at pH 5.88 (Region: Aliphatic): *(file name: wcp4_123_TRIW_4Py_091023 [Spectrum 1]).*

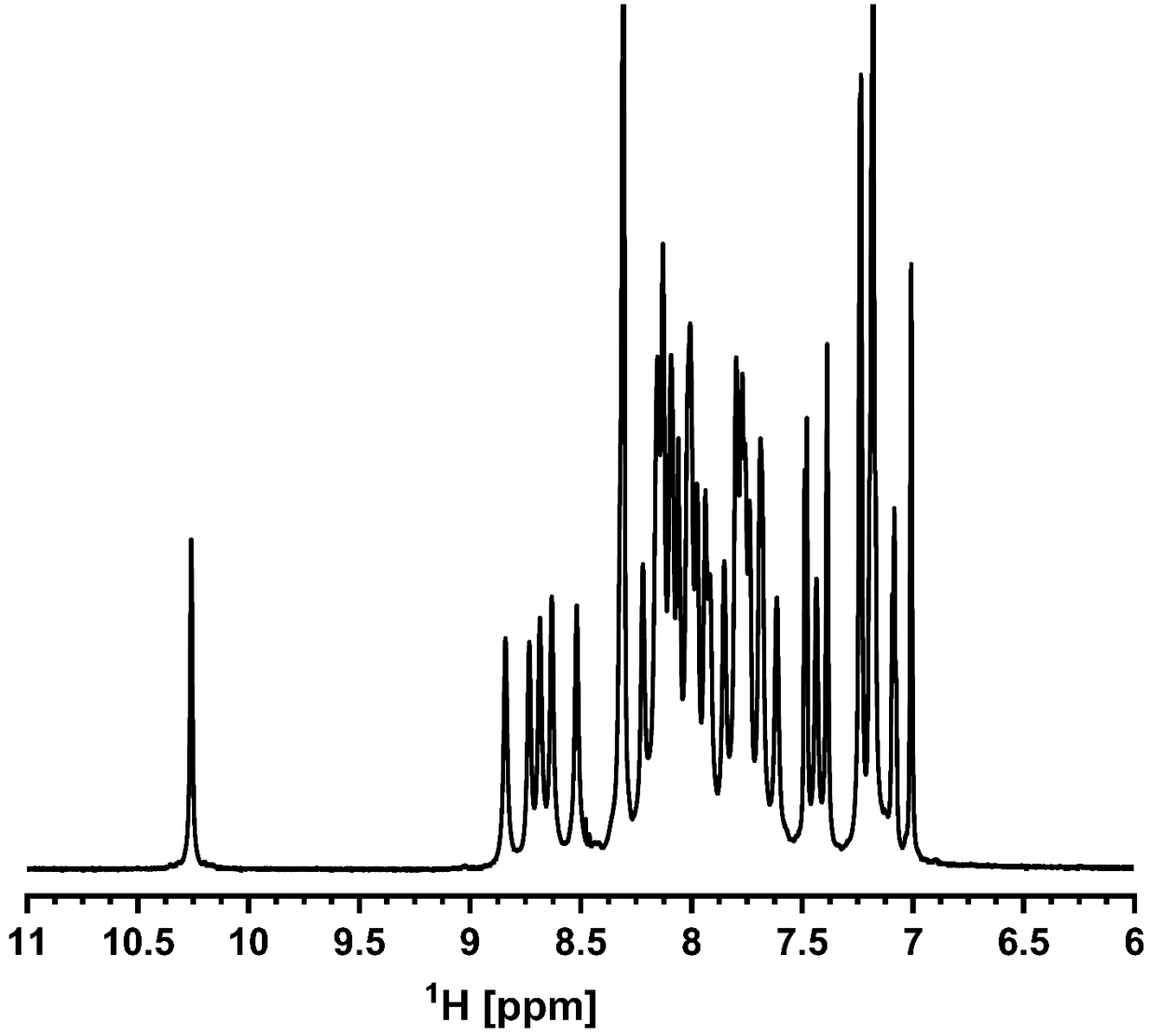


Figure A-7: ^{1}H-NMR of apo-TRIW-4'Py at pH 5.88 (Region: Aromatic): *(file name: wcp4_123_TRIW_4Py_091023 [Spectrum 1]).*

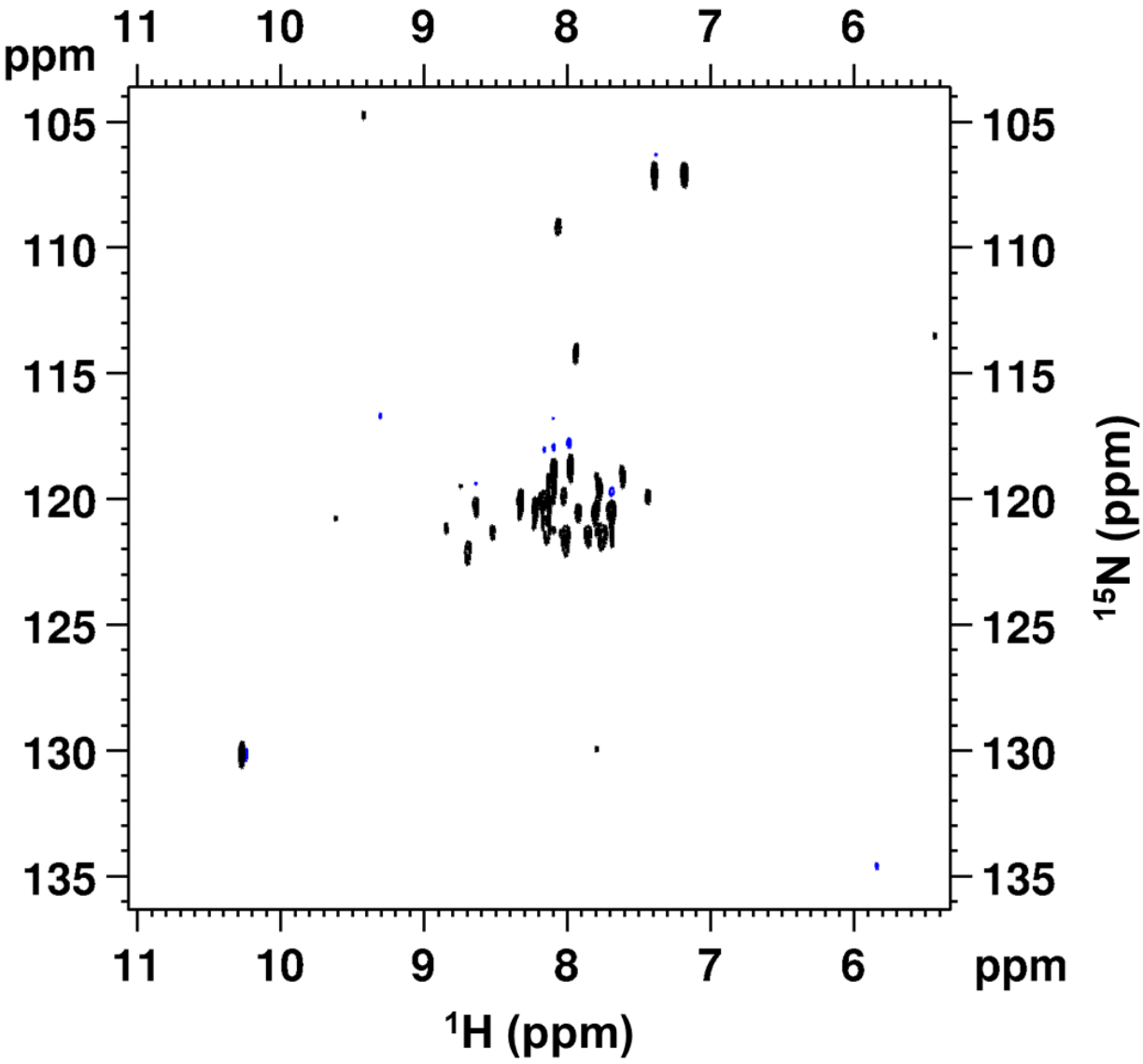


Figure A-8: ^{1}H-^{15}N NOESY of apo-TRW-4'Py at pH 5.88 (Region: Amide): mixing time=100 ms *(file name: wcp4_123_TRIWL23_4Py_091023 [Spectrum 2]).*

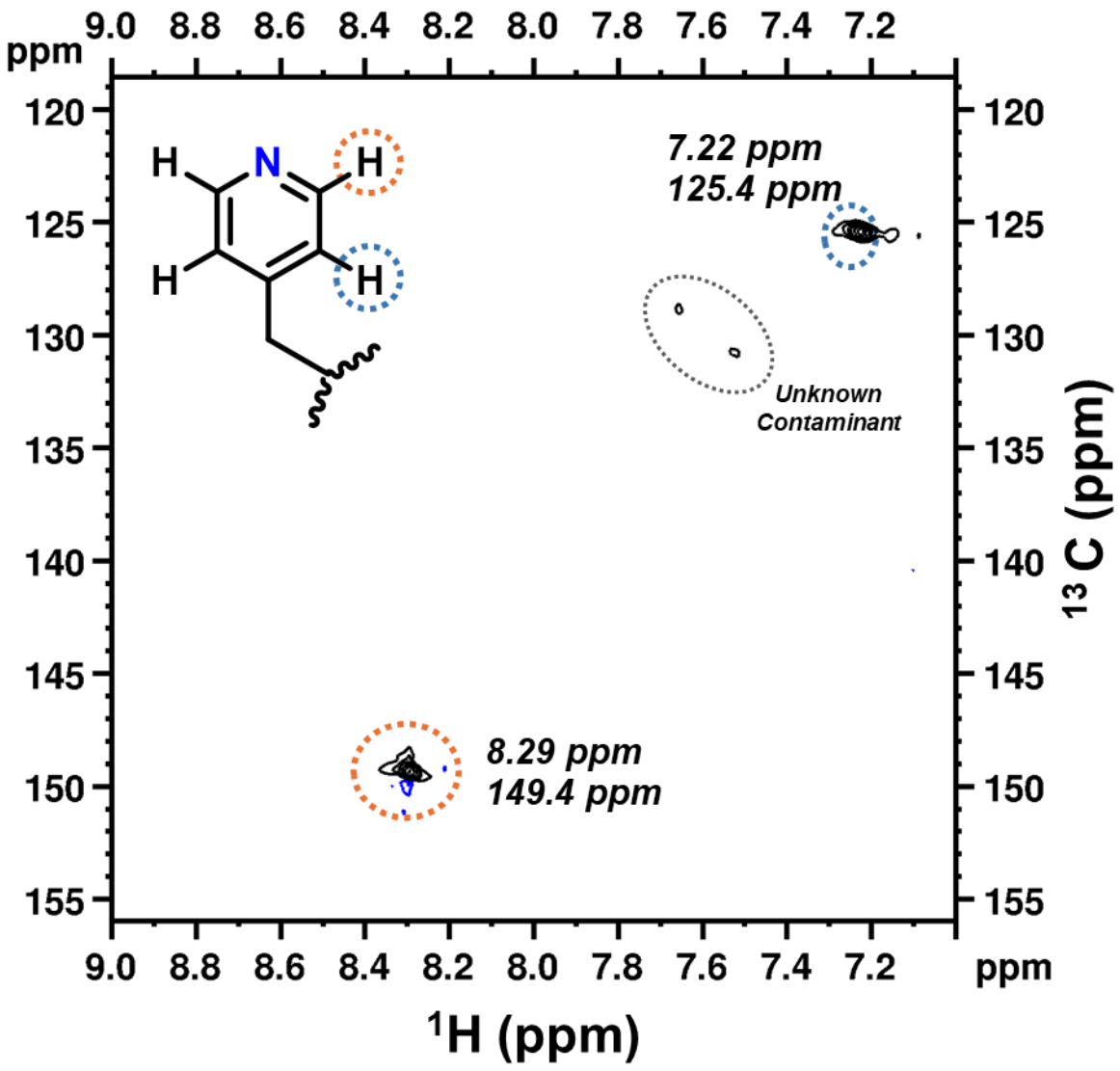


Figure A-9: ^{1}H-^{13}C HSQC NMR of apo-TRI-4'Py pH 5.00 (Region: Aromatic): delay constant #2 = 145 Hz *(filename: wcp3_126_TRIL23_4Py_pHTit_091122 [Spectrum 13])*.

The unknown contaminant is common across many samples throughout the NMR work in this thesis. Many attempts have been made to purify away or identify this molecule using mass spectroscopy without any progress. However, within the limitations of the experiments in this appendix, this contaminant does not bind either Cu(I) nor Cu(II).

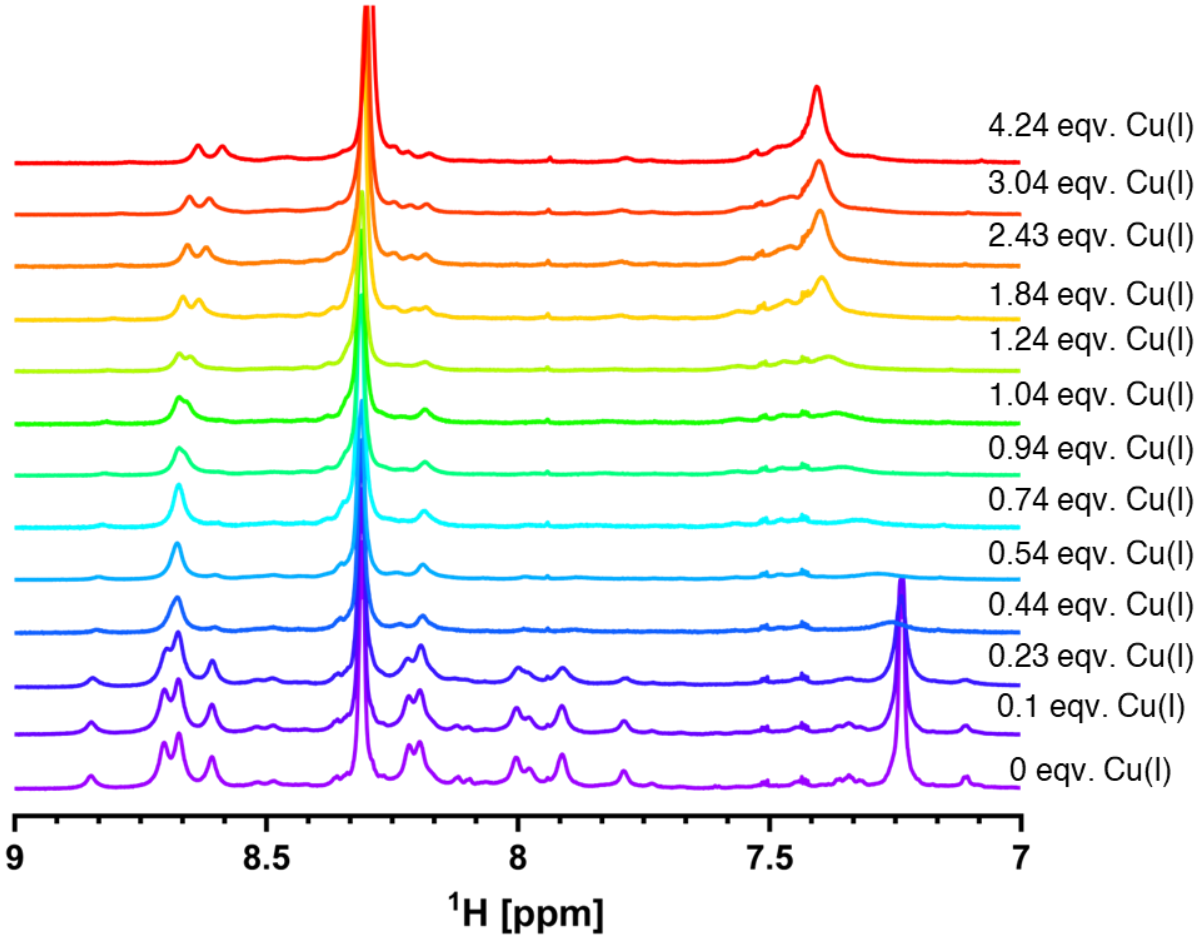


Figure A-10: ^{1}H-NMR of Cu(I)[MeCN]$_4$ titration TRI-4'Py 10% D_2O v/v at pH 5.90 (Region: Aromatic): *(file name:wcp3_178_TRIL23_4Py_CuITitrationpH5p9_111522).*

Upon the addition of Cu(I)[MeCN]$_4$, an intensity attenuation of the meta proton (the 7.24 ppm peak) is accompanied by a small downfield shift up 0.54 eqv. Cu(I). Further addition of Cu(I) yields at least two pyridine nitrogens (Figure A-13) at δ^{15}N values within range of those reported in Cu(I) histidine/Pyridine complexes.[2] *However, more experiments are needed to confirm the ortho-proton invariancies to Cu(I) binding (8.29 ppm), which is in opposition to those reported with Cu(I)-pyridine complexes.*[1] *These experiments should include using $CuSO_4$ and sodium ascorbate to yield the appropriate reduced enzyme to ensure the acetonitrile solution does not prevent the binding of Cu(I) to the enzyme (see Chapter II-NMR section).*

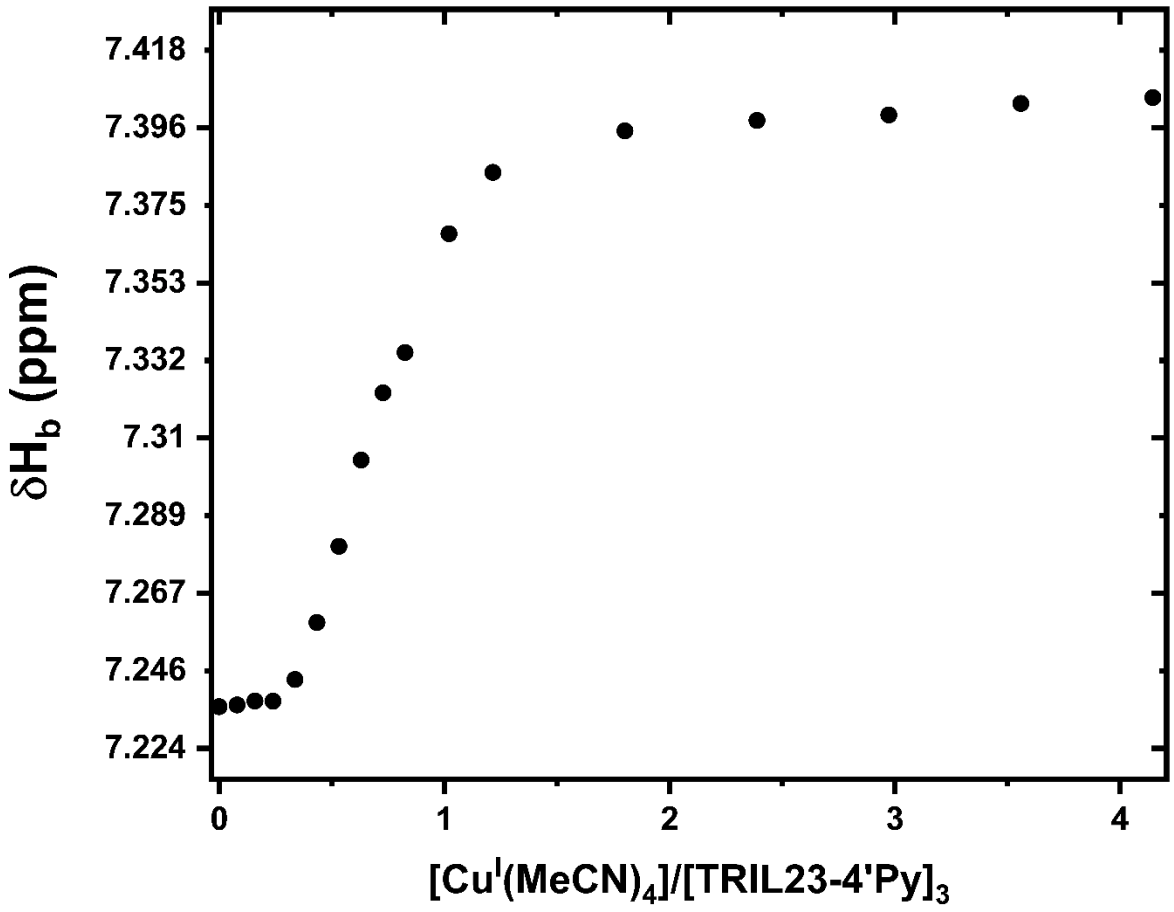


Figure A-11: Progression curve of Cu(I)[MeCN]$_4$ titration of TRI-4'Py following the meta-proton on the pyridine ligand.

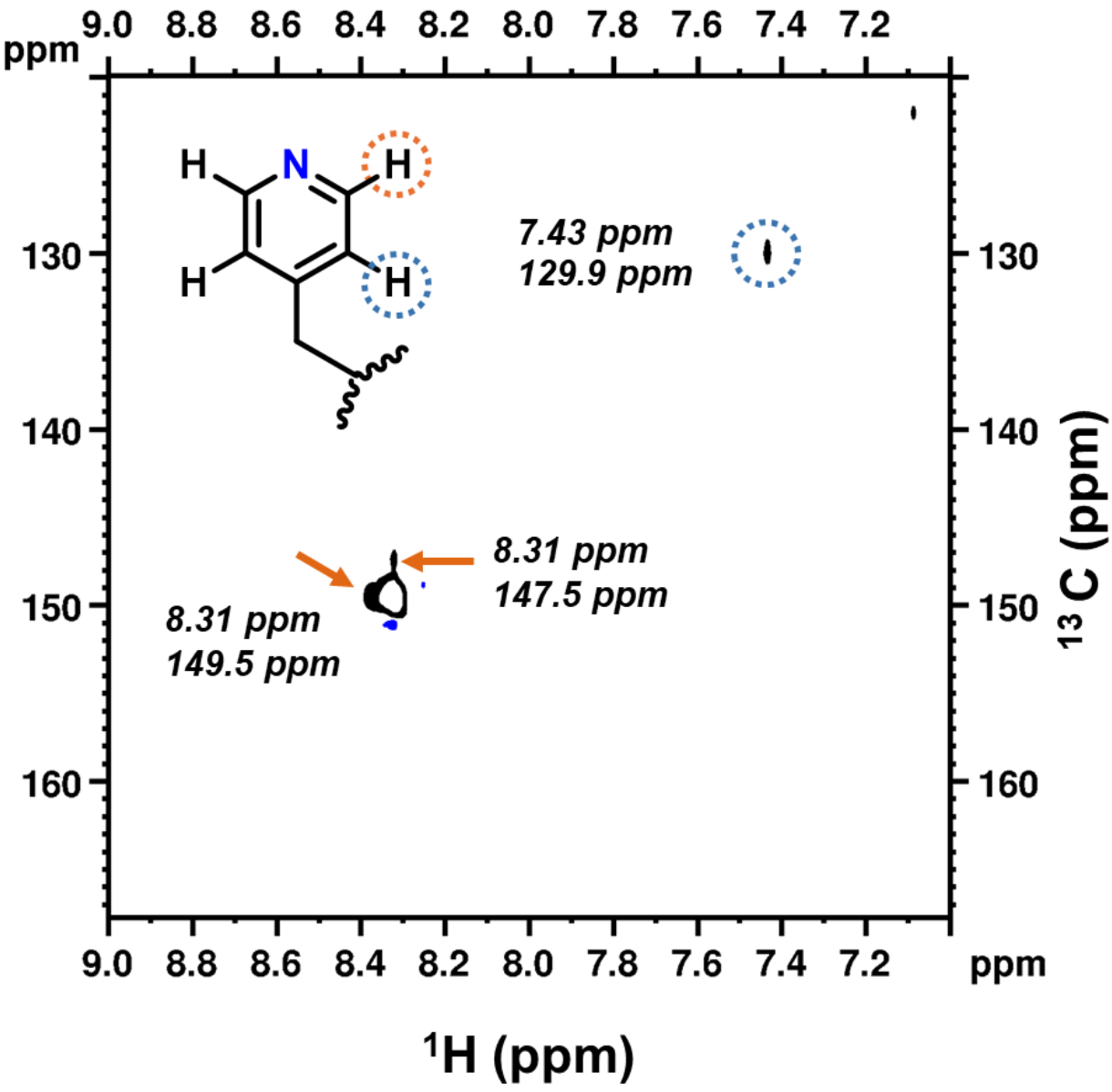


Figure A-12: ^{1}H-^{13}C HSQC NMR of 1.04 eqv. Cu(I)[MeCN]$_4$ TRI-4'Py at 10% D_2O v/v pH 5.90 (Region: Aromatic): delay constant #2 = 145 Hz *(file name: wcp3_178_TRIL23_4Py_CuITitrationpH5p9_111522 [Spectrum 15]).*

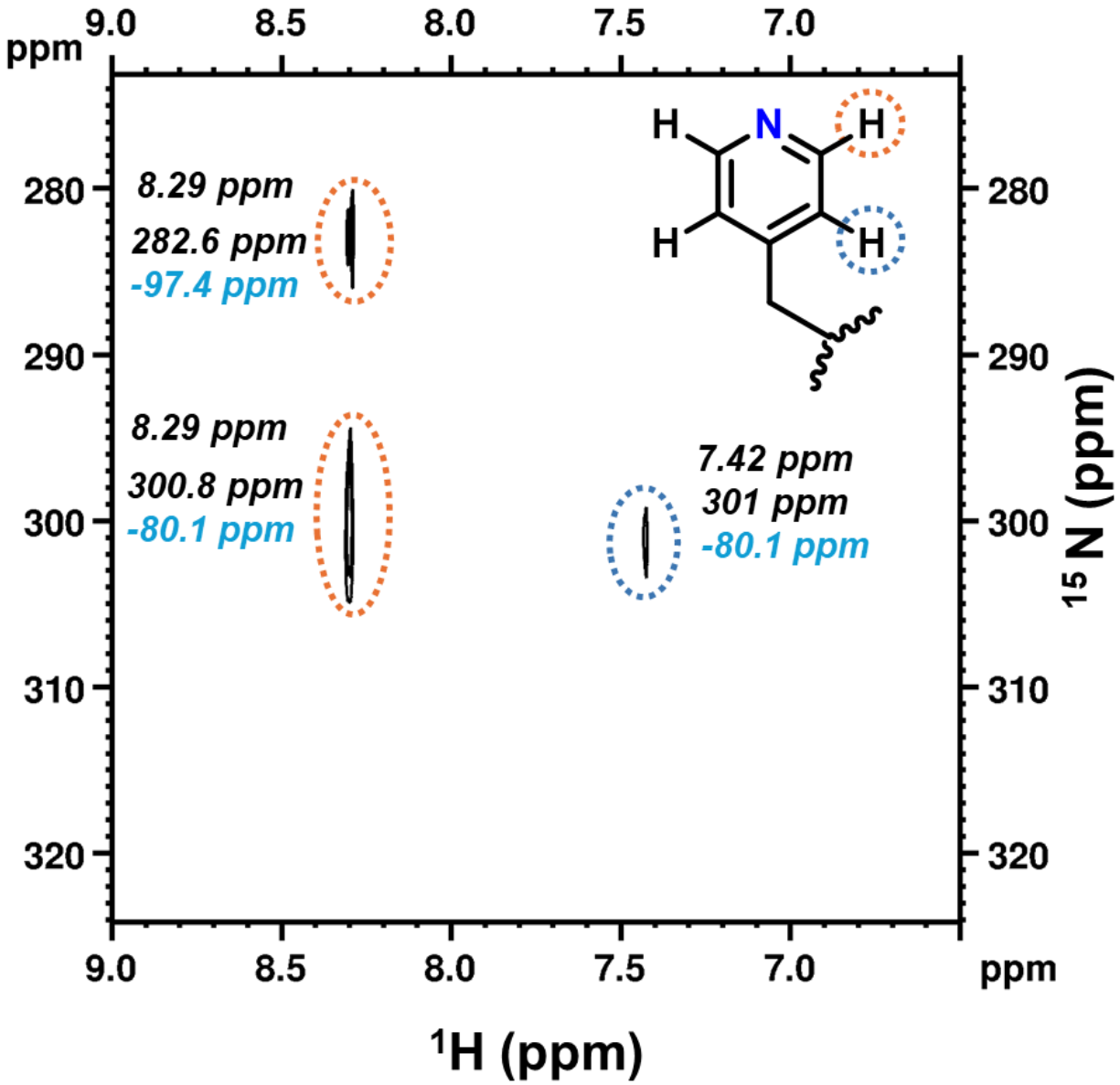


Figure A-13: ^{1}H-^{15}N HMBC of 4.239 eqv Cu(I)[MeCN]$_4$ TRI-4'Py 10% D_2O v/v at pH 5.90 (Region: Aromatic): delay constant #13=5 Hz *(file name: wcp3_178_TRIL23_4Py_CuITitrationpH5p9_111522 [Spectrum 16])*. Blue ^{15}N ppm values are externally referenced to nitromethane to match the ^{1}H-^{15}N HMBC reference of the Cu(I)-pyridine complex's in Ref. 2.

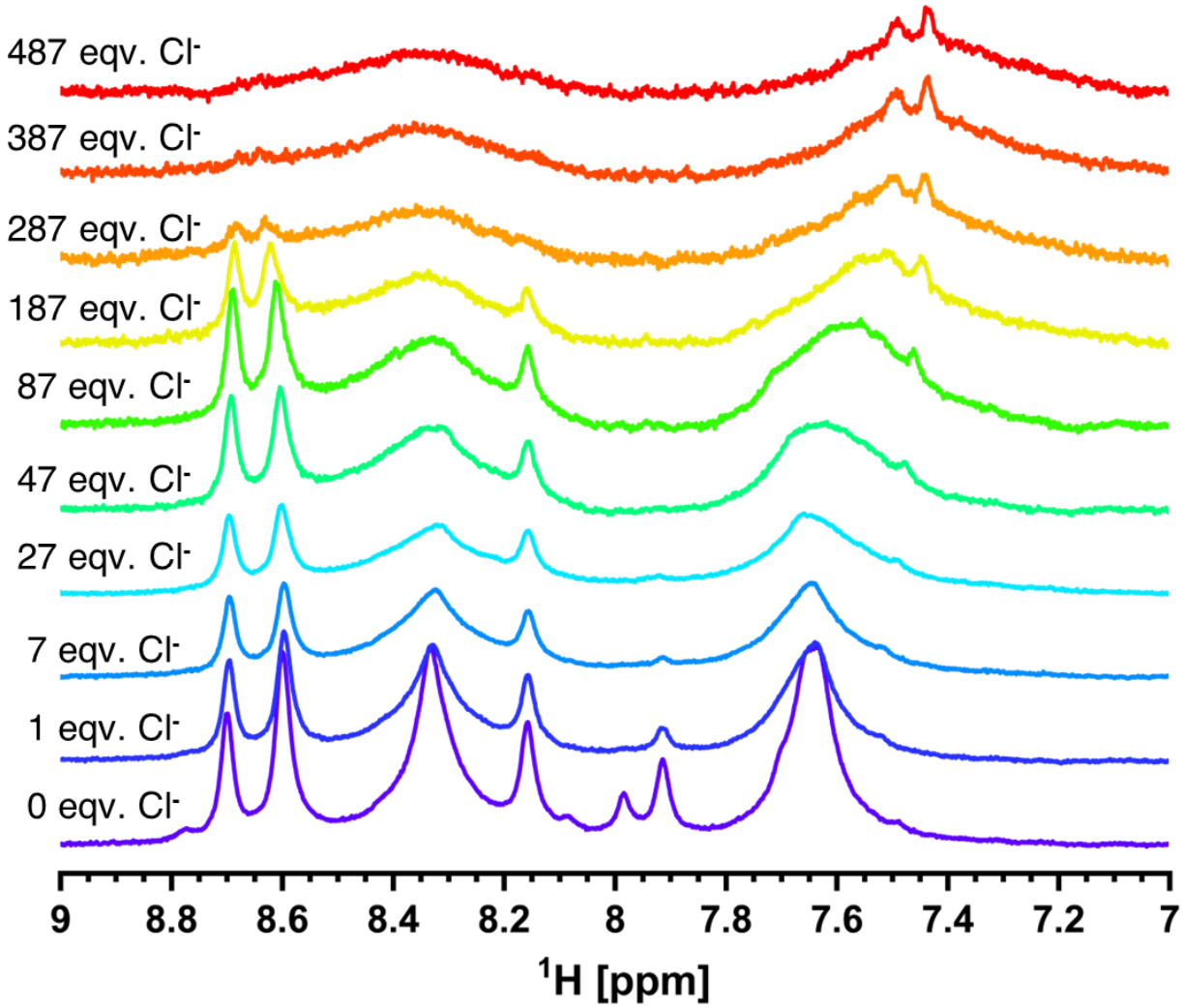


Figure A-14: ^{1}H-NMR NaCl titration of Cu(I)-TRI-4'Py [1 eqv. Cu(I)[MeCN]$_4$] 10% D_2O v/v at pH 5.90 (Region: Aromatic): *(file name: wcp3_108_TRIL23_4PyCuI_Cl_Titration).*

The amide backbone protons (see Figure A-8) merge into the baseline in ^{1}H NMR with increasing addition of NaCl, likely as a result of an increase exchange rate with D_2O, as reported by Tadeo et al.[8]*. These amide protons are closely associated near the active site, as oxidation to the Cu(II) form in TRI-3'Py eliminates these amide peaks (See Figure A-25). From the EXAFS in Chapter III, the binding of Cl^- to the reduced enzyme leads TRI-4'Py to adopt a different coordination geometry which may cause disorder (chemical disoperation) near the active site. Another interpretation of the data is the Cl^- aids in disproportion of Cu(I) to Cu(0) and Cu(II), where the paramagnetism leads to the broadening. However, the shifts in Figure A-16 are consistent with the leucine layers rearranging to accommodate the Cl^- ion near the copper site.* <u>Note</u>*: The broadening of the ortho and meta pyridine protons (8.34 ppm and 7.64 ppm, respectively) is likely not a result of the large concentration of NaCl to interfere with proper tuning and matching of the deuterium signal by the NMR probe (i.e., the ^{1}H peaks at 7.45 ppm in the 487 eqv. Cl^- spectrum).*

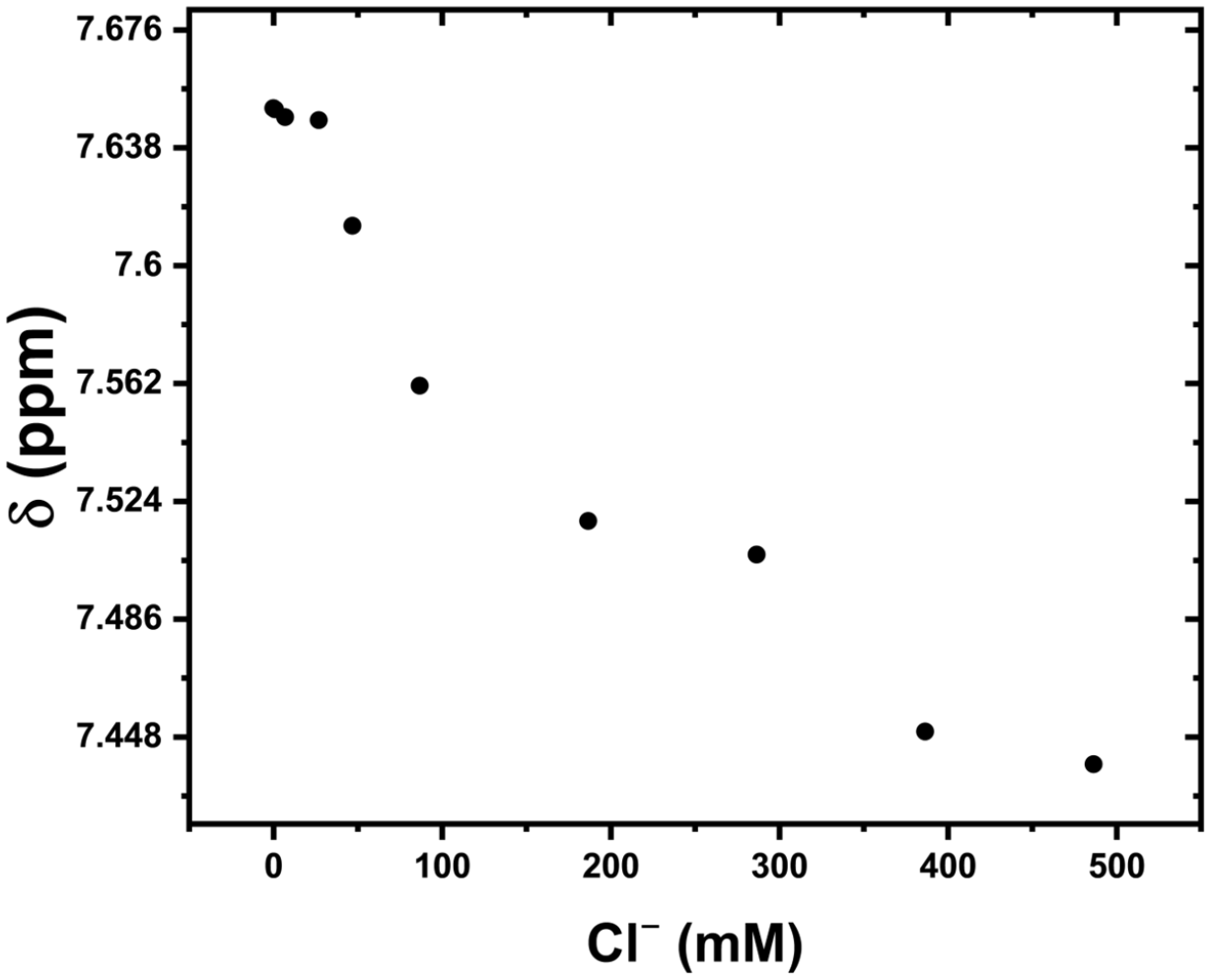


Figure A-15: Progression curve of NaCl titration of Cu(I)[MeCN]$_4$ titration of Cu(I)-TRI-4'Py following the meta-proton on the pyridine ligand.

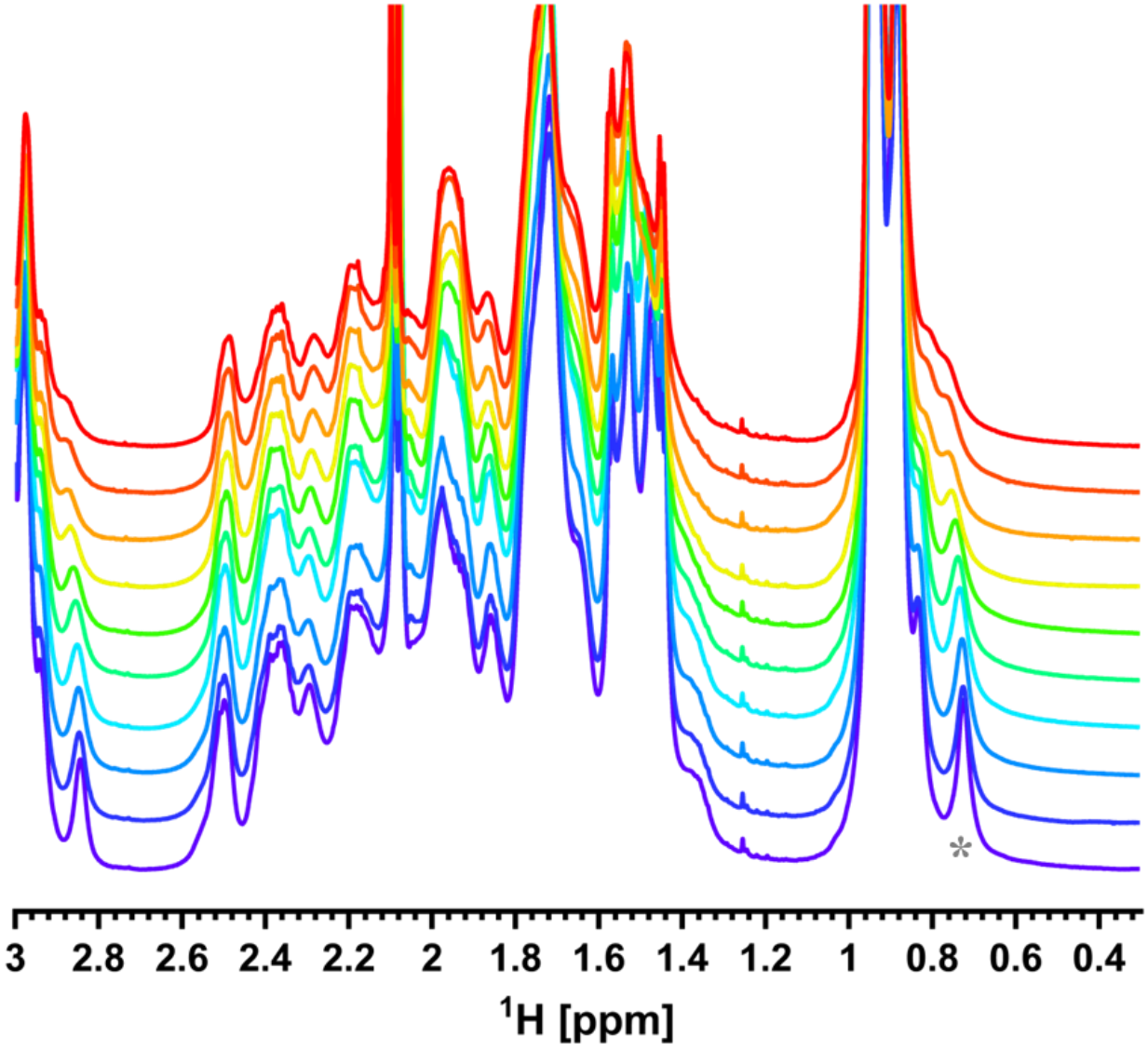


Figure A-16: ^{1}H-NMR NaCl titration of Cu(I)-TRI-4'Py [1 eqv. Cu(I)[MeCN]$_4$] 10% D_2O v/v at pH 5.90 (Region: Aliphatic): *(file name: wcp3_108_TRIL23_4PyCuI_Cl_Titration).*

Protein: TRI-4'Py L19A and TRIW-4'Py L19A

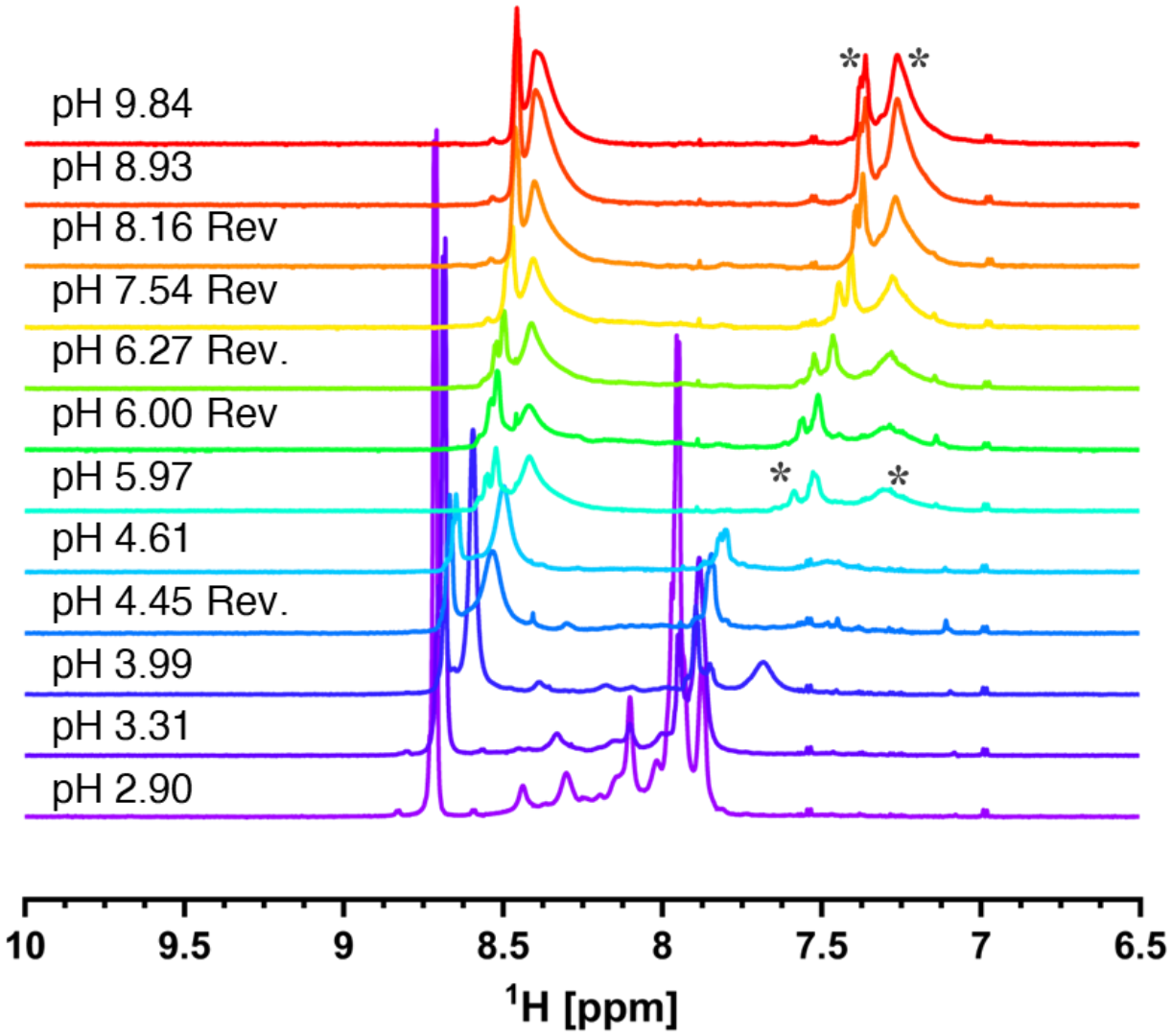


Figure A-17: ^{1}H-NMR pH Titration of apo-TRI-4'Py L19A in 10% D_2O v/v (Region: Aromatic): *(file name: wcp3_176_TRIL19AL23_4Py_pHTitration_111422)*. "Rev" implies the spectrum is collected in the reverse direction upon pH 9.84 was reached. Ortho protons (*).

Visual inspection of the *pH titration of the apo-TRI-4'Py L19A suggests reversibility in the deprotonation equilibriums within the pH range of 4.45 to 9.84. The ^{1}H-NMR and ^{1}H-^{13}C HSQC spectra (Figure A-19) pH 5.97 suggest there are at least two populations of ortho pyridine protons on the 4'Pyridine ligand. The two populations are clear in the ortho-protons at pH 5.97 and pH 9.84 in the figure above. In the presence of 1.0 eqv of Cu(I), these protons resolve to a single peak as seen in Chapter II (Figure II-9).*

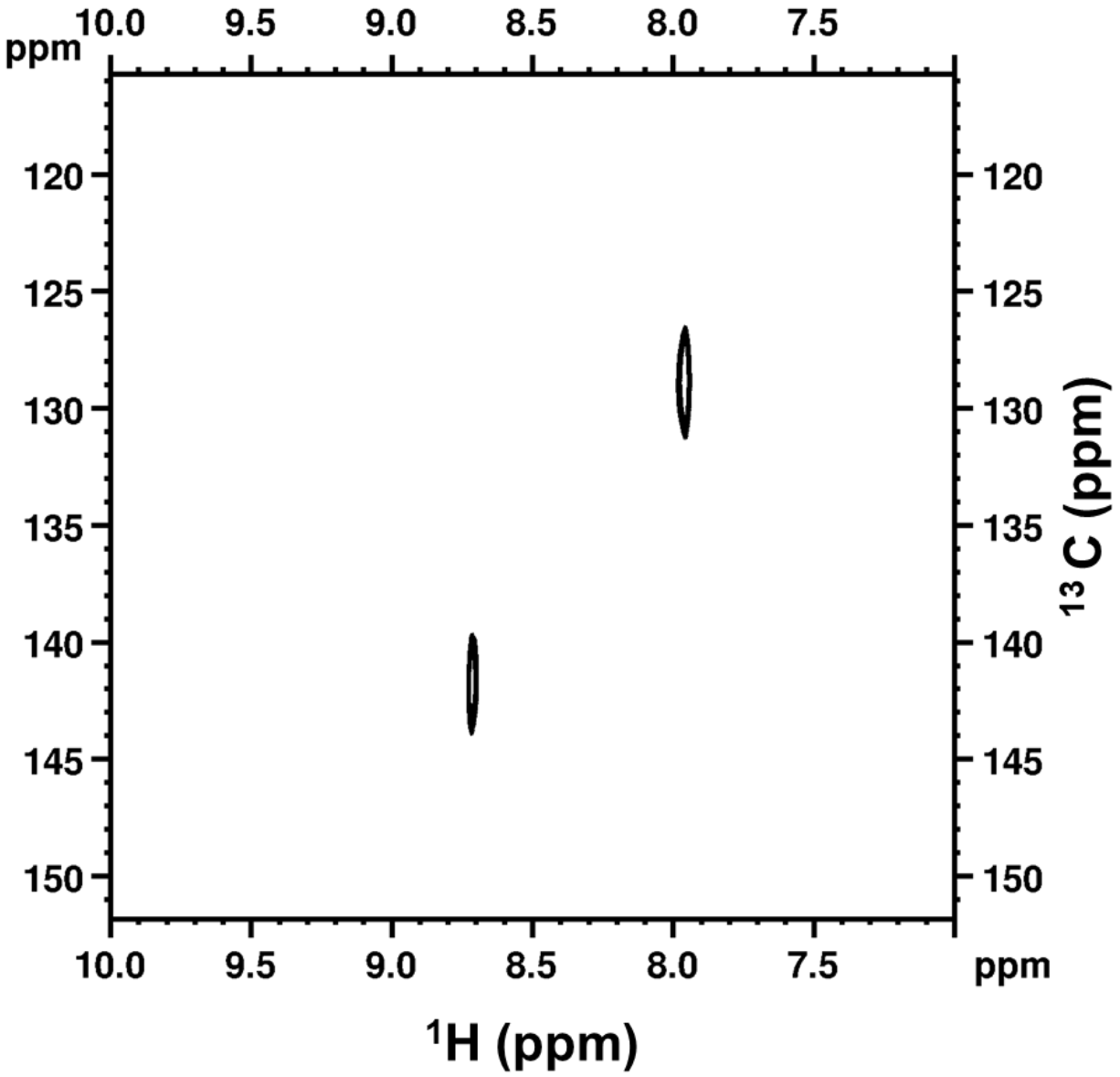


Figure A-18: ^{1}H-^{13}C HSQC NMR of apo-TRI-4'Py L19A at pH 2.90 (Region: Aromatic): delay constant #2 = 145 Hz *(file name: wcp3_176_TRIL19AL23_4Py_pHTitration_111422 [Spectrum 3])* .

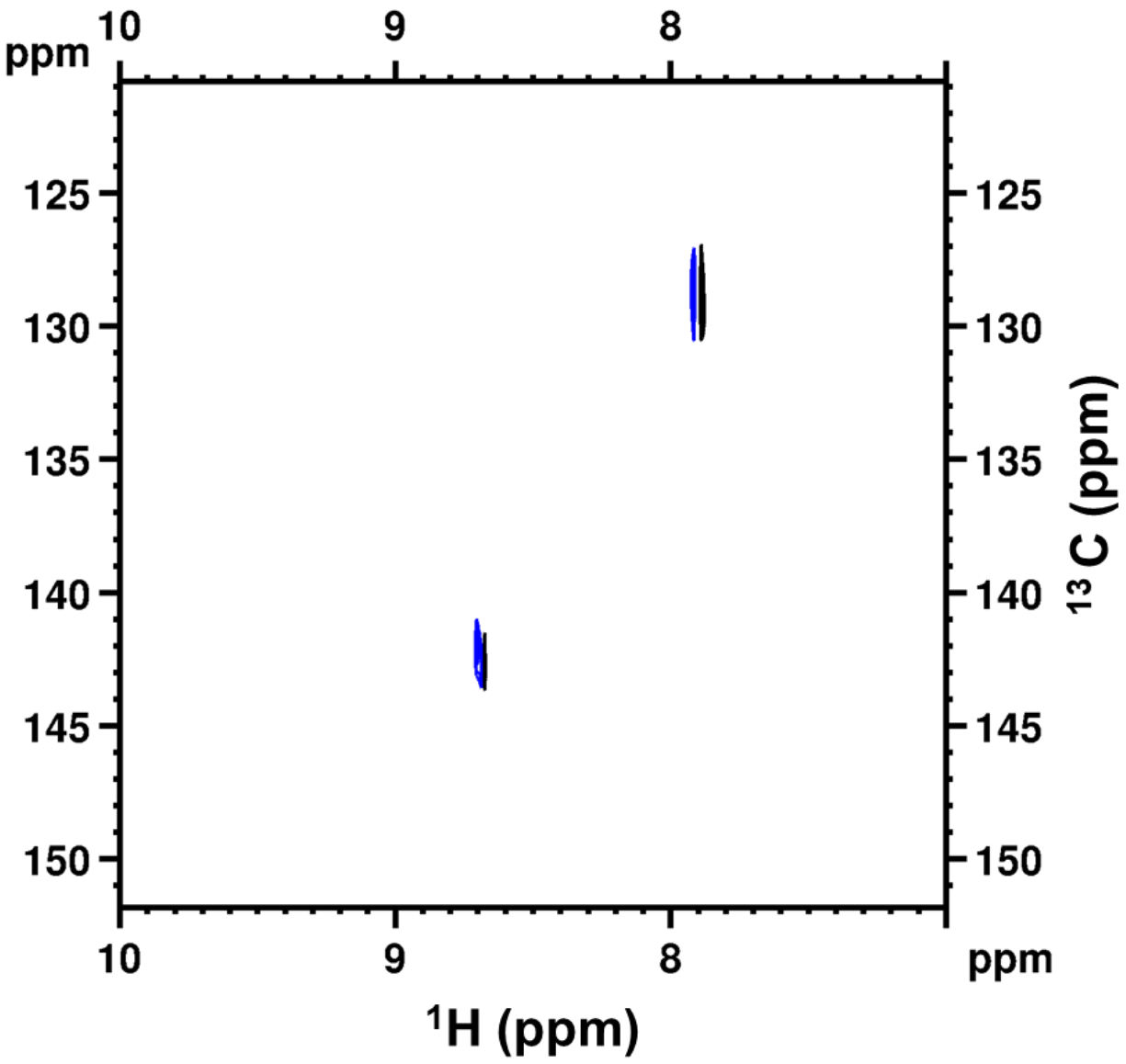


Figure A-19: ^{1}H-^{13}C HSQC NMR of apo-TRI-4'Py L19A at pH 3.99 (Region: Aromatic): delay constant #2 = 145 Hz (*file name: wcp3_176_TRIL19AL23_4Py_pHTitration_111422 [Spectrum 7])* .

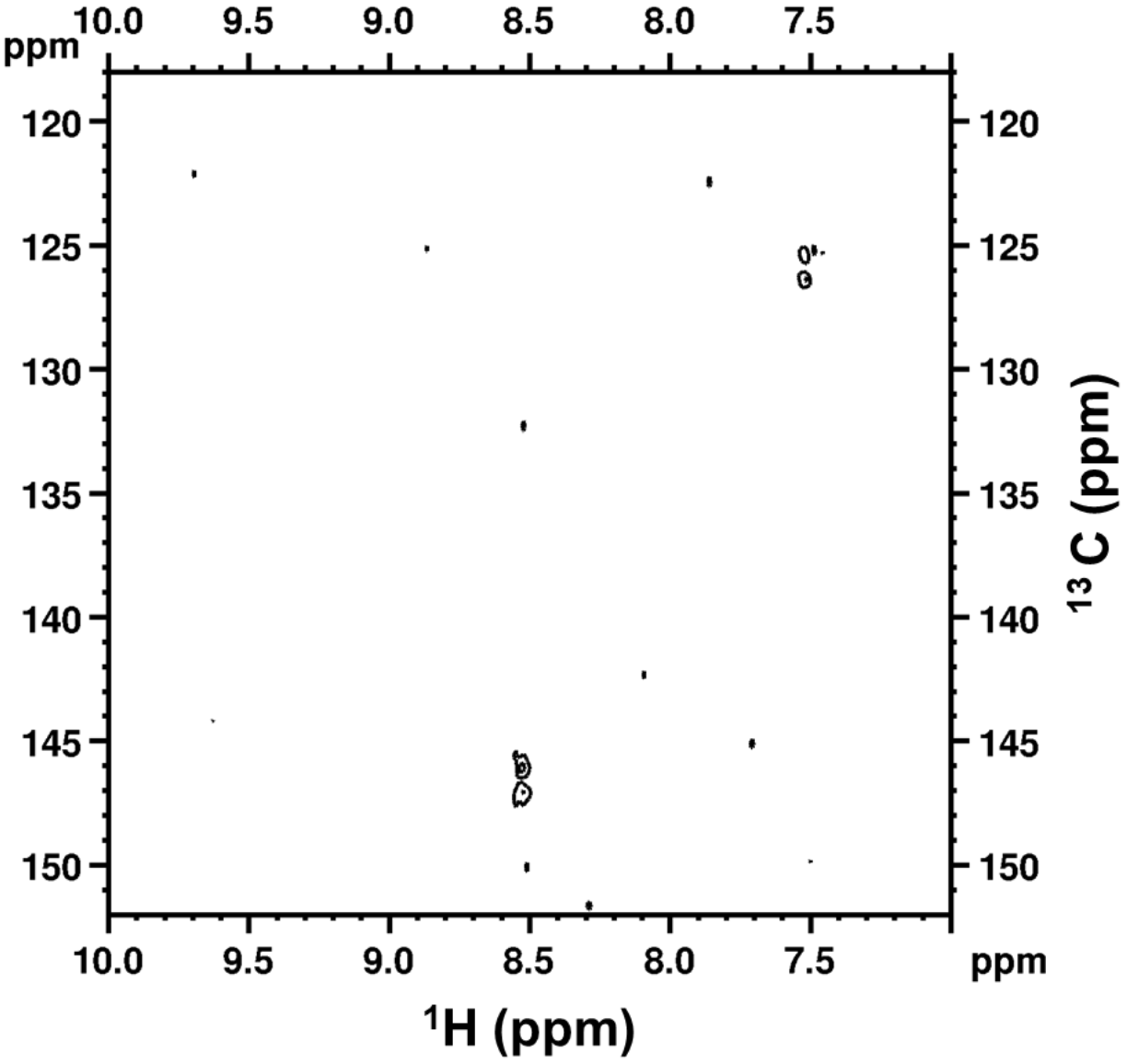


Figure A-20: ^{1}H-^{13}C HSQC of apo-TRI-4'Py L19A at pH 5.97 (Region: Aromatic): delay constant #2 = 145 Hz *(filename: wcp3_176_TRIL19AL23_4Py_pHTitration_111422 [Spectrum 10]).*

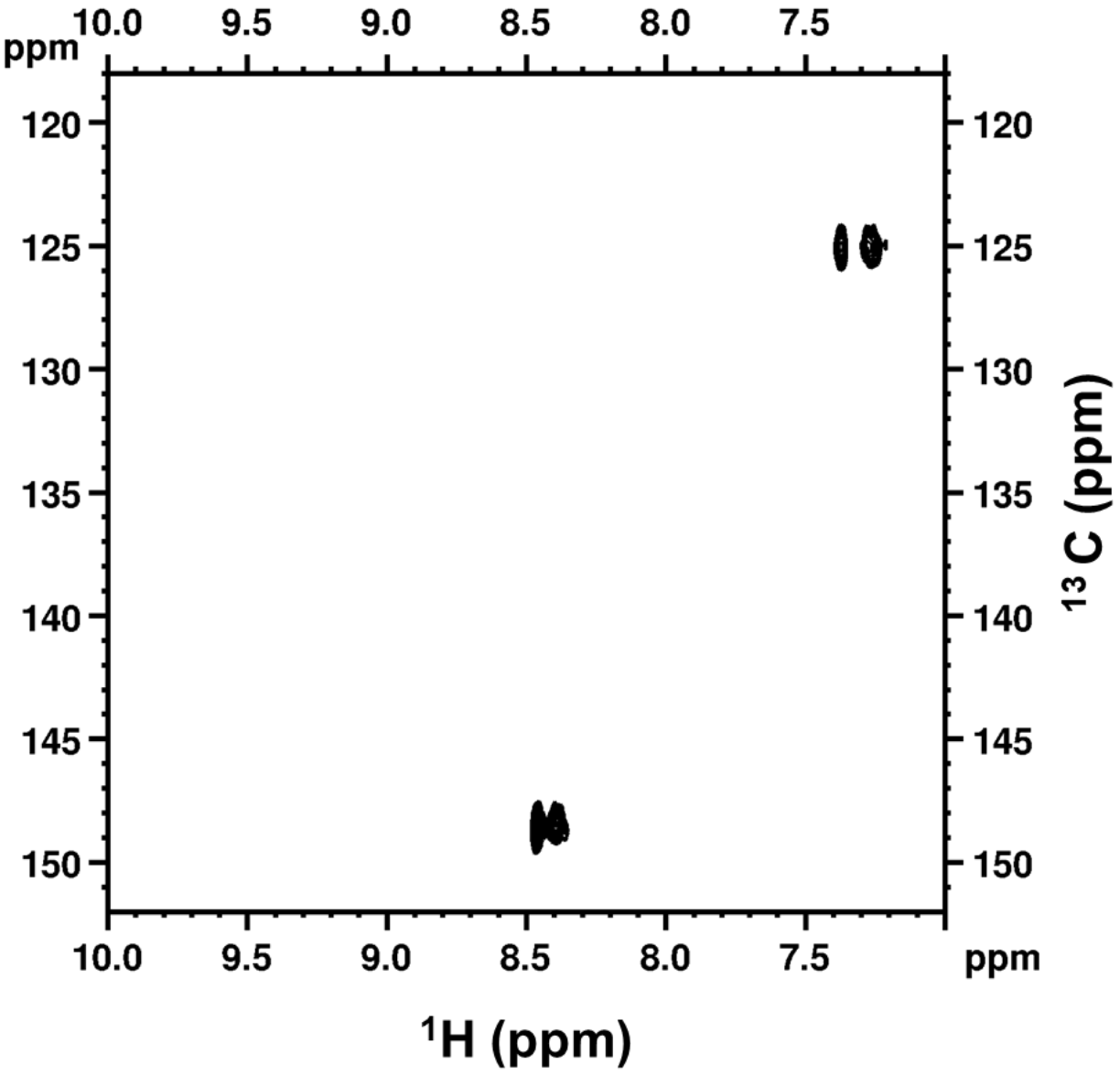


Figure A-21: ^{1}H-^{13}C HSQC NMR of apo-TRI-4'Py L19A at pH 9.84 (Region: Aromatic): delay constant 2 = 145 Hz *(filename: wcp3_176_TRIL19AL23_4Py_pHTitration_111422 [Spectrum 14]).*

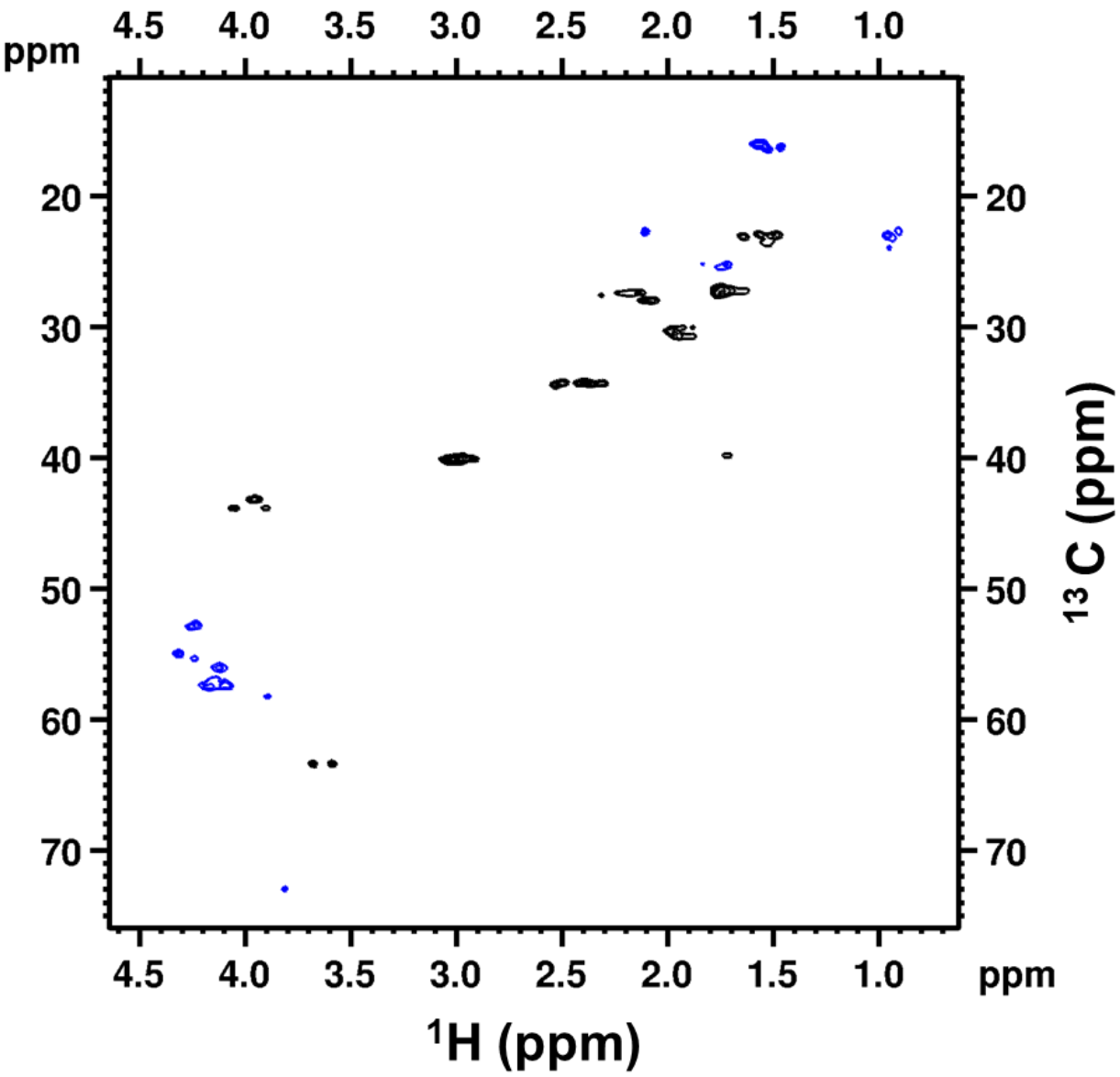


Figure A-22: ^{1}H-^{13}C HSQC of apo-TRI-4'Py L19A at pH 5.94 (Region: Aliphatic-sidechains): delay constant #2 = 145 Hz *(filename: wcp4_54_TRIL19AL23_4Py_Cu_titration_050623 [Spectrum 4]).*

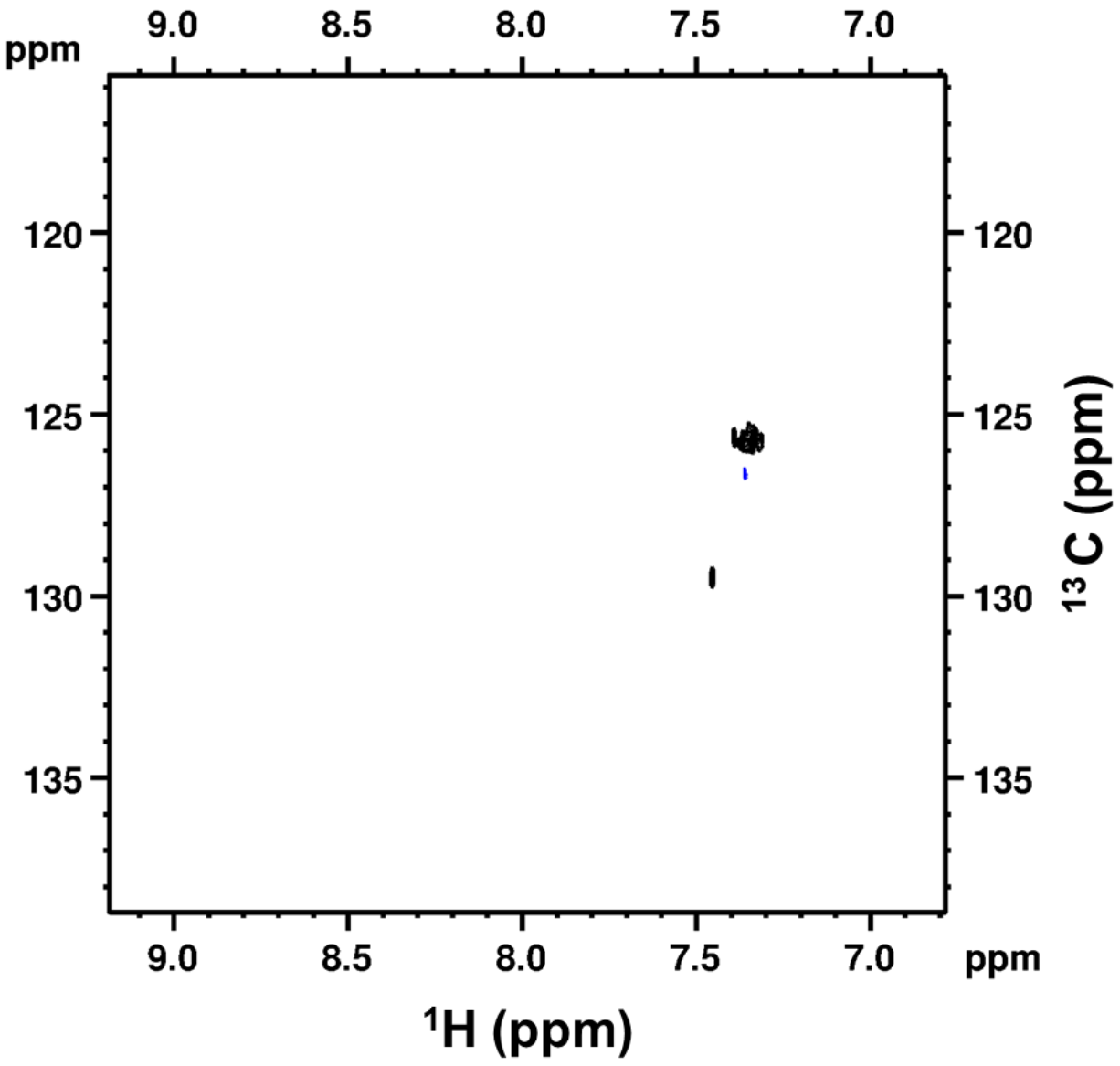


Figure A-23: ^{1}H-^{13}C HSQC NMR of 3.7 mM TRI-4'Py L19A 0.3 eq. $CuSO_4$ (10 eq. sodium ascorbate) at pH 5.94 (Region: Aromatic): delay constant #2 = 145 Hz *(filename: wcp4_54_TRIL19AL23_4Py_Cu_titration_050623 [Spectrum 7]).*

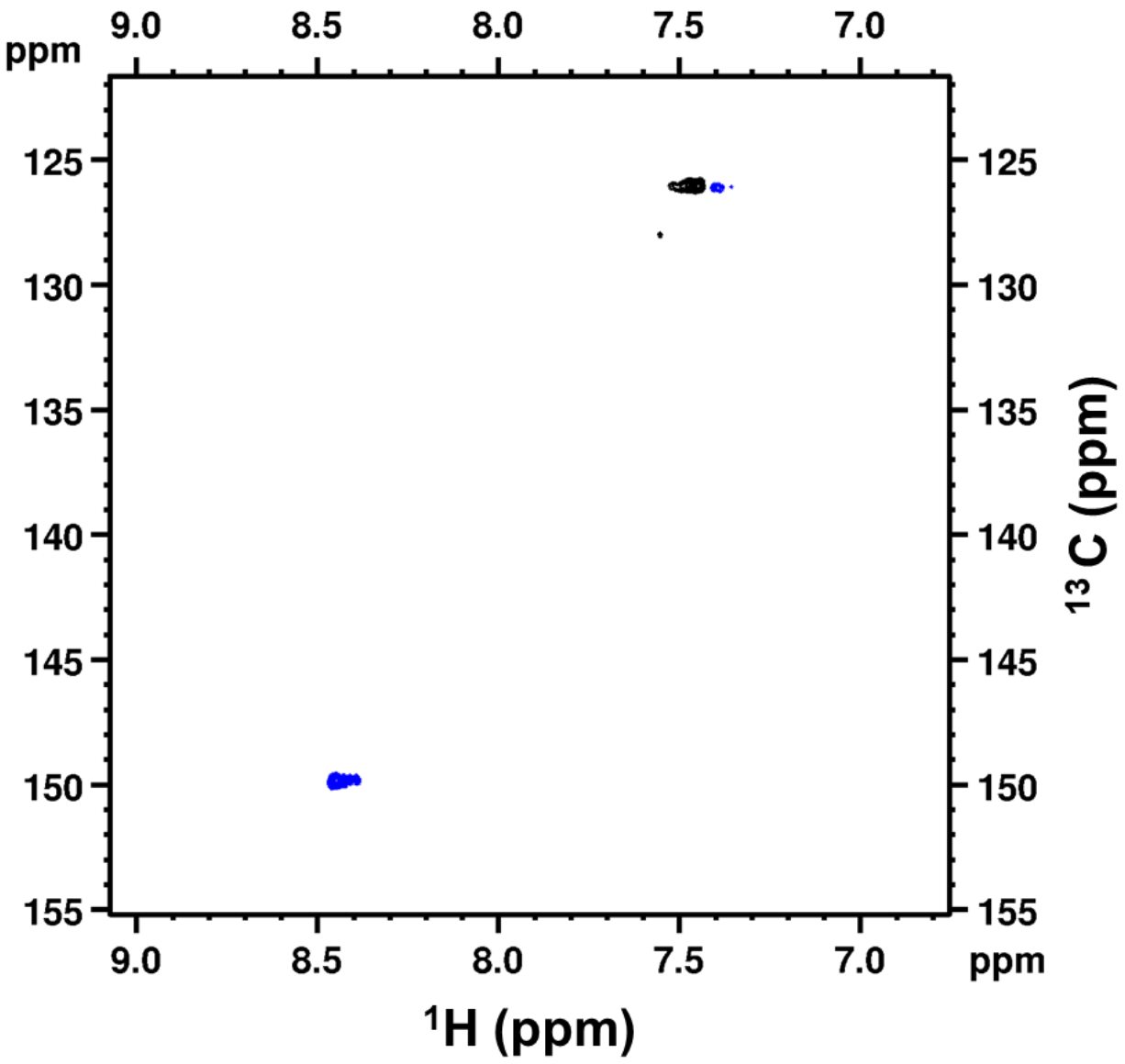


Figure A-24: ^{1}H-^{13}C HSQC NMR of 3.7 mM (TRI-4'Py L19A)$_3$ 0.7 eq. $CuSO_4$ (10 eq. sodium ascorbate) at pH 5.94 (Region: Aromatic): delay constant #2=145 Hz *(filename: wcp4_54_TRIL19AL23_4Py_Cu_titration_050623 [Spectrum 10-2]).*

Protein: TRI-3'Py

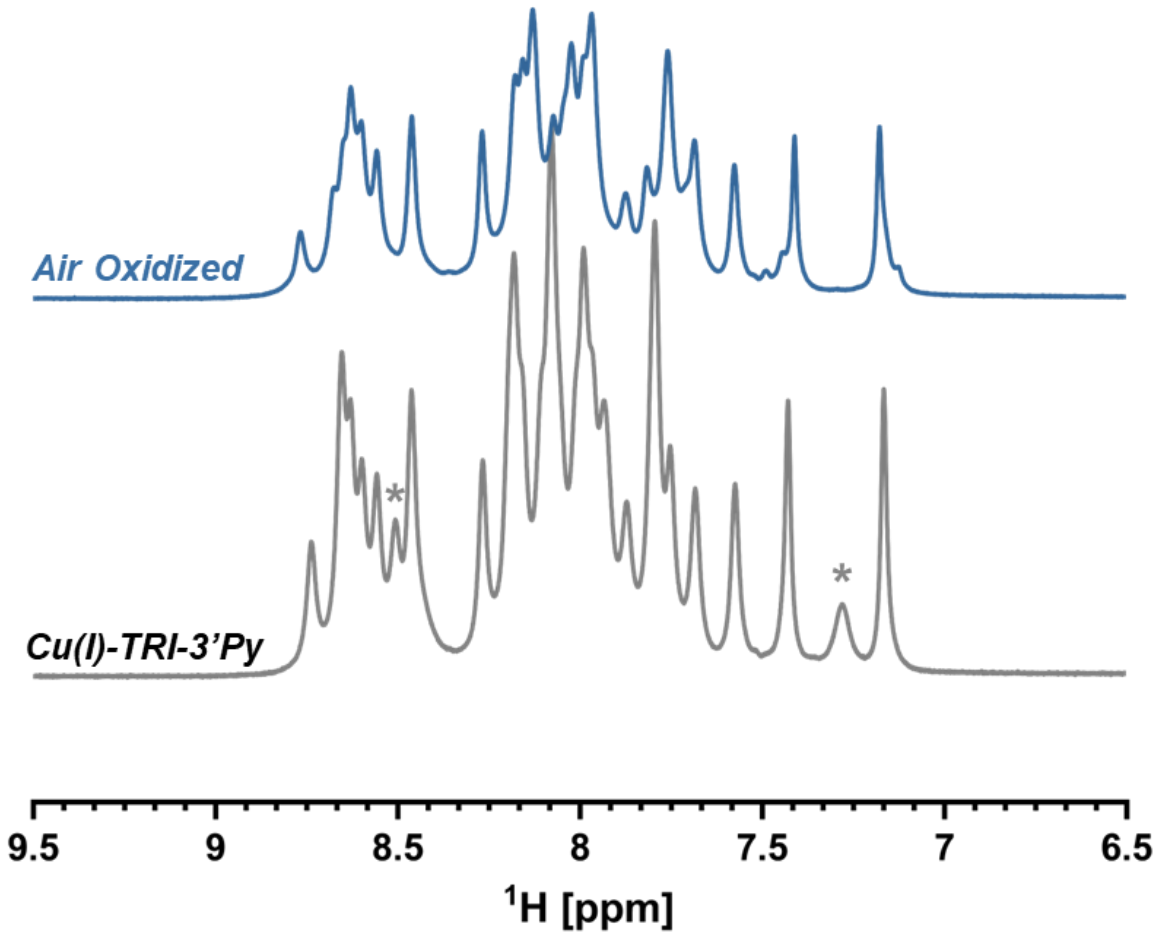


Figure A-25: ^{1}H-NMR of Cu(I)-TRI-3'Py at pH 5.91 vs. the oxidized enzyme (Region: Aromatic): *(filename: wcp4_44_TRIL23_3Py_Cu_titration_042723 [Spectrum 4]).*

Based on the ^{1}H-^{13}C HSQC assignments in Chapter II (Figure II-8), the oxidation of the Cu(I)-TRI-3'Py resulted in loss of the pyridine proton peaks. For example, the ortho- protons and meta-proton intensity is lost due to the paramagnetism of the d^9 configuration of the Cu(II) bound to the pyridine active site (shorter T_1 relaxation rates). The remaining amide protons are not in proximity to the Cu(II) ion, and therefore, the relaxation rates are not substantially impacted. However, it should be noted that upon oxidations, perturbation in both the chemical shifts and intensity of some amide protons can be observed when comparing to the two spectra.

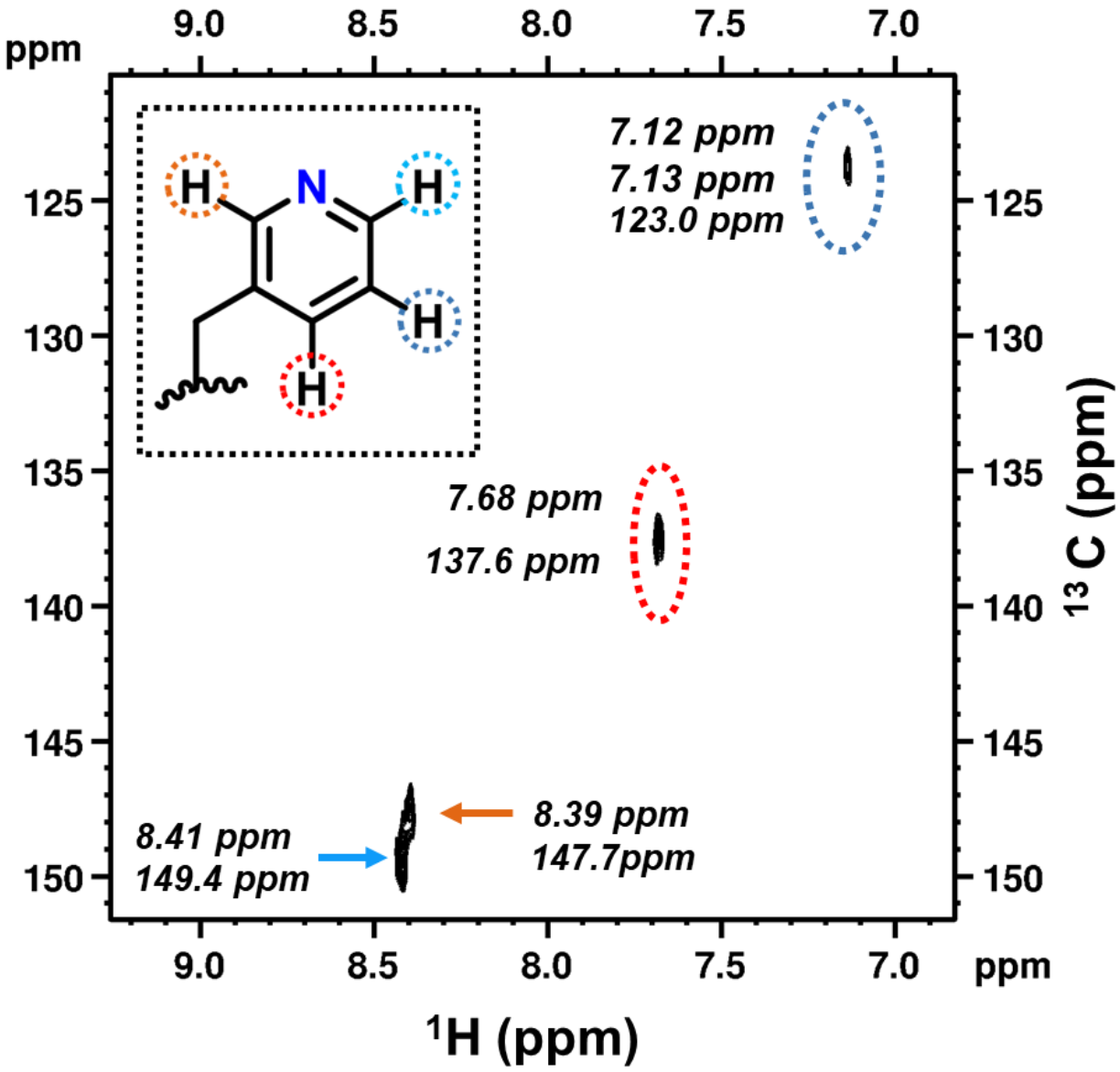


Figure A-26: ^{1}H-^{13}C HSQC NMR of 2.2 mM TRI-3'Py 0.3 eq. $CuSO_4$ (10 eq. sodium ascorbate) at pH 5.93 (Region: Aromatic): delay constant #2=170 Hz *(filename: wcp4_54_TRIL23_3Py_Cu_titration_050623 [Spectrum 4]).*

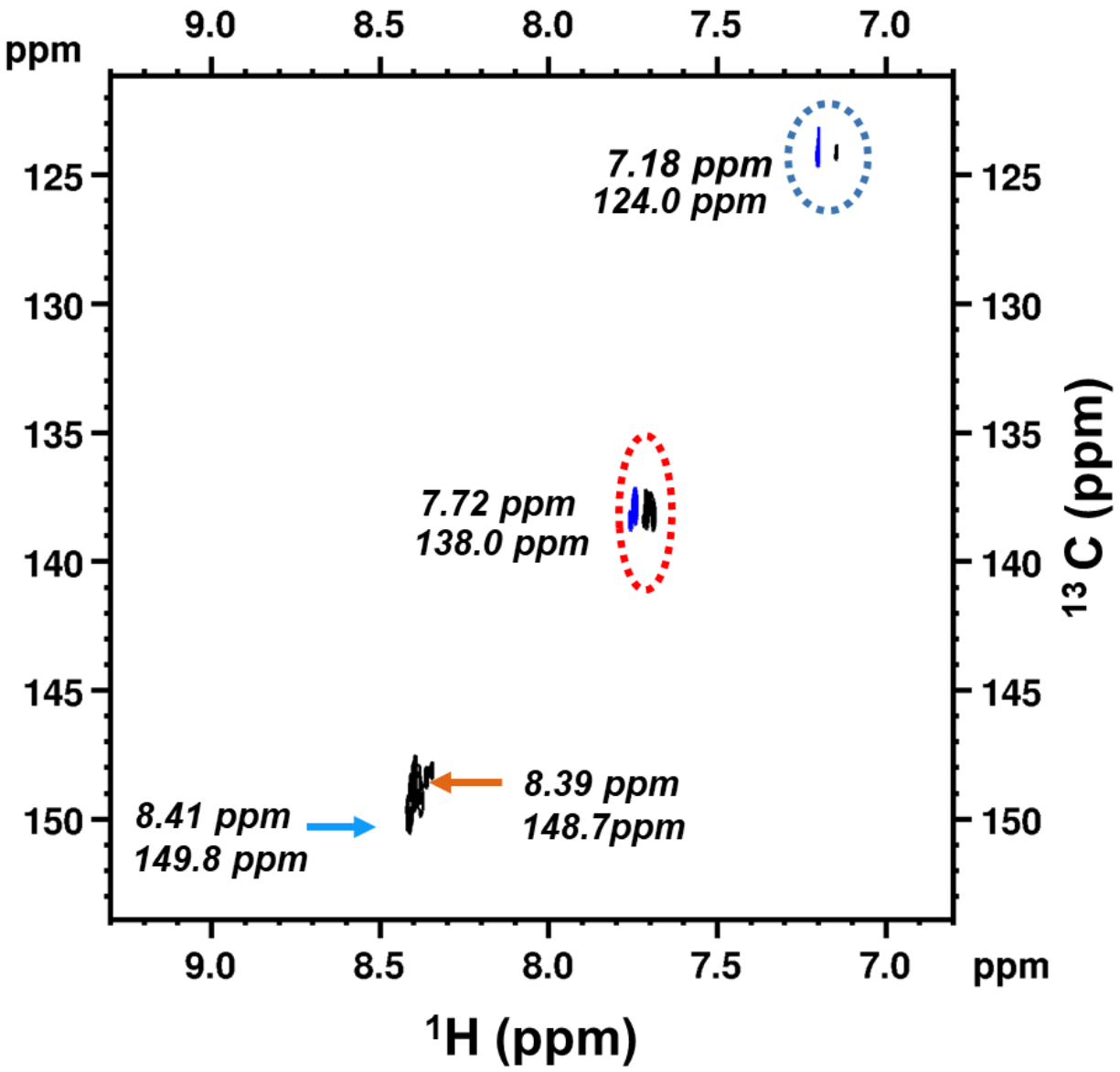


Figure A-27: ^{1}H-^{13}C HSQC NMR of 2.2 mM TRI-3'Py 0.5 eq. CuSO4 (10 eq. sodium ascorbate) at pH 5.93 (Region: Aromatic): delay constant #2 = 170 Hz *(filename: wcp4_54_TRIL23_3Py_Cu_titration_050623 [Spectrum 6]).*

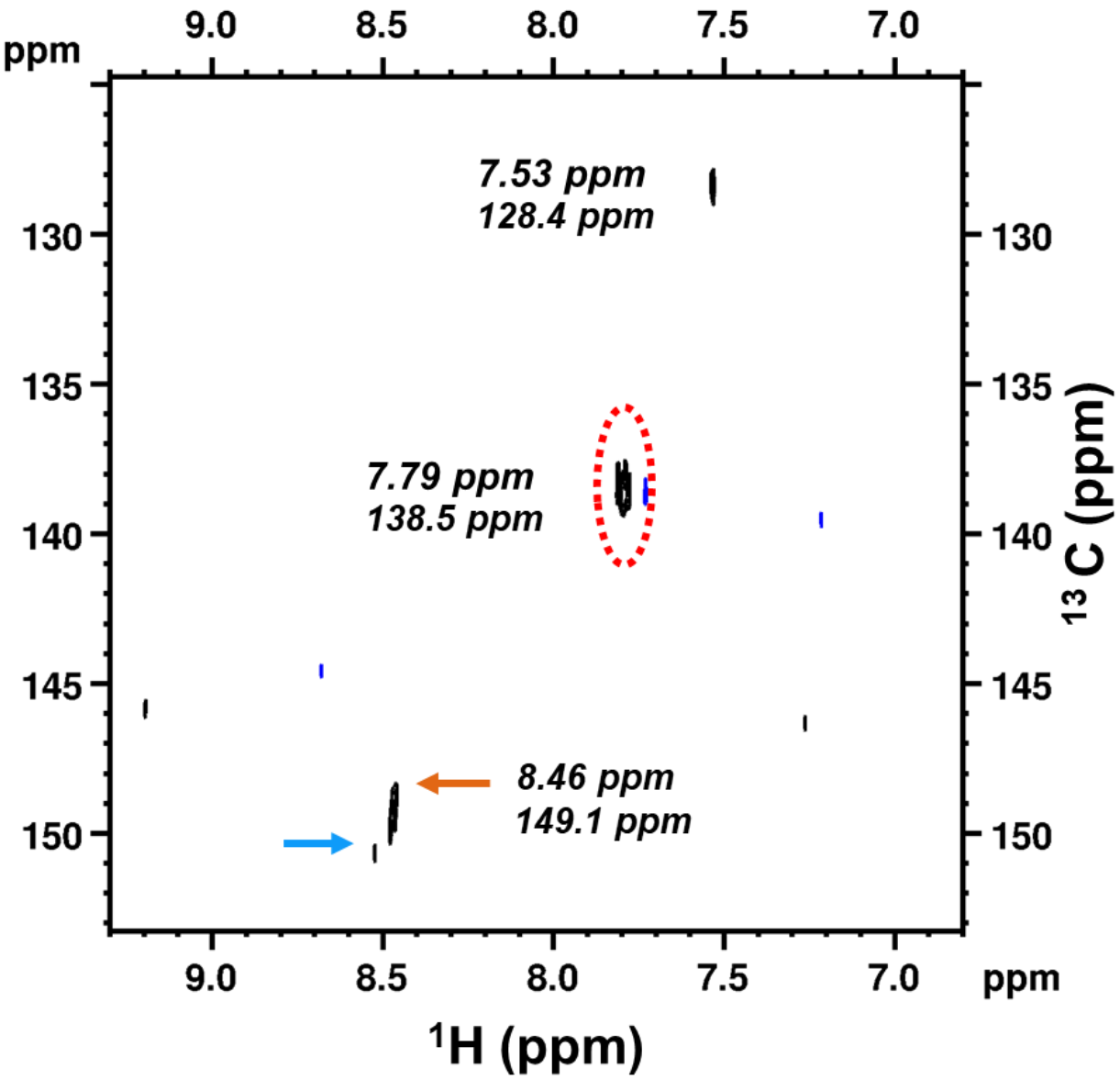


Figure A-28: ^{1}H-^{13}C HSQC NMR of 2.2 mM TRI-3'Py 0.7 eq. $CuSO_4$ (10 eq. sodium ascorbate) at pH 5.93 (Region: Aromatic): delay constant #2 = 170 Hz *(filename: wcp4_54_TRIL23_3Py_Cu_titration_050623 [Spectrum 8]).*

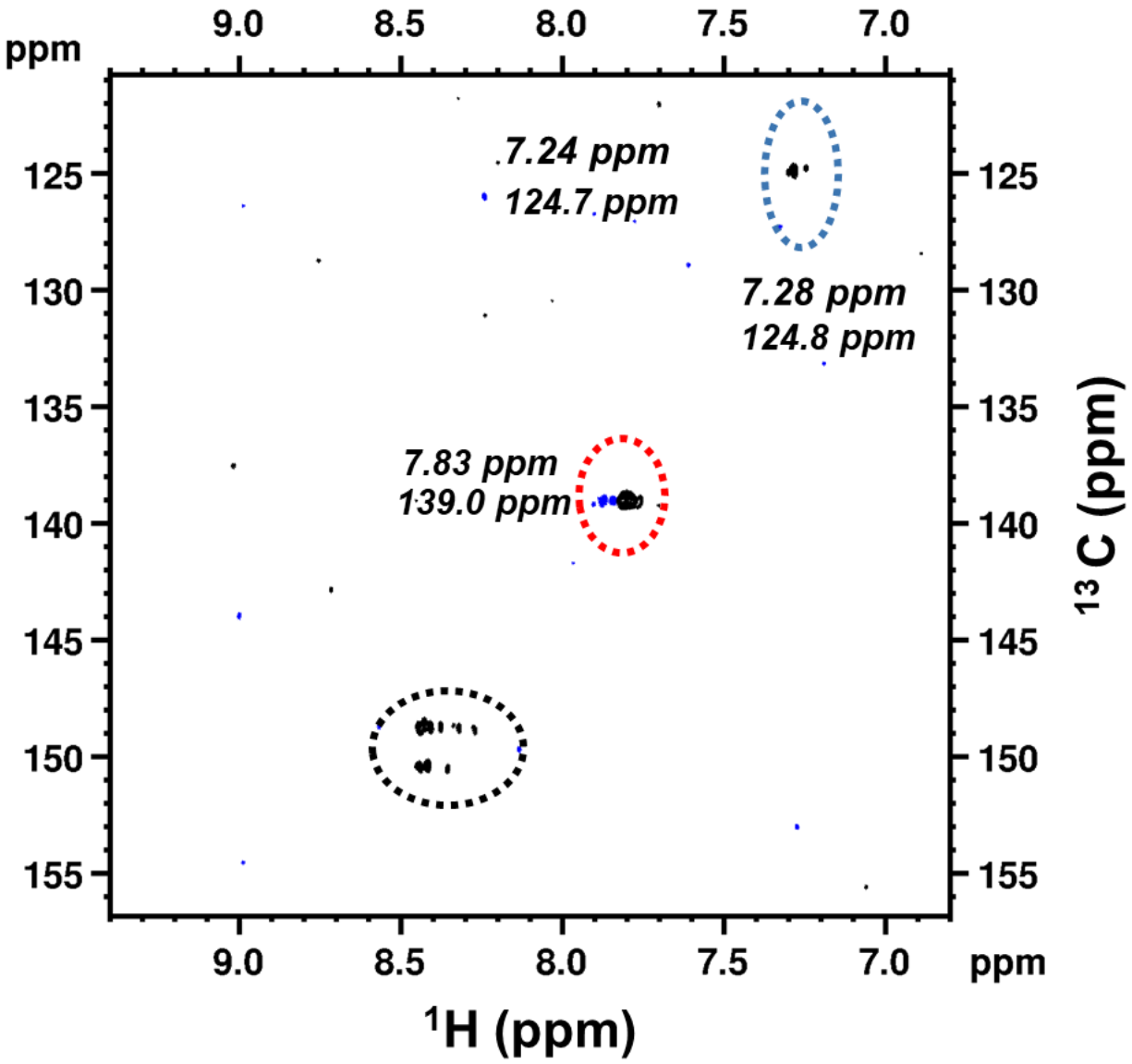


Figure A-29: ^{1}H-^{13}C HSQC NMR of 2.2 mM TRI-3'Py 1.0 eq. $CuSO_4$ (10 eq. sodium ascorbate) at pH 5.93 (Region: Aromatic): delay constant #2 = 170 Hz *(filename: wcp4_44_TRIL23_3Py_Cu_titration_042723 [Spectrum 5]).*

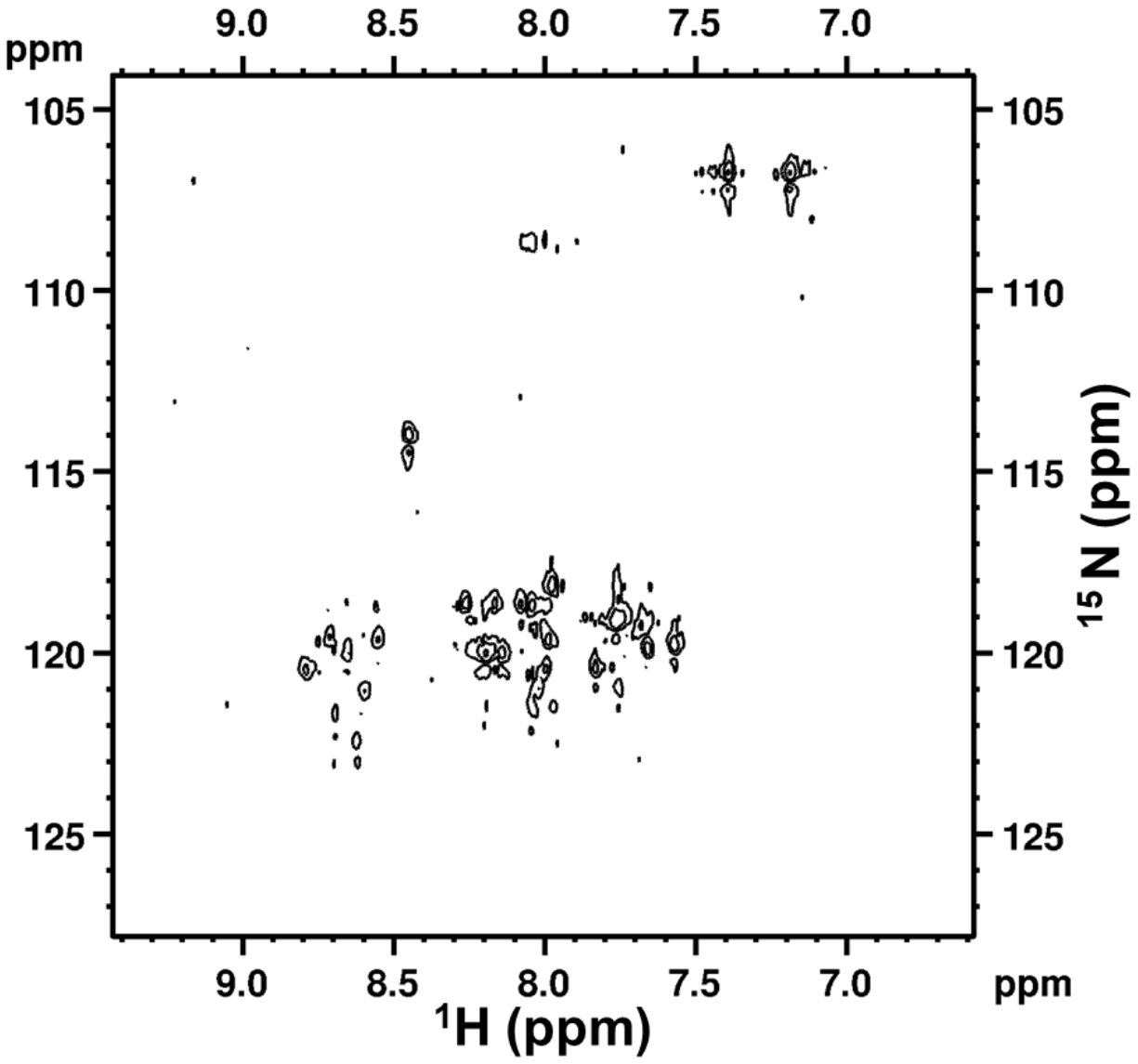


Figure A-30: ^{1}H-^{15}N NOESY of apo-TRI-3'Py at pH 5.88 (Region: Amide): mixing time=200 ms (*file name: wcp4_17_TRIL23_3Py_Cu_titration_031523 [Spectrum 6]).*

A.2 Chapter IV Nuclear Magnetic Resonance Data

Protein: GRW-3'Py

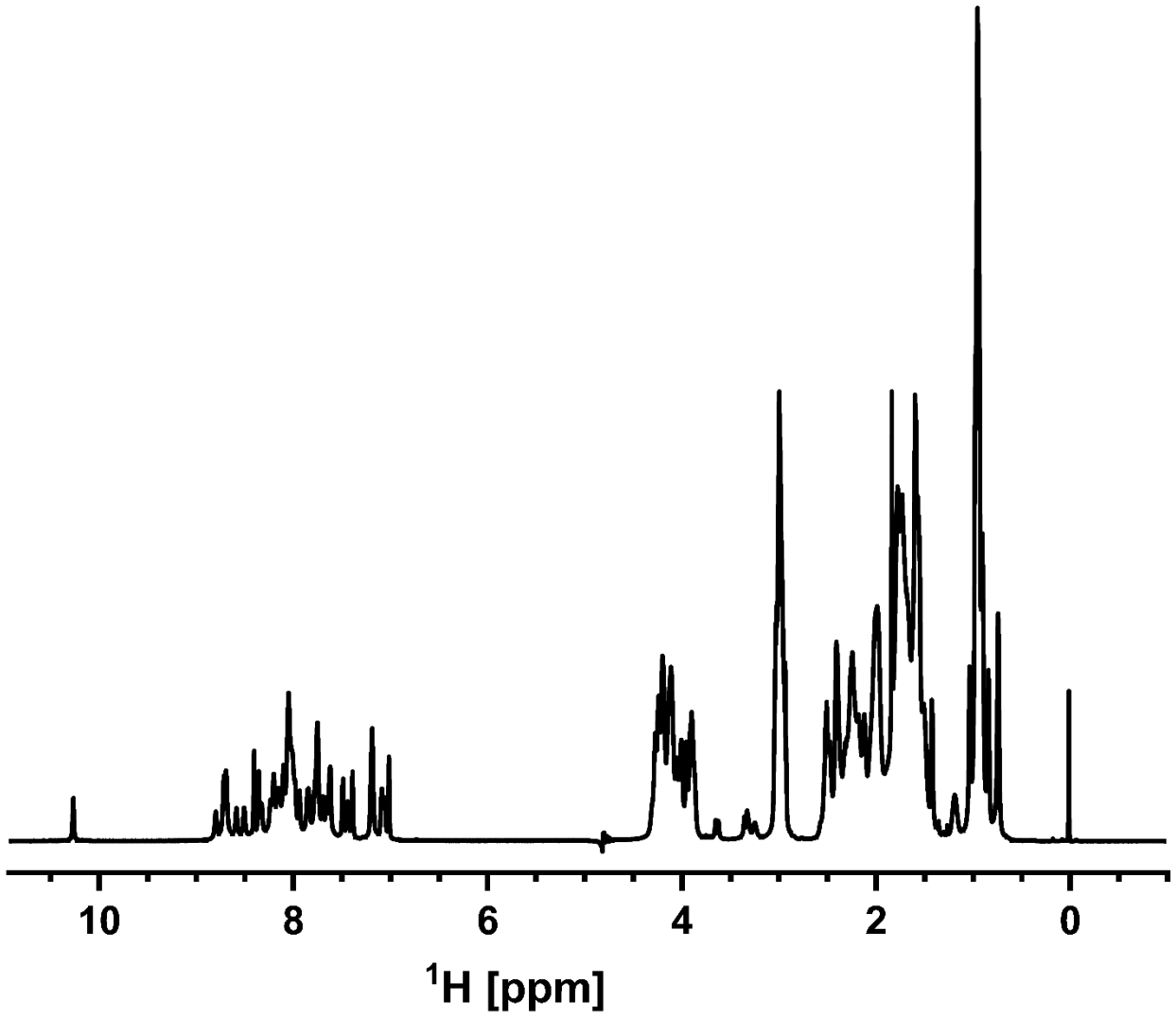


Figure A-31: ^{1}H-NMR of apo-GRW-3'Py at pH 5.97 (Region: Overview): (*file name:wcp4_121_GRWL30_3Py_090423 [Spectrum 1]).*

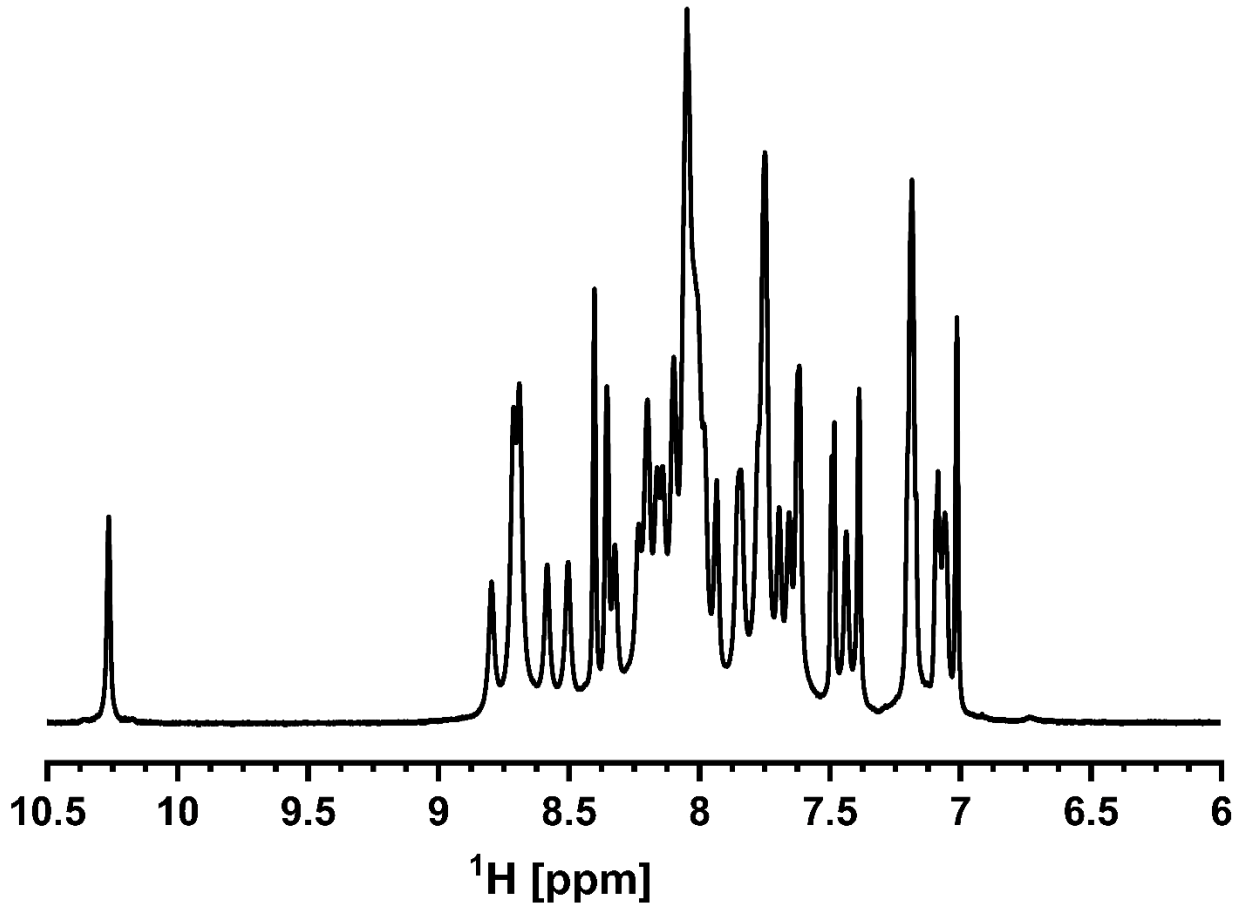


Figure A-32: ^{1}H-NMR of apo-GRW-3'Py at pH 5.97 (Region: Amide/Aromatic): (*file name:wcp4_121_GRWL30_3Py_090423 [Spectrum 1]).*

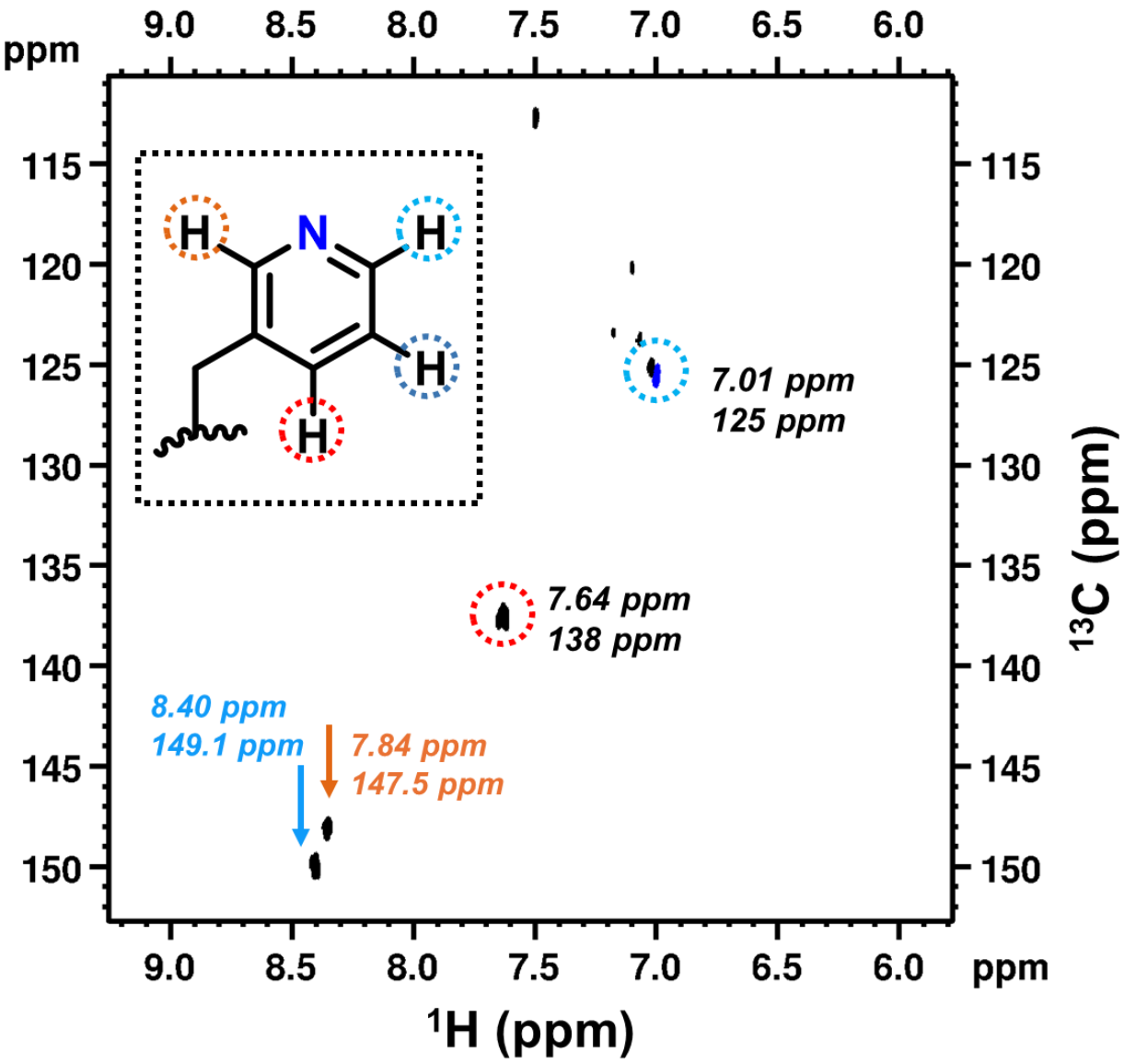


Figure A-33: ^{1}H-^{13}C HSQC NMR NMR of apo-GRW-3'Py at pH 5.97 (Region: Aromatic): *(file name: wcp4_121_GRWL30_3Py_090423 [Spectrum 2]).*

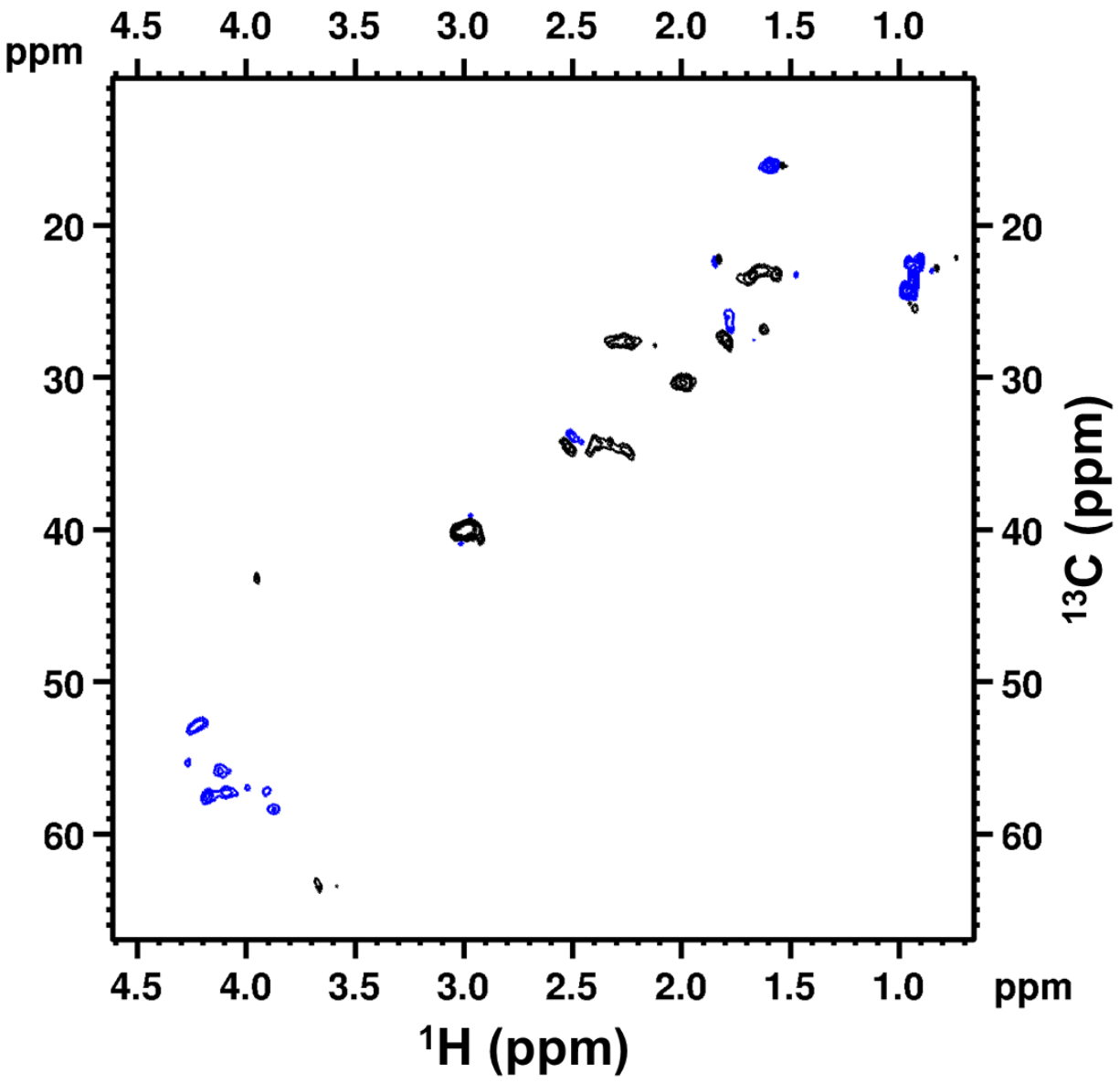


Figure A-34: ^{1}H-^{13}C HSQC of apo-GRW-3'Py at pH 5.97 (Region: Aromatic): delay constant #2 = 145 Hz *(file name: wcp4_121_GRWL30_3Py_090423 [Spectrum 7]).*

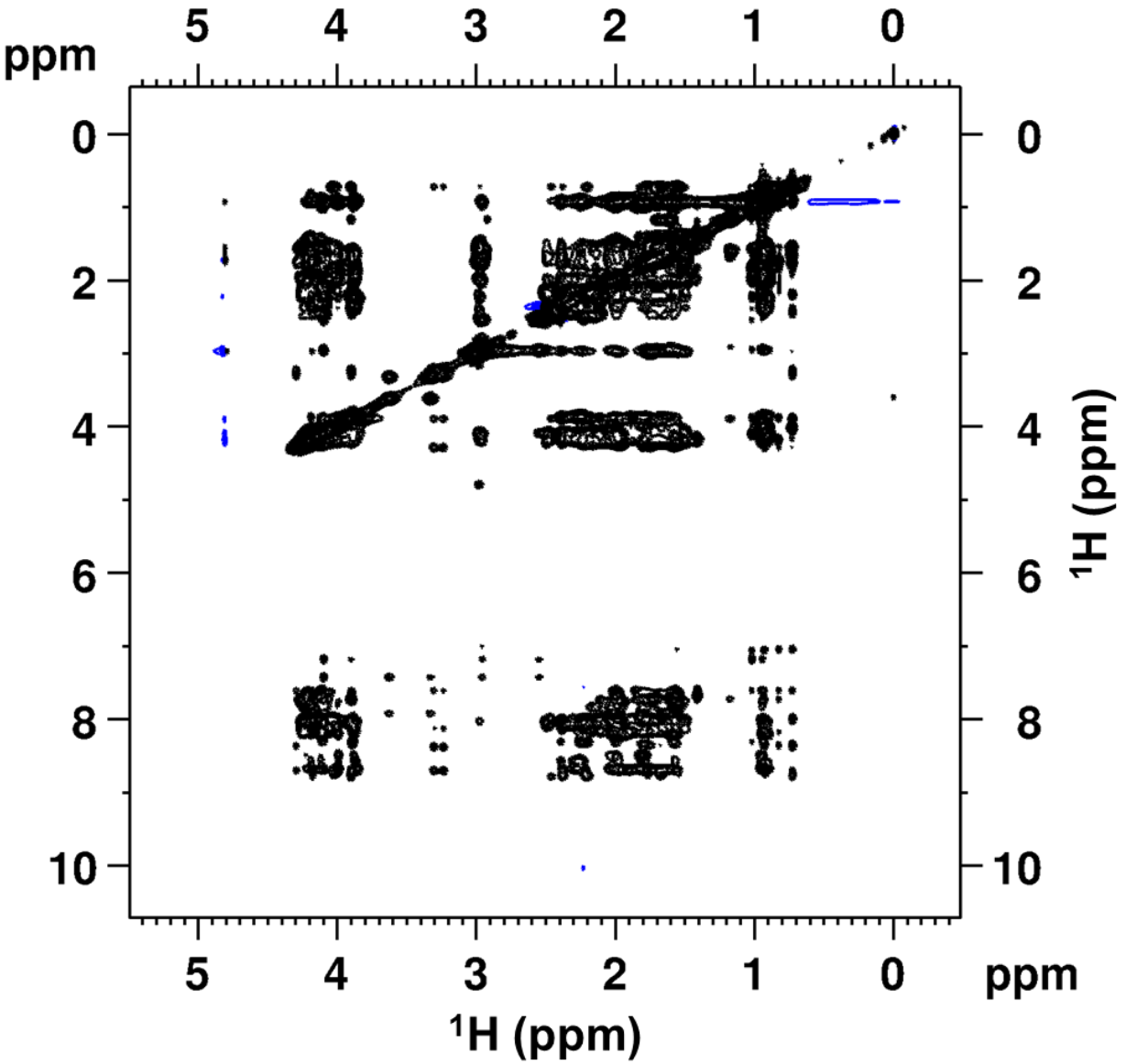


Figure A-35: ^{1}H-^{1}H NOESY of apo-GRW-3'Py at pH 5.90 (Region: Overview): mixing time=100 ms *(file name: wcp4_121_GRWL30_3Py_090423 [Spectrum 10]).*

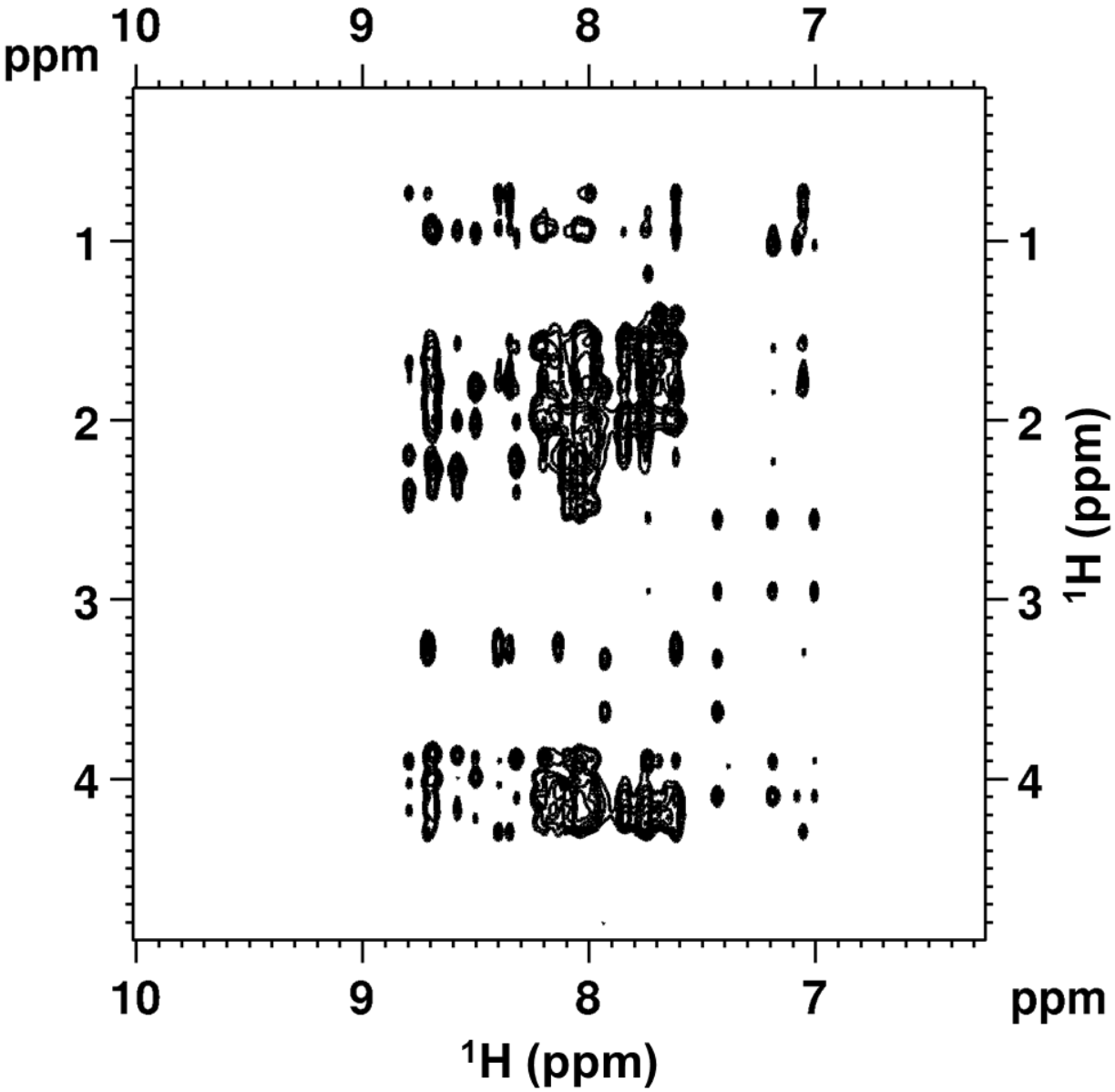


Figure A-36: ^{1}H-^{15}H NOESY of apo-GRW-3'Py at pH 5.90 (Region: Amide/Aliphatic): mixing time=100 ms *(file name: wcp4_121_GRWL30_3Py_090423 [Spectrum 10])*.

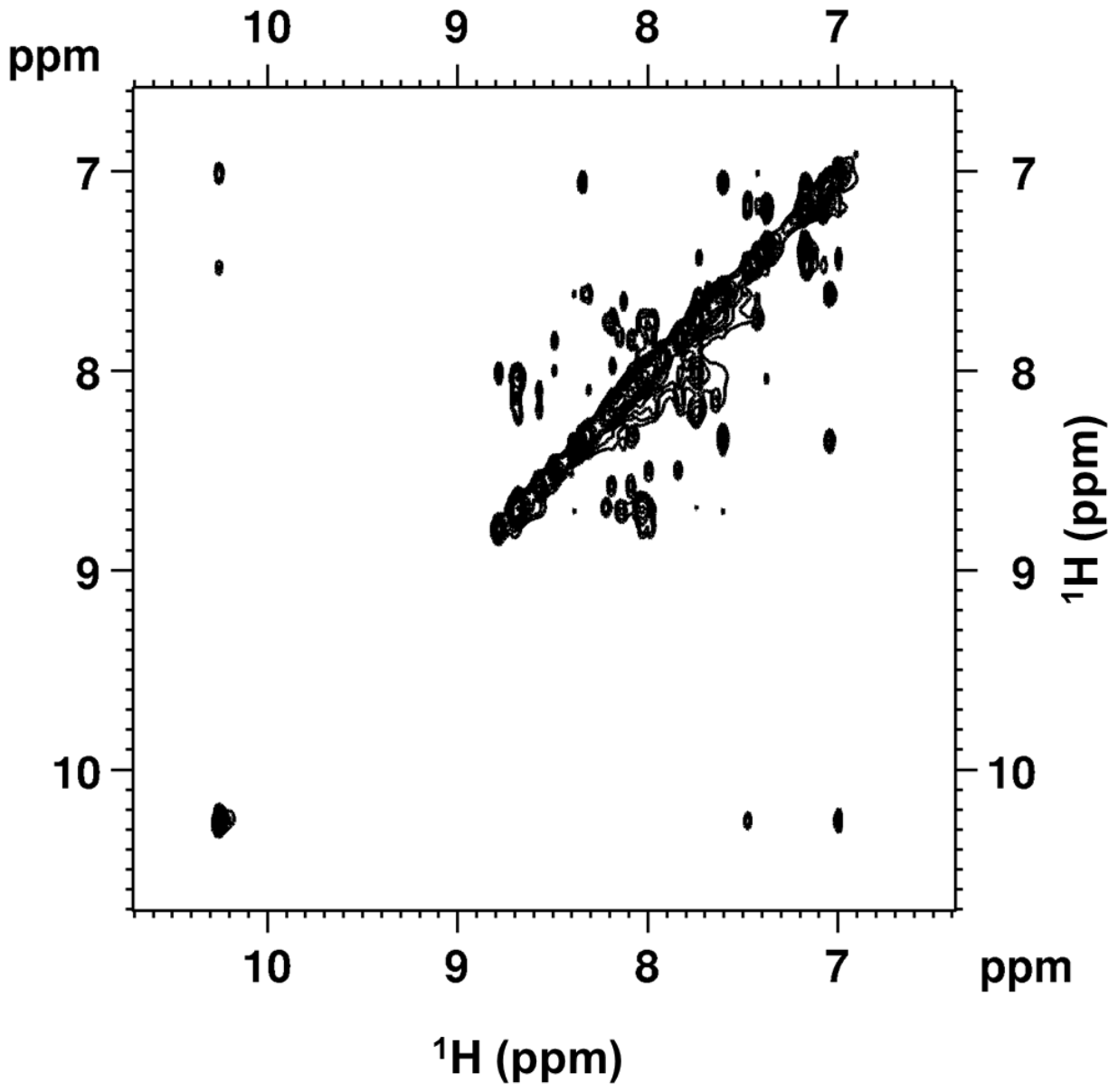


Figure A-37: ^{1}H-^{15}H NOESY of apo-GRW-3'Py at pH 5.90 (Region: Amide/Amide): mixing time=100 ms *(file name: wcp4_121_GRWL30_3Py_090423 [Spectrum 10]).*

Protein: GRW$_{stam27(AE3'Py)}$

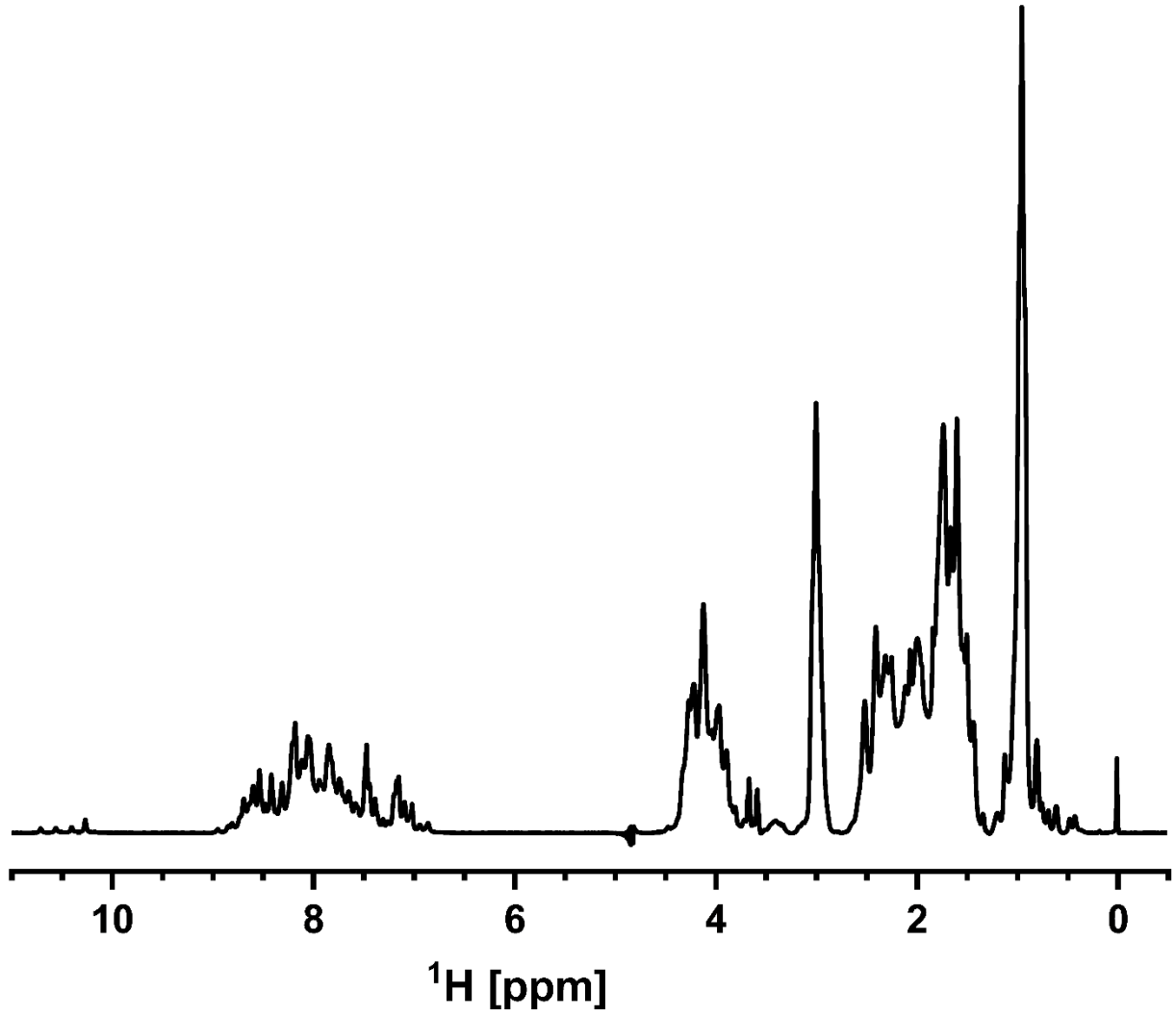


Figure A-38: ^{1}H-NMR of apo-GRW$_{stam27(AE3'Py)}$ at pH 5.97 (Region: Overview): *(file name: wcp4_122_GRWstamAE3Py_090523 [Spectrum 3]).*

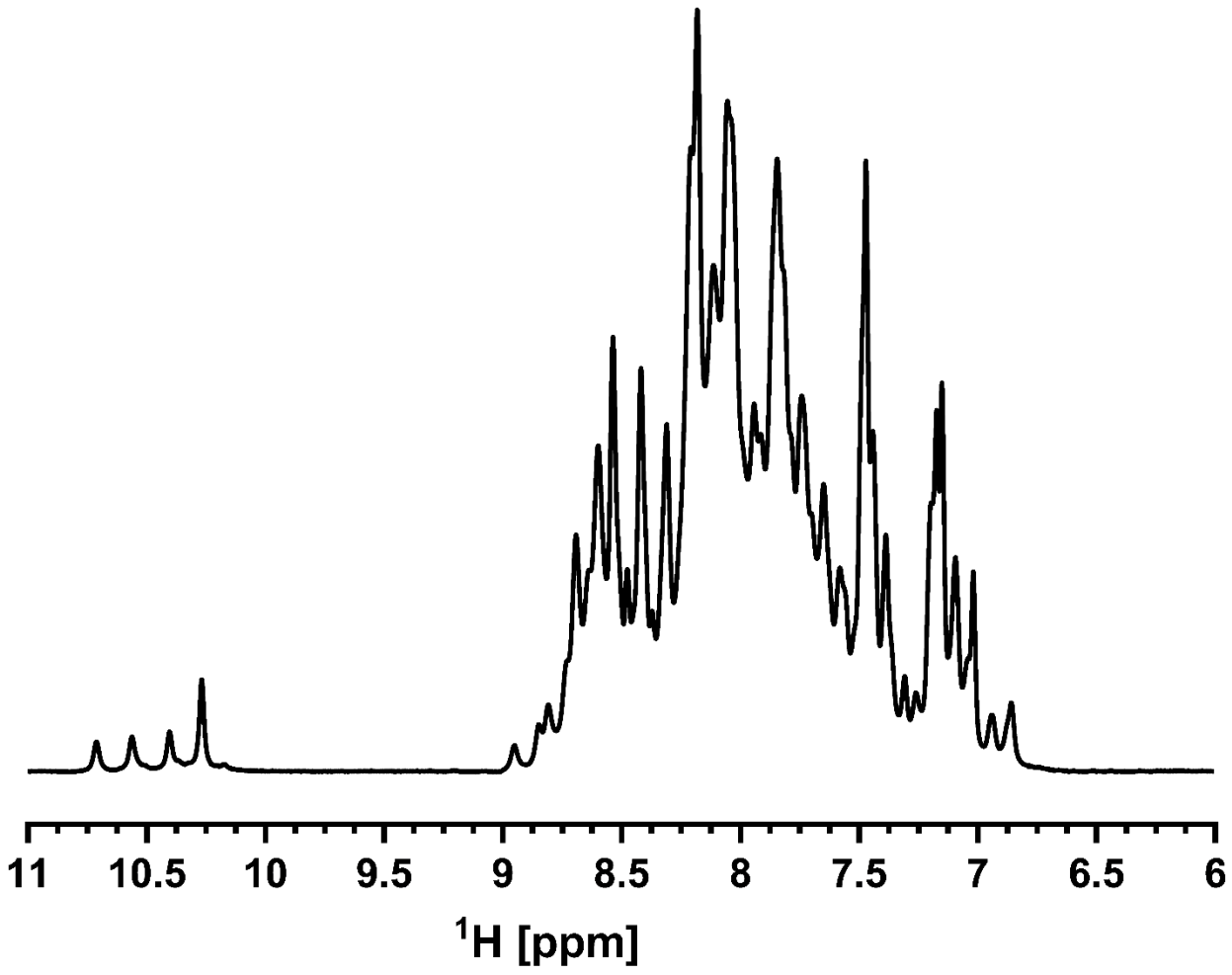


Figure A-39: ^{1}H- NMR of apo-GRW$_{stam27(AE3'Py)}$ at pH 5.97 (Region: Aromatic): delay constant #2 = 145 Hz *(file name: wcp4_122_GRWstamAE3Py_090523 [Spectrum 3]).*

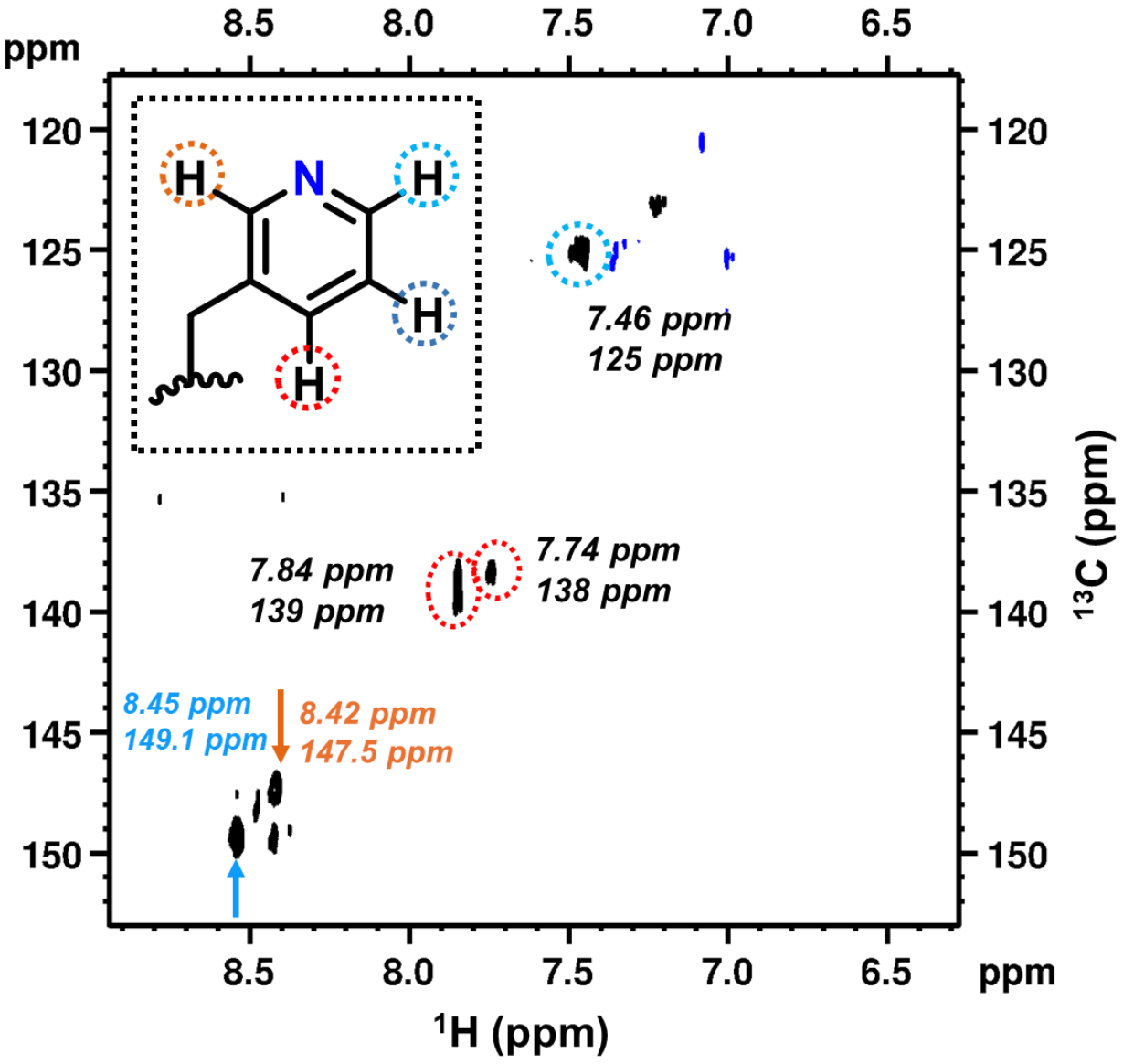


Figure A-40: ^{1}H-^{13}C HSQC NMR of apo-GRW$_{stam27(AE3'Py)}$ at pH 5.97 (Region: Aromatic): delay constant #2= 145 Hz *(file name: wcp4_122_GRWstamAE3Py_090523 [Spectrum 2]).*

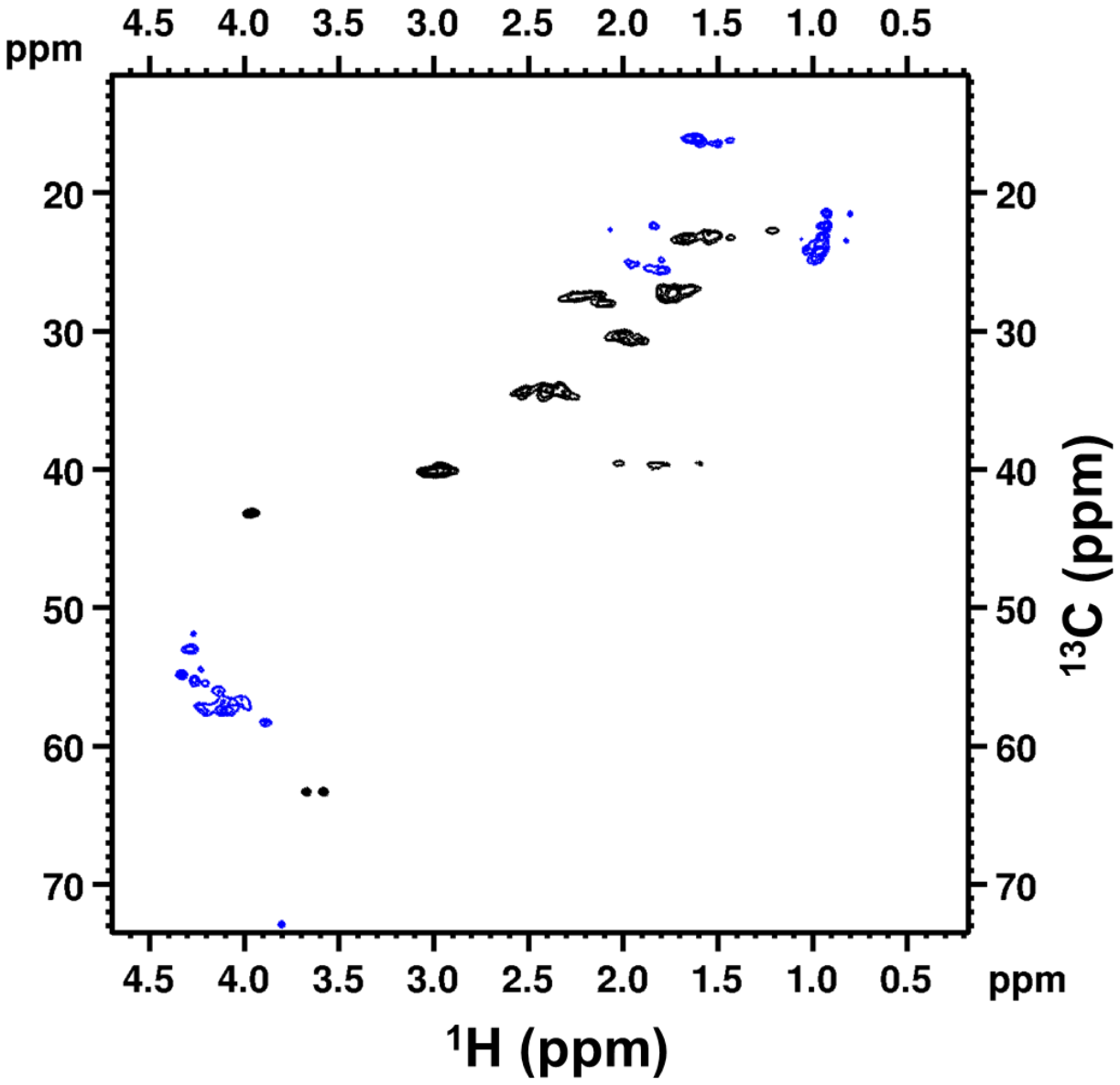


Figure A-41: ^{1}H-^{13}C HSQC NMR of apo-GRW$_{stam27(AE3'Py)}$ at pH 5.97 (Region: Aromatic): delay constant #2 = 145 Hz *(file name: wcp4_122_GRWstamAE3Py_090523 [Spectrum 6]).*

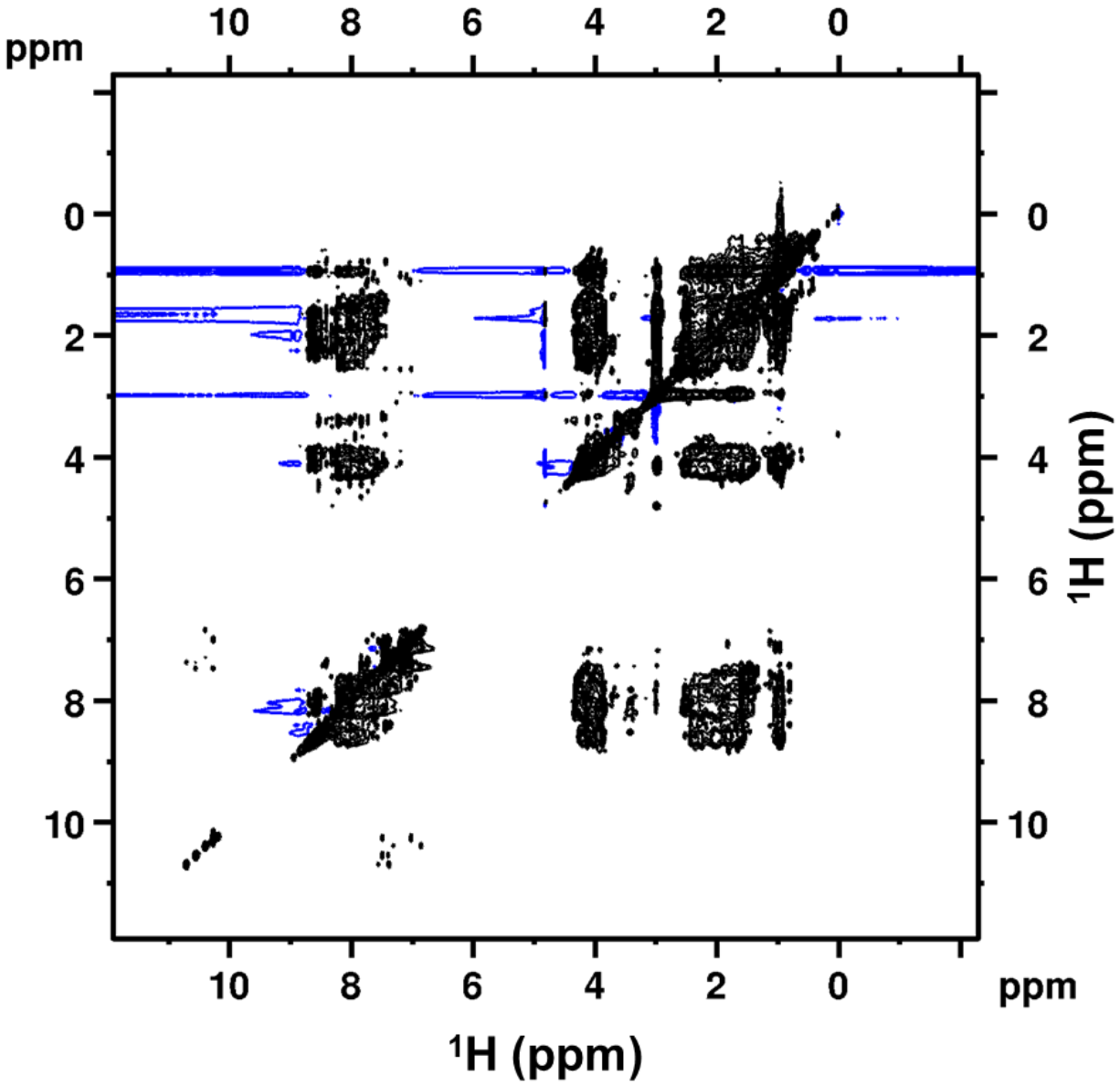


Figure A-42: ^{1}H-^{1}H NOESY of apo-GRW$_{stam27(AE3'Py)}$ at pH 5.97 (Region: Overview): mixing time=100 ms *(file name: wcp4_122_GRWstamAE3Py_090523 [Spectrum 12]).*

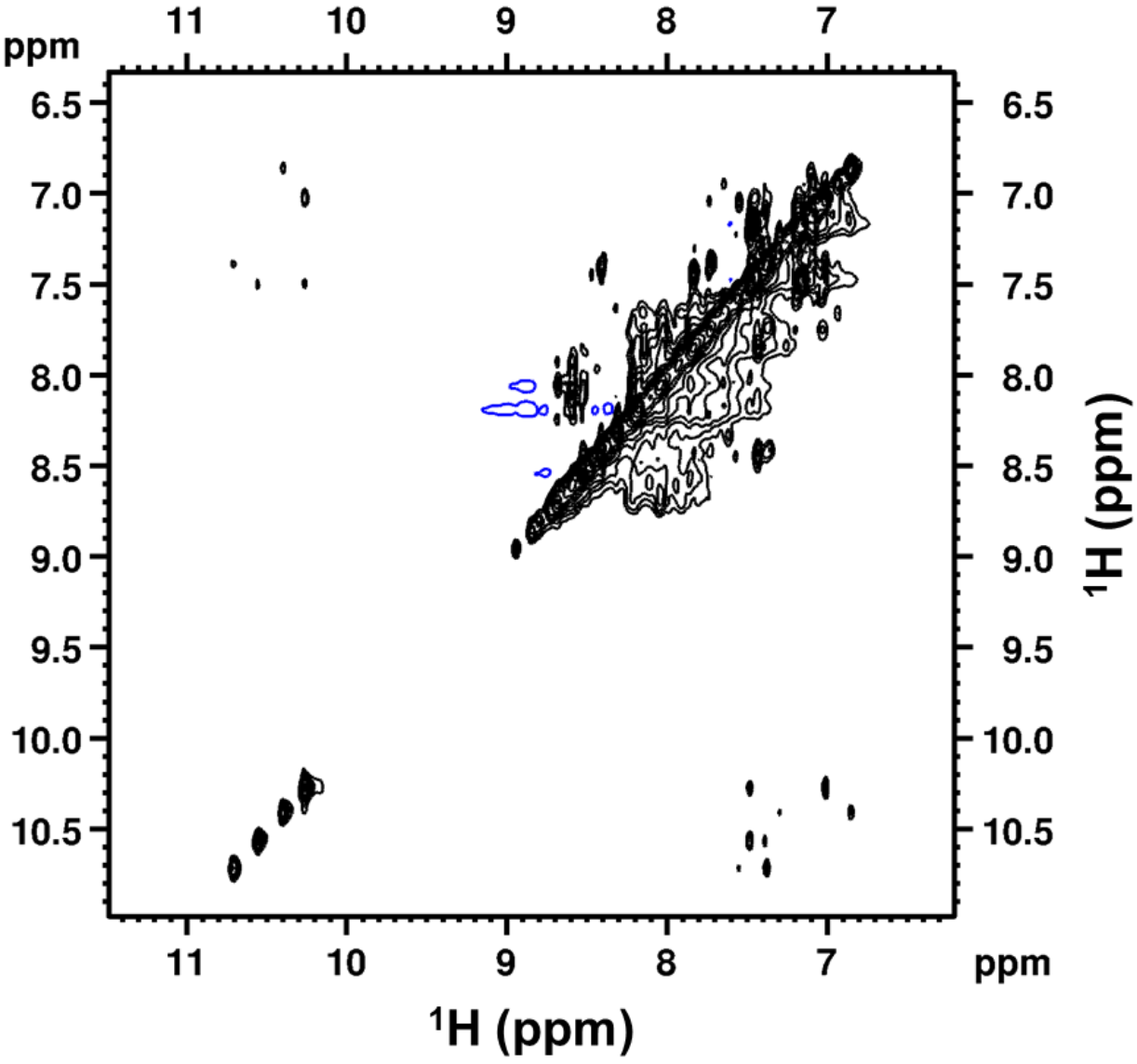


Figure A-43: ^{1}H-^{1}H NOESY of apo-GRW$_{stam27(AE3'Py)}$ at pH 5.97 (Region: Amide/Aromatic): mixing time=100 ms *(file name: wcp4_122_GRWstamAE3Py_090523 [Spectrum 12]).*

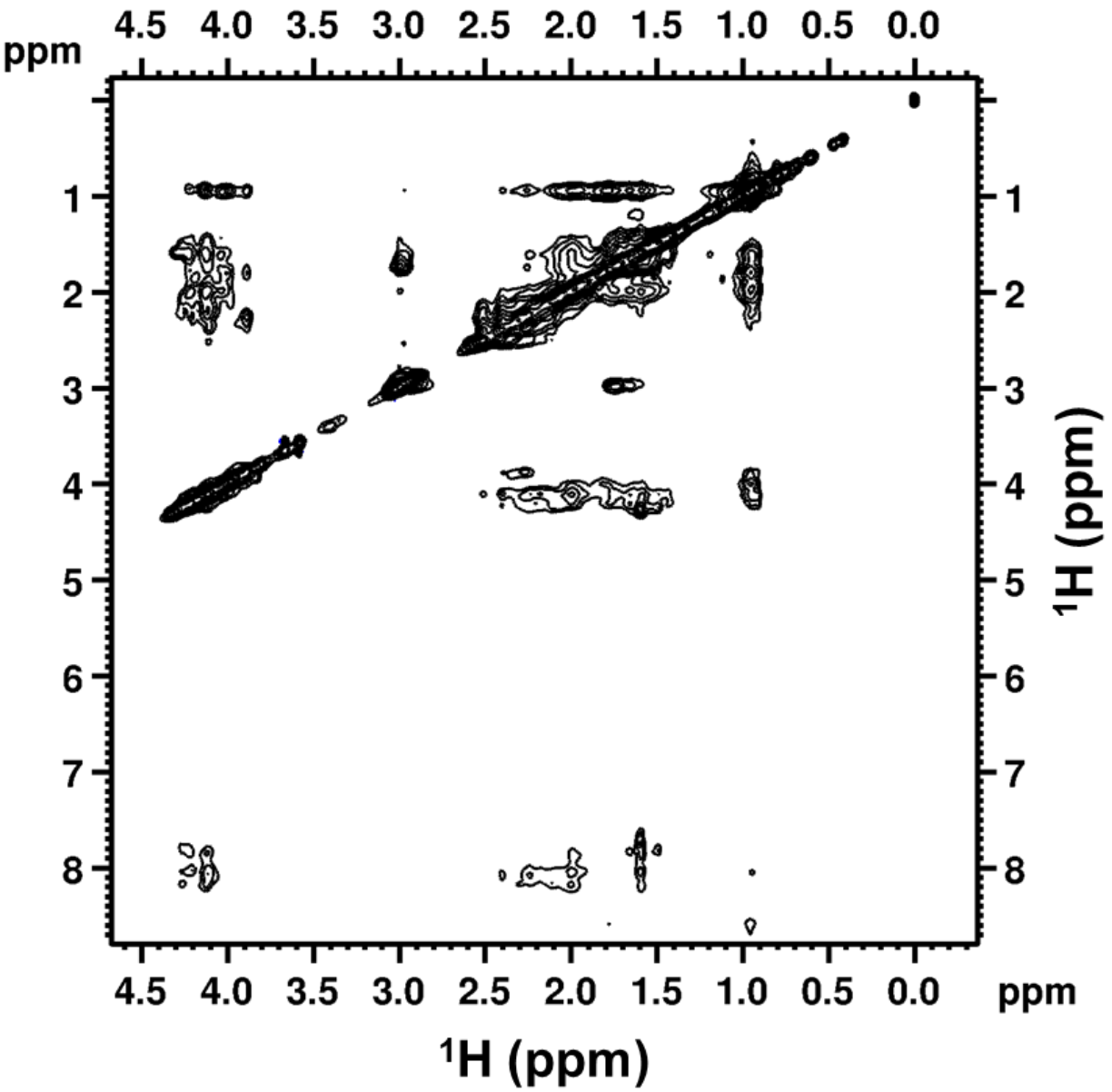


Figure A-44: ^{1}H-^{1}H NOESY of apo-GRW$_{stam27(AE3'Py)}$ at pH 5.97 (Region: Amide/Aliphatic): mixing time=100 ms *(file name: wcp4_122_GRWstamAE3Py_090523 [Spectrum 12]).*

Protein: GRW-4'Py

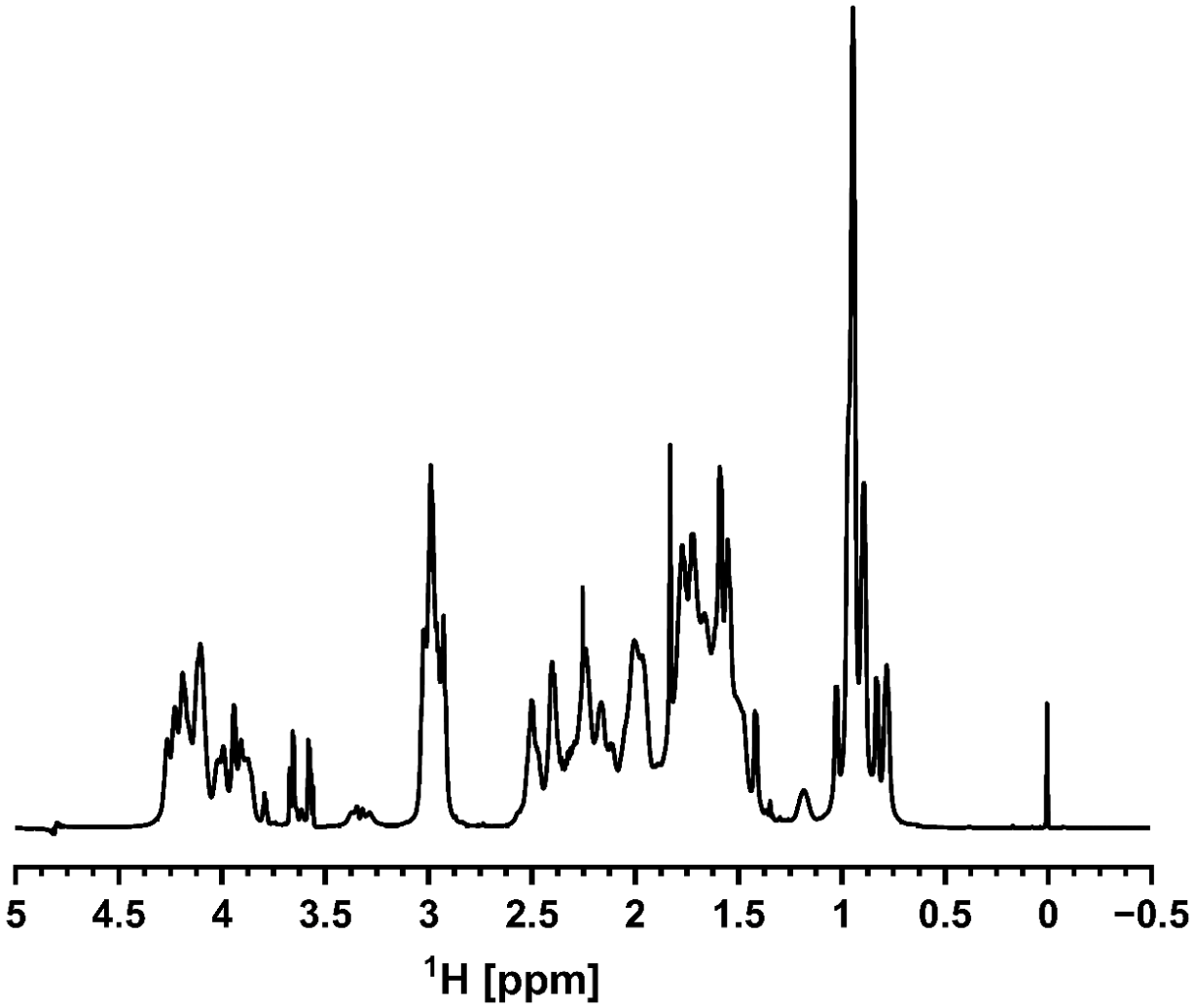


Figure A-45: ^{1}H-NMR of apo-GRW-4'Py at pH 5.90 (Region: Aliphatic): *(filename wcp4_123_GRWL30_4Py_091223 [Spectrum 1]).*

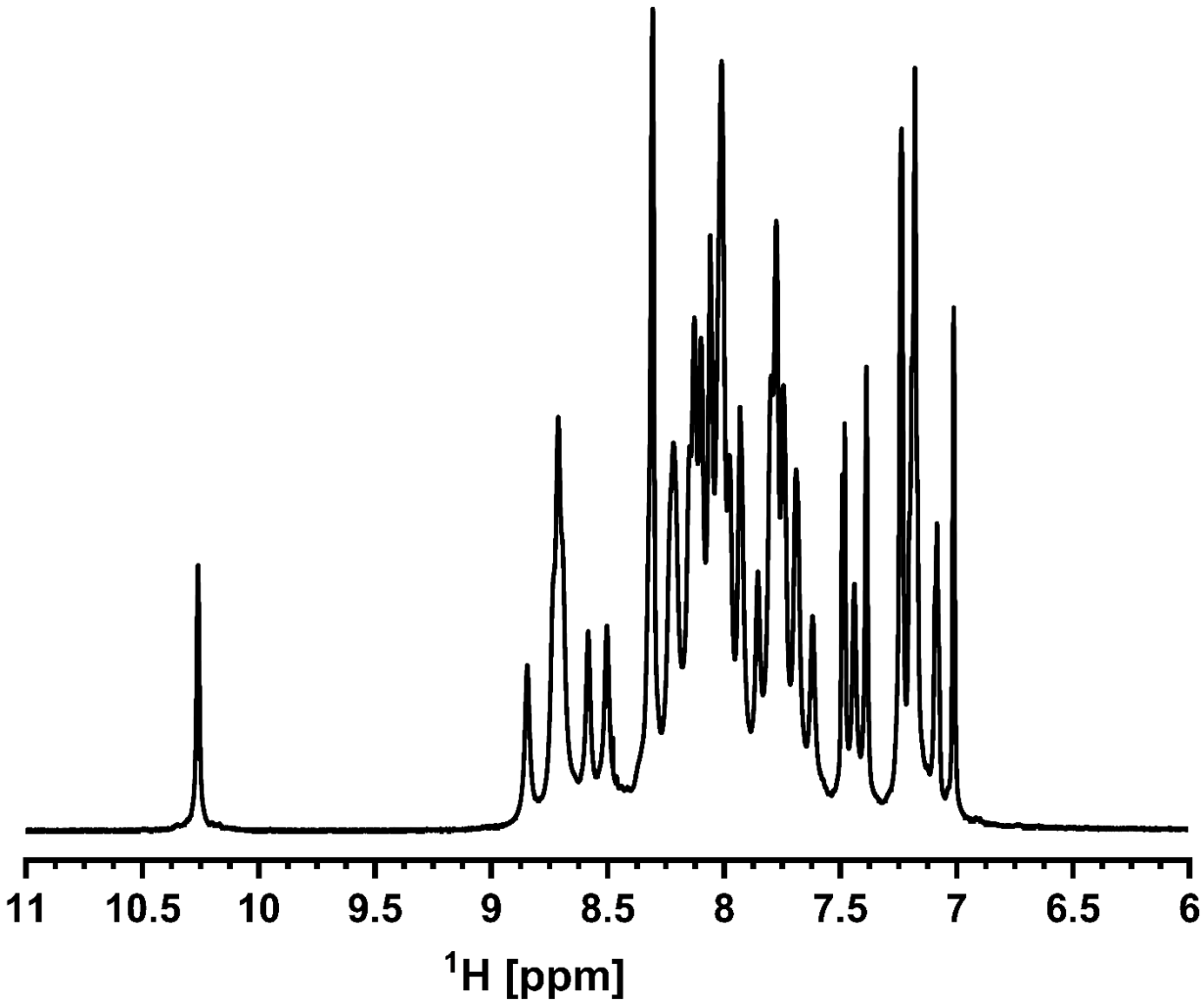


Figure A-46: ^{1}H- NMR of apo-GRW-4'Py at pH 5.90 (Region: Amide/Aromatic): *(filename wcp4_123_GRWL30_4Py_091223 [Spectrum 1]).*

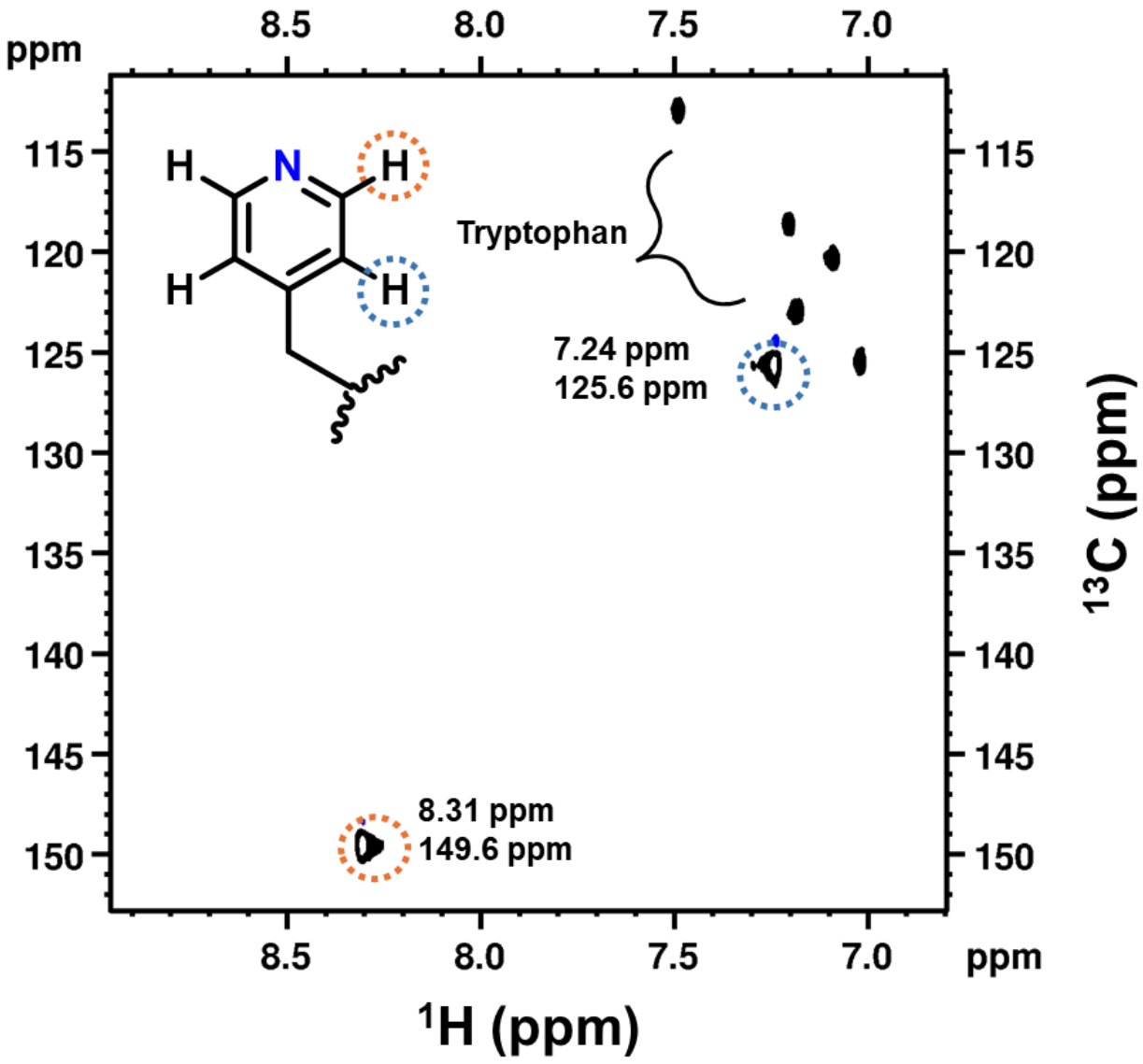


Figure A-47: ^{1}H-^{13}C HSQC of apo-GRW-4'Py at pH 5.90 (Region: Aromatic): delay constant #2 = 170 Hz *(file name: wcp4_123_GRWL30_4Py_091223 [Spectrum 4]).*

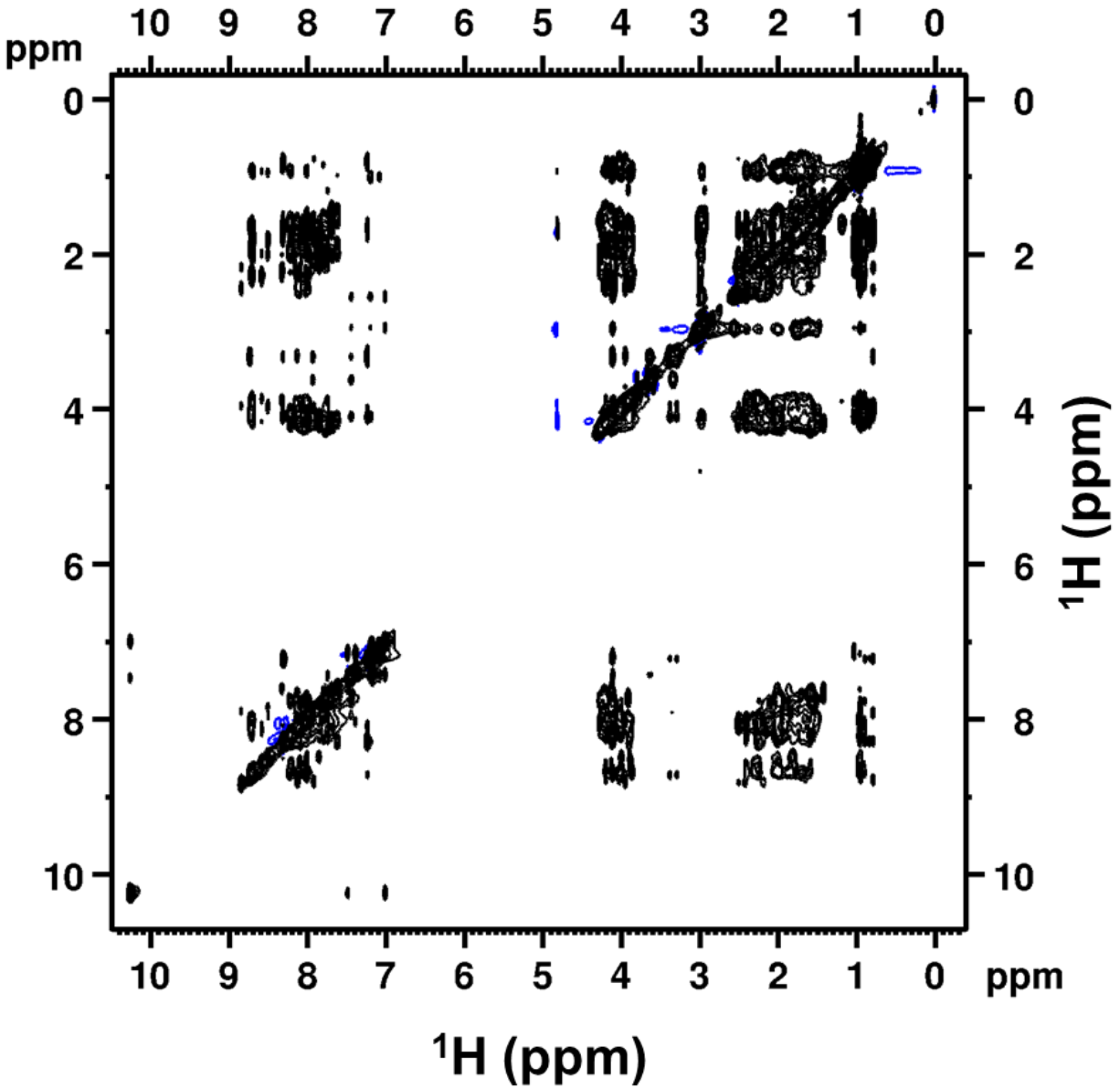


Figure A-48: ^{1}H-^{1}H NOESY of apo-GRW-4'Py at pH 5.90 (Region: Overview): mixing time=100 ms *(file name: wcp4_123_GRWL30_4Py_091223 [Spectrum 2]).*

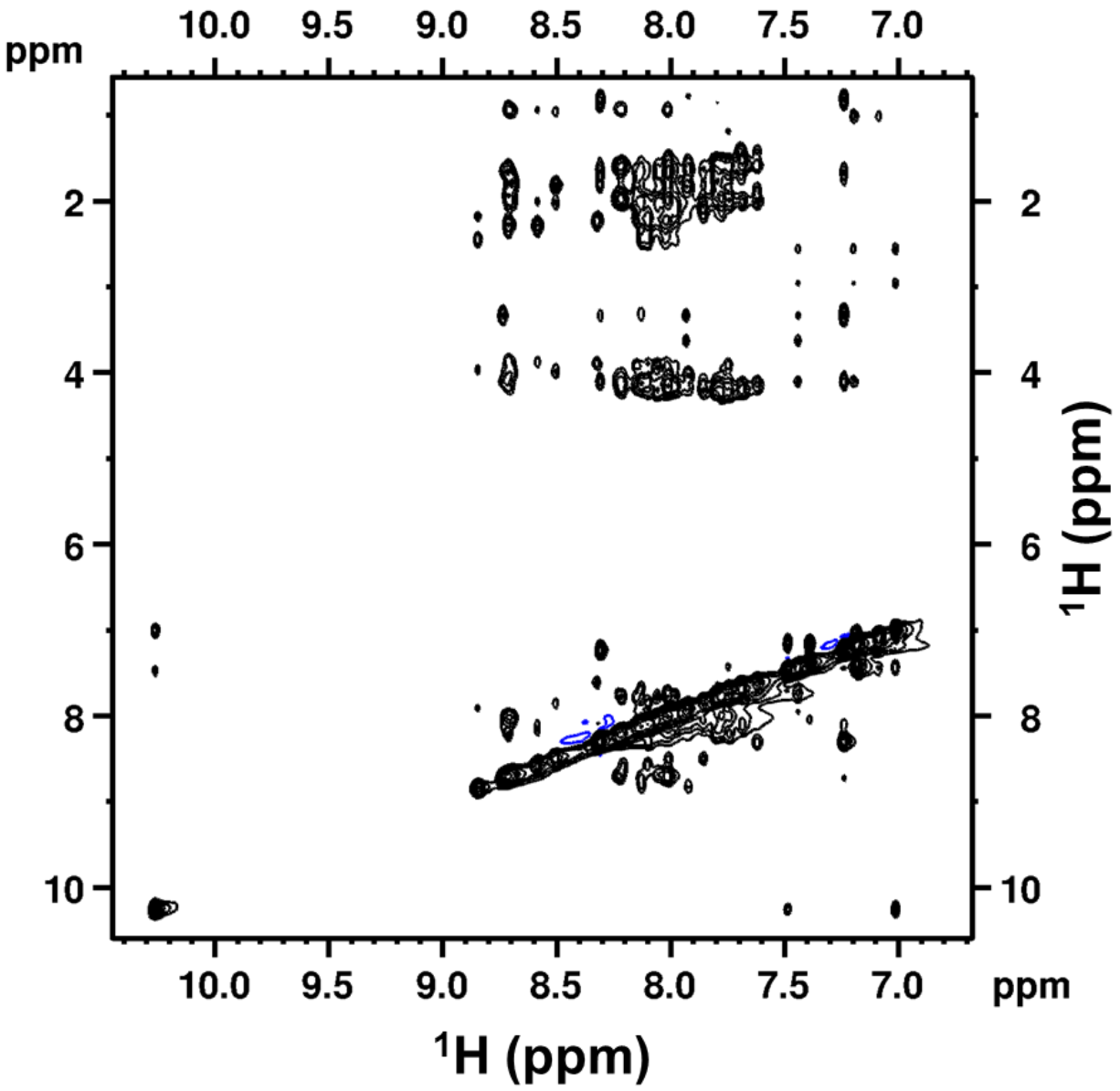


Figure A-49: ^{1}H-^{1}H NOESY of apo-GRW-4'Py at pH 5.90 (Region: Amide/Aliphatic): mixing time=100 ms *(file name: wcp4_123_GRWL30_4Py_091223 [Spectra 2]).*

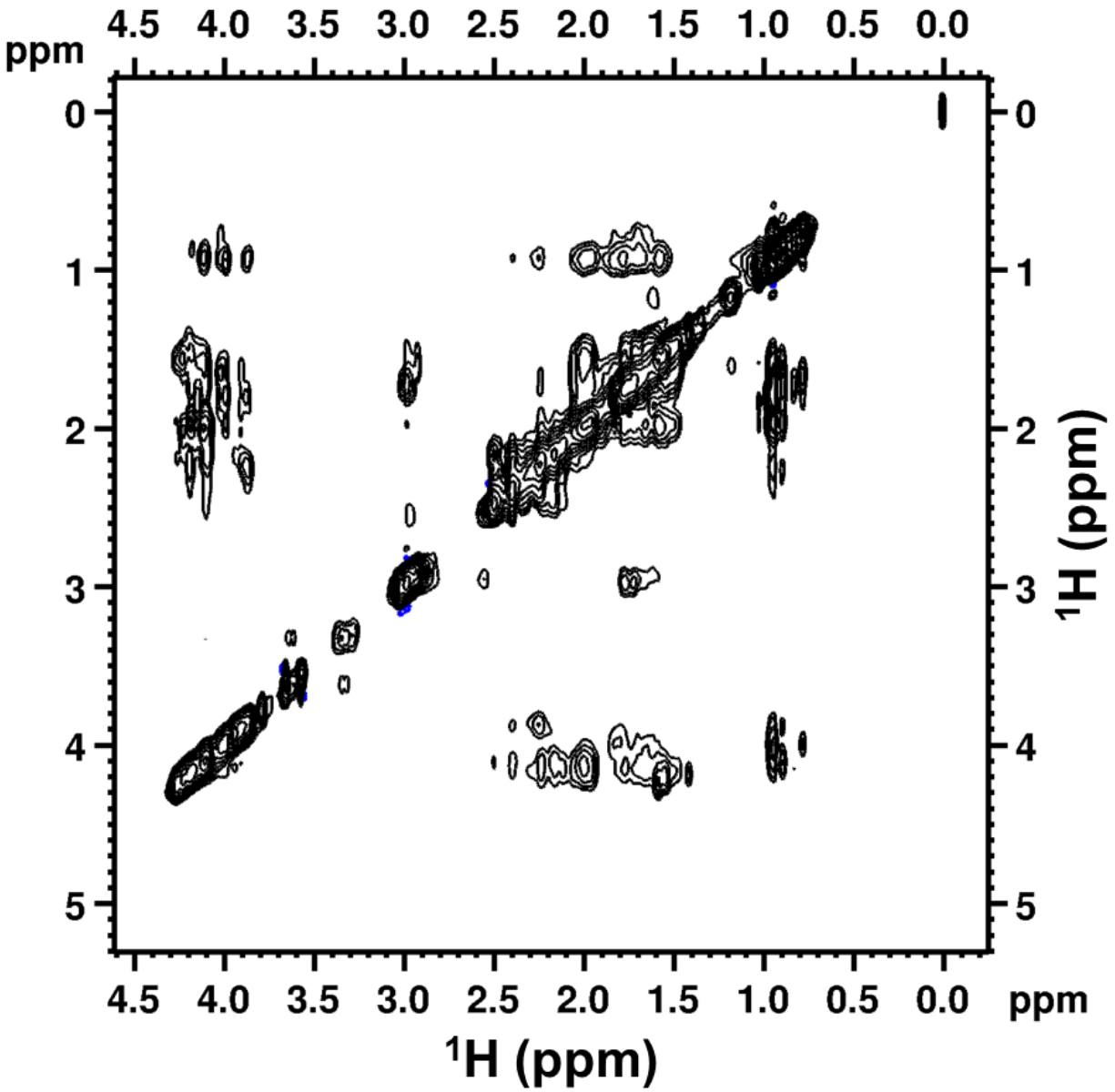


Figure A-50: ^{1}H-^{1}H NOESY of apo-GRW-4'Py at pH 5.90 (Region: Aliphatic): mixing time=100 ms *(file name: wcp4_123_GRWL30_4Py_091223 [Spectra 2]).*

Protein: GRW$_{stam27(AEL)}$L33-4'Py

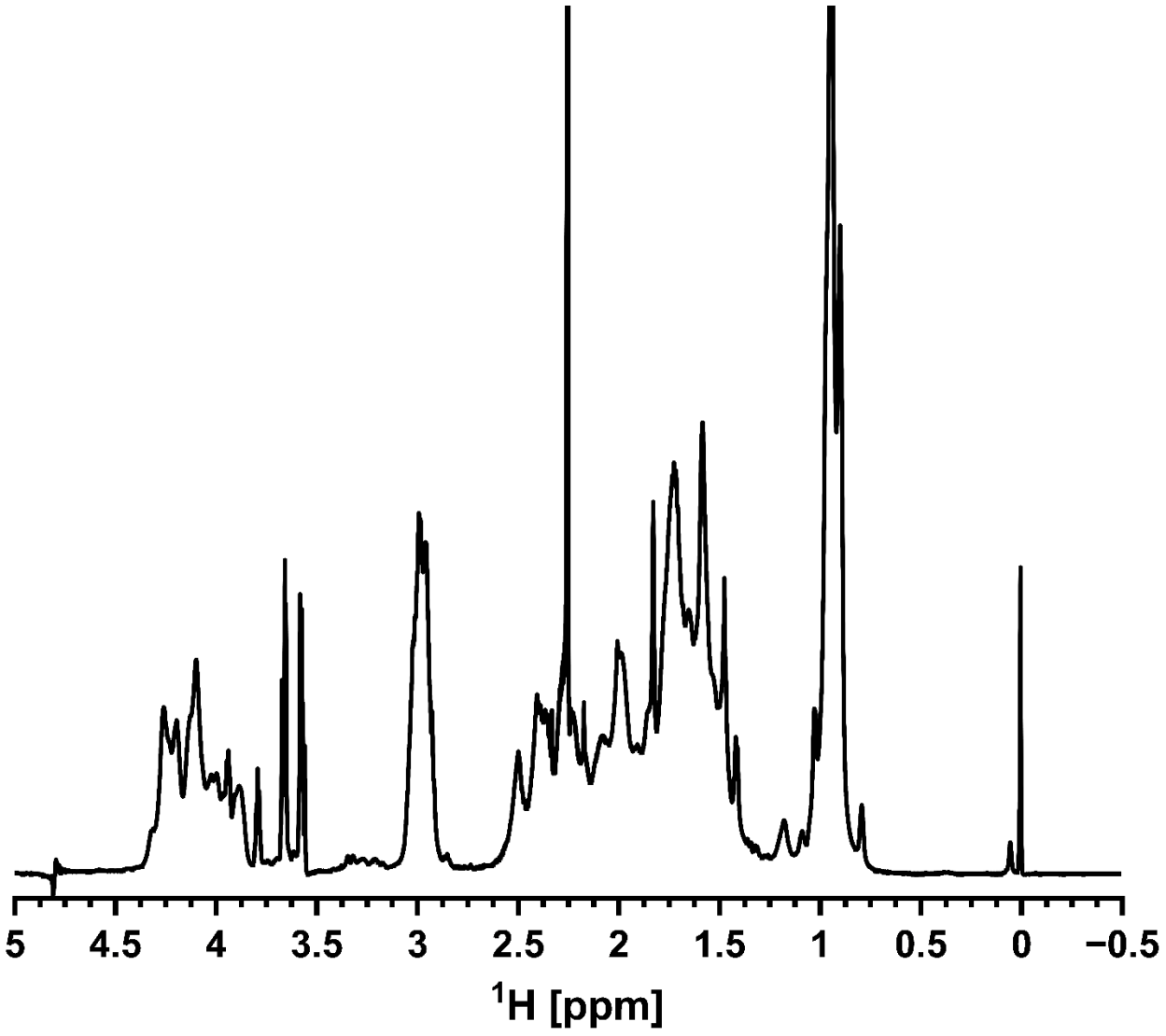


Figure A-51: ^{1}H-NMR of apo-GRW$_{stam27(AEL)}$L33-4'Py at pH 5.97 (Region: Aliphatic): *(file name: wcp4_123_GRWstamAEL27L33_4Py_091023 [Spectrum 1]).*

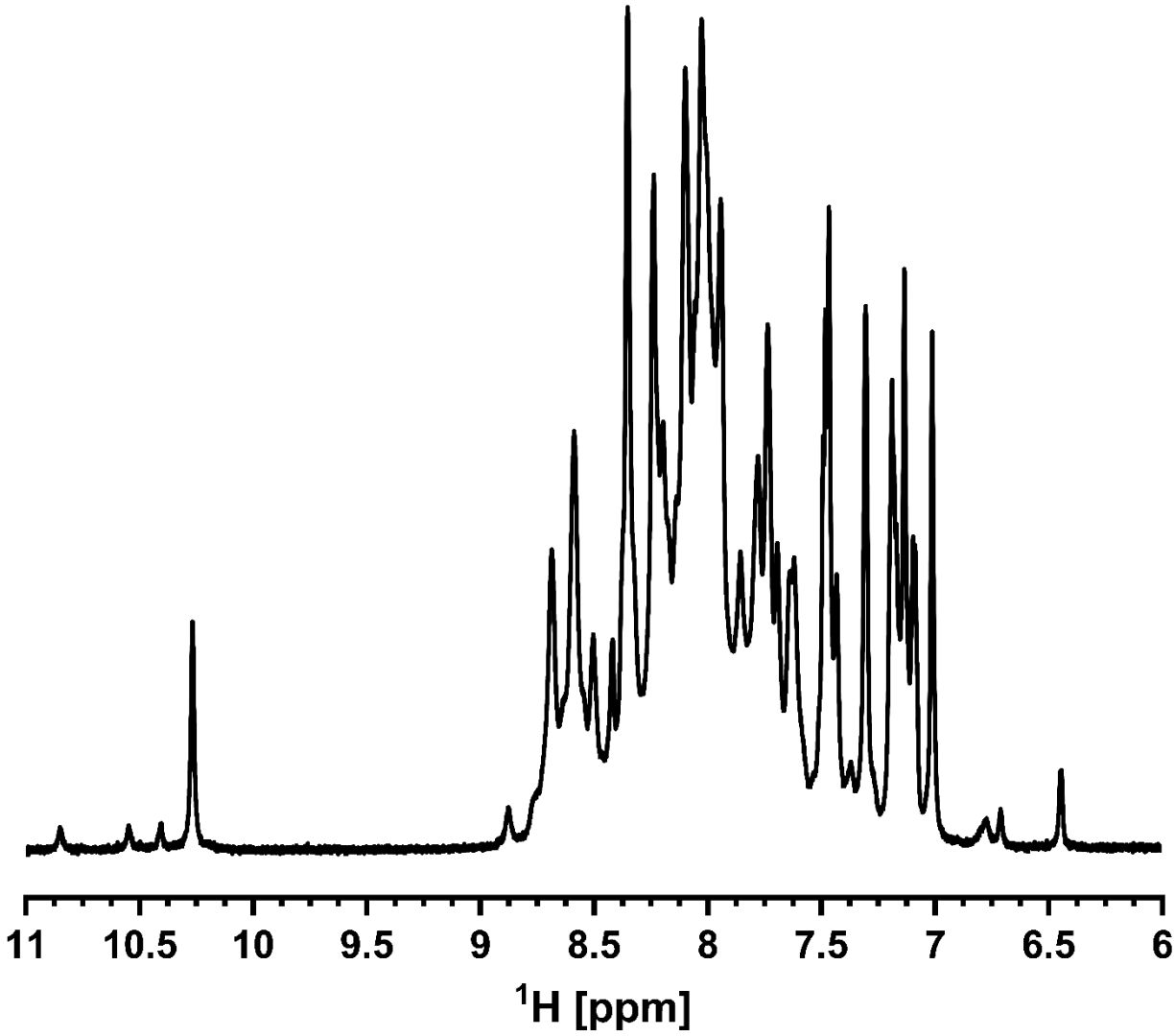


Figure A-52: ^{1}H-NMR of apo-GRW$_{stam27(AEL)}$L33-4'Py at pH 5.97 (Region: Aliphatic): *(file name:wcp4_123_GRWstamAEL27L33_4Py_091023 [Spectrum 1]).*

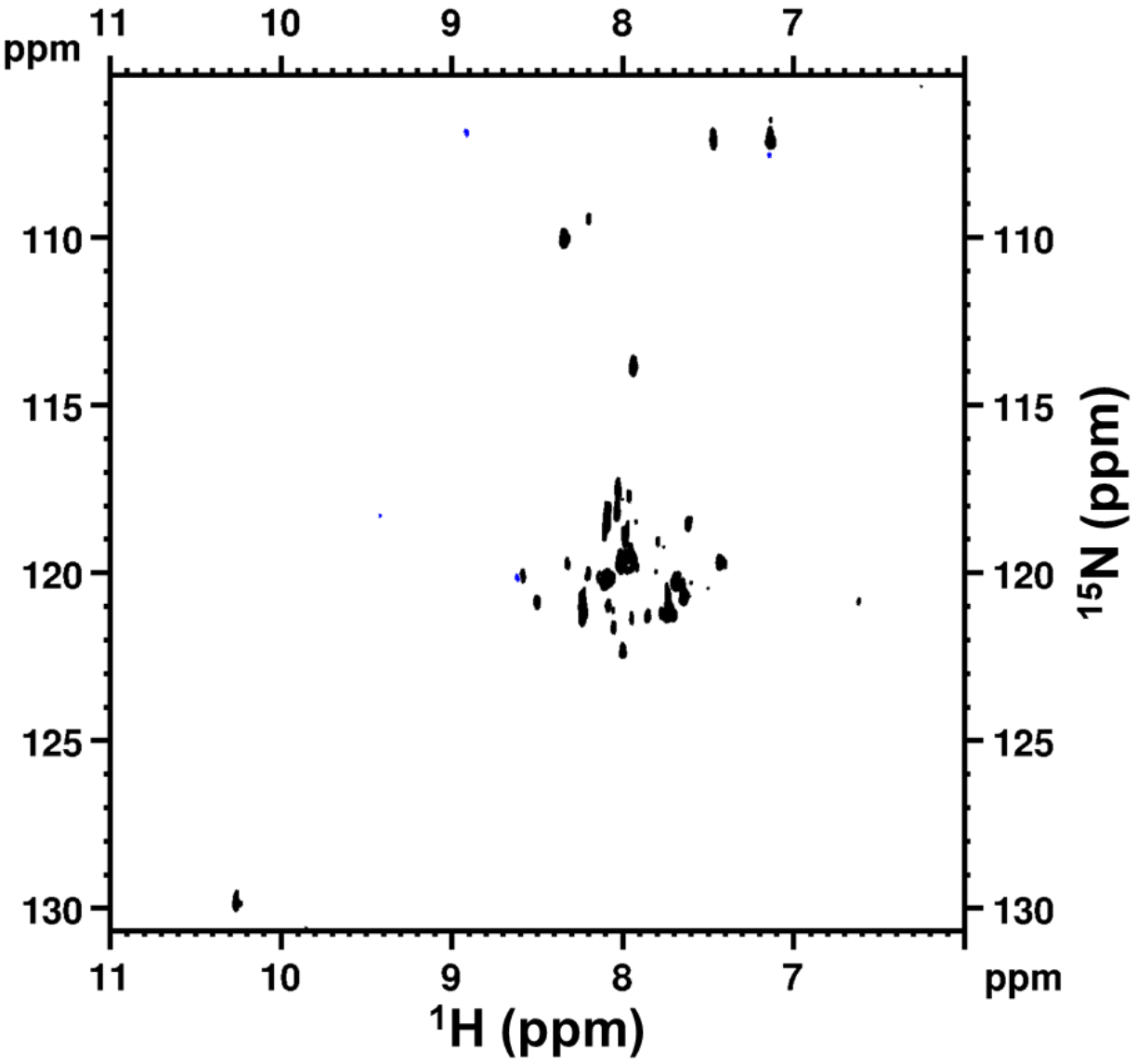


Figure A-53: ^{1}H-^{15}N NOESY of apo-GRW$_{stam27(AEL)}$L33-4'Py at pH 5.97 (Region: Overview): mixing time=100 ms *(file name: wcp4_123_GRWstamAEL27L33_4Py_091023 [Spectrum 6]).*

Protein: GRW$_{stam27(AEA)}$L33-4'Py

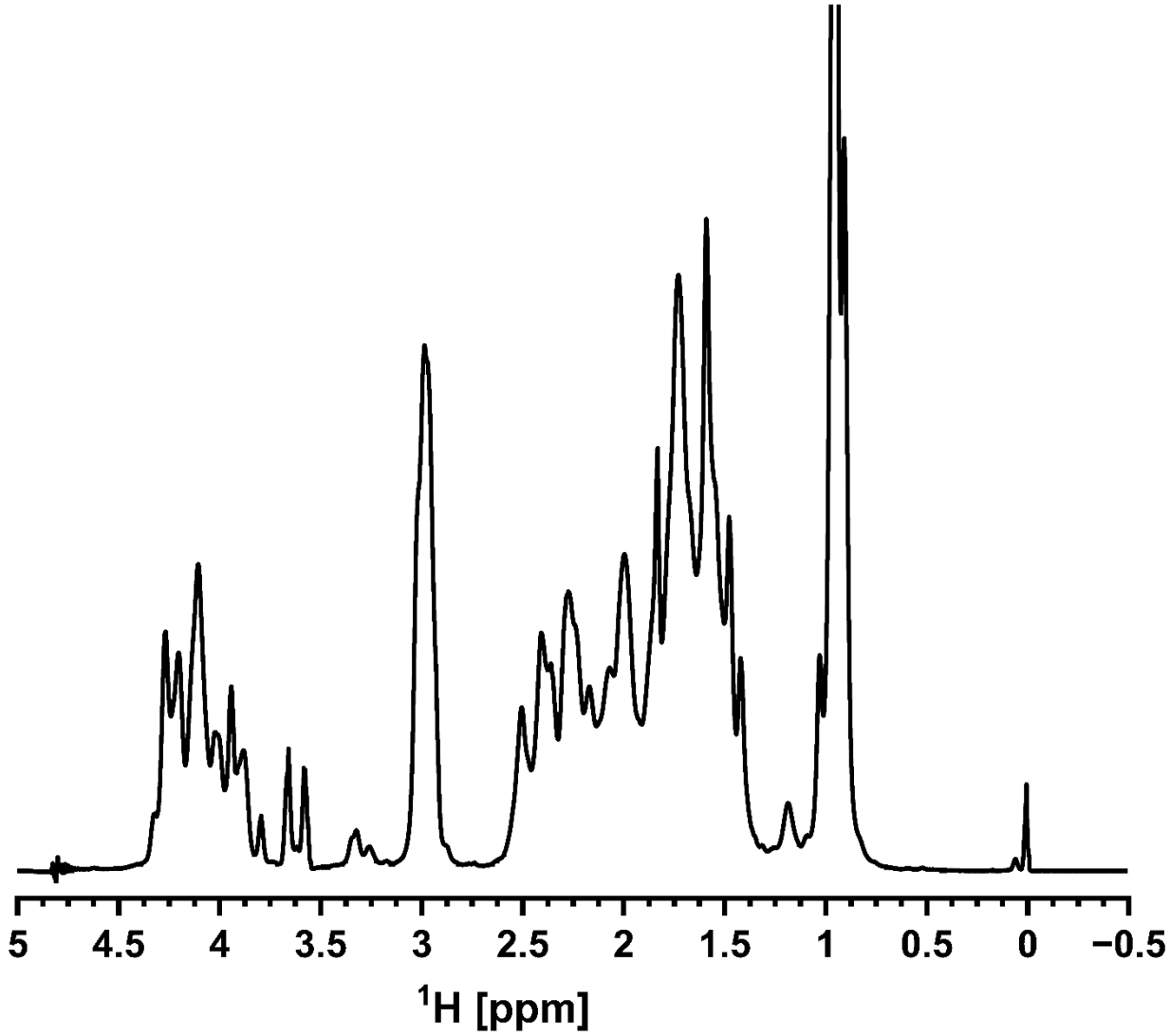


Figure A-54: ^{1}H-NMR of apo-GRW$_{stam27(AEA)}$L33-4'Py at pH 5.87 (Region: Aliphatic): *(file name: wcp4_123_GRWstamAEAL33_4Py_090823 [Spectrum 1]).*

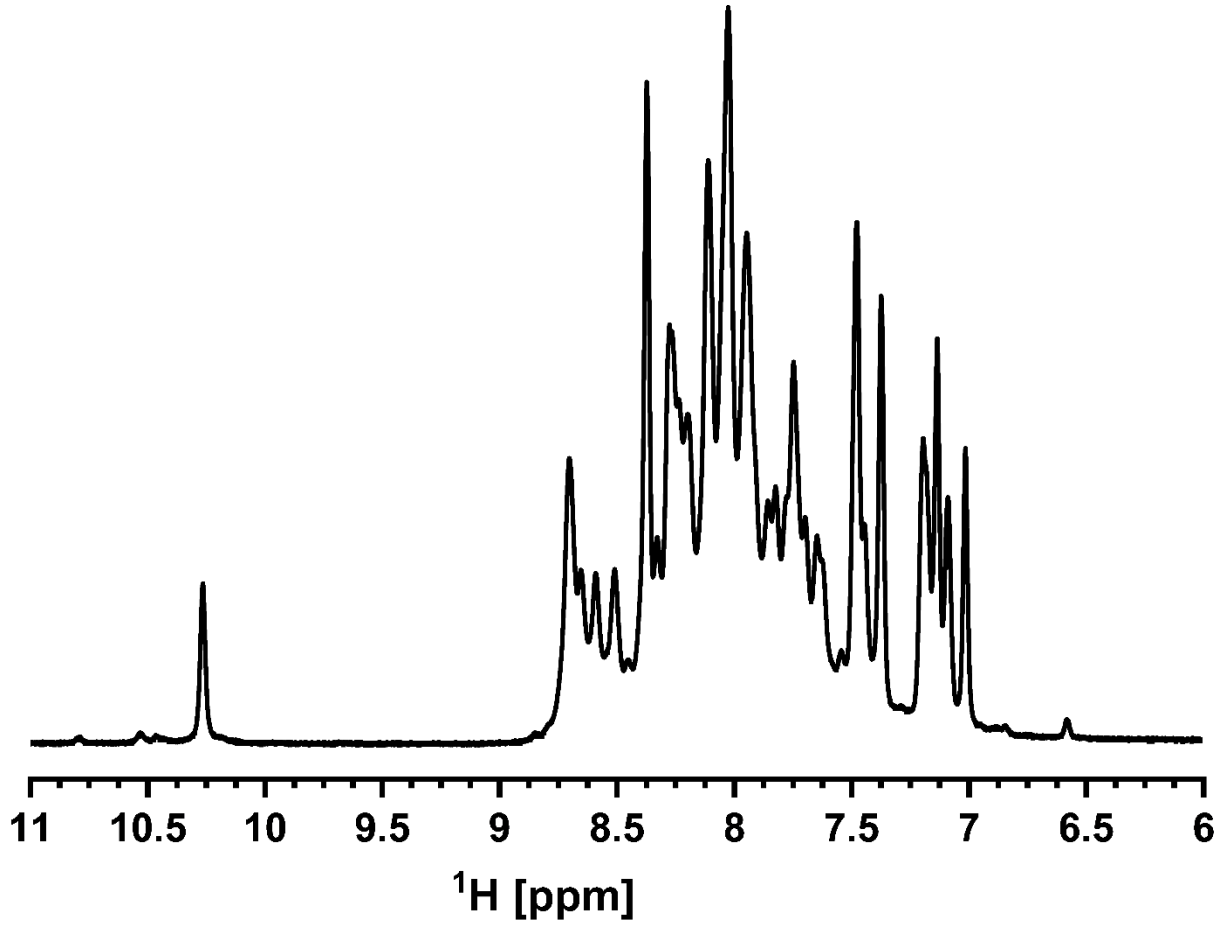


Figure A-55: ^{1}H- NMR of apo-GRW$_{stam27(AEA)}$L33-4'Py at pH 5.87 (Region: Amide/Aromatic): *(file name: wcp4_123_GRWstamAEAL33_4Py_090823 [Spectrum 1]).*

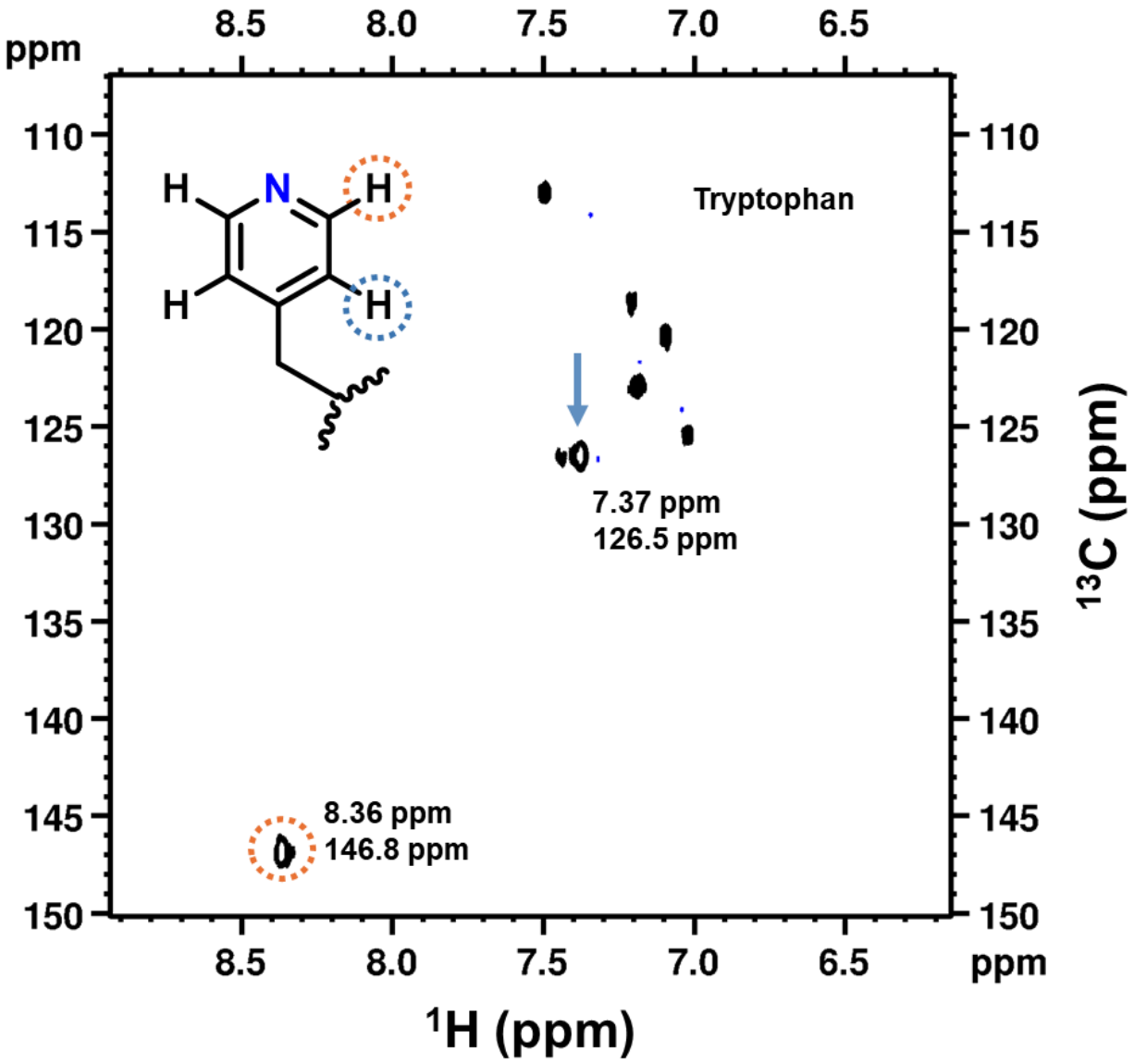


Figure A-56: ^{1}H-^{13}C HSQC NMR of apo-GRW$_{stam27(AEA)}$L33-4'Py at pH 5.87 (Region: Aromatic): delay constant #2 = 170 Hz *(file name: wcp4_123_GRWstamAEAL33_4Py_090823 [Spectrum 2]).*

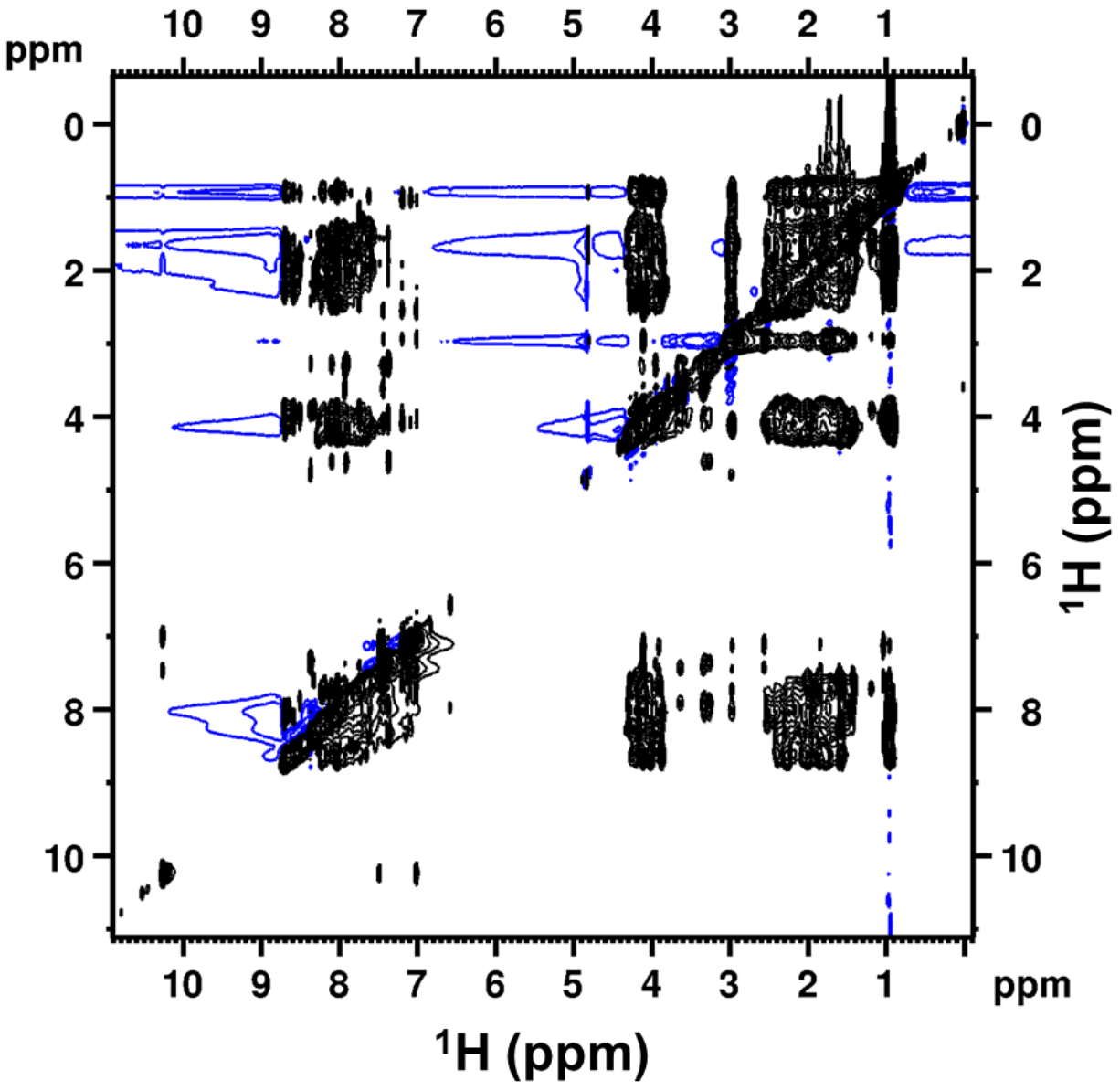


Figure A-57: ^{1}H-^{1}H NOESY of apo-GRW$_{stam27(AEA)}$L33-4'Py at pH 5.87 (Region: Overview): mixing time=100 ms *(file name: wcp4_123_GRWstamAEAL33_4Py_090823 [Spectrum 6]).*

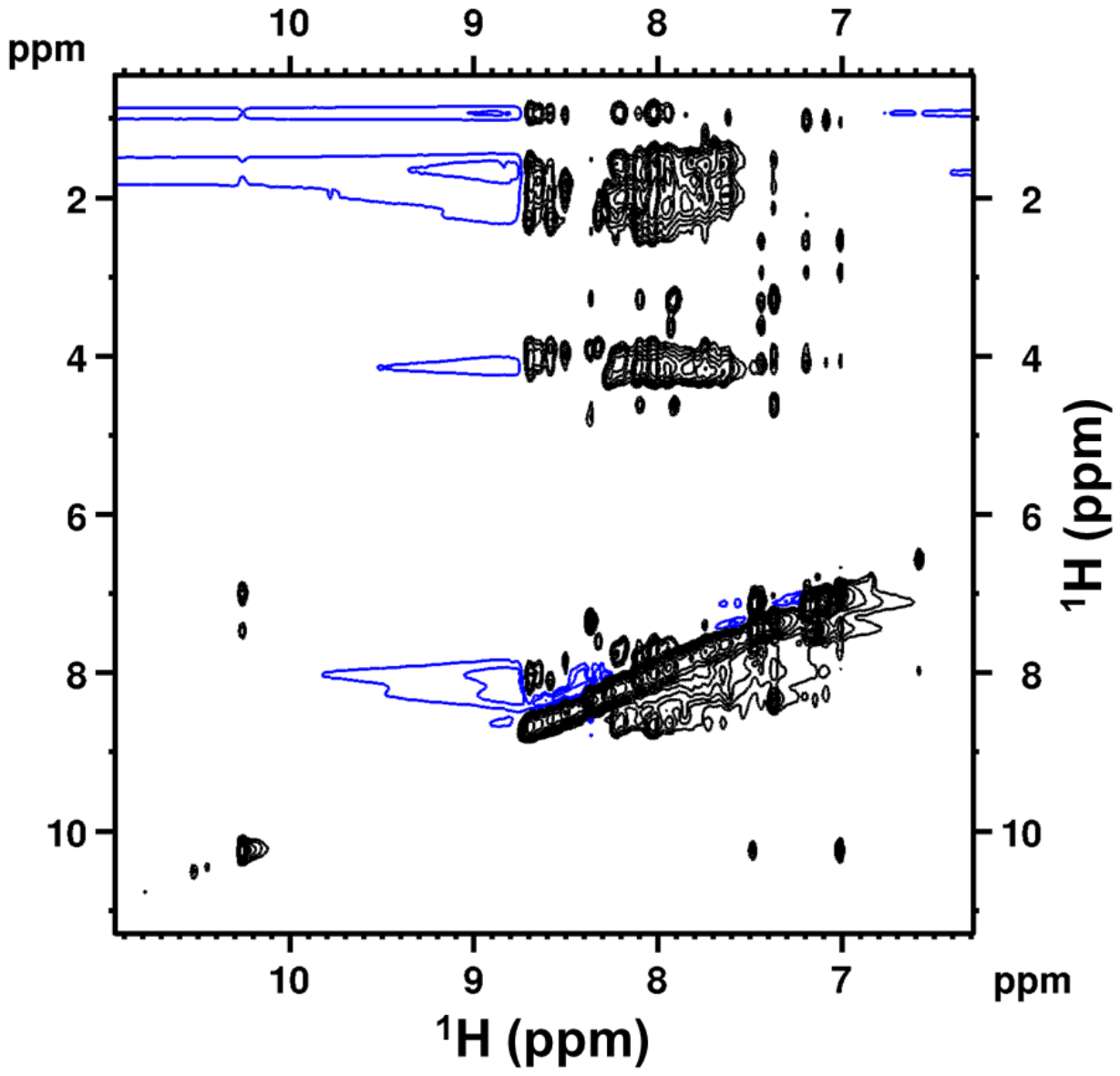


Figure A-58: ^{1}H-^{1}H NOESY of apo-GRW$_{stam27(AEA)}$L33-4'Py at pH 5.87 (Region: Amide/Aliphatic): mixing time=100 ms *(file name: wcp4_123_GRWstamAEAL33_4Py_090823 [Spectrum 6]).*

References:

(1) Kitagawa, S.; Munakata, M.; Miyaji, N. New Mixed-Ligand Copper(I) Complexes with 2,2′-Bipyridine and Their NMR Spectra. *Inorg. Chem.* **1982**, *21* (10), 3842–3843.

(2) Gerz, I.; Jannuzzi, S. A. V.; Hylland, K. T.; Negri, C.; Wragg, D. S.; Øien-Ødegaard, S.; Tilset, M.; Olsbye, U.; DeBeer, S.; Amedjkouh, M. Structural Elucidation, Aggregation, and Dynamic Behaviour of N,N,N,N-Copper(I) Schiff Base Complexes in Solid and in Solution: A Combined NMR, X-Ray Spectroscopic and Crystallographic Investigation. *Eur. J. Inorg. Chem.* **2021**, *2021* (46), 4762–4775.

(3) Harris, R. K.; Becker, E. D.; de Menezes, S. M. C.; Goodfellow, R.; Granger, P. Nuclear Spin Properties and Conventions for Chemical Shifts (IUPAC Recommendations 2001†). *eMagRes* **2007**, *2007* (11), 1795–1818.

(4) Willker, W.; Leibfritz, D.; Kerssebaum, R.; Bermel, W. Gradient Selection in Inverse Heteronuclear Correlation Spectroscopy. *Magn. Reson. Chem.* **1993**, *31* (3), 287–292.

(5) Plegaria, J. S.; Dzul, S. P.; Zuiderweg, E. R. P.; Stemmler, T. L.; Pecoraro, V. L. Apoprotein Structure and Metal Binding Characterization of a de Novo Designed Peptide, A3DIV, That Sequesters Toxic Heavy Metals. *Biochemistry* **2015**, *54* (18), 2858–2873.

(6) Bax, A.; Summers, M. F. 1H and 13C Assignments from Sensitivity-Enhanced Detection of Heteronuclear Multiple-Bond Connectivity by 2D Multiple Quantum NMR. *J. Am. Chem. Soc.* **1986**, *108* (8), 2093–2094.

(7) Lichter, R. L.; Roberts, J. D. 15N Nuclear Magnetic Resonance Spectroscopy. XIII. Pyridine- 15N. *J. Am. Chem. Soc.* **1971**, *93* (20), 5218–5224.

(8) Tadeo, X.; Castaño, D.; Millet, O. Anion Modulation of the 1 H/ 2 H Exchange Rates in Backbone Amide Protons Monitored by NMR Spectroscopy. *Protein Sci.* **2007**, *16* (12), 2733–2740.